europhysics conference abstracts

22nd European Physical Society Conference on

Controlled Fusion and Plasma Physics

Bournemouth, 3rd-7th July 1995

Editors: B E Keen, P E Stott and J Winter

Contributed Papers, Part III

'ublished by: The European Physical Society

'eries Editor: Prof. R Pick, Paris

Managing Editor: G Thomas, Geneva

Volume 19C

Part III

22nd European Physical Society Conference on

Controlled Fusion and Plasma Physics

Bournemouth International Centre, United Kingdom

3-7 July 1995

Editors: B.E. Keen, P.E. Stott and J. Winter

europhysics conference abstracts

22nd European Physical Society Conference on

Controlled Fusion and Plasma Physics

Bournemouth, 3rd-7th July 1995

Editors: B E Keen, P E Stott and J Winter

Contributed Papers, Part III

Published by: The European Physical Society

Series Editor: Prof. R Pick, Paris

Managing Editor: G Thomas, Geneva

Volume 19C

Part III

EUROPHYSICS CONFERENCE ABSTRACTS is published by the European Physical Society, © 1995.

The Proceedings may be purchased from "The Publications Officer, The JET Joint Undertaking, Abingdon, Oxon, OX14 3EA, UK".

Preface

The 22nd European Physical Society Conference on Controlled Fusion and Plasma Physics, under the auspices of the Plasma Physics Division of the European Physical Society, was hosted by and local arrangements were made by the JET Joint Undertaking, Abingdon, UK. Following the guidelines of the Board of the EPS Plasma Physics Division, the 1995 Conference included topics from the areas of: Tokamaks; Stellarators; Alternative Magnetic Confinement Schemes; Magnetic Confinement Theory and Modelling; Plasma Edge Physics; Plasma Heating; Current Drive and Profile Control; Diagnostics; and Basic Collisionless Plasma Physics.

The scientific programme and paper selection was the responsibility of the International Programme Committee appointed by the Board of the EPS Plasma Physics Division. The Programme Committee selected 492 contributed papers (out of 600 submitted abstracts) for presentation as posters in four sessions at the meeting. In order to maintain participants interest throughout all four poster sessions, the sessions were not divided into topic groups, but a mixture of posters from all topic groups was arranged at each session. As a consequence, the Proceedings of the Conference are published in four volumes, which correspond to the four poster sessions (Sessions P, Q, R and S) rather than to the Topic Groups.

In 1994, for the 21st EPS Conference, the Board of the EPS Plasma Division agreed to an important change in the arrangements for contributed papers. The Proceedings were printed after the meeting, allowing a later submission date for abstracts and giving authors the opportunity to present latest results in the four-page papers. This arrangement was continued for the 22nd EPS Conference, in 1995. Consequently, authors of contributed papers handed in their four-page papers to the Scientific Secretary during the conference and these are reproduced in these volumes.

According to EPS Plasma Physics Division regulations, the Conference Proceedings contain the four-page papers of all those contributions for which at least one author was a registered participant at the Conference. There are 462 papers which satisfy this condition. The four volumes of the proceedings will be mailed to all registered participants of the Conference.

The papers of the nine Review Lectures and 18 Topical Lectures will be published in a Special Issue of the journal "Plasma Physics and Controlled Fusion", which will also be mailed to all registered participants.

B E Keen, P E Stott and J Winter

July 1995

Acknowledgements

The Conference Organisers gratefully acknowledge financial support from the following:

The European Commission
Holec Projects bv
Thomson Tubes Electroniques
Brush Wellman Inc
Institute of Physics Publishing
Ansaldo
Spinner GmBH
E Zanon Spa
Linde Cryogenics Ltd
JET Joint Undertaking

Programme Committee

J Winter	(KFA, Jülich, Germany - Chairman)
F Alladio	(ENEA Frascati, Italy)
A Bers	(MIT, Cambridge, USA)
A Bondeson	(Uppsala University, Sweden)
M Chatelier	(CEA, Cadarache, France)
R O Dendy	(UKAEA, Culham Laboratory, UK)
J R Drake	(RIT, Stockhom, Sweden)
V E Golant	(Ioffe Institute, St Petersburg, Russia)
O Gruber	(IPP, Garching, Germany)
N J Lopes-Cardozo	(FOM, Nieuwegein, The Netherlands)
J Sanchez	(CIEMAT, Madrid, Spain)
F Sluijter	(Eindhoven University, The Netherlands - Chairman, Plasma Physics Division EPS
P E Stott	(JET Joint Undertaking, Abingdon, UK)

Local Organising Committee

P E Stott	Chairman
B E Keen	Scientific Secretary
G Blankenback (Mrs)	Conference Secretary
J H C Maple	
K R Musgrave	
C Norris (Mrs)	Finance Officer

Contents

Part III: Poster Session R

Title	Presenting Author	Page No:
• Local Transport Investigations of Different L- and H-mode Discharge Phases in ASDEX-Upgrade	Alexander M	III-001
• Confinement of High β_{pol} Plasmas in JET	Sips G	III-005
• Sawtooth Heat Pulse Propagation: Ballistic Response and Fourier Analysis	Jacchia A	III-009
• Isolation of the Role of Ion Mass from the Influence of Profile and Beam Deposition Changes in Isotope Scaling Studies on TFTR	Synakowski EJ	III-013
• Relevance of Present Day High Field Confinement Results for the IGNITOR Experiment	Bombarda F	III-017
• Transport Analysis of FTU Plasmas with High Power Density ECRH at 140 GHz	Buratti P	III-021
• Experimental Determination of the Dimensionless Parameter Scaling of Energy Transport in Tokamaks	Luce TC	III-025
• The Time Behaviour of the Heat Conductivity during L-H-L Transitions in JT-60U	Neudatchin S	III-029
• Confinement at Tight Aspect Ratio in START	Walsh M	III-033
• Transient Electron Heat Transport Experiments in the W7-AS Stellarator and the RTP Tokamak	Peters M	III-037
• Isotope Effect on Hard X-Ray Intensity Spectra	Rodriguez-Rodrigo L	III-041
• Advances in Understanding of Disruptions and MHD in TFTR	Fredrickson E	III-045
• Disruptions, Vertical Instabilities and Halo Currents in COMPASS-D	Morris AW	III-049
• Measurements of Profile Changes prior to and during Sawtooth Crashes on TEXTOR Tokamak	Fuchs G	III-053
• The Effect of a Sawtooth Crash on Fast Particle Behaviour	Jarvis ON	III-057

Title	Presenting Author	Page No:
• Spatial Localization of Turbulence during the Sawtooth Crash	Hennequin P	III-061
• Measurement of m=1 Magnetic Field Perturbartions during Sawtooth Activity in the TEXTOR Tokamak	Koslowski H	III-065
• Runaway Electrons in the ASDEX Upgrade Tokamak - A Free Electron Maser	Kurzan B	III-069
• Tomography Research for Sawtooth Crash Mechanism and Influence of the Biased Electrode on Sawtooth Behaviour in HL-1	Dong JF	III-073
• Locked MHD-Modes in T-10 Tokamak	Ivanov N	III-077
• Direct Measurement of TAE, EAE and Multiple Kinetic TAE in JET	Fasoli A	III-081
• Radiation in JET's Mark I Divertor	Reichle R	III-085
• Improved Plasma Purity in the JET Pumped Divertor	Stamp MF	III-089
• Modification of the ASDEX-Upgrade Divertor	Bosch HS	III-093
• Effects of Field Reversal in ASDEX-Upgrade	Laux M	III-097
• Power Losses during Divertor Biasing and Detachment Experiments: Biasing Effects on Impurity Levels and Transport in TdeV	Stansfield BL	III-101
• Radiation Distributions in Detached Divertor Operation on DIII-D	Leonard AW	III-105
• Atomic Physics and Plasma-Wall Interaction Effects on Particle Screening and Radiative Behaviour of Ergodic Divertor Edge Plasmas in TORE SUPRA	de Michelis C	III-109
• Edge Localised Modes in TCV Tokamak	Weisen H	III-113
• Studies of X-Point Plasmas in the START Tokamak	Sykes A	III-117
• Impurity Ion Emission and Edge Transport during ELMy H-modes in the New JET Divertor Configuration	O'Mullane MG	III-121
• Comparison of Transition to ELM-Free H-mode Regime on COMPASS-D and ASDEX Upgrade	Valovic M	III-125
• W7-AS with Modified Mirror Ratio at High-1 Values	Rau F	III-129
• Drift Reversal in the W7-X Advanced Stellarator	Cooper WA	III-133
• Simulation and Analysis of Neutral Particle Spectra for W7-AS	Wolle BKR	III-137
• Correlation Between Helium Particle Transport and Electron Density Profiles in W7-AS	Hirsch M	III-141

Title	Presenting Author	Page No:
• Transport Studies of Injected Impurities in the Stellarator Wendelstein 7-AS	Burhenn R	III-145
• Island Divertor Studies for the Stellarator Wendelstein 7-X	Kisslinger J	III-149
• Results from Thomson Scattering and Electrostatic Probe Measurements in the Extrap T1 Reversed-Field Pinch	Moller A	III-153
• First Results from Extrap T2 Reversed-Field Pinch	Brunsell P	III-157
• Effects of the Impurities on the Loop Voltage in RFX	Carraro L	III-161
• Influence of Parallel Viscosity on Tearing Mode Stability Boundaries	Xie H	III-165
• Sawtooth Model for ITER	Porcelli F	III-169
• Scaling Laws for the Amplitude, Period, and Crash Time of Sawtooth Oscillations	Thyagaraja A	III-173
• Kinetic and Hydrodynamic Descriptions of Wave Scattering and Transformation in Plasmas	Sitenko A	III-177
• Hot Plasma Effects on the Collective Scattering of Electromagnetic Fluctuations	Heikkinen JA	III-181
• A Symmetric Electron-Cyclotron Emission from Non-Thermal Plasmas Subject to a Generalized Kirchhoff's Law	Bornatici M	III-185
• Trapped Particle Precessional Drifts in Arbitrary Aspect Ratio Tokamaks with Shaping Consequences for Stability	Roach CM	III-189
• The Effect of Shearless Stellarator Rotational Transform on the Tokamak Plasma Stability	Subbotin A	III-193
• Derivation of Bohm's Coefficient of the Magnetic Field Diffusion in Frame of 2-D EMHD Model	Zabajdullin OZ	III197
• Refined Numerical Modelling of Fusion Product Measurements	Beikert G	III-201
• The Hall Effect in Plasmas: Enhanced Propagation Rate of Magnetic Field Propagation and Short-scale Plasma-Field Mixing in Plasma Focus Experiments	Kukushkin A	III-205
• Plasma Edge Turbulence Numerical Study with a Vlasov Eulerian Code	Fijalkow E	III-209
• Non-Linear Heat Pinch in a Tokamak	Haines M	III-213
• Neoclassical Theory of Poloidal Rotation Damping	Morris R	III-217
• Scale-Invariant Plasma Motions near X-Points	Schep TJ	III-221

Title	Presenting Author	Page No:
• Investigation of Low Radiation Collapses in Stellarator Plasmas	Ochando MA	III-225
• Dimensional Analysis of L-H Power Threshold Scalings	Kerner W	III-229
• Long Term Applications of High β Spherical Tokamaks	Hender TC	III-233
• Effect of Edge Localized Modes (ELMs) on Edge Electron Density and Temperature Profiles and Impurity Transport in ASDEX Upgrade	Suttrop W	III-237
• Variation of Power Density Decay Lengths in the SOL of ASDEX Upgrade Measured by Thermography and Langmuir Probes	Herrmann A	III-241
• Scrape-off Layer Power and Pressure Balance in ASDEX-Upgrade	Pitcher CS	III-245
• ELM-Resolved and Ion Temperatures from Neutral Fluxes	Stober J	III-249
• Density Profiles in the ASDEX Upgrade Scrape-Off Layer	Schweinzer J	III-253
• The Behaviour of Divertor and Scrape-Off Layer Parameters in JET	Davies S	III-257
• Edge Pressure Gradients and Velocity Shear Behaviour during H-modes and ELMs in the New JET Divertor Configuration	Hawkes N	III-261
• The SOL in Diverted Discharges in the Texas Experimental Tokamak (TEXT)	Rowan W	III-265
• Influence of L- and H-mode and Rotational Transform on the Edge Density Profiles in W7-AS	Zoletnik S	III-269
• ELM Related MHD Activity on the Compass-D Tokamak compared with ASDEX-Upgrade	Buttery RJ	III-273
• Edge Modes as ELM Events	Pogutse O	III-277
• The Effects of ELMs on the Plasma Edge of JET	Lingertat J	III-281
• Instabilites of Debye Layers in Experiments on Imitation of SOL Plasma-Surface Interactions	Kurnaev V	III-285
• Effect of the Toroidal Field Reversal on Divertor Asymmetries	Chankin A	III-289
• Divertor Plasma Detachment in JET	Monk RD	III-293
• The Location of the Separatrix in the JET Divertor and SOL	Erents K	III-297

Title	Presenting Author	Page No:
• Investigation of Opacity in the Tokamak Divertor Region	Lovegrove T	III-301
• The Influence of Divertor Geometry on JET Discharges	Loarte A	III-305
• Power Deposition Studies in the JET Mark I Pumped Divertor	Clement S	III-309
• Divertor Similarity and Multi-machine Scaling Experiments	Vlases G	III-313
• Power and Particle Flux to the Neutraliser Plates of the TORE SUPRA Ergodic Divertor	Grosman A	III-317
• Analysis of Particle Flow in the DIII-D SOL and Divertor	Porter G	III-321
• An Investigation of the Extent of Divertor Detachment in ALCATOR C-Mod	Lipschultz B	III-325
• Electron Energy Distribution Function in Edge Plasma of TF-2 Tokamak	Bogomolow L	III-329
• Low Frequency Plasma Heating and Current Drive Regimes for Ignitor	Moroz PE	III-333
• Toroidal Velocity and Ripple Losses in TORE SUPRA with LH, ICRF, and Combined Additional Heating	Platz P	III-337
• ICRF Preionization and Plasma Production in TEXTOR	Koch R	III-341
• Auxiliary Heating Experiments with a Tungsten Test Limiter in TEXTOR 94	Van Oost G	III-345
• The Nonlocal Drift-Kinetic Quasilinear Theory of Radiofrequency Heating in Magnetic Traps	Kasilov S	III-349
• Fokker-Planck Solver with Spatial DIffusion of the Driven Currents	Shkarofsky IP	III-353
• Simulations of Filling the Spectral Gap with Lower Hybrid Waves	Pattikangas T	III-357
• Modelling of LH Current Drive and Profile Control Experiments on JET	Fischer B	III-361
• ICRF Heating and Current Drive Experiments in TFTR	Majeski R	III-365
• First Results from LHCD in COMPASS-D	Warrick CD	III-369
• Advanced Current Density Profiles for Non-Inductive TORE SUPRA Operation	Kazarian-Vibert F	III-373
• ITER Plasma Diagnostics	De Kock L	III-377
• Multiple Neutron Spectrometer Diagnostic for ITER	Källne J	III-381

Title	Presenting Author	Page No:
• Diamond Detector Application for ITER SXR-imaging	Krasilnikov A	III-385
• Impurity Induced Neutralization of Alpha-particles and Application to ITER Diagnostics	Korotkov A	III-389
• Advances in Neural Network Applications for COMPASS-D and ITER	Windsor CG	III-393
• TPX Diagnostics for Tokamak Operation, Plasma Control and Machine Protection	Edmonds P	III-397
• Tomographic Reconstruction of the Radiation Distribution during Neon Puff Experiments in ASDEX Upgrade and JET	Fuchs JC	III-401
• Spatial Distribution of Electron Density Fluctuations Measured using CO_2 Laser Phase Contrast Method on Heliotron-E	Kado S	III-405
• Spectroscopic Determination of Ion Temperatures in the Divertor of ASDEX Upgrade	Lieder G	III-409
• Multichannel YAG Thomson Scattering on CHS	Yamada I	III-413
• In Situ Measurement of Neutral Beam Divergence using Spectral Asymmetry in Motional Stark Effect in a Tokamak	Xu J	III-417
• First Results with the Rotating Polarization Polarimeter at RTP	Rommers JH	III-421
• Diagnosis of Nonthermal ECE by means of Combined LFS ECE, HFS ECE and ECA Measurements	van Gelder JFM	III-425
• Modulational Instability of Electromagnetic Waves in Collisional Dusty Plasmas	Shukla P	III-429
• Modulational Instability of Packets of Lower-Hybrid Waves	Popel SI	III-433
• Combined Diagnostic Methods of Non-LTE Dense Pulsed Plasma	Zhovtyansky V	III-437
• Non-Linear Effect in Coupling of Electrostatic Waves	Riccardi C	III-441
• The Condition of the Existence Electrostatic Waves in an Electron Beam-Plasma System	Nejoh Y	III-445
• Computational Studies of Generation and Control of Ion Source Plasmas	Ido S	III-449
• The Operational Characteristics of a Molten and Damaged Beryllium Divertor Target in JET	Tubbing B	III-453
• Resistivity Profile Effects in Numerical Magnetohydrodynamic Simulations of the Reversed Field Pinch	Sátherblom HE	III-457

Local Transport Investigations of different L- and H- Mode Discharge Phases in ASDEX- Upgrade

M. Alexander, L. Giannone, O. Gruber, S. de Pena Hempel, J. Köllermeyer, G. Pereverzev, J. Schweinzer, ASDEX- Upgrade and NI teams

Max- Planck- Institut für Plasmaphysik, D- 85748 Garching, Federal Republic of Germany

Introduction

The transport physics of both the electrons and ions in tokamaks are not well understood up to now. For the test of existing and the development of new theories it is necessary to have well analysed discharges in the different operating regimes of a tokamak. In this work ASDEX-Upgrade discharges in the Ohmic- mode, L- mode, H- mode with type I ELMs and the recently discovered CDH- mode [1] are analysed.
For the local analysis with the ASTRA code [2] the profiles of the electron temperature T_e, ion temperature T_i, electron density n_e, radiation p_{rad}, effective charge Z_{eff} and the results of magnetic measurements have been used. ASTRA is a fully time dependent transport code for both analysis and simulation with a non circular 2D equilibrium code included. Here we concentrate on the analysis of the energy transport.
For the analysis of sawtooth propagation an existing code using the maximum entropy principle and working in cylindrical geometry has been extended [3, 4].

Results and Discussion

Consistency checks

For meaningful analysis all results of the diagnostics as Thomson scattering and ECE for T_e, passive CX from the centre and boundary (LENA) and CXRS for T_i, interferometry and Li beam diagnostic for n_e, and bolometry for radiation have been checked carefully against each other. We first checked the agreement of the kinetic energy W_{kin} against the equilibrium (W_{equ}) and diamagnetic (W_{dia}) energies including the energy contribution of the fast ions. In all investigated neutral beam discharges the contribution to the plasma energy by the fast ions never exceeds 20% of the kinetic energy. This is due to the relatively high densities in ASDEX Upgrade discharges secondly. During the whole analysis the current diffusion equation was solved. The resulting loop voltage was compared with the measured one to get a check on T_e and Z_{eff} from Bremsstrahlung. The bootstrap current never exceeded 20% of the total current. The beam driven current is negligible (<2%) due to the nearly perpendicular injection. All presented analyses were taken in stationary phases of Deuterium discharges.

Ohmic discharges

In all analysed discharges the ion thermal diffusivity χ_i exceeded the electron thermal diffusivity χ_e. For instance the analysis of the Ohmic discharge #4783 shows χ_i to be nearly 2 to 4 times higher than χ_e (Fig. 1) and approximately 5 times higher compared with χ_{CH} [4]. This is confirmed by ion temperature transport simulations with fixed T_e and n_e (Fig. 2). The accuracy of the central ion temperature has been further checked by the comparison of a simulated neutron rate with the measured one.

High power L- mode discharge

For the L- mode discharge #6056 the analysis of the power balance diffusivities gives χ_i values approximately twice as high as χ_e. χ_e is at the highest T_e gradient about 1 m^2/s

(Fig. 3). The investigations of the sawtooth propagation gives values for χ^{hp}/χ_e in the range from 8 to 15 (Fig. 3). This is a similar value as given from TFTR [6], but large compared with other experiments, reporting a range of 1 to 4 [7]. These heat pulse investigation will be engrossed by using modulated ECRH.

H- mode with type I ELMs

In ELMing H- mode discharges the effect of the power losses by ELMs are time averaged and included into the heat transport coefficients. The type I ELM H- mode discharge # 6196 shows no reduction in the heat transport compared with the L- mode discharge (Fig. 4). This is only partly described by the lower plasma current and higher heating power of the H- mode discharge, but reflects our finding [8] that the L- mode confinement with heating powers corrected for radiation close to the L-H transition power threshold is much better than described by the former L- mode scalings and approaches the H- mode values. The higher χ_e's outside $\rho_{tor} = 0.6$, ρ_{tor} being the normalised toroidal flux coordinate, may be caused by the lower radiation power P_{rad} normalised to the heating power P_h inside the separatrix of this discharge. To assess the enhanced ion diffusivity, transport simulations of T_i in the same way as described in the Ohmic case above are shown in Fig. 5. Only an enhancement of χ_{CH} by a factor of 4 can satisfactorily reproduce the ion temperature on a wide range of ρ_{tor}. Such an enhancement in χ_i may be due to η_i driven modes, because $\eta_i > 1.5$ at all radial positions. This is true for all the different discharges presented in this paper.

In the discharge #5024 the total radiation was increased with additional Ne puffing above 50% of the heating power, without loosing type I ELMs (#5024). The energy confinement time of 75ms is only slightly higher than in # 6196 and close to the DIII-D/ JET /ASDEX- Upgrade and the elmy ITER H92P scaling [8]. But the ion heat diffusivity is apparently reduced. To assess the error bars a special statistical analysis was made therefore. 50 statistically varied T_e, T_i and p_{rad} profiles have been calculated assuming an error of about 10% in the temperatures and radiation. With these input profiles 50 analyses were done and the standard deviations of χ_i and χ_e could be determined, represented by the error bars of Fig. 6. In the near future it is planned to extend and improve this method.

CDH- mode

Enhancing the impurity radiation loss and the neutral gas pressure in the divertor further, the CDH- mode [1] is obtained. For the analysis of the CDH- mode discharge # 6136 it is assumed that T_i is equal to T_e, as no ion temperature measurements are available. At the high density of $> 10^{20} m^{-3}$ this assumption is allowed. Thus we calculated in addition to χ_e and χ_i (Fig. 7a) a $\chi_{eff} = 0.5\ (\chi_e + n_i/n_e \cdot \chi_i)$ (Fig. 7b). After switching off the impurity puffing a type I ELM H-mode appears again, so that within one shot both H- mode types can be compared. The difference in χ_{eff} is nearly negligible, which also holds comparing it with the type I ELM discharge # 5024 (see above). This is in agreement with the nearly unchanged global energy replacement time [8], and with simulations of similar discharges using the BALDUR code [9]. Comparing the individual transport coefficients shows an enhancement of χ_e for the type I ELM phase between ρ_{tor}=0.6 and 0.9 which may be caused both by the shifting of the power deposition profile towards the edge (due to the about 10% higher electron density and the reduced radiation power) and the reduced density peaking compared with the CDH- phase.

Summary

The ion thermal diffusivity exceeds the electron thermal diffusivity in all analysed discharges and is well above the neoclassical value. The heat pulse transport coefficient for electrons is strongly enhanced compared with the power balance results pointing towards a strongly nonlinear dependence of the transport on temperature and its gradient.
The confinement of L- mode discharges close to the L-H transition approximates the H-mode confinement, both locally and globally.
The thermal transport of CDH- and type I ELM H- mode phases are about equal both comparing them in a single discharge or in different discharges. However, changes in the particle transport are obvious from the density peaking observed in the CDH- mode. This may be connected with the enhanced edge radiation profile and the corresponding peaking of the radiation corrected heat deposition, as is indicated already in other enhanced confinement regimes.

References

[1] O. Gruber, et al., Phys. Rev. Letters 74 (1995) 4217
J. Neuhauser, et al., this conference
[2] G. V. Pereverzev et al., IPP 5/42 (1991)
[3] K. S. Riedel, et al., Nucl. Fusion 28 (1988) 1509
[4] L. Giannone, et al., Proc. 17th Europ. Conf. on Contr. Fus. and Plasma Heating, Amsterdam (1990) 191, and L. Giannone, et. al., this conference
[5] C. S. Chang and F. L. Hinton, Phys. Fluids 29 (1986), 3314
[6] E. D. Fredricksen, et al., Nucl. Fusion 26 (1986) 849
[7] N. J. Lopes Cardozo and J. C. M. De Haas, Nucl. Fusion 30 (1990) 521
[8] F. Ryter, et al., this conference
[9] G. Becker, et al., this conference

Figures

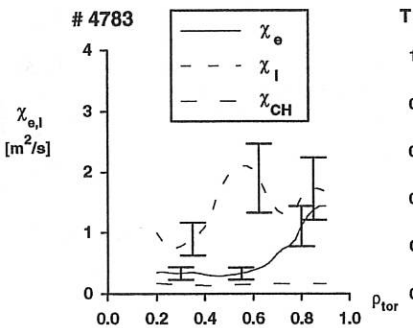

Fig. 1: Thermal diffusivities of electrons χ_e and ions χ_i and neoclassical diffusivity of Chang and Hinton χ_{CH} for Ohmic discharge #4783. I_p = 600kA, B_t = -2T, $\langle n_e \rangle = 3.2 \cdot 10^{19} m^{-3}$, P_{OH} = 580kW.

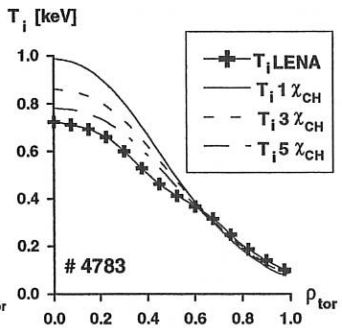

Fig. 2: Simulated Ti profiles with χ_i = 1-5 χ_{CH}. T_e, n_e fixed.

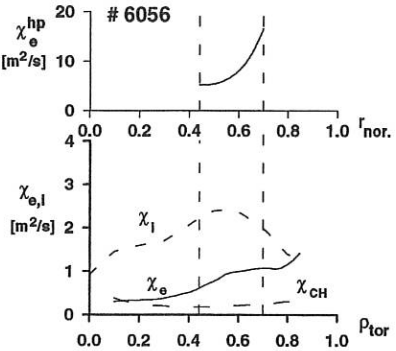

Fig. 3: Comparison of χ_e, χ_i and χ_{CH} for L- mode discharge #6056 with χ_e^{hp} for sawtooth propagation and the power balance analysis. I_p = 1MA, B_t = 2.5T, $<n_e>$ = 5.2 • $10^{19}m^{-3}$, P_{NI} = 2.8MW.

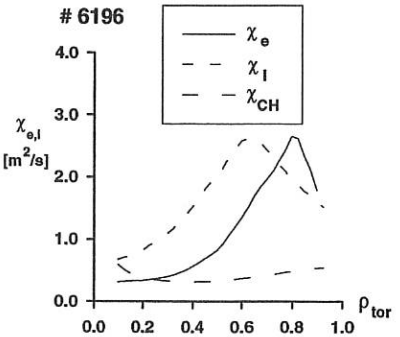

Fig. 4: χ_e, χ_i for a H- mode discharge with Type I ELMs (#6196) and χ_{CH}. I_p = 800kA, B_t = -2.5T, $<n_e>$ = 5.5 • $10^{19}m^{-3}$, P_{NI} = 5.2MW

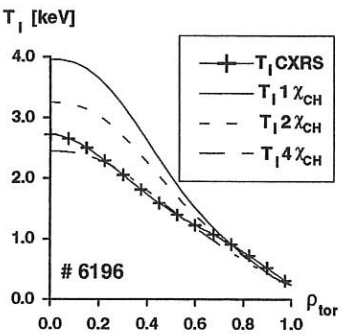

Fig. 5: Simulated T_i profiles with $\chi_i = 1-4 \cdot \chi_{CH}$. (#6196) T_e, n_e fixed.

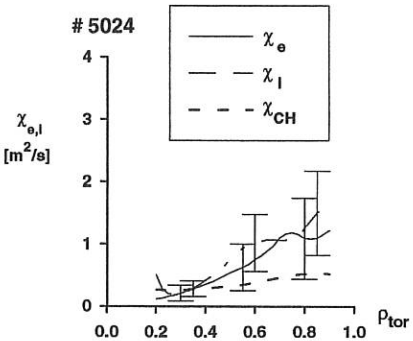

Fig. 6: χ_e, χ_i and χ_{CH} for a H- mode discharge with type I ELMs and Ne puffing . I_p = 1MA, B_t = -2.5T, $<n_e>$ = 1 • $10^{20}m^{-3}$, P_{NI} = 7.9MW

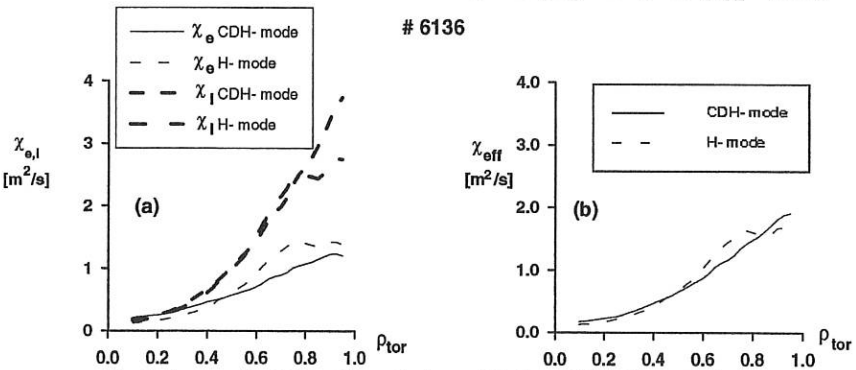

Fig. 7: a) χ_e, χ_i for CDH and H- mode phases of discharge #6136 . b) χ_{eff} for both phases. I_p = 1MA, B_t = -2.5T, $<n_e>$ = 12 • $10^{19}m^{-3}$, P_{NI} = 7.7MW

CONFINEMENT OF HIGH β_{POL} PLASMAS IN JET

A.C.C. Sips, C.D. Challis, C. Gormezano, C.W. Gowers, G.T.A. Huysmans,
S. Ishida*, F.G. Rimini, B.J.D. Tubbing and D.J. Ward.
JET Joint Undertaking, Abingdon, Oxon, OX14 3EA, United Kingdom.
* JAERI, Naka Fusion Research Establishment, Ibaraki-ken, 311-01 Japan.

INTRODUCTION

Experiments aimed at examining the confinement characteristics of plasmas with high values of poloidal beta (β_{pol}) have been performed over a wide range of plasma parameters in JET. In previous JET campaigns high β_{pol} plasmas were achieved in conditions of very high confinement ($\tau_E/\tau_{ITER89L\text{-}P} \approx 3.7$) [1,2]. In these ELM free H-mode plasmas the high confinement phase collapsed after an uncontrolled rise of the plasma density. In the JET pumped divertor campaign the aim of the experiments was to achieve high β_{pol} in quasi steady state conditions to study the confinement. The results of these studies are presented.

EXPERIMENTAL BACKGROUND

ELMy H-mode plasmas form the basis of these experiments in which the stored energy and density typically achieve quasi stationary conditions early in the heating phase (Fig. 1).

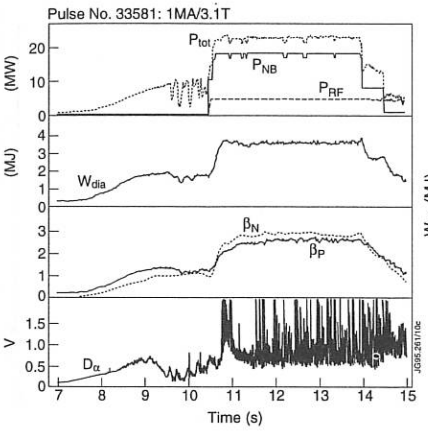

Figure 1: A high beta poloidal discharge

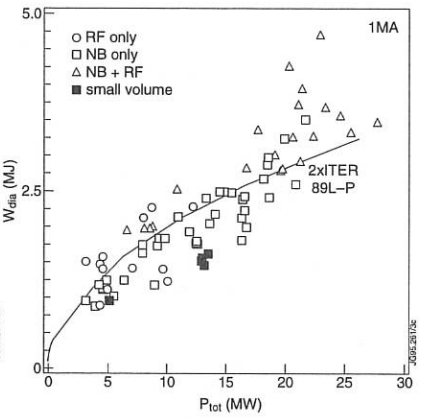

Figure 2: Stored energy vs. input power.

High combined heating powers are used (maximum: 28 MW, for several seconds) mainly at 1 MA with a variation of the toroidal field from 1.0 to 3.4 Tesla. Carbon tiles were installed in the JET divertor and the divertor cryo-pump was used extensively.

CONFINEMENT

In previous JET campaigns, ELM free H-mode were obtained at 1 MA/3.1 Tesla with only 7 MW of ICRH power in double null X-point discharges. High β_{pol} was achieved by virtue of the very high confinement ($\tau_E/\tau_{ITER89L\text{-}P} \approx 3.7$) achieved in these conditions. However, the high confinement regime was only transient.

In the JET pumped divertor campaign the aim of the experiments was to achieve high β_{pol} in quasi steady state conditions to study the confinement. Compared with previous campaigns the pumped divertor geometry offers better power handling and the divertor cryo-pump can be used to control the density. However, the experiments are at reduced volume and are single null X-point plasmas.

It was found that H-modes in the JET pumped divertor configuration are naturally ELMy, allowing quasi steady state operation at high poloidal beta. In these conditions the stored energy (W_{dia}) reaches typically twice the prediction of the ITER89L-P scaling expression up to the maximum additional heating power of 28 MW (Fig. 2). The confinement is independent of the additional heating method. In the high combined heated discharges a beta limit has not yet been reached [4].

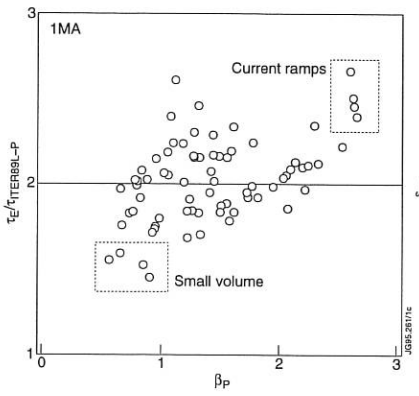

Figure 3: H-factor (ITER89L-P) vs. beta poloidal

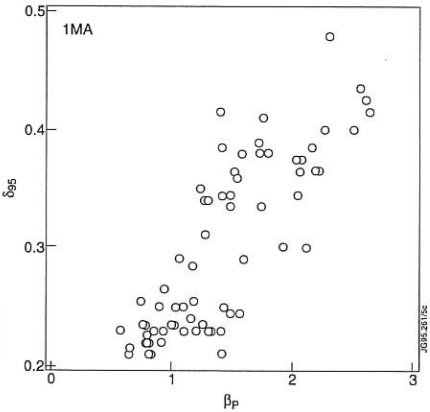

Figure 4: Triangularity (δ_{95}) vs. beta poloidal.

From these results it can be concluded that there is no apparent increase in confinement over H-mode scaling with β_{pol} (Fig. 3). High β_{pol} plasmas become naturally triangular (δ_{95}), despite this increased triangularity the confinement in these ELMy H-modes does not improve (Fig. 4).

SMALL VOLUME PLASMAS

The data presented in the previous section also contain a variation of the aspect ratio. Dedicated experiments have been performed in 'small volume' plasmas in JET in which the volume has been reduced from 85 m^3 to 55 m^3. The confinement in these small volume plasma is not much different from the large volume plasmas. However, at 1 MA the confinement of the small volume plasmas is slightly below the H-mode scaling (Fig 3). When included in the data a possible increase in the H-factor (ITER89L-P) with plasma volume in JET is found. But, a comparison of discharges on the same day at 1.5MA shows no difference between large and small volume plasmas [3]. The reduction in the H-factor compared to the rest of the 1 MA data may then be due to the fact that the divertor cryo-pump was not used and the discharges were heavily gas fuelled to prevent neutral beam shinethrough, both of which might lead to a higher ELM frequency.

TRANSIENT ELEVATED CONFINEMENT

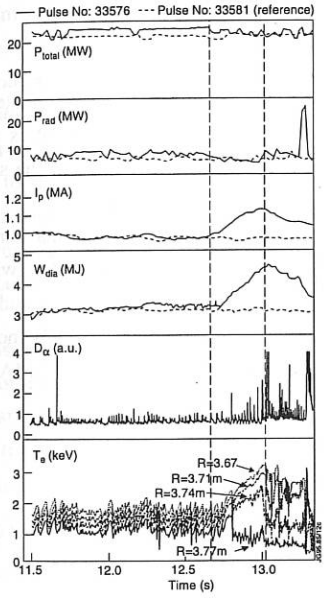

Figure 5: High beta poloidal with current ramp.

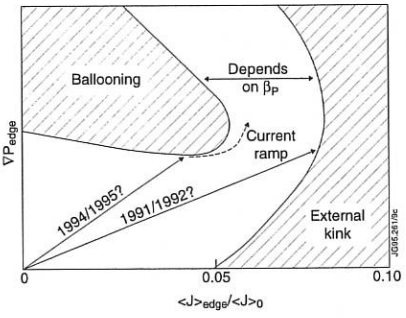

Figure 6: Stability diagram [5].

In some high β_{pol} discharges it is observed that the stored energy can suddenly increase at constant input power, correlated with oscillations in the plasma current at high β_{pol}. This was exploited by pre-programmed ramps of the plasma current (ramp up). The edge temperature increases just after the current ramp but the ELMs do not cease, i.e. not a transition to ELM-free H-mode (Fig. 5).

A speculative explanation is offered as follows: In the JET pumped divertor configuration the edge pressure is limited by the first stability ballooning limit. Access to 2nd stable regime exists in the plasma periphery at high β_{pol} and will allow an improved confinement regime during the heating. However, the ratio of $j_{edge}/\nabla P_{edge}$ is not large enough, due to reduced edge collisionality, despite the divertor cryo-pump which helps to keep the edge density low. The plasma needs a modest increase in j_{edge}. With a current ramp in the high β_{pol} phase, the link between ∇P_{edge} and j_{edge} will be broken and the edge current density is increased (Fig. 6).

The current ramps may be used to extend the high β_{pol} regime to give improved confinement at higher currents by starting at 1 MA level and high β_{pol} and using the current ramp to 'kick' the plasma into the VH mode regime. After the current ramp, the improved confinement of the VH mode regime may be stable due to a larger bootstrap current at the edge generated by increased pressure gradients. However, such a plasma may destabilise external kinks modes due to the high edge current density.

CONCLUSIONS

There is no apparent increase in confinement over H-mode scaling at high β_{pol} in quasi steady state ELMy H-mode conditions (β_{pol} up to 2.7). In this regime the confinement is also insensitive to the heating method, toroidal field and plasma shape, although at 1 MA the small volume plasmas exhibit confinement parameters at the lower end of the spectrum.

Transient improved levels of confinement can be induced with plasma current ramps (up!) with the plasma already at high beta poloidal. A possible explanation is that, with a current ramp during the high β_{pol} phase, the link between ∇P_{edge} and j_{edge} is broken and the current density is increased in conditions where access to second stability exists (VH mode). Current ramps could be used to achieve high β_{pol} and high fusion performance at $I_p \geq 2$ MA.

REFERENCES

[1] C.D. Challis, et al., Nucl Fusion **33** (1993) 1097.

[2] P.N. Yushmanov, et al. ,Nucl Fusion **30** (1990) 1999.

[3] S. Ishida, et al., APS Conference, Minneapolis (1994).

[4] C.D. Challis, et al., this conference.

[5] G.T.A Huysmans, et al., this conference.

Sawtooth Heat Pulse Propagation: Ballistic Response and Fourier Analysis

A.Jacchia, F.De Luca[1], G.Gorini[1], P.Mantica, N.Deliyanakis[2], M.Erba[2], L.Porte[2]
Istituto di Fisica del Plasma, Associazione EURATOM-ENEA-CNR, 20133 Milano, Italy
[1]Dipartimento di Fisica, Università degli Studi di Milano, 20133 Milano, Italy
[2]JET Joint Undertaking, Abingdon, OX143EA, United Kingdom

Sawtooth (ST) heat pulse propagation has been widely used to determine the "perturbative" electron heat diffusivity, χ_e^P, from heat pulse data [1]. The ratio of χ_e^P with the electron heat diffusivity from steady-state power balance analysis, χ_e^{PB}, is usually observed to lie in the range $1<\chi_e^P/\chi_e^{PB}<5$, and can be explained by a non-linear (or offset-linear) dependence of the heat flux on the temperature gradient.

The temperature perturbation following a ST crash is the result of an MHD instability. This instability is generally observed to be very fast (timescale $\tau_{ST}\approx 100\ \mu s$) and localised within the so-called mixing radius (r_{mix}). The observation of the so-called ballistic heat pulse propagation in TFTR [2], however, has revealed a more complex picture of the ST event, with two phases: the crash phase, occurring on a fast time scale τ_{ST} and confined within r_{mix}; and the ballistic phase, occurring on a slower time scale τ_b and characterised by enhanced transport over a significant portion of the plasma volume extending outside r_{mix}.

Unfortunately, the need for very fast measurements of the electron temperature has so far limited the investigation of the two phases of the ST crash. It is therefore of interest to see if any method exists for detecting anomalies in the ST heat pulse propagation when measured with diagnostics with moderate (1-10 kHz) time resolution.

In order to look for non-diffusive features of ST heat pulses in JET, Fourier analysis was applied to JET data in [3]. The Fourier method is very sensitive to non-diffusive features in the heat pulses. It is also more sensitive to noise in the data. The newly available heterodyne ECE electron temperature diagnostic in JET provides an opportunity for a more detailed analysis of heat pulse propagation in JET.

Simulation of a ballistic heat pulse

The assumption that χ_e be a function of local macroscopic plasma parameters is not valid in the case of a ballistic heat pulse. The enhancement of χ_e following the ST crash can be modelled heuristically by assuming that χ_e is enhanced by a coefficient which is an explicit function of time (t) and radius (r): $\chi_e=\gamma(t,r)\chi_{e0}$. In this expression, χ_{e0} is the power balance diffusivity without any enhancement. The equation for the perturbed electron temperature, $\tilde{T}_e$, is [4]

$$\frac{3}{2}n_{e0}\dot{\tilde{T}}_e-\nabla\cdot\left[n_{e0}\gamma(r,t)\chi_e^P\nabla\tilde{T}_e\right]=\nabla\cdot\{[\gamma(r,t)-1]n_{e0}\chi_{e0}\nabla T_{e0}\} \qquad (1)$$

The usual diffusion equation for $\tilde{T}_e$ is recovered by taking $\gamma=1$. Apart from the enhancement of χ_e^P on the left hand side, one can see that the ballistic effect contributes an additional (time dependent) source term to the right hand side.

Examples of simulated ballistic heat pulses can be obtained by solving Eq.1 numerically after having specified the functional expressions of $\gamma(r,t)$, $\chi_e^p(r)$, $\chi_{e0}(r)$, $n_{e0}(r)$ and $T_{e0}(r)$, as well as the initial and boundary conditions for $\tilde{T}_e$. The simulation analysed here was obtained with the following specifications. For the equilibrium quantities,

$$n_{e0}(r) = n_0\left[1-\left(\frac{r}{a}\right)^2\right]+n_a,\quad T_{e0}(r) = T_0\left[1-\left(\frac{r}{a}\right)^2\right]^4,\quad \chi_{e0} = \chi_0+(\chi_1-\chi_0)\left(\frac{r}{a}\right)^2,$$

where the numerical values $n_0=3.46\cdot10^{19}$ m^{-3}, $n_a=0.12\cdot10^{19}$ m^{-3}, $T_0=7$ keV, $\chi_0=0.5$ m^2/s, $\chi_1=2$ m^2/s have been used. The plasma minor radius was a=1 m. For the perturbation quantities, $\chi_e^p=\chi_{e0}$, $\gamma(r,t) = [1+\delta\exp(-t/\tau_b - k\,r^2)]$, with $\delta=35$, $\tau_b=1$ ms and $k = 16$ m^{-2}. The ST crash was assumed to occur at t=0. The simulation was performed starting from a standard prescription for the initial temperature perturbation profile with $r_{mix}=0.29$ m. As a boundary condition, $\tilde{T}_e$ was assumed to vanish at r=a.

Fourier analysis of a ballistic heat pulse

Fourier analysis of the simulated heat pulse is performed using the procedure of Ref.[3] to which we refer for details. The quantities of interest are the gradient of the phase (φ') and the logarithmic gradient of the amplitude (A'/A) of the Fourier transform $T_\omega=Ae^{i\varphi}$ of $\tilde{T}_e$. For a purely diffusive heat pulse, $\varphi'=(A'/A)_g$, where $(A'/A)_g=A'/A+1/2r-1/2r_n$ and $r_n=-n_{e0}/n_{e0}'$. The value of χ_e^p is determined from $\chi_e^p=\chi_g^p \equiv \frac{3}{4}\omega/\left[\varphi'(A'/A)_g\right]$. The Fourier analysis represents an unambiguous method to establish the diffusive nature of a heat pulse. Non-diffusive features will show up in the analysis in the form of a difference between φ' and $(A'/A)_g$. Only if $\varphi'=(A'/A)_g$ we expect χ_g^p to provide the correct numerical value for χ_e^p.

The results of the Fourier analysis of the ballistic simulation are shown in Fig.1. At r=0.5m, the pulse is still strongly influenced by the ballistic effect: φ' is nearly independent of frequency and is significantly lower than $(A'/A)_g$. χ_g^p exceeds χ_e^p by a factor 2-3. At r=0.6 m, φ' and $(A'/A)_g$ are still significantly different although the error on χ_e^p is only 10-30% in this case. In order to observe a purely diffusive behaviour of the pulse, one has to go as far as r=0.7 m. There the agreement between φ' and $(A'/A)_g$ is very good. Clearly, the ballistic effect is quite strong in this simulation: despite the mixing radius is $r_{mix}=0.29$ m, one has to go to $r>2r_{mix}$ before the heat pulse is purely diffusive. Other combinations of parameters will result in more or less favourable conditions for diffusive propagation. The point made here is that if a diffusive region exists, it can be recognised by Fourier analysis. Of course the possibility for the Fourier analysis to recognise a diffusive pulse is limited by the s/n ratio of the measurement. In cases where Fourier analysis is not possible, other approaches must be used in order to recognise the diffusive region of the pulse. A possible approach is to study the initial perturbation of the pulse.

In Fig.2, the temperature perturbation profile for the ballistic simulation is shown at t=0.5 ms and t=1 ms (at t=0, the perturbation vanishes outside r_{mix}). One can see that within 1 ms of the ST crash, the perturbation has extended over a region well beyond r_{mix} as a result of the ballistic enhancement of the diffusivity. The perturbation is negligibly small for r>0.6-0.7 m, both

at t=0.5 ms and t=1 ms. Now r≈0.6-0.7 m is just where the heat pulse starts to be diffusive according to Fourier analysis. This simple observation justifies the approach used, for instance, in previous analyses of JET ST heat pulses [5]. There r_{mix} was defined heuristically as the radius beyond which the initial perturbation vanished, and standard heat pulse analysis was carried out for $r>r_{mix}$.

Fourier analysis of a JET heat pulse

The new ECE heterodyne diagnostic covers most of the electron temperature profile. The space resolution can be inferred from Fig.3, which shows the temperature profile just before a ST crash and about 200-300 μs afterwards (a) as well as their difference (b). The difference profile has the role of initial perturbation for the heat pulse, in the sense discussed in the previous section. The corresponding normalised mixing radius value is $\rho_{mix}\approx 0.7$; this is more than twice the value of the inversion radius ($\rho_{inv}=0.32$).

Fourier analysis (Fig.4) must be restricted to the region $\rho>0.7$ in order to provide a good determination of χ_e^P. The values of φ' and $(A'/A)_g$ in the region $\rho>0.7$ are plotted vs frequency in Fig.4a and confirm the diffusive behaviour of the heat pulse. The χ_e^P value is $\chi_e^P=3.5\ m^2/s$. It is interesting to see what would be the consequence of including data with $\rho<\rho_{mix}$ in the analysis. This is shown in Fig.4b, where the values of φ' and $(A'/A)_g$ in the region $\rho>0.6$ (7 channels) are plotted. The values of φ' are seen to be significantly smaller than their true value, while the value of $(A'/A)_g$ has remained unchanged. This result is similar to the analysis of the ballistic heat pulse shown in Fig.1. Given the time resolution of the diagnostic, however, it is not possible to decide whether the heat redistribution causing the large r_{mix} value occurs on a fast (τ_{ST}) time scale or on a slower (ballistic) time scale.

The large ρ_{mix} value of this heat pulse prevents a meaningful comparison between perturbed (χ_e^P) and power balance (χ_e^{PB}) diffusivity values due to the large uncertainties in χ_e^{PB} near the plasma edge. Other ST heat pulses measured with the heterodyne diagnostic have smaller ρ_{mix} values and confirm the result $\chi_e^P/\chi_e^{PB}\approx 2\text{-}4$ typical of JET plasmas.

Conclusions

Application to a simulated ballistic ST heat pulse has shown that Fourier analysis can identify the plasma region (far from the mixing radius) where the heat pulse is diffusive. This region coincides with the region where a diagnostic with moderate (≈1 kHz) time resolution would find a negligible initial perturbation. Both Fourier and initial perturbation analysis can be used on JET ST pulses to identify the diffusive region of the pulse.

[1] N.J.Lopes Cardozo, to appear in Plasma Phys. Contr. Fusion (1995).

[2] E.D.Fredrickson et al, Phys. Rev. Lett. 65 (1990) 2869; Nucl. Fusion 33 (1993) 1759.

[3] P.Mantica et al, Nucl. Fusion 32 (1992) 2203.

[4] A.Jacchia et al, in preparation.

[5] N.J.Lopes Cardozo et al, in Proc. 18th Eur Conf Berlin, Vol 15C, Part I, EPS (1991) 193.

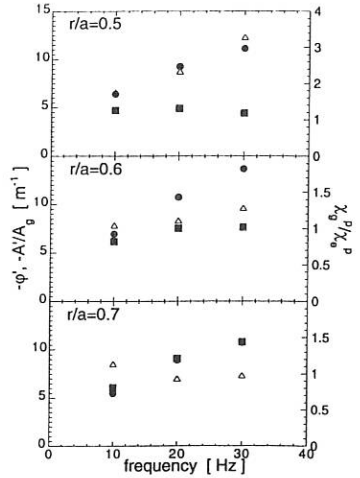

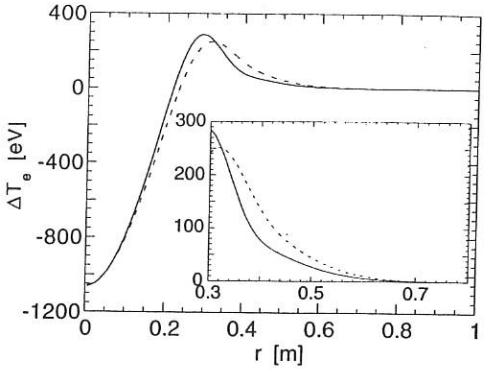

1. *Values of φ' (squares) and $(A'/A)_g$ (circles) obtained from a simulated ballistic ST heat pulse at three different locations in the plasma, plotted vs frequency. The χ_g^p value (open triangles) normalised to the input χ_e^p value is also shown on the same plots.*
2. *Spatial profile of $\tilde{T}_e$ at t=0.5 ms (full line) and t=1 ms (dashed line). The same profiles are plotted in the insert over the radial range 0.3<r<0.8.*

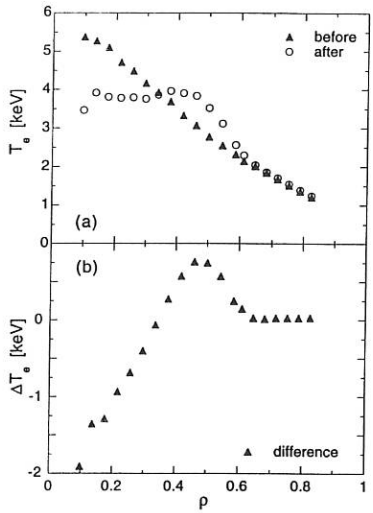

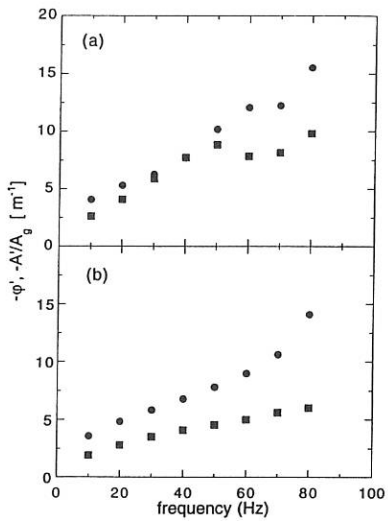

3. *Change in the T_e profile due to a ST instability in JET discharge #23425 as recorded by the ECE heterodyne diagnostic (time resolution Δt=0.5 ms) at selected radial locations. This was a discharge with B=3.4 T, I_p=3.5 MA, $\langle n_e \rangle = 1.4 \cdot 10^{19}$ m^{-3}, $\langle T_e \rangle$=2 keV, P_{OH}=1.5 MW, P_{RF}=3.8 MW. The ST instability occurs at t=50.815 s. The $\tilde{T}_e$ profile extends out to ρ≈0.6-0.7.*
4. *Values of φ' and $(A'/A)_g$ from the ST heat pulse of Fig.3. The derivatives are calculated over (a) the 4 outermost ECE channels (0.7<ρ<0.85) and (b) the 7 outermost ECE channels (0.6<ρ<0.85).*

Isolation of the Role of Ion Mass from the Influence of Profile and Beam Deposition Changes in Isotope Scaling Studies on TFTR

E.J. Synakowski, C.W. Barnes, R.E. Bell, R.V. Budny, C.E. Bush, Z. Chang, D. Ernst, B. Grek, L.C. Johnson, H. Park, J. Schivell, S.D. Scott, J.D. Strachan, G. Taylor, M.C. Zarnstorff, and the TFTR Group
Princeton Plasma Physics Laboratory, Princeton, New Jersey, 08543 USA

I. Introduction -- Deuterium-tritium operation in TFTR supershot plasmas [1,2] has been characterized by a strong, favorable dependence of heating and confinement on isotopic mix [3,4]. Past studies of the supershot regime have indicated that local transport is reduced as T_i/T_e is increased [5], suggesting that a small isotope effect is amplified by a strong dependence on this temperature ratio. Recent isotope scaling studies indicate that an improvement in the local ion thermal conductivity persists for deuterium- and tritium-injection plasmas at the same value of T_i near r/a = 1/3. However, it is useful to reduce local profile effects as much as possible by examining plasma pairs of different isotopic mix that are similar throughout the cross section. If such similar pairs can be found, an ion mass effect would be unambiguously identified by examination of the total stored energy, rather than a local transport analysis. In addition, differences in beam physics may play a role in the apparent improvement in ion temperature and global confinement in plasmas fueled with tritium neutral beams. These two issues are potentially related, as the stronger coupling of tritium beam ions to thermal and impurity ions tends towards higher ion temperatures. Also, the differing velocities of the beam ions might lead to changes in beam-thermal ion coupling large enough to influence the thermal ion stored energy and ion temperature, resulting in an apparent increase in confinement time during T-beam injection that would be attributed to the difference in thermal ion mass alone.

In this paper, we isolate the mass effect from these confounding influences in two ways. In both techniques, plasma pairs with D-only neutral beam injection (D-NBI) and T-only neutral beam injection (T-NBI) are examined. The first pair (Section III) had the same neutral beam injection power. The effects of changes in energy and particle deposition are studied by simulating the ion temperature (T_i), electron temperature (T_e), and electron density (n_e) profiles for the T-NBI case. The calculation was performed by holding constant all of the measured quantities, except the single one to be simulated. For the T_i simulation, the ion thermal conductivity χ_i as determined for the D-NBI plasma was used with the calculated T-NBI sources to evaluate the new T_i profiles. A similar procedure was followed in simulating T_e (the electron thermal conductivity χ_e from the D-NBI case was used) and n_e (the effective electron particle diffusivity D_{eff} from the D-NBI was used). For the second study (Section IV), the pair is composed of a 20 MW D-NBI and a 15 MW T-NBI plasma. The D-NBI and T-NBI plasmas had total stored energies of 3 MJ, and had similar profile shapes and scale lengths, allowing the effects of average ion mass on confinement to be separated from those due to changes in the values and gradients of T_i, T_e, n_e and toroidal rotation velocity V_ϕ.

II. Background -- Past studies have emphasized comparing carefully matched sets of D-NBI and T-NBI plasmas, for which all the externally controlled discharge parameters and the target plasma are nominally identical. The T-NBI plasmas consistently showed improved performance compared to their equal power D-NBI counterparts. For a typical pair of 18 MW, 1.6 MA deuterium and tritium plasmas from this study, the T-NBI plasma had a ~25% higher central ion temperature and a 5-10% higher central electron temperature. The measured plasma density profiles had the same shape, but the D-NBI plasma density was ~ 10% lower. The improvements are evident in the plasma stored energy W_{tot}, as measured by magnetics: for the same heating power, W_{tot} is up to 25% higher in plasma fueled with tritium beams relative to comparable deuterium plasmas. Some of the increase can be attributed to classical effects such as the increased energy stored in unthermalized beam ions during tritium beam injection and energy stored in the unthermalized fusion alpha component, but up to 65 - 80% of the total increase in W_{tot} in high power plasma pairs arises from additional energy stored in the thermal ions and electrons. This indicates a favorable dependence of thermal τ_E on tritium content in these plasmas. The transport coefficients of these plasmas show improvement primarily in the ion thermal conduction and electron particle confinement. Differences in the electron thermal conductivity are small.

Local transport coefficients are inferred using the steady-state transport code SNAP [6] As input, the code uses the measured temperature and density profiles and impurity content. The thermal conductivities χ_i and χ_e, and effective electron particle diffusivity D_e are defined by $Q_{i,e} \equiv -\chi_{i,e}\, n_{i,e} \nabla T_{i,e} + 3/2\, \Gamma_{i,e} T_{i,e}$ and $\Gamma_e \equiv -D_e \nabla n_e$, where Q_i and Q_e are the total ion and electron radial energy fluxes, Γ_e and Γ_i are the electron and ion radial particle fluxes, and $n_i = \Sigma n_j$ is the total thermal ion density. Here, $T_i(r,t)$ and $V_\phi(r,t)$ were determined by measuring emission from carbon impurity ions with charge exchange recombination spectroscopy (CHERS). $T_e(r,t)$ was determined from ECE spectroscopy, and $n_e(r,t)$ was inferred from measurements by a ten-channel infrared interferometer array. The ion depletion was calculated using tangential visible-bremsstrahlung measurements for Z_{eff} and X-ray spectroscopy measurements of metallic concentrations. This code modelled the deposition of the injected beam neutral atoms, and the subsequent slowing down and losses of the fast ions. Classical differences expected in beam deposition between T- and D-NBI plasmas are included in the analysis. For example, the lower beam particle velocity of T-NBI broadens the power deposition profile. Also, the lower T beam velocity also increases the fraction of beam power collisionally coupled to thermal ions, and reduces the coupling to thermal electrons.

III. Simulation of T-NBI plasma with D-NBI transport coefficients -- Ambiguities introduced by differences between D- and T-beam physics are removed by simulating in SNAP the T-NBI plasma profile of interest, using the transport coefficient pertaining to it from the SNAP analysis of the D-NBI plasma. All but the simulated quantity's

measured radial profiles are held to the T-NBI values. With differences in particle and energy sources thus removed, any change between the simulated and measured profiles can be attributed to a mass effect alone. Results from this simulation are shown in Fig. 1.

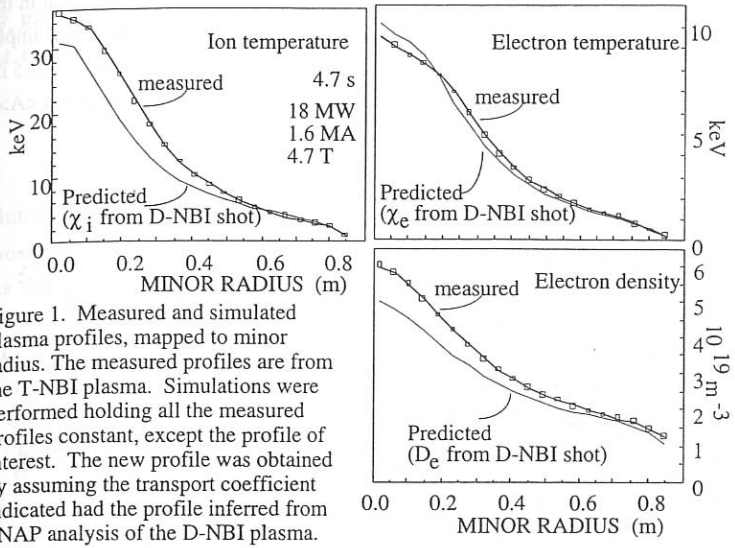

Figure 1. Measured and simulated plasma profiles, mapped to minor radius. The measured profiles are from the T-NBI plasma. Simulations were performed holding all the measured profiles constant, except the profile of interest. The new profile was obtained by assuming the transport coefficient indicated had the profile inferred from SNAP analysis of the D-NBI plasma.

As was seen in the SNAP analysis of the local transport coefficients, the clearest indication of an isotope effect is found in the ion thermal transport and electron particle transport. This manifests itself here as a difference between the predicted and measured profiles of T_i and n_e. The similarity in the predicted and measured T_e is not surprising, since the values of χ_e inferred from the SNAP analysis are quite similar. Since differences in the beam physics have been removed, this implies that inferred and measured improvements in confinement are not due to secular changes in beam particle and energy deposition. Note that the difference between predicted and measured values of T_i is smaller than the inferred change in χ_i itself between the two plasmas, since not all of the ion power is conducted. At the half-radius, 30% is expected to be transferred to the electrons collisionally, while 23% is transported by ion particle convection.

IV. T- and D-NBI Plasmas With Similar Profiles -- Although D- and T-only injection at the same power yields substantially different background plasma profiles, it is possible to construct pairs with more similar profiles by reducing the power in the T-NBI case. Data from such a pair is shown in Fig. 2. The central carbon profiles, inferred from CHERS (not shown), and the central Z_{eff} are similar as well. Differences in the V_ϕ profile outside of R = 2.9 m (r/a = 0.2) are quite small, reducing the possible influence of changes in velocity shear on the total confinement [7,8]. The total plasma stored energies are the same to within a few

percent, as are the individual stored energies of the ions and electrons. Significantly, the power required to establish these plasmas was 15 MW for the T-NBI case, and 20 MW for the D-NBI case. The measured confinement times were 195 ms and 153 ms in the T- and D-NBI plasmas, respectively. This clearly demonstrates that there is an enhancement in confinement in the T-NBI case that is not related to local changes in background plasma parameters. This implies a strong dependence on confinement on ion mass alone: the average ion mass <A> was 2.5 in the T-NBI case and 1.9 in the D-NBI plasma, leading to a scaling with average ion mass <A> that is approximately $\tau_E \propto \langle A \rangle^{1.0}$.

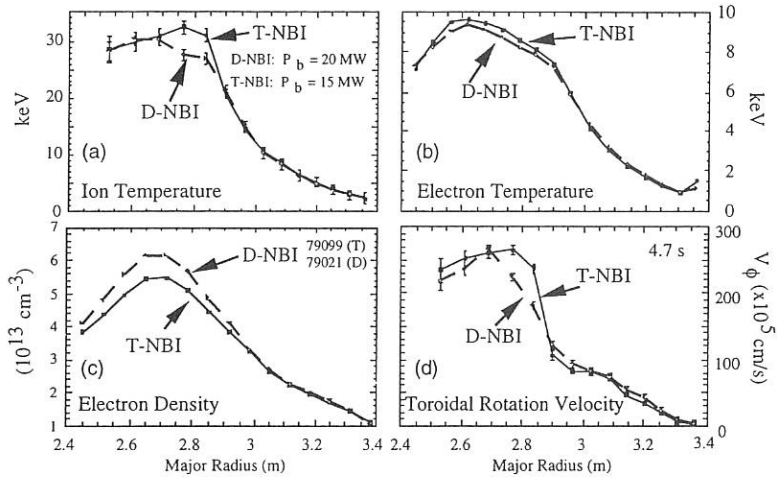

Figure 2. Measured radial profiles of the 15 MW T-NBI plasma and the 20 MW D-NBI plasma. Shown are (a) the ion temperature, (b) the electron temperature, (c) the electron density, and (d) the toroidal rotation velocity.

This work was supported by the U.S. DOE Contract No. DE-AC02-76-CHO3073.

1 J.D. Strachan *et al.*, Phys. Rev. Lett. **72** (1994) 3526.
2. R.J. Hawryluk *et al.*, Phys. Rev. Lett. **72** (1994) 3530.
3 S.D. Scott *et al.*, Physica Scripta **51** (1996) 394.
4 M.C. Zarnstorff *et al.*, Heating and Transport in TFTR D-T Plasmas, paper IAEA-CN-60/A-2-I-2, presented at the Fifteenth International Conference on Plasma Physics and Controlled Nuclear Fusion Research (Seville, Spain, 1994).
5 D. Meade *et al.*, Recent TFTR Results, paper IAEA-CN-53/A-1-1, presented at the Thirteenth International Conference on Plasma Physics and Controlled Nuclear Fusion Research (Washington D.C., USA, 1990).
6 H. Towner *et al.*, Rev. Sci. Instrum. **63** (1992).
7 T. Fukuda *et al.*, Phys. Rev. Lett. **72** (1994) 3662..
8 R.J. La Haye *et al.*, General Atomics Report GA-A21544, April 1994, submitted to Phys. Rev. Lett.

Relevance of Present Day High Field Confinement Results for the Ignitor Experiment*

F. Bombarda†, B. Coppi, W. Daughton, L. Sugiyama, C. Fiore, S. Golovato, M. Graf, M. Greenwald, A. Hubbard, J. Irby, B. LaBombard, E. Marmar, M. Porkolab, J.E. Rice, Y. Takase, S.Wolfe

Massachusetts Institute of Technology, Cambridge, MA 02139, USA

†Associazione Euratom-ENEA sulla Fusione, Frascati, 00044 Italy

1. Introduction

Ignitor has been the first experiment designed to reach ignition conditions [1]. For this it relies on the favorable confinement and purity properties of the high density plasmas, demonstrated by the compact, high field line of experiments represented by the Alcator A, C, and C-Mod machines at MIT and the FT and FTU machines at Frascati. The two machines presently in operation, C-Mod and FTU, display different confinement properties, in spite of their common plasma density range. On C-Mod, the ohmic energy confinement time τ_E is 2-3 times higher than predicted by the neo-Alcator scaling, it shows a positive dependence on plasma current I_p, and possibly on the inverse of the collisionality parameter ν_e^*; FTU follows the neo-Alcator scaling [2]. Geometry, in particular elongation, and possibly the edge conditions at the lowest densities, may play a determining role in establishing the transport regimes. The presence of the divertor, on the other hand, seems to be beneficial but not so crucial.

2. Alcator C-Mod Energy Confinement

An analysis of the C-Mod confinement properties has been carried out over a recent set (from December '94 to June '95) of ohmic and ICRF heated discharges at 5.3 T, covering a wide range of parameters (line average density $\bar{n}_e$= 0.5–4.5 × 10^{20} m^{-3}, plasma current I_p= 0.4–1.2 MA, elongation κ = 1.5–1.8), but no H-mode conditions. The improvement in confinement with plasma current is shown in Fig. 1, for ohmic discharges. It has been observed that, at a

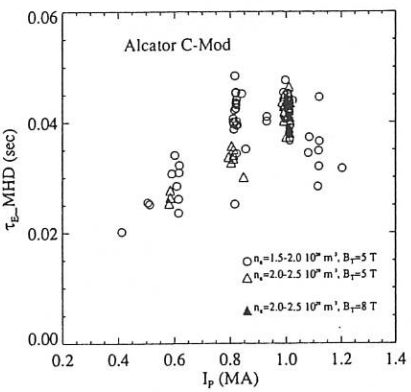

Fig.1: τ_E as function of plasma current at 5.3 T

* Sponsored in part by the U.S. Department of Energy and by ENEA of Italy

given value of I_p, the ohmic power increases with density, whereas the magnetic stored energy W (from the EFIT code [3]) remains essentially constant; as a consequence, τ_E decreases with density. β_{pol}, on the other hand, shows a very limited variation for all ohmic plasmas (see Fig. 2). The previously reported consistency of the experimental results with the ITER89_P scaling [4] is, to some extent, the result of the relation between P_{OH} and n_e.

We found that the C-Mod ohmic energy confinement time scales with the inverse of the electron collisionality parameter ν_e^* (see Fig. 3) :

$$\nu_e^* = \frac{\nu_e \varepsilon^{-3/2}}{\omega_b} = 2.8 \times 10^{-2} q R \varepsilon^{-3/2} \lambda \frac{\overline{n}_{20}}{T_e^2} Z_{eff} \qquad (1)$$

where ν_e is the electron collision frequency, ω_b the trapped electrons bounce period, ε the torus aspect ratio, R the major radius in m, T_e the electron temperature in keV, λ the Coulomb logarithm normalized to 15, $\overline{n}_{20}$ the electron line average density in units of 10^{20} m^{-3} and Z_{eff} the plasma effective charge; all quantities are calculated at approximately 1/3 of the minor radius, where the gradients are steepest. This correlation is not found when additional RF Ion Cyclotron heating is applied. In these cases, τ_E degrades with power, similar to other experiments, and a strong increase of β_{pol} is observed, with good ion and electron heating [5].

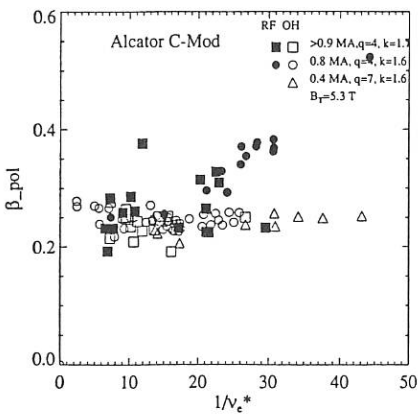

Fig. 2: β_{pol} for ohmic and RF discharges

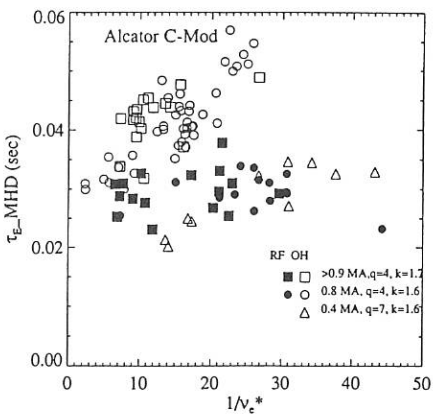

Fig. 3: τ_E (MHD) vs collisionality

It should be remarked that some uncertainty is associated with the determination of the stored energy from the magnetic equilibrium reconstruction, particularly for low values of β_{pol} and of stored energy, that could possibly introduce spurious effects on the data. However, the calculation of the stored energy from the kinetic measurements is also affected by both instrumental errors and by the effects of some approximations, at present under careful assessment, and the particular trend of τ_E with density, which is clear from the magnetic data, is not evident from the limited number of kinetic calculations that could be performed.

Indeed, simulations of C-Mod discharges using the 1 1/2 - D transport code BALDUR [6], with the assumption of neoclassical ion transport and an anomalous thermal electron transport coefficient D_{JA}, containing a nearly linear dependence on I_p and only a weak function of n_e, is found to reproduce quite well the measured electron temperature and density profiles of ohmic plasmas.

3. Comparison with FTU and prospects for Ignitor

Alcator C-Mod is a particularly significant machine for checking the extrapolations involved for some of the Ignitor parameters. For example, the peak current density, the electron density and the elongation in C-Mod have already reached the design values envisaged for Ignitor and C-Mod complements FTU in providing useful and relevant information. The transport properties in FTU seem to be quite different from C-Mod, and in broad terms they can be described as following a neo-Alcator scaling up to $\langle n_e \rangle q_a = 3 \times 10^{20}$ m^{-3} and then saturating [2]. The saturation has been attributed to the filling up of the ion energy reservoir: when T_i reaches T_e (at $\langle n_e \rangle \approx 1 \times 10^{20}$), then τ_E saturates at a typical value of 40 – 50 msec. A detailed comparison between experimental determinations and theoretical predictions of various quantities (radial plasma flow velocity, Z_{eff} and stored energy) has led to the conclusion that FTU plasmas are in better agreement with the extended neoclassical theory [7]. Contrary to C-Mod, β_{pol} is found to be a function of I_p.

One of the main differences between the two machines is the plasma shape, FTU having a circular plasma cross section limited by one or two poloidal limiters, and C-Mod characterized by a highly elongated shape and a divertor. Elongation may be a relevant parameter: the preliminary analysis of a series of low κ discharges on C-Mod seems to recover some of the neo-Alcator scaling characteristics. This is a favorable indication for Ignitor (R=1.32 m, a= 0.47 m, κ=1.8, $I_p \leq 12$ MA, B_T=13 T, $n_{e0} \cong 10^{21}$ m^{-3}, $T_{e0} \leq 15$ keV), which will have a similar κ to C-Mod, and will operate at lower values of ν_e^*, so that the confinement can be expected to present the improvements generally associated with the higher values of I_p and the larger dimensions of the machine.

On the other hand, the role of the divertor looks less crucial. On C-Mod, an experiment done to highlight the difference between limiter and divertor geometry showed an improved screening for metals and non-intrinsic recycling impurities when in the divertor configuration, but little or no effect on the energy confinement. Similar results were obtained on FTU, where an injection of impurity (argon) to the point of substantially raising Z_{eff} did degrade the confinement as much [2].

The attainment of an H-mode in Ignitor is not required to reach ignition and, on the basis of present power threshold scalings, the available power in Ignitor (20 MW) is not sufficient to achieve H-mode conditions at full parameters, even considering the C-Mod lower coefficient

[8]. However, the actual dependence of the threshold on the toroidal field and the effect of density peaking have yet to be fully verified.

Since both FTU and C-Mod have an all metal first wall, their low density plasmas are dominated by high Z impurities (Ni for FTU, Mo for C-Mod). A comparison of the edge conditions shows that FTU edge temperatures (20-30 eV) are typically lower than in C-Mod (≤60 eV), for similar SOL densities, while the connection lengths are shorter. Although the details of the SOL may differ between the two machines, their common characteristic is that all impurities are very effectively screened from the main plasma as the density is raised above 10^{20} m^{-3}, without any particular wall conditioning. From the results obtained by both machines, it appears that the high Z materials used for the plasma facing components are not a hindrance for reaching high performances in ohmic conditions, with values of Z_{eff} steadily decreasing with increased density, and, indeed, they may be necessary to attain the high values of n_e required in Ignitor to approach ignition. It can also be observed that the expected power loads on the first wall in Ignitor, under normal ignition conditions, will be similar or lower than the present ones on C-Mod.

Acknowledgments

The authors wish to thank R. Bartiromo, M. Leigheb, and F. Alladio for providing FTU data and useful comments.

References

[1]Coppi B., Nassi M., Sugiyama L.E., *Physica Scripta* **45** 112 (1992)

[2]Bombarda F., Bracco G., Buratti P., et al., *Proceed. of the 20th EPS Conf. on Controlled Fusion and Plasma Physics*, Lisbon 1993, **17B I** 29

[3]Lao L.L, St. John H., Stambaugh R.D., et al., *Nuclear Fusion* **25** 1611 (1985)

[4]Greenwald M., et al.,to be published in *Proceed. of 15th Interntl Conf. on Plasma Physics and Controll Nuclear Fusion Research*, Seville 1994, (or PFC/JA-94-29)

[5]Golovato S., et al., to be published in *Proceed. of the 11th Topical Conf. on Radio Frequency Power in Plasmas*, Palm Springs, CA 1995, AIP N.Y.

[6]Coppi B. et al., *Proceed. of the 21th EPS Conf. on Controlled Fusion and Plasma Physics*, Montpellier 1994, **18B III** 520

[7]Bracco G., Segre S.E., Zanza V., et al., *Nuclear Fusion* **34** 863 (1994)

[8]Snipes J.A., et al., *Proceed. of the 21th EPS Conf. on Controlled Fusion and Plasma Physics*, Montpellier 1994, **18B III** 1542

Transport Analysis of FTU Plasmas with High Power Density ECRH at 140 GHz

P. Buratti, O. Tudisco, V. Zanza and FTU Team
Associazione Euratom-ENEA sulla Fusione, C.E. Frascati, C.P. 65
00044 Frascati, Roma, Italy

A. Bruschi, S. Cirant, G. Granucci, S. Nowak, A. Orefice, A. Simonetto, G. Solari
Istituto di Fisica del Plasma, Associazione Euratom-ENEA-CNR, via Bassini 15,
20133, Milano, Italy

1. Introduction

The effect of auxiliary heating on local transport properties has been studied in a series of ECRH experiments carried out on the FTU tokamak (R_0=0.935 m, a=0.3 m) with 0.4 MW of injected microwave power at 140 GHz [1] Equatorial low field side launch of ordinary polarized waves was used. For on-axis heating experiments the vacuum magnetic field at $R=R_0$ was B=5.2 T, corresponding to fundamental resonance at the plasma magnetic axis, while the field was increased to 5.8 T for off-axis heating.

The electron density at the resonance position varied from 0.6 up $1.7\times10^{20}m^{-3}$, i.e. up to 70% of the critical density. Central temperatures in the ohmic phase were in the range 1÷2 keV; some sawtooth free discharges were characterized by strong central radiation, and by slightly hollow profiles.

The ECRH pulse duration was limited to 15 ms by the power supply available at the time, while the energy confinement time ranged from 28 to 50 ms. In spite of the short pulse duration and of the relatively low radiofrequency power (35÷60% of the ohmic power), large temperature increases (from 0.9 to 3.5 keV) and large temperature gradients (up to 40 keV/m) were obtained for central heating, owing to the large ECRH power density.

2. Changes in temperature profiles during ECRH

Ray tracing calculations typically predict power deposition within 10% of the plasma minor radius [2], owing to the narrow antenna pattern and to the high single pass absorption, which in all cases exceeds 90%. Electron temperature profiles have been measured by a 12-channel grating polychromator tuned to the second electron cyclotron harmonic. This instrument was not influenced by the gyrotron radiation, in fact the signals did not change during the gyrotron power switch on (about 100 μs) and the measured temperature increases were in very good agreement with Thomson scattering data [3]

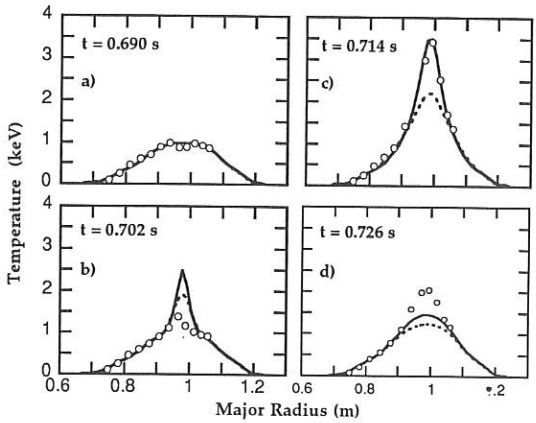

Fig. 1: *T_e profiles for shot #8282 ($B_0 = 5.2$ T; $n_e(0)=0.95\times10^{20}m^{-3}$; Ip=379 kA; $q_a=5.8$; $Z_{eff}=1.5$; $\tau_E=28$ ms; ECRH pulse 0.7÷0.715 s). a) ohmic phase; b) early in the ECRH pulse; c) at the end of the ECRH pulse and d) after the ECRH pulse. Solid and dashed lines refer to simulations with χ_e fixed at the ohmic profile and to χ_e increasing as $T_e^{3/2}$ respectively. Dots represent experimental data.*

The response of temperature profiles in sawtooth free discharges is very sensitive to the resonance location: central heating gives rise to strong peaking (Fig. 1), while off-axis heating has nearly no effect on the central temperature (Fig. 2); there is therefore no evidence of temperature profile resiliency, at least over times of the order of half energy confinement time and much shorter than the resistive diffusion time, which is about 100 ms. Similar results have been obtained by ICRH on JET [4].

Although the tendency of profile peaking around the heating radius is still observed on the short time scale also in sawtoothing discharges, the reconnection at the sawtooth crash reduces the average temperature peaking during central heating, while during off-axis heating the sawtooth period increases, giving rise to a build-up of central temperature (Fig. 2) which is small but has been systematically observed.

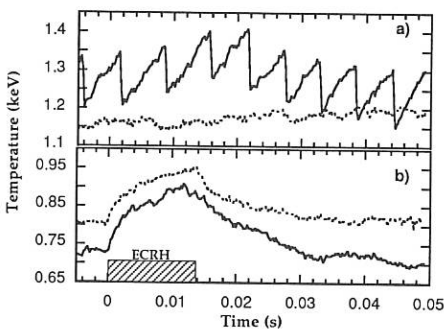

Fig. 2: *Temperature evolution for off-axis heating (B_0=5.8 T); a) r=0; b) r=11 cm (resonance position). Solid and dashed lines refer to shots #8313 (sawtoothing) and #8159 (sawtooth free) respectively.*

3. Comparison with transport calculations

In order to evaluate the effect of heating on the electron heat diffusivity χ_e, the temperature evolution measured in a sawtooth free shot (Fig. 1) with central heating has been compared to predictive transport calculations. Sawtooth free shots are preferable for simulations as no model for convective transport due to sawtooth reconnections is required. The transport code uses the 2-D flux surfaces as given by equilibrium reconstruction, so that all quantities are either flux functions or flux surface averages. Measured radiated power and electron density profiles are used. Ohmic power and electron-ion energy exchange are calculated self-consistently assuming Spitzer resistivity and neoclassical ion energy transport. The ECRH power deposition profile was calculated assuming that all the launched power is deposited according to the single-pass absorption profile calculated by the ray tracing code [2]. The code can be run in an interpretative mode, in which the measured electron temperature is an input data, while the electron heat diffusivity profile χ_e is an outcome.

The predictive analysis during the additional EC heating pulse is carried out assuming that the χ_e profile remains equal to the one determined in the ohmic phase by running the code in the interpretative mode. The χ_e profile is ill-measured in the central region, where radiation is strong and the T_e profile is hollow; in this region a flat χ_e is assumed (Fig. 3).

The prediction is in very good agreement with the measurement for the channels that are well outside the heated region, and with the measured temperature at the end of the pulse for all the channels (Fig 1), while the predicted rise is much faster than measured at the beginning of the ECRH pulse in the directly heated region. In this particular shot the discrepancy could be explained by a broadening of the power deposition profiles, but in other cases [5] there may be a relevant amount of missing power.

The Te profiles measured at the end of the ECRH pulse cannot be reproduced

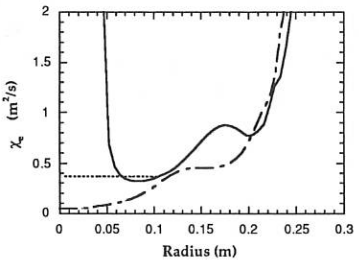

Fig. 3: *Electron heat diffusivity profiles for shot #8282. Solid line: χ_e from the interpretative code in the ohmic phase (t=0.690 s); dashed line: flattened χ_e assumed in the predictive code; dot-dashed line: χ_e from the interpretative code after the ECRH pulse (t=0.726 s).*

if χ_e is increased during ECRH; an example with χ_e increasing as $T_e^{3/2}$ is shown in Fig. 1.

After the ECRH pulse the measured T_e profile remains more peaked than the one predicted with the pre-ECRH χ_e profile (see Fig. 1d); in this phase the interpretative analysis gives very low χ_e values in the central region (Fig. 3). The main difference between this regime and the one observed before the ECRH pulse is a reduction of radiation near the plasma center, which allows a more accurate power balance in that region.

4. Discussion

In the experiments reported in this paper a large increase of the central electron temperature lasting for half confinement time was not accompanied by a degradation of the local energy transport properties. This indicates that L-mode behaviour could be associated with effects that could not be produced due to the limited ECRH power and pulse duration, i.e. either with strong ion heating, or with electron heating in the outer plasma regions, or its onset could take place on times comparable with the resistive diffusion time.

References

[1] S. Cirant et al., IAEA/CN/60/G-P-6, 1994

[2] A. Bruschi et al., this Conference

[3] S. Cirant et al., *High power heating of the FTU tokamak plasma at the fundamental electron cyclotron resonance of 140 GHz*, The 11th Topical Conf. on Radio Frequency Power in Plasmas, May 17-19 -- Palm Springs, California

[4] B. Balet, J. G. Cordey, D. G. Muir, G. L. Schmidt, Nucl. Fusion **32** (1992) 1261

[5] G. Granucci et al., this Conference

Experimental Determination of the Dimensionless Parameter Scaling of Energy Transport in Tokamaks

TC Luce and CC Petty
General Atomics, San Diego, California 92186-9784, U.S.A.

1. Introduction

Controlled fusion experiments have focused on the variation of the plasma characteristics as the engineering or control parameters are systematically changed. This has led to the development of extrapolation formulae for prediction of future device performance using these same variables as a basis. Recently [1], it was noticed that present-day tokamaks can operate with all of the dimensionless variables which appear in the Vlasov-Maxwell system of equations (including device geometry) at values projected for a fusion powerplant with the exception of the parameter ρ_*, the gyroradius normalized to the machine size. The scaling with this parameter is related to the benefit of increasing the size of the machine either directly or effectively by increasing the magnetic field. It is exactly this scaling which is subject to systematic error in the inter-machine databases and the cost driver for any future machine. If this scaling can be fixed by a series of single machine experiments, much as the current and power scalings have been, the confidence in the prediction of future device performance would be greatly enhanced. While carrying out experiments of this type, it was also found that the ρ_* scaling can illuminate the underlying physics of energy transport. Conclusions drawn from experiments on the DIII–D tokamak in these two areas are the subject of this paper.

2. Background

The fundamental assumption is that the energy diffusivity χ can be written as $\chi = \chi_B \rho_*^\alpha F(\beta, \nu_*, q, R/a, \kappa, T_e/T_i, \dots)$, where χ is normalized to χ_B, the Bohm diffusivity, by convention. The goal is to change ρ_* while holding the functional F fixed to determine α. As explained elsewhere [2], $\alpha = 1$ is known as gyro-Bohm scaling, $\alpha = 0$ is Bohm scaling, $\alpha = -1/2$ is Goldston scaling, and $\alpha = -1$ is stochastic scaling. Drive-wave theories of cross-field transport generally have gyro-Bohm scaling.

Experiments in L–mode plasmas with low β ($\beta_N \sim 0.5$) and high q ($q \sim 7$) found [2] that the global confinement scaling changed from gyro-Bohm scaling to Bohm scaling as the density increased. However, these experiments allowed for the first time separate determination of the ρ_* scaling of the electron and ion diffusivity. The experiments clearly showed that the electron scaling was always gyro-Bohm, while the ion scaling was always Goldston. The global scaling varied with the fractional power exhausted in the electrons. The strong deviation of the ion scaling from gyro-Bohm remains unexplained; however, one hypothesis is that it arises from orbit averaging over the turbulence when the ion gyroradius is larger than the turbulent eddy size. The ion scaling should return to gyro-Bohm in the limit $\rho_* \to 0$.

Another series of experiments [3] designed to lie on a dimensionless scaling path to ITER was performed in H mode plasmas at lower safety factor ($q = 3.8$) and higher β ($\beta_N \sim 2.2$). The result was that both the electrons and ions (and therefore the global) scaling was gyro-Bohm. This result leads to a very optimistic confinement prediction for ITER, as discussed below.

3. Understanding the Ion ρ_* Scaling

Equally interesting is the dramatic change in ion ρ_* scaling. Four quantities have changed between the two experiments — L mode to H mode, which changes the density scale length; high q to low q, which changes the shear length; low β to higher β; and $T_e/T_i > 1$ to $T_e/T_i < 1$. These variations are listed in the order in which the effect of their variation will be tested. The density scale length is interesting since it changes dramatically in the classic phenomenology of the transition from L mode with peaked profiles to H mode with flat profiles. The magnetic shear length is chosen because the current scaling is the strongest of the engineering parameter scalings. Also, scale lengths rather than the dimensionless quantities themselves are chosen because of the working hypothesis of orbit averaging. If the turbulent eddy scale is determined by some scale length in the plasma, then a dramatic change in that scale length would correspondingly change the critical ρ_* at which the ion scaling transitions from gyro-Bohm to $\alpha < 0$. The new experiments reported here are the first in a series to investigate the source of the variation in the ion ρ_* scaling.

The strategy to find the effect of the density scale length L_n on the ion ρ_* scaling was to run L–mode discharges with dimensionless parameters as close as possible to the H–mode discharges discussed above. The aspect ratio, elongation, q_{95}, and T_e/T_i were nearly the same; however, it was not possible to remain in L mode with as high triangularity or β. With this caveat, any change in the ion ρ_* scaling will be attributed to the change in L_n. Some of the dimensionless parameters for a pair of such L–mode discharges are shown in Fig. 1. Also shown are the parameters from one of the ITER-like H–mode discharges for comparison. The ratio of the diffusivities for electrons, ions, and a single fluid are shown in Fig. 2. The electron diffusivity has gyro-Bohm scaling as always, but the ion scaling is now approximately Bohm. The single fluid scaling lies about halfway between indicating a nearly even split of the transported power between electrons and ions. This global scaling is reminiscent of the original dimensionless scaling experiments on DIII–D which for low-q, L–mode discharges found a global scaling between Bohm and gyro-Bohm [1]. Unfortunately, the scaling of the individual species could not be determined in those experiments due to the high density.

The correlation between the ion ρ_* scaling and the density scale length can be clearly seen using all of the datasets for which the ion ρ_* scaling can be determined (Fig. 3). While the two quantities are correlated, causality is much more difficult to establish.

The same unknown mechanism which controls the ion ρ_* scaling could also affect the particle transport.

4. Prediction of Future Device Performance

The H–mode discharges discussed above have the same dimensionless parameters as the ITER EDA design from summer 1994, with ρ_* increased by a factor of 8. The DIII–D plasma scales to a plasma at $a = 3.01$ m, $I = 19.6$ MA, and $P_{\rm fus} = 1.5$ GW (with 50% tritium). The power necessary to support the profiles against the gyro-Bohm scaled transport is only 41 MW (with no mass compensation for tritium), considerably less than the 300 MW of α-heating power. The bremsstrahlung losses of $\sim$ 70 MW must also be included, but the total losses are less than the α power. Therefore, gyro-Bohm scaling provides a large ignition margin.

It is implicitly assumed in this extrapolation that the discharge will be H mode. Dimensionless scaling formulae for the H–mode threshold are now available [4]. Along a ρ_* scaling path, the formula $P_{\rm H} \propto n^{0.75}BS$ (where S is surface area) has a Goldston ρ_* scaling (ρ_*^{-3}). [It is interesting to note that this is the same scaling as the original L–mode ion ρ_* scaling, suggesting the transition is related to ion transport. However, the comments which follow pertain to any H–mode threshold scaling stronger than gyro-Bohm as $\rho_* \rightarrow 0$.] The H–mode threshold curve crosses the gyro-Bohm confinement projection at a ρ_* value between DIII–D and the design point (see Fig. 4). Therefore, while the confinement would be excellent for the ITER design, there is no gyro-Bohm scaling path to the point, since the threshold scaling predicts L mode at the design point. Presumably, the power required to continue the dimensionless scaling path would then follow the Goldston scaling of the threshold. There is evidence of this from recent JET data [5]. The larger ρ_* discharges from JET lie along the gyro-Bohm path from DIII–D, but the smallest ρ_* point tracks the threshold curve, giving Goldston scaling (see Fig. 4). Based on this interpretation, either the fusion powerplant must operate at the H mode threshold with relatively poor confinement or an ignition point must be found well on the H–mode side of the threshold. This suggests operation at higher β through more highly shaped tokamaks or, if necessary, actively controlled advanced tokamaks.

This is a report of work sponsored by the U.S. Department of Energy under Contract No. DE-AC03-89ER51114.

References

[1] Waltz RE, DeBoo JC and Rosenbluth MN, *Phys. Rev. Lett.* **65** 2390 (1990)

[2] Petty CC, Luce TC, *et al.*, *Phys. Rev. Lett.* **74** 1763 (1995); Luce TC, Petty CC, *Physica Scripta*

[3] Petty CC, Luce TC, *et al.*, *Phys. Plasmas* **2** 2342 (1995)

[4] Iter H-Mode Database Working Group, *Proc. 21st EPS Conf. on Controlled Fusion and Plasma Physics* (1994), Vol I, p 334

[5] Balet B, this conference

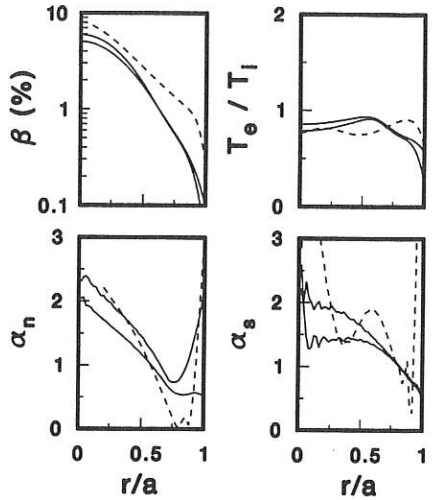

Fig. 1: Dimensionless parameters for the higher-β L–mode discharges (solid lines). The data for the H–mode discharge is shown for comparison (dashed line). The quantities α_n and α_s the power to which a parabolic radial dependence must be raised to get the local scale length for density and shear, respectively.

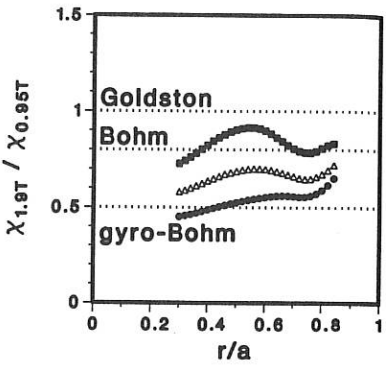

Fig. 2: Ratio of diffusivities for higher-β L–mode discharges. The filled squares are the ion data, the filled circles are the electron data, and the open triangles are the effective diffusivity data.

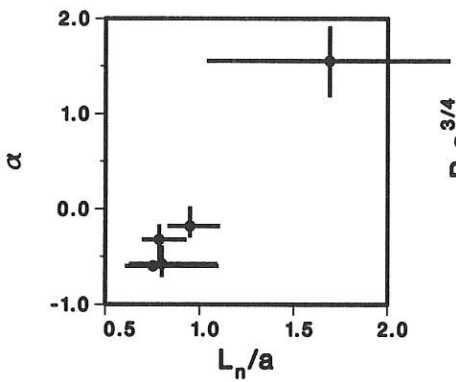

Fig. 3: Exponent of ρ_* scaling versus density scale length. Points are average values for ρ = 0.5–0.7. Bars are range of values not error.

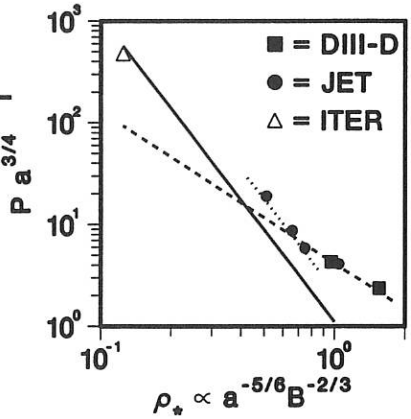

Fig. 4: Loss power versus ρ_* for a ρ_* scan. The appropriate "dimensionless" variables are plotted (constants with dimensions are not shown). The dashed line is a gyro-Bohm extrapolation based on the DIII–D points only. The solid line is the H–mode threshold from Ref. 4. The dotted line is twice the power threshold.

THE TIME BEHAVIOR OF THE HEAT CONDUCTIVITY DURING L-H-L TRANSITIONS IN JT-60U

S.V. Neudatchin*, H. Shirai, T. Takizuka, N. Isei , Y. Kamada,
Y. Koide, D.G. Muir**, M. Sato, M. Azumi
Japan Atomic Energy Research Institute, Naka Fusion Research Establishment,
Naka-machi, Naka-gun, Ibaraki-ken, 311-01, Japan
* Russian Scientific Centre "Kurchatov Institute", Moscow, Russia
** JET Joint Undertaking, Abingdon, Oxfordshire, UK

1. Introduction

An understanding of the time evolution of local transport coefficients during transitions between various confinement regimes is important to clarify the physical mechanisms responsible for the anomalous transport observed in tokamak plasmas. In relation to L-H-L transitions, soft termination and strong ELMs on JET, the time evolutions of electron temperature, T_e, ion temperature, T_i, electron heat diffusivity, χ_e, and ion heat diffusivity, χ_i, have been analyzed and reported previously [1-4]. The simultaneous T_e response (with few millisecond uncertainty) was clearly seen at $0.2 < r/a < 1$. It was shown that χ_e changes across almost all plasma volume on a millisecond time scale (more than a hundred times faster than the energy confinement time τ_E). The values of χ_e jumps were estimated without knowledge of power balance conductivity before and after transition. In the "traditional" picture, the L-H or H-L transition occurs near the plasma surface and the confinement improvement in plasma interior is then evolved on a time scale of the order of τ_E [5].

The possible explanation for the coefficients jump is that a part of the anomalous transport is controlled by "noise pumping" created by strong periphery turbulence [6]. The density fluctuation level and the correlation width measured with correlation reflectometry technique decrease simultaneously with χ_e variation at the L-H-L transitions on JET [3,4]. The similar picture of the density turbulence behavior during transitions was observed in JT-60U [7].

In this paper, an analysis of the L-H-L transition dynamics on JT-60U is presented. We restrict the analyses here for the case of L-H-L transitions after the improved confinement with high H-factor (ratio of τ_E to $\tau_E^{ITER89P}$) is well developed.

2. Jumps of χ at L-H-L transitions on JT-60U

The waveform of a 3 MA /4T hot ion H mode pulse 16130 (q_{eff}=3.8, V~68 m^3) [7] are shown in Fig. 1. The $T_e(r,t)$ is observed with the multi-channel ECE grating polychromator. The positions of measurement are shown by $\rho = r/a$.

It is clearly seen in Fig. 1 that the growth of the stored energy, W, is interrupted by a series of ELMs. The decay of all ECE signals is clearly

seen during the short L-mode phase for an approximately 30 ms time interval pointed as A-B. After the time B, the confinement is almost restored in the ELM-free H-mode phase. The L-mode again occurs at the time C. The τ_E value decreases by factor of two. The beginning of the decay of ECE signals and the $H\alpha$ jump (about 10 ms uncertainty) occur simultaneously. Moreover we see an interesting and unusual feature of the transition C. The T_e decay for $0.2 < r/a < 0.4$ starts earlier than that around r/a=0.8. This rules out the possibility of the heat pulse propagation from the periphery. In this particular case, χ_e for $0.2 < r/a < 0.4$ jumps up immediately and χ_e around r/a=0.8 increases gradually.

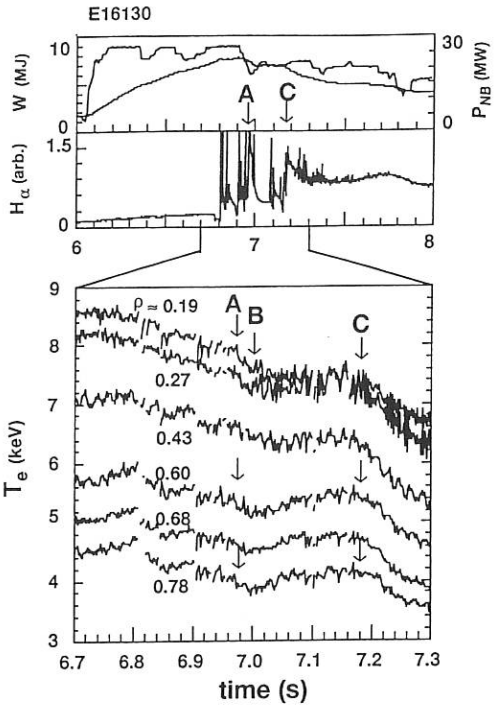

Fig.1 Waveform of pulse 16130

The value of χ_e jump, $\delta\chi_e$, is estimated in a limited space-time region from simple formula which was checked with transport codes [1-4]. The value of $\delta\chi_e$ is about 0.75 m^2/s for r/a=0.35 and 0.6 m^2/s for r/a=0.64 at 30 ms after H-L transition at time C in Fig. 1.

The evolution of plasma parameters in a 3.5 MA/4.1T hot ion H-mode pulse 17058 is shown in Fig. 2. The growth of W is interrupted by an H-L transition at the time D and the confinement does not recover later. The sawtooth crash occurs about 50 ms after the transition. The values of $\delta\chi_e$ are about 0.65 m^2/s and 0.85 m^2/s for r/a=0.61 and 0.71, respectively.

The time evolution of the T_i profile, $T_i(r,t)$, is evolved similarly to $T_e(r,t)$. The clear correlation between $T_i(r,t)$ and the toroidal rotation velocity, $V_t(r,t)$, is clearly seen in Fig. 2. The values of $\delta\chi_i$ are estimated on the assumption that $T_i(r,t)$ evolution started together with $T_e(r,t)$. The value of $\delta\chi_i$ is about 0.55 m^2/s for r/a=0.56. This picture is typical for many 3.5 MA / 4 T H mode pulses.

The evolution of $T_i(r,t)$ during L-H-L transitions in a 2 MA / 4.1 T pulse 17038 (q_{eff}=5.8 and V=68 m^3) is shown in Fig. 3. The values of $\delta\chi_i$

at the L-H transition are 0.64 and 0.93 m^2/s at r/a =0.55 and 0.63, respectively, which are higher than those in low-q discharges.

3. Conclusion and discussion

We have analyzed L-H-L transitions in 8 high field pulses, in which plasma parameters varied as 2 MA < I_p < 4 MA, 3.8 T < B_t < 4.2 T, 2.9 < q_{eff} < 5.8, 20 MW < P_{NB} < 30 MW, 5 MJ < W < 8.5 MJ during time intervals studied. The simultaneous T_e response (with uncertainty of order 10 ms) is clearly seen over 0.2 < r/a < 0.9. This evolution is not explained as the result of the heat pulse propagation (HPP) from the periphery, but can be described as the result of the fast χ_e jump over 0.2< r/a < 0.9. The fast variation of χ (at least 20-40 times less than τ_E) inside almost all plasma volume is a new finding of the L-H-L transitions in JT-60U. The T_e response in the central region (r/a ~ 0.3) often delays comparing with that in the outer region (r/a ~ 0.5), which may show the importance of HPP in the central region similarly to JET results [1-4]. The values of $\delta\chi_e$ ~ 0.75 m^2/s were obtained for 0.35 < r/a < 0.75, 4.3 keV < T_e < 5.5 keV and 5.5 keV/m < ∇T_e

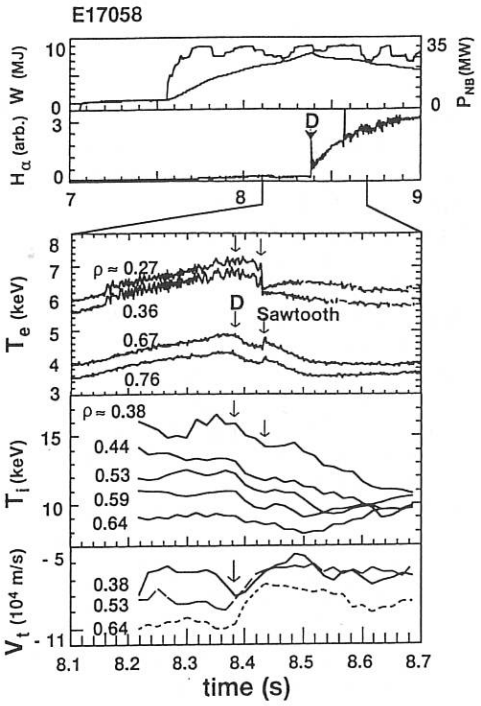

Fig.2 Waveform of pulse 17058

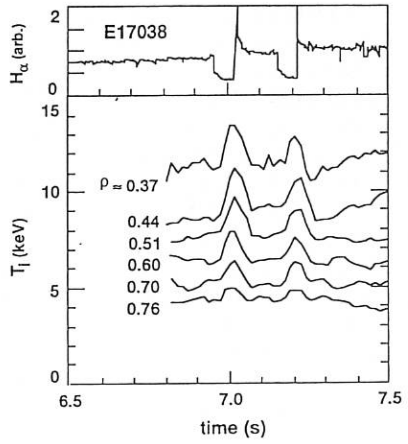

Fig.3 Waveform of pulse 17038

< 12 keV/m. They usually increase with radius.

We have also evaluated $\delta\chi_i$ in 5 pulses. The values of $\delta\chi_i$ were similar to $\delta\chi_e$ for $0.5 < r/a < 0.77$, 2.0 MA $< I_p <$ 3.5 MA, 3.8 T $< B_t <$ 4.2 T, 7.5 keV $< T_i <$ 11 keV and 15 keV/m $< \nabla T_i <$ 19 keV/m. They usually increase with radius as the same as $\delta\chi_e$.

Now we discuss about the characteristics of $\delta\chi$ comparing our results and JET data [1-4]. The values of $\delta\chi_e$ in JT-60U and JET are similar. The expression of $\delta\chi_e \sim q^2\nabla T_e/B_t$ in JET [3] is applied to the JT-60U data, but the poor agreement is found (the error is about factor 2). As for the ratio, $\delta\chi_i$ / $\delta\chi_e$, it is almost unity for JT-60U pulses with $B_t \sim 4$ T, while it is about 3 for one low field JET discharges (3 MA/1.9 T) [3,4]. We have analyzed $\delta\chi_i$ for a low field JT-60U discharge 17298 (1.5 MA/2.5 T) [7]. We could not evaluate $\delta\chi_e$ because of large noise level in ECE data. The values of $\delta\chi_i$ for L-H transition were about 1.3 m^2/s at r/a=0.52 and 2.0 m^2/s at r/a=0.6. These values are similar to those in JET. Jumps of χ_i and χ_e may have different dependences on plasma parameters.

If we combine the low field JET and JT-60U data with high field JT-60U data, we find a negative dependence of $\delta\chi_i$ on B_t like $1/B_t$. Therefore the ratio of $\delta\chi_i$ / $\delta\chi_e$ may have a negative dependence on B_t. The tendency of the negative dependence on I_p is also seen for $\delta\chi_i$. The increase of χ_i with decrease of I_p in JT-60U L-mode plasmas was obtained from the power balance analysis [8]. These dependencies are in qualitative agreement with each other.

We will further investigate $\delta\chi_e$ and $\delta\chi_i$ with the ECE measurement at low field and the high time resolution Ti measurements in new JT-60U experiments.

We wish to acknowledge Dr. J.G. Cordey for fruitful discussions and encouragement.

[1] S.V. Neudatchin, J.G. Cordey, D.G. Muir, "The time behaviour of the electron conductivity during L-H and H-L transitions in JET, JET-P(93) 58 (1993).
[2] S.V. Neudatchin, J.G. Cordey, D.G. Muir, in Contr. Fusion and Plasma Phys., (Proc. Eur. Conf. Lisboa 1993), Vol. 17c, part 1, EPS (1993) 83.
[3] J.G. Cordey, D.G. Muir, S.V. Neudatchin, V.V. Parail, et al., Plasma Phys. and Contr. Fusion, 36, suppl.(7)A, (1994) A267.
[4] J.G. Cordey, D.G. Muir, S.V. Neudatchin, V.V. Parail, et al., Nucl. Fusion, 35 (1995) 101.
[5] R.J. Groebner, Phys. Fluids B,5 (1993) 2343.
[6] B.B. Kadomtsev, Plasma Phys. and Contr. Fusion, 34 (1992) 1931.
[7] T. Fukuda , M. Kikuchi, Y. Koide, M. Sato, Y. Neyatani, M. Azumi, Plasma Phys. and Contr. Fusion, 36, suppl.(7)A, (1994) A87.
[8] H. Shirai, T. Takizuka, M. Azumi, in Proc. Int. School of Plasma Physics, Varenna, Italy, (1993) 33.

Confinement at Tight Aspect Ratio in START

M J Walsh, R.A.Bamford, P.G.Carolan, J Connor, J.G. Ferreira[+], D H Goodall, M Gryaznevich, J Hugill, I Jenkins, R Martin, S Manhood, C Ribeiro[*], C Roach, D C Robinson, V Shevchenko[#], A Sykes, T N Todd, J Tomas and H R Wilson

UKAEA Government Division, Fusion, Culham, Abingdon, Oxon, OX14 3DB, UK. (EURATOM/UKAEA Fusion Association), [+]INPE, Sao Jose des Campos, Brazil, [*]University of Sao Paulo, Brazil, [#]TRINITI, Troitsk, Moscow Region, 142092 Russia

1 Introduction

In an attempt to elucidate the global confinement properties of the START device and hence contribute to the understanding of the tight aspect ratio tokamak in general, a series of measurements of the energy confinement time, τ_E covering a wide variation of parameters has been made. The START device with R_0~0.2-0.35m, a~0.14-0.29m[1,2] can presently operate at aspect ratio A~1.3, with plasma currents in the range of 50-250kA, central electron temperatures between 100-1000eV, central ion temperatures between 75-150eV and line averaged electron densities between $3x10^{18}m^{-3}$ and $1x10^{20}m^{-3}$. Values of total beta, β_T, and normalised beta, β_N, of ~3.9% and ~1.8 respectively have been achieved in Ohmic discharges.

2 Measurements

The measurements for this study featured the following ranges of parameters, plasma current, I_p~50-180kA, line averaged density, n_e~1-5.5x$10^{19}m^{-3}$ and toroidal field, B_T~0.2-0.4T. All the plasmas mentioned in this report were limiter discharges formed in deuterium with a major radius of approximately 0.25m, with the exception of two double-null divertor discharges[3]. The START device has mainly aluminium surfaces exposed to the plasma with the exception of the central limiter which is made from graphite and the coil cases which are stainless steel. The vacuum vessel is regularly boronised by glow discharge with a mixture of trimethyl boron and helium.

In this data-set estimates of τ_E are based on measurements of the electron temperature and electron density profiles on a shot-to-shot basis by a scannable single point Thomson scattering system. The ion temperature is measured using a 5-channel (100eV-10keV) neutral particle analyser (NPA). The data was recorded at a time in the discharge when the main parameters (plasma current, major radius, line averaged electron density and loop voltage) were close to steady state. Typical experimental errors on the values of τ_E are ±20%. The effect of radiated power was not included in the calculations.

3 Main Results

Figure 1(a) shows a graph of central electron temperature versus plasma current, obtained for n_e~2-3x$10^{19}m^{-3}$ and B_T~0.38T. In this case there is a clear trend of increasing temperature with plasma current. For the same conditions, figure 1(b) shows a plot of measured energy confinement time versus plasma current. In this case the confinement is around 1 ms for a current of 100kA, with a slight decrease at higher currents typical of an ohmically heated plasma. Scaling with density shows an initial increase at lower densities with a flattening-off at higher densities (n_e~5x10^{19}m-3) for R~0.25m, k~1.4, Ip~100kA.

In order to relate the data values to those from other devices, a range of well known scaling laws have been used. These have arisen as a result of analysis of data from a wide range of machines, all of which are at a significantly higher aspect ratio. The main laws selected are neo-Alcator, Rebut-Lallia (R-L), T-10, Connor-Lackner-Gottardi (C-L-G), ITER89-P and recent ITER-92 ELMy and ELM-free H-mode scalings. Most of these scaling laws are only valid in certain regimes such as L-mode, Ohmic or H-mode.

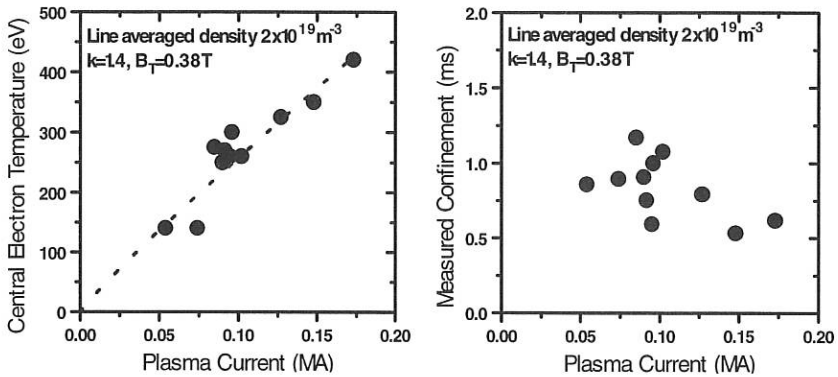

Figure 1: (a)Temperature and (b)confinement scaling with plasma current in START.

Neo-Alcator is valid only for Ohmic regimes and figure 3 shows that START data is typically a factor of 2 above this prediction. A few data points which are less than this value are close to the I/N limit ($N=\pi abn_e$) where radiative losses are significant.

Typically for START, the measured confinement is above that predicted by C-L-G(Figure 3). This is a modified version of Lackner-Gottardi scaling with the free parameters chosen to fit the results from a whole range of devices from Pulsator to JET, in both Ohmic and L-mode. The version of Rebut-Lallia used (having a coefficient of 2 in front) is generally optimistic for the present data set (see Figure 3). The T-10/Merezhkin-Mukhovatov scalings show reasonable agreement with the data-set but this may be fortuitous, since it predicts a linear dependence with magnetic field which is not observed when this variable is isolated. When compared with ITER89-P, values of H approaching 1 are observed (see Figure 3). It should be noted that the

ITER-92 ELM-free and ELMy H-mode scaling laws generally predict values of τ_E less than the ITER89-P L-mode scaling for START. This obvoiusly casts some doubt on the validity of these scalings at small aspect ratio.

Local transport versions of the above scaling laws are being tested to try to establish a good modelling base for the tight aspect ratio tokamak. This is discussed separately[5]. No clear evidence of a transition to an improved confinement regime has been seen in the two double-null divertor plasmas, although these have Ohmic power levels above the level sufficient for the Ohmic H-mode transition on COMPASS-D[6] and other devices. More recent DND discharges at higher densities do suggest access to improved confinement[3].

4 Ion temperature scalings

Estimates for the ion energy confinement time calculated by assuming electron collisional heating alone, give values for τ_{Ei} of between 1.7 and 3ms. These values support the global energy confinement data.The START NPA data show good agreement with the ion temperature predictions of Artsimovich, which can be seen in Figure 2.

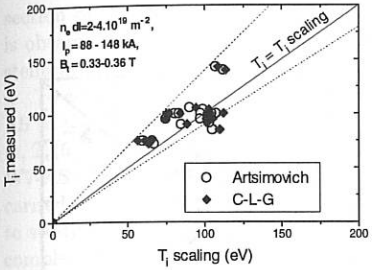

Figure [2] A comparison of measured ion temperatures on START with the Artsimovich and Connor-Lackner-Gottardi scalings (C-L-G with $C_p = 4.8\times10^{-6}$).

Provided $T_e \geq 1.5 \times T_i$, then ;

$$T_i^A(eV) = 2.8\times10^{-6} \times \frac{\left(I_p(A)B_\phi(T)R^2(m)\overline{n}_e(m^{-3})\right)^{1/3}}{A_i^{1/2}(amu)}$$

The Connor-Lackner-Gottardi model of energy confinement scaling includes a modification due to tight aspect ratio geometry. The equivalent ion temperature scaling is:

$$T_i^{CLG}(eV) = C_p \frac{\left(I_p(A)B_\phi(T)R^2(m)\overline{n}_e(m^{-3})\right)^{1/3}}{A_i^{1/2}(amu)} \cdot \left(\frac{k^2}{\left(1+K^2\right)}\frac{1}{f_g}\right)^{1/3}, \text{ where } f_g = \frac{1.17-0.65\varepsilon}{\left(1-\varepsilon^2\right)^2},$$

with ε = a/R and $K^2 = k^2\left(1+2\delta-1.2\delta^3\right)$, with δ = the triangularity. This gyro-Bohm law predicts essentially the same scaling as the neo-classical formula of Artsimovich, although it does differ numerically by a small factor for ions in the plateau regime. From typical START plasmas C_p is found to be 4.68×10^{-6}.

5 Conclusions and Discussion

The results reported here represent the most systematic set of confinement data from any tight aspect ratio tokamak to date and extend the conventional tokamak database to a new domain. The key result is that $\tau_{E(kin)}$ values of a few milliseconds have been observed in the START device. The results show that energy confinement in the START device is better than that predicted by Connor-Lackner-Gottardi, neo-Alcator and H-mode scalings while somewhat below ITER89-P L-mode scaling. Values of total beta of 3.9% and normalised beta of 1.8 have been achieved using Ohmic heating alone.

Acknowledgement

This work was funded jointly by the UK Department of Trade and Industry and EURATOM.

References

1) A. Sykes *et al*, Nuclear Fusion 32(6) 694 1992
2) M.Walsh *et al*, EPS 1993, Lisbon, Volume 17C,1-28
3) A.Sykes *et al*, this conference
4) Artsimovich L.A., Nuclear Fus. **12** 215, 1972.
5) C. Roach *et a* , this conference.
6) S.J.Fielding *et al*, this conference.

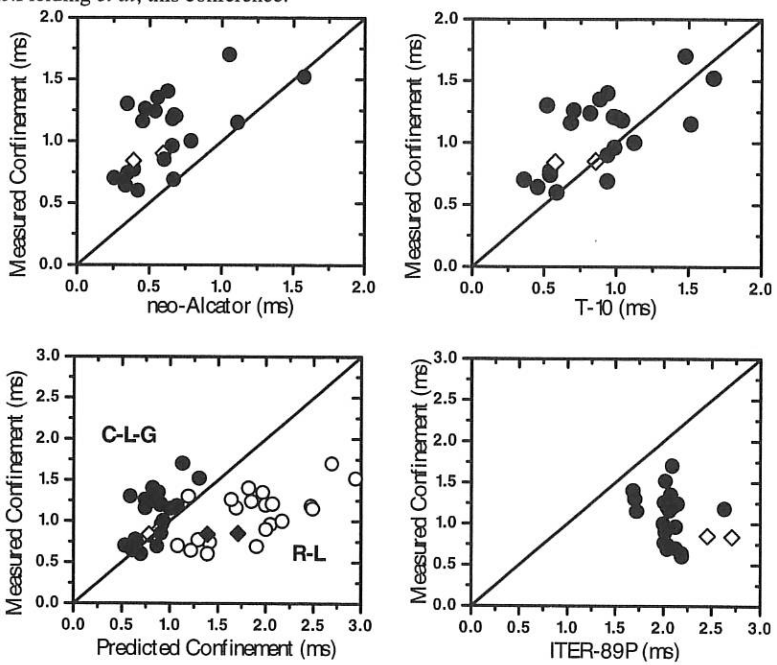

Figure 3 Comparison of global confinement scalings with START data.

Transient electron heat transport experiments in the W7-AS stellarator and the RTP tokamak

M. PETERS, H.J. HARTFUSS[1], U. STROTH[1],
V. ERCKMANN[1], G.M.D. HOGEWEIJ, N.J. LOPES CARDOZO,
AND THE RTP AND W7-AS TEAMS

FOM Instituut voor Plasmafysica 'Rijnhuizen', Associatie EURATOM-FOM,
P.O.Box 1207, 3430 BE Nieuwegein, The Netherlands
[1]Max-Planck-Institut für Plasmaphysik, EURATOM-IPP Association,
85748 Garching, Germany

1. Introduction

In this paper, the question will be addressed as to whether electron heat transport is, as commonly hypothesized, a function of the local thermodynamic variables such as the electron temperature (T_e), its gradient (∇T_e) and the electron density (n_e). An alternative model, presented by Stroth [1], is that upon a change in heating power level, the radial electron heat diffusion coefficient (χ_e) undergoes a change over the entire plasma cross section on a timescale smaller than the diffusive transport timescale. Evidence for this is obtained from an ECH switch-on (SECH) experiment in the Wendelstein 7 advanced stellarator (W7-AS) [1].

To address this question transient transport experiments have been performed on W7-AS ($a \leq 0.18$ m, $R \simeq 2$ m, $T_e(0) < 3.5$ keV) and the RTP tokamak ($a = 0.165$ m, $R = 0.72$ m, $T_e(0) < 3.5$ keV) using ECH to locally perturb T_e. The ECH systems on both RTP and W7-AS allow shaping of the T_e-profile. Modulated-ECH (MECH) experiments have been carried out on both machines under similar conditions while varying the T_e-profile shape to study the dependence of transport on T_e and its gradient separately. Furthermore, to complement the experiment reported in [1], an SECH experiment has been carried out in RTP.

2. SECH experiment in the RTP tokamak

In the flat top of an Ohmic target plasma ($B = 2.04$ T, $I_p = 80$ kA, $q_a = 4.8$, $Z_{eff} = 1.7$) 110 GHz ECH (330 kW) is applied from the low field side and absorbed on the second harmonic resonance located on the plasma magnetic axis. The profiles of T_e and n_e are measured with the Thomson-Scattering system which measures at 100 radial positions (-5 cm < r < 11 cm) simultaneously. To record the entire time-evolution of the profiles the discharge has been reproduced 20 times while varying the timelag (Δt) between ECH switch-on and the Thomson-laser pulse. ECH switch-on causes T_e and n_e to increase and decrease respectively, resulting in a monotonic increase of electron plasma pressure with time. In Fig. 1 the stored electron energy (W_e) within respectively 5 and 11 cm plasma minor radius is plotted versus Δt along with the results of local transport simulations. The evolution of $T_e(r)$ and $n_e(r)$ cannot be reproduced with a model of the type: $\chi_e \propto (T_e)^\alpha/n_e$ or $\chi_e \propto (\nabla T_e)^\alpha/n_e$. Limiting the dependencies of χ_e to T_e, ∇T_e and n_e results in a too fast increase of $T_e(r)$ in the first few ms. Good agreement is found with a model: $\chi_e(r) \propto (\int_0^r p(\rho)\rho d\rho)^{0.5}/n_e(r)$, where p(r) is the total power heating density. This model implies that χ_e responds to changes of the applied ECH power level on timescales smaller than the diffusive transport time scale and over the entire plasma cross section. This

result is confirmed by the comparison of the experimental T_e-profiles with the simulations in Fig. 2.

3. MECH experiment in the RTP tokamak

In the flat top of an Ohmic target plasma ($B = 2.2$ T, $I_p = 80$ kA, $q_a = 5.2$) 110 GHz ECH (350 kW) is applied from the low field side and absorbed on the second harmonic resonance located at 7 cm to the low field side of the magnetic axis. This strong and localized heating results in a flattening of the steady state T_e-profile which is a unique feature of the RTP experiment [3]. In addition, on-axis 60 GHz MECH is used to generate heat pulses the propagation of which yields an estimate of χ_e. By choosing the duty cycle to be 0.2 and 0.8 respectively the time-averaged on-axis ECH power can be changed by a factor 4 resulting in a variation of ∇T_e over the same range (see Fig. 3). Meanwhile the harmonic content of the perturbation remains fixed which allows a straightforward comparison of the phases and the amplitudes of the heat pulses. In Fig. 4 it can be seen that for the fundamental and the second harmonic frequencies the phases and amplitudes are essentially the same for ∇T_e differing a factor 4. From the data an explicit dependency of χ_e on ∇T_e stronger than $\chi_e \propto \nabla T_e^{0.25}$ can be excluded. Previously, sawtooth heat pulse propagation experiments at RTP yielded that an explicit T_e-dependence stronger than $\chi_e \propto T_e^1$ can be excluded [4].

4. MECH experiment in the W7-AS stellarator

In W7-AS similar ECH power modulation experiments have been carried out recently. Making use of both 70 GHz ECH (2×180 kW) and 140 GHz ECH (400 kW, on-axis and off-axis) a large variety of T_e-profile shapes was obtained at various plasma densities. An example is given in Fig. 5. The ECH modulation yielded good heat pulse propagation data. Analysis is still in a preliminary stage.

5. Conclusion and discussion

In the RTP tokamak, the evolution of $T_e(r)$ in the transient phase following a change of ECH power indicates that a local description of electron heat transport is not feasible. Instead, the data suggests an explicit and non-local dependence of χ_e on the applied heating power. This result strongly resembles evidence from the W7-AS stellarator [1]. It can be shown that this dependence of χ_e does not affect the estimation of other (T_e and ∇T_e) dependencies of χ_e by MECH experiments [2].

MECH experiments at RTP imply that if an explicit dependence of χ_e on ∇T_e exists it must be weaker than $\chi_e \propto (\nabla T_e)^{0.25}$.

MECH experiments at the W7-AS stellarator yielded good heat pulse propagation data for a large variety of T_e-profile shapes and at various densities. Analysis is in a preliminary stage.

Acknowledgement

This work has been carried out under the Euratom-FOM association agreement with financial support from NWO and Euratom. Discussions with F. DeLuca, G. Gorini, A. Jacchia and P. Mantica are gratefully acknowledged.

References

[1] U. Stroth, Physica Scripta, Vol. 51, p. 655 (1995)

[2] M. Peters, to be published.

[3] G.M.D. Hogeweij, this conference.

[4] G.M.D. Hogeweij, Proc. 21^{st} Conf. on Contr. Fusion and Plasma Phys. Montpellier 1994, Vol. 18B, part 1, p. 66.

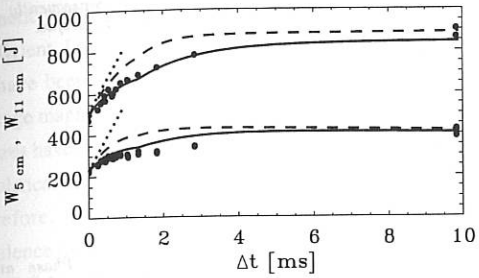

Figure 1: *From the SECH experiment in RTP the stored plasma energy (W) within minor radius of 5 and 11 cm versus Δt. The dots denote the Thomson-scattering data. The dashed line is the result of local transport simulation using $\chi_e(r) \propto T_e(r)^{1.5}/n_e(r)$, whereas the solid line represents $\chi_e(r) \propto (\int_0^r p(\rho)\rho d\rho)^{0.5}/n_e(r)$ where p is the total heating power density.*

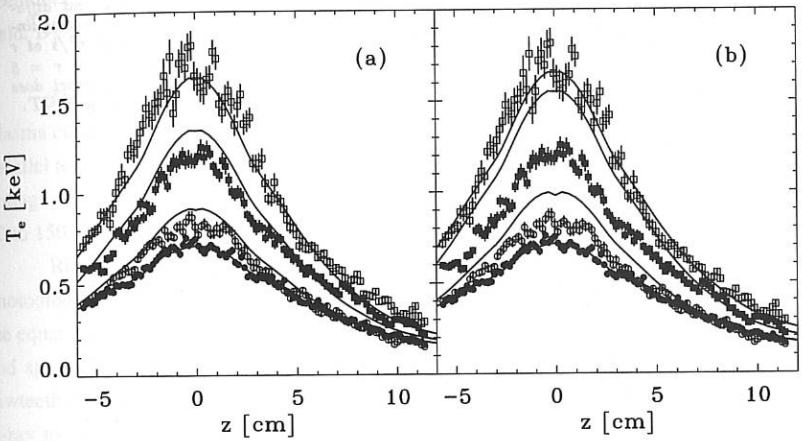

Figure 2: *In both* **(a)** *and* **(b)** *the measured T_e-profiles for $\Delta t < 0$ (closed circles), 0.25 ms (open circles), 1.33 ms (closed squares) and 9.83 ms (open squares) are given. The solid lines represent the model simulations using $\chi_e(r) \propto (\int_0^r p(\rho)\rho d\rho)^{0.5}/n_e(r)$ in* **(a)** *and $\chi_e(r) \propto T_e(r)^{1.5}/n_e(r)$ in* **(b)** *where p is the total heating power density.*

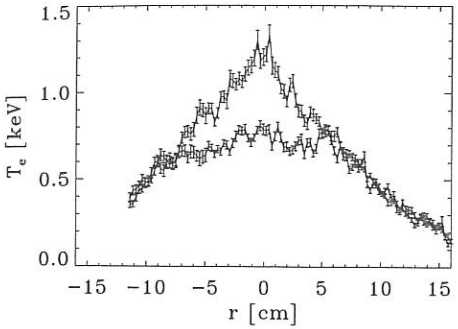

Figure 3: *T_e-profiles from 110 GHz off-axis heated RTP discharges with in addition 60 GHz MECH for duty cycle = 0.2 and 0.8 respectively. A higher duty cycle implies a higher time-averaged ECH power and consequently a more peaked T_e-profile.*

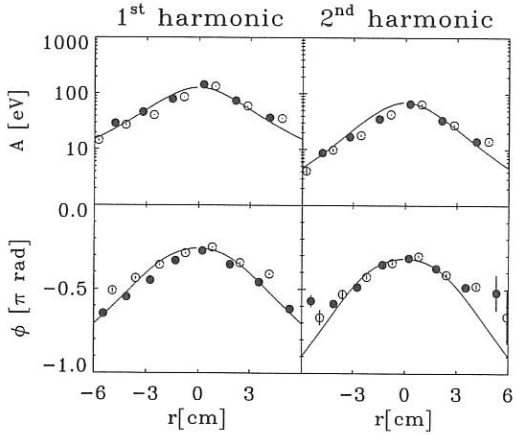

Figure 4: *Phase and amplitude profiles of 2 RTP discharges with a ∇T_e that varies over a factor 4, fitted with a simulated solution of the linearized heat diffusion equation. χ_e varies linearly between 0.5 m^2/s at r = 0 and 2 m^2/s at r = 5 cm. Clearly, transport does not depend strongly on ∇T.*

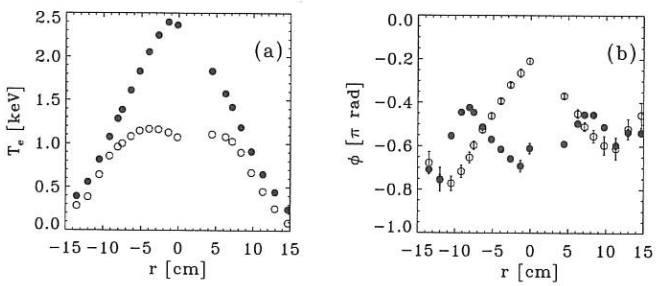

Figure 5: *In* (a) *Time-averaged T_e-profiles from ECH discharges in the W7-AS stellarator are given. The flat profile is obtained with 2^{nd} harmonic off-axis ECH at 140 GHz. When on-axis 70 GHz ECH is added T_e becomes peaked. Since both ECH sources were modulated heat pulse propagation is available. In* (b) *the phases of both the outgoing (open circles) and the ingoing heat pulses (closed circles) are shown for the case with the peaked T_e-profile. As can be seen the data is of high quality.*

ISOTOPE EFFECT ON HARD X-RAY INTENSITY SPECTRA

L. Rodríguez-Rodrigo, F. Castejón, F. Medina, M.A. Ochando.
Asociación EURATOM/CIEMAT para Fusión, 28040 Madrid, Spain

Spectroscopic observations and sawteeth propagation of soft and hard X-ray fluxes analyses in TJ-I tokamak suggested that the isotope effect could be related to a reduction of magnetic turbulence [1]. On the other hand, in TJ-I tokamak, average magnetic line diffusion coefficient, D_M, radial magnetic correlation length, k_r^{-1}, and runaway diffusion coefficient, D_r, have been obtained in hydrogen (H) plasmas, using hard X-ray intensity spectra [2]. Average magnetic turbulence level can also be deduced from this method. In fact, hard X-ray features have been explained in terms of runaway electron kinetic effects induced by magnetic turbulence, namely orbit averaging of turbulence and energy dependence of radial diffusion. Therefore, if transport improvement in deuterium (D) plasmas were due to a magnetic turbulence decrease, since runaway electrons suffer rare collisions and are little sensitive to electric fields, changes in magnetic turbulence characteristics should be detected in the hard X-ray intensity spectra signature. Using this method, magnetic turbulence characteristics have been obtained from hard X-ray spectra in H and D discharges for a scan in toroidal magnetic field, B_T.

These experiments have been carried out in TJ-I tokamak: R_0=0.30m, a=0.10 m; Plasma current, I_p, varied from 24 to 36 kA; toroidal magnetic field, B_T, from 0.8 to 1.4 T, parallel to I_p, and line averaged electron density, n_e, was kept around 1.5×10^{19} m^{-3}. Plasma voltage, V_p, changed from 2.5 to 5 V. Under these conditions ohmic power P, changed from 60 to 150 kW and the safety factor, q(a), from 2.5 to 6.5.

Radial distribution of the soft X-ray emission was obtained using two fan-like PIN photodiode arrays, 10 channels each along 10 chords, and two NaI (Tl) detectors, located on the equatorial plane, tangentially to the magnetic axis, were used to obtain hard X-ray fluxes and spectra. Oscillations detected by soft X-ray arrays could not be clearly identified as sawteeth and soft X-ray intensity profiles were used to follow possible profile changes. Hard X-ray spectra were measured with an energy resolution of 30 keV to guarentee the detection of low energy photons, by accumulation of data from at least 10 reproducible discharges for time windows of 5 ms. All the spectra, from H and D presented two slopes (black circles in figures 1a and 1b).

From spectra the following characteristics were directly deduced: the first slope energy ε_φ, the critical energy ε_k, from which the second part of the spectra appears, and the cut-off energy ε_{max}, where photon statistics drastically falls. Measured hard X-ray spectra are fitted

to the runaway intensity emission calculated from the distribution function given in [2] (white circles in figures 1a and 1b).The mean energy $\varepsilon_{\varphi 2}$ of runaway electrons with energies higher than ε_k, is deduced analytically.

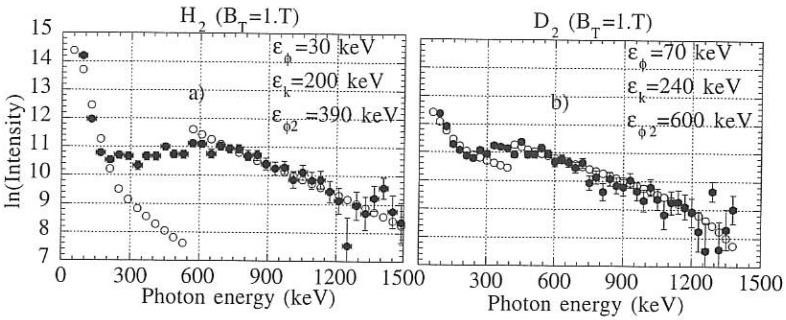

Figure 1. Hard X-ray spectra in hydrogen (a) and deuterium (b).

Using the method described in [2], the magnetic line diffusion coefficient is inferred:

$$D_M = \frac{eV_p a^2}{\mu_0^2 2\pi R}\frac{1}{\varepsilon_\varphi} \qquad (1),$$

which is related to the magnetic turbulence level as follows:

$$D_M(r) = \sum_{mn} qR\left(\frac{\tilde{B}_{mn}}{B_T}\right)^2 \delta(r - r_{mn}) \qquad (2),$$

where a and R are the minor and the major radii respectively and μ_0 is the first zero of the Bessel function I_0. The radial correlation length is given by:

$$k_r^{-1} = \frac{q}{m_e c\omega_{ce}}\varepsilon_k \qquad (3),$$

The runaway diffusion coefficient is obtained from the expression:

$$D_r = D_M|v_{||}|Y \qquad (4),$$

where $v_{||}$ is the runaway velocity and Y is the drift modification factor depending on $\Delta = k_r d_r$, being d_r the runaway electron drift. Typical drifts for each part of the spectra are obtained from ε_φ and $\varepsilon_{\varphi 2}$. In the data analysis k_r and d_r represent higher limit values since q is taken as $q(a_p)$, where a_p is the plasma radius.

Raw data obtained from spectra give for hydrogen ε_φ=25-65 keV, ε_k=200-275 keV, $\varepsilon_{\varphi 2}$=325-625 keV, and for deuterium ε_φ=50-100 keV, ε_k=200-350 keV, $\varepsilon_{\varphi 2}$=525-675 keV, ε_{max} varies from 1500 to 2500 keV in both cases.

Magnetic fluctuation level are obtained from expression (2) and are represented versus B_T and P in figures 2a and 2b.

It can be observed that b/B_T are higher for hydrogen than for deuterium for the same parameter range and that their dependencies on B_T are opposite, decreasing with B_T for H and almost constant for D. b/B_T clearly increases with P for H and is also practically constant for D.

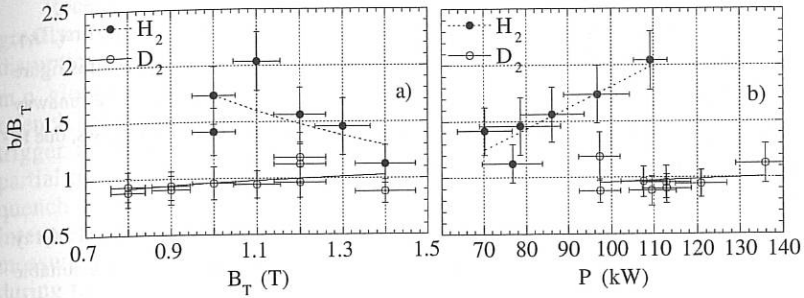

Figure 2: Magnetic fluctuation levels for hydrogen and deuterium versus toroidal magnetic field, B_T, (a) and versus ohmic power P (b).

For H, the following scaling law is found:

$$\frac{b}{B_T} \sim P^{1\pm0.4} B_T^{-0.6\pm0.3} \qquad (5),$$

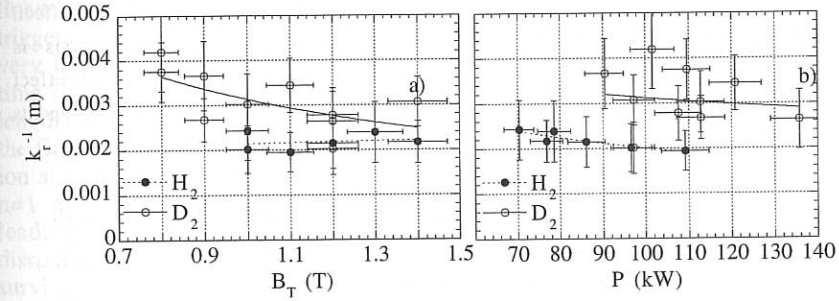

Figure 3: Radial correlation length of the magnetic turbulence for hydrogen and deuterium versus toroidal magnetic field, B_T, and versus ohmic power P (b).

This result is in agreement with previous scaling law obtain for D_M in H discharges with B_T inverted in relation to I_p [2] and with results obtained in ASDEX tokamak [5]. For D, no dependence either on B_T or on P could be extracted from our data.

The values of k_r^{-1} are deduced from expression (3) and represented in figure 3 as functions of B_T and P. In this case the radial correlation length is larger for D than for H giving for deuterium a decreasing tendency and slower than the previous one observed for H in TJ-I tokamak [2], and in ASDEX [5]. There is no dependence of k_r^{-1} on the ohmic power, in spite of the parallel slowly decreasing behaviour observed in figure 3b. The former result is again in good agreement with those obtain in [5].

Runaway diffusion coefficients can be inferred using expression (5) for the first, D_{r1}, and second slope, D_{r2}, of hard X-ray spectra, and are illustrated in figure 4. From this figure it is shown that magnetic turbulence levels are lower in D than in H and therefore runaway diffusion is higher in H. It can also be seen that D_{r2} are smaller than D_{r1} in both gases, due to the runaway averaging effect when they overcome the critical energy ε_k.

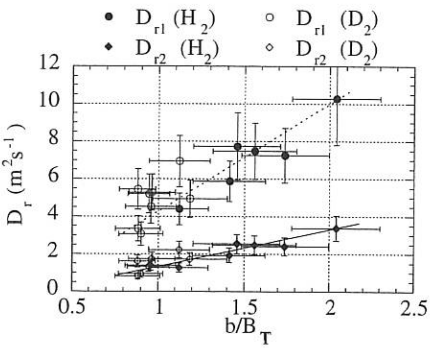

Figure 5: Runaway diffusion coefficient obtained hard X-ray spectra from the first slope (Dr1) and from the second one (Dr2).

In conclusion, hard X-ray spectra measurements are a suitable diagnostic to evaluate magnetic turbulence. On the other hand, magnetic turbulence levels are lower in deuterium than in hydrogen plasmas, while radial correlation length detected by runaway electrons seems to be higher in deuterium. That fact suggests that magnetic turbulence reduction could be an isotope effect. More detailed data analysis is necessary to infer isotope effect relevance for fusion machines and its relation with magnetic turbulence.

1-Zurro B. et al. *21st EPS Conf. on Contr. Fusion and Plasma Phys.* **18B** I 162 (1994).

2-Rodríguez-Rodrigo L., Castejón F. *Physical Review Letters* **74** 3987 (1995).

3-Gurevich A.V. et al. *Nucl. Fusion* **27** 453 (1987).

4-Myra J.R., Catto P.J. *Phys. Fluids B* **4** 176 (1992)

5-Kwon O.J. et al. *Nuclear Fusion* **28** 1931 (1988).

Advances in Understanding of Disruptions and MHD in TFTR*

E Fredrickson, Z Chang, R Budny, D. Darrow, E Mazzucato, R Nazikian,
A. Janos, K. M. McGuire, R. Majeski, C. Phillips, G. Schilling, G Taylor,
R. Wilson and S Zweben
Princeton University, Plasma Physics Laboratory, Princeton, NJ 08543, USA

S. Mirnov and I. Semenov
Triniti, Moscow Reg., USSR

Major and minor disruptions in the DT campaign

Recent experiments on TFTR with extensive diagnostic coverage have greatly expanded understanding of disruptions at high β. The high β disruption occurs in three stages as shown in Figure 1. In the first stage low m,n global modes grow at rates 10^3-10^4/sec prior to the first thermal quench (about 3.427sec in Figure 1). The global modes in some cases, trigger moderate n (10-20) ballooning modes[1-3]. This stage ends in a partial quench of ion energy and a quench of the electron temperature. The quench of the electron energy is of uncertain size due to uncertainties in the interpretation of the 2nd harmonic electron cyclotron emission (ECE) measurements. During the second stage locked modes, possibly generated during the initial thermal quench or growing out of the n=1 precursor kink, likely appear. Impurities, resulting from the heat deposition on the limiter enter the plasma and begin to radiatively cool the plasma. The second stage ends in a global reconnection of magnetic flux possibly involving an (m,n)=(1,1) internal mode as in the high density disruption [4]. This results in a complete electron and ion thermal quench, followed by the slower current quench, (phase III).

The first stage typically begins with a rapid growth of the n=1 kink-like mode. The theoretical model of this not complete - as q(0) is often less than unity, the (1,1) mode is ideally unstable and it must be assumed that it is non-linearly saturated at a low level. The n=1 , in many cases (possibly all) triggers a toroidally localized ballooning modes. The ballooning modes have very large growth rates ($\approx 10^5$/sec), begin near the q=1 radius and by the time of the disruption extend to the edge of the plasma. The short scale lengths of the moderate n ballooning modes may allow rapid reconnection of the flux surfaces leading to global stochasticity and the partial/full quench of ion and electron thermal energy. This sequence of events, the growth of the n=1 mode and the triggering of toroidally localized ballooning modes leading to a thermal quench, are considered the trigger for high β disrputions on TFTR. For relatively mild thermal quenches, the plasma can survive this, but invariably has severely reduced performance due largely to

the presence of MHD activity or to the influx of hydrogen or impurities generated by the deposition of heat on the limiter.

Measurements of ECE, used to deduce T_e, are complicated during the initial thermal quench by the strong non-thermal emission during the quench. Further, following the thermal quench there is in some cases evidence that the ECE is cut-off or refracted by a high density plasma ($10^{21}/m^3$) near the grating polychromator (GPC) μwave horn. This is deduced from data from two toroidally separated GPC's. In Figure 2 are shown the evolution of the electron temperature profiles measured by two GPC's during the first thermal quench of the disruption shown in Fig. 1. At one toroidal location a GPC measures a plasma with $T_{eff}(0) > 6$ keV, 126° toroidally away the ECE level is nearly zero, $T_{eff} < 1$ keV. Even more extreme examples have been observed following other disruptions. This cut-off of the ECE can last up to 3msecs (throughout phase II). Similar cut-offs have been observed during density limit disruptions. However, in those cases it lasted less than 100μsec. These observations are preliminary and further work is planned.

The second stage of the disruption begins after the first thermal quench. The initial electron thermal quench is not accompanied by a full ion thermal quench as fast measurements of the neutron emission rate show only a 20% drop or less at this time. In this example the drop in neutron rate was much less (Fig. 1). The second stage can persist for as long as 10 msec, excluding minor disruptions where the second stage does not result in a major disruption. There is some evidence, from numerically integrated Mirnov coil data, that locked modes are present and growing during the second stage. The external locked mode diagnostic can not respond on timescales much less than 20msec, the wall penetration time for the radial field. While some losses of fusion products occur during the first thermal quench, more are lost during the second phase as can be seen in the fourth trace of Figure 1. Perhaps most importantly, impurities and cold hydrogenic species generated by the rapid deposition of energy on the limiters are cooling the plasma. The electron temperature profile evolution during this period is very similar to that seen in high density disruptions.

At the end of this period there is a large positive spike in the plasma current suggesting that a reconnection of the current column takes place. The fast (10kHz) measurement of the plasma current shows a positive current spike of 10% - but lasting only 1 msec as compared with several msec in high density disruptions. As in the high density disruptions this appears to be inititiated by an internal m/n=1/1 mode based on the data from two GPC's. In Figure 3 are shown the evolution of electron temperature profiles from the two GPC's. The temperature collapse is consistent with an internal

(1,1) mode, although in this example it does not appear to have the cold bubble topology. This reconnection causes the final ion and electron thermal quench (neutron rate drop) leading to the third and final phase of the disruption, the current quench.

Toroidal Alfvén Eigenmodes

Toroidal Alfvén Eigenmodes and other Alfvénic modes have been predicted to be destabilized by the presence of a fusion α population in TFTR and future D-T machines, possibly resulting in significant loss of the fast α population. In the experiments performed to date, there has been no conclusive evidence of fusion-α driven Aflvénic modes. Studies of Alfvén modes driven by ICRF generated tail ion populations are the best method of benchmarking the MHD codes used to predict TAE stability in ITER.

In ICRF heated plasmas a second, independent branch of fast ion driven Alvénic modes has been found[5]. Direct measurements with a toroidal Mirnov coil array of the n number of these ICRF generated Alfvénic modes shows that the mode numbers for the two branches cover the same range, providing confirming evidence that two types of modes are present (Fig. 4). At the onset time of the mode the frequency is above that of the TAE modes and the signal is very weak on the Mirnov coils, but strongest on the core channel of the reflectometer. Over a period of about 100-200msec, the frequency drops and the signal becomes stronger on the Mirnov coils, i.e., at the plasma edge and all but disappears from the core reflectometer channel. The rapid drop in frequency, not caused by density changes, suggests that the mode is affecting the fast ions, possibly moving fast ions outward in minor radius. The mode may then follow the fast ion population outward in radius.

The experimental discovery of this new mode illustrates the importance of experiments dedicated to the search of fast ion driven instabilities. Measurements of the damping rate of TAE modes by external excitation would not find these modes, nor properly describe their properties. The mode, in the initial 'linear' phase is strongly localized in the plasma core - thus not accessible with external excitation. Secondly, the mode resonance probably does not exist in the absence of the fast ion population and is not describable by perturbative MHD codes, nor by perturbative experiments (external excitation) in plasmas without fast ion components[6].

*Supported by DoE contract No. DE-AC02-76-CHO-3073

[1] E. Fredrickson accepted for publication at Phys. of Plasmas (1995)
[2] C. C. Hegna and J. D. Callen, Phys. Fluids B **4**, 3031 (1992)
[3] W. Park et al., submitted to Phys. of Plasmas (1995)
[4] Fredrickson, E. D., K M McGuire, M G Bell, et al., Nucl. Fusion **33**, 1993.
[5] E Fredrickson, submitted to Nucl. Fusion (May 1995).
[6] L. Chen, Physics of Plasmas **1** (1994) 1519.

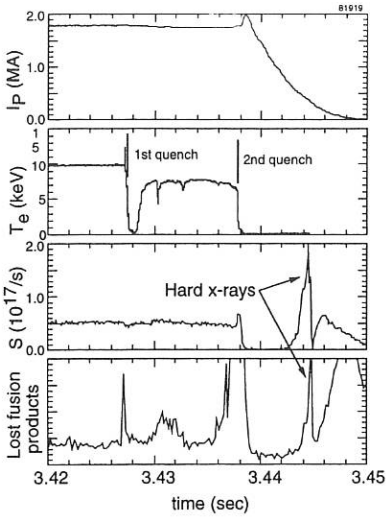

Figure 1 Plasma current, electron temperature, neutron rate and 'lost α' signal.

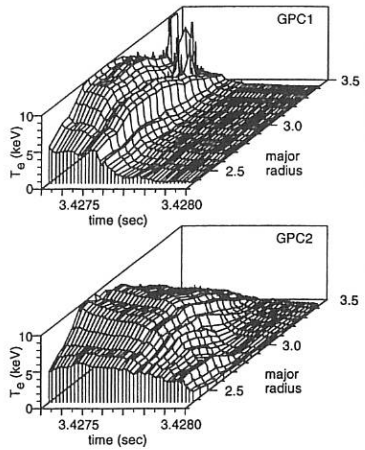

Figure 2 Electron temperature profiles during the first thermal quench at toroidal locations separated by 126º.

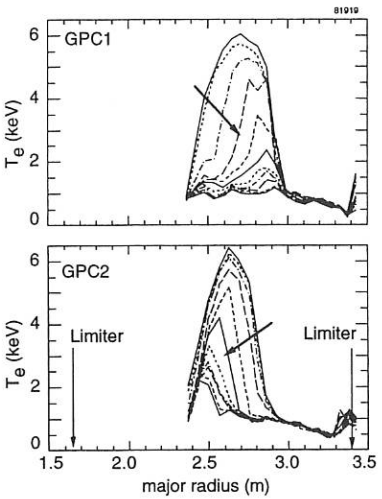

Figure 3 Electron temperature profiles during the second thermal quench, spacing is 10 μsec.

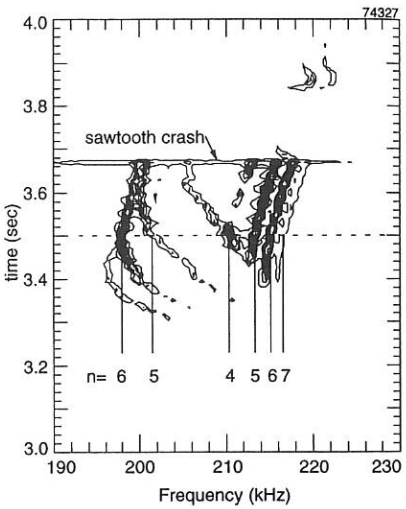

Figure 4 Contours of the Mirnov coil spectrogram showing mode frequency vs. time and the toroidal mode numbers.

DISRUPTIONS, VERTICAL INSTABILITIES AND HALO CURRENTS IN COMPASS-D

A W Morris, L C Appel, G G Castle, P J Knight, S J Manhood, M Valovič, P Vyas*
and the COMPASS-D Team.

UKAEA Government Division Fusion, Culham, Oxon OX14 3DB UK
(UKAEA/EURATOM Fusion Association)

* *Department of Engineering Science, University of Oxford, UK*

1 Introduction

COMPASS-D ($R = 0.56$m, $a \sim 0.18$m, $I_p \lesssim 320$kA, $B_\phi \leq 2.1$T) is routinely operated in a single-null divertor configuration (SND) with elongation $\kappa = 1.5 - 1.6$, similar to JET and that proposed for ITER. Disruptions have been studied in H-modes, at the experimental β-limit ($\beta_N \sim 2.0$), at $q_{95} \sim 3$ and in the presence of applied helical error fields. Disruptions characteristics such as quench times, current decay rates and halo currents are measured.

2 The COMPASS-D plasma control system

The plasma current, vertical and radial fields and plasma shape are controlled by independent decoupled power supplies and windings - no control matrices are used. For the data described here, the current in the shaping windings is pre-programmed, and so there will be small shape changes due to changes in β_p, l_i. The poloidal field (PF) coil configuration is shown in Fig 1.

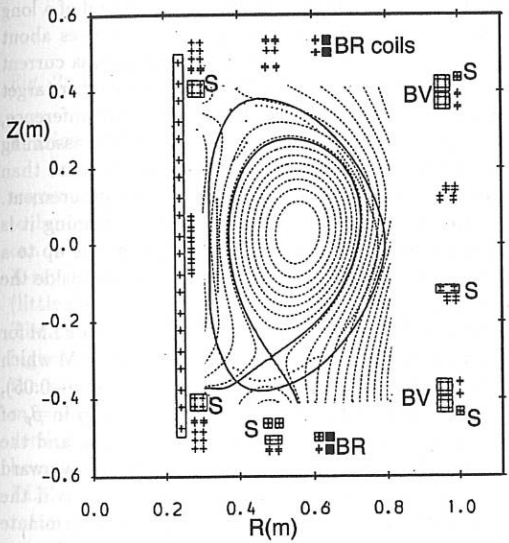

Fig. 1: *Cross-section of COMPASS-D showing the PF coils used and a typical single null equilibrium. The control (BR, BV) and shape (S) coils are marked. Other coils are used for the magnetising and fast vertical field control.*

The analogue $P + D$ controller for z_p consists of a velocity (D) signal from 8 pickup coils (B_θ) inside the 3mm thick inconel vessel (τ_{wall} measured to be $\sim 300\mu$s for B_R), and

a signal from 4 axisymmetric flux loops outside the vessel which give a measure of the position of the current centroid (for the P-term). A fast transistor amplifier (60/120V, 5kA, 6kHz bandwidth) provides both the slow position control and the fast control of the vertical instability. The P and D gains are separately programmable during the discharge, and have been adjusted empirically to provide a critically-damped response to disturbances and give good control over a wide range of plasma parameters with a single pair of time-independent gains. Control is lost for open-loop growth times below $200-300\mu$s, usually triggered by external disturbances (ELMs, Mirnov oscillations, 600Hz thyristor switching noise from the poloidal field power supplies). If the velocity signal is replaced with the unintegrated flux loop (FL) signal, the control range is much reduced due to the screening of the vacuum vessel. The H_∞ control theory can be used to improve the stability margin using the FL signals only, and preliminary results confirm this to be the case, but the vessel screening means it is still less effective than the hybrid configuration. This is explored quantitatively by applying the process of "system identification": random perturbations of the position reference signal are applied to the closed loop system and the resulting response analysed to yield the open-loop response of the plasma. The resulting Nyquist diagrams show that the closed loop stability margin is substantially smaller for the FL-only system [1]. The growth rate of the vertical instability has been measured in closed loop (as the plasma shape is varied), and the results, together with measurements of the growth rate when position control is finally lost, are in agreement with calculations with the PACE code, which models the plasma as movable rigid filaments and the vessel as fixed resistive and inductive filaments.

3 Vertical displacement events and halo currents

Fig. 2 shows a vertical displacement event following a large ELM (at the end of a long ELM-free period in an Ohmic H-mode). In this example the plasma only moves about 5cm before the energy quench occurs, q_{95} reducing to ~ 3, after which the plasma current decays and halo currents flow. I_{halo} is measured by shunts ($\sim 2\text{m}\Omega$) on the divertor target tiles at a single toroidal location. Each of the tiles covers $\frac{1}{16}$ of the toroidal circumference, and a poloidal length of about 8cm. For the example shown $I_{halo} > 40$kA, assuming axisymmetry, and in other cases $I_{halo} > 80$kA is measured, corresponding to more than 40% of the initial plasma current, and close to $100\%I_p$ at the time of the measurement. Reversing B_ϕ causes the halo current to reverse direction, as expected, confirming it is paramagnetic. There is some preliminary evidence of toroidal variation (perhaps up to a factor 2) from differences in the change in B_ϕ from poloidal arrays of detectors inside the vessel at two toroidal locations ($\Delta\phi = 180°$).

There does not need to be any significant shift of the plasma at the time of an ELM for the system to lose control, and the observed motion immediately following an ELM which does not lead to a VDE is modest - at most 2-3mm for a large ELM ($\delta(\beta_p + l_i/2) \sim -0.05$), generally downwards and inwards. For a typical COMPASS-D equilibria a drop in β_p of 0.05 is calculated to result in the position of force balance between the plasma and the poloidal field coils moving up (away from the X-point) by 4mm, leading to a downward force from the poloidal field coils. For this case the plasma moves 30mm in 1ms if the motion is only limited by the resistive wall. The great majority of plasmas terminate moving vertically downwards. 76% of a database of 1009 disruptions in the flat-top or current decay move downwards, and many of the upward disruptions correspond to overstable oscillations of the control system before termination.

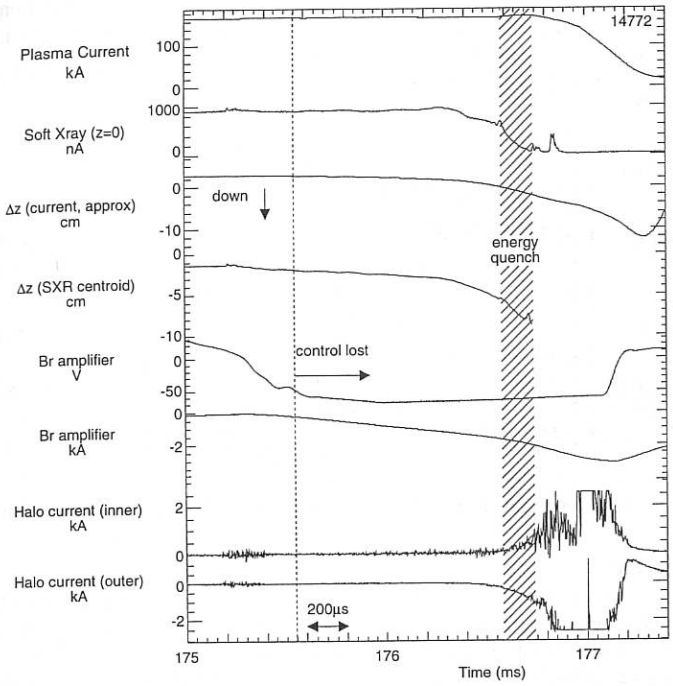

Fig. 2: *Vertical displacement event on COMPASS-D triggered by a large ELM at 175.2ms.*

4 Disruption precursors and characteristics

In general, disruptions in SND plasmas on COMPASS-D do not follow a conventional sequence of a two-stage energy quench followed by a current quench - the process appears to be nearly continuous. The current decay rate as measured inside the vacuum vessel can be as high as 500MA/s and energy quench times are 50-200μs from the central soft X-ray flux, or $100-1000\mu$s from the average X-ray emission over the whole detector array (little data is available for high β_N shots due to hard X-ray emission at the disruption). The current quench time (90% to 10%) varies between 0.2-1.5ms, with indications that higher densities correspond with longer quench times (I_p and energy). At the β-limit [2] the precursor appears to be a resistive mode, predominantly $m = 2, n = 1$, but with $m = 3, n = 2$ components which leads to a fast loss of plasma energy, and often loss of vertical position control. Disruptions are rare in ELMy H-modes - high densities have only been achieved in ELM-free periods. ELM-free H-modes terminate in large spontaneous ELMs or else an $m = 2$ mode appears (Fig. 3). The $m = 2$ mode is generally slowly rotating and either triggers a large ELM and a VDE, or a transition to L-mode when recovery is possible, or else the m=2 mode leads to an energy quench directly (Fig. 3). Disruptions can also be triggered by error-fields in ELM-free H-mode [4] at densities much higher than would be expected from low density results on COMPASS-D and the

Fitzpatrick-Hender scaling for Ohmic plasmas [4]. In these cases the stationary driven island triggers a giant ELM in much the same way as a natural m=2 mode - i.e. it is not the m=2 mode that seems to be immediately responsible for the disruption.

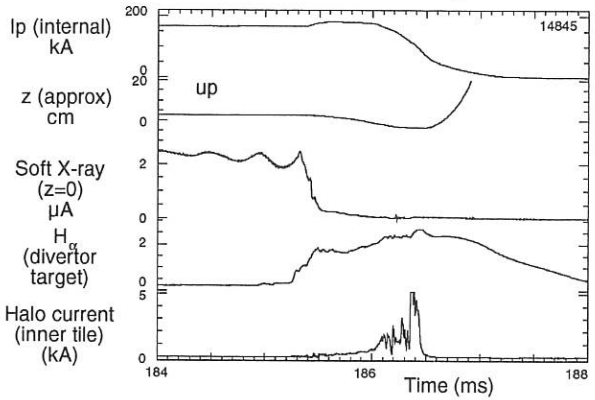

Fig. 3: *Disruption after an $m = 2$ mode in ELM-free H-mode, and preceeding a VDE.*

5 Summary

A relatively simple vertical position control system allows reliable position control, and growth rate measurements (in closed loop) are in good agreement with calculations using a rigid-body model of the plasma with a resistive wall. All disruptions in SND configurations on COMPASS-D lead to large vertical displacements with the large majority directed towards the X-point at the bottom of the vessel. The plasma current decays rapidly (0.2-1.25ms, and up to 500MAs^{-1}) but there are indications that slower decays occur at higher plasma densities. The energy quench timescale also varies between 50 and 200μs. In H-modes disruptions follow large ELMs at the end of ELM-free periods, and lead to loss of vertical position control. H-modes with infrequent or no ELMS can also be susceptible to m=2 modes which lead to giant ELMS or energy quenches. Halo currents appear during the vertical motion and decay of I_p and, assuming axisymmetry, correspond to over $40\%I_p$(flat-top). The experimental β-limit is a consequence of large $m = 2, n = 1$ modes.

This work is jointly funded by the UK Department of Trade and Industry and EURATOM.

[1] P Vyas, A W Morris, and D Mustafa. *Proc 18th Symp. Fusion Technology, Karlsruhe, to be published* (1994).

[2] D Gates et al. The effect of current profile control on the β-limit in the COMPASS-D tokamak. *This conference* (1995).

[3] R J Buttery et al. ELM-related MHD activity on the COMPASS-D tokamak compared with ASDEX-Upgrade. *This conference* (1995).

[4] G J McArdle et al. Instability control on COMPASS-D. *This conference* (1995).

Measurements of Profile Changes Prior to and During Sawtooth Crashes on TEXTOR Tokamak

G. Fuchs, H.R. Koslowski, P.C. de Vries and G. Waidman

Abstract

The rotation of the plasma has been stopped in TEXTOR tokamak by properly adjusting the neutral injection power. Under these conditions a dipole like plasma flow across the $q = 1$ surface could be observed better.

1. Introduction

Since the discovery of the sawtooth oscillations in tokamaks by S.von Goeler [1] the physical reason for the sudden crash is still not clear. Recently a number of models have been put forward in order to give an explanation [2, 3, 4, 5]. These models are in agreement with the experimental finding [6] that the value of the safety factor q stays below 1 during the entire sawtooth period. As the above models all employ different physical mechanisms, more experimental evidence is needed in order to make a distinction.

2. Experimental procedure

The experiments reported here have been done with the HCN interferometer – polarimeter, the electron cyclotron emission radiometer ECE, and the soft x–ray pin diode cameras SXR on TEXTOR. The devices have all been described elsewhere [7, 8, 9]. To get a better view on the crash event we have slowed down and brought to a standstill the plasma rotation near the $q = 1$ surface. In ohmic discharges the TEXTOR plasma rotates poloidally in the paramagnetic direction all the way from the magnetic axis to the limiter edge. The rotation can be reversed with neutral beam injection in direction of the plasma current. To stop rotation we can adjust the injection power either by the extraction voltage or by the width of the exit slit made up by a V–shaped target; only the latter method does work for small powers. The sense of rotation and the frequency of the precursor oscillations have been monitored by the SXR.

The measured profile data can be decomposed to space and time eigenfunctions using the method of singular value decomposition

$$A = U \cdot \Lambda \cdot V^T, \tag{1}$$

where A is the matrix containing the measured data versus time in the rows and versus radius in the columns, U gives the time eigenfunctions, V those in space and Λ contains the

eigenvalues. We may note that the Radon transform[1] $\mathcal{R}$ operates on the space functions only, i.e.

$$\mathcal{R}^{-1}A = U \cdot \Lambda \cdot \mathcal{R}^{-1}V^T, \tag{2}$$

from which it follows, that structures seen in U do apply to the raw and inverted data as well.

3. Results

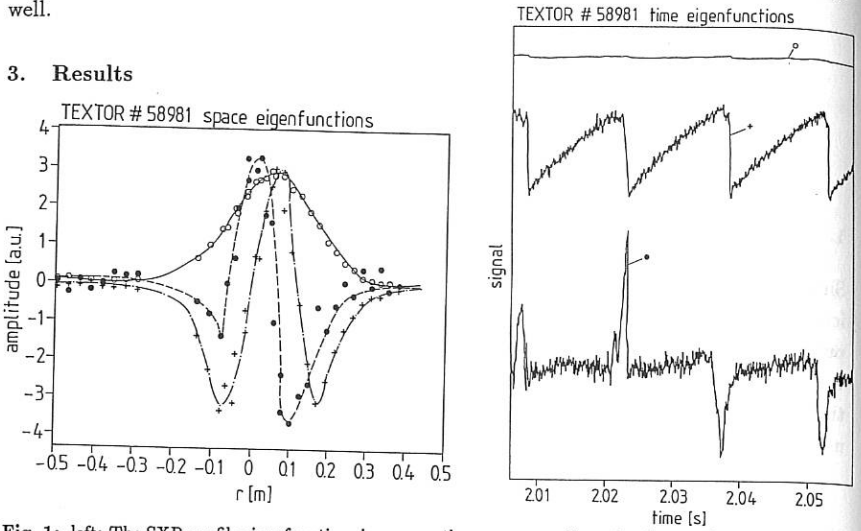

Fig. 1: left: The SXR profile eigenfunctions in space o:the average profile +:the changes due to sawtoothing •:the changes due to a m=1 structure growing. right: The time traces of matrix U for the eigenfunctions 1 to 3.

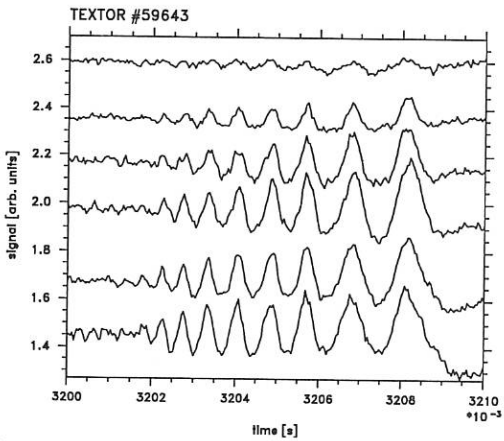

Fig. 2: The electron temperature measured with the ECE from the $q = 1$ surface toward the magnetic axis (from top to bottom).

An example showing the first 3 eigenfunctions in space and time for a case where the plasma rotation has been halted is shown in fig.1. They represent the average profile, the sawtoothing and an $m = 1$ structure. The space eigenfunctions are pretty much the same in case the plasma rotates, (cf. [8]), the same is true for the time eigenfunctions for the average and sawtoothing contributions. The function, which shows the evolution of the $m = 1$ structure shows positive or

[1] this and its inverse $\mathcal{R}^{-1}$ give the tomographic projection and its inverse

negative peaks. We interpret this as indicative for the growth of an $m = 1$ island near the $q = 1$ surface. The phasing of this island in space takes random values, i.e. there is no direction prefered for the outflow of the plasma during the crash.

From the measurement of the Faraday rotation angle in the mid-plane and the measurement of the electron temperature with the ECE we can state that the interior of the island near $q = 1$ is colder than the x–point region (for more details on this see [10]). For rotating islands we see a flat portion develop on the ECE signals starting near $q = 1$ and growing toward the magnetic axis (cf. fig.2). If we assume, that a flat portion during the minimum in an ECE signal is caused by the island interior passing the resonant volume of the particular channel, we can deduce that the island grows to a width of about 5 cm when the sawtooth crash occurs. The diameter of the $q = 1$ surface was about 20 cm, therefore there is no reconnection on the time scale of the island growth seen during the precursor phase. From the magnitude of the disturbed magnetic field in the midplane as measured by Faraday rotation we may likewise deduce that there cannot be reconnection at least in the ohmic case [10].

During the crash of the sawtooth we see a pulse on the different core diagnostics. This pulse shows up on the SXR (cf. fig.3) on one side only, whereas there is a depression

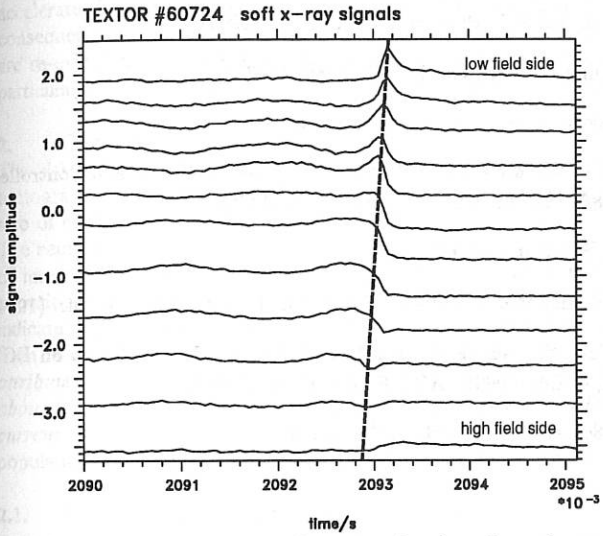

Fig. 3: The signals from SXR across the $q = 1$ surface the peak occuring at the end of the sawtooth ramp up indicates a plasma flow moving with about 500 m/s all the way across the q=1 surface.

on the other side. The pulse has a width of several hundred μs, which is under usual conditions in the order of the precursor period. In case we slow down or stop the plasma rotation this pulse becomes better visible. We interpret the pulse and its dependence on radius and time as indicative for a movement of the plasma in one direction across the

interior of the $q = 1$ surface, i.e. the flow field is that of a dipole and not that of a radial outflow, i.e. of a monopole. The speed of that flow can be inferred from fig.3 to about 500 m/s. After the pulse has reached the $q = 1$ surface at the one side, there is shortly afterwards a small pulse at the other side. This we may interpret in such a way that it circles along the $q = 1$ surface around that torus to the other side.

4. Conclusions

In conclusion we may say, that an island grows before the sawtooth crash near the $q = 1$ surface, however, it stays limited in size. Just before the crash there appears a dipole like flow with about 500 m/s across the interior of the $q = 1$ surface. These findings favor the models, which predict such a flow, namely [3, 5].

References

[1] v.Goeler S., Stodiek W. and Sauthoff N., Phys. Rev. Lett. 33 1201 (1974)

[2] Lichtenberg, A.J., Itoh, K., Itoh, S.I., Fukuyama, A., Nucl. Fus. 32, 495 (1992)

[3] Biskamp, D. and Drake, J.F., Phys. Rev. Let. 73 971 (1994)

[4] Rogister A. and Ding Li, Jül. Report 2799 Jülich (1993)

[5] Fuchs G. and Zhukov V. submitted for publication

[6] Soltwisch H, Stodiek W., Manickam J., Schlüter J.; Plasma Physics and Controlled Nuc. Fus. Res. 1986 Proc. Int. Conf. Kyoto V1 263 (1986)

[7] Soltwisch H; Rev. Sci. Inst. 57 1939 (1986)

[8] Fuchs G., Miura Y. and Mori M.; Plasma Physics and Controlled Nuc. Fus. (1994)

[9] Waidmann, G., Cao, Y., Jadoul, M., Kardon, B.; Proc. EC-7 Workshop on ECE and ECRH, Hefei, China (1989); IAEA-Publ p.92 Sept (1990)

[10] Koslowski, H.R., Soltwisch, H., Stodiek, W.; this issue

THE EFFECT OF A SAWTOOTH CRASH ON FAST PARTICLE BEHAVIOUR

O.N.Jarvis, J.M.Adams[1], D.Bond[1], M.Hone, P.J.A. Howarth[2], M.J.Loughlin, F.B.Marcus, G.Sadler, P. van Belle and N.Watkins[1]
JET Joint Undertaking, Abingdon, Oxfordshire, U.K.
[1]AEA Technology, Harwell, Oxon OX11 0RA, UK
[2]University of Birmingham, U.K.

1. Introduction

That the spatial distribution of fast particles in a tokamak is significantly perturbed by the action of a sawtooth crash is widely accepted. Observations at JET for ohmic plasmas show that the total neutron emission yield displays weak but abrupt falls at each sawtooth crash. With ICRF heating, the effect on the neutron emission is more dramatic and studies of ^{3}He-d fusion product proton emission showed [1] that accelerated ions are expelled from the centre of the plasma. With neutral beam heating, strong effects of the sawteeth on neutron emissivity profiles have been observed (with both d-d and d-t plasmas) [2]. On the other hand, the total 14 MeV neutron emission from burnup of the fusion product tritons released from d-d reactions are at most marginally affected *as are their profiles* [3]. Finally, measurements of the profiles of gamma-rays emitted from nuclear reactions between highly energetic fast ions accelerated by ICRF heating with impurity ions [4] showed the sawtooth crash to have a minor consequence on the bulk of the fast ion spatial distribution. In this paper, these gamma-ray data are re-examined and we find that the crash does have an important effect on the orbits of a particular class of fast ions. It will be argued that all the above observations are consistent.

2. Gamma-ray tomography

The 19-channel neutron profile monitor installed on the JET tokamak has permitted tomographic inversions to be obtained of line-averaged d-d and d-t fusion neutron data and also of nuclear reaction neutron and gamma-ray data for a variety of plasma conditions [2-5]. The neutron and gamma-ray signals of present interest originate within the plasma as a result of interactions between ^{3}He ions accelerated during ICRF heating experiments with plasma impurities (mainly ^{12}C and ^{9}Be). The deduced 2-D profiles of the gamma-ray emission clearly indicate the presence of a localized source of emission in addition to the distributed emission from banana orbits with turning points at the resonance layer. *This localized source is attributed to a class of particle with orbits having rather small poloidal excursions, centred about 15 cm to the low-field side of the resonance layer and circulating in the direction of the current (the co-direction).* These ions represent no more than 10% of the total fast ion population but generate a very sharp off-axis peak in the 2-d emission contour plot [5].

2.1. Sawtooth example - gammas and neutrons

A unique example of a major sawtooth crash [4] in a 5 MA plasma showed that particles with turning points at the resonance layer are little affected while the class of particle responsible for the sharp peak in the emission profile is strongly reduced in magnitude (fig.1). The gamma-ray tomography shows that the global gamma-ray emission falls by less than 20% at the crash, consistent with the reduced slowing down time due to the fall in central electron temperature - implying that most of the fast ions remained near the plasma centre. The global neutron emission falls by 50% in the 50 ms following the crash, with a time constant consistent with slowing down at r/a $\approx$ 0.7; a signal is indeed observed with the profile monitor at this radius.

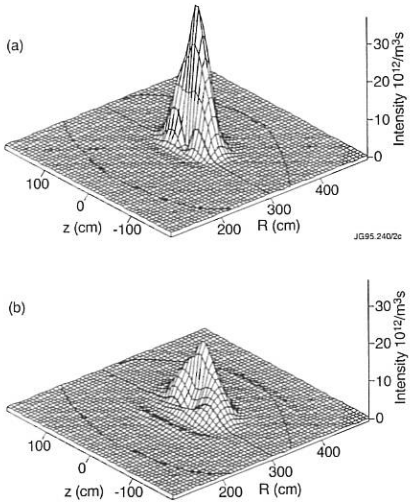

Fig.1.

Tomographic reconstruction of the gamma-ray emission profiles
(a) before and
(b) after, the sawtooth crash at 10.17 secs in discharge 23230.

The time traces (fig.2) show the appearance at about 9 s of a new source of neutrons, growing in magnitude to the level of the d-d fusion emission but with no additional gamma-ray emission from the plasma. This new source is evidently a new reaction with a high reaction threshold; $^{12}C(^{3}He, n)^{14}O$ is an obvious candidate as the threshold is -1.148 MeV and no gamma-radiation is expected until an excess of about 5 MeV in kinetic energy becomes available. We associate the 50% fall in global neutron emission as being due to this reaction and with the disappearance of the hot-spot feature (the co-passing ions). It follows that the particles following these localized orbits must possess above-average energies, explained as being a result of acceleration by the RF waves by virtue of a Doppler frequency shift effect

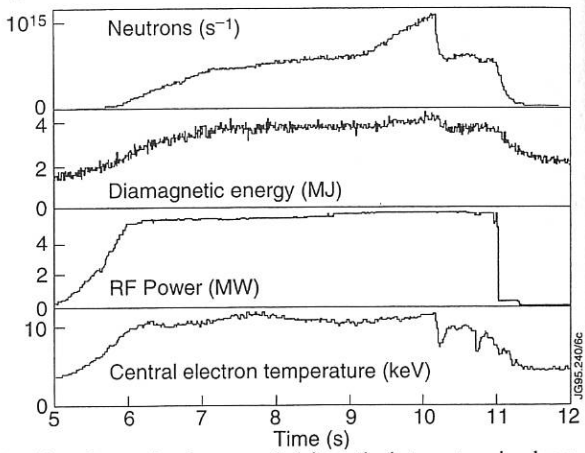

Fig.2

Time traces for discharge 23230, showing the rise in neutron emission despite the constancy of RF power and the standard plasma parameters.

which sustains their parallel velocities. Co-passing ions expelled from the hot-spot region leave the influence of the RF and will slow down rapidly, as observed.

2.2. Interpretation

We may now speculate as to how a sawtooth crash might affect the RF-generated fast particles in the central region. It is believed that the crash is an m=1, n=1 kink instability that takes place suddenly and with a duration of order 50 μs in JET. This instability affects the plasma pressure and may involve a reconnection of field lines [6]. We assume the current channel becomes deformed, distorting the flux surfaces. Electrons and thermal ions, being closely tied to flux surfaces, should follow precisely the motion of the field lines, whereas MeV ions accelerated by RF heating (the majority having large D-shaped orbits with turning points in the resonance layer) are only loosely coupled to the flux surfaces and are insensitive to any local disturbances. The main concentration of fast ions is at the resonant surface, close to the machine mid-plane. With the thermal ions and electrons being displaced by the crash, but not the bulk of the RF-accelerated ions, then the resulting charge separation should cause an electrical field to be set up that possesses a scale length of the magnitude of the displacement of the disturbance. Fig. 3 illustrates the situation that would then exist in the absence of any relaxation of the displaced core along the field lines. The parallel relaxation would, of course, be rapid. However, the final cross-field relaxation could take several milliseconds (hundreds of times longer than the orbital period of energetic passing particles).

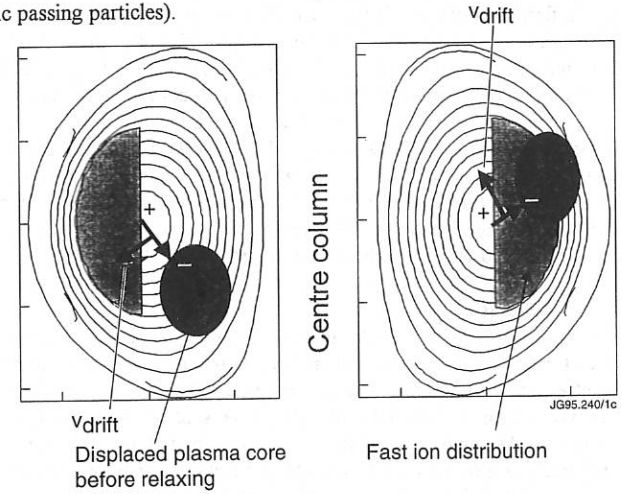

Fig.3
Illustrating the charge separation and resulting $E \wedge B$ drifts suggested as a mechanism for the expulsion from the central plasma region of a selected class of fast ions by the action of a sawtooth crash.

The transitory electrical field will induce a vertical **ExB** drift of the poloidally localized particles. (Since the duration of the sawtooth crash is much greater than the gyration period of the fast ions, we expect magnetic moment conservation to apply). The co-passing particles thus have their orbits transformed into off-axis banana orbits with turning points outside the inversion radius. The trapped ions possessing turning points at the resonance layer spend little time in the region of this electrical field and so should not be greatly affected.

3. Ohmic heating, ICRF-heating, beam-heating, fusion product tritons.

In the absence of ICRF-heating, there should be no large-scale electrical field generation. The electrons and ions will be redistributed uniformly by mechanisms such as those outlined by Kadomtsev [6] and later workers; the global thermal neutron emission will drop because the particles within the original q=1 surface will have become dispersed within an enlarged, cooler, volume and the previously peaked temperature profile will have become flattened.

As described here, with ICRF heating a particular set of the accelerated ions will have their orbits shifted vertically until they have turning points at or beyond the edge of the sawtooth disturbance. These particles subsequently perform an orbital motion in outer regions of the plasma not previously accessible. This explains the very sharp (picket-fence) signals observed when recording the 16 MeV fusion product protons from ^{3}He-d reactions using an in-vessel silicon diode detector [2,7].

With neutral beam (D^0) injection heating, there are three fusion reaction contributions to the neutron emission to be distinguished: beam-beam, beam-plasma and thermal. The sawtooth performance of the thermal contribution has been discussed above. Those beam ions orbiting within the central region of plasma affected by the crash are mostly on passing orbits (for JET). As the injected ions have relatively low energy, they tend to follow the field lines around the flux surfaces, becoming redistributed along with the thermal ions. A sudden redistribution of the beam ions has negligible immediate consequences on the beam-plasma global emission; however, the spatial redistribution is observable through the 2-D profile [2]. Ref. [3] concluded that a discharge for which the beam-plasma neutron emission was wholly dominant would not display significant neutron sawtoothing, either globally or locally, because central flattening of a relatively broad distribution, which is the case for beam-plasma dominant discharges, would produce no observable effect on the neutron emission. Beam-beam contributions are only important when the beam-ion density profiles are peaked, in which case the distinct broadening of the profile greatly reduces the beam-beam contribution.

Finally, as mentioned in the Introduction, the 14 MeV neutron emission from burnup of fusion product tritons shows no global and weak spatial changes with sawteeth [3], despite their birth radial profile being the same as the 2.5 MeV neutron emission profile. 14 MeV neutron production is heavily biased towards tritons at 200 keV, which have the same velocity as 140 keV beam deuterons. The weak spatial redistribution of the tritons [3] is consistent with the finding for beam ions in beam-plasma dominated discharges.

4. Conclusion

The study [1] of 16 MeV proton emission from ICRF-heated plasmas demonstrated dramatically that accelerated ions are expelled completely from the inner region of a plasma by the effects of a sawtooth crash, giving a misleading impression of the importance of the effect. The work reported here indicates that the bulk of the accelerated ions barely responds to the crash and that only a special class of accelerated particle is significantly disturbed. The mechanism responsible for this effect is peculiar to ICRF-generated fast ion distributions. In the absence of ICRF heating, highly energetic (several MeV) ions would be expected to be redistributed along with the sawtooth crash to the extent that their orbits are guided by the flux surfaces. At lower energies (~100 keV), and in hot plasmas, little distinction between the behaviour of thermal and fast ions is expected.

5. References

1. G.Sadler et al, Europhysics Conference Abstracts, Vol. 10C, Part 1 (1987)105.
2. F.B.Marcus et al, Plasma Physics and Controlled Fusion 33 (1991) 277.
3. F.B.Marcus et al, Nuclear Fusion 34 (1994) 687.
4. G. Sadler et al, Proc. IAEA Technical Meeting on Alpha-particles in Fusion and Plasma Physics, Aspanas, July 1991, Vol.1, p 97.
5. P.J.A.Howarth et al, Europhysics Conference Abstracts, Vol. 18B, Part 1, p. 262.
6. B.Kadomtsev, Sov. J. Phys. 1 (1975) 389.
7. O.N.Jarvis et al., Europhysics Conference Abstracts, Vol. 18B, Part 1, p. 270.

Spatial Localization of Turbulence During the Sawtooth Crash

P. Hennequin, F. Gervais, A. Quéméneur, A. Truc.
PMI-CNRS (UPR 287), Ecole Polytechnique, F-91128 Palaiseau (France).

P. Devynck, C. Laviron, A. L. Pecquet.
Association Euratom-CEA, CEN Cadarache,
F-13108 Saint-Paul-lez-Durance Cedex (France).

Introduction

While observed for many years, sawtooth activity in tokamak remains an open question, mainly because of the variety of observed behaviour and discrepancies between experimental observations and theoretical explanations. Onset of turbulence during the process has been suggested both theoretically [1] and experimentally [2,3] as a possible mechanism to account for unexplained features of the sawtooth crash, especially the rapid crash time scale.

Transient density fluctuations related to the sawtooth crash have been measured on the Tore Supra tokamak to characterize the turbulence and test the theoretical models. A previous study [4] provided mainly the temporal characteristics of that specific turbulence, and a more detailed analysis is presented below dealing with its spatial structure.

Experimental procedure

Experiments have been performed in standard Tore Supra ohmic discharges (n_e = 4 10^{19} m^{-3}, T_e = 1.5 keV, Ip = 1.7 MA, B_T = 3.8 T, $q(a)$ = 3.3, $r_{q=1} \approx$ 25 cm). Sawteeth observed in such discharges have a typical period of 80 ms, a typical crash time of 100 μs, and relative variation of electron temperature (density) of about 15% (5%).

Density fluctuations $\tilde{n}(\vec{k}, t)$ were measured via collective scattering of a CO_2 laser light (Altair experiment) at different locations of the vertical measurement volume: along a nearly central chord (X = 7 cm from the center of q = 1 surface), near the q=1 surface (X = 23 cm) and outside this surface (X = 30 cm). The observed fluctuation wave vector $\vec{k}$ is directed horizontally towards low field side in the poloidal plane of scattering experiment.

Temperature and density evolutions (ECE emission, interferometry, soft X-ray emission) and scattering signals were simultaneously analysed to observe the plasma behaviour on a fast time scale. Figure 1 illustrates the main features of the crash as seen on the contour plot of the emissivity map, obtained by tomographic reconstruction of soft X-ray

Figure 1

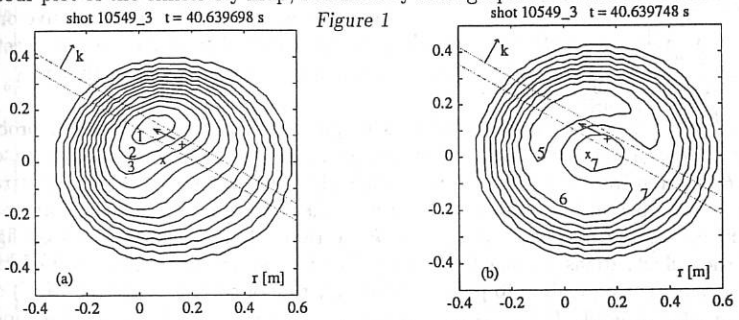

signals, at two times during a crash: first a fast displacement (50 μs) of the hot core (indicated by an arrow on figure a), and a poloidally asymmetric temperature collapse

(b) (50-70 μs). The initial kink-like motion is a $m = 1$, $n = 1$ mode, according to spatial variation of signals in each diagnostic port; equivalent relative location of the scattering chord is reported in X-ray diagnostic port and plotted in dashed line in fig. 1. The angle between the corresponding hot core displacement direction in the scattering experiment section, and $\vec{k}$ direction (fig. 5) will be noted θ from now on. Hot core fast displacement direction is statistically evenly distributed in all poloidal directions for our set of ohmic shot sawteeth.

General features

A detailed analysis of the scattering signal has shown [4] a first burst of density fluctuations, appearing synchronously with the fast displacement of the hot core at the beginning of the crash (referred to as 'first phase'); a stronger burst appears when central temperature collapses and heat flows outside the inversion surface ('second phase').

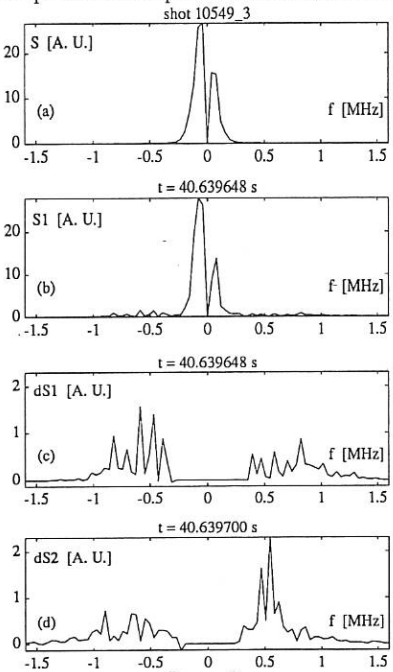

Figure 2

As turbulence during the crash has been seen to be enhanced mainly in high frequency range (.4 to 1.6 MHz), the following treatment, illustrated on figure 2, was done to discriminate this specific turbulence from broadband quasi-stationary one (QS) generally associated to anomalous transport. Four spectra corresponding to $k = 4$ cm^{-1} are plotted: (a) is the average spectrum performed before and after the crash to evaluate QS contribution (means over about 50 spectra), (b) $S_1(\omega)$ is performed during the first phase of the crash (for typically 50 μs), (c) is the 'specific' fluctuation spectrum $dS_1(\omega)$ obtained by computing the difference between (b) and (a); (d) $dS_2(\omega)$ is the specific one during the second phase, using the same procedure. Furthermore heterodyne detection allows determination of the direction of propagation of density fluctuations with negative frequency corresponding to fluctuations propagating in the $\vec{k}$ direction. The transient fluctuations appears either on positive or negative frequency side of the specific spectrum, depending on the sawtooth analysed.

As an $m = 1, n = 1$ mode is doubtless implicated in the sawtooth crash process, levels and propagation direction have been systematically related to direction of hot core motion θ, inferred from emissivity maps at the end of first phase: figure 1 (a) illustrates the case of an upward hot core displacement in the scattering experiment port nearly perpendicular to the analysed wave vector $\vec{k}$; corresponding specific spectra on figure 2 (c,d) show fluctuations flowing both along $\vec{k}$ and opposite to $\vec{k}$. The ratio of mean quadratic value corresponding to positive frequency side of specific spectrum (dS_+) over the whole integral level (dS) is used to quantify the information about the direction of propagation ($dS_+/dS \approx 0.5$ in the presented case).

Density fluctuation propagation direction during the crash.

The ratio dS_+/dS, plotted on figure 3 versus θ, shows a strong correlation between the propagation direction inferred from the spectra shape and kink-like motion; dashed lines indicate angles corresponding to kink-like motion towards the scattering volume intersection with $q = 1$ surface (see figure 5): as shown in figure 3 (a), during the first phase, fluctuations propagate mainly in the direction opposite to the hot core motion.

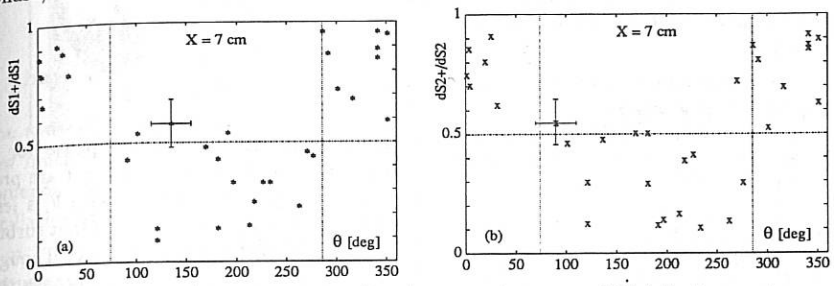

Figure 3 : Fluctuation propagation direction versus hot core poloidal displacement.

This is still the case during second phase (figure b); though hot core motion is no longer valid because of temperature collapse, we still relate fluctuation propagation direction to it as it is characteristic of the mode. Fluctuations seem to propagate towards colder zone of fast collapse of the temperature, which is seen on emissivity maps to invade the $q = 1$ surface from a side, quite opposite to the hot core location at the end of the first phase.

Spatial localisation of turbulence

On figure 4 is plotted the total fluctuation level dS_1 corresponding to a central chord of measurement, versus θ: turbulence level is strongly correlated with the poloidal position of the hot core at the end of the first phase; it can vary by a factor up to 6 to 10 and is roughly higher when the hot core coincides with the scattering measurement chord (for $X = 7$ as well as $X = 23$ cm). Levels are similar for motion towards interior and exterior ($\theta \approx 0°$ or $180°$), the slight difference being due to the 7cm shift of the scattering chord.

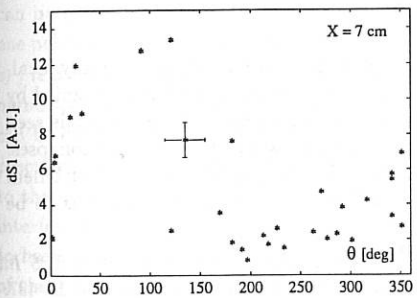

Figure 4: turbulence level versus θ (first phase)

Surprisingly there is an asymmetry between hot core moving upwards ($\theta \approx 90°$) and downwards ($\theta \approx 270°$), though both corresponds to a motion close to the scattering volume, in a symmetrical direction with respect to the equatorial plane. This could be explained by Doppler shift of specific spectrum due to plasma rotation ($v \approx V_{de}$) on either higher or lower frequency depending on the fluctuation propagation direction and localisation: due to kink motion, compression on $q = 1$ surface induces two fast flows along separatrix (figure 5): fluctuations propagate from hot core compression zone along q=1 surface at a velocity about 5-10 times larger than hot core motion, and are detected near hot core while their level and velocity are high enough compared to QS one:

on one side, fluctuations flowing against plasma rotation are seen on turbulent spectra in the QS turbulence frequency range and are not taken into account in our treatment. This hypothesis has been checked numerically, and agreement with both spectra shape and turbulence level behaviour versus θ is rather good (to be published).

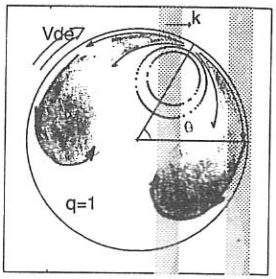

Figure 5: schematic vue of turbulence and scattering experiment geometry.

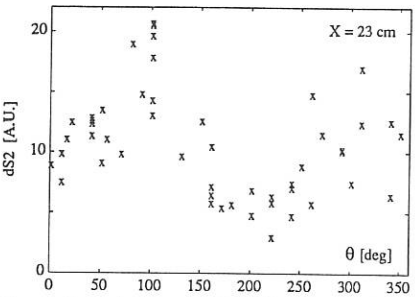

Figure 6: turbulence level (collapse phase)

Levels associated to collapse phase for a scattering chord located near $q = 1$ are presented in figure 6: variation with θ is less pronounced, probably indicating that turbulence is less localised at that stage. Though correlation with θ is less clear because the fast collapse zone is wide and not always in opposite direction to hot core motion, we can infer that maximum fluctuation level is reached when one side of the colder zone invades the observation volume, as if turbulence was located in the two frontier zones shown in grey on figure 5.

No enhanced turbulence has been observed for a chord passing outside $q = 1$ surface.

The enhancement of turbulence levels during collapse by a factor 50 to 200 compared to the QS one in the corresponding region shows that onset of turbulence could explain the fast heat transport outside $q = 1$ surface, which is two orders of magnitude higher compared to QS one. These density fluctuations can be the sign of magnetic and/or electrostatic turbulence; it is not elucidated whether they are associated to convection by plasma flow or conduction during the whole process.

Conclusion

Transient density fluctuations measured during the sawtooth crash are spatially localized within the $q = 1$ surface: initial kink-like motion of the hot core is accompanied by fluctuations flowing in opposite direction along $q = 1$; higher level of turbulence is seen during fast collapse, coming from two more central zones where temperature collapses. Theoretical models implying onset of stochasticity [5,6] have predicted some turbulent zone near destroyed $q = 1$ separatrix, but detailed dynamical behaviour still has to be clarified.

[1] M. A. Dubois and A. Samain. *Nuclear Fusion*, **20**, 1101, (1980).

[2] F. Gervais *et al. Proc. of the 16th EPS Int. Conf. on PPCF* (Venice 1989), Vol. II, 497.

[3] R. Nazikian *et al. Proc. of the 18th EPS Int. Conf. on PPCF* (Berlin 1991), Vol. I, 265.

[4] A. Truc *et al. Proc. of the 20th EPS Int. Conf. on PPCF* (Lisbonne 1993), Vol. II, 497.

[5] R. Sabot *et al. Proc. of the 14th IAEA Int. Conf. on PPCF* (Wurzburg 1992), Vol. I, 409.

[6] A. J. Lichtenberg *et al. Nuclear Fusion*, **32**, 495, (1992).

Measurement of m=1 Magnetic Field Perturbations during Sawtooth Activity in the TEXTOR Tokamak

H. R. Koslowski, H. Soltwisch*, and W. Stodiek†
Institut für Plasmaphysik, Forschungszentrum Jülich GmbH,
Ass. EURATOM-KFA, D-52425 Jülich, Germany

1. Introduction

The sawtooth activity is one of the unresolved problems in tokamak research. Up to now much work has been contributed to investigate the underlying physics of this phenomenon. One feature of the sawteeth commonly observed is the concomitant precursor oscillation starting some ms before the sawtooth collapse. This perturbation shows an $m = 1$ behaviour and is related to poloidally asymmetric deformations of the electron temperature and density distributions. The growth rate and spatial extension of this mode is often used as experimental evidence for different theoretical models. Most of the experimental work done so far is based on the analysis of the soft X-ray emission from the plasma core which is a well established diagnostic on nearly all tokamaks. The electron cyclotron emission as well as measurements of the electron density profile give additional information. On the TEXTOR tokamak we have extended the existing nine-channel interferometer/polarimeter by a horizontal probing beam with high time resolution. This allows us to detect also the magnetic perturbation field during the presence of the precursor oscillations.

2. The Horizontal Polarimeter at TEXTOR

A detailed description of the nine-channel FIR-interferometer/polarimeter at TEXTOR can be found elsewhere [1]. In brief, the plasma is probed with nine vertical channels in one poloidal cross section. Along each line of sight the line integrated electron density $\overline{n_e} = c_I \int n_e ds$ as well as the Faraday rotation angle $\alpha = c_F \int n_e \vec{B} \cdot \vec{ds}$ are measured. Applying numerical inversion procedures the local electron density and the poloidal magnetic field can be determined. In order to measure the displacement of the magnetic axis during the precursor phase an additional probing beam in the horizontal midplane has been added to the instrument. For technical details of this extension we refer to [2]. The horizontal interferometer and polarimeter are equipped with He-cooled InSb-detectors which prove to have an excellent signal to noise ratio. In addition, the application of digital filtering of the measured signals results in a time resolution for the Faraday rotation signal better than 100 μs. As a further option the beat frequency of the heterodyne system can be increased by frequency shifting the reference beam (i.e. the local oscillator) with a second rotating grating, thus allowing a time resolution up to $10 - 20$ μs in future experiments.

*Institut für Experimentalphysik, Ruhr-Universität Bochum, D-44780 Bochum, Germany
†Plasma Physics Laboratory, Princeton University, Princeton N.J. 08544, USA

3. First Experimental Results

Figure 1a shows a Poincaré plot of the magnetic field lines, where inside the $q = 1$ radius a helical perturbation of the form $\vec{B}_1 = \nabla \times (\vec{\xi} \times \vec{B}_0)$ has been added to the poloidal field component. The excursion of the magnetic axis is given by $\vec{\xi} = \xi_0(\cos(\theta - \varphi), \sin(\theta - \varphi), 0)$, $\vec{B}_0$ is the sum of the toroidal and the unperturbed poloidal field. The plot shows the typical $m = 1$ island structure. The near-circular flux surfaces inside the $q = 1$ surface are shifted towards the X-point. The solid lines represent the probing beams of the interferometer/polarimeter which are able to detect the island structure. Two channels of the vertical interferometer at major radius locations of $R = 175$ cm and $R = 185$ cm measure the electron density on both sides of the magnetic axis ($R_{mag} \approx 180$ cm for standard discharge conditions). The horizontal polarimeter and interferometer probe the plasma at $z = 0$ along a line through (or near) the magnetic axis.

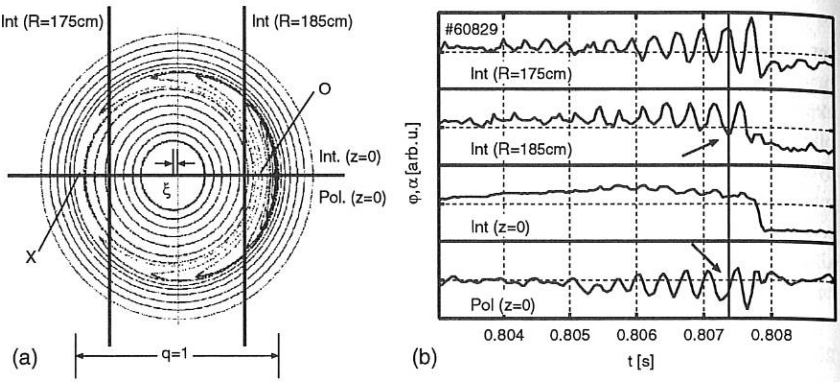

Fig. 1: (a) Poincaré plot of a model field structure with an $m = 1$ island and location of the probing beams (b) Interferometric and polarimetric measurements of a sawtooth in a standard OH discharge

In figure 1b typical data of the interferometer and polarimeter during the precursor phase of an OH discharge are displayed. The vertical interferometric probing beams at $R = 175$ cm and $R = 185$ cm show a modulation with opposite phase. The oscillations are due to the fact that the magnetic island rotates in the poloidal cross section, thus giving a signal modulation because of the difference in electron density at the X-point and the O-point, respectively. The horizontal interferometer signal exhibits only a small oscillation amplitude whereas the polarimeter signal (lower trace in figure 1b) has a pronounced modulation during the precursor phase. The latter may be expressed as

$$\alpha = c_F \int n_e \, \vec{B} \cdot \vec{ds} \sim \int n_{e0} \, \vec{B}_0 \cdot \vec{ds} + \int \tilde{n_e} \, \vec{B}_0 \cdot \vec{ds} + \int n_{e0} \, \vec{\tilde{B}} \cdot \vec{ds} + \mathrm{O}(\tilde{n_e}\vec{\tilde{B}}),$$

where the electron density and the magnetic field have been written as the sum of a time averaged and a time modulated quantity. The first term on the right hand side is

a constant Faraday rotation produced by the mean values of $\vec{B}$ and n_e, and the second term gives the modulation of the rotation angle caused by the modulation of the electron density. Both vanish if the alignment of the probing beam is exactly perpendicular to the toroidal and the unperturbed poloidal field. For the present setup it has been checked that contributions from incorrect alignment are small. The third term accounts for the varying magnetic field and is, therefore, important for the actual measurement. Here the modulation of the Faraday rotation signal is due to the rotation of the $m = 1$ perturbation field.

The vertical line in figure 1b makes clear that the modulation of the Faraday rotation angle exhibits a phase angle of 90° with respect to the line integrated electron densities measured along the vertical chords. A maximum or minimum of the interferometric measurement corresponds to a vertical orientation of the perturbing field, therefore the polarimetric measurement is zero. In the geometry of figure 1a the $m = 1$ perturbation rotates counter-clockwise[1]. The signal from the horizontal polarimeter has a positive sign if the plasma is shifted downwards and vice versa[2], or, in other words, it is positive when the X-point of the magnetic island is below the horizontal midplane. At the time marked in figure 1b the X-point crosses the horizontal midplane from top to bottom, i.e. the X-point is located at the high field side. The density measurement at $R = 185$ cm (low field side) shows a minimum. From this measurement we can conclude that the flat part of the density profile during the precursor phase is at the O-point of the island.

From earlier investigations of the precursor oscillation on the density and temperature signals we know that the flat parts of both profiles correspond to each other [3], i.e. the flattening of the temperature profile is at the O-point of the island, too. Therefore the SXR signals should normally show the same behaviour. This has been assumed so far for the interpretation of the measured data and is now confirmed by the polarimetric measurement.

Figure 2a shows a time trace of the horizontal polarimeter during the flat top phase of an OH discharge. The precursor oscillations grow up to amplitudes of about $0.2° - 0.3°$ and vanish after the sawtooth crash. In figure 2b the amplitude of the mode oscillation is plotted as a function of the time difference prior to following sawtooth crash. The data from many sawtooth events under the same discharge conditions are collected. The solid line represents an exponential fit to the data. The growth rate of the $m = 1$ mode is about 600 s^{-1}. The precursor amplitude at the start of the sawtooth crash is 0.26°. If we approximate the Faraday rotation angle by $\alpha = c_F n_{e1} \overline{B_1} d_1$ where n_{e1} is the average electron density within the $q = 1$ surface, d_1 its diameter, and $\overline{B_1}$ is the average perturbation field along the intersection of the line of sight and the $q = 1$ surface, we get an average field strength of $\overline{B_1} = 110$ G. The shift of the plasma core corresponding to this mode amplitude is about 1 cm. Assuming a smooth q-profile with $q_0 \approx 0.75$ and without a local flattening at the $q = 1$ surface, the corresponding island width is a small

[1]The sense of rotation has been measured with two soft X-ray cameras in one poloidal cross section of the plasma. (G. Fuchs, private communication)

[2]This has been checked by running a discharge with a programmed vertical displacement

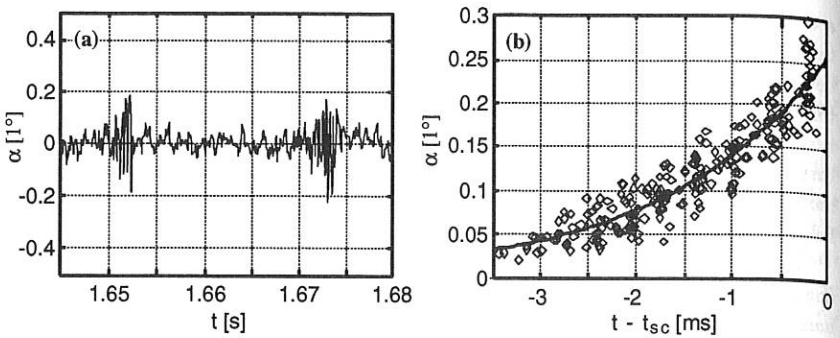

Fig. 2: (a) Sawtooth precursor oscillations measured with the horizontal polarimeter (b) ◇ amplitude of the precursor vs the time prior to the sawtooth crash — exponential fit to the data

fraction of the $q = 1$ radius ($w/r_1 \leq 0.25$). Under these conditions full reconnection is not likely to occur. This conclusion is in agreement with previous measurements according to which the central safety factor increases by only 6% from before to after the sawtooth crash interval in a standard Ohmic discharge [4, 5].

4. Conclusion

First results from the new fast horizontal polarimeter at TEXTOR show that the flat part of the density profile is at the O-point of the island. The magnitude of the magnetic $m = 1$ perturbation in OH discharges at the time of the sawtooth crash is about 110 G for the average perturbation field. The perturbation field has a growth rate of about 600 s^{-1}. Further investigations covering the whole range of operating conditions as well as measurements with improved time resolution are underway at present.

References

[1] H. Soltwisch, *Rev. Sci. Instruments* **57** 1939 (1986)

[2] A. Cosler, E. Kemmereit, and H. Soltwisch, *Proc. 15th IEEE/NPSS Symp. on Fusion Engineering*, vol. 1, p. 93 (1994)

[3] H. R. Koslowski and A. Krämer-Flecken, *Proc. 19th Eur. Conf. on Controlled Fusion and Plasma Physics*, Innsbruck, Vol. I, p. 383 (1992)

[4] H. Soltwisch, W. Stodiek, J. Manickam, J. Schlüter, *Proc. 11th International Conf. on Plasma Physics and Controlled Nuclear Fusion Research*, Kyoto 1986, Vol. 1, p. 263, IAEA, Vienna

[5] H. Soltwisch, H. R. Koslowski, *Plasma Phys. Control. Fusion* **37** 667 (1995)

Runaway Electrons in the ASDEX Upgrade Tokamak - A Free Electron Maser

B Kurzan, KH Steuer, W Suttrop, G Fußmann, ASDEX Upgrade Team
IPP Euratom Association, Boltzmannstr. 2, 85748 Garching, Germany

1 Introduction

The dynamics of runaway electrons in tokamaks is governed by the acceleration in the toroidal electric field, the deceleration by synchrotron radiation losses, collisions and the ripple resonance mechanism. The last effect generates a relativistic monoenergetic electron beam, which can amplify the spontaneously emitted radiation of the runaways as a free-electron maser.

2 Dynamics of runaway electrons in tokamaks

Runaway electrons in a tokamak plasma are being accelerated in the toroidal electric field, decelerated by the emission of synchrotron radiation and they collide with the plasma particles. In this paper we show, that a resonance between their gyromotion and the ripple of the magnetic field, which for highly relativistic electrons is $(n\,N_{Coil}\,c)/R = (e\,B)/(\gamma_n\,m_e)$ (n: toroidal harmonic of the ripple, N_{Coil}: number of main field coils, which is 16 on ASDEX Upgrade, c: speed of light, R: major radius of the tokamak, e: elementary charge, B: magnetic field, γ_n: relativistic gamma factor of the runaways, m_e: electron rest mass) determines their final energy. This is found when investigating their Bremsstrahlung spectra on ASDEX (fig. 1). In a ripple resonance Lorentz forces due to the ripple field perpendicular to the drift

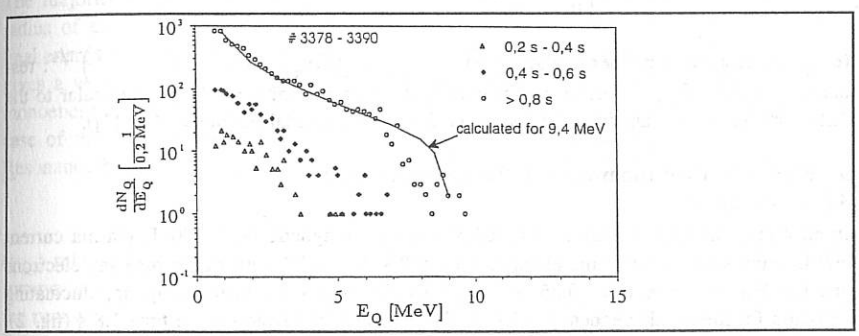

Fig. 1: The Bremsstrahlung spectra of runaways in ASDEX generated at the beginning of the discharges and hitting a tungsten target grow harder with time. From 0.8 s on the spectrum is stationary and can be explained by monoenergetic runaway electrons of energy 9.4 MeV, *which is resonant with the 7th harmonic of the magnetic ripple (*B = 2.2 T*)*

surfaces increase the gyromotion and decrease the guiding centre velocity, which is nearly parallel to the magnetic field. If the ripple harmonic is so strong that the gyration velocity and thus the pitch angle are increased so much while passing over the resonance that the synchrotron radiation losses equal the energy gain in the electrical field, the runaways are not further accelerated. In ASDEX Upgrade the resonant interaction of the gyromotion with the

ripple field is not randomized by an overlap of neighbouring resonances as suggested by [1] and thus quasilinear diffusion of the gyration momentum, since here due to the small ripple the resonances do not overlap. Pitch angle scattering by collisions of the runaway electrons with the plasma particles randomizes the phase difference between the gyromotion and the magnetic ripple field sufficiently for the motion of the runaway electrons to be described very well by an analytic diffusion coefficient for the pitch angle. The dynamic of the runaways in a tokamak is described by the relativistic Fokker-Planck equation

$$\frac{\partial f}{\partial t} + \frac{\partial}{\partial \vec{p}} * \left[\left(\vec{F}_E + \vec{F}_C + \vec{F}_S + \vec{F}_R \right) f \right] = 0 \tag{1}$$

(f: distribution function, $\vec{p}$: momentum vector of the runaway electrons) with the electrical force $\vec{F}_E$, the friction force $\vec{F}_C$ [2], the retarding force $\vec{F}_S$ due to incoherent synchrotron radiation [3] and the diffusive flow of the pitch angle due to ripple resonance,

$$\vec{F}_R f = m_e c \frac{\sqrt{1-\mu^2}}{q} \frac{\partial}{\partial \mu} \left(q^2 D_{\vartheta\vartheta R} f \right) \vec{e}_\vartheta \tag{2}$$

($\mu = \cos(\vartheta)$, with ϑ as pitch angle, $q = |\vec{p}| / (m_e c)$, $\vec{e}_\vartheta$: direction of increasing pitch angle) with

$$D_{\vartheta\vartheta R} = \begin{cases} \frac{\pi}{32} \frac{eB}{m_e \sqrt{q^2+1}} \left(\frac{\delta B_{nm}}{B} \right)^{\frac{3}{2}} \frac{\sqrt{\mu}}{\left(1-\mu^2\right)^{1/4}}, \\ \qquad \text{if } |\, q - q_{nm}(\mu)\, | < \Delta q_{nm}(\mu) \\ 0 \quad \text{else} \end{cases} \tag{3}$$

($q_{nm}(\mu)$: resonance momenta, $\Delta q_{nm}(\mu) = q_{nm}(\mu)\left[(\delta B_{nm}\,\mu)/B\right]^{1/2}\left(1-\mu^2\right)^{1/4}$: resonance widths, δB_{nm}: Fourier coefficients of the magnetic ripple field perpendicular to the drift surfaces of the runaways for the toroidal (n) and poloidal harmonics (m) [1]).

3 Energy-blocked runaways - A free electron maser

3.1 Observation

In an ohmic divertor discharge in ASDEX Upgrade (magnetic field 2.90 T, plasma current 600 kA, line-averaged thermal electron density $3 * 10^{19}\ m^{-3}$) containing runaway electrons generated at the time $t = (0.35 \pm 0.01)$ s by delaying the density ramp up, fluctuating emission (spikes) with frequency (116 ± 4) GHz starts to develop at the time 1.8 s (fig. 2). Spikes at other frequencies of the microwave region develop in discharges with other values of the plasma density and the magnetic field. This phenomenon has not yet been explained.

3.2 Interpretation

Simulating the dynamics of the runaways for the discharge discussed with the Fokker-Planck equation (1) gives different final energies of the runaways depending on the position of their drift surfaces in the plasma: The runaways near the plasma centre are not captured in a ripple resonance, because of the small ripple there. At the plasma edge the runaways are energy blocked in a high toroidal harmonic of the ripple, which is very strong there, corresponding to a low final energy of the runaways. With [4] one can assume a near parabolic density profile

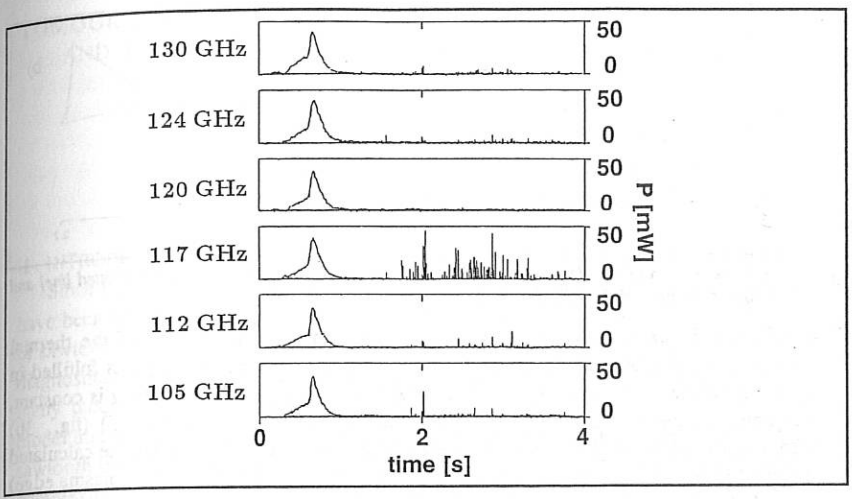

Fig. 2: The contimous emission in the first second of the discharge stems from the just generated suprathermal electrons. With increasing energy of the runaways this emission is shifted to higher frequencies. When the runaways have reached their maximal energy, fluctuating emission (spikes) starts to develop in the channel, which is sensitive to radiation with frequency 117 GHz. *Since in the neighbouring channels the intensity of the spikes is much lower, the emission frequency is* (116 ± 4) GHz .

for the runaways. So these calculated energies apply only to a minority of the runaways. The majority of the runaways, located at about the small plasma radius $a/\sqrt{3}$ (a: minor radius of the plasma), is captured in the 8th toroidal ripple resonance, corresponding to a final energy of 11.5 MeV. Solving the stationary Fokker-Planck equation ($\partial f/\partial t = 0$ in (1)) gives a very narrow energy spread of the runaways ($\Delta E/E \approx 8 * 10^{-3}$). This extremely monoenergetic runaway beam can amplify radiation as a free-electron maser, which in the case of the runaways gyrating in the magnetic field of the tokamak is a Cyclotron-Auto-Resonance-Maser (CARM) [5]. The frequency of the amplified resonant radiation is

$$\nu = \frac{\nu_{ce}}{1 - n\,\beta\cos(\vartheta_M)} \qquad (4)$$

(ν_{ce}: relativistic gyration frequency of the runaways, n: refractive index, β: velocity of the runaways, normed to the speed of light, ϑ_M: pitch angle, where the distribution function of the runaways in momentum space has its maximum). The radiation can be amplified only, if the electromagnetic wave moves along the drift velocity of the runaways for a sufficient long time. Since the width $1/\gamma$ rad = 0.04 rad of the radiation cone emitted along the direction of the momentary velocity of the runaways is smaller than the pitch angle $\vartheta_M \approx 0.2$ rad, the spontaneously emitted radiation cannot follow the resonant runaways for a sufficient long time. The electromagnetic wave of frequency (4), which is emitted in the direction of decreasing refractive index (fig. 3a) is bent to the tangential direction after a radial displacement of about 1 cm. This displaced radiation can be amplified, if the resonance frequency does not change with the position, $\vec{\nabla}\nu = 0$. The refractive index must then vary as:

$$(\partial n/\partial z)_p = 0\,, \quad (\partial n/\partial R)_p = \left[1/\left(\beta\cos\left(\vartheta_M\right)\right) - n\left(\vartheta_M, R\right)\right]/R\,. \qquad (5)$$

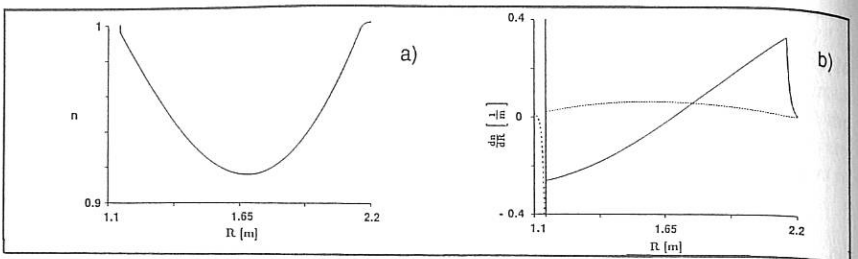

Fig. 3: refractive index n of the plasma at 116 GHz *(a), comparison between the postulated (dotted line) and the real change (solid line) of the refractive index with the major radius (b)*

The refractive index for a cold plasma [6] depends on both the density of the thermal electrons and the magnetic field. Since the latter does not change with z, (5) is fulfilled in the equatorial plane of the plasma, where the flux surfaces, on which the density is constant, are tangential to the z-direction. Comparing the real change $\partial n/\partial R$ with (5) (fig. 3b) gives to major radii, where both meet. However only at the outer plasma edge the calculated frequency (122 $\pm$ 9) GHz (runaway energy 11.5 MeV, $\vartheta_M = 0.207$ rad at the plasma edge) agrees with the observed frequency (116 $\pm$ 4) GHz. This resonant position exists only for an exponentially decaying thermal electron density (Scrape-off layer), as observed on ASDEX Upgrade. It is deduced from the spectral width $\Delta\nu_{1/2} \lessapprox 4$ GHz, that the monochromatic wave puls is so long [7], $L_P \gtrapprox \nu/\left(\Delta\nu_{1/2}\right)(c/\nu_{ce}) = 3.2$ m, that it must be bent along the runaway path for the time of amplification. This so-called optical guiding is inherent in the free-electron maser mechanism [7]. The finite length L_P is due to the loss L of the curved guided wave, $L = \exp(-c\,t/L_P)$. The gain G of the maser increases with the density of the runaways. For an overall amplification bigger than one, the loss must be compensated by the gain, $G * L > 1$. This gives the lower limit $n_R \gtrapprox 2 * 10^{13}\ m^{-3}$ for the density of the runaways. This is much lower, than the line-averaged density of $3 * 10^{14}\ m^{-3}$ obtained from measuring the Bremsstrahlung intensity of the runaway electrons inside the vessel. So the density profile of the runaways is peaked.

4 Conclusion

The dynamics of runaway electrons in tokamaks is describable by a relativistic Fokker-Planck equation. Solving this equation gives the maximal energy of the runaways. This is especially important for the planned ITER tokamak.

References

[1] L. Laurent, J. M. Rax, Europhysics Letters 11 (3), 219 (1990)
[2] J. W. Connor, R. J. Hastie, Nuclear Fusion 15, 415 (1975)
[3] J. Schwinger, Physical Review 75 (12), 1912 (1949)
[4] O. J. Kwon et al., Nuclear Fusion 28 (11), 1931 (1988)
[5] S. K. Ride, W. B. Colson, Appl. Phys. Let. 54 (14), 1302 (1989)
[6] T. H. Stix, Waves in Plasmas (American Institute of Physics, New York, 1992)
[7] J. B. Murphy, L. Pellegrini in *Laser Handbook, Vol. 6*, edited by W. B. Colson, C. Pellegrini, A. Renieri (Elsevier Science Publishers B. V., 1990)

TOMOGRAPHY RESEARCH FOR SAWTOOTH CRASH MECHANISM AND INFLUENCE OF THE BIASED ELECTRODE ON SAWTOOTH BEHAVIOR IN HL-1

J.F.Dong, G.C.Guo, Y.Z.Zhong, L.W.Yan, Z.H.Wang,
Q.D.Gao, L.B.Ran, E.Y.Wang, Y.Liu, G.Yang and B.Z.Fu
(Southwestern Institute of Physics, Chengdu, Sichuan, 610041)

I. INTRODUCTION

Since the plasma sawtooth phenomena were observed in 1974 ,the sawtooth oscillations have been an important subject related to confinement and heating process. Different types of sawtooth oscillations in tokamaks have been studied by soft x-ray diode arrays and other diagnostics[1]. In order to explain the crash mechanisms of different sawtooth oscillation, many theoretical models have been proposed, for example Kadomtsev model, Wesson model and Sato-Hagayama model and so on. These theoretical models have explained some sawtooth oscillation phenomena, but they can't explain all sawtooth oscillations due to the complexity of sawtooth phenomena. Accompanying the development of the soft x-ray tomographic technique and application of the new measurement methods, e.g., current density profile, the study on the sawtooth crash mechanism is caused stronger interest once again.

Different types of sawtooth oscillations have been observed during HL-1 tokamak discharges for eight years. In this paper, two kinds of sawteeth collapse mechanism have been studied by two-dimension tomographic code[2] , and the influence of the biased electrode on sawtooth behavior have been abserved in HL-1.

II .TOMOGRAPHY OF CRASH PROCESSES FOR TWO TYPES OF SAWTEETH

We have observed sawtooth-like, monster sawtooth in the HL-1 tokamak plasma[3] . Their collapse mechanisms are analyzed initially by the tomographic method in this section.

1) Reconstruction For Sawtooth-like With m=2 precursor oscillations

Fig.1 shows the soft x-ray emission signals which are transiting into the sawtooth-like from normal sawtooth under higher density discharge. As compared with normal sawtooth, both the inversion radius and the period of the sawtooth-like oscillation are larger than that of normal sawtooth. When the sawtooth-like oscillation appearing, the MHD perturbation measured by magnetic probes are enhanced rapidly. The modes of located at the symmetry two sides to plasma center are in phase,so they have m=2 mode structure. According to theoretical analysis, the development and evolution of magnetic islands for m=2/n=1 and m=3/n=2 have been calculated by the interaction between quasi-linear tearing mode and impurity radiation and may produce the similar relaxation[4]. It indicated that the m=2 MHD instability play an important role in the sawtooth-like crash.

The crash process of sawtooth-like have been reconstructed by the tomographic technique in Fig.1, and the relevant discharge parameters are as follows:

R=102cm, a=18cm, B_T=2.4T, I_p=128kA, $\bar{n}_e=5.4*10^{13}cm^{-3}$

Firstly, the hot core is at the plasma center and the plasma temperature is peak in Fig.1(a). In Fig.1(d,e,f,g), a hydrodynamic flow with a cold bubble exists in plasma and moves from the outside into the center of plasma with a velocity about 1700m/s. Secondly, the hot core is broken into two parts, then the cold bubble is expanded, and pushes the hot core out toward the plasma edge continuously. Finally, the hot core becomes into two crescent. The temperature of the cold bubble rises gradually due to the ohmic heating and forms a new hot core. According to the Wesson model, the flow is a convective which is caused by a quasi-interchange mode instability. The convective flow leads to crash. In the Sato-Hagayama model[5], the reconnection of magnetic field lines is driven by a kink flow. The plasma inside the new flux surface is ohmically heated and becomes a new hot spot.

2) Reconstruction For The Monster Sawtooth

The monster sawteeth with 44*ms* in the HL-1 Ohmic discharge have been observed. They appeared during high density discharges with strong gas puffing.

Discharge parameters with monster sawteeth are as follows:

B_T=2.3T, I_p=110kA, $\bar{n}_e$=6.9*10^{13}cm^{-3}

Fig.2 is soft x-ray reconstruction image of the monster sawtooth oscillation from the HL-1 tokamak plasma and the region of each frame is $x=-13.3cm \rightarrow +13.3cm$ and $y=-13.3cm \rightarrow +13.3cm$.In Fig.2, a cold bubble dashed into the plasma center quickly along with a flow and pushed the original hot core outwards. The cold bubble growed gradually and led to the temperature dropping and flatting of core plasma within larger area (see frame *b,c,d,e,f*). The original hot core is pressed to out of the $q=1$ surface, next the $m=2/n=1$ mode structure appears, and then the core plasma is ohmically heated, finally becomes a new hot spot gradually, while the original hot core becomes two cold crescent (see frame g,h,i,j,k). The reconstruction results for the crash process of the monster sawtooth are in accordance with MNPHOB's model basically[6] .

The sawtooth oscillation limited the heating and confinement to the core plasma. Once the oscillation is suppressed, the energy confinement time will go up 20% and increase greatly the ratio of the fusion reaction,which becomes into an important subject,especially for monster sawtooth. It stimulates people to try to find out the reasons why the sawtooth is stabilized. The accumulation of the impurity at the plasma center makes it possible that the central current density distribution become hollow and lead to the $q(0)$ larger than 1,which stabilize the growth of $m=1$ mode. It may be an explanation why the monster sawtooth is formed in HL-1 tokamak plasma .

III. THE INFLUENCE OF THE BIASED ELECTRODE ON SAWTOOTH BEHAVIOUR

The influence of the biased electrode on sawtooth behavior have been studied in HL-1.The L-H transition is triggered by setting up positive radial electric field in the edge by means of electrode .Simultaneously,with the increase of energy confinement the sawtooth periods are apparently prolonged. The reduction of the electron thermal conductivity, χ_e ,which deduced from the propagation of the heat pulse induced by sawtooth in the biasing phase,is observed,and the reduction of $\chi_e$at the low field side is more than the one at the high field side(Fig 3), this indicating that the effect of bias on the confinement at low

field side is stronger than the one at the high field,i.e., the improvement in confinement with H-mode is poloidally asymmetric,with the greatest improvement occurring on the low field side.The improvement in energy confinement is corresponding with the reduced electron thermal conductivity and the prolonged sawtooth period.

REFERENCES

[1] K. Mcguire, Callen J.D., et al European Physical Society,134(1985).

[2] J. F. Dong , et.al., Nuclear Fusion and Plasma Physics (in Chinese), 11(4), 246(1991).

[3] G. C. Guo, et al., "HL-1 Soft X-ray Tomography and the Study of the Plasma Sawtooth and the Mode Activity", Private Communication (1993).

[4] L. W. Yan, et al., Nuclear Fusion and Plasma Physics (in Chinese),10(2),112(1988).

[5] Y. Hagayama, Phys.Rev.Lett., 61(16), 1839(1988).

[6] С.В. МИРНОВ, "ФИЗИЧЕСКИЕ ПРОЦЕССЫ В ПЛАЗМЕ ТОКАМАКА" (1983).

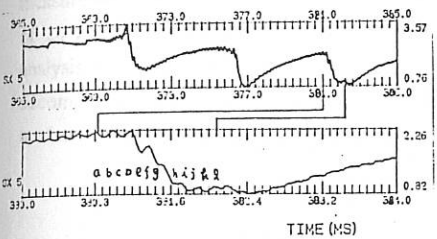

Fig 1. Tomographic reconstruction image of the sawtooth-like during the m=2 precurser oscillations.

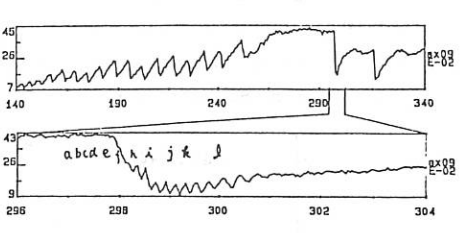

Fig 2.Contour plots of the soft x-ray during a mouster sawtooth crash.

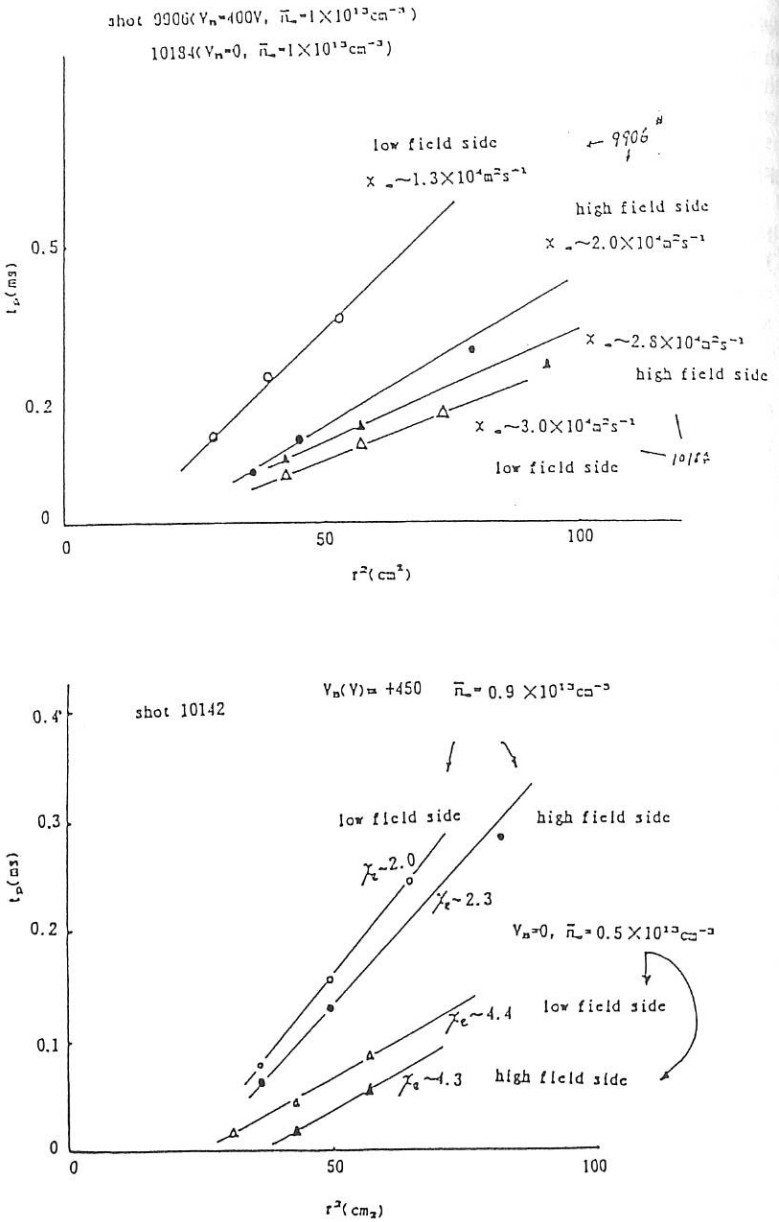

Fig.3 Arrival time of heat pulse peak on high (full dots) and low (open dots) field sides versus r^2.

LOCKED MHD-MODES IN T-10 TOKAMAK

Ivanov N.V., Kakurin A.M., Kovrov P.E., Martynov D.A., Novikov A.Yu., Volkov V.V.
RRC "Kurchatov Institute", Nuclear Fusion Institute
Ploschad Kurchatova, 1, Moscow, 123182, Russia

1. Introduction

The mode-locking phenomenon was investigated both at the current ramp-up stage of the discharge and at the stage of the current plato. Under the measurements the main attention was paid to rotation and locking of the poloidal magnetic field perturbations at plasma edge.

2. Experimental arrangement

The experiments were performed in OH and second-harmonic-ECRH discharge regimes differing in safety factor q(a)=2-4 and line-average plasma density $\overline{n}_e=(0,5\text{-}4)\cdot10^{13}cm^{-3}$. Various scenarios of current ramp-up and gas puffing were used. The measurements of the poloidal magnetic field perturbations have been carried out with an array of 24 magnetic probes uniformly disposed along the minor bypass of the torus. For data analysis a computer code has been developed which allowed to perform the spatial Fourier decomposition of the perturbations and to calculate angular velocities of the separated MHD-modes rotation.

3. Experimental results

3.1. Low-density discharges

A well reproducible low-density ($\overline{n}_e=1\cdot10^{13}cm^{-3}$) regime with q(a)=2.75 was chosen for the mode-locking investigations. The regime was characterized by a periodical repetition of the m=2 mode locking during the whole quasi-stationary stage of the discharge. Each mode-locking event was accompanied by a rise of the mode amplitude and by a minor disruption. A typical dependence of the inverse value of the m=2 mode instant frequency upon time and poloidal phase of the mode for this regime in case of Ohmic heating is shown in Fig.1(a). Note that the mode-locking takes place at the mode poloidal phase values approximately constant for all the mode-locking events. It means that the magnetic island structure rotation periodically interrupts at certain spatial positions.

In this regime the central ECR heating resulted in a significant acceleration of the m=2 mode rotation and in the mode-locking suppression, as it is shown in Fig.1(b). Along with the rise of the mode frequency a decrease of the mode amplitude was observed. The ECRH effect on the m=2 mode frequency was stronger at higher values of the absorbed EC power and at lower values of the plasma density, as it is shown in Fig.2. The effect of the ECR heating on

the mode rotation depended on the toroidal magnetic field and on the corresponding position of the second harmonic ECR layer in plasma (see Fig.3). An appreciable rise of the m=2 mode frequency was observed in the case of central ECR heating. In the cases of the plasma periphery heating this effect decreased and probably changed its sign.

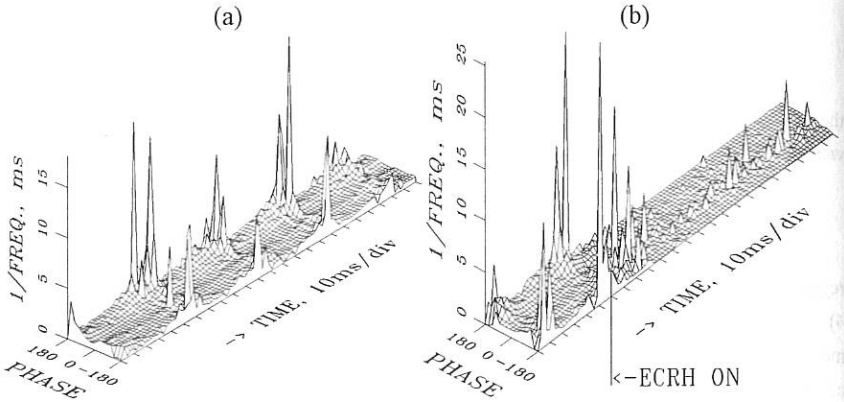

Fig.1. The time variation of the dependence of inverse value of the m=2 mode instant frequency on the poloidal phase of the mode: in OH discharge (a) and under central ECR heating (b). Unintegrated signals of the magnetic probes were used. Each peak corresponds to a strong decrease of the mode frequency, i.e. to the mode-locking event.

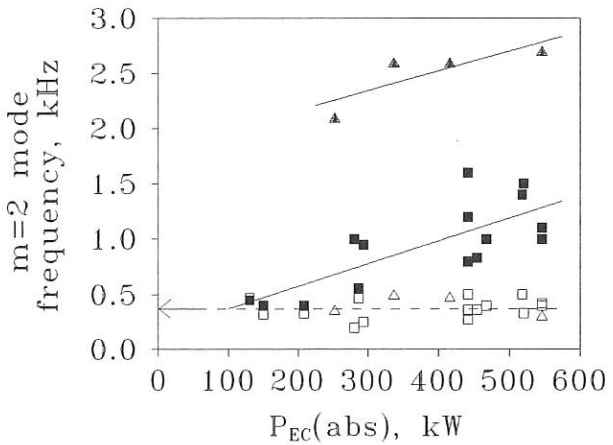

Fig.2. The dependencies of the m=2 mode frequency variation under ECRH upon the absorbed EC power at two plasma density ranges: $\overline{n}_e=(0.7\text{-}0.8)\cdot10^{13}cm^{-3}$ *(open triangles - before, filled triangles - under ECRH);* $\overline{n}_e=(0.8\text{-}1.1)\cdot10^{13}cm^{-3}$ *(open squares - before, filled squares - under ECRH).*

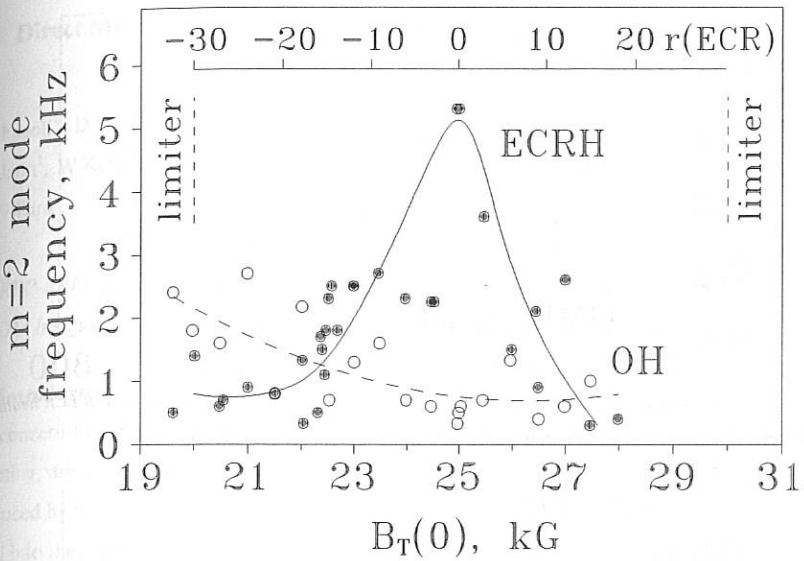

Fig.3. The time-average (over 10 ms) m=2 mode frequency versus toroidal magnetic field and corresponding position of the second harmonic ECR layer: open circles - Ohmic regime, filled circles - ECRH regime.

3.2. Low q(a) discharges

In Ohmically heated T-10 plasma with $\overline{n}_e=(3\text{-}4)\cdot10^{13}cm^{-3}$ the lowest achievable value of the cylindrical safety factor, q(a)=1.9, was determined by the m=2 mode-locking and subsequent major disruption at the current ramp-up stage of the discharge. Under the input ECRH power more than 0.5 MW the central auxiliary heating allowed to avoid the mode-locking and the subsequent major disruption at q(a)=1.9 and to reach the plasma current value at the quasi-stationary stage of the discharge, corresponding to q(a)=1.8. In these experiments the auxiliary heating was applied 100 ms before the achievement of the q(a)=1.9 value. In cases of approximately equal ECRH power, the total ECRH effect on the discharge development depended on the heating duration, as it is seen in Fig.4. In conditions of a sufficiently long ECRH pulse, plasma remained stable at the quasi-stationary stage of the discharge even after the end of the ECRH.

As it is shown in Fig.5, the central ECR heating allowed to restore the discharge after the beginning of the current-quench in the mode-locking induced major disruptions.

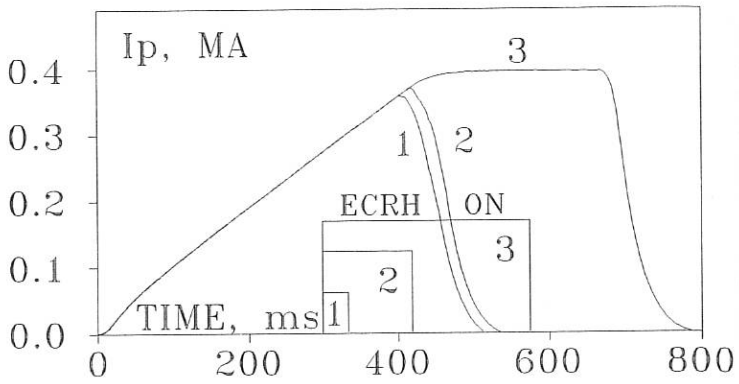

Fig.4. The time evolution of the plasma current in three tokamak discharges, differing in central ECR heating duration. The time duration of the auxiliary heating application is indicated by rectangles.

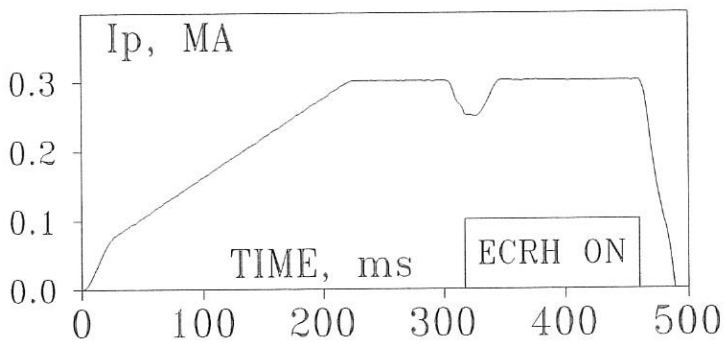

Fig.5. The time evolution of the plasma current in a discharge with the central ECRH applied in the current-quench stage of a mode-locking induced major disruption.

4. Conclusions

The presented experimental results can be explained from the existing point of view that the rotation of the magnetic islands in tokamak plasma is determined by a number of different competitive factors. The error-fields of the tokamak magnetic system contribute to the slowing-down of the MHD-mode rotation and can cause the mode-locking in definite spatial positions.

The effect of the central auxiliary heating on the mode-locking phenomenon can be probably attributed to an increase of the plasma pressure gradient in the vicinity of the resonant magnetic surface and hence to a strengthening of the factors, accelerating the magnetic islands rotation, i.e. the electron diamagnetic drift and plasma drift in the radial electric and toroidal magnetic fields.

Direct Measurement of TAE, EAE and Multiple Kinetic TAE in JET

A.Fasoli[1], D.Borba, N.Delyanakis, J.A.Dobbing, D.J.Campbell, C.Gormezano, J.Jacquinot, A.Jaun[1], W.Kerner, H.Holties[2], P.Lavanchy[1], J.B.Lister[1], J.-M.Moret[1], L.Porte, S.Sharapov, L.Villard[1]

JET Joint Undertaking, Abingdon, Oxfordshire, OX14 3EA, UK

[1]*CRPP-EPFL, Ass. Euratom-Swiss Confederation, 21 av. des Bains, CH-1007 Lausanne*

[2]*FOM Institute for Plasma Physics, Rijnhuizen, Nieuwegein, Netherlands.*

1. Introduction

A concern for tokamak reactors is that alpha particles, providing the main source of plasma heating, drive Alfven Eigenmodes (AE) unstable and in turn be subject to anomalous transport induced by these modes [1]. Experimental investigations into the AE linear stability properties and into the features determining their effects on particle orbits appear necessary.

2. The JET AE Active Diagnostic

To obtain this information a new AE active diagnostic has been developed at JET, combining excitation by external antennas with coherent detection of various probing signals, including the impedance of the driven saddle coils, the voltage on non excited saddle coils and magnetic coils, 8 ECE and 8 reflectometer signals [2]. The JET saddle coils are driven by a 3 kW amplifier in the range 30-300 kHz. The antenna currents (<30 A) generate low-n magnetic perturbations much smaller than those predicted to affect the particle transport significantly.

3. TAE and EAE Excitation and Identification

Many global AE have been driven in the frequency range from 50 kHz to 300 kHz and identified as Toroidicity or Ellipticity induced AE from their frequency dependence on density and magnetic field. The eigenmodes appear as resonances in the antenna/detector transfer function. The corresponding poles and residues provide the mode frequency, the total damping rate, $\gamma = \gamma_{damping} - \gamma_{drive}$, and the spatial structure. In Fig. 1 we see an example of a driven AE resonance, with the identification of the observed mode as a TAE being presented in Fig. 2.

4. Direct Measurement of TAE/EAE damping rates

Damping rates were measured in a wide variety of conditions, with 1 MA$<I_p<$3 MA, $1x10^{19}$ $m^{-3}< \bar{n}_e <5x10^{19}$ m^{-3} and 1 T$<B_{tor}<$3.5 T [2]. The results with both odd and even low-n

excitation span several orders of magnitude, from $\gamma/\omega < 0.1\%$ to $\gamma/\omega > 10\%$, suggesting that different absorption mechanisms dominate according to the configuration of each specific shot. Greatly differing damping rates were measured in similar discharges with different profiles of g $= 1/(q\rho^{1/2})$, the function determining the AE gap alignment and hence the significance of continuum damping (Fig. 3). With a strong radial dependence of g(r) (a), strong continuum damping occurred with $\gamma/\omega \sim 5\%$. g(r) in curve (b) was flatter and led to a more 'open' gap structure with much less damping.

5. AE spectrum in heated plasmas: kinetic AE

AE experiments have also been undertaken in additionally heated plasmas, to extend the parameter range for the damping measurements, to assess the driving effects of resonant fast particles and to study the AE spectrum in the presence of non-ideal MHD effects. A sudden change was observed in the spectra as T_e, T_i , T_e/T_i and the magnetic shear were increased by means of high current ohmic heating, NBI, Lower Hybrid Heating (LHH), ICRH, or fast plasma current ramps. This transition appeared clearly in high current ohmically heated plasmas (Fig. 4). The single peak TAE observed for low I_p is transformed into a multiple structure of less damped peaks at higher I_p, corresponding to a hotter plasma. As these modes are externally driven with $|n|=2$, with negligible plasma rotation, they cannot correspond to Doppler shifted peaks of different n. Similarly, multiple resonances with the same toroidal mode number characterised the spectrum of driven magnetic and density perturbations in the TAE range with LHH and moderate ICRH (Fig. 5). This first observation of driven density perturbations emphasises the non-ideal MHD character of the modes. Comparable spectra in the TAE/EAE gap frequency range, with similar peak frequency spacing, resonance width and mode numbers, have been driven during discharges with other additional heating methods. In most cases the observed structures consisted of several resonances with regular frequency spacing and damping rates significantly lower than for the corresponding 'cold' TAE. As they appear in experimental conditions which correspond to the predicted departure from ideal MHD behaviour due to kinetic effects, the observed modes are identified as kinetic AE [4].

6. Excitation of AE by non-linear beating of ICRH waves

The excitation of AE by ICRH beat waves was investigated experimentally. The frequencies of two different ICRH modules were mixed together to produce a beat wave signal at Δf, then used as the reference of the AE synchronous detectors. TAE were excited when Δf coincided

with the TAE gap centre frequency (Fig. 6). The relatively large amplitudes for the TAE driven by ICRH beat waves suggest that this non-linear excitation method could allow investigations into the effects of AE on particle orbits and should be taken into account in ICRH heated thermonuclear plasmas.

7. Conclusions

The successful implementation of a new active diagnostic for AE has allowed us to drive TAE and EAE in linearly stable conditions and to measure, for the first time, their damping rates in a variety of plasma conditions. Weakly damped, multiple kinetic AE have been excited and detected in the TAE/EAE gap frequency range on the JET heated plasmas. Resonant excitation of TAE by ICRH beat waves has also been demonstrated experimentally. The combination of these linear and non-linear studies should provide insight into the AE stability and their effects on alpha particles' dynamics in future ignition experiments.

The Authors would like to thank the JET Team for experimental support. This work was partly supported by the Fonds National Suisse pour la Recherche Scientifique.

References

[1] C.Z.Cheng, L.Chen, M.S.Chance, *Annals of Physics* **161**, 21 (1985).
[2] A.Fasoli et al., *Phys. Rev. Lett.*, in press (1995).
[3] D.J.Sigmar, C.T.Hsu, R.White and C.Z.Cheng, *Phys. Fluids B* **4**, 1506 (1992).
[4] R.R.Mett and S.M.Mahajan, *Phys. Fluids B* **4**, 2885 (1992).

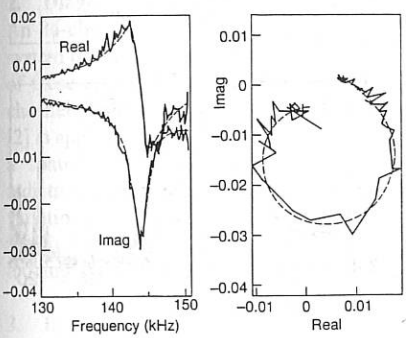

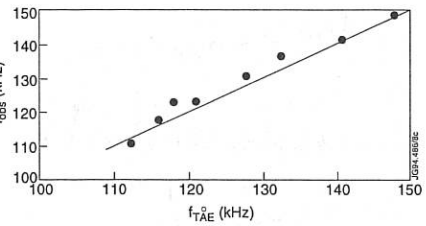

Fig. 2 Measured eigenfrequency vs $f_{TAE}^{0}=v_A/2\pi qR$, the TAE gap centre, calculated for q=1.5 (#31591). B_{tor} was varied linearly between 2.2 and 3 T.

Fig. 1 TAE resonance in ohmic plasma (#31638). Real and imaginary parts (left) and complex plane representation (right) of a magnetic probe signal, normalised to the driving current. A fit with a transfer function of order 5/2 is shown, giving f_{obs}=144.2 +-0.1 kHz, $\gamma/2\pi$=1400 +-100 s^{-1}, $\gamma/\omega \cong 1\%$.

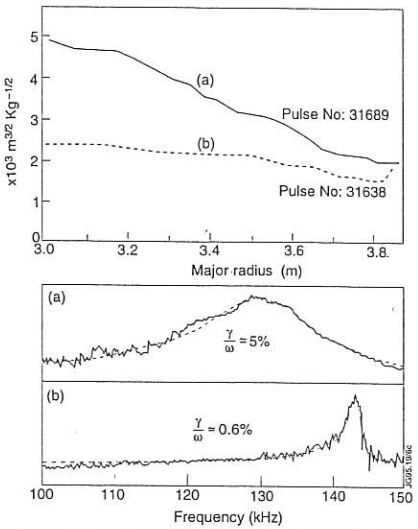

Fig. 3 The relationship between the profile of $g(r)=1/(q(r)\rho(r)^{1/2})$ and the TAE damping. Excitation peaked at $|n|=2$ was used for both discharges; ohmic plasma, with $\bar{n}_e \cong 4x10^{19}$ m^{-3}; (a) $B_{tor} \cong 1.8$ T. (b) $B_{tor} \cong 2.8$ T.

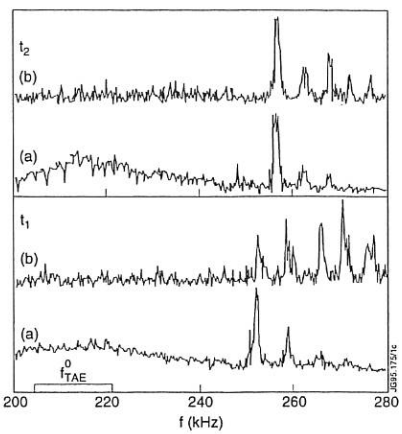

Fig. 5 Spectrum of magnetic (a) and density perturbations at r/a~0.5 (b), with LHH (2.5 MW) and ICRH (6 MW). Two successive scans in shot #33157, at $t_1 = 19$ s and $t_2 = 20$ s, are shown. $I_p \sim 3$ MA; $B_{tor} \sim 3.2$ T; $T_e \sim 6.3$ keV; $T_i \sim 2.9$ keV.

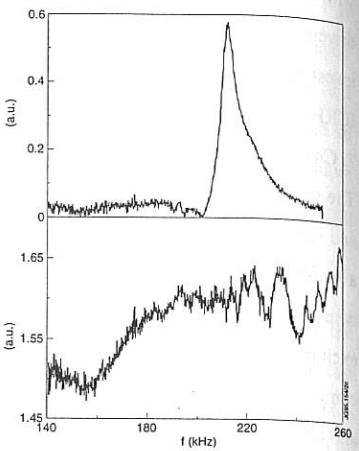

Fig. 4 δB_{pol} probe signals for moderate (top: t=3.5 s; $I_p \sim 2$ MA; $B_{tor} \sim 2.5$ T; $T_e \sim 2.2$ keV; $f_{TAE}^0 \sim 200$ kHz) and high plasma current (bottom: t=9.5 s; $I_p \sim 4.1$ MA; $B_{tor} \sim 2.9$ T; $T_e \sim 3.2$ keV; $f_{TAE}^0 \sim 180$ kHz) in shot #34073.

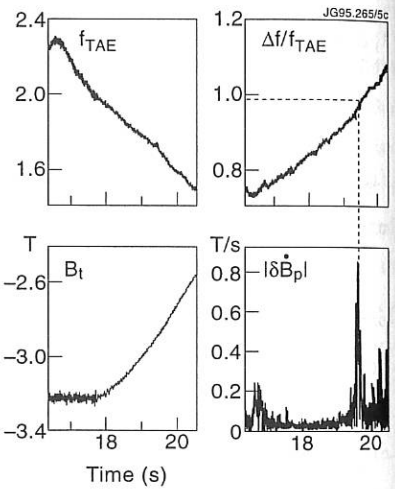

Fig. 6 Observation of TAE driven by ICRH beat waves in shot #35051. Each module is in dipole configuration for hydrogen minority heating, with $f_{1,2} \sim 43$ MHz, and coupled power ~1MW; $I_p \sim 3$ MA; $T_e \sim 5$ keV.

Radiation in JET's Mark I Divertor

R. Reichle, D.V. Bartlett, D.J. Campbell, H. Chen[1)], J.C. Fuchs[2)], R.M. Giannella, N.A.C. Gottardi[3)], N. Hawkes[4)], L.D. Horton, H.J. Jäckel, L. Lauro-Taroni, A.C. Maas, R.D. Monk[5)], M.G. O'Mullane[6)], L. Porte, R. van der Linden, M. von Hellermann, J. Wesson

JET Joint Undertaking, Abingdon, Oxon, OX14 3EA, UK
[1)] Southwestern Institute of Physics, Chengdu, China
[2)] Max Planck Institut für Plasmaphysik, Boltzmannstr. 2 Garching D-85748, Germany
[3)] Commission European Community, DGXVII, E2 Bâtiment Cube, L 2920 Luxembourg
[4)] UKAEA, Fusion, Culham Laboratory, Abingdon, Oxon, OX14 3DB, UK
[5)] Royal Holloway College, University of London, Surrey, TW20 OEX, UK
[6)] Physics Department, University College Cork, Ireland

1. Introduction

The most promising technique to avoid overheating of the target plates in large tokamaks is to increase radiative and charge exchange losses from the plasma. JET has performed many experiments with high recycling and radiative divertor operation in which this technique worked successfully. With intrinsic impurities - predominantly carbon - radiative detachment could only be achieved in ohmic and L-mode discharges [1]. This contribution concentrates on discharges with sufficient input power and impurity seeding to give better confinement than L-mode together with radiative divertor conditions. The radiation distribution is measured with JET's bolometer system and evaluated with the ADMT (Anisotropic Diffusion Model Tomography) program and an Abel inversion technique. Since the gain in longevity of the target is usually accompanied by a loss in core plasma performance the correlation between the two is also investigated.

2. Diagnostic and Analysis Details

An 84-channel high temperature bolometer system has been installed at JET [1]. The new system operates without cooling inside JET's vacuum vessel up to 320°C. A maximum of 20 of these channels looking into or near the divertor were used simultaneously. The old 34-channel Bolometer [3] has been modified to improve divertor viewing. The ADMT method [2] is applied to reconstruct the emissivity profiles from these 54 bolometer lines of sight with a spatial resolution of 8 cm. For the reconstructions it is assumed that the variation of the radiation perpendicular to the field lines in the poloidal plane is 5 times larger than the variation parallel to them. In the divertor a 5 to 20 times larger spatial variation is assumed than in the bulk section. For Abel inverted profiles the horizontal 10-channel bolometer array looking at the upper half of the plasma is used.

3. Discharge selection

Nitrogen seeding was most frequently used to achieve high power radiative divertor operation in JET, followed by neon and argon. The discharges discussed here are heated by 10-18 MW NBI at I_p= 2-3 MA and B_T= 2-3 T on the horizontal target plates. As far as the radiation is concerned, these observations are representative also for operation on the side plates and for both beryllium or carbon target plates and conditions with and without Cryo-pump.

4. A typical discharge evolution in the high radiative regime

Discharge 34343 is a 2 MA / 2 T discharge with strong nitrogen seeding at 18 MW of NBI heating power (fig. 1). With the onset of the nitrogen influx the radiation rises especially in the divertor. At first the radiation maximum is well below the X-point. With the build up of the nitrogen and the rise of Z_{eff} from 2 to 3.5 the radiation maximum smoothly moves upwards and when the total radiated power has reached 70% of the input power the radiation has detached from the target and assembled around the X-point (fig. 2 and 3). JET has also cases in which a substantial up/down oscillation is superimposed to this movement [4]. The discharge can remain in the detached state for a long time and it can be terminated without disruption. However, this example has a radiation collapse during which the whole plasma surface radiates strongly, after too much radiation condensation in the X-point has occurred.

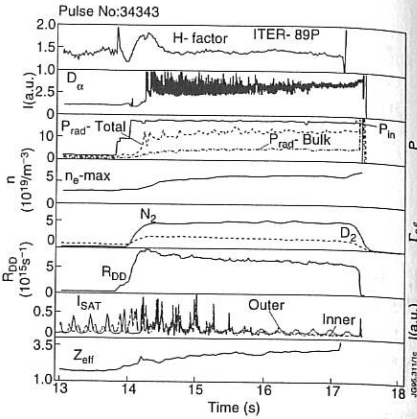

Fig. 1: Nitrogen seeded discharge evolution.

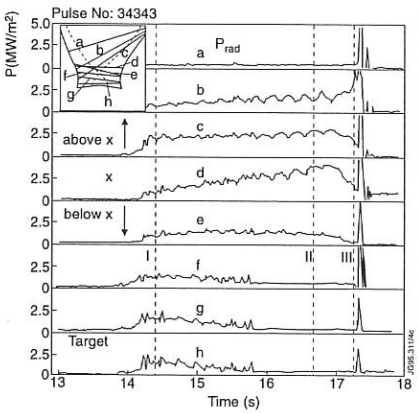

Fig. 2: Divertor radiation measurements.

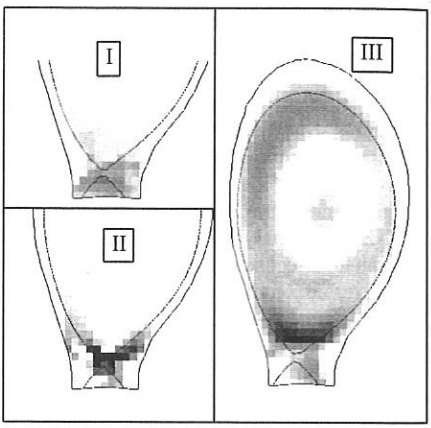

Fig. 3: Radiation reconstructions.

5. Underlying physics of this radiation behaviour

Due to the shallow magnetic field line angle near the X-point, the electron temperature gradient in the poloidal plane is largest there and the X-point is a natural cold spot. In coronal equilibrium the emissivity coefficients for light impurities peak between 10 eV (carbon, nitrogen) and 40 eV (neon). For short residence times these values are higher (20 to 200 eV). As for Marfes, there is the tendency to bring down the temperature locally to the temperature of the maximum of the emissivity. Due to the steep natural temperature gradient (fig. 3), this formation is stabilised at the X-point after the radiative zone has moved up from the target. VUV measurements of the relative intensities of the different ionisation stages corroborate this view [5]. As long as the radiation peak stays at the bottom of the steep temperature gradient this 'divertor Marfe' is stable. With a further rise of the radiative loss fraction, the radiation peak moves up further, the steep gradient disappears and the temperature along the whole plasma surface collapses.

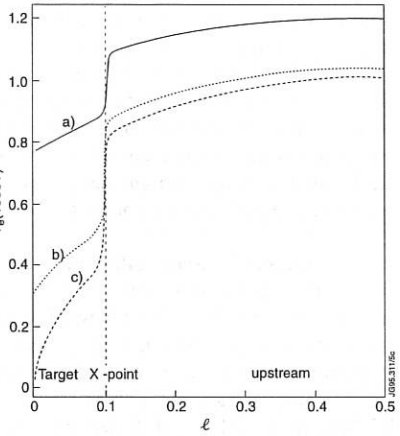

Fig. 4: Electron temperature along a flux contour close to the separatrix in the poloidal plane with its total length l normalised to 1 for a radiated fraction of the input power increasing from a) to c).

6. Comparison between intrinsic impurities, nitrogen, neon and argon

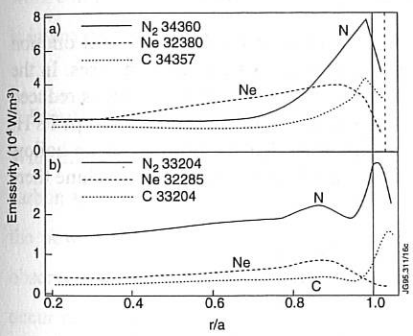

Fig. 6: Nitrogen, neon and carbon - horizontal radiation profiles: a) Abel inversion, b) predictive code result.

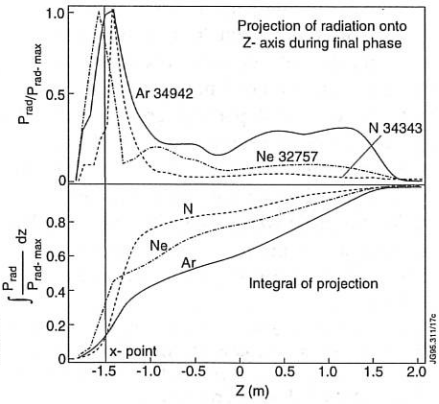

Fig. 7: Projection of reconstructed radiation distributions for nitrogen, neon and argon onto the vertical axis and its integral.

The radiation shell in carbon and nitrogen dominated discharges has a sharp maximum near the separatrix. The neon radiation shell extends deeper inside. Abel inverted bolometer measurements and simulations performed with a time dependent predictive impurity transport code based on charge exchange measurements agree in this respect (fig. 4). The ratio of divertor to bulk radiation increases from carbon and nitrogen (2:1) over neon (1:1) to argon. The peakedness of the X-point radiation increases from argon over neon to nitrogen. All these observations reflect that the temperature at which emissivity coefficient has its maximum rises from carbon and nitrogen over neon to argon. In the detached condition only a small proportion of the radiation comes from below the X-point. Contrary to the nitrogen cases, the local radiation maximum in the divertor achieved with neon is still below the X-point, because full detachment was not obtained (fig. 5).

7. Correlation between radiation, performance and impurity accumulation

Observations common to nitrogen and neon are: by increasing the radiated power fraction from 30% towards 70% the edge electron temperature and the neutron rate decline and the ITER-89p H-factor is reduced from 2 to 1.5 (fig. 6). A 1 MA / 1.4 T discharge close to the Greenwald-limit with 65% radiative losses and an H-factor of 1.75 may be seen as an indication of possible improvements when approaching the normalised beta limit. The density remains unaffected by a rising impurity radiation fraction in the nitrogen case. Less neon input was needed to achieve the same radiated power fractions. This is probably due to the different recycling behaviour. In the neon cases usually a substantial confinement loss coupled with a loss of central density occurred when increasing the radiated power fraction. This performance loss stopped progress to radiated power fractions above 65%. The fuel dilution by electrons from neon remains small and is smaller than in equivalent nitrogen cases. In the neon discharges, it could be established, that while the electron temperature profile is reduced by the increasing impurity radiation, the edge ion temperature is more robust and keeps its H-mode like shape with a high edge pedestal. The light impurity density profiles remain hollow throughout JET-discharges. With strong deuterium fuelling from the top of the machine there is evidence of impurity screening (see also:[6]).

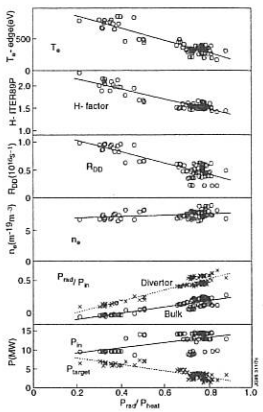

Fig. 6: Statistical analysis of nitrogen seeded discharges

References

[1] R. Reichle et al., 36th APS Plasma Physics, Minneapolis, Minnesota, 7-11 Nov. 1994

[2] J.C. Fuchs et al. , Contrib. 21st EPS, Montpellier, France, June 27 - July 1, 1994

[3] K.F. Mast, H. Krause, Rev. Sci. Instr. 56(5), 1985, p.969

[4] R.D. Monk et al., these proceedings

[5] M.G. O'Mullane et al. 'Analysis of Emisssion Spectra from MARFES in JET',22nd IOP Plasma Physics Conference, 10-13 April Oxford, U.K.

[6] P. Harbour et al., these procedings

Improved Plasma Purity in the JET Pumped Divertor

M F Stamp and M von Hellermann

JET Joint Undertaking, Abingdon, Oxon, OX14 3EA, UK

1. Introduction

The enhancement of fusion reactivity by the control of plasma impurities is a key aspect of the JET Pumped Divertor and it is anticipated that several factors should contribute to improved plasma purity in the Mk.1 Pumped Divertor.

The improved design, which avoids exposed edges and has an increased wetted area, is expected to reduce the incidence of impurity blooms during high power heating experiments.

The improved closure to escaping neutrals at moderate plasma density should give rise to higher divertor electron densities and lower divertor electron temperatures, leading to a reduced impurity source and cleaner plasmas.

The establishment of a detached divertor regime should further reduce the flux of energetic particles to the target, further reducing the source of sputtered impurities.

The line-average Z_{eff}, derived from visible bremsstrahlung measurements at 523.5nm, is used as a routine monitor of the plasma cleanliness and visible spectroscopy (including a new survey spectrometer, see section 5) is used to measure the fuel and impurity sources. This work compares data from old (1991/2) and recent (1994/5) plasmas to see if the plasma purity is improved with the JET Mk.1 pumped divertor.

2. Impurity Blooms

With the old divertor, carbon blooms were generated after 10MJ had been deposited on the carbon target plates [1]. With the Pumped Divertor the strike points can be swept to spread the power load and so keep the target plate temperature low. Carbon blooms are now not observed, even with 100MJ deposited on the carbon divertor tiles [2,3]. Beryllium blooms occur at a much lower tile temperature, so blooms are avoided by tripping off the additional heating when the tiles approach melting temperature. Nevertheless, about 60MJ has been deposited on the beryllium divertor target, without a bloom [3].

3. Plasma Purity

Figs.1a,b show a comparison of plasma parameters, including Z_{eff}, and vertical D_α (as a measure of the wall recycling) for a selection of Hot-Ion H-modes using the old and new divertors. The figures are remarkably similar in Z_{eff} (about 1.8), electron density (the faster density rise in the 1994/5 data is a result of a higher NBI particle source) and vertical D_α signal. It is noteworthy that the D_α signals are constant while the central density is rising rapidly.

Fig.2 shows the same comparison for two Steady-State H-Modes, with 7MW heating power. This time there is a difference; Z_{eff} is about 1.3 in the pumped divertor plasma, and is much higher, about 2.0 in the old divertor comparison.

Radiative divertors were produced in 1991/2 on the beryllium divertor target with a Z_{eff} of about 1.4 [1]. In 1994/5, many radiative divertor plasmas have been produced on the carbon and beryllium targets [4], with a Z_{eff} of about 1.2 (no impurity seeding).

4. Discussion

We need to understand why the old and new divertors behave the same at low density (Hot-Ion H-Mode), but differently at higher density (Steady-State H-Mode).

Typical target plasma densities for Task Force 'D' (TFD) H-Mode studies were $>8x10^{19}m^{-2}$, due to NBI requirements in the plasma configurations that were used. At such densities Z_{eff} is close to 1. The NBI fuelling produces an increased electron density (n_e) at both the inner and outer target plates. The electron temperature (T_e) rises from about 25 to 35eV in the outer divertor and drops to 10eV or less in the inner divertor (fig.3a). Consequently there is little change in the sputtering yields, and Z_{eff} stays close to 1. Similar H-Modes in 1991/2 had a lower divertor n_e and a higher divertor T_e [5], and therefore a higher sputtering yield.

The Hot-Ion H-modes of TFH have a significantly lower target plasma density and consequently a higher Z_{eff}. During the Hot-Ion H-Mode the line integral electron density increases but the divertor n_e stays constant, as shown both by the Langmuir probes and the spectroscopic ratio of D-beta/D-gamma (fig.3b). The divertor T_e also seem constant; 50eV at the inner divertor, and about 80eV in the outer divertor (though the outer divertor signals are very noisy). This is the same edge behaviour as found in 1991/2.

5. New Visible Survey Spectrometer

The new diagnostic is a novel multi-track F/2 survey spectrometer [6] with a 1024x1024 pixel CCD camera as detector. It covers 420-730nm with a spectral linewidth of 1.0nm FWHM. A portion of the spectrum is shown in fig.4. Note the presence of molecular bands from CD and BeD.

6. Summary

Improved divertor design and sweeping of the strike points has eliminated impurity blooms on the carbon targets. Blooms on the beryllium targets are avoided by tripping off the additional heating power.

The JET Pumped divertor produces generally cleaner plasmas than the old divertor at moderate to high central plasma density. For the low density Hot-Ion H-Modes, the cleanliness is the same.

The improved Z_{eff} is due to operation at a core plasma density that results in relatively low divertor electron temperatures, and relatively high divertor electron density. The low electron temperature minimises the physical sputtering source.

Molecular emission (CD, BeD) is seen regularly from the divertor target plates. The importance of chemical sputtering still needs to be assessed, but it is clearly not significantly contaminating the plasma core.

7. References

[1] C G Lowry et al., J.Nucl. Mat. **196-198** 735 (1992).

[2] D J Campbell and the JET Team, Proceedings of 15th IAEA, Seville, paper IAEA-CN-60/A-4-I-4 (1994).

[3] S Clement et al, this conference.

[4] G Matthews et al., this conference.

[5] S Clement et al, Paper at the 35th APS, St.Louis (1993).

[6] M F Stamp, to be submitted to Rev. Sci. Instr.

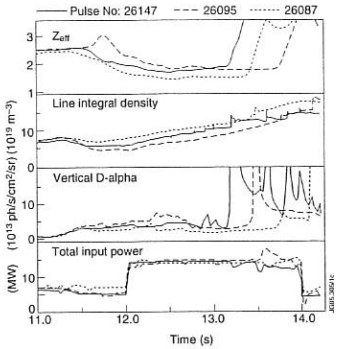

Figure 1a: Plasma parameters for pulse numbers 26147, 26095, 26087; 3MA plasmas from 1991 on the old divertor carbon target.

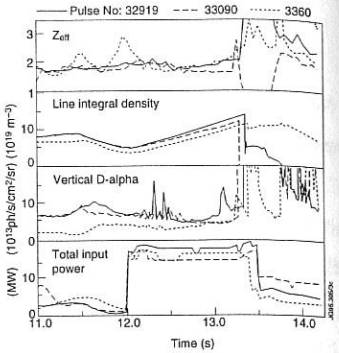

Figure 1b: Plasma parameters for pulse numbers 32919, 33090, 33680; 3MA plasmas from 1994/5 on the new pumped divertor carbon target.

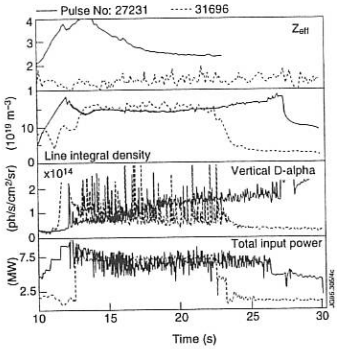

Figure 2: Comparison of two similar Steady-State H-Modes. Even though the line integral density is nearly the same, Z_{eff} is much lower in the pumped divertor case.

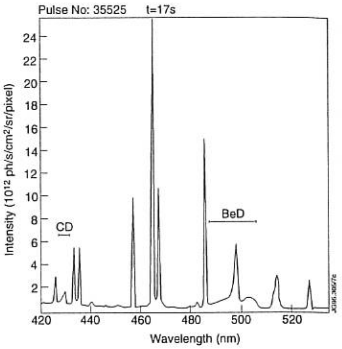

Figure 4: Portion of the spectrum from the inner beryllium target of the JET pumped divertor.

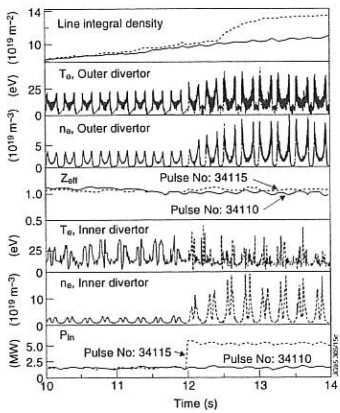

Figure 3a: Evolution of the edge parameters during NBI heating. The inner and outer divertor electron densities rise, but electron temperatures hardly change. The strike points are swept.

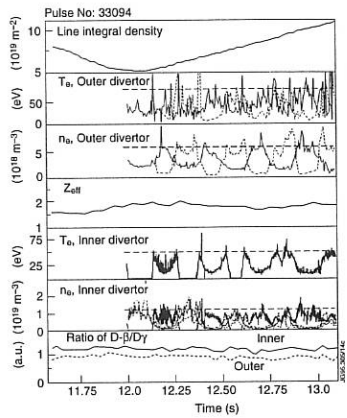

Figure 3b: Evolution of the edge parameters in a Hot-Ion H-Mode. The divertor electron temperature is constant, and high. The divertor electron density is also constant (or even falling), and low. The strike points are swept.

Modification of the ASDEX-Upgrade Divertor

H.-S. Bosch, D. Coster, O. Gruber, M. Kaufmann, W. Köppendörfer, K. Lackner, J. Neuhauser, R. Schneider, B. Streibl, and the ASDEX-Upgrade team
Max-Planck-Institut für Plasmaphysik, EURATOM Association, D-85748 Garching

1. Introduction

The most challenging issue in the design of ITER is a divertor concept which simultaneously provides tolerable power loads on the target plates and sufficient particle exhaust. Presently different divertor concepts, based on power and momentum removal by neutrals, are being discussed. The basis of these concepts is a detached plasma in front of the target plates with strong radiation cooling in the scrape-off layer plasma.

Such concepts, however, have to be tested first in present fusion experiments, and ASDEX-Upgrade will modify its present divertor to do so [1]. It is especially suited for such a task, as the magnetic configuration – when scaled to ITER – looks very similiar, and there is enough space in the lower half of the vacuum vessel to install a new divertor, because such modifications had already be envisaged from the beginning.

Two different concepts, the vertical target plates (LYRA) and the GAS BAG are considered for ASDEX Upgrade. In both configurations the length of the divertor leg will be increased compared to the present divertor in order to increase the volume of the radiating plasma. For the LYRA vertical target plates have been chosen in order to reflect the neutrals, created at the target, directly back to the separatrix, where the power conducting layer is situated.

A flexible arrangement of additional baffle elements will further allow to modify the neutral flux circulation in the divertor chamber.

2. Modelling of different divertor scenarios for ASDEX-Upgrade

To check the underlying physics ideas and to study the effect of geometrical differences, 2D-modelling calculations using the B2-EIRENE code package have been performed for three different configurations, the present divertor I, the LYRA and the GASBAG. Similiar simulations have been done for the ITER concepts [2].

The calculational grids and the approximated in-vessel-structures for the three ASDEX-Upgrade configurations are shown in figure 1. The LYRA uses inward-inclined target plates to direct (unlike in the present divertor I) the recycling neutrals towards the region of highest energy flux close to the separatrix. The exact shape has been derived from the criterion of constant energy flux density onto the target (using the observed power decay legths). The upper parts of the LYRA-target plates run parallel to the flux surfaces and serve as baffles to reduce the backflow of neutrals into the main chamber.

The GASBAG uses only small target plates in a rather open divertor chamber to allow a global gas flow pattern also to the outside of the divertor fans. Towards the main chamber, however, the divertor is well closed, very similiar to the LYRA configuration. Figure 2 shows the pressure drop from the midplane to the target plate for a density sccan for all three configurations. This pressure drop is defined as the ratio of the flux-surface integrated pressure at the midplane to the one at the target plate

$$p^* = \frac{\int_{midplane} p \cdot (1 + M^2)\, d\Psi}{\int_{targetplate} p \cdot (1 + M^2)\, d\Psi}$$

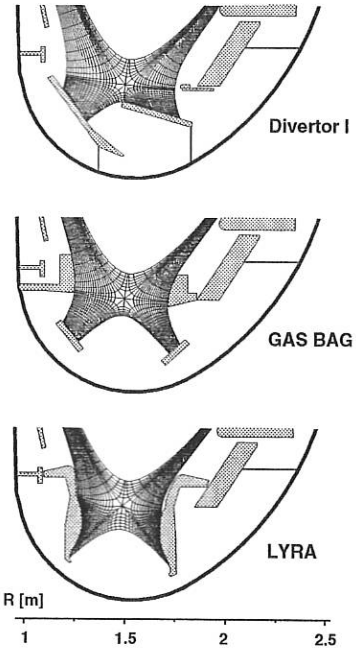

Fig. 1 Calculational meshes for the B2-EIRENE simulations of different ASDEX-Upgrade divertor configurations

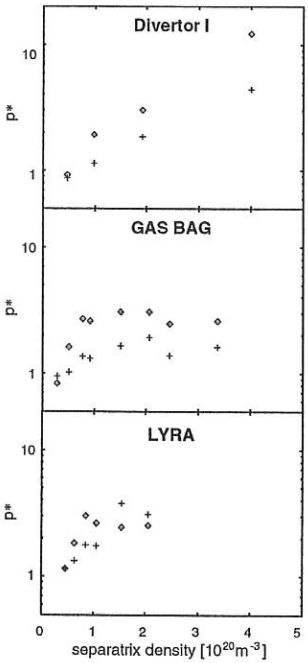

Fig. 2 Momentum loss from midplane to inner target ($\diamond$) and to outer target plate (+). $P_{heat,sep} = 7.5\ MW$.

when M is the Mach number of the flow.

These calculations were done for pure hydrogen plasmas with an input power of 7.5 MW into the scrape-off layer. It is clearly seen that in the GAS BAG and the LYRA configuration detachment occurs at lower separatrix density as compared with divertor I. This is due to the better confinement of neutrals to the divertor region. However, the detachment at both divertor legs is rather asymmetric for the GAS BAG, where the inner divertor detaches much earlier.

Stronger control of the neutral gas with structural elements in the private flux region should allow to symmetrise the GAS BAG, but also to increase the effect of the neutrals if they are preferentially feed back rather close to the target plates.

3. Modelling of baffle structures for the LYRA-configuration

To study this, we have simulated pure hydrogen plasmas in the LYRA-configuration (now with an input power of 5 MW into the SOL) with different dome-shaped baffles (restricting the gas

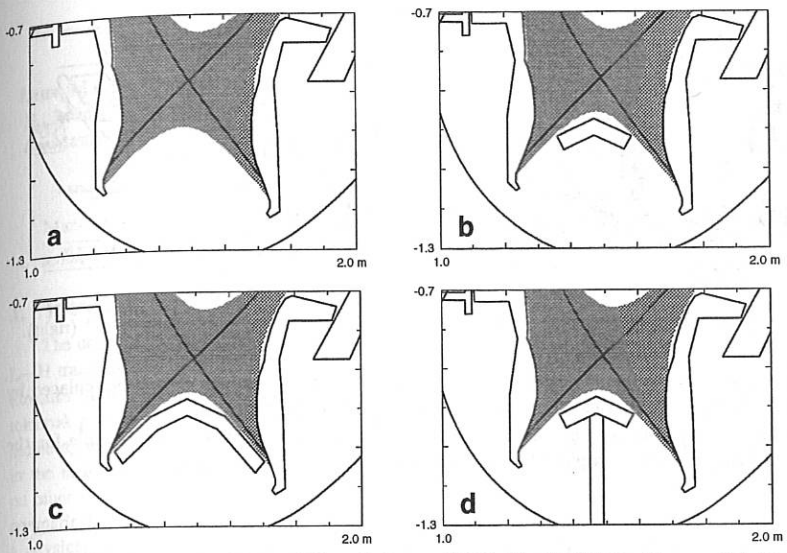

Figure 3: Divertor geometry for modelling of the pure LYRA (a), the LYRA with a small baffle (b), a wide baffle (c), and a septum (d).

flow towards the main plasma) and a septum (separating the both divertor legs), as shown in figure 3. The separatrix density for this comparison is $3 \times 10^{19}\ m^{-3}$.

The short baffle (figure 3b) strongly decreases the neutral density below the X-point. However, the influence on the target plate conditions is almost negligible. This is different for the long baffle (figure 3c), which covers such a large fraction of the private flux region that the total recycling of neutrals is strongly decreased. Therefore electron temperature increases at the separatrix, where the plasma was detached for the pure LYRA and the LYRA with the short baffle. The septum (figure 3d) acts for these plasma conditions almost identical to the long baffle.

4. Design and construction of divertor II

Currently three different options are followed simultaneously, the LYRA and GAS BAG 2 (both similiar to the configurations in figure 1), and GAS BAG 1, which has vertical target plates with a smaller angle of incidence, resulting in a better spred of the power conducted to the target plate. The first configuration to be installed in ASDEX Upgrade is the LYRA, and later the GAS BAG configurations are to be studied. The basic idea underlying the engineering design of divertor II is the request for a fast change ($\sim$ 3 months) between different options. Therefore the base of all configurations is a common water-cooled support structure holding different target plate modules. Fig. 3 shows the cross-section of the LYRA and GAS BAG 1. It can be seen that also the retention modules stay the same in the different configurations. Only the transition

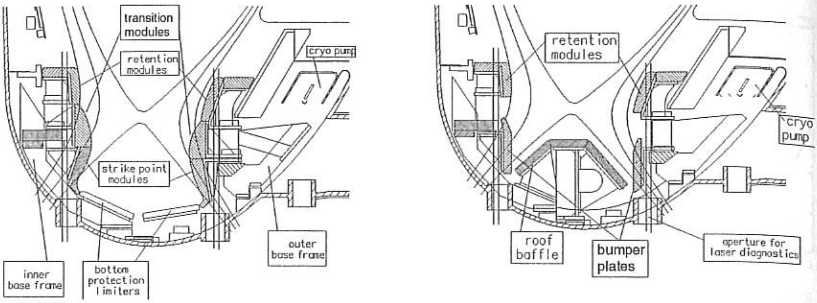

Figure 4: Cross-section of the LYRA-configuration (left) and of the GASBAG configuration 1 (right).

modules and the strike-point modules of the LYRA have to be removed and to be replaced by the respective bumper plates when converting to a GAS BAG configuration.

The strike-point modules and the bumper plates will be fabricated from CFC, while for the other modules fine grain graphite has a sufficient power handling capability.

Especially with the LYRA the conductance to the pumping channel is strongly reduced. To make up for this, and to enhance flexibility for operation in general, additional pumping capacity is necessary. Therefore a liquid helium cooled cryo pump with a nominal pumping speed of about 100 m^3/s will be installed behind the passive stabiliser. This pump is also shown in figure 4. The present turbomolecular pumps, for comparison, have a pumping speed of 13–17 m^3/s for D_2 and He, depending on the pressure. The cryo pump will also be able to pump He, using Ar frost, however, with a pumping speed much lower than that for D_2. The pump will have a small chevron at the bottom side to thermalise fast neutrals from the plasma. With the GAS BAG configurations an additional baffle for particle thermalisation might become neccessary, which could be installed between retention module and bumper plate.

5. Summary

The ASDEX-Upgrade divertor will be modified to handle higher divertor power loads connected to higher auxiliary heating power available in 1997, and to test new divertor concepts that are presently discussed for ITER.

The new configurations have been modelled with B2-Eirene to check the underlying ideas. These simulations show a much better recycling of the neutrals, mainly due to geometric differences, leading to easier access to detachment. However, the both divertor legs are strongly different, and it should be possible to influence these differences with additional baffling structures in the private flux region. So far modelling of such baffles has shown an influence on the neutral gas distribution, but only small effects on the divertor plasma.

Construction of the LYRA configuration is under way. Starting in May of 1996, it will be installed in ASDEX-Upgrade, and operation will resume at the beginning of 1997.

[1] BOSCH, H.-S. et al., Extension of the ASDEX Upgrade programme: Divertor II and tungsten target plate experiment, Technical Report 1/281a, IPP, Garching, Germany, 1994.

[2] SCHNEIDER, R. et al., J. Nucl. Mater. **220–222** (1995) 1076.

Effects of toroidal field reversal in ASDEX Upgrade

Laux, M., Herrmann, A., Neu, R.,Weinlich, M., Pitcher, S.C.[1], Schweinzer, J., Hirsch, S., Napiontek, B., Rohde, V., Büchl, K., Kallenbach, A., Bosch, H.-S., Ryter, F., Mertens, V., Gruber, O., Carlson, A., Mast, F., , Neuhauser, J. , Haas, G., Fuchs, Ch., Junker, W., Field, A.R., Wenzel, U., Lieder, G., ASDEX Upgrade Team, NI Team

Max-Planck-Institut für Plasmaphysik, EURATOM Association, Garching and Berlin, Germany
[1] CFFTP, Toronto, Canada

1. Introduction

The dependence of general parameters describing state and performance of the tokamak plasma (like L→H transition power or the density limit) on the orientation of the toroidal field [1,2] and, therefore the direction of the grad B - drifts, confirms the importance of an understanding of field reversal processes. In tokamak plasmas numerous effects are reported to depend on the orientation of the toroidal magnetic field including the symmetry of particle and power deposition at inner and outer divertor plates, radial profiles in the edge and SOL regions, the recycling pattern, etc. [3,4,5]. Usually all these effects depend also on other control parameters of the discharge like the power, the density, etc.. Therefore, only a detailed comparison of several discharges representing essentially different types of plasmas can reveal clues for a physical explanation of the field reversal effects. Such a comparison for ASDEX Upgrade and first attempts to identify the underlying physical processes are the aim of this paper. A discussion of possible modifications of the major impurity sources like the divertor plates and the inner and outer walls will be given, whereas a treatment of the very complicated influence of the field orientation on the impurity transport is beyond the scope of this paper.

2. Experiments

A large variety of discharge parameters is included in the comparison : plasma current 0.6 ... 1.0 MA, line averaged central densities 1.1×10^{19} ... 1×10^{20} m^{-3}, strength of the toroidal magnetic field 1.2 ... 2.5 T, and heating power 1 ...10 MW. This parameter space includes L- and H-mode for both field orientations, attached and detached conditions at the target plates, MARFE formation at the x-point and excursions of the MARFE at the high-field side. All discharges are in deuterium having single null configuration with the x-point at the bottom of the machine. Magnetic field as well as the plasma current are assumed to be positive if they point counter-clockwise looking from the top of the machine. The "normal" situation in ASDEX-Upgrade is negativ B_t-field and positive I_p-current (grad B - drift for ions downwards to the bottom divertor). In field-reversal experiments only the direction of B_t was changed.

3. Diagnostics

Video cameras and arrays of Dα diodes were used to monitor changes of the recycling pattern and the development of radiating structures. A bolometer system is used to determine the radiated power and an IR diagnostics to measure the power deposited onto the divertor plates. The IR-camera and the Langmuir-probes mounted flush into the plates deliver power and particle fluxes, respectively, and provide information about in/out asymmetries. Movable Langmuir-probes are installed in the outer midplane and in front of the divertor plates. A Bragg-spectrometer observes CVI and OVIII radiation to monitor the impurity concentration in the central column. The divertor and the boundary layer spectrometers observe the distribution of the emissivity of few spectral lines in the plasma boundary and the outer divertor leg, respectively. Radial boundary density profiles in the midplane are determined by observation of an injected 35 kV Li-beam.

4. Results and Discussion

The experimental investigation of plasmas with ion grad B-drift pointing away from the divertor has been motivated by the observation that there is a more equal distribution of the power load between the inner and outer divertor plates reducing the peak load [3]. For a large ensemble of discharges representing different plasmas states (ohmic, L- and H-mode), different line averaged central densities $\bar{n}$, and slightly different plasma currents I_p (0.8 ... 1MA) the dependence of this in/out ratio of deposited power is shown in Fig. 1 as a function of the product nB_t. Despite the large scatter of the data it can be stated that (i) the ratio falls with $|\bar{n}B_t|$ at low densities for both field orientations; (ii) it rises again for large negative $\bar{n}B_t$, but there are no experiments at high enough positive $\bar{n}B_t$ to confirm this branch for reversed fields; (iii) the slope of the low-density branch is steeper at normal field, so that for a small positive $\bar{n}B_t$ the ratio appears closer to unity compared to a negative $\bar{n}B_t$ having the same absolute value. The same form of the dependence of the ratio on density implies that, generally, the change with field reversal is minor compared to the variation with the density itself.

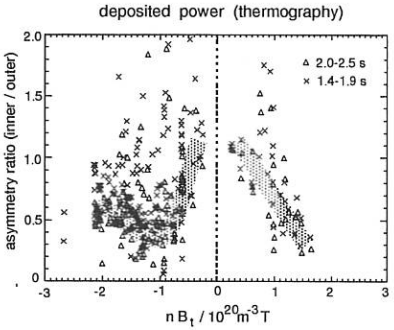

Figure 1 Ratio of power flux to the inner and outer divertor plate vs. $\bar{n}B_t$ (various discharge types)

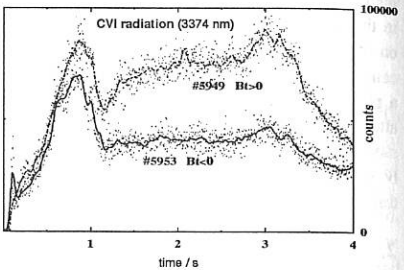

Figure 2 Line integrated emissivity of CVI radiation from the central plasma column

In ASDEX Upgrade the most striking property of discharges with ion-grad B drift away from the divertor is the higher impurity content (e.g. C and O) of the central column (Fig. 2) leading to a 10% to 30% higher Z_{eff}. In a series of ohmic shots with reversed field covering densities from 1.1×10^{19} to $4.6\times10^{19}m^{-3}$ the C emissivity in the column (monitored by the intensity of a CVI spectral line) was found to change non-monotonically – a minimum appears at $2...3\times10^{19}m^{-3}$ (for 0.8 MA ohmic). Close to such densities the divertor of ASDEX-Upgrade becomes cold (<10 eV), the plasma begins to detach from the divertor plates: a pressure drop is gradually developed and the C-radiation retracts from the plate surface to the x-point [2]. Fig. 3 illustrates both stages. For $\bar{n} = 2\times10^{19}m^{-3}$ (the attached case) the CIII intensity in front of the outer plate is twice as high for reversed B_t as for normal field orientation, whereas for $4\times10^{19}m^{-3}$ (detaching) about the same amount of radiation comes from the x-point region for both field orientations. The estimation of CIII particle fluxes from spectroscopic observations of the inner heat shield during earlier experiments ($\bar{n} > 3\times10^{19}m^{-3}$) revealed a higher and top-bottom asymmetric influx of carbon for reversed field cases compared to the normal orientation [6]. Changes in the radiation detected by 10 bolometer channels distributed along the inner shield confirm this observation but indicate influences of the density as well.

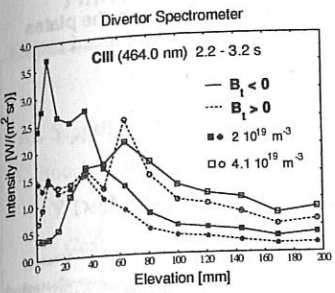

Figure 3 Line integrated emissivity of CIII vs. distance from the outer divertor plate (elevation) in ohmic discharges

interaction with the tiles in the reverse field case. These observations are confirmed completely by measurements using the movable Langmuir-probe at the outer midplane. Additionally, the long term observation of the ASDEX Upgrade discharges using TV-cameras and $D\alpha$-detectors showed typical differences in the recycling pattern for both field orientations, e.g. there was remarkably more recycling detected at the ICRH safe-guard limiters during shots with positive B_t.

Langmuir-probes installed in the divertor plates and on a movable arm in front of the plate are used to identify changes of the radial profile of power and particle fluxes, the potential, or the streaming velocity along field lines. The reversal of the magnetic field seems to change the potential distribution close to the strike zone of the separatrix completely and a flow reversal in front of the outer plate could be detected by a Mach probe (fig. 5). There are examples where the small radial zone of maximum power deposition which is normally located somewhat outside the strike point (in the scrape-off layer) switches into the private flux region during field reversal (fig. 6).If the direct introduction of material eroded from the plate into the private flux region can lead to a more efficient impurity fuelling through the

The radial profiles of the plasma density at the outer midplane observed by an active Li-beam diagnostic differ if the field direction changes (fig. 4). For positive B_t the profile reaches radially further out, especially for higher density (a shift of some mm due to uncertainties in equilibrium reconstruction is possible). The radial positions of additional bumps appearing in the profiles could be identified as projected locations of inner structures like the ICRH safe-guard limiters etc. The fact that at those bumps the profile becomes locally flat contradicts the principal shortening of connection lengths by additional inner structures and, therefore, points to ionization of neutrals recycling from these inner structures. This can be taken as evidence for a strong

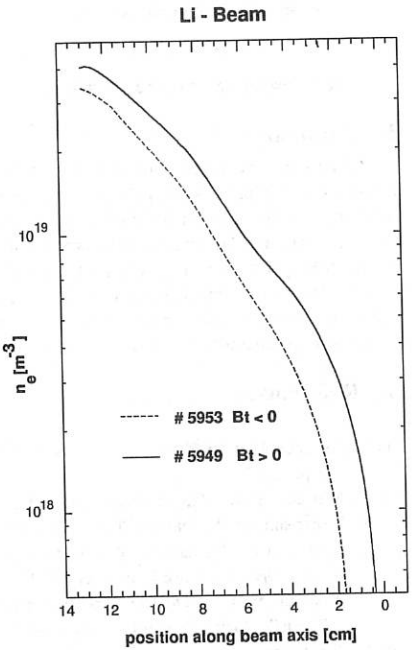

Figure 4 Radial density profiles at the outer midplane from the Li-beam dignostic (absolute position along the beam axis)

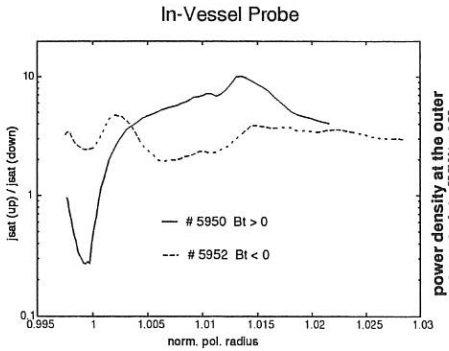

Figure 5 Radial profile of the upstream/downstream ratio of ion saturation currents representing the parallel flow velocity of ions above the outer plate

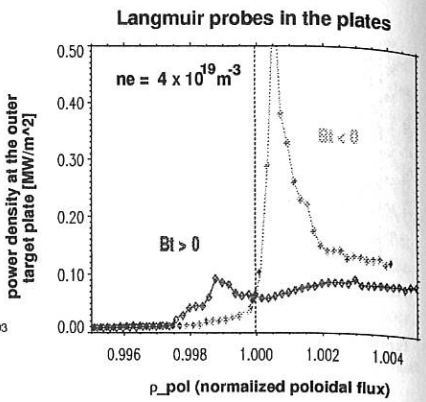

Figure 6 Deposited power density along the outer divertor plate from the probes

x-point region can only be speculated.

5. Summary

Effects of field reversal on the radial density profile in the scrape-off layer and the particle and power deposition profiles along the divertor plates are observed. Flatter profiles are responsible for higher recycling at walls and inner structures and, probably, enlarge the C-production as well. All effects appeared to depend strongly on density. The location of the peak power load on the plate changes with respect to the strike point, indicating a possible activation of a different transport channel (via the private flux region). In addition impurity transport in the divertor plasma may have changed (flow reversal in parts of the divertor). All this can contribute to a higher impurity influx leading to a larger impurity content observed experimentally in the main plasma for reversed field.

6. References

[1] K. Lackner, Plasma Phys. Contr. Fusion, Vol. 36 Suppl., No. 12 B, 1994, p. B79

[2] V. Mertens, et al., Plasma Phys. Contr. Fusion, Vol. 36, No. 8,1994, p.1307

[3] A. Herrmann, et al., Plasma Phys. Contr. Fusion, Vol. 37, No. 1,1995, p.17

[4] A. Loarte, et al., "Overview of JET Results with the Mark I Divertor", IPP-DoE Divertor Workshop, May 16.-17. 1995, Garching

[5] N. Asakura, et al., "Field Reversal Effects on Particle and Heat Fluxes in Divertor on JT-60U", 11th PSI Conf.. May 23.-27. 1994, Mito

[6] M. Kaufmann et al., Plasma Phys. Contr. Fusion, Vol. 35 Suppl., No. 12 B, 1993, p. B205

Power Losses During Divertor Plate Biasing and Detachment Experiments; Biasing Effects on Impurity Levels and Transport in TdeV

BL Stansfield, N Richard, R Marchand, J Mailloux, E Haddad, H-H Mai, BC Gregory, C Boucher, JP Gunn, J-L Lachambre, F Meo, B Terreault, A Côté, C Côté, R Décoste, Y Demers, J-L Gauvreau, F Martin, A Sarkissian, W Zhang and the TdeV team

Centre canadien de fusion magnétique*, Varennes, Québec, Canada J3X 1S1

* Supported by AECL, Hydro-Québec, and the Institut national de la recherche scientifique

1. Power losses and detachment

The power distribution and the divertor plasma parameters were measured as a function of the core line-average density, with the divertor plates grounded and with negative divertor biasing [1], in both ohmic and auxiliary-heated discharges. For these experiments, a single null (top) configuration was used, with I_p=190 kA, B_ϕ=1.8T, and the ion ∇B drift away from the divertor. The lower hybrid heating system [2] delivered 550 kW, injected counter to the ohmic current. Radiated power is measured by bolometers. Of special interest is a pair of bolometers which give measurements from two vertically separated regions in front of the divertor plates. An IR camera measures the spatial distribution of the heat load on both the inner and outer divertor plates, and the total energy absorbed by the plates is measured by imbedded thermocouples. The outer divertor is composed of horizontal and oblique plates, and the power to them is monitored separately. There is an array of 16 flush-mounted probes in the horizontal divertor plate. A rotating periscope is installed in the divertor, for spectroscopic imaging of the divertor plasma. In the SOL the main diagnostics are provided by a Fast-Scanning Probe on the bottom, and a "Gundestrup" Probe [3] on the outer midplane.

The global power balance shown in Fig. 1 is generally quite good for ohmic discharges, and with divertor plate biasing. Of the non-radiated power, most goes to the outer divertor, with outer/inner ratios of about 2-4. With negative biasing the outer divertor is active, and this ratio increases, reaching values of about 6-8. With RF heating, on the other hand, a significant amount of power is not accounted for, due to toroidal asymmetries and power deposited on uninstrumented machine components. The increase of the measured outer/inner ratio with biasing is not as dramatic here as in the ohmic case.

As the line average density increases, the fraction of the input power radiated from the main

plasma increases, and the power and particle fluxes to the divertor plates decrease. At the same time, however, although the total power deposited in the outer divertor is decreasing, an increasing fraction of this power is deposited on the oblique plates, even though great care was taken to maintain the magnetically-determined strike-point at a constant position on the horizontal plate. Measurements of the electron pressure in the SOL, and near the horizontal plate calculated from divertor probe measurements and from ratios of HeI line intensities [4] are shown in Fig. 2(a) as a function of the core density. It is relatively constant at low density, and comparable to the pressure in the main SOL. At densities above $5x10^{19}$ m^{-3}, the divertor pressure drops rapidly. At these densities, both the electron temperature and the electron density decrease in the divertor, resulting in a pressure gradient between the X-point and the divertor plate. Spectroscopic imaging of the divertor plasma shows that the density near the divertor throat continues to rise as the line-average density is increased, while that near the plate decreases. This redistribution of the fluxes is consistent with a change of the spatial distribution of the radiation losses from the divertor plasma: at low density, a larger fraction of the divertor radiation comes from a region near the horizontal plate, while at higher densities, the zone of strongest radiation moves away from the target toward the X-point (Fig. 2(b)). The density at which detachment occurs varies approximately linearly with SOL power per particle. Increasing the ohmic power results in higher edge T_e, and detachment occurs at higher density. Because of increased recycling, RF heating does not appreciably change T_e in the edge, and therefore the detachment threshold increases only slightly.

Simulations were made with the B2.5 code (a modified version of B2 [5]) for edge and divertor plasmas corresponding to ohmic discharges without biasing. The power flux into the SOL, as well as the approximate powers delivered to the inner and outer divertor plates were modelled with anomalous particle and energy diffusion coefficients $D_\perp$=0.2, $\chi_{i,e\perp}$=0.6 m^2 s^{-1}. At the boundary between the SOL and the central plasma, it was necessary to assume T_i=3T_e for low density discharges, and $T_i \approx T_e$ for higher densities, in order to reproduce correctly the deposited powers. As the density is increased at the midplane, the density at the horizontal divertor plate increases, T_i and T_e decrease monotonically, but no detachment was observed.

2. Effect of Biasing on Central Impurity Transport

Experiments were performed in L-mode at $\bar{n}_e = 2.5x10^{19}$ m^{-3}, I_p = 190 kA and B_ϕ = 1.5 T in double null H_2 and neon doped (0.3%) discharges. Carbon and oxygen intrinsic impurities, and

neon and aluminium injected impurites were studied using VUV monochromators [6,7] and soft X-ray cameras [8], both with spatial and temporal resolution. Spectral lines of C IV, O VII, Ne IX and Al XI were studied. Fig. 3 shows typical experimental results for 3 impurity line intensities as a function of minor chordal distance at different biasing voltages. Chordal profiles of soft X-rays doubled in intensity as V_{bias} increased from -130 to +130 V. For laser-ablated Al, both the decay time of the central soft X-ray signal and the Al XI line intensity doubled as V_{bias} increased from -250 to +250 V. These experimental results were interpreted using the MIST code [9] and a soft X-ray model code [10]. The C IV results showed that the diffusivity increased (decreased) by 15% for V_{bias} = +200 V (-200). Analysis of C IV, O VII, Ne IX, soft X-rays and laser ablation indicated that the inward convection velocity increases (decreases) by 30% for V_{bias} = +200 V (-200), while the impurity levels are increased (reduced) by 25-50% for V_{bias} = +200 V (-200). It is interesting that impurity transport within the separatrix is affected by potentials applied to the central plasma as a whole via the divertor plates. A possible explanation [11] is that modifications of the poloidal and/or toroidal ion rotation in the SOL (both observed), caused by a changing radial electric field, are carried into the central confined plasma by anomalous viscosity. The radial electric field within the separatrix is therefore altered, changing the radial convection through either the neoclassical model [12] or the model proposed by Horton and Rowan [13].

References

[1] Décoste R, Lachambre J-L, Abel G et al, *Phys. Plasmas* **1** 1497 (1994)

[2] Demers Y, Côté A et al, *Proc. 21st EPS Conference on Cont. Fusion and Plasma Physics, Montpellier*, Vol. III 1086 (1994)

[3] MacLatchy CS, Boucher C et al, *Rev. Sci. Instrum.* **63** 3923 (1992)

[4] Schweer B, Mank G et al, *J. Nucl. Mater.* **196-198** 174 (1992)

[5] Braams BJ, Ph.D. Dissertation, University of Utrecht (1986)

[6] Haddad E et al, *Plasma Phys. Contr. Fusion* **34** 579 (1992)

[7] Mai HH et al., *Rev. Sci. Instr.* **57** 866 (1986)

[8] Janicki C et al, *Rev. Sci. Instr.* **63** 4410 (1993)

[9] Hulse RA, *Nucl. Tech. Fusion* **3** 259 (1983)

[10] Janicki C, Internal Report CCFM RI 370e (1992)

[11] Haddad E et al, Internal Report CCFM RI 433e (1995)

[12] Stringer TE, *Nucl. Fusion* **32** 1421 (1992)

[13] Horton W and Rowan WL, *Phys. Plasmas* **1** 901 (1994)

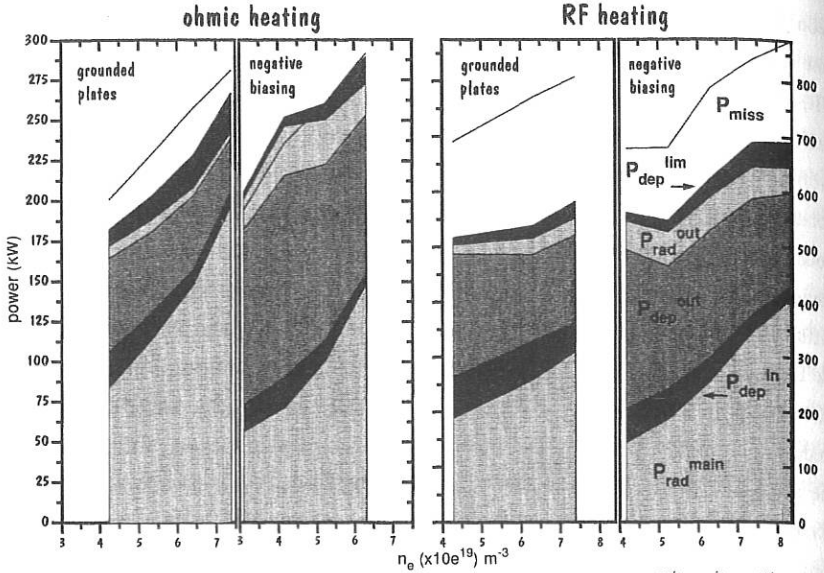

Fig.1 - Power balance for ohmic and RF heated discharges, without and with biasing, for n_e scans. P_{rad}^{main}, P_{dep}^{in}, P_{dep}^{out}, P_{rad}^{out} and P_{dep}^{lim} represent respectively the power radiated from the main plasma, deposited on inner divertor plates, deposited on outer divertor plates (including throat baffle), radiated from outer divertor and deposited on limiters. P_{miss} is the missing power.

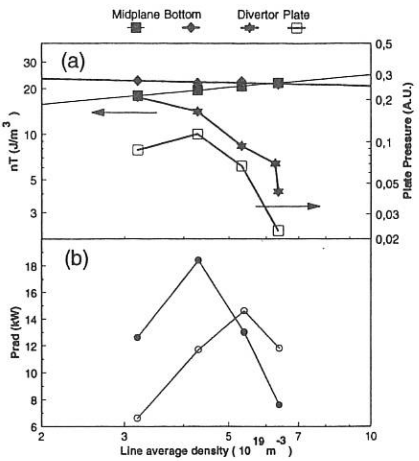

Fig 2- Signatures of plasma detachment for ohmic discharges with negative biasing. **(a)** *Electron kinetic pressure in the SOL (midplane and bottom) and in the divertor from He I ratios and flush mounted probes.* **(b)** *Radiated power in the outer divertor integrated from the plate to 4 cm below the plate (solid circles) and from 5 cm to 9 cm below the plate (open circles)*

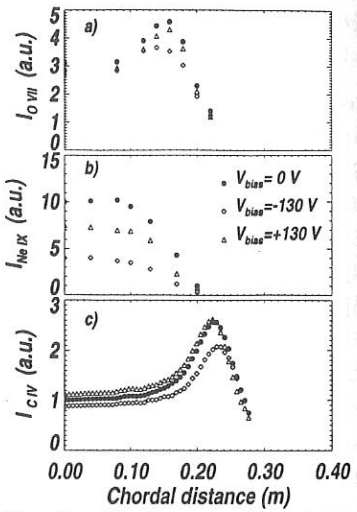

Fig. 3 Chord averaged emission profiles of 3 spectral lines in the VUV (O VII at 1623.7Å, Ne IX at 1248.3Å and C IV at 1548.2Å)

RADIATION DISTRIBUTIONS IN DETACHED DIVERTOR OPERATION ON DIII–D*

A.W. Leonard, S.L. Allen,† M.E. Fenstermacher,† D.N. Hill, † C.J. Lasnier, †
W.M. Meyer,† T.W. Petrie, J.G. Watkins,Δ R.D. Wood,† and The DIII–D Team

General Atomics, P.O. Box 85608, San Diego, CA 92138-9784

Enhanced radiative losses with accompanying divertor heat flux reductions have been achieved on DIII–D by the puffing of deuterium and/or neon gas [1]. In addition these highly radiating, reduced divertor heat flux regimes have been extended to lower core plasma density through cryopumping in the divertor. This paper describes the magnitude, distribution and other characteristics of the radiation obtained during these experiments. Radiated power is measured by two poloidally separated 24-channel bolometer arrays. One array views from above, the other from below the midplane. The radiated power profile is reconstructed by assuming constant emissivity on a flux surface for the core and SOL plasma and parameterizing the divertor radiation by flux surface and distance above the divertor floor [2]. Images of visible line radiation in the divertor provide information about the distribution of impurities; *e.g.*, a tangential image is inverted to provide a poloidal profile of the emissivity. The core plasma impurity densities are measured by charge-exchange spectroscopy techniques.

1. Deuterium Injection

The target plasma for the gas injection experiments is a 1.6 MA, 2.1 T single-null ELMing H–mode plasma with ~8 MW of injected power and the ∇B drift direction toward the X-point. With no additional gas puffing IR cameras measure the highest heat flux at the outboard strikepoint at ~6.0 MW/m^2 but ≤1.0 MW/m^2 at the inboard strikepoint. Conversely, the divertor radiation is much greater in the inboard divertor than the outboard [3]. This radiation pattern obtained from inversion of the bolometer data, is shown in Fig. 1(a). Sufficient deuterium puffing, ~100 torr-ℓ/s for ~500 ms, produces an abrupt transition to a highly radiating state in the outboard divertor [4]. The increased radiation in the outboard divertor [Fig. 1(b)] extends from the X-point to the divertor target peaking at ~10 W/cm^3. This radiating state is also characterized by a drop in peak outboard divertor heat flux by a factor of 3–5 and a decrease in plasma flux and pressure at the strikepoint as measured by Langmuir probes. In the inboard divertor there is no significant change after the transition. Through the transition the plasma remains in H–mode with confinement at ~2 x L–mode.

By summing specific regions of the reconstructed radiation profile, loss channels for the injected power can be identified. Before puffing, 18%–20% of the injected power is lost

*Work supported by the U.S. Department of Energy under Contract Nos. DE-AC03-89ER51114, W-7405-ENG-48, and DE-AC04-94AL85000.
†Larwrence Livermore National Laboratory.
ΔSandia National Laboratory.

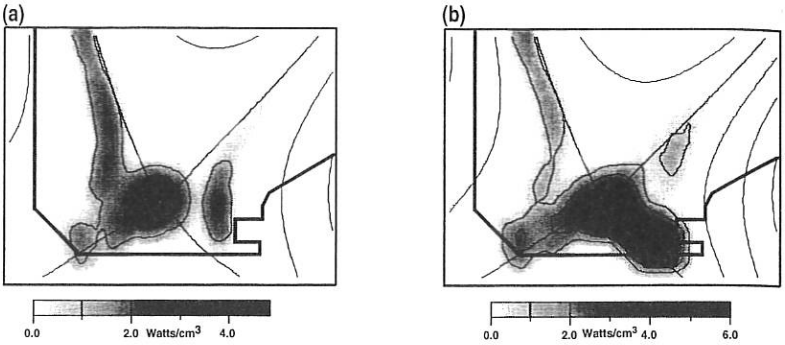

Fig.1. Divertor radiation distribution for (a) no additional gas puffing and (b) deuterium puffing until radiative regime obtained

through radiation in the core and SOL. In the divertor, radiation accounts for another ~30% of the power with most of that in the inboard side. The balance of the injected power is observed as divertor plate heat flux, with ≥3/4 of that in the outboard strike-point. A detailed accounting of power balance during ELMing H–mode in DIII–D is given in Ref. [3]. After injection, the outboard divertor radiation increases from 7% of the injected power to 30%. With the extra gas there is a moderate increase in central density, from 7.8×10^{19} m^{-3} to 8.9×10^{19} m^{-3} while the core and SOL radiation modestly increase from 19% to 23% of the injected power. The increase in total radiation is offset by a corresponding decrease in divertor heat flux. A summary of radiation distribution is presented below.

	No Gas	D_2 Puffing	D_2 with Pumping
Core & SOL	20%	23%	23%
Outboard Divertor	7%	31%	31%
Inboard Divertor	21%	16%	21%
Total Radiation	48%	71%	76%

The fractional contributions to radiation from neutral hydrogen and impurities have not yet been measured on DIII–D. With complete graphite coverage carbon is expected to be the dominant impurity. Carbon concentrations of ~1.5% have been measured in the core plasma by charge-exchange spectroscopy for these discharges. Inverted poloidal profiles of visible CIII emission from camera images present a pattern similar to that for radiated power. Visible CIII emission is concentrated along the inner leg of the divertor before deuterium puffing, but then increases to a greater level along the outboard divertor after the radiative transition. Given the measured carbon concentrations and the region of highly radiating CIII, the intrinsic carbon impurity probably represents a significant fraction of the increase in radiated power. Measurements on JT-60U have shown that carbon contributes approximately

half of the radiation observed during highly radiating divertor discharges [5]. Measurements of these contributions on DIII–D are planned for the future.

Divertor pumping on DIII–D has allowed operation of ELMing H–mode plasmas at lower central density [6]. Puffing of deuterium into these pumped plasmas has produced a similar increase in divertor radiation and reduction in heat flux as the non-pumped case. These plasmas have a ~25% lower core density and maintain good H–mode confinement. The divertor radiation profile, shown in Fig. 2, while yielding the same total power has a more even distribution of radiation along the inboard and outboard divertor legs. Otherwise the magnitude and distribution of radiation are very similar. This result represents a significant step in the effort to independently control the core and divertor plasmas.

2. Neon Injection

Puffing of neon gas has also been effective in reducing peak divertor heat flux. For neon puffing the increase in radiation occurs inside the separatrix. With sufficient neon to produce a heat flux reduction of a factor of 3–5, the radial profile of the radiative emissivity peaks at 0.5 W/cm^3 just inside the separatrix, from ρ = 0.8–1.0, as shown, in Fig. 3. A core neon concentration of 1.5% for this case was measured in the central plasma. The total radiation increases to 65%–70% of the injected power. The mantle of radiation inside the separatrix is roughly equal in magnitude to the divertor/X-point radiation. A radiation distribution summary is given in Table I. The total divertor radiation decreases somewhat and moves up the divertor

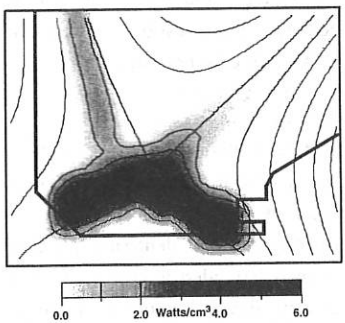

Fig. 2. Divertor radiation in radiative regime at lower density with pumping.

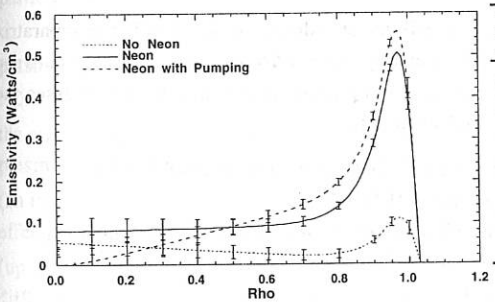

Fig. 3. Radial profile of radiative emissivity in core plasma with no gas puffing, neon injection and neon injection with pumping.

Table 1

Radiative Power Loss	Neon Injection	Neon with Pumping
Core &SOL	42%	48%
Mantle, ρ = 0.8–1.0	24%	33%
X-point/ divertor	23%	21%
Total Radiation	65%	69%

leg into the X-point region. The divertor radiation distribution is illustrated in Fig. 4. Visible CIII images show a decrease in emissivity in the X-point region. Though significant power is lost inside the separatrix, H–mode confinement is maintained. However, the ELM character is strongly affected, with the ELMs decreasing in frequency to ~5–10 Hz and increasing in amplitude to produce a strong modulation in the central plasma density of ~15%.

Divertor pumping has also been applied to neon injection. When injecting neon into a pumped plasma with 25% lower central density, a similar mantleof radiation and heat flux reduction is produced as for the nonpumped case. The core radiation profile is also shown in Fig. 3. The X-point/divertor radiation, though remaining similar in magnitude to the nonpumped plasma, moves back to the inboard leg of the divertor. The ELMs are again reduced in frequency and of larger amplitude producing a significant modulation of the main plasma density. A method of ELM control must be found, such as in the ASDEX-U CD H–mode [7], in order to practically make use of edge plasma radiation for power dissipation.

3. Conclusion

Attractive methods of reducing peak divertor peak divertor heat flux have been demonstrated by the injection of either deuterium or neon gas. With deuterium injection the radiation is extended along the divertor leg effectively dissipating much of the injected power. Much of the increased radiation likely comes from the intrinsic carbon impurity. More modeling is needed to determine if such a scenario can be utilized in larger size devices. The attainment of a highly radiating divertor at reduced central plasma density is also encouraging. This implies a flexibility to optimize the core plasma conditions yet maintain a reduced divertor heat flux if the right conditions are met.

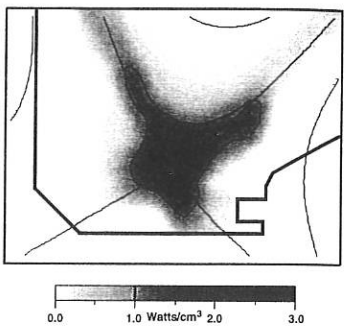

Fig. 4 Divertor radiation distribution with neon injection

Neon injection has demonstrated the possibility of radiating power inside the separatrix before it reaches the divertor. Better understanding and control of the relationship between H–mode power threshold, ELM characteristics and plasma density are needed to asses the applicability of this scenario for ITER-sized tokamaks.

[1] Petrie T W, Buchenauer D, Hill D N et al., *J Nucl. Mater.* **196-198** 848 (1992)
[2] Leonard A W et al., *Rev. Sci Instrum.* **66** 1201 (1995)
[3] Leonard A W,et al., Proc 11th Conf. Plasma Surface Interaction, Mito (Japan) 1994
[4] Petrie T W et al., submitted to Nucl. Fusion
[5] Kubo H., et al., *Nucl. Fusion* **10** 1427 (1993)
[6] Mahdavi M A et al., Proc of 20th EPS Conference on Controlled Fusion and Plasma Physics, Lisbon (Portugal) Vol. **17C**, Part II 647 (1993)
[7] Gruber O, Kallenbach A, Kaufmann M submitted to Phys. Rev. Lett.

ATOMIC PHYSICS AND PLASMA-WALL INTERACTION EFFECTS ON PARTICLE SCREENING AND RADIATIVE BEHAVIOUR OF ERGODIC DIVERTOR EDGE PLASMAS IN TORE SUPRA

C. DeMichelis, A. Grosman, C. Chamouard, Ph. Ghendrih, C. Grisolia, R. Guirlet, W. Hess, M. Mattioli, P. Monier-Garbet

Association Euratom-CEA sur la Fusion Controlée, DRFC, C.E. Cadarache, 13108 St. Paul-lez-Durance (France)

1. INTRODUCTION. One of the most spectacular effects of the Ergodic Divertor (ED) in Tore Supra (TS) is its capability to screen intrinsic impurities [1, 2] (mainly carbon in TS, an all carbon, actively cooled, tokamak), thus purifying the plasma core ($r/a \leq 0.8$) with practically no change in its confinement properties [3]. This was quite unexpected, since the ED theory does not foresee a drastic increase of particle transport (contrary to the large predicted effect on heat transport). The interpretation of this ED-induced impurity screening is quite complicated, since it involves the interplay among particle transport, atomic physics, and plasma-wall interaction phenomena. Moreover, it was hoped that the ED would allow a considerable increase of the radiated power fraction, thus reducing heat load problems. Both these topics are discussed here, where we try to clearly state our present understanding of these problems, which has been aided by the study of the behaviour of both intrinsic and injected impurities. The ED-induced, edge plasma characteristics, relevant to the particle effects discussed in this paper, are: a relatively large (10-15 cm) radial extension of the affected edge (both ergodic and laminar layers), characterized by a substantially reduced particle confinement time, a flat electron temperature, T_e, profile (between 40 and 80 eV, depending on the electron density, n_e), between at least $0.9 \leq r/a \leq 1$, and a relatively large, up to 7 cm, scrape-off (laminar) region [3].

2. SCREENING. We shall start with a review of the experimental results (the screening factor is defined as the ratio of the central particle densities with and without ED). For all particles, screening is proportional to the perturbation strength, i.e., to the ED current I_{ED}.

i- Deuterium is strongly screened. In D plasmas, n_e decreases (Fig. 1) as soon as the ED is switched on (n_e decreases much more in the ergodic layer, $r/a \geq 0.8$, than in the confined plasma); at the same time all the Dα signals (an indication of recycling) increase: these two effects indicate a decreased peripheral particle confinement time. The value of the n_e decrease (up to 50% of the average density) and its time constant depend on the wall conditions. It is difficult to maintain n_e at the pre-programmed value when switching on the ED at the current plateau, since this induces a very large gas injection, eventually leading to a disruption. This

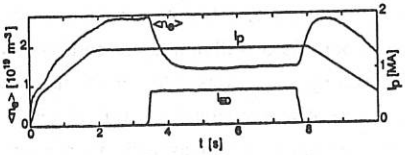

Fig.1- ED deuterium plasma.

problem has been solved by switching on the ED at the beginning of the current ramp up, thus ensuring a smooth transition to the divertor configuration (typically a D injection of a few $Pa.m^3\ s^{-1}$ is necessary to obtain $\langle ne \rangle \cong 4\ 10^{19}\ m^{-3}$, i.e., a filling efficiency of a few %).

ii- Helium is practically not screened. In He plasmas, n_e remains practically constant when applying the ED. The fuelling efficiency is ≥ 80 % . The impurity screening factor is somewhat less than for D plasmas.

iii- Intrinsic impurities. Carbon is efficiently screened: a screening factor of 0.2 to 0.4 is found, depending on wall conditions and fuelling gas (Fig. 2). Screening is somewhat better with boronized walls. Oxygen is less screened; however, if the O data is normalized to the Dα measurements (proportional to the D flux), it falls in line with C (Fig. 3). Chlorine, present in small quantities only in high density plasmas, is very efficiently screened, especially with boronized walls.

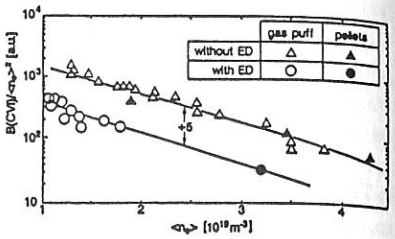

Fig.2- C concentration in ED and limiter D plasmas as function of $\langle n_e \rangle$.

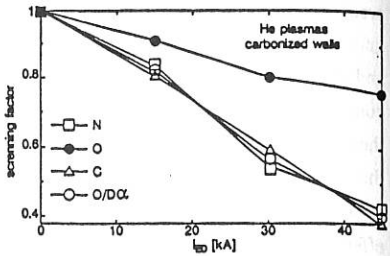

Fig.3- C, O, and N concentrations in He plasmas as functions of I_{ED}.

iv- Injected impurities. We shall neglect laser blow-off injection of metals, since (although non perturbative for the core plasma) it is locally (at the periphery where the neutrals enter the plasma) very perturbative, and burns through the ergodic layer. Nitrogen, argon, and neon have been injected. N and Ar are both screened approximately as C (for N, screening is better with boronized walls), and are both partially recycling impurities (Ar more than N), because of wall retention. Ar wall trapping has been systematically investigated by measuring the Ar particle balance, using RGA (residual gas analysis) and flowmeter measurements. Fig. 4 shows that the integrated quantity of deposited Ar particles (for a series of consecutive shots during a radiative layer experiment with Ar injection) increases continuously: Ar accumulates in the vessel walls. Gas recovery at the end of the shot larger than the injected quantity is obtained for disruptive plasmas (black circles) and non-disruptive plasmas without Ar injection. Similar results are obtained for N.

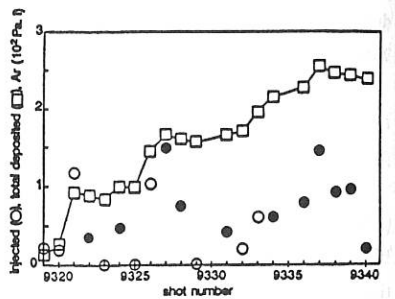

Fig.4- Injected (circles), and integrated quantity deposited in the walls (squares), for Argon

Both impurities end up in the wall, and are (at least partially) released in subsequent shots, thus preventing shot to shot reproducibility. Neon, on the other hand, is an almost completely recycling impurity, practically not screened: the injected quantity is completely recovered at the end of the shot. RGA measurements show that mass 22 (representing neon) has an exponential decay with a time constant of 17 s (very close to the vessel Ne pumping time constant), to be compared to 50 s for a non-ED limiter plasma. This difference is probably due to the lower energy, with the ED, of the impinging Ne ions, because of the lower edge T_e value, leading to a shallower ion penetration in the wall.

A discussion of these results must start with the observation that 'pumping' (either active pumping or wall retention) is an absolute prerequisite for particle screening. Indeed, a completely recycling particle, even if ionized in the ED region, will eventually enter the confined plasma if there is no means to pump it out . D is well screened, even when the usual wetted carbon surfaces are saturated, because the different ED connections give access to larger interaction areas. However, even for a partially or non-recycling particle, screening can only be effective if the neutral ionization length λ_i ($=v_o/n_e\langle\sigma v\rangle_{ion}$, where v_o is the velocity of incoming neutrals and $\langle\sigma v\rangle_{ion}$ the ionization rate coefficient) is shorter than the ED layer extent, λ_{ED} (in which case, the wider sol and reduced edge particle confinement time increase the screening). Estimations of λ_{ED}/λ_i show that only backscattered particles have a finite probability of entering the confined plasma (for backscattering, we have taken the value $3T_e^e$ for the incident particle energy, T_e^e being the value in the ED layer). For both He and Ne neutrals, a large fraction is expected to be backscattered; moreover, both have low ionization rates and are not pumped, thus explaining the poor screening. Finally, since D is efficiently screened, backscattering cannot play a major role, and most of the population must be of Franck-Condon origin; indeed, Dα line profile measurements show an average energy of 3.5 eV, with practically no underlying hotter component.

3. RADIATION. One of the possible solutions to the wall heat load problem is to radiate a large fraction of the input power; this involves the injection of impurities and requires that they do not pollute the confined plasma. The ED screening properties are a distinct advantage; however, they would require active pumping, since using the wall retention capability gives rise to shot to shot irreproducibility, due to the subsequent release (indeed, we have not been able to reliably operate with Ar or N). We have therefore injected Ne (preferred to He because of its larger cooling rate at the relevant T_e) into relatively high power (up to 5.5 MW of ICRH) ED plasmas, thus increasing the radiated power by approximately 1.5 MW (up to

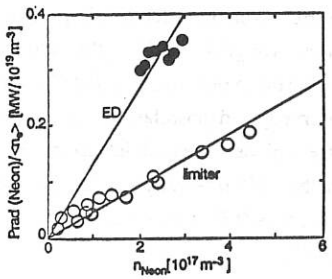

Fig.5-Normalized Ne radiation power as function of Ne density in the plasma core.

~80% of the total), at the expense of an increased central impurity content (since Ne is not screened): $n_{Ne}/n_e \cong 0.7\%$ for $\sim 10^{19}$ Ne atoms injected. The ED effect is seen here in the increased radiation efficiency (Fig. 5): three to four times less Ne is sufficient to obtain the same radiated power as in similar , non-ED, limiter plasmas. Larger radiated powers were obtained in these experiments only at the expense of the onset of a Marfe-like structure at the high field side [4] (the normal radiative pattern in ED plasmas is with a strong radiating layer on the low field side), accompanied by an outside detachment. Although the increased Ne radiation efficiency may be partially due to the ED-induced T_e profile (constant at the right value over a larger edge layer), two other effects are known to increase the impurity radiative rate: transport modifications and charge exchange (CX) recombination [5]. Reduced particle confinement times in the ED layer (resulting in increased recycling) have been inferred from D injection and spectroscopically from N injection [2]. CX recombination requires a large neutral D density at the edge; although we have no direct measurement of the edge neutral density, the importance of CX processes in ED plasmas is demonstrated by comparing experimental values and simulations for two CX sensitive C spectral line intensity ratios, $G=I_{CV}/R_{CV}$ and $\rho=Ly\alpha/R_{CV}$ ($Ly\alpha$=CVI 33.74 Å, R_{CV}=CV 40.27 Å , resonance line , and I_{CV}=CV 40.73 Å, intercombination line), Fig. 6. The G-ratio is an inverse function of T_e at tokamak electron densities; it is increased by CX recombination of H-like C ions. The $Ly\alpha/R_{CV}$ ratio, on the other hand, is an indication of the relative amounts of H-like and He-like C ions, and decreases as a consequence of the increased peripheral recycling in the ED layer. Indeed, a stronger peripheral recycling increases the He-like C ion density with respect to that of H-like C ions, since the latter are located in the confined plasma, where the perturbation has vanished [1]. In order to correctly simulate both line intensity ratios with the ED [6], it is necessary to increase simultaneously the diffusion coefficient in the ED layer (by a factor of approximately three, roughly within the completely stochastic region where a flat T_e profile is observed) and postulate the existence of a large peripheral neutral deuterium density n_o (in the 10^{16} m^{-3} range at the CV emitting layer, $r/a \approx 0.85$, and in the 10^{17} m^{-3} range at $r/a = 1$).

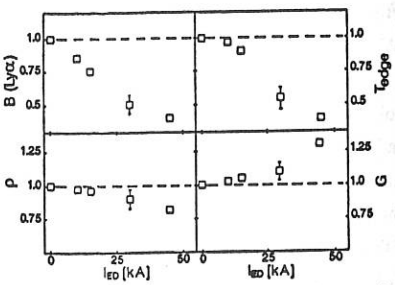

Fig.6- Variation with I_{ED} of C Lyα radiance, edge T_e, and ratios G and ρ, normalized to I_{ED}=0.

REFERENCES. [1] C. Breton et al, Nucl. Fusion 31, 1774 (1991). [2] C. DeMichelis et al, J. Nucl. Mater. 196-198, 485 (1992). [3] C. DeMichelis et al, Nucl. Fusion, to be published. [4] W.R. Hess et al, Plasma Phys. Contr. Fusion, to be published. [5] D.E. Post, J. Nucl. Mater. 220-222 (1995) 143. [6] M. Mattioli et al, Nucl. Fusion, to be published.

Edge Localized Modes in the TCV Tokamak

H. Weisen, M.J. Dutch, A. Pochelon, A. Hirt, R.A. Pitts, F. Hofmann, M. Anton,
B.P. Duval, J.B. Lister, J.-M. Moret, Ch. Nieswand, and G. Tonetti
Centre de Recherches en Physique des Plasmas, EPFL
Association EURATOM-Confédération Suisse, CH-1015 Lausanne

1. Introduction

The TCV tokamak [1] has produced a large number of diverted SN and DN plasmas, as well as limited plasmas. Following boronization in 1994 virtually all discharges with the ion ∇B drift towards an X-point and several elongated limited plasmas have produced Ohmic H-modes [2]. The typical SN discharge shown in fig.1 demonstrates most of the features observed in H-modes. Transitions can be 'dithering', with the D_α level switching between L-mode and H-mode levels. They can also feature ELMs with pulses of D_α emission well above the L-mode level. Following the transition there generally is an initial ELM-free period. In the example presented there is a short period of irregular 'mossy' ELMs causing low amplitude fluctuations on the D_α signal, followed by several Large ELMs which significantly reduce the energy confinement time and interrupt the density rise and a final period of mossy ELMs. The plasma density rises rapidly in the absence of Large ELMs. Mossy ELMs have their largest amplitude in the divertor and do not appear to affect confinement. In the absence of Large ELMs H-modes frequently terminate in high density disruptions, sometimes at the Greenwald limit $\langle n_e \rangle_{GL} = 0.27\ I_p/a^2$.

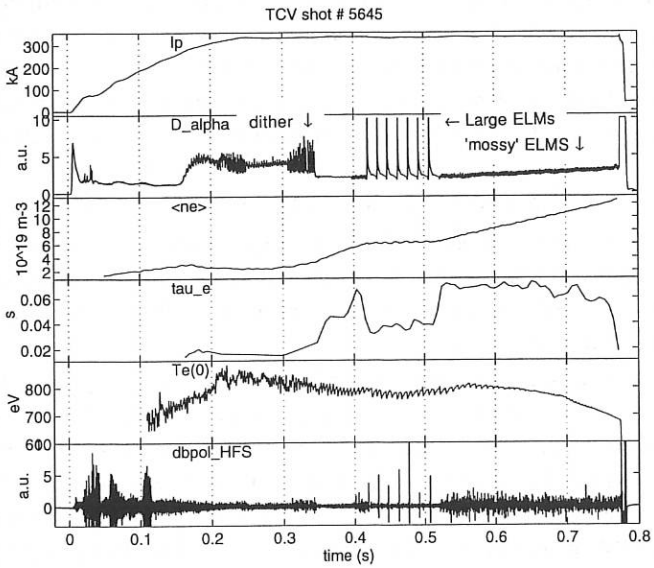

Fig.1 Typical Ohmic H-mode evolution in the Single-Null configuration (fig.2b)

2. Large ELMs

The magnetic signature of Large ELMs features a dominant m=1, n=0 (fast vertical displacement) together with an m=2,3, n=1 mode. Higher order modes could not be measured because of hardware limitations. Both coherent and turbulent precursors have been observed, beginning 0.1-3 ms before the D_α pulse.

ELM effects have been studied in detail in two configurations, a Double-Null D shaped configuration (DN) with κ=1.7, δ=0.7, Ip=390 kA and a Single Null configuration with the X-point at the top (favourable ion drift, SN) with κ=1.6, δ=0.4, Ip=330 kA (fig.2).

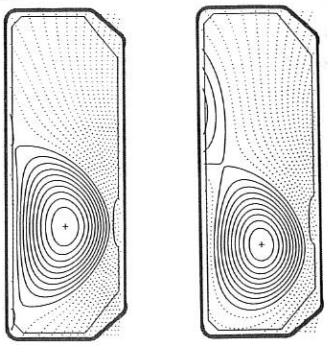

Fig.2 Configurations for ELM studies. Left: DN, right SN

In the SN plasmas these ELMs cause changes in electron content and stored energy of the order of 10% [3] . The X-ray emission from the plasma edge is dramatically affected. The emission rises at the arrival of heat pulses released by sawtooth collapses and falls as a result of the energy loss associated with each ELM. A single ELM may cause the emission to fall by a factor of 2 within 0.1 ms. It is interesting to note that in ELMy H-modes these discrete MHD events (sawteeth and ELMs) appear to dominate the power balance at the edge transport barrier. In DND the ELM effects are 2-3 times smaller.

The effect of ELMs on global confinement has been investigated as a function of ELM frequency. We may take a time average (over many ELMs) of the usual particle balance and obtain

$$\langle \dot{N}_{eff} \rangle / N = \Phi_{in}/N - 1/\tau_{up} + (\langle \Delta N \rangle / N) f_{ELM}$$

where the first term on the left hand side is the rate of change of the particle content averaged of many ELMs. τ_{up} stands for the underlying (ELM-free) particle confinement time and Φ_{in} is the particle source. Analogous expressions hold for the impurity content, N_z, and the stored energy W.

The experimental time traces were divided into windows with roughly constant ELM frequency, for which quantities of interest and their rates of change were sampled. In both the DN and the SN cases the average rates of change in electron content from a 4 channel FIR interferometer, impurity content estimated from an X-ray measurement [4], stored energy from the equilibrium reconstruction vary nearly linearly with f_{ELM} up to a maximum frequency, ~300 Hz for DN and ~120 Hz for SN (figs.3 and 4). Above these frequencies irregular ELMs and returns to L-mode are often observed.

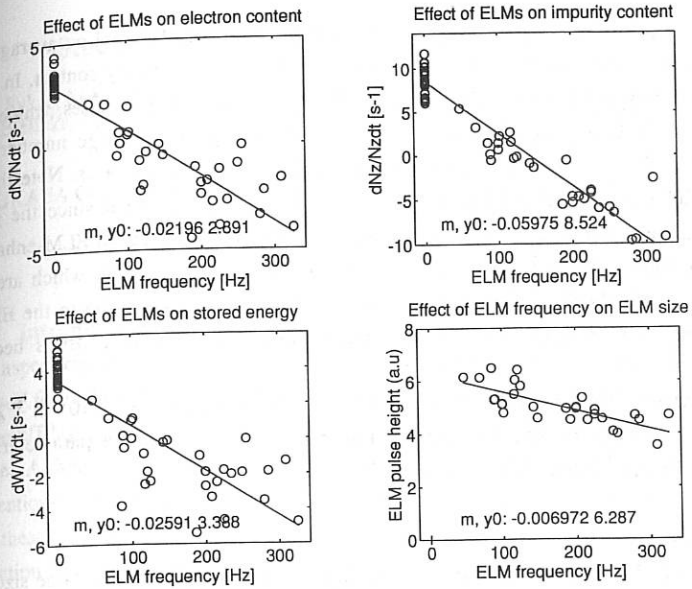

Fig. 3 *Rates of change of electron content, impurity content and stored energy versus ELM frequency in DN H-modes. The right bottom right figure shows the pulse height of the D_α emission.*

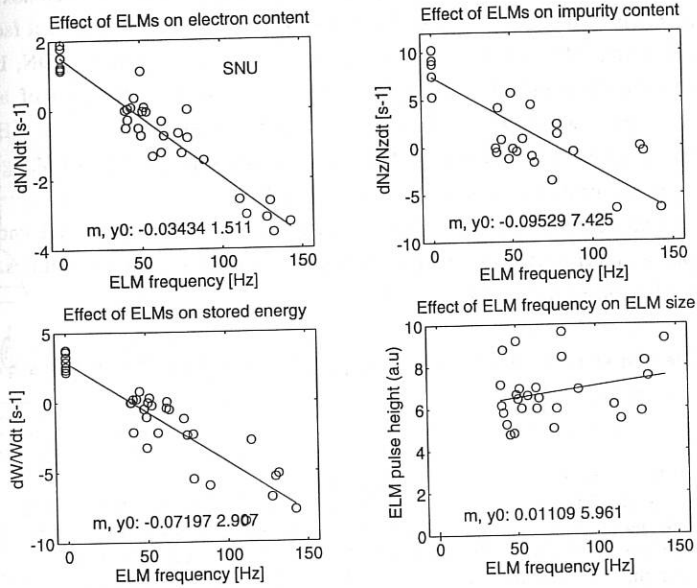

Fig. 4 *As fig.3 but for SN*

From the slopes of the fitted lines we see that in DND these ELMs expel on average 2% of the electron content, 2.5% of the stored energy and 6% of the impurity content. In SNU the corresponding numbers are 3.5%, 7% and 9%. The height of the D_α pulses, which may be indicative of ELM size, vary little with ELM frequency. These large numbers are confirmed by direct measurements of $\Delta N_e/N_e$ and $\Delta W/W$ in selected cases. Note that as far as particles are concerned the loss fraction should be taken as net since the gross outward flux caused by the ELMs may be partly offset by an influx due to ELM-enhanced recycling at the walls. Also the X-ray estimates for the impurity content, which are still based on a single chord and cannot take into account profile changes due to the ELMs, may be subject to revision when more comprehensive impurity diagnostics become available.

In DN stationary conditions are obtained for $f_{ELM} \approx 120$ Hz, with $\langle n_e \rangle \approx 8 \cdot 10^{19} m^{-3}$, $Z_{eff} \approx 1.6$ and $\tau_e \approx 0.7\, \tau_{eu}$. In SN, stationary conditions with similar plasma parameters are obtained for $f_{ELM} \approx 50$ Hz, due to the larger ELM size.

3. Discussion

Although Large ELMs have been observed in ohmic H-modes in TCV, their large size and probable pressure (gradient) threshold, indicated by the requirement of an ELM-free period lasting for 20 ms or more before the first Large ELM occurs following an L-H transition, suggest they may be related to type I ELMs observed in devices with auxiliary heating. The instability threshold for Large ELMs also depends on configurational factors, as apparent from the ELM control experiments [5]. In these experiments in DN, Large ELMs were induced or inhibited depending on the sign of the imbalance of a DN configuration. When the ion ∇B drift was away from the 'active' X-point Large ELMs appeared after an initial ELM-free period. This opens up the possibility of controlling both the evolution of H-modes and the size (ΔW, ΔN) of the ELMs.

The smaller ELMs observed near L-H and H-L transitions may be of type III. We know of no counterpart, in other devices, of 'mossy' ELMs, although detachment instabilities have been suggested as an explanation [6].

Acknowledgements: This work was partly supported by the Fonds National Suisse de la Recherche Scientifique.

References:

[1] J.-M. Moret et al., this conference (invited)
[2] F. Hofmann, J.B. Lister et al, Plasma Phys. Contr. Fusion **36**, (1994) B277.
[3] H. Weisen et al., 17th Symp. Plasma Phys. and Techn., Prague, June 1995.
[4] H. Weisen, D. Pasini, A. Weller et al., Rev. Sci. Instrum **62** (1991) 1531
[5] M. Dutch, F. Hofmann, et al., accepted for Nuclear Fusion (Letters), 1995.
[6] M.A. Mahdavi, personal communication, June 1994

Studies of X-point plasmas in the START tokamak

A Sykes, M.Booth, G Counsell, K Erents, J Ferreira+, D H J Goodall, M Gryaznevich, J B Hicks, J Hugill, I Jenkins, P Knight, G Maddison, S Manhood, R Martin, M Price, C Ribeiro‡, D C Robinson, V Shevchenko*, M J Walsh

UKAEA Government Division, Fusion, Culham, Abingdon, Oxon, OX14 3DB, UK
(UKAEA/EURATOM Fusion Association)
+ INPE, Sao Jose des Campos, Brazil
‡University of São Pãulo, Brazil
* TRINITI, Troitsk Moscow Region, 142092 Russia

1 Introduction

Low aspect ratio plasmas in START (A = R/a ~ 1.3) are normally obtained in the 'natural divertor' form characteristic of the low A tokamak [1], in which a substantial fraction of the scrape-off-layer (SOL) escapes interaction with the centre post and is led off into an exhaust plume. Although this remains a promising feature of low-A tokamaks, for comparison with conventional tokamaks a variety of X-point configurations are now under study in START. To date, these are obtained by passing an attractive current in a pair of poloidal field coils; denoted 'induction coils' in Fig 1.

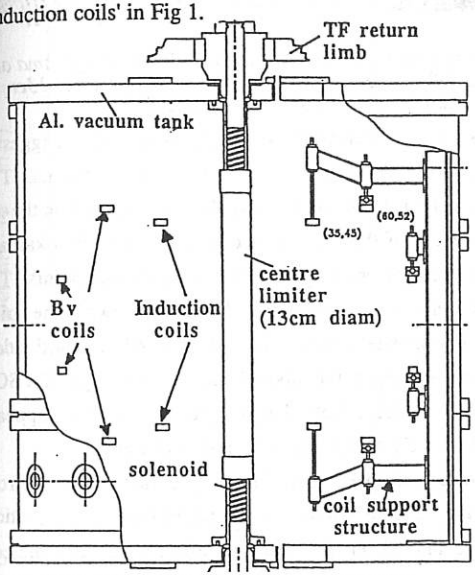

Fig 2 *Schematic of the present layout of START*

By this means a range of double null divertor (DND) and single null (SND) X-point plasmas can be obtained.

The equilibrium properties of these configurations are compared with visible light images of the plasma in section 2. Preliminary investigations of the turbulence and scrape-off layer (SOL) characteristics of these configurations, using high speed video, probe and reflectometer techniques are discussed in section 3 and comments on confinement given in section 4.

2 Equilibria in START

Standard plasmas are described in [2,3], and have plasma currents up to 250kA.

By passing current (of the same sign as the plasma current) in the 'induction' coils a range of X-point configurations can be obtained. As the X-point current increases, the plasma first

becomes elongated; then gradually separated from the central limiter; then forms a double X-point plasma. At first the X-point is close to the induction coil and a double 'footprint' is seen on each coil case as shown in Fig 2. This plasma has elongation $\kappa = 1.75$ and is vertically stable without active feedback.

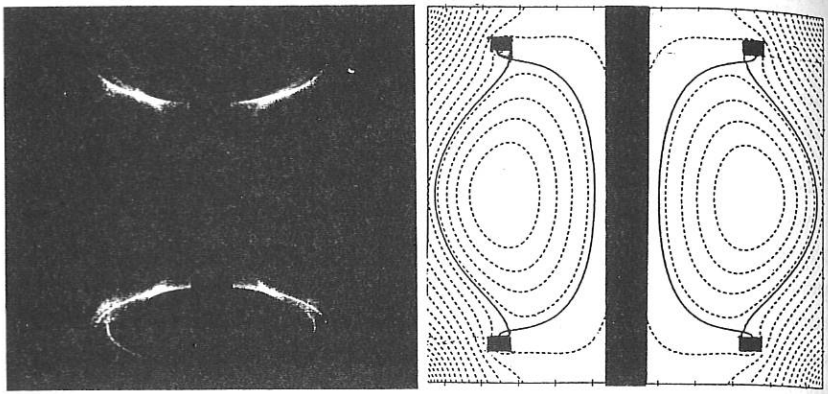

Fig 2 Photograph and equilibrium model of DND plasma in START. The plasma and centre rod currents are 100kA, 500kA respectively, and the centre column is 13cm in diameter. Note the 'shadows' cast by the Rogowski coil (lower left).

The image of the plasma boundary is now much sharper, and high speed videos suggest a greatly reduced level of fluctuations in the emitted light from the edge of the plasma. The picture also reveals remarkable toroidal symmetry of the diverted plasma footprints on the top and bottom coil cases. There is no beading of the light, as is commonly seen in tokamaks having targets composed of tiles, nor is there any braiding or splitting of the strike-points. The Rogowski coils around the upper and lower coil case targets cast distinct shadows in the strike point emissions, extending toroidally in opposite senses at the inboard and outboard sides, consistent with plasma transport to Bohm sheaths at the inboard and outboard ends of a SOL magnetic flux tube meeting a material boundary. Note that the plasma boundary appears especially sharp on the inboard side, where the toroidal field is 5 - 6 times larger.

The X-point coils, radius 35cm, have recently been moved to a separation of 90cm (from 80cm) and DND plasmas of elongation $\kappa \sim 2$ are obtained. At still higher I_{coil}/I_{plasma} ratios, the X-point is further from the coil case and the separatrix can completely surround the coil case.

3 Turbulence and SOL characteristics

A high speed video camera, with speeds of up to 40,500 frames/s, shows that the SOL of a 'natural divertor' plasma is turbulent with considerable 'flare' activity outside the apparent plasma edge (Fig 3a). In contrast, the X-point plasmas generally show a sharp edge with low

fluctuation level, in the emitted light and without external flares (Fig 3b). When viewed by more conventional optical devices, the fluctuations and flare activity produce a broad, fuzzy plasma edge and a surrounding halo.

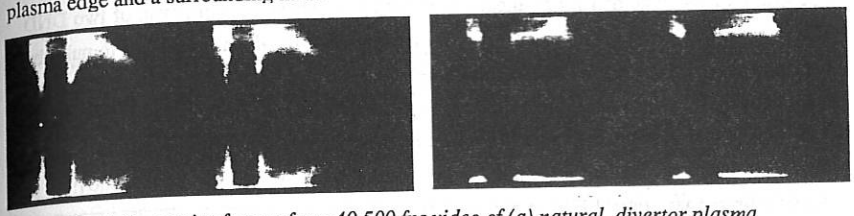

Fig 3 *Successive frames from 40,500 fps video of (a) natural divertor plasma (b) X-point plasma. Apart from X-point coil currents, conditions are identical in these two successive shots.*

Probe measurements of the 'natural divertor' plasmas have been reported in [4,5], and the results reflect the video observations; a high fluctuation level and a broad SOL (Fig 4, circles). In contrast, investigation of the edge regions of X-point plasmas of the type shown in Fig 2 indicate much reduced fluctuation levels and a SOL about 10 times narrower (Fig 4, squares).

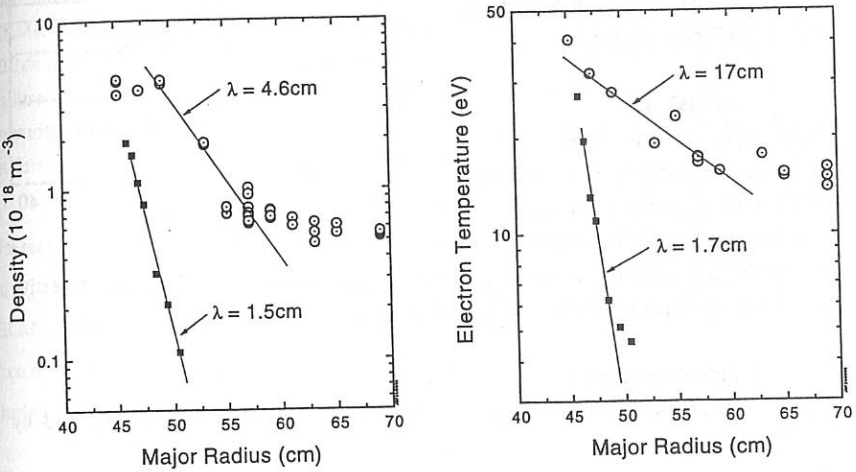

Fig 4 n_e and Te profiles in the SOL for 'natural divertor' (circles) and X-point configurations (black squares)

Note that flux tubes in the outer SOL are considerably shorter in the DND configuration, since they extend from one coil case to the other (connection length ~4m), rather than the entire length of the exhaust plume (overall length 12 ~ 16m). The factor 10 reduction in measured SOL width λ is consistent with the model proposed by Peng and Hedrick [6] for the minimum thickness of an SOL based on marginal stability to ideal ballooning modes, which implies $\lambda \propto L^2$.

4 Energy confinement

The reduced turbulence apparent in the DND plasmas could lead to steeper edge gradients, lower losses and improved confinement, and reflectometry measurements do indicate a steepening of the edge density gradient [7]. Estimates of energy confinement of two DND discharges are reported at this conference [2], using profiles obtained from pulse to pulse by Thomson scattering. These discharges are at relatively low plasma current and density, and show no clear evidence of improved energy confinement; their power density exceeds the ASDEX - Upgrade H-mode threshold [8] by a factor > 2, but β_N in both discharges is about one half of the threshold $\beta_N \sim 1$ recently suggested for transition to ELM-free H-mode [9].

Recent discharges (June 1995) at higher plasma currents and densities do show several features associated with transition to an improved confinement regime (Fig 5), in particular a spontaneous increase in density and stored energy after the X-point configuration is formed. However, the energy confinement of these discharges has not yet been evaluated.

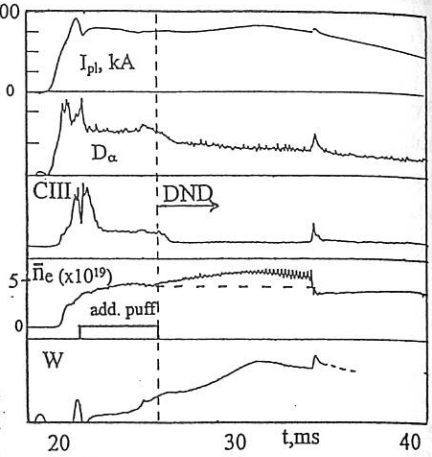

*Fig 5 waveforms of *25402*

Conclusions

X-point plasmas in START have been studied at elongations up to 2. Probe analysis shows a factor 10 reduction in SOL width when compared to the 'natural' plasma configuration. Recent discharges at high density and plasma current show features suggestive of improved confinement, but this is still to be quantified.

Acknowledgements

This work was jointly funded by the UK Department of Trade and Industry and by EURATOM.

References

[1] A Sykes, Plasma Physics and Controlled Fusion, Suppl. (12) B 36 p393, 1994
[2] M J Walsh et al, this conference
[3] M Gryaznevich et al, this conference
[4] J G Ferreira et al, in Proc. of 20th EPS conf., Lisbon 1993
[5] S K Erents et al, in Proc. of 11th PSI Conference, Ibaraki-ken 1994
[6] Y-K M Peng & L Hedrick, ITER Technical Meeting, Garching Feb 1994
[7] V Shevchenko et al, this conference
[8] F Ryter et al, in Proc of 20th EPS Conf, Lisbon, 1 (1993) 23
[9] M Valovic et al, this conference

Impurity Ion Emission and Edge Transport during ELMy H Modes in the New JET Divertor Configuration.

M G O'Mullane[1,2], H Chen[3], I H Coffey[4], N C Hawkes[2], M von Hellermann, L Lauro-Taroni, N J Peacock[2], A Rookes[5]

JET Joint Undertaking, Abingdon, Oxon., OX14 3EA, UK

[1]University College Cork, Ireland, [2]EURATOM-UKAEA Fusion Association, Culham Laboratory, Abingdon, Oxon., UK, [3]Southwestern Institute of Physics, Chengdu, China, [4]Queens University Belfast, Northern Ireland, [5]Imperial College, London, UK

Introduction

In H modes, impurities are expected to show accumulation. Experiments in DIII-D [1] have shown that the controlled removal of impurities is possible with long periods of grassy ELMs. An H-factor of 1.5 is maintained in these steady state discharges. In contrast, giant ELMs cause periodic collapses in confinement and can expel 5–10% of plasma energy on a millisecond timescale. They have the additional deleterious effect of being a source of fresh impurity influxes following energy deposition on the target plates. Clearly it is important to understand the impurity behaviour during these giant ELMs.

The typical giant ELM is triggered by a fast (τ~0.2ms) MHD event [2]. During this time the temperature in the outer part of the plasma falls on the same timescale with a concomitant rise in D_α. After the giant ELM (Type I) crash there may be a series of smaller, higher frequency, ELMs (Type III?) before H-mode is re-established. Alternatively the recovery to H mode can be free of D_α fluctuations. High time resolution ECE temperature measurements, fig.1, show that during this recovery period the temperature returns to its pre-ELM value.

The impurity transport behaviour of Neon (from gas puffing) during H mode with giant ELMs is modelled. Transport following the giant ELM and during the recovery of H mode are interpreted as distinct transport phases.

Impurity Transport Simulation of Giant ELMs

The SANCO 1.5-D impurity transport code has been used in all simulations. Particle transport is described by a diffusive and convective part with the flux of each ionisation stage

$$\Gamma_i = -D(\psi,t)\nabla \cdot n_i + V(\psi,t)n_i$$

The transport functions (D,V) are heuristically chosen and the solution is iterated until the transport is consistent with experiment.

In the case of low amplitude grassy ELMs it is possible to average the transport over a number of ELM periods (i.e. when total radiation is not perturbed). In the case of giant ELMs the transport is time-dependent.

A phenomenological model of impurity transport, within the constraints of the two function (D,V) formalism, during H modes with giant ELMs is proposed. The model assumes that H mode is established. Following the giant ELM crash there is a period of enhanced diffusion before ELM-free conditions are restored. This will be referred to as the H→L hybrid phase. It is characterised by smaller, high frequency, mini-ELMs and the recovery of the edge temperature during these mini-ELMs. The transitions between H-mode and the hybrid H→L phase and back to H-mode are modelled by a sharp switch (< 1ms) in the diffusion coefficient only. Both transport profiles are kept constant throughout each phase.

Experimental Observations

The impurity transport model requires many parameters that can vary both spatially and temporally. The model inputs are electron temperature and density profiles and a source function describing the impurity influx. The success, and limitations, of the model depend on these inputs and on the experimental data used for comparison to the simulation results.

Temperature and density are measured with ECE (15ms time resolution) and LIDAR (50ms). The source function follows the peripheral NeVII ($2s^2 - 2s2p$ 465.22Å) time history as measured by a survey VUV spectrometer (11ms). The instrumental time resolutions are not fast enough to follow the ELM event in detail.

The location of the transport barrier removes a free parameter from the simulations. Its location and width are found from the edge charge exchange measurements [4]. The change in density of Ne^{10+} inside and outside of the transport barrier is shown in fig.2. The barrier is located between r=3.68m and r=3.70m, corresponding to a normalised radius of 0.93. The change in the gradient of the ion temperature near the edge gives a barrier width of ~1cm.

There is *no* on-axis accumulation of Neon. Charge Exchange Recombination Spectroscopy (CXRS) shows hollow profiles. This necessitates the introduction of an outward convection term [3] (see fig.3).

The penetration of the ELM into the plasma column is followed from the time histories of the intrinsic impurities. NiXXV radiates at T_e ~ 500–700eV which, depending on plasma conditions, corresponds to radii of r ~ 0.7a – 0.9a. Fig.4 shows that, within the time resolution of the spectrometer, the impurities react simultaneously with the ELMs. In other discharges ELMs are seen clearly in the ClXV signal (T_e ~ 300–400eV) but not in the NiXXV. The penetration depth appears to depend on the abruptness of the recovery following the ELM crash.

Results

The model is adjusted to match the total number of Neon particles, the profile of the Ne^{10+} and impurity line intensities. A sudden drop (<1ms) in diffusion *only* following the ELM models the evolution of the Ne^{10+} profile (see fig.4). A transport barrier is essential throughout the simulation. A 'standard' convection of ($V=-2Dr/a^2$) during the H→L hybrid phase destroys the hollow profile. The allowable values of D(r) are intermediate between H and L mode

$$D_H(r)\ x2 < D_{H\rightarrow L}(r) < D_H(r)\ x4$$

where the L mode factor is typically x6–10 of H-mode value. Although the location is more important there is a sensitivity to the size of the barrier

$$-7\ ms^{-1} < V_{r=0.95a}(r) < -10\ ms^{-1}$$

There is qualitative agreement between the Ne^{10+} behaviour on either side of the transport barrier. Changes in diffusion during the H mode recovery have not been investigated although the simulations hint that there may be some change over the ELM-free part.

Conclusions

An impurity transport model has been applied to describe the behaviour of impurities during H mode with giant ELMs. There is a period of enhanced diffusion following the ELM crash. Although it can be interpreted as a H→L transition there is *no change in the convection barrier* and the change in diffusion is intermediate between the H and L mode values.

It is necessary to improve the time resolution, to sub-ms times, over that of present day spectroscopic instruments in order to follow the evolution of the transport barrier itself and the detailed behaviour of impurities during the ELM.

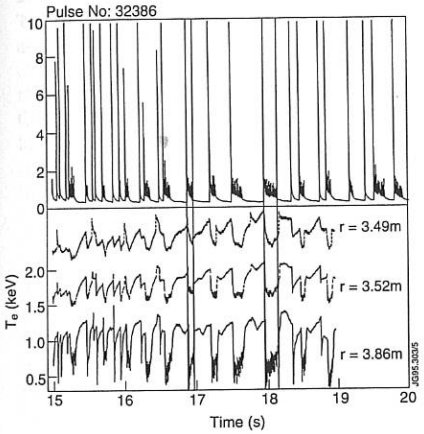

Fig.1 Edge T_e measurements during giant ELMs.

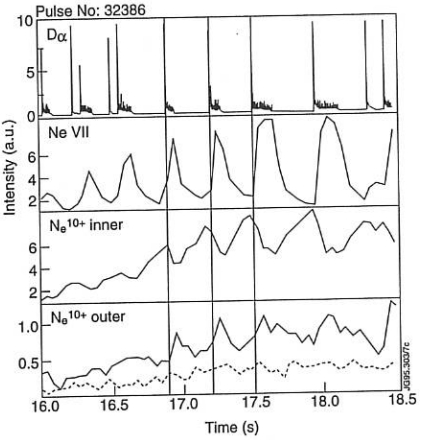

Fig.2 Evolution of spectroscopic signals.

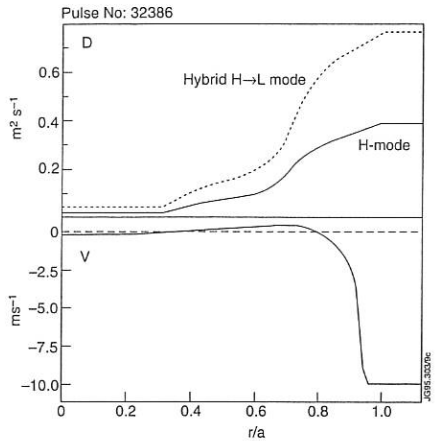

Fig.3 Transport profiles used in simulation.

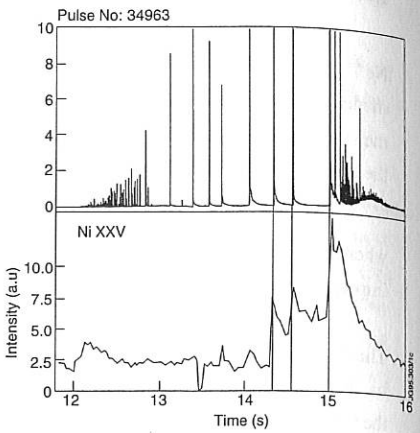

Fig.4 Time evolution of NiXXV showing ELMs

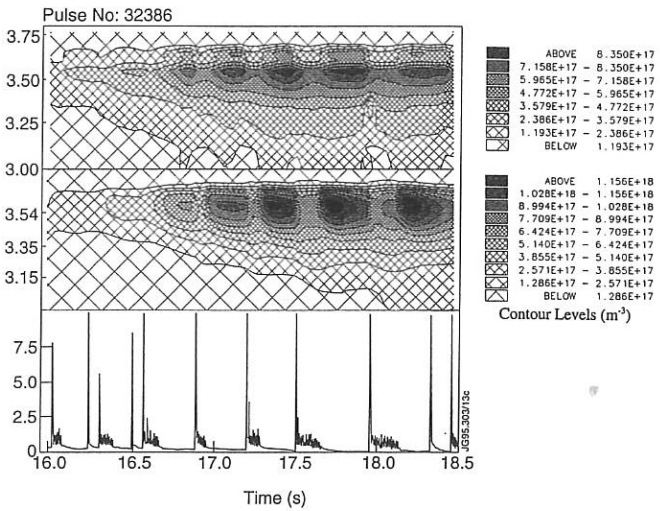

Fig.5 Comparison between Ne^{10+} profile from CXRS and simulation.

References

[1] DIII-D Team, 13th IAEA Conf. Washington, IAEA-CN-53/A-I-4,1990

[2] V V Parail et al., 15th IAEA Conf. Seville, IAEA-CN-60/A-2-II-3, 1995

[3] L Lauro-Taroni, 21st EPS Montpellier, I-120, 1994

[4] N C Hawkes, This conference

Comparison of Transition to ELM-free H-mode regime on COMPASS-D and ASDEX Upgrade

M Valovič J Ashall, S J Fielding, D A Gates, C G Gimblett, J Hugill, A W Morris,
M Maraschek*, W Schneider*, F Ryter,* H R Wilson, H Zohm*,
COMPASS-D Team and ASDEX Upgrade Team*
UKAEA, Fusion, Government Division, Culham, Abingdon, Oxon OX14 3DB, U.K.
(EURATOM/UKAEA Fusion Association)
*Max-Planck-Institut für Plasmaphysik, EURATOM-Association D-85740 Garching

1. Introduction

There is a general consensus that the transition from L-mode to H-mode confinement regimes is caused by a reduction of fluctuations at the plasma edge. In this case a parameter might exist which monotonically changes when plasma evolves from L-mode to ELM-free H-mode. In this study we test the hypothesis that this parameter is plasma pressure. We use the volume averaged plasma pressure and therefore we assume that profiles are self similar up to the transition to ELM-free H-mode. A restricted dataset from COMPASS-D and ASDEX Upgrade is used. Comparison of these two machines is interesting because both use single null X-point separatrix, boronized walls and have similar aspect ratio R/a=3.3, elongation κ=1.6-1.7 and low triangularity δ_{up}=0.0, δ_{down}=0.28-0.48. The machines differ considerably in size: R=0.56m, Ip=130-200kA, B_T=0.8-1.9T for COMPASS-D and R=1.65 m, Ip=0.75-1MA, B_T=1.0-2.5T for ASDEX Upgrade and different heating methods are used: Ohmic and ECR heating in COMPASS-D and Ohmic, NBI and ICR heating on ASDEX-Upgrade.

The transition to ELM-free H-mode does not necessarily coincide with the conventional L-H transition. The H-mode threshold is studied most extensively in the framework of the ITER H-mode database [1]. The H-mode power threshold on COMPASS-D is discussed in more detail in [2].

2. COMPASS-D data

Transition to or from ELM-free H-mode is typically identified by bursts on the H_α emission each associated with an increase in MHD activity observed on Mirnov coils at the outboard side at r/a=1.36. Duration of the ELM-free H-mode in COMPASS-D is 10-80 ms. For Ohmically heated plasma magnetic signals have a characteristic precursor-burst structure. The frequency of these bursts decreases when approaching ELM-free H-mode and according to conventional classification they can be called type-III ELMs. However, in the Ohmic plasma the power $P=P_{OH}-dW/dt$ is observed to be approximately constant when approaching ELM-free H-mode. However, parameters which monotonically increase are the volume-averaged plasma pressure $\langle p\rangle \propto W_{dia}$ and plasma density. Therefore in this case the conventional power dependence of event repetition rate ν for type-III ELMs $d\nu/dP<0$ should be replaced by

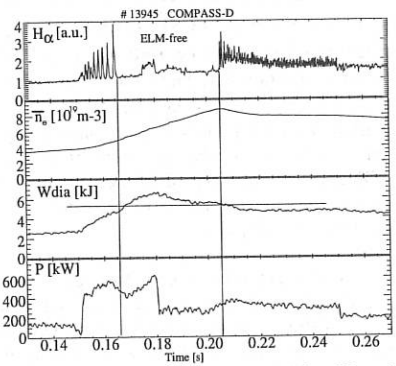

Fig. 1: Transition to and from ELM-free H-mode regime for ECRH discharge at $1\omega_{ec}$. I_p=208 kA, B_T=-1.9 T, $P=P_{OH}+P_{EC}$ - dW/dt.

$dv/d\langle p\rangle<0$. With ECR heating, the transition to an ELM-free regime is also associated by with a drop in the H_α emission and level of MHD fluctuations on the Mirnov coils. However, at low densities with ECRH, the observed H_α and MHD fluctuations just before the transition to the ELM-free regime do not clearly consist of separated events, indicating probably the scale of structures finer than the diagnostic resolution. With ECRH at higher densities, the transition to ELM-free regime appears with the Hα/MHD-events having $dv/d\langle p\rangle < 0$, similar to the Ohmic heating case. Fig. 1 shows such a transition. It is seen that the ELM-free period coincides with the period when the plasma pressure exceeds a certain threshold. Transitions to and from the ELM-free regime occur at the same value of $\langle p\rangle$. However, the density approaches the cut-off value towards the end of the ELM-free period and thus the power absorption profile is uncertain.

Next we test the hypothesis that the criterion for transition to ELM-free H-mode can be expressed in terms of the plasma pressure. As a simplest global dimensionless scaling we plot in Fig. 2 the values of toroidal beta at the transition to ELM-free regime v.s. the safety factor. Here, $\beta_T = 2\mu_0\langle p\rangle/B_T^2$, where B_T is the toroidal magnetic field at the geometric plasma radius and $q_* = 5a^2B_T/(RI_{P_{MA}})(1+\kappa^2)/2$ [3]. The data show that with both Ohmic and ECR heating, ELM-free H-mode is triggered approximately along the line of constant normalised beta $\beta_N = \beta_T(\%)aB_T/I_P(MA) \sim 1$. This line well separates the ELM-free regimes from L-mode or type-III ELMy regimes. This criterion also holds for Ohmically heated plasma in helium where the heating power is typically 1.5 times higher than in deuterium. For ECR heating at fundamental resonance, the transition occurs at similar beta for both lower $n \approx (1.5\text{-}1.9)\times10^{19}$ m^{-3} and medium $n \approx (3.5\text{-}4.8)\times10^{19}m^{-3}$ line-averaged densities, although the required RF power in the first case is about 2× higher. The exception however, ECRH plasmas at $2\omega_{ec}$ where the density is low $n \approx (0.7\text{-}1.4)\times10^{19}m^{-3}$ and the transition is at higher beta, or even no transition is observed despite $\beta_N > 1$. These plasmas have very low electron collisionality. An ELM-free regime has not been obtained on COMPASS-D for any discharges with the unfavourable ion gradB drift direction i. e. away from the X-point.

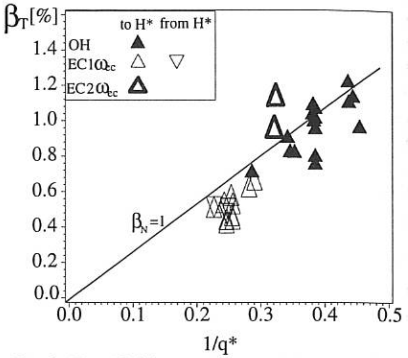

Fig. 2: Toroidal beta at the transition to or from ELM free H-mode regime.

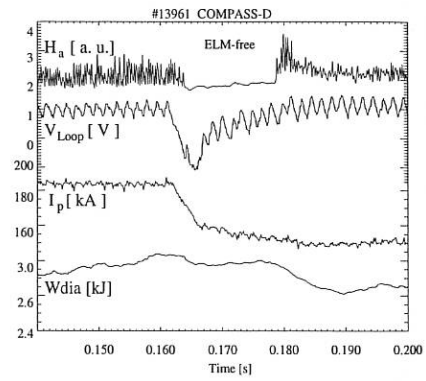

Fig. 3: Effect of current ramp down on transition to ELM-free regime.

Preliminary experiments have been performed in order to test the dependence of the transition to ELM-free regime on the edge current density, using current ramp down in Ohmically heated discharges. It was found that in discharges close to a H-mode transition current ramp down can induce transiently the ELM-free regime as illustrated in Fig. 3. Application

of ramp down during an ELM-free period never triggered ELMs or L-mode.

3. ASDEX Upgrade data

On ASDEX Upgrade, the ELM-free regime is also established through a period of events on the H_α emission which are accompanied by activity as detected by Mirnov coils in the outboard mid plane (r/a=1.28). With ion gradB drift towards the X-point, type-III ELMs or 'late dithering cycles' [4] occur, but not for the other direction. However, in this second case 'L-mode fluctuations' grow with time and power. Fig. 4. shows transitions to and from the ELM-free regime with unfavourable ion gradB drift.

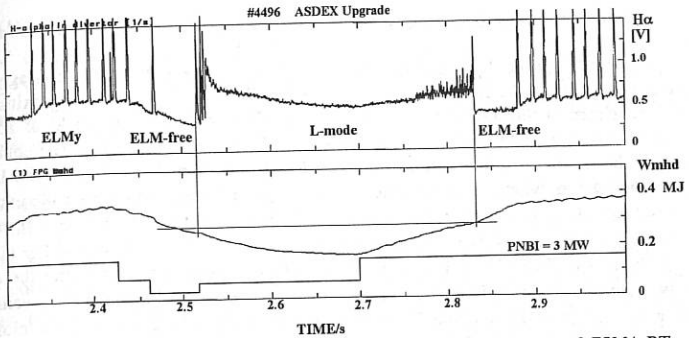

Fig.5: Transition to and from ELM-free regime on ASDEX-Upgrade. Ip=0.75MA,BT=+2T.

As on COMPASS-D, both transitions occur at approximately the same values of volume averaged plasma pressure $\langle p \rangle \propto W_{mhd}$. Fig. 5. summarises the values of β_T at transitions to and from the ELM-free regime for NBI, ICRH and OH heating and both directions of toroidal magnetic field. COMPASS-D data are shown for comparison. It is seen that the transition in ASDEX Upgrade appears close to the same value of β_N as on COMPASS-D, however, the scatter increases towards low q values. Concerning the asymmetry in the B_T direction, inspection of similar shots with $B_T=\pm 2T$ (##4388, 4387) reveals that at the transition to the ELM-free regime W_{mhd} is the same within 10% for both field directions while the heating power P_{NBI} is 2× larger for unfavourable ion gradB.

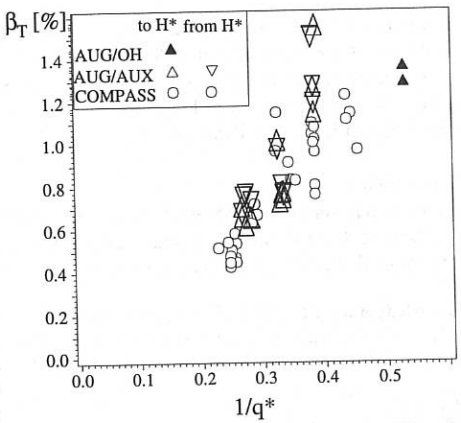

Fig. 5: β_T at transition to and from ELM-free H-mode on ASDEX Upgrade. COMPASS-D data from Fig. 2 are shown for comparison.

4. Discussion

One possible explanation for these observations might be the stabilising effect of plasma pressure. Ideal MHD theory predicts that the plasma edge is stable against the pressure driven (flute) instabilities due to the favourable averaged curvature at the edge where q>1 [5]. This stable system can be de-stabilised by increasing the edge current density or by non-zero resistivity. In order to restore stability the plasma pressure should exceed the offset given by destabilising mechanisms. For the case of finite edge current density the criterion for linear stability (peeling modes) [6] can be re-written in terms of volume average beta as:

$$\beta_T > 2\sqrt{(1+\kappa^2)/2\kappa^2}\,\frac{L_p}{a}\,s\,\frac{j_a}{\langle j\rangle}\times\frac{1}{q^2} \qquad (1)$$

where $s=aq'/q$, $L_p=<p>/p'$, prime denotes derivative at the edge, $< >$ denotes volume average, j is the total current density and j_a the current density at the edge. This formula predicts approximately the observed dependence of threshold beta on q for COMPASS and ASDEX-Upgrade, as above. Also the threshold in beta is independent of machine size if the profiles are similar. The equation (1) also predicts the observed induced transition into ELM-free H-mode on COMPASS-D by plasma current ramp-down, which is expected to reduce $j_a/<j>$, although the increase of q during ramp down is expected to reduce the threshold beta as well. On the other hand, $j_a/<j>$ is expected to increase due to the bootstrap current and thus can explain the increase of threshold β_T at low density $2\omega_{ec}$ ECRH in COMPASS-D. For order-of-magnitude comparison we re-write the edge current density factor as $sj_a/<j>=s(1-s/2)$ having a maximum at s=1. For this s and for a value of edge pressure gradient $L_p/a\approx 1/10$ equation (1) predicts stability for $\beta_T > 0.92$ % at q=3 i. e. close to the value at which transition to ELM-free H-mode is observed. The second de-stabilising effect, finite resistivity [7], is known to be relevant [8] but is not discussed here.

If a transition to ELM-free H mode occurs above a critical plasma pressure then some of the dependencies in the representation of the threshold in power P_{th} can be explained by the behaviour of energy confinement time τ_E. Hysteresis can be a consequence of the discontinuity of τ_E at the transition. The increase of P_{th} at low densities, observed in COMPASS-D [2] and other devices, can be a consequence of the dependence $\tau_E \propto n$.

5. Conclusions

The transition to and from ELM-free H-mode is observed to occur at a threshold $\beta_T \times q$ ($\beta_N \cong 1$) on both COMPASS-D and ASDEX-Upgrade. Preliminary comparison with ideal MHD peeling mode theory shows that it could explain some of these observations.

Acknowledgement. Discussions with Dr R J Hastie are gratefully acknowledged. This work was jointly funded by the UK Department of Trade of Industry and EURATOM and was performed under a collaboration agreement between the COMPASS-D and ASDEX-Upgrade Teams.

References

[1] Ryter F et al, *Proc. of 21st EPS Conf. on Contr. Fus. and Pl. Phys.* **I** 334 (1994)
[2] Fielding S J et al, *this Conference*
[3] *ITER documentation Series* **No 21** 18 IAEA Vienna (1991)
[4] Zohm H et al, *Plasma Physics and Controlled Fusion* **37** *437 (1995)*
[5] Shafranov V D, Yurchenko E I, *Soviet Physics JETP* **26** 682 (1968)
[6] Connor J W, Hastie R J and Wilson H R, *private communication*
[7] Drake J F and Antonsen T M Jr, *Phys. Fluids* 27 898 (1984)
[8] Guzdar P N et al, *Phys. Fluids* **B5** 3712 (1993)

W7-AS with Modified Mirror Ratio at High ι-Values

F. Rau, C.D. Beidler, J. Das, G. Kühner, E. Harmeyer, J. Kißlinger, H. Niedermeyer, H. Ringler, E. Würsching, H. Wobig, W7-AS Team, ECRH Group

Max-Planck-Institut für Plasmaphysik, IPP-EURATOM-Association
D-85748 Garching, Germany

A series of operation points is established in this paper for the three configuration types "R", "M" and "A" with modified mirror ratio in W7-AS, at various values of the edge rotational transform ι_a>0.49. We use stationary low-β plasmas in order to compare to vacuum field calculations. The first part of this paper describes vacuum field properties for the three configuration types, the second part gives experimental data.

The number of trapped particles and their localization can be modified in W7-AS by a change of the mirror ratio, defined as MR = (B_{36} - B_0) / (B_{36} + B_0), via the axis field values at the toroidal angles ϕ=0 and 36° in the 5 field periods of the device. This is done by different input currents in the non-planar coils at ϕ=36° compared to the currents in the other non-planar coils. The mirror ratio changes its sign in "R" with MR=10% and "A" with MR = -10%. A new configuration type, "M" with minimum values of MR < 1 %, is introduced in the vicinity of the standard case, "S". In all cases the field value B_{36} is kept to ≈1.26 T for ECRH plasma production and heating: the average axis field is largest in "A" and lowest in "R". The sizes of the edge magnetic surfaces differ at ϕ=0 and 36°: for "R" they are larger at ϕ=0 than at 36°, and *vice versa* for "A".

Vacuum fields for various values of ι_a are shown in Fig.1 for "R" and "A" with MR = ±10 %, as well as for "M" with MR ≈0.2 %. No vertical fields are applied. The input data for the calculations are from actual shot data, except for the case at ι_a=5/7. The plasma edges are corrugated according to the effective main resonance, ι_a=5/N, with N=7 to 10 in the range of interest. The corrugation increases with decreasing local shear and is largest in "A" near ι_a=5/9 (not shown in the figure). Internal islands at ι=5/9 (or 5/10) can exist within closed edge surfaces in the vacuum fields of "R", "S" and "M" at slightly differing ι−values on axis. The radial extension of these islands increases towards the edge, it is smaller in "R" than in "M". Higher-order resonances, e.g. the combinations of 5/10 and 5/9 => 10/19 or 5/9 and 5/8 => 10/17 can be seen in the vacuum fields at specific ι−values. Fig.2 summarizes the dependences of minor radius, global shear and global well depth *vs* ι_a for the three configuration types. The minor radius is defined by the average size of the 'last closed' surface not touching the inboard limiters or by the size of the separatrix; its value shrinks with increasing ι_a. When changing from "R" via "M" to "A" at ι_a=0.55, the minor radius stays between 15 and 16 cm, the magnetic well deepens from -0.7 to -1.3%, but the shear is reduced from 6% for "R" to nearly zero for "A". This is accompanied by a minimum of the minor radius at the 5/9 resonance in the latter configuration. Similar minima are indicated for "R" and "M" at ι_a=5/8.

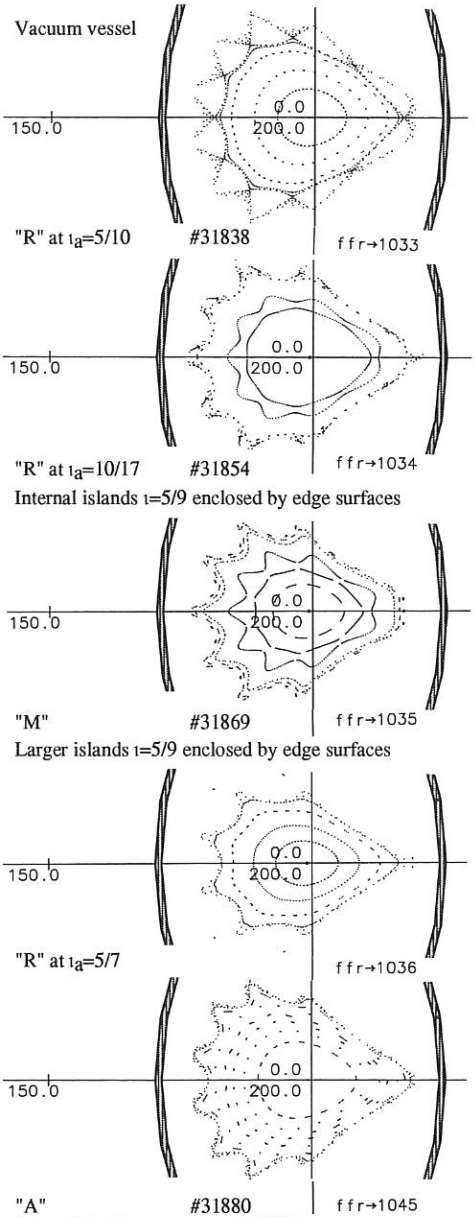

Fig.1: Magnetic surfaces in W7-AS at modified mirror ratio, ϕ=0.

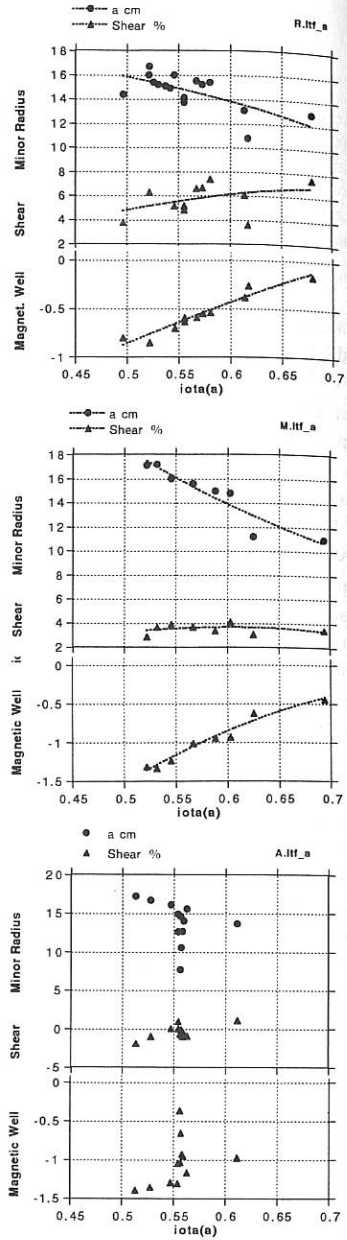

Fig.2: Minor radius, shear and magnetic well for "R", "M" and "A" versus ι_a.

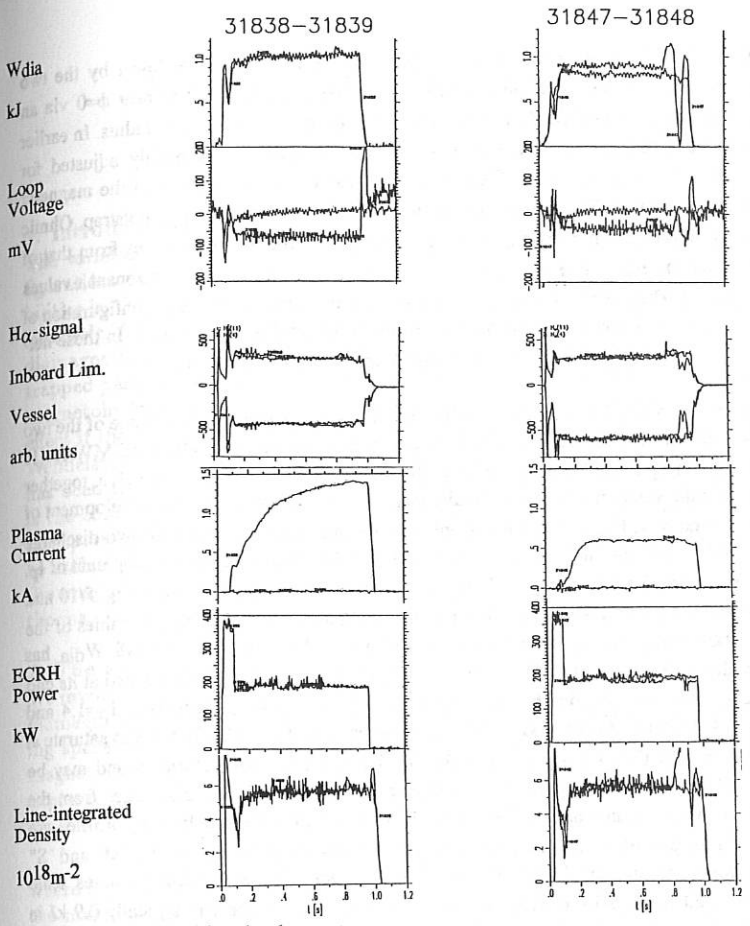

Fig.3 "R" I_p=0 and free development

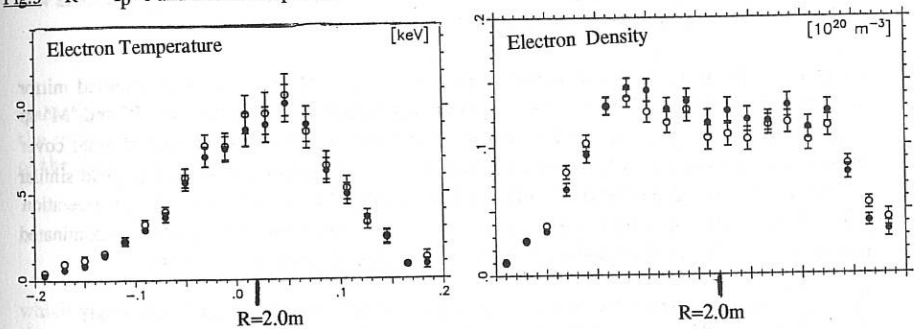

Fig.4: Thomson profiles for "R" at 0.54 s : #31838 I_p=0 (dots) ; #31839 Free development (circles).

Experimental details. The plasma radius, a, was set in W7-AS until 1994 at low ι by the two movable main limiters at ϕ=36°, and subsequently by the fixed inboard limiters near ϕ=0 via an appropriate axis shift by a vertical field. At high ι the separatrix defines the plasma radius. In earlier experiments with modified mirror ratio the edge rotational transform was mainly adjusted for $\iota_a \approx 0.34$, see /1/ and /2/. Any increase in β causes an increase of ι in the vicinity of the magnetic axis; other changes of the ι-profile are correlated with residual plasma currents I_p, (bootstrap, Ohmic and/or electron-cyclotron-driven current). Then the resulting ι-profile locally deviates from that of the vacuum field, and its edge value differs from ι_a. Effects of magnetic islands at resonant ι-values are difficult to predict. They may also change the plasma radius. Details of the edge configuration of the standard case, "S", and results of correlated experiments for $I_p \approx 0$ are given in /3/. In these net-current-free plasmas, the bootstrap current was compensated by an Ohmic current.

Plasma start-up in the present investigation is with ≈0.4 MW input power. After 0.1s one of the two gyrotrons is switched off, the second one is continued at a moderate power of about 0.2 MW for 1s pulse time. The line-integrated density is controlled by feed-back of an external gas valve, together with recycling from the vessel walls. We study discharge pairs with $I_p \approx 0$ and a free development of the residual plasma current. Fig.3 gives for example various quantities of interest for two discharge pairs in"R", #31838 and #31847 at $I_p \approx 0$, as well as #31839 and #31848 with free development of I_p. Minor radii of 14.3 and 13.8cm, average axis fields of 1.16 and 1.14 T, and values of ι_a=5/10 and 0.55, resp., are calculated in the vacuum configurations of these discharges. Identical values of the diamagnetic energy, $W_{dia} \approx 1.1$kJ, are obtained in the pair #31838-39; in #31847-48 W_{dia} has successively smaller values by ≈10%. The discharge #31847 ($I_p \approx 0$, $\iota_a \approx 0.55$) is influenced at its end by an edge probe. This perturbation should be neglected. Free-developing currents of I_p=1.4 and 0.6kA are seen in #31839 and #31848, with differing time behavior: I_p in #31839 tends to saturate at about 1s near the end of the discharge, that of #31848 has a much faster saturation and may be influenced by ι_a=5/9. Values of $\iota_p \approx 4I_p/(Ba^2) = 0.02$ and 0.01 result for these discharges from the cylindrical approximation using vacuum field data. Peaked T_e and slightly hollow n_e profiles are nearly identical for the pair of discharges shown in Fig.4, profiles of other cases in "R", "M" and "S" (two discharge pairs) are similar, T_e profiles in "A" are broader, however. Central values scale roughly as W_{dia} in all cases. With increasing ι_a the values of W_{dia} decrease to typically 0.9 kJ in "R" and "M"; the observed H_a-signals at the inboard limiter show small variations, those at the wall tend to increase marginally. No space-resolution of H_a-signals was attempted.

Summary and conclusions: Three configuration types, "R", "M" and "A" with modified mirror ratio are investigated in W7-AS at ι_a>0.49 by extending vacuum field properties for "R" and "M" up to $\iota_a \approx 0.7$ and for "A" up to $\iota_a \approx 0.6$. Initial experimental data with low-power ECRH plasmas cover the transition towards separatrix-dominated cases for "R" and "M" up to $\iota_a \approx 0.58$, and yield similar T_e- and n_e-profiles with central values of 0.8-1.3 keV and $1.4\text{-}1 \times 10^{19} m^{-3}$, resp.. The new operation points thus provide a basis for further more detailed studies of the transition from limiter-dominated to separatrix-dominated configurations, magnetic islands and effects of trapped particles.

/1/ F. Rau et. al., 21st EPS Montpellier 1994, Eur. Conf. Abstr., Vol.18B I, 400 (1994)
/2/ F. Rau et. al., 10th Int. Stell. Conf. Madrid (1995), in press
/3/ J. Das et al., paper submitted for this conference

Drift Reversal in the WVII-X Advanced Stellarator

D. Clément and W. A. Cooper
CRPP/EPFL, Association Euratom/Confederation Suisse,
Lausanne, Switzerland

1. Introduction

The variation of the magnetic field along a field line in fusion plasma confinement configurations causes particles to become mirror-trapped. These particles can trigger instabilities in the fluid plasma which can have important implications especially if they are energetic. The sign of the ratio of the bounce-averaged magnetic drift frequency to the diamagnetic drift frequency constitutes a useful and important measure of the impact of trapped particles on instabilities. The application of a Schwarz inequality shows that for magnetohydrodynamic (MHD) modes, energetic trapped particles exercise a stabilising effect if the ratio is positive, but no conclusions can be drawn if it is negative [1]. In the Wendelstein WVII-X device [2], the effect of trapped particles on ballooning instabilities has been examined by Nührenberg and Zheng [3]. Another important class of instability is the *collisionless trapped particle mode* ($CTPM$) [4], which can enhance anomalous transport losses. These modes that are localised in regions of unfavourable curvature can be stabilised by the digging of a magnetic well at finite β that reverses the direction of the magnetic drifts. In this work, we examine the conditions that lead to the reversal of the magnetic drift frequencies in the WVII-X Advanced Stellarator.

2. The equations

We invoke the ballooning representation in order to calculate the ratio ot the magnetic to diamagnetic drift frequencies because local stability properties are evaluated in ballooning space in order to reconcile conditions of periodicity in toroidal systems with finite magnetic shear [5]. In the ballooning space, the magnetic drift frequency is given by the expression

$$\omega_{dj} = -\frac{1}{\Omega_j}\left[\left(\frac{B\times k_\perp\cdot\kappa}{B}\right)v_\parallel^2 + \left(\frac{B\times k_\perp\cdot\nabla lnB}{B}\right)\frac{v_\perp^2}{2}\right], \tag{1}$$

where $\Omega_j = Z_j eB/M_j$ is the cyclotron frequency of a particle of species j, $\kappa = (b\cdot\nabla)b$ is the magnetic field line curvature and b is the unit vector along the magnetic field lines. The diamagnetic drift frequency is

$$\omega_{*j} = -\frac{p_j}{\Omega_j\rho_{Mj}}\frac{B\times k_\perp\cdot\nabla lnN_j}{B}, \tag{2}$$

where p_j is the pressure, N_j is the density, $Z_j e$ is the electronic charge, $\rho_{Mj} = M_j N_j$ is the mass density and M_j is the mass of the particles of species j. We express the ratio of the diamagnetic drift frequency to the bounce-averaged magnetic drift frequency as

$$\frac{1}{R} = \frac{(-1)\int_{\theta_{min}}^{\theta_{max}} d\theta\sqrt{g}\frac{B}{v_\parallel}}{\int_{\theta_{min}}^{\theta_{max}} d\theta\frac{\sqrt{g}}{v_\parallel}\left[\left(\frac{B\times\nabla S\cdot\nabla(p+B^2/2)}{B^3}\right)v_\parallel^2 + \left(\frac{B\times\nabla S\cdot\nabla B}{B^2}\right)\frac{v_\perp^2}{2}\right]}, \tag{3}$$

which is evaluated in the Boozer magnetic coordinate system [6] (s,θ,ϕ), where s labels that radial variable, θ is the poloidal angle and ϕ is the toroidal angle. In this coordinate system, the magnetic field B lines are straight, hence the wave vector $k_\perp = \nabla S$ in ballooning space is given by $\nabla S = \nabla\phi - q\nabla\theta - q'(\theta-\theta_k)\nabla s$, where q is the inverse

of the rotational transform and prime (′) denotes the derivative with respect to s. The integration with respect to θ between the bounce points θ_{min} and θ_{max} are evaluated on a fixed magnetic field line $\alpha = \phi - q\theta$ which reflects the coordinates being straight. The factor (-1) in the numerator is a result of the normalisation of the diamagnetic drift frequency that we have imposed to unity taking into consideration that the density profile is assumed monotonically from the centre to the edge of the plasma to make its sign negative.

3. Description of the results

We calculate three dimensional (3D) equilibria with nested magnetic flux surfaces that model the WVII-X device with the VMEC code [7]. We map these equilibria to the Boozer magnetic coordinates with the modules of the TERPSICHORE stability code that perform this task [8]. To evaluate the bounce averages, we chooses $\theta = \theta_{max}$ and evaluate the pitch $\lambda = 1/B(\theta_{max})$ and then follow the field line to search for θ_{min} that satisfies $B(\theta_{min}) = B(\theta_{max})$ to a prescribed absolute error, typically 10^{-11}. We then apply a Simpson rule to performe the bounce average integrations. We have benchmarked the calculations with results presented for the tight aspect ratio START tokamak [9]. We find good agreement with respect to the drift reversal of the barely trapped particles and with the observation that the fraction of drift-reversed particles does not change with β. Some discrepancies are observed in the shape of the $1/R$ curve for deeply trapped particles that can be attributed to the difference in the models employed. The mod-B distribution in WVII-X on a surface with $s = 10/18$ is illustrated in Fig. 1. As an initial application for WVII-X, we have considered the evaluation of $1/R$ on two different field lines $\alpha = -1$ and $\alpha = -1 - 2\pi/5$, which due to stellarator symmetry describe in fact the same field line (Fig. 1). The results are essentially identical. The calculation of $1/R$ shows that the grad-B drifts dominate over the curvature drifts because the trapped particle orbits are confined to the straight sections of the WVII-X device. It also shows that the magnetic well is an important factor associated with drift reversal. At low β, only the barely trapped particles have orbits of sufficient toroidal extent to sample the well to reverse their drifts. The bulk of the trapped particles do not drift-reverse except for a small fraction of deeply trapped particles near the magnetic axis. This is shown in Figs. 2a-2c. As we raise β, we find that the fraction of drift-reversed particles increases significantly at $\beta = 1.5\%$ and that virtually all trapped particles reverse their magnetic drifts near the MHD limit of $\beta = 5\%$. The drift reversal is caused by the enhancement in the magnitude of the radial gradient of the Jacobian $\sqrt{g}$ which is associated with a deepening of the magnetic well with β and the steepening of the radial gradient of the poloidal current flux. The fraction of drift-reversed particles on flux surfaces with $s = 3/18$, $s = 10/18$ and $s = 16/18$ occupy the solid regions in Figs. 2a-2c for $\beta = 0.15\%$, in Figs. 2d-2f for $\beta = 1.5\%$ and in Figs. 2g-2i for $\beta = 5.3\%$.

4. Summary and conclusions

In summary, we have analysed the conditions for drift reversal in the Wendelstein VII-X Advanced Stellarator. For this purpose, we have evaluated the bounced-averaged drifts in ballooning space because local stability of a plasma is commonly investigated after invoking the ballooning mode transformation (in order to reconcile conditions of periodicity in systems with shear). The calculations are performed in the straight field line Boozer magnetic coordinates . At low β, we obtain that the helically (toroidally) trapped particles have bounced-averaged drift frequencies of the same (opposite) sign compared with the diamagnetic drift frequency (assuming monotonically descreasing density pro-

files). As β increases, we find that the fraction of trapped particles that experience drift reversal also increases (manifested by a change in the sign of the ratio of the drifts). This increase is attributed mainly to the modification of the grad-B drift due to the combination of a favourable variation of the radial gradient of the Jacobian (which is related to a deepening of the magnetic well with β) and a steepening of the poloidal current flux gradient. Near the MHD β limit of 5%, nearly all the trapped particles become drift-reversed. This could have very favourable implications for anomalous transport in the WVII-X.

References

[1] Rosenbluth M N et al, *Phys. Rev. Lett.* **51** 1967 (1983)
[2] Beidler C. et al., *Fusion Technol.* **17** 148 (1990)
[3] Nührenberg J and Zheng L J, *Proc. 20th EPS Conf. Contr. Fusion Plasma Phys.* ECA17c I-413 (1993)
[4] Rosenbluth M N and Sloan M L, *Phys. Fluids* **14** 1725 (1971)
[5] Connor J W, Hastie R J and Taylor J B, *Phys. Rev. Lett.* **40** 396 (1978)
[6] Boozer A H, *Phys. Fluids* **23** 904 (1980)
[7] Hirshman S P and Betancourt O, *J. Comput. Phys.* **96** 99 (1991)
[8] Anderson D V et al, *Int. J. Supercomp. Appl.* **4** 34 (1990)
[9] Roach C M, Connor J W and Janjua S J, *Culham Laboratory Report* **281** (1995)

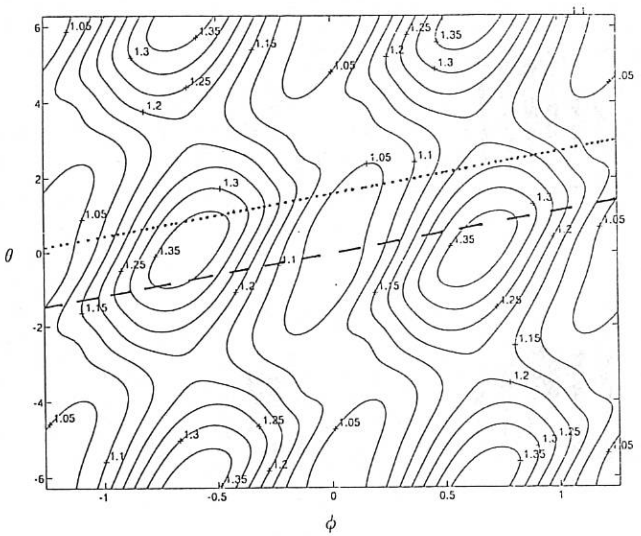

Figure 1: The mod-B contour distribution in WVII-X on a flux surface with $s = 10/18$ at $\beta = 1.5\%$ peeled open over the poloidal and toroidal Boozer magnetic coordinate angles θ and ϕ, respectively. This distribution covers two field periods $-2\pi/5 < \phi < 2\pi/5$ and two poloidal transits $2\pi < \theta < 2\pi$. The dashed line corresponds to the trajectory of the magnetic field line labelled $\alpha = 0$ and the dotted line corresponds to the field line with $\alpha = 2\pi/5$ or alternatively can be considered as the $\alpha = 0$ line but one field period downstream.

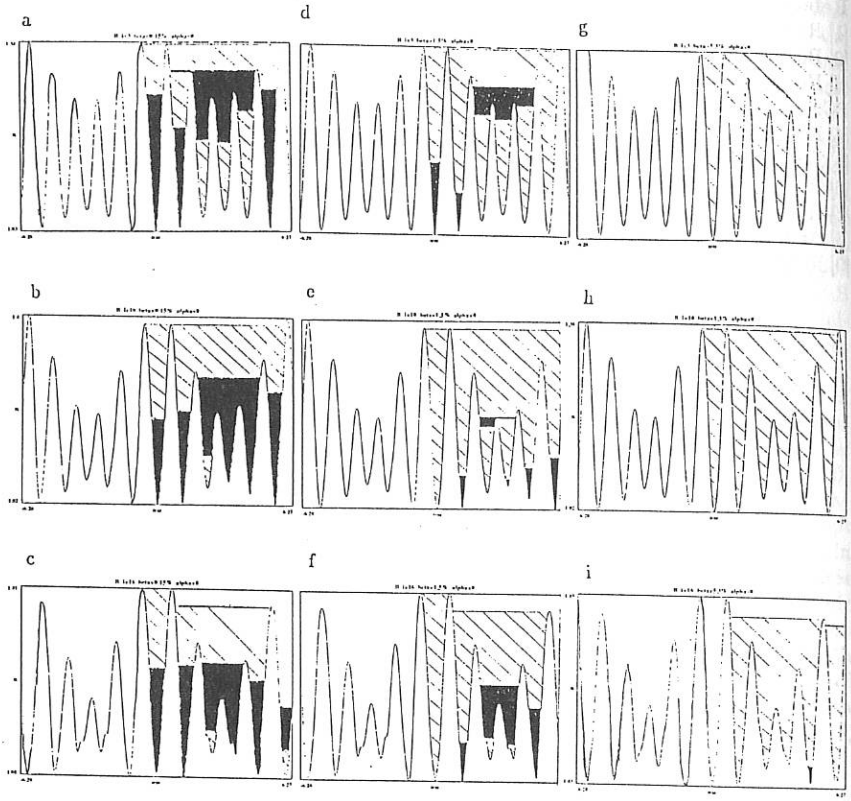

Figure 2: The magnitude of the magnetic field in WVII-X as a function of the poloidal angle θ along the field line $\alpha = 0$ for a) $\beta = 0.15\%$ and $s = 3/18$, b) $\beta = 0.15\%$ and $s = 10/18$, c) $\beta = 0.15\%$ and $s = 16/18$, d) $\beta = 1.5\%$ and $s = 3/18$, e) $\beta = 1.5\%$ and $s = 10/18$, f) $\beta = 1.5\%$ and $s = 16/18$, g) $\beta = 5.3\%$ and $s = 3/18$, h) $\beta = 5.3\%$ and $s = 10/18$, and i) $\beta = 5.3\%$ and $s = 16/18$. Trapped particles that experience drift reversal are confined in the solid regions and those do not drift-reverse are located in the hatched regions.

Simulation and Analysis of Neutral Particle Spectra for W7-AS

N. Rust, B. Wolle, K. Hübner, M. Kick*), F.P. Penningsfeld*), U. Stroth*), H. Walter

Institut für Angewandte Physik, Universität Heidelberg, D-69120 Heidelberg, Germany

*) Max-Planck-Institut für Plasmaphysik

Association EURATOM-IPP, D-85748 Garching, Germany

1. Introduction

Good confinement of energetic ions is one of the optimization criteria for the W7-X stellarator [1]. Therefore, it is of importance to improve present experimental and theoretical methods for the investigation of the physics of fast particle confinement. Here, we present first results of a detailed experimental and theoretical study on analysis and interpretation of non-thermal neutral particle spectra for W7-AS which are strongly related to the ion energy distribution.

2. Experimental Setup

The neutral particle diagnostics (NPA) at W7-AS consists of 4 neutral particle energy-analysers, built and calibrated up to 22 keV at Joffe Institute [2]. They have lines-of-sight in a vertical plane and are mounted on a lift that can be moved in vertical direction. A neutral particle diagnostic beam with an energy of 22 keV is passing vertically through the plasma center. This allows spacially resolved measurements at the crossing-points of the beam with the lines-of-sight of the analysers. The observation angle of the diagnostic system is about 35° to the magnetic field lines. For the measurement of the ion energy distribution two analysers are used, each having 10 energy channels.

3. Neutral Particle Flux

The local charge-exchange particle flux $S(v,\mu,t)$ from the plasma is given by

$$S(v,\mu,t) = g\, n_i\, n_0\, f(v,\mu,t)\, \langle\sigma\, v\rangle_{cx} \cdot \exp\left[-\int_0^a \frac{1}{v}\left(n_i \langle\sigma\, v\rangle_{cx} + n_e \langle\sigma\, v\rangle_e\right)\right] . \qquad (1)$$

Here, $f(v,\mu,t)$ is the time-dependent 2D ion velocity distribution, v is the particle velocity, $\mu = v_{\parallel}/v_{\perp}$ the pitch-angle, g is a geometrical factor, n_i and n_0 are the ion and neutral particle densities, $\langle\sigma\, v\rangle_{cx}$ and $\langle\sigma\, v\rangle_e$ are the rate coefficients for charge-exchange and electron impact ionization [3]. The exponential factor of eq. 1 describes the absorption of the particles on their trajectory through the plasma which is important for the low-energy part in the measured spectra and depends on the absolute values of the ion and electron density profiles.

4. Simulation of the Ion Distribution Function

For the comparison with the measured neutral particle spectra it is important that the simulation of the ion velocity distribution includes pitch-angle scattering. Therefore we calculate the non-thermal ion velocity distributions of neutral-beam-heated ions by using the time-dependent 2D Fokker-Planck code NRFPS [4] which solves the Fokker-Planck equation for the velocity distribution $f(v, \mu, t)$.

Numerical calculations were carried out for W7-AS discharges with H^0-injection into H^+-plasma. The central density was 2.8×10^{19} m^{-3}, the central electron and ion temperatures were 0.5 and 0.44 keV, respectively. The injection angle of the neutral-beam injection was 22°. The electron temperature and density were taken from Thomson scattering and the ion temperature was taken from the neutral particle diagnostics. The deposition profile for the injected particles was calculated with the 3D Fafner code. Since Z_{eff}-measurements were not available, $Z_{eff} \approx 2$ due to carbon impurities was assumed. Fig. 1 shows the calculated ion velocity distribution for some different pitch-angles in the presence of neutral-beam injection.

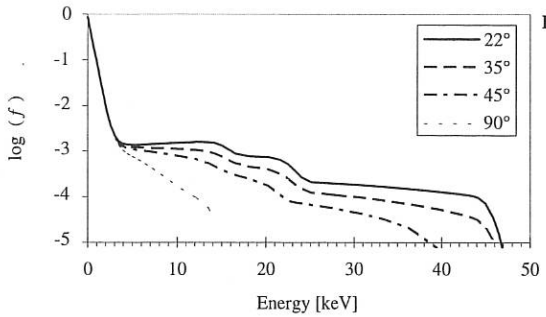

Fig.1: Calculated normalized ion velocity distribution for different pitch-angles.

The plasma data are: $n_e = 2.8 \times 10^{19}$ m^{-3}, $Z_{eff} = 2$, $T_e = 0.5$ keV, $Ti = 0.44$ keV and 45 keV injection with a power density of $H_0 = 1.2$ W/cm^3.

For detailed analysis of the NPA spectra it is important to understand the influence of the different plasma parameters on the fast ion distribution. Therefore we carried out numerical studies varying one plasma parameter and keeping the others unchanged.

We found that a change in the electron temperature of 15 % has little effect on the ion-distribution function below 5 keV and the high energy part is changing by less than 20 %. This is in the order of the error of the NPA measurements. A change of the ion temperature directly changes the slope in the low-energy part of the distribution function but has no effect on the high-energy range.

Lowering the electron density leads to an increase of the non-thermal part at the cost of the thermal part (below ≈ 5 keV). However, we found that a small change in the electron density of about 5 to 10 % has no measurable effect on the ion distribution function.

An decrease of Z_{eff} from 2 to 1 enhances the plasma ion density. This leads to an enhanced pitch-angle scattering and an depletion of the particle distribution function at the injection energy. Our calculations show that Z_{eff} is a critical parameter in the high-energy region (see fig. 2).

5. Comparison of the flux calculation and measurements

In order to compare the calculated ion distribution function $f(v,\mu,t)$ with experimental data, a theoretical particle flux from the plasma $S(v,\mu,t)$ was calculated according to eq. 1. The absorption term in eq. 1 was calculated with respect to the real stellarator geometry.

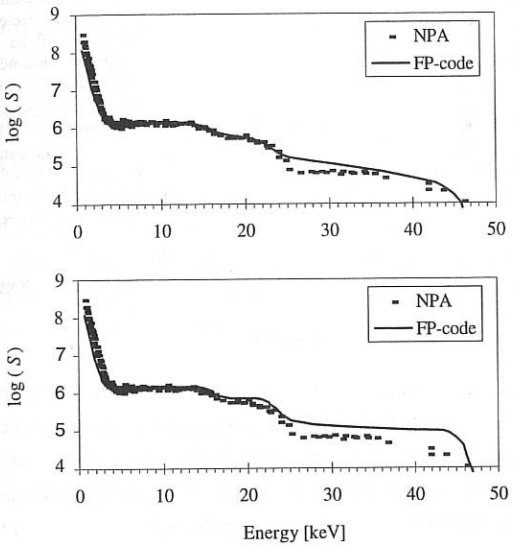

Fig. 2: Comparison of calculated neutral particle flux with experimental data.
$n_e = 2.8 \times 10^{19}$ m^{-3}
$T_e = 0.5$ keV
$T_i = 0.44$ keV
2a: $Z_{eff} = 2$

2b: $Z_{eff} = 1.5$

Fig 2. shows the comparison of these calculations with the experimental result for the Z_{eff} values of 2 (fig. 2a) and 1.5 (fig. 2b). From thermal energies up to energies of 24 keV the comparison between the measurement and the calculation is rather good. Small discrepancies in the low-energy region may result from uncertainties in the absorption term due to errors in the density profiles. Larger deviations above 24 keV show the importance of using accurately measured Z_{eff}-values. Additional work needs to be done for the investigation of the ion velocity distribution in this energy-region. The comparison is also sensible on the energy calibration of the NPA that has to be set properly.

6. Effects of field ripple on fast particle confinement

The good agreement of the calculations with the experimental data up to 24 keV will, for the future, allow to investigate the influence of global Alfén waves [5] and the losses due to vertical drifts of magnetically trapped particles (1/v regime).

First measurements observing slowing-down particles from the neutral particle diagnostic beam in the presence of a changed toroidal field ripple show a clear coherence between the fast particle loss and the toroidal field ripple.

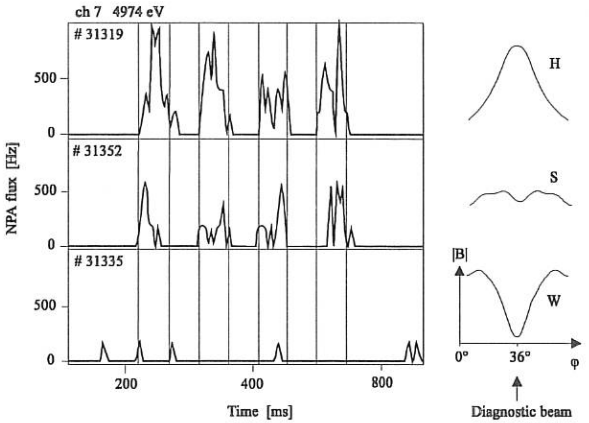

Fig. 3: NPA flux at an enegy of 4974 eV for different magnetic configurations. Particles are injected during four 50 ms diagnostic beam-pulses beginning at 240 ms at an toroidal angle φ of about 36°.
H: Precence of a magnatic hill (passing particles).
S: Standard configuration with a small magnetic well.
W: Presence of a deep magnetic well (trapped particles).

In fig. 3, the neutral particle flux at the energy of 4976 keV is shown for the different magnetic field configurations indicated in the right. If the diagnostic beam is injected in a magnetic hill position, the fast ions are passing particles and therefore confined. They can be observed. The NPA flux decreases if a small well is present (standard configuration) and all particles are trapped and therefore lost if the beam is injected in a strong magnetic well.

References

[1] G. Grieger et al., Phys. Fl. B4 (7) 1992 p.208
[2] V.V. Afrosimov et al., Sov. Phys. Tech. Phys. 28, 43 (1978)
[3] R.L Freeman, E.M. UKAEA Research Group Culham Laboratory, CLM-R 137 (1974)
[4] B. Wolle et al, Plasma Phys. Contr. Fusion 34, 1051 (1994).
[5] A. Weller et al, Phys. Rev. Lett. 72 (1994) 1220-1223.

Correlation between Helium Particle Transport and Electron Density Profiles in W7-AS

M. Hirsch, J. Baldzuhn, B. Brañas*, E. de la Luna*, W. Ohlendorf
Max-Planck-Institut für Plasmaphysik, EURATOM-Ass, 85748 Garching, Germany
*Asociación EURATOM-CIEMAT, Madrid, Spain

Introduction

To test the validity of a neoclassical description for impurity transport measured impurity profiles can be compared with code calculations. At W7-AS density profiles of impurities are obtained from active charge exchange spectroscopy CXRS by means of a diagnostic neutral beam injector. For the neoclassical transport of He the IONEQ code predicts, that the He III profile has a similar shape than the profile of the electron density. In the gradient region of the core plasma the required electron density profile can be measured from mm-wave reflectometry with a high spatial and temporal resolution. A comparison between these density profile and the measured He III profile should show, whether a neoclassical description is valid or anomalous contributions to He particle transport exist.

Electron density fluctuations possibly generate anomalous transport. An anomalous component in He transport therefore could be correlated with the density fluctuation level as it is measured with reflectometry.

Electron density profiles and density fluctuations measured by reflectometry

At W7-AS edge density profiles and electron density fluctuations are measured by a broadband heterodyne reflectometer [1]. The system is operated in extraordinary mode polarization probing densities 1 to $6 \cdot 10^{19}$ m^{-3} within less than 1ms. Depending on plasma conditions radial positions range from $0.3 < r/a < 1.1$, with $a \leq 18$cm. Gaussian beam optics for final signal launch and detection permits a beam waist of less then 2cm at the plasma location. The mm-wave launched to the plasma is amplitude modulated, and both the phase of the modulation envelope and the phase of the carrier are measured simultaneously. From the phase of the modulation envelope, i.e. the time delay of the reflected signal, the density profile n(r) is obtained. For the profile recovery by numeric Abel inversion an edge profile up to the lowest probed density has to be assumed. It is fitted to the probed part via the gradient. The density profiles obtained by that for the investigated discharges agree with Thomson scattering and Lithium beam data. An example is shown in Fig.1.

Phase fluctuations of a reflected mm-wave give information about the density fluctations at or close to the probed cut-off layer [2]. Heterodyne detection technique allows to measure the required phase fluctuations independent of fluctuations in the amplitude of the reflected signal. Coherent contributions to the phase spectrum, e.g. modes, are filtered

numerically and only the turbulent component of the spectrum is taken into account. The density fluctuation level $\Delta n(r)$ is evaluated from the rms value of the measured phase fluctuations $\Delta\Phi$, using the local gradient grad[n(r)] of the density profile:

$$\Delta n(r) = (4\pi)^{-1} \cdot \lambda_{eff} \cdot \text{grad}[n(r)] \cdot \Delta\Phi \, .$$

The effective probing wavelength λ_{eff} is obtained from numerical calculations [1][3]. For each discharge density fluctuation profiles are measured under stationary plasma conditions with the mm-wave frequency ramped up every 10ms to probe the different radial positions. An accurate knowledge of the local density gradient is crucial for the estimation of the density fluctuation level. Therefore the density profile is taken with the mm-wave frequency sweeping continuously over the entire range before and after the fluctuation measurement. The relative density fluctuations $\Delta n/n$ obtained with this methode for the same discharge with profiles shown in Fig.1 are given in Fig.3. For all discharges $\Delta n/n$ increases towards the edge with typical values of 10 to 15% at the limiter respective the separatrix position. As an example the fluctuation profiles from a density scan at fixed ECRH heating power are summarized in Fig. 2.

CXRS-Measurement and Code-Calculations of He-Profiles

Density profiles of fully stripped He are obtained by active charge exchange spectroscopy CXRS. A diagnostic neutral beam injector is pulsed with 10 Hz to allow for a subtraction of background light originating from the plasma edge. The density of He III is derived from the CX spectral light intensity of He II at 4686 Å, which occurs after charge exchange with the beam neutrals. The CX light is guided by a turnable mirror to a 1.26m grating spectrometer to resolve the single CXRS spectral lines. One radial position can be chosen per discharge. To maintain constant He density conditions for a series of discharges, a short He gas puff is applied at the beginning of each shot. Due to a recycling coefficient $R \approx 1$ an almost constant helium concentration of about 1% is obtained for the whole discharge.

For the calculation of the He III density profile the neutral beam attenuation in the plasma is calculated by an iterative algorithm, taking into account charge exchange and ionization by the background plasma as well as by the impurities. Ion temperatures are obtained from the Doppler broadening of CXRS spectral linewidth. For the ion density $n_i(r)=n_e(r)$ is assumed and the electron density n(r) with $(0<r<a)$ is taken from Thomson scattering measurements. A detailed description of the whole procedure is given in [4]. Fig. 3 shows the He III density profile (open circles) for the discharge taken as example.

With the IONEQ code [5] impurity density profiles can be calculated using a neoclassical transport model. For each flux surface a set of coupled continuity equations is solved which take into account radiation, ionization and recombination as well as diffusive

and convective transport. The measured density and temperature of the „background" electrons and protons and a background neutral gas profile are required as input parameters.

He-transport and electron density profile

He-transport properties and electron density fluctuations have been characterized for different plasma conditions and heating scenarios. ECRH-, NBI-heated and discharges with combined heating covering central densities 2 to $10 \cdot 10^{19}$ m^{-3} have been studied.

The neoclassical transport model predicts that the He III density profile shape is very close to the density profile of the electrons. An example of calculated He density and the respective electron density profile used as an input is shown in Fig.3. For the calculation the central He III density is fixed to 1% relative concentration.

Within the experimental error we find that the measured He III density profile shape (see e.g open circles in Fig.3) is consistent with the calculated one [6]. As density profile information is available from reflectometry in the gradient region, Fig. 4 compares the gradient of the measured He-profiles at r/a=0.9 with the respective gradient of the measured electron density for a number of different discharges. Within the limits of experimental error no significant deviation from the results of the corresponding neoclassical calculation (black dots and line) is observed. So far our result supports the conclusion that He-particle transport in W7-AS can be described quite well with the neoclassical theory only, without the assumption of an additional anomalous contribution.

Access to possible anomalous transport contributions is given from the deviations between measured and calculated He III profiles. Electron density fluctuations possibly generate anomalous transport. In this case anomalous contributions to the impurity transport should be related the density fluctuation profile obtained by reflectometry (black dots in Fig.3). Nevertheless up to now we find that deviations between measured and calculated He III profiles are below the level of experimental error. Dynamic He-profile measurements as a finer instrument for particle transport are subject to further investigations. Due to their increased information on He-transport and the detailed knowledge of the electron density profile in the gradient region also minor anomalous contributions to impurity transport can be adressed.

References

[1] H. J. Hartfuß, T. Estrada, M. Hirsch, T. Geist, J. Sanchez, *Rev. Sci. Instrum.* **65 (7)**, 2284 (1994).

[2] B. Brañas, M. Hirsch, V. Zhuravlev, E. de la Luna, T. Estrada, T. Geist, H. J. Hartfuß, J. Sánchez, this conference.

[3] T. Estrada, J. Sánchez, H. J. Hartfuß, M. Hirsch, T. Geist, *IAEA Technical Committee Meeting on Stellarators and other helical confinement Systems*, Garching, Germany, 10-24 May 1993, p 292, (1993).

[4] J. Baldzuhn, W. Ohlendorf, A. Weller, R. Burhenn, M. Kick, W7-AS-Team, *Proc. of the 20st EPS Conference on Controlled Fusion and Plasma Physics,* Lisboa, vol.III, p.1207 (1994).
[5] Weller et al., Phys. Rev. Lett. **49**, 1408 (1991).
[6] R. Burhenn et al., this conference.

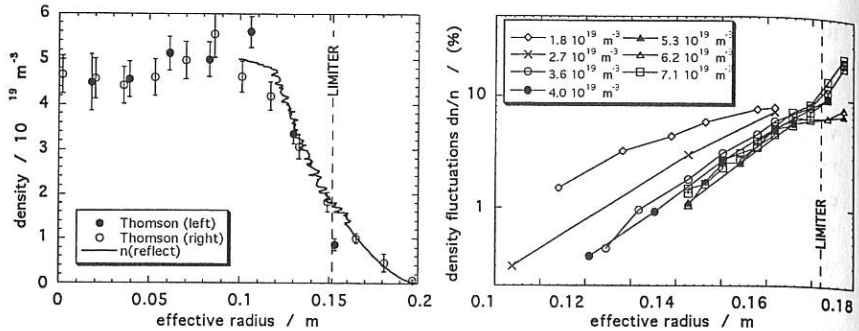

Fig.1: Electron density profiles measured with Thomson scattering and reflectometry for a ECRH heated discharge (B=2.5T, iota = 0.34). The plasma edge as determined from the limiter position and magnetic field configuration is shown as dashed line.
Fig.2: Density fluctuation profiles for a series of ECRH heted discharges (P=450kW) with different densities.

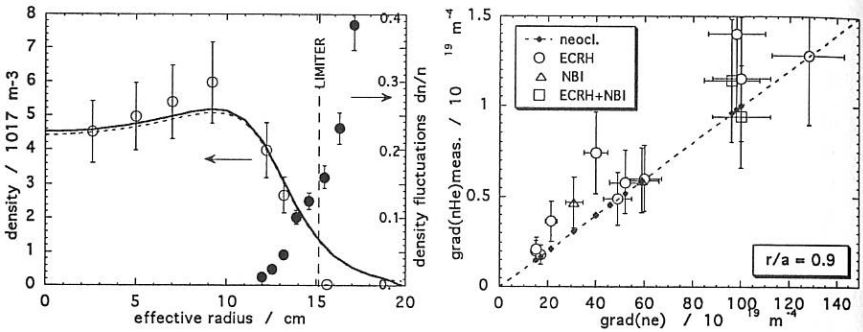

Fig. 3: HeIII density measured with CXRS (open circles) compared with IONEQ code calculations (thick line) for the same discharge as Fig.1. The calculated He density fits with the electron density (dotted line). Electron density fluctuations (filled circles, right scale) typically show values of 10-15% at the limiter (dashed line).
Fig. 5: Comparison of electron density gradient with HeIII gradient at r/a=0.9. The respective results of the neoclassical calculation are shown for comparison.

Transport Studies of Injected Impurities in the Stellarator Wendelstein 7-AS

R.Burhenn, H.Hacker, L.Ledl, E.Unger, J.Baldzuhn, J.V.Hofmann, A.Weller,
W7-AS Team, ECRH Group[1], NI Group
Max-Planck-Institut für Plasmaphysik, EURATOM Ass., D-85748 Garching, FRG
[1]Institut für Plasmaforschung, Universität Stuttgart, D-70569 Stuttgart, FRG

1. Introduction

In contrast to strong efforts concerning the improvement of energy confinement in fusion plasma devices, the confinement of so-called impurity atoms released from plasma facing in-vessel components by plasma-wall interaction should simultaneously be as worse as possible. Their presence in the plasma can cause a strong reduction of the plasma temperature by impurity radiation cooling and a significant dilution of the fusion mixture, both, depending on its concentration, having serious effects on the ignition criteria for a fusion plasma. For these reasons, there is an urgent need to understand the impurity transport, especially with respect to steady-state operation of future fusion devices. For toroidal plasmas the neoclassical transport theory describes the collisional dissipation. Often, however, a large fraction of the transport cannot be explained by this theory alone and the difference is attributed to additional turbulent transport which is not yet well understood. It is important to find out whether the impurity transport in the stellarator W7-AS is basically governed by turbulent mechanisms or possibly is described by collisional transport. In the latter case an understanding of the nature of the impurity transport is provided with the possibility to predict the behaviour in future devices.

The study of the non-stationary temporal behaviour of non-intrinsic impurity tracers injected into the plasma is a well-known technique to investigate impurity transport. At W7-AS, laser blow-off and gas-oscillation experiments have been performed in ECR-heated discharges and were simulated by the transport and radiation code SITAR.

2. Injection methods

With laser blow-off technique the impurity material (Al, Fe) under investigation, being evaporated (thickness 1μm) onto the surface of a glas substrate, is ablated by a short pulse of a focussed (≈ ϕ 2-3mm) Q-switched ruby laser beam (1J, 30ns) into the stationary phase of an ECR-heated plasma discharge. From the temporal evolution of spectral lines from different ionization states (Al IX-XIII, Fe XVI-XXI) of the tracer, directly following the injection, information about its transport can be derived. With exception of the soft-X camera only central line-of-sight observation was possible. Additional observation of lowest ionization states (Al I-III) along the injection path confirmed the already known feature, that the impurity beam consist of a short pulse (≈50μs width) of fast neutrals followed by a broader distribution (≈1-3ms

width) of slower clusters. The relative abundance depends strongly on the laser energy density on the target and on the target thickness [1]. Measurements of the penetration depth of the clusters into the plasma reveal that their deposition takes place at the last close flux-surface whereas a large amount of the neutral component is already ionized outside the plasma edge and probably lost. Hence, a source function was used in the code simulations having similar time behaviour as the emission of the lowest ionization states and being localized at the plasma edge for both impurity species.

Another powerful method for impurity transport investigation applied at W7-AS is the gas-oscillation technique [2], which provides better access to the radial dependence of the transport. Here, a gaseous impurity tracer (e.g. H_2S for S, F_3CH for F) is injected by a sinusoidal modulated gas valve (5-10Hz) at the vessel wall during the whole stationary phase of the plasma discharge. Depending on the radial transport, the tracer wave penetrates into the plasma, steadily undergoing a phase delay and damping of its amplitude relative to its source function at the plasma edge. The required source function was again obtained by observing spectral lines of lowest ionization states (S II, F II) along the injection path. The soft-X camera turned out to be the most suitable tool for measuring the radial phase and amplitude profiles of the impurity wave. Although the soft-X camera cannot distinguish between different spectral lines, the observed spectral range could be restricted to line radiation from helium- and hydrogen-like ions by using proper absorption filters (25 µm Be for S, 5 µm Be for F) in front of the camera. In a further step, these line-of-sight integrated and filtered radial profiles were simulated by the transport and radiation code SITAR.

3. Code simulation

The transport and radiation code SITAR [3] time-dependently solves the complete set of coupled continuity equations for all ionization states z. These calculations can be done either with an ansatz for the particle fluxes Γ derived directly from neoclassical transport theory or using an heuristic ansatz $\Gamma=-D(\delta n/\delta r)-vn$ with selectable radial values for the diffusion coefficient D and the convection velocity v, being identical for all ionization states. In the expression for the neoclassical fluxes originally implemented in the code [3] several coefficients which had been approximated by constant values, were replaced by collisionality dependent analytical expressions [2,4] in order to consider correctly the contributions from the different transport regimes (Banana-Plateau and Pfirsch-Schlüter transport). The influence of the impurity background on the tracer transport is considered by a single species only, represented by one typical ionization state, being radially fixed to the electron density profile. Electron transport is not calculated and hence not selfconsistently taken into account.

Concerning the errors of the neoclassical simulations, the calculations are highly sensitive on the radial profiles of electron and ion temperature and electron density as well as the reasonable

consideration of - possibly more than one - additional background impurity. Uncertainties in these input data can cause significant errors (factors 1.5-2) in the simulated results.

4. Results and Discussion

At the low shear stellarator W7-AS (R=2m, a=12-18cm, B_0=1.25/2.5T, $0.25 \leq (t=1/q) \leq 0.7$) a variety of experimental plasma conditions were investigated by laser blow-off measurements. No difference in the transport behaviour was observed between injected iron and aluminium. The following results were obtained with aluminium as tracer. The confinement time τ_{Al} was calculated from fitting the temporal decaying part of the line radiation from highest ionization states by a function $\exp(-t/\tau_{Al})$ and represents the impurity transport in the core plasma. From a statistical analysis (53 discharges) the following scaling law was derived for $n_{eo} \leq 5 \cdot 10^{19}$ m^{-3}:

$$\tau_{Al}[ms] = 4.6 \cdot 10^{2}\ a_p[m]^{2.4\ (\pm 0.4)}\ B_o[T]^{0.3\ (\pm 0.2)}\ P[MW]^{-0.8\ (\pm 0.2)}\ n_{eo}[10^{19} m^{-3}]^{1.2(\pm 0.2)}$$

(plasma radius a_p, magnetic field B_0, ECR heating power P, central electron density n_{eo}). Unfortunately, Z_{eff} could not be taken into account, because Z_{eff}-measurements were not avaiable for most of the discharges. Additionally, no clear dependence on the rotational transform as well as the working gas (H,D) could be identified. Nevertheless, there is a clear and stable dependence of the confinement time on the plasma density, the heating power and the plasma radius. Compared to the energy confinement time τ_E, obtained from the ratio of plasma energy (diamagnetic loop) and heating power, a nearly proportional relation $\tau_{Al} \cong 4\tau_E$ was found.

Concerning the density dependence of the transport, similar results were obtained from gas-oscillation method during a density scan [2] (a_p= 18cm, B_0= 2.5T, P= 450kW, $t = 1/q \cong 1/3$) with sulfur as a tracer. For these discharges Z_{eff} changed inversely to the electron density.

Fig.1 shows the overall phase delay between a central channel of the soft-X camera and the source function (S II) at the plasma edge for the different densities. This is compared with neoclassical expectations. In fig.2 the corresponding central diffusion coefficients D, derived from the simulations of the experimental results are plotted versus the electron density, together with results from laser blow-off experiments at B_0=1.25T.

For the lowest density the measured phase delay is smaller and consequently the transport higher than neoclassically predicted. This is also confirmed by simulations of the radial profiles of phase and amplitude, requiring enhanced values for the diffusion coefficients. To match the experimental results, the neoclassical fluxes had to be enlarged by factors of 2-4. Although this deviation is close to the errors of the simulations, the tendency is obvious and supported by laser blow-off measurements at lowest density. This discrepancy might be explained either by additional turbulent transport or - in particular under these low-density conditions, where the

coupling of electrons and ions is weak - the neglection of electron transport and resulting radial electric fields in the simulation .

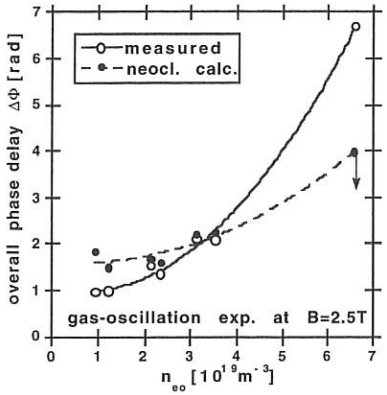

Fig.1: Measurements and neoclassical calculations of the phase delay between plasma center and boundary.

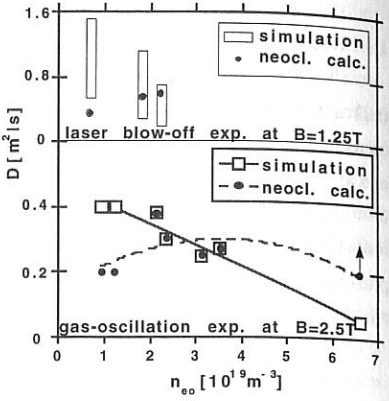

Fig.2: Diffusion coefficients from simulation of gas-oscillation and laser blow-off experiments compared with neoclassical calculations.

At medium densities the experimental data are in agreement with the neoclassical simulations within the errors, but with a trend towards better agreement using reduced neoclassical fluxes at increased density. Due to the optimization of the magnetic field topology in W7-AS, a reduction of the Pfirsch-Schlüter-currents by a factor 2 is predicted, so that the experimental findings would not be in contradiction to expectations.

At the highest density, however, the transport seems to be only explainable using a drastic reduction of the neoclassical fluxes by factors of 4-10 in the simulations, which is not yet understood and subject to further investigations. The corresponding data points in fig.1 and 2 (with arrow) represents the upper/lower limit with respect to uncertainties of the input data.

Close to the plasma edge nearly no phase delay was observed, indicating an enhanced radial transport in this region. This was confirmed by measurements of radial line radiation profiles of fluorine (FV-VII) from ionization states, which are located in this region. These profiles could be simulated only with a transport exceeding the neoclassical one by an order of magnitude.

References

[1] L.F.Ledl, IPP-Report IPP III/202, 1995

[2] E.Unger, PhD thesis, Max-Planck-Institut für Plasmaphysik, 1995, (to be published)

[3] WVII-A Team, NI Group, Nucl. Fusion 25(11)1593 1985

[4] G.Fußmann, IPP-Report IPP 1/273, 1992

ISLAND DIVERTOR STUDIES FOR THE STELLARATOR WENDELSTEIN 7-X

J. Kißlinger , C. D. Beidler, E. Harmeyer, F. Rau, H. Renner, H. Wobig
Max-Planck-Institut für Plasmaphysik, IPP-EURATOM Association
D-85748 Garching bei München, Germany

Introduction – Wendelstein 7-X (W7-X), the large advanced stellarator developed by IPP Garching, aims to operate with H_2/D_2 plasmas towards reactor-relevant parameters and to demonstrate steady-state operation. This calls for active particle and energy exhaust by an effective divertor. The chosen Helias configuration for this experiment is optimized [1] for good confinement and stability properties. The main data of this machine with 5 field periods and modular superconducting coils are: $R_0 = 5.5$ m, a $= 0.52$ m, $B_0 = 3$ T. The rotational transform ι at the edge is adjustable from $\iota = 5/6$ to $\iota = 5/4$; in the standard case $\iota = 5/5$. Associated magnetic islands provide an inherent divertor configuration, no extra divertor coils are required. The island divertor concept [2, 3] utilizes these islands and their separatrices. Increasing the shear at the boundary either by modification of the coil system [4] or by means of additional control coils generates outside the LCMS an ergodized layer, structured by remnants of islands.

Design of target plates – The divertor is designed to accomodate the entire ι-range, different island sizes and positions and even an "ergodized" boundary layer. Therefore a divertor with baffle plates has been chosen, carefully adjusted to the various magnetic field geometries while avoiding the problem of leading edges. Ten independent divertor units (two per field period) are arranged toroidally along the "helical edge"; see Fig. 1. Each of these units consists of modularized target plates, baffle plates, cryo-pumps and a control coil. The target plates are composed of single water-cooled elements which are able to remove a heat load of 10 MW/m^2 /5/. In order to concentrate the neutrals in the divertor region and minimize the interaction of high-energy neutral particles with the vessel, the target plates are combined with baffle plates.

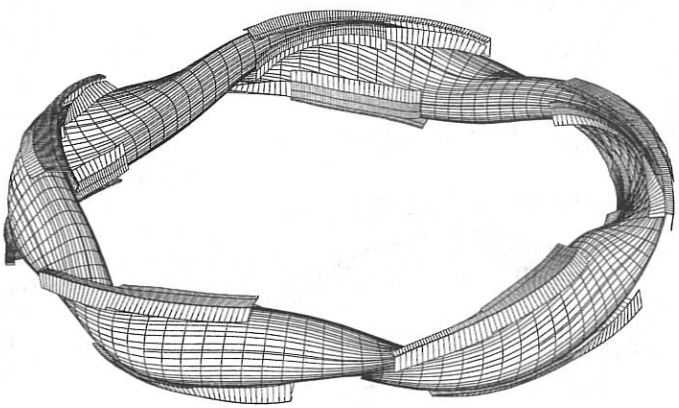

Fig. 1: Magnetic surface, target plates (finer segmentation) and baffle plates (coarser segmentation).

Variation of the island size – A crucial value for the proper functioning of the island divertor is the radial size of the island which governs the distance between target and separatrix and the length of a field line (inside the island, near the separatrix) which connects two target plates. Both parameters depend on the Fourier components of the magnetic field, B_{mn}, at the rational $\iota = m/n$. These field components increase with lower numbers for m and n and may be influenced by currents due to finite plasma pressure. A system of 10 control coils will be installed which generates magnetic field components to control the island size. These saddle-shaped loops have dimensions of 0.25x1.8 m^2, are integrated in the 10 divertor units and are located behind one of the baffle plates. Currents of up to 25 kA in these coils allow the variation of size and phase of the islands, and also the introduction of an ergodic region at the plasma boundary. Fig. 2 shows Poincaré plots of the standard case with currents of $I_{cc} = 0$ and $\pm 15kA$ in the control coils. Depending on current polarity the islands are either enlarged or reduced. The islands can be reduced to a small size, larger currents increase again the island size with reversed O- and X-point. The connection length and the width of the SOL decreases with increasing the island size. A further application of the control coils is the compensation of symmetry breaking error fields, (e.g. due to small construction inaccuracies of the device) achieved by individual currents in each control coil.

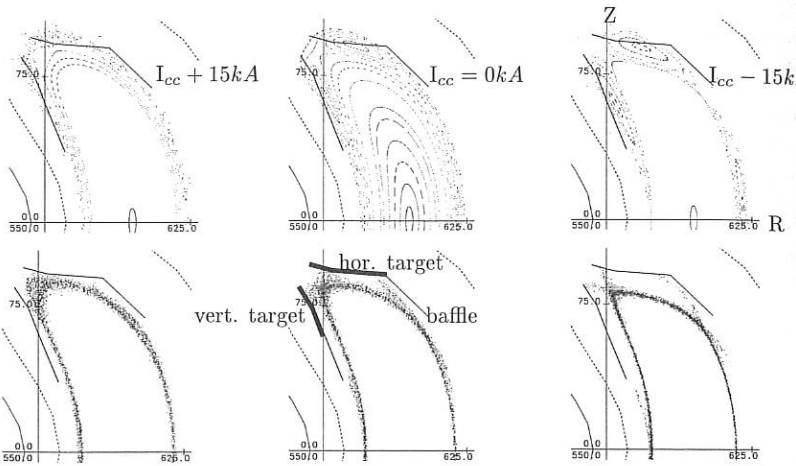

Fig. 2: Variation of island size by control coils. Poincaré plots of magnetic surfaces at $\varphi = 0$ and SOL simulation with the Monte-Carlo code, reduced island $I_{cc} = +15kA$, enlarged islands $I_{cc} = -15kA$.

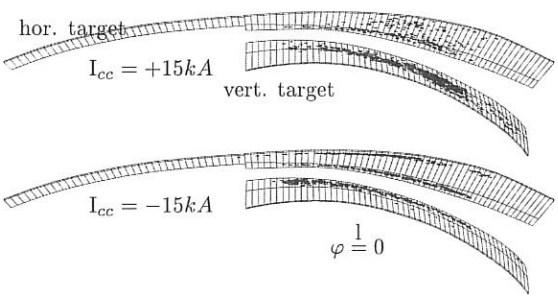

Fig. 3: Power deposition on the targets with the reduced islands and enlarged islands size.

SOL-modelling – In a first step to simulate the SOL a Monte-Carlo method was used to calculate the particle and energy transport along and perpendicular to the field lines for the parameter range of the magnetic configuration. From these calculations the power densities and neutral sources on the target and baffle plates are estimated (fig. 2 bottom row and fig. 3, [2, 3]).

A second approach to model the SOL is via the multi-fluid code B2 for simulation of edge plasmas [6]. Since B2 is a 2D-code the geometry of the plasma edge must be averaged (distances) or integrated (areas and volume) in the toroidal direction. The code is based on a rectangular grid which can be generated only approximately in the W7-X case. Due to the five-fold symmetry it is sufficient to calculate one island region (a sector of 1/5 of the poloidal circumference), corresponding to a single null geometry. The main geometrical differences to a tokamak of a comparable size are:

- The connection length is longer due to the larger aspect ratio and the small rotational transform inside the island.
- The distance between the target and the main plasma is smaller.
- The ratio of volumes in the private regions to the volumes inside the islands is larger because there are 5 X-points.

The first two points come closer to the tokamak values with increasing island size, the third one with increasing ι.

For the calculations the following boundary conditions are used: plasma density and power flux are prescribed at the connection to the main plasma in radial direction; zero gradients of all plasma variables are assumed at the symmetry planes in poloidal direction; low temperature (2eV) and zero density are preset at the boundary towards the wall (private region and O-points); the condition $V_{||} = c_s$ is used towards the targets. The thermal diffusivity for electrons and ions is set to $1m^2/s$ and the particle diffusivity to $0.5m^2/s$. The present study is made without impurity radiation and with a simple neutral particle recycling model (included in B2) with a recycling coefficient to the wall of 1 and to the targets of 0.98. In this investigation the plasma density at the separatrix midplane is varied from 1.5 to $5 \cdot 10^{19}/m^3$, the power reaching the SOL from 1 to 2 MW per island (total 5 to 10 MW), the ratio of B_θ/B by factors $F_c = 1$ to 8 to simulate a decrease of the connection length by this factor. Fig. 4 shows the geometry of the averaged grid of one island and the electron temperature distribution for a case with midplane separatrix density $n_s = 5 \cdot 10^{19}/m^3$, heating power 2 MW and $F_c = 2$. The left and right side of the grid are connected with the neighbouring island (simulated in the calculations by the symmetry planes).

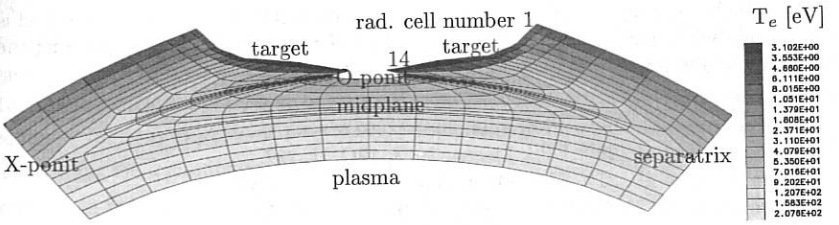

Fig. 4: Geometry of the averaged grid of one island and distribution of the electron temperature.

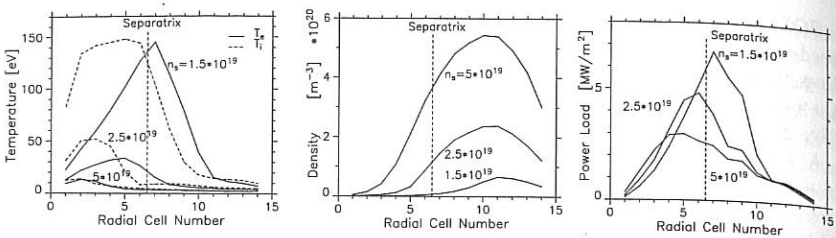

Fig. 5: Temperature, density and power loads vs the radial cell number. Parameter is the separatrix density n_s at the midplane. Cell 1 to 6 are in the private region. $F_c = 2$.

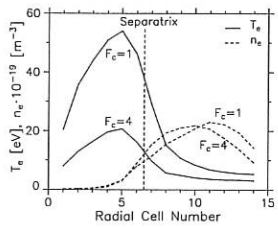

Fig. 6: Temperature and density at the target plate with F_c as parameter.

In Fig. 5 temperature, density and power load are shown at the target plates vs the radial cell number with n_s as parameter. From these figures we conclude that the high recycling regime is reached at a separatrix density $n_s = 2.5 \cdot 10^{19}/m^3$ due to the increase of the density towards the targets by up to a factor of 9 compared with n_s. The power density looks very moderate, but one must recall that this is an average value along the wetted length of the target plates. The maximum value derived by the simple Monte-Carlo model with constant parameters everywhere is about 8 MW/m^2 for the standard case with a toroidal average of about 4 MW/m^2. The influence of the connection length L_c is shown in Fig. 6. A drop in the temperature of more than a factor of 2 results at the targets and a factor of about 1.5 at the separatrix midplane when L_c is shortend by a factor of 4. The density profile at the target is shifted somewhat towards the separatrix with about the same maximum value. At the separatrix midplane the density is reduced by about 6%.

Summary and Conclusion – The island divertor concept of W7-X provides a flexible solution for the energy and particle exhaust and allows variations of the rotational transform, island size and position, or to choose configurations with an ergodic boundary. A critical issue of the island divertor concept is the stability of the islands against modifications of the vacuum field by finite β effects or by construction errors in the coil system, breaking the five-fold symmetry. The control coils in W7-X allow the compensation of error fields and finite β effects (which are rather small in W7-X due to the optimized configuration) on the islands. The calculation with the B2-code show that the high-recycling regime can be reached at a moderate density, the power load is comparable with that obtained by previous Monte-Carlo calculations. Shortening the connetion length lowers the temperature at the targets and at the midplane.

References

[1] Grieger G., et al., Phys. Fluids B4, 2081 (1992).
[2] Kißlinger J., et al., 20^{th} EPS, Lisboa, 1993, 17C, II, 787.
[3] Kißlinger J., et al., 21^{st} EPS, Montpellier, 1994, 18B, I, 368.
[4] Strumberger E., 21^{st} EPS, Montpellier, 1994, 18B, II, 702.
[5] Greuner H., et al. 18^{th} SOFT, Karlsruhe, 1994, PA-039.
[6] Braams B.J., Ph.D. Thesis, Rijksuniversiteit Utrecht (1986).

Results from Thomson scattering and electrostatic probe measurements in the Extrap T1 reversed-field pinch

A. Möller, A. Welander, J.H. Brzozowski and G.X. Li

Division of Fusion Plasma Physics, (Association EURATOM-NFR), Alfvén Laboratory, Royal Institute of Technology, S-100 44 Stockholm, Sweden

1. Introduction

Information about the radial profiles of electron density $n_e(r)$ and temperature $T_e(r)$ is important in the study of energy and particle transport in confined plasmas. On the Extrap T1, as on all RFP experiments, diagnostic access is limited due to the necessity of minimising magnetic field errors due to large penetrations through the conducting shell. The available diagnostics for measurements of n_e and T_e include a 5 J ruby laser Thomson scattering equipment for measurement of the on axis density $n_e(0)$ and temperature $T_e(0)$ at one time into the discharge, a CO_2 laser interferometer which gives a time resolved chord averaged density N, and an electrostatic probe which measures the time evolution of n_e and T_e in the edge region of the plasma. In addition spectroscopic measurements of line ratios of O^{+3}, O^{+4}, and O^{+5} and measurements of soft x-ray continuum intensity ratios are used to derive weighted chord averaged T_e values. In order to estimate profiles, results from these different measurements are used in parametric models of $n_e(r)$ and $T_e(r)$. By this technique, a study of the scaling of the profiles with global plasma parameters has been conducted and in some cases the time evolution of their mean values has also been measured. In the edge region of the plasma the average radial particle flux resulting from electrostatic fluctuations has been estimated for different plasma currents.

2. Profile measurements

The scaling of $T_e(0)$ and $n_e(0)$ measured in the middle of the discharge (at the time 325 μs) with plasma current is shown in fig.1a, the data shows a close to linear increase of $T_e(0)$ and a slight increase of $n_e(0)$. An additional result is that the n_e profile is not much affected by the magnitude of the plasma current. In fig.1b the scaling of density (at the time 325 μs) with the gas filling pressure is shown and in fig.1c and d the time evolution of the mean profile is given. The radial particle flux $\Gamma(r)$ may be obtained from these measurements using the continuity equation for ions $\partial n_i/\partial t = -\nabla\cdot\Gamma + \sigma(T_e) n_0(r) n_e(r)$ with the source term $\sigma(T_e) n_0(r) n_e(r)$ representing the ionisation rate of incoming neutrals. The ionisation rate coefficient $\sigma(T_e)$ is known and only weakly T_e dependent, the neutral gas density $n_0(r)$ however needs to be modelled. The peakedness of n_e (given by $n_e(0)/N$) is found to scale with $1/N$ rather than I/N

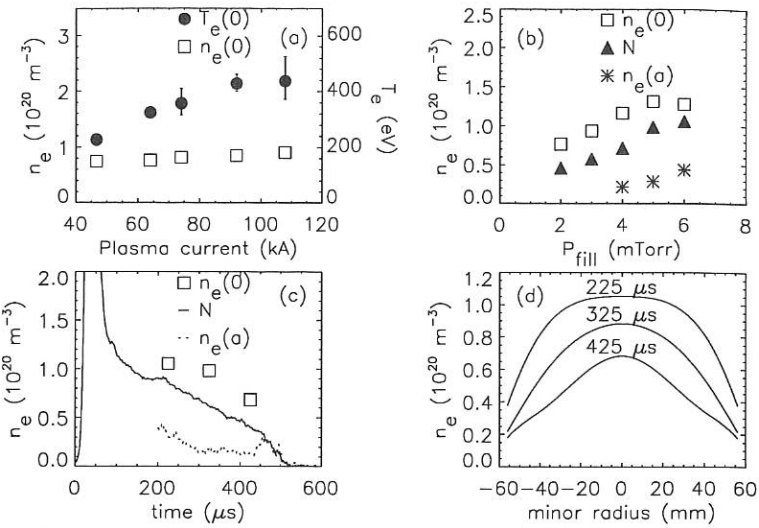

Fig.1: Scaling measurements of a) central density and temperature with plasma current and b) density with gas filling pressure at the time 325 μs. In c) the time evolution of mean values of central, line averaged and edge densities are shown and in d) the resulting profile estimates.

(I being the plasma current) as observed for instance in RFX [1], the scaling seems independent of the gas filling pressure and of time. The observed scaling can be understood by considering the source term, at higher density the neutrals from the wall are ionised more efficiently and a smaller fraction penetrates deep into the plasma thus resulting in a more edge weighted ionisation profile.

3. Edge Particle Transport

Results from other RFPs have pointed out electrostatic fluctuations as being the major drive of particle flux in the edge plasma, e.g. [2], thus saying that $\Gamma \approx \Gamma_{E\times B}$ (the electrostatic fluctuation driven, radial particle flux). For the modelling of the particle transport attempts have been made to estimate $\Gamma_{E\times B}$ with triple Langmuir probe technique using a probe head carrying an array of four probe tips arranged in a square 3.5 mm on edge. $\Gamma_{E\times B}$ is calculated as the product of the imaginary part of the cross correlation spectra of density and plasma potential fluctuations $C_{n\phi}$ and the toroidal wave vector, divided by the time averaged magnetic field. Fig.2a shows the absolute value of $C_{n\phi}$ and fig.2c the resulting $\Gamma_{E\times B}$ as a function of frequency in a series where I and the pinch parameter Θ were held constant at 62 kA and 1.8 respectively.

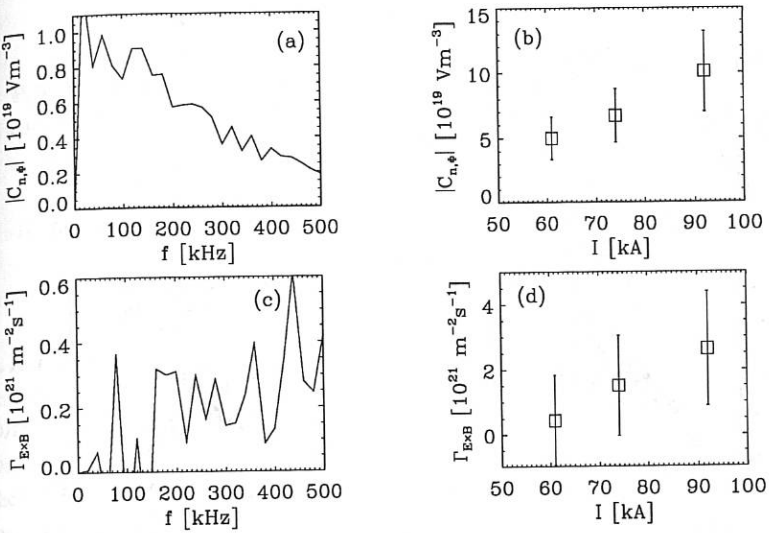

Fig.2: Electrostatic transport measurements showing a) /Cnf/ and c) $\Gamma_{E\times B}$ as functions of frequency. To the right frequency integrated quantities of b) /Cnf/ and d)$\Gamma_{E\times B}$ are shown as functions of plasma current.

The short duration of the T1 pulses, 500 μs, limits the frequency resolution of the spectra since only 50 μs time traces can be used for calculation. The integrated $\Gamma_{E\times B}$ in the displayed frequency range is $5\cdot10^{21}$ $m^{-2}s^{-1}$, which is about 20% of the total particle losses deduced from H_α line emission under similar conditions [3].The low frequency peak at 0-100 kHz, resulting from coupling with internal tearing modes [4] present in the cross power spectrum does not contribute significantly to $\Gamma_{E\times B}$, while the major particle flux takes place in the frequency region above 100 kHz. The bandwidth of the measurement was limited to 500 kHz by low-pass filters while the $\Gamma_{E\times B}$ spectrum suggests that there may be particle transport induced by higher frequencies. Measurements without the filters have shown substantial levels of fluctuations in this range. Figures 2b and 2d show frequency integrated $/C_{n\phi}/$ and $\Gamma_{E\times B}$ in a I scan where Θ was held constant at about 1.6. The total particle flux varies only slowly with I [3] indicating that an increasing fraction of the particle flux is driven by electrostatic fluctuations at larger currents. The limited bandwidth of the measurements may be one reason why the measured $\Gamma_{E\times B}$ is generally lower than expected, ranging from 5% to 20% of the total particle losses. New measurements are needed to investigate the frequency region above 500 kHz in order to get a total picture of the electrostatic fluctuation driven particle transport.

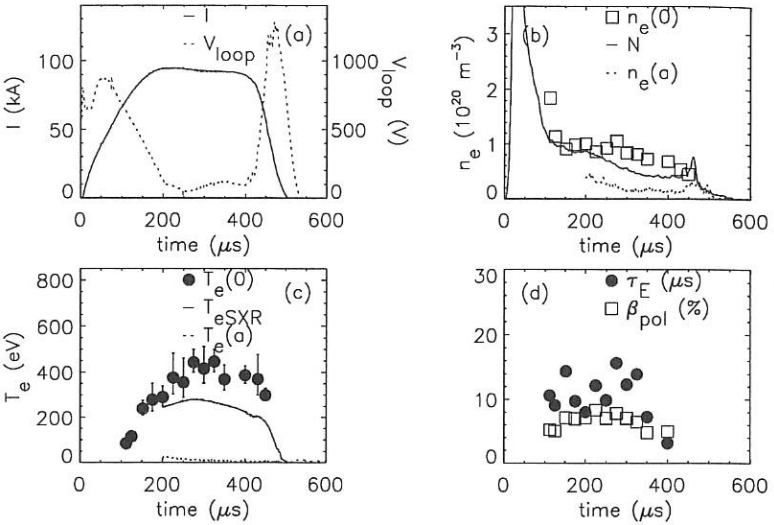

Fig.3: Ensemble averages over a number of reproducible discharges of a) Plasma current I and loop voltage V_{loop}, b) Central, line averaged and edge electron density, c) Central, soft x-ray and edge electron temperature, and d) poloidal β and energy confinement time.

4. Summary

Information about the electron density and temperature mean radial profiles including their time evolution has been obtained from a combination of different diagnostics in the Extrap T1. The density profile is seen to be peaking with lower densities which is attributed to the deeper penetration of neutrals towards the plasma centre. The experimental data will be used in a more detailed study of particle and energy transport. In addition direct measurements of the particle flux driven by electrostatic fluctuations in the frequency range 0-500 kHz at the plasma edge have been carried out, however it is likely that higher frequency components also contribute to the flux, necessitating further measurements. Fig.3 shows a typical discharge in the Extrap T1 including calculated poloidal β values and energy confinement times based on the obtained profiles.

References

[1] S. Martini et al.,proc. 21:st EPS conf. contr. Fus. Pl. Phys., part **I**, 454 (1994)

[2] T.D. Rempel et al., Phys. Fluids B **4(7)**, 2136 (1992)

[3] G.X. Li et al., These proceedings

[4] S. Mazur et al., Nucl. Fus., **34(3)**, 427 (1994)

First results from Extrap T2 reversed-field pinch

P. R. Brunsell, H. Bergsåker#, J. H. Brzozowski, J. R. Drake, B. Emmoth#, T. Fall*, G. Hedin, A. Hedqvist*, G. Hellblom, P. Hörling*, D. Larsson#, G. Li, S. Mazur, A. Möller, P. Nordlund, E. Rachlew-Källne*, J. Sallander*, H.-E. Sätherblom and A. Welander

Division of Fusion Plasma Physics, (Association EURATOM-NFR), Alfvén Laboratory
** Dept. of Physics I, # Dept. of Physics-Frescati*
Royal Institute of Technology, S-10044 Stockholm, Sweden

1. Introduction

In June of 1994 plasma operation started in the Extrap T2 reversed-field pinch, the former OHTE [1]. This medium size RFP (R/a=1.24 m/0.183 m) features a resistive shell (τ=1.5 ms). One major aim of the experiment is to study long pulse sustainment of RFP with a resistive shell. During this first phase of operation, pulses have been achieved with lengths up to 10 ms, corresponding to 6-7 shell times. Plasma first wall is completely covered with graphite armour. A second goal of the experiment is to study density control with the graphite wall. Helium glow discharge cleaning is successfully used to reduce the hydrogen loaded in the wall [2]. Plasma loop voltage is strongly reduced by helium glow discharge cleaning, suggesting that plasma resistance may be affected by impurity accumulation on the wall.

2. General characteristics of T2 RFP discharges

About 1000 plasma discharges have been made to date. During the initial phase of T2 RFP operation, plasma currents are around I_ϕ=150 kA and toroidal loop voltages are in the range V_ϕ=100-150 V. A typical RFP discharge is shown in Fig. 1. Discharge wave forms resemble those previously observed in the OHTE machine [1]. The plasma current is increased to its maximum during a 2 ms period by firing capacitor banks in two stages. The current is then maintained for a total of about 10 ms by a low voltage, electrolytic sustaining bank which is triggered at t=2.5 ms. The pinch parameter $\Theta=B_\theta(a)/\langle B_\phi\rangle$ is in the range Θ=1.8-2.0 and the reversal parameter is $F=B_\phi(a)/\langle B_\phi\rangle$=-(0.2-0.4). The plasma density pulse form is similar to the plasma current wave form, as is typical for graphite wall RFP's but in contrast to the decaying density in metal wall RFP's without active fuelling.

During this initial phase of T2 operation, the necessary vertical magnetic field for toroidal equilibrium is provided partly by the transformer iron core and partly by the OHC primary currents. The distribution of primary currents between inboard and outboard side is controlled by a shot-to-shot variable choke inductance in series with the inboard coils. Optimisation of the inductance value was a requirement for long pulses. The vertical plasma displacement is small and relatively stationary. With optimum inductance, the radial

displacement of the outermost closed plasma flux surface relative to the liner is kept less than about 2 mm for most of the discharge duration. However, there is a persistent radial drift which increases toward the end of the discharge. It seems therefore likely that the lack of precise equilibrium control is the cause of the termination of the discharge.

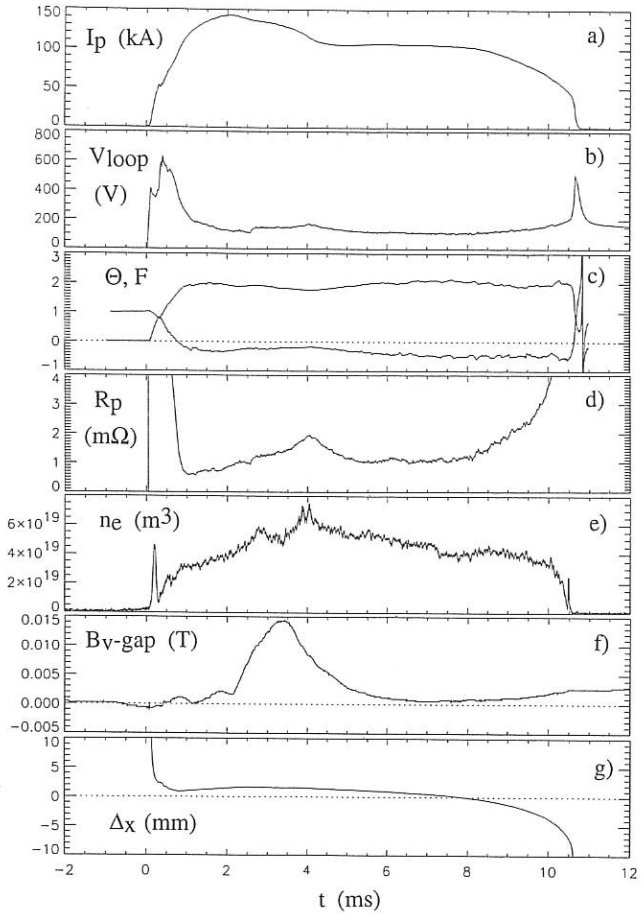

Fig. 1 RFP Discharge wave forms, a) Plasma current, b) Loop voltage, c) Pinch parameter Θ and reversal parameter F, d) Plasma resistance, e) Plasma density, f) Vertical magnetic field at the shell gap g) Radial equilibrium displacement of outermost flux surface

In the discharge shown in Fig. 1, a temporarily increased plasma resistance is observed around t=4 ms, causing a drop in the plasma current. The gap vertical field is observed to increase during a 1.5 ms period before the plasma resistance peak and reaches a maximum value of about 10 % of the main poloidal magnetic field slightly before the resistance peak. At the time of maximum resistance there are clearly noticeable density spikes, suggesting increased plasma wall interaction. It is likely that the observed resistance increase is caused by MHD modes which become wall locked near the gap, causing a locally large magnetic field error. However, after t=4 ms the gap field decreases and reaches a low value after 2 ms of around 1 % which is maintained during the rest of the discharge. Also the plasma resistance becomes low again and the plasma current is maintained. The discharge seems to '"self-heal" from the wall locked modes as observed in earlier OHTE operation [1]. Sometimes the sudden resistance increase occurs without a corresponding increase of the gap vertical field, which suggests that the modes may also lock at other toroidal positions than the shell gap.

3. Wall conditioning and density control

The experiment is operated with H_2 or D_2 gas and the electron density is in the range 1 - $6x10^{19}$ m^{-3}, depending on the condition of the graphite wall. The ratio I/N correspondingly varies in the range 3 - $15x10^{-14}$ Am. Total radiated power is typically 10-20% of ohmic input power in this density range. The density is practically independent of filling density and mainly determined by hydrogen recycling on the graphite wall. Density is typically increasing during a series of shots as the wall is loaded with hydrogen. Applying helium glow discharge cleaning effectively reduces the hydrogen wall concentration and low density plasmas can easily be produced again.

Plasma loop voltage is reduced by helium glow discharge cleaning. The lowest plasma resistance, around R_p=0.7 mΩ at I_p=150 kA which is comparable with previous OHTE operation, is typically achieved after glow discharge cleaning. The He GDC also reduces the plasma density in the RFP shots following immediately after the He GDC. Helium glow discharges every 10-20 RFP shots have been necessary for obtaining low density and low resistance RFP discharges. However, for a given plasma current the density is usually gradually increasing, shot by shot, after a He GDC. The increase in density and the increase in loop voltage is not simply related. There is an optimum situation 5-10 discharges after a GDC where the resistance is lowest (Fig. 2). This may be due to start-up problems which are more evident in the first discharges or to the existence of an optimum (intermediate) density.

It is clear that the graphite wall allows us to operate in a quite wide density range where the radiated power fraction is low. Although there is no direct control of the plasma density in the present situation, the He GDC is effective to reduce the density, while loading

of the graphite wall in RFP discharges normally increases the density. It may be possible to utilise these features to investigate further the question of optimum density.

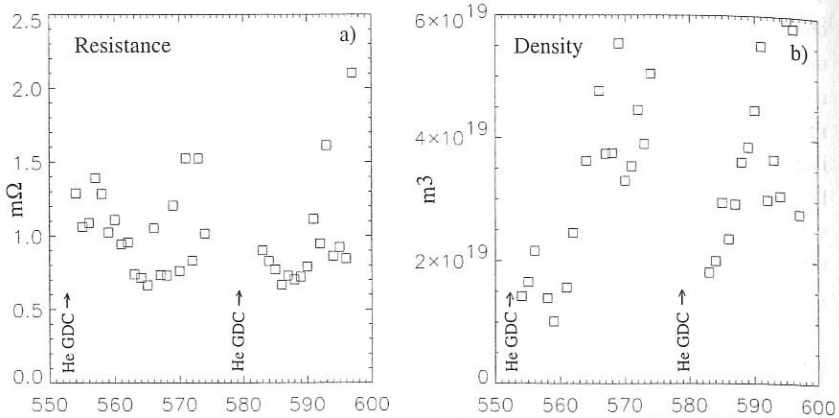

Fig.2 Plasma parameters vs. shot number. All shots with plasma current around 150 kA.. Helium glow discharge cleaning is indicated with arrow. a) Plasma resistance, b) Plasma density.

4. Summary

Pulse lengths in T2 are at present up to 10 ms, corresponding to 6-7 shell times. Events are seen where the plasma resistance temporarily increases, sometimes coincident with the growth of an error vertical magnetic field near the shell gap indicating wall locking of MHD modes near the gap. However, the plasma "self-heals" as the large gap error field subsequently disappears and the plasma resistance recovers a low value. The experiment is operated with electron densities in a wide range (n_e=1-6x10^{19} m^{-3}) depending on the condition of the graphite wall. Low density discharges are obtained by applying He GDC to reduce the hydrogen wall concentration. He GDC every 10-20 RFP shots have been necessary for obtaining low plasma density and low plasma resistance. The lowest plasma resistance (R_p=0.7 mΩ at I_p=150 kA) is comparable with previous OHTE operation [1].

The authors wish to thank the engineering and technical staff at the Alfvén laboratory for their work with the construction and operation of the T2 experiment. This research was performed under an Euratom-NFR association agreement with funding from NFR and Euratom.

References

[1] P. Taylor, et al., 15:th European. Conf., Dubrovnik, 1988, Europhys. Conf. Abstracts, Vol. 12B, Part II, (1988) 573.

[2] H. Bergsåker, et al., at this conference

Effects of the Impurities on the Loop Voltage in RFX

L.Carraro, P.Innocente, M.E. Puiatti, F.Sattin, P. Scarin, M. Valisa,

Gruppo di Padova per Ricerche sulla Fusione

Associazioni EURATOM-ENEA-CNR-Università di Padova

Corso Stati Uniti, 4 - 35127 Padova (Italy)

Introduction.

The laws determining the loop voltage in Reversed Field Pinches have been for long a matter of debate due to the difficulties to experimentally evaluate the classical resistive dissipation, the power consumption required to produce and maintain the reversed configuration against resistive diffusion (dynamo) and other processes such as helicity losses at the edge [1,2,3]. This paper focuses on the analysis of the impurity contributions to the loop voltage in RFX, where the presence of the modes locking at the wall in all the discharges [4] has characterised significantly the plasma wall interactions, causing in approximately 50 % of the high current experiments (0.7-0.9 MA) the appearance of carbon blooming [5]. These phenomena have sometime seriously limited the plasma performance but have also enriched the Z effective database so as to allow a statistical analysis. The results show that, with the existing machine geometry and control,minimizing the contribution of the sources of loop voltage enhancement already recognized in RFX, such as horizontal shift, field errors at the gaps [4] and vertical field distribution [6], a pedestal of approximately 15 V still characterises the loop voltage.

Zeff measurements

In RFX, Zeff is essentially determined by the contents of carbon and oxygen. Only occasionally negligible emission from Ni X, Ni XI and Ni XII has been observed, especially at the beginning of the discharge. Contributions from boron have never seriously affected the plasma dilution and only in a small number of circumstances fluorine has been observed in the plasma due to the sublimation of insulating materials exposed to particle fluxes drifted by large field errors into the diagnostic ports. Zeff has been estimated by measuring the averages over 20 ms of the absolute intensities of carbon and oxygen hydrogen-like and helium-like resonant lines by means of an absolutely calibrated grazing incidence spectrometer [7] and deducing the contribution of the non emitting ionisation states with a 1-D collisional-radiative impurity diffusion code [8]. The RFX experimental line emission is well reproduced when an outward diffusive term D ~ 10-20 m^2/s and a pinch convective term V(a)=1-2 D/a m/s (a is the minor radius) are assumed in the simulation.

Attempts to derive Zeff from the continuum emission in a presumably line free visible region of the spectrum have resulted in signals probably contaminated by the strong edge radiation associated to the plasma wall interactions. Zeff from visible continuum was found to be reasonably close to the one calculated from the resonant impurity lines only in experiments aimed at minimising the toroidal field ripple, where in fact the CCD cameras have shown a

smoother interaction outside the regions affected by the locking of the modes. The impurity diffusion model has not been applied to all of the discharges, but instead its typical results have been used to formulate a fast algorithm to provide Zeff directly from the experimental emissivities of the carbon and oxygen resonant lines. To compute the excitation coefficients of the carbon lines the electron temperature derived from the intensity ratio of the intercombination to resonant CV lines was considered, while for the oxygen lines the use of central electron temperature from the SiLi detector has been found to reproduce well the results of the code.

Results

A selection has been made among 1000 shots at high current and 300 at low current by including only discharges featuring a horizontal shift between 0 and 1.5 cm , field errors at the gaps of the conductive shell below 5% and vertical field decay index of about -1.5. These intervals are the results of experimental optimisation processes to minimise the loop voltage. The relation between Zeff and the on axis V_{loop} in high current (0.7-0.9 MA) discharges is shown in Fig.'s 1a and 1b for two electron density intervals. A linear unweighted fit is drawn in the figures; with this linear scheme, the loop voltage dependence on Zeff shows the presence of a pedestal of 8 to 15 V (+/- 5).

At currents of 500-600 KA a pedestal of about 10 Volts is found. A weighted fit was not considered because the experimental error for each datum was difficult to define and the errors on the pedestals given above should be considered as underestimated. Another, more precise way of verifying the presence of an anomalous additive contribution to the loop voltage, is to consider the relationship between the on axis Spitzer loop voltage V_S and the on axis loop voltage V_{loop}, taking into account only the discharges with the best dilution, namely with Zeff comprised between 1.2 and 1.5. In this way, the consequences of the error in the determination of Zeff are minimised. To evaluate the on axis Spitzer loop voltage V_S, the electron temperature measured with a Si(Li) detector and the current density on axis extrapolated from a μ&p model [1] are used. Fig. 2 shows the results for the two plasma current values. The data refer to different density values (from $3\ 10^{19} m^{-3}$ to $7\ 10^{19} m^{-3}$) and are the result of an average over 5 to 10 discharges. According to this analysis the loop voltage may be expressed as $V_{loop}=17(15)+2.1(2.8)V_S$, the values within brackets referring to the low current case. The proportionality factor between V_{loop} and V_S accounts for the loop voltage necessary to sustain the helicity [9]. The pedestals found in this way are compatible with the previous ones and the good correlation factors seem to suggest that the difference found above with density and current was mostly an effect of the experimental uncertainties in Zeff. Also here it should be stressed that a weighted fit would probably imply a larger error and that therefore these values should be considered with some care. The same data of Fig. 2 are replotted in Fig.3 as a function of I/N (N being the linear density) together with V_{loop} .

Fig. 's 4 and 5 show the time evolution of plasma current, electron density , C V emission and loop voltage for the shot # 4694. At about 50 ms the C V emission suddenly increases and a

similar behaviour is found on the loop voltage which rises from 35 to 60 V. The enhanced carbon influx causes a slight increase in the electron density and a decrease in the electron temperature from 330 to about 250 eV. The radiated power almost doubles and the enhancement of the plasma resistivity causes a premature decrease of the plasma current whose sustainement lasted up to 80 ms. Zeff has been calculated at 40 and 60 ms from the 20 ms averages of the grazing incidence spectrometer measurements and changes from 1.6 to 2.8. This variation is compatible with the existence of a pedestal of 23 V in the loop voltage, which is a little higher than the values found above with a statistical analysis.

Conclusions

The effective charge has been estimated in the RFX shots from the emissivities of the resonant lines of carbon and oxygen hydrogen-like and helium-like states and by computing the contribution of the totally stripped atoms by means of a collisional radiative transport code. These estimates suffer from a number of uncertainties primarily associated to the presence of poloidal and toroidal asymmetries in the plasma wall interactions that cannot be included in a 1-D model. The statistical analysis of the dependence of Zeff on the loop voltage for fixed electron temperatures shows that a pedestal of the order of 15 V appears to exist in the loop voltage. This value is confirmed by a slightly different approach where the on axis Spitzer resistivity is computed only for those shots with very low Zeff, minimising in such a way the effects of the uncertainties on the effective charge not associated to systematic errors. The experimental uncertainties are such that possible dependences of the pedestal on current or density are not discriminated. Presently the origins of the loop voltage anomaly have not been uniquely identified. From the results of other experiments, the further reduction of the field errors induced by the presence of the gaps in the stabilising shell is expected to reduce the pedestal [9,10,11] ; with this aim, active and passive control systems of the field errors are being implemented for the next RFX operations.

Acknowledgements

One of the authors (F.S.) would like to thank Dr.M.Mattioli for helpful discussions and assistance during his stay in the Laboratory of Cadarache.

References

[1] Ortolani s. Plasma Phys. and Contr. Fusion **31 (10)** 1665 (1989)
[2] Jarboe T.R.,.Alper B. Phys.Fluids **30 (4)** 1177 (1987)
[3] Tsui H.Y.W. Nucl.Fusion **28 (9)**,(1988) 1543
[4] Buffa A. et al. ,21st EPS Conference, Montpellier 27 June-1July 1994, Vol. I , 458
[5] Carraro L. et al. , "Impurity Influxes and Production Mechanisms in RFX", this Conference
[6] Bettini P. et al , "Improved RFX Operation by Active Magnetic Field Control", this Conference
[7] Schwob,J.L.et al.,Rev.Sci.Instrum., **58(9)**, (1987) 1601
[8] Carraro L. et al., Physics of Alternative magnetic Scheme, Varenna 15-24 October 1990,p.1019
[9] Alper B. et al., Plasma Phys. and Contr. Fusion **30 (7)**, (1988) 843
[10] Almagri A.F. et al. Phys.Fluids B, **4 (12)**, (1992) 4080
[11] Shimada T. et al, Proc. of 11th Int. Conf. on Plasma Physics and Contr. Nuclear Fusion , Kyoto (1986) Vol II, 453

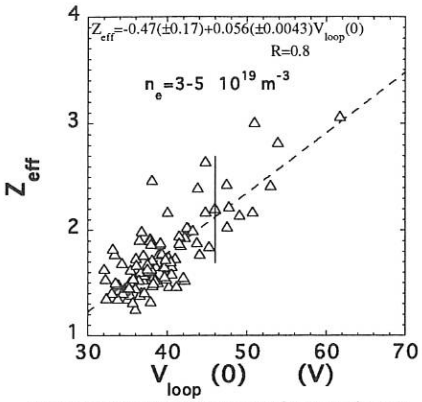

Fig.1a Relation between loop voltage on the axis and the effective charge for high current, low density discharges

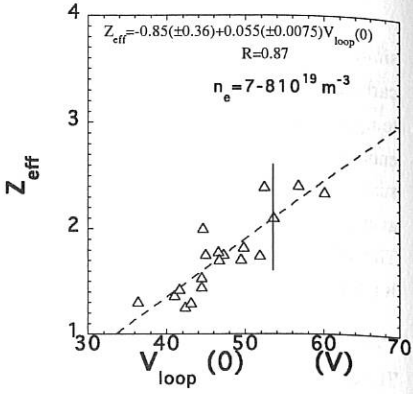

Fig.1b Relation between loop voltage on axis and effective charge for high current, high density discharges

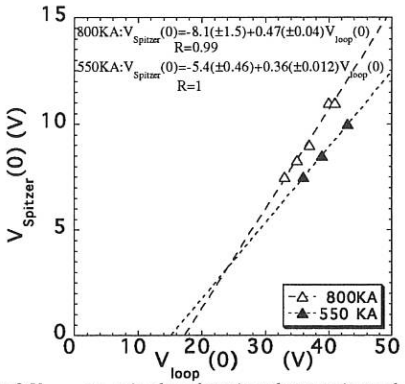

Fig.2 $V_{Spitzer}$ on axis plotted against the experimental Vloop on axis is shown for high and low current discharges. Averaged values among shots in which Zeff is between 1.2 and 1.5 are considered.

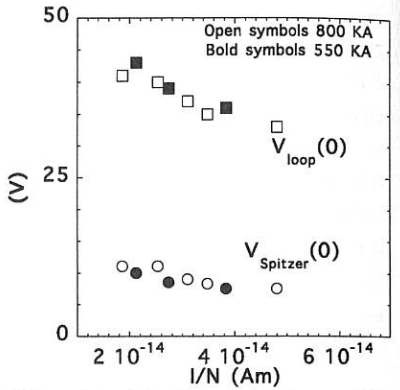

Fig.3 Same data of Fig. 2 are replotted versus I/N. Loop voltage on axis, as functions of I/N is also shown.

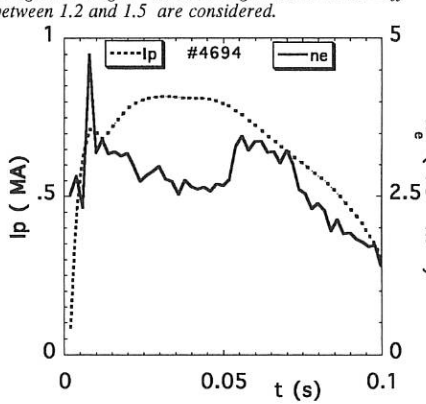

Fig.4 Time evolutions of plasma current and density in a high current shot with carbon blooms.

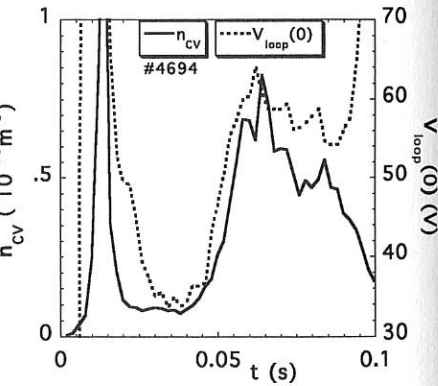

Fig.5 CV density and loop voltage on axis versus time for the same shot of Fig.4

INFLUENCE OF PARALLEL VISCOSITY ON TEARING MODE STABILITY BOUNDARIES

H. X. Xie and A. Bondeson
Department of Technology, Euratom-NFR/Fusion Association,
Uppsala University, Box 534, S-751 21 Uppsala, Sweden

I. INTRODUCTION

In linear theory,[1,2] resistive modes in tokamaks are strongly stabilized by pressure gradients combined with favorable curvature for $q > 1$. This stabilization, the so-called *Glasser* effect, depends on particle dynamics along the magnetic field lines, or the coupling of tearing mode to "sound waves". It was recently pointed out[3] that the finite beta stabilization may be eliminated by a sufficiently large parallel viscosity. In the present paper, we reexamine the influence of a parallel viscosity on tearing mode stability assuming that the parallel viscosity originates from *collisionless* ion Landau damping. We find that the Glasser effect is rather robust and that parallel viscosity only gives modest modifications of the stability limits.

The stability boundaries for tearing modes in tokamaks with a circular cross-section, are constructed numerically for various values of resistivity and pressure. The results are presented in an $l_i - q_a$ diagram to facilitate comparison with experiments. Such comparison shows that at least some stabilization over the cylindrical low-β result is needed to explain experimental results. Even rather moderate S-numbers ($\sim 10^7$) bring the resistive stability boundary quite close to the ideal one. Both are in reasonable agreement with experimental results. By including the stabilizing effect of conducting walls we conclude that the lower limit in l_i is mainly set by ideal modes.

II. EFFECT OF PARALLEL VISCOSITY

We model ion Landau damping by adding a viscous force $-2\kappa\rho\gamma\xi_{\|}v_{\rm thi}\left|k_{\|}\right|$ along the magnetic field lines. From a resistive layer analysis we have obtained an analytical expression for the critical Δ', valid when the viscosity coefficient κ is sufficiently large.[4] In the limit of small $|D_s|/\Gamma\beta$ (where D_s is the Suydam parameter, Γ the adiabatic index, and $\beta = 2p/B^2$), the critical Δ' is given by

$$L_R\Delta_c{}' = 3.115\ (-D_s)\beta^{-1/6}\kappa^{-1/3} \tag{1}$$

where $L_R = aS^{-1/3}(q/naq')^{1/3}$ is the resistive layer width. In the limit $|D_s|/\Gamma\beta >> 1$,

$$L_R\Delta_c{}' = 1.919\ (-D_s)^{2/3}\beta^{1/6}(\Gamma/\kappa)^{1/3} \tag{2}$$

When κ and Γ are of order unity, these results are not significantly different from those of Glasser, et al[1] for $\kappa = 0$. This indicates that the pressure effect is rather robust to collisionless parallel viscosity.

We have made fully toroidal computations including parallel viscosity using the MARS code.[5] We have chosen a circular equilibrium with $R/a = 3$, $q_0 = 1.025$, $q_a = 2.3$ and $< \beta >= 0.84\%$. The resistive interchange parameter is $D_R \approx -3.67 \times 10^{-2}$ at the $q = 2$ surface. For a collisionless plasma a reasonable approximation is $\kappa = 0.9$ and $\Gamma = 3/2$. Figure 1 shows critical S as a function of κ. The prediction $S_{crit} \propto \kappa$ from (1) and (2) is well verified for $\kappa > 0.35$, where marginal stability occurs at zero frequency. The critical Lundquist number is rather weakly influenced by the parallel viscosity.

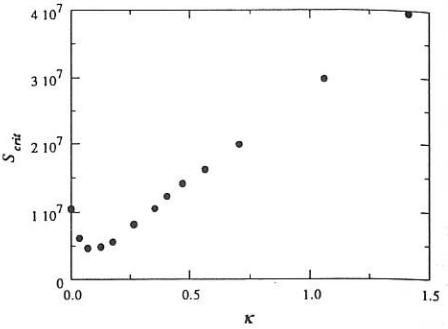

Fig.1: Critical Lundquist number versus parallel viscosity coefficient, κ

III. RESISTIVE STABILITY BOUNDARIES

Using the MARS code, we have constructed stability boundaries for tearing modes in tokamaks. The profiles of pressure and surface averaged toroidal current I^* have been prescribed as

$$dp/d\Psi = p_0\,(1 - \Psi/\Psi_a)\,, \qquad I^* = I_0[1 - \Psi/\Psi_a]^\alpha,$$

where α controls the peaking of the current profile and the internal inductance l_i. We have studied the stability of equilibria with fixed Troyon coefficient $g = \beta/(I/aB)$ by adjusting p_0 and α. The dependence of ideal MHD limits on Troyon coefficient g is shown in Figure 2. The upper limit of l_i is indicated as the line $q_0 = 1$. This is essentially the stability limit for the internal kink mode in

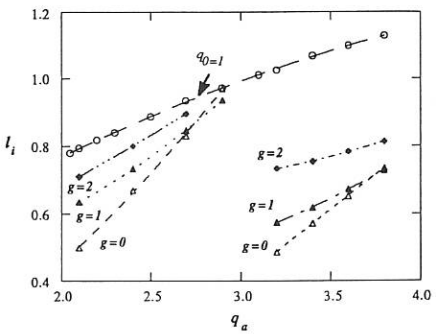

Fig.2: Ideal MHD stability boundaries for different Troyon coefficients $g = \beta/(I/aB)$

resistive MHD[5] (although experimental evidence indicates that q_0 often remains < 1 throughout the sawtooth cycle). The lower limit is set by the free boundary $n = 1$ kink mode. Figure 2 shows that this mode is strongly destabilized by pressure when q_a is just above an integer. For q_a just below an integer, the dependence is weaker, and for q_a just below 3 the pressure tends to stabilizing. This indicates that the mode behaves like an interchange mode, stabilized by favorable averaged curvature, rather than as a ballooning mode. Comparison with experimental $l_i - q_a$ diagrams (JET,[6] Tore Supra[7]) indicates that the experimental results are consistent with the ideal stability boundaries. The JET results[6] for the lower l_i-limit correspond well to the ideal MHD limit of Figure 2 for $g \approx 1.5$. The favorable effect on the beta limit, indicated by the empirical scaling $g \approx 4l_i$ for ballooning modes[8] is confirmed in a qualitative sense, but Figure 2 shows that the $n = 1$ beta limit is a more complicated function of q_a.

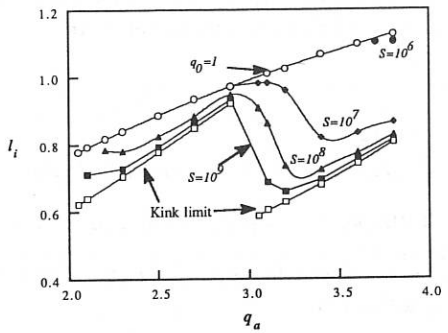

Fig.3: Resistive MHD stability diagram for $g = 1$ without a conducting wall. The lower lines show the ideal kink limit. The top line represents $q_0 = 1$

We have computed resistive $n = 1$ stability limits at various Lundquist numbers S and a fixed Troyon coefficient $g = 1$.

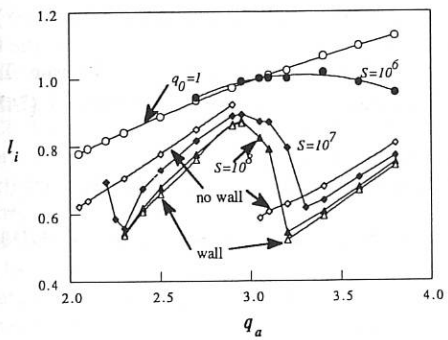

Fig.4: Resistive MHD stability diagram with a conducting wall at $b = 1.3a$.

The results are shown together with the ideal stability limits, in Figure 3 for the case without a conducting wall, and in Figure 4 with a wall at radius $b = 1.3a$. Figure 3 shows that $m = 3/n = 1$ tearing mode (for $3 < q_a < 4$) is largely stabilized without a conducting wall if $S \geq 10^8$, while the $m = 2/n = 1$ tearing mode (for $2 < q_a < 3$) requires somewhat larger S for stability. Notably, there is no stable region with $q_0 > 1$ and $q_a \leq 4$ if $S \leq 10^6$. Figure 4 shows that with a perfectly conducting wall at $b = 1.3a$, the $m = 2/n = 1$ and $m = 3/n = 1$ modes are largely stabilized if $S \geq 10^7$. We

note that for $S \geq 10^7$, the resistive stability limits with a wall at $b = 1.3a$ and Troyon factor $g = 1$ are almost everywhere *less* restrictive than the ideal limits with the wall at infinity. Therefore, for rotation frequencies sufficient to give wall stabilization for resistive, but not for ideal modes, the lower limit for l_i is set mainly by ideal external kink modes.

Previous work[9,10] has shown that, even in the absence of toroidal stabilization, tearing modes may be stabilized by tailoring current profile so that it is locally flattened near low-order rational q. For the case with no pressure and the present choice of current profiles, we find that tearing modes are always unstable for $q_a \leq 4$ even with an ideal wall at $b = 1.3a$. This indicates that the toroidal stabilization of tearing modes[1] is effective, although it is difficult to say whether the result for the critical S-number is quantitatively correct.

References

[1]A. H. Glasser, J. M. Greene, and J. L. Johnson, *Phys. Fluids* **18**, 875 (1975).

[2]R. J. Hastie, A. Sykes, M. Turner, and J. A. Wesson, *Nucl. Fusion* **173**, 515 (1977).

[3]R. Iacono, A. Bhattacharjee, C. Ronchi, J. M. Greene, and M. H. Hughes, *Phys. Plasmas* **1**, 2645 (1994).

[4]H. X. Xie and A. Bondeson, to appear in *Phys. Plasmas* **2**, (1995)

[5]A. Bondeson, G. Vlad, and H. Lütjens, *Phys. Fluids* **B4**, 1889 (1992).

[6]J. A. Wesson et al, *Nucl. Fusion* **29**, 641 (1989).

[7]D. Edery, et al, in *Proc. 14th IAEA Meeting*, (Würzburg, 1992), Vol 1, p. 279.

[8]E. J. Strait, M. S. Chu, J. R. Ferron, L. L. Lao, E. A. Lazarus, T. H. Osborne, T. S. Taylor, and A. D. Turnbull, in *Pro. 18th Controlled Nuclear Fusion Research* (IAEA, Vienna, 1993), Vol. I, p. 167.

[9]A. H. Glasser, H. P. Furth, and P. H. Rutherford, *Phys. Rev. Lett.* **38**, 234 (1977).

[10]C. Z. Cheng, H. P. Furth and A. H. Boozer, *Plasma Phys. Controll. Fusion* **29**, 351(1987)

Sawtooth model for ITER

Franco Porcelli, Dipartimento di Energetica, Politecnico di Torino, Italy
D. Boucher and M. N. Rosenbluth, ITER JWS, San Diego, CA, USA

INTRODUCTION. Sawtooth activity is expected to play an important role in ITER plasmas, especially in view of the relatively high values of the normalized beta parameter, $\beta_N \sim 2$ and low values of the safety factor near the plasma edge, $q_\psi \sim 3$, which entail large values of the sawtooth mixing radius, r_{mix}, at which ITER discharges are intended to operate. We present preliminary simulations of sawtooth activity in ITER based on the PRETOR transport code and on the threshold condition for the onset of sawteeth outlined below.

INSTABILITY THRESHOLD. The following practical instability criterion has been implemented in the PRETOR code. Sawtooth crashes are triggered when either of the two following conditions is met:

1. $-\delta\hat{W}_{core} > c_h \omega_{Dh} \tau_A$
2. $-\delta\hat{W} > -c_\rho \hat{\rho}$ and $\omega_* < c_* \gamma_\rho$

The auxiliary condition $\omega_{Dh} > \omega_*$ is easily satisfied in ITER when the fast ions have energies above a few hundred KeV. The inequality $\omega_* < c_* \gamma_\rho$ can be transformed into a critical shear criterion for instability. In these equations, $\delta\hat{W}_{core} = \delta\hat{W}_{mhd} + \delta\hat{W}_{KO}$ is the core plasma potential energy, with $\delta\hat{W}_{KO}$ the part related to the thermal collisionless trapped particles, $\delta\hat{W} = \delta\hat{W}_{core} + \delta\hat{W}_{fast}$, with $\delta\hat{W}_{fast}$ the fast ion contribution. The potential energy terms are normalized so that, when $\delta W = \delta W_{mhd} < 0$, the ideal-MHD growth rate is $\gamma_{mhd}\tau_A = -\delta\hat{W}$. Furthermore, ω_{Dh} is the precessional drift frequency, ω_* is the thermal diamagnetic frequency, $\hat{\rho} = \rho_i / r_1$ is the normalized thermal ion Larmor radius, r_1 is the q=1 radius, τ_A is the Alfven time, $\gamma_\rho = C_\rho(\tau)\hat{\rho}^{4/7} S^{-1/7} s_1^{6/7} \tau_A^{-1}$ is the m=1 semi-collisional growth rate, $C_\rho(\tau) = [2(1+\tau)/\pi]^{2/7}$, $\tau = T_e/T_i$, $s_1 = r_1 q'(r_1)$ is the magnetic shear parameter at the q=1 surface and S is the magnetic Reynolds number. The numerical factors c_h, c_ρ and c_* are of order unity.

This stability threshold can be used to analyze the possibility of sawtooth control in ITER by means of fast ions, either arising from neutral beam injection or by thermonuclear reactions, and by means of current drive. The influence of fast particles is explicitly taken into account by the stabilizing $\delta\hat{W}_{fast}$ term. As far as current drive is concerned, all the terms in the threshold condition depend upon the q profile. Reducing the magnetic shear around the q=1 surface has a stabilizing effect on two counts: firstly, it becomes easier to satisfy the criterion $s_1 < s_{crit}$ for stable operation, which is relevant when $\delta\hat{W} < \hat{\rho}$ and the density profile is relatively peaked; secondly, $\delta\hat{W}$ is inversely proportional to the local magnetic shear, so that for positive $\delta\hat{W}$ the stable domain $\delta\hat{W} > \hat{\rho}$ can be accessed by reducing s_1.

PRETOR SAWTOOTH SIMULATIONS. We present preliminary simulations of the sawtooth period in ITER based on the PRETOR transport code and the proposed sawtooth model. All cases shown correspond to ignited scenarios with the following plasma parameters [1]: a = 2.80 m, R = 8.14 m, Bt = 5.68T, Ip = 21 MA, κ = 1.6, fusion

power = 1.5 GW. An important assumption is made in these simulations, namely that after each sawtooth crash the profiles are relaxed according to the Kadomtsev complete reconnection model. This amounts to setting the value of q on axis equal to unity after each sawtooth crash, while the q profile increases slightly as a function of radius up to $r = r_{mix}$. The temperature and density profiles are flattened up to r_{mix} to a value corresponding to particle and energy (magnetic plus thermal) conservation. In Figures 1-2, repetitive sawtooth oscillations with a period of about 120 s are shown. Figure 1a compares the values of $\gamma_{core}\tau_A \equiv -\delta\hat{W}_{core}$ and of $c_h\omega_{Dh}\tau_A$. It is clear from this figure that $\delta\hat{W}_{core}$ is negative for most of the sawtooth ramp. On the other hand, the condition $-\delta\hat{W}_{core} < c_h\omega_{Dh}\tau_A$ is always satisfied. These results indicate that in this representative simulation the core plasma is unstable to ideal MHD internal kink modes, but the alpha particles act to suppress the instability. Indeed, the modified potential energy, $\delta\hat{W} = \delta\hat{W}_{core} + \delta\hat{W}_{fast}$, is positive throughout the sawtooth ramp, as indicated in Fig. 1b. One concludes that the relevant threshold for the onset of the sawtooth crash is $\delta\hat{W} = \hat{\rho}$ in this example. Values of $\delta\hat{W} < \hat{\rho}$ cannot be stabilized by diamagnetic frequency effects because of the rather flat density profile assumed in this simulation, which is intended to reproduce an H-mode discharge. Figure 1c shows the break up of the various terms constituting the potential energy functional (only the absolute values are shown in the figure). The MHD term is separated into the part corresponding to a circular cross section plasma (indicated by δW_{Bussac}) and the part due to cross section shaping (δW_{elong}). The fast particle term, δW_{fast}, dominates over all the other terms, however it decreases rapidly during the sawtooth ramp because of the expanding q=1 region. The elongation term is never important in this simulation, while the Kruskal-Oberman term plays a role only at the beginning of the ramp, when the q profile is still rather flat and close to unity. Fig. 2a shows the profiles of temperature and Fig. 2b the safety factor profiles just before and after the sawtooth crash. The density profiles remain flat throughout the sawtooth crash and the mixing radius is located at about 65% of the minor radius.

We have also studied variants of the above scenario. We found that the mixing radius can be reduced to 50% of the minor radius by decreasing the plasma current to 18 MA and adding 50 MW of off-axis current drive (with an assumed efficiency $\gamma = 0.2\ 10^{20} \mathrm{MA/MW/m^2}$). Another variant consists in delaying the onset of sawteeth activity by applying early heating. We found that by applying heating 20s before the current flat top, a sawtooth free period of more than 500s can be acheived (the first sawtooth crash has a normalised mixing radius of 66%).

The criterion for fishbone excitation has not yet been fully studied as it depends on the details of the treatment of the ion inertial layer. We however project that, in view of the large banana width of the fast particles, fishbones would only lead to a modest flattening of the alpha profile.

DISCUSSION AND CONCLUSIONS. The alpha particles play an important role in these simulations. Without the alpha particle contribution, the core plasma would be unstable to ideal internal kink modes and the sawtooth period would be of the order

of 1 s, which is the characteristic time scale for the peaking of the pressure profile. With the alpha particle contribution, sawteeth with a duration of order 100 s are observed in the simulations. The sawtooth-free period is limited by the expansion of the q=1 radius, and the relevant instability threshold, $\delta\hat{W} = \hat{p}$, is crossed when r_1 / a reaches a value of about 0.5. According to Kadomtsev 's relaxation model, the corresponding mixing radius for these long duration crashes can be as large as $r_{mix} / a \sim 0.7$. The observed sawtooth-free period in ITER simulations can be interpreted as follows. The resistive diffusion time in ITER is about 100 times longer than in JET, where long duration sawteeth are observed routinely in the presence of ICRH minority fast ions. Thus, a long duration sawtooth of 100 s in ITER should be compared with a "mini-monster" of about 1s in JET (long sawtooth free periods in JET can exceed 3 s). It is important to recognize that the rate of current density diffusion in ITER is very low: starting from a Kadomtsev-relaxed q profile, the q=1 radius takes about 100 s before reaching about 50% of the plasma minor radius. These results depend to some extent on the adopted Kadomtsev model. A note of caution should be introduced, as recent observations have indicated that Kadomtsev relaxation is not always consistent with the experimental data. In particular, the value of q on axis is often observed to remain well below unity throughout the sawtooth cycle. The likely consequence of incomplete reconnection is a reduction of the sawtooth-free period in ITER by perhaps as much as a factor of two, as it would take a shorter time for the q=1 radius to reach 50% of the plasma minor radius starting from a partially reconnected q profile. Another consequence would be a reduction of the sawtooth mixing radius. Clearly, these are important aspects, therefore we conclude that a characterization of the incomplete reconnection process is perhaps the most urgent sawtooth theoretical issue to be resolved.

In conclusion, we have presented a sawtooth model for ITER. The first simulations indicate that sawtooth suppression by alpha particles can occur transiently in ITER for periods of the order of 100 s. These periods are terminated by crashes with a mixing radius easily exceeding 50% of the plasma minor radius. Our model is rather preliminary and directions for possible improvements have been indicated. One question that is left unanswered is the desirability of transient sawtooth suppression. On one hand, the ignition margin for ITER - derived in [1] using the conservative assumption that central profiles would be flattened in case for instance of frequent sawteeth activity - would be increased further if sawteeth were stabilized because of the more peaked pressure profiles normally observed during long sawtooth free periods. On the other hand, we cannot say at present whether good confinement can persist after a long duration sawtooth crash with a large mixing radius. It appears that this important question can only be answered by *ad hoc* experiments in existing Tokamaks, that would operate simultaneously at high $\beta_N \sim 2$ and low $q_{95} \sim 3$. This is precisely one purpose of the ITER Demonstration Discharges experiments which are currently being undertaken on all major Tokamaks worldwide.

[1] ITER Interim Design Report - June 1995.

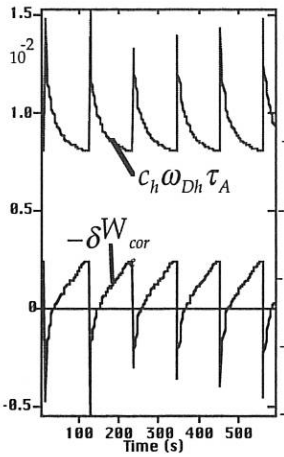

Fig. 1a: Constraint (1) always satisfied

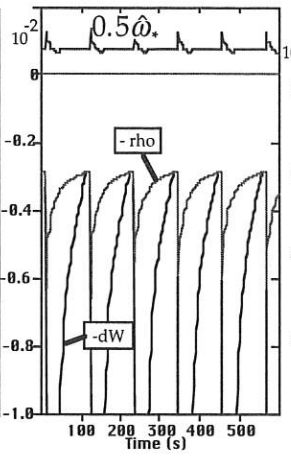

Fig. 1b: Crash triggered when:(2) -dW = -ρ

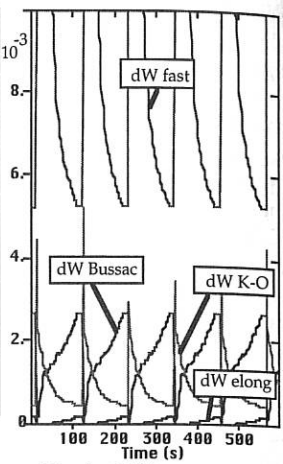

Fig. 1c: Different terms composing dW.

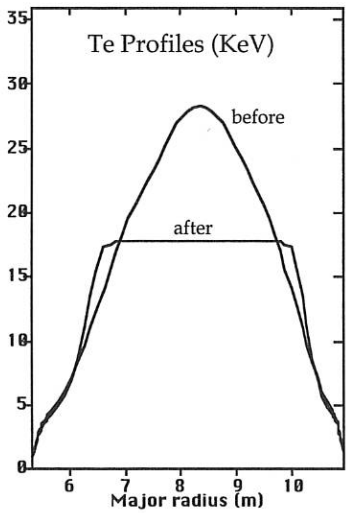

Fig. 2a: Temperature profile change for a reference ignited ITER plasma.

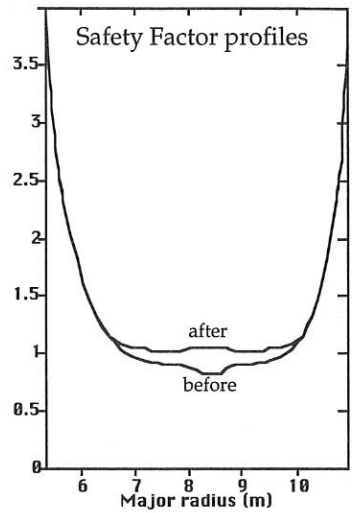

Fig. 2b: Safety factor change for a reference ignited ITER plasma.

Scaling Laws for the Amplitude, Period and Crash time of Sawtooth Oscillations

A. Thyagaraja and F.A. Haas*
UKAEA Government Division, Fusion, Culham, Abingdon, OX14 3DB, UK.
* Oxford Research Unit, The Open University, Boars Hill, Oxford.
(UKAEA/Euratom Fusion Association)

1. Introduction: In recent papers [1,2,3] a dynamical model of sawteeth in tokamaks based on a nonlinear, turbulence-driven thermal instability in the $q < 1$ core was developed. It involves a pair of coupled nonlinear ordinary differential equations governing the temporal evolution of the core-averaged plasma temperature and the core averaged magnetic turbulence energy. The model predicts that, a) the sawtooth temperature amplitude is proportional to the shear parameter, b) the period is proportional to amplitude and core confinement time, with a factor to take account of neoclassical losses, and c) that the crash time is proportional to the toroidal Alfvén time and varies inversely with the amplitude. It describes the complete, nonlinear limit cycle temporal dynamics of sawteeth without invoking any MHD instability.

2. Model Equations: The model leads[3] to the following equations for the 'core' temperature, $T(t)$ and the magnetic turbulence energy, $< (\frac{\delta B_\theta}{B_{z0}})^2 >$, the latter evaluated at $r = r_1$. We use nondimensional forms for the reduced variables, $Z(t) = \frac{T(t)}{T_{\rm mean}}$, and $W(t)$, the heat flux from the core due to the turbulence. W is a direct measure of the magnetic turbulence energy. Here, $T_{\rm mean}$ denotes the sawtooth-averaged core temperature.

$$\tau_s^* \frac{dZ}{dt} = 1 - W - \frac{\tau_s^*}{\tau_{NC}} Z \qquad (1)$$

$$\frac{\tau_s^*}{2} \frac{dW}{dt} = \Lambda(Z-1)W\phi(W) + F(Z,W) \qquad (2)$$

The following definitions apply (see [2,3] for details): $\tau_s^* \equiv \frac{3N_0}{2\pi^2\gamma r_1^2 n_0(0)} \frac{I^2(r_1)}{r_1^2 P_0 c^2}$,$\tau_A = \frac{r_1}{V_{\rm Alfvén}}$, $W(t) \equiv \frac{4\pi\tau_s^* r_1 \chi_\parallel(r_1)}{3N_0} \mid \frac{dp_0}{dr} \mid_{r_1} \frac{\pi\gamma c^2 r_1^2 n_0(0)}{I^2(r_1)} \left\langle \left(\frac{\delta B_\theta}{B_{z0}}\right)^2 \right\rangle_{r_1} \equiv \frac{\chi_\parallel(r_1)}{\chi_{\perp \rm eff}} \left\langle \left(\frac{\delta B_\theta}{B_{z0}}\right)^2 \right\rangle_{r_1}$, $\chi_{\perp \rm eff} \equiv (\frac{r_1 L_{p_0}}{\tau_s^*}) \frac{3\left[1 - \frac{\mu}{6}(1+q_0+q_0^2)\right]}{4}$, $\frac{1}{L_{p_0}} \equiv \frac{1}{p_0(r_1)} \mid \frac{dp_0}{dr} \mid_{r_1}$. We then have, $\Lambda \equiv \frac{9}{4}(\frac{r_1}{R})^2(\frac{\tau_s^*}{\tau_A})$ and $\Theta \equiv (\frac{\chi_{\perp \rm eff}}{s^2 V_{the} R})(\frac{R}{r_1})^2$. The profile constants $\gamma, \mu \simeq 1$([2]).

The function F is determined in terms of the core parameters and the two spatial moments, Z, W thus:

$$F(Z,W) = (\frac{\gamma}{8})(\frac{r_1}{R})^2 W(1-\Theta W)\left[1 + (\frac{\tau_s^*}{\tau_A})(\frac{r_1}{R})^2 s(\phi(W))^{1/2}\right]\left[W - 1 + (\frac{\tau_s^*}{\tau_{NC}})Z\right] \qquad (3)$$

The time-scale τ_s^* is proportional to the ratio of the poloidal magnetic field energy to the power input appropriate to the core and can be usefully thought of as measure

of the heating rate normalised to the poloidal field energy. By definition, the energy confinement time of the core, $\tau_E \propto \tau_s^* \beta_{pol}$, where β_{pol} is the poloidal beta of the core. The time τ_{NC} represents the neoclassical loss rate of the core. The dimensionless parameter, Λ is closely related to the ratio of the sawtooth period to the crash time and is a function of core parameters such as $\frac{r_1}{R}, \frac{\tau_s^*}{\tau_A}$, where τ_A is the Alfvén time appropriate to the problem. It is usually a large number ($\simeq 10^2$—10^4). The parameter Θ represents the saturated turbulence level at the crash. The function, $\phi(W) \equiv \frac{2W}{1+W}$ represents the saturation of turbulent particle transport at large amplitudes. The sawtooth period (τ_{period}), crash time (τ_{crash}) and the amplitude, $Z_{max} = \frac{T_{max}}{T_{mean}}$ are then calculated by solving the above equations subject to arbitrary initial conditions.

Although the neoclassical loss and the F term are usually small compared to the other terms on the RHS of Eqs.(1,2) derived in [1], they ensure that the system, (a) has true limit cycle behaviour characteristic of driven dissipative systems leading to a prediction of the amplitude (unlike the previous model [1]), and (b), is 'structurally stable' to neoclassical energy losses.

3. Analysis of the Equations and Scalings: In physically interesting cases, the parameters satisfy certain orderings: $\Lambda \gg 1$, $\Theta \ll 1$, $\tau_A \ll \tau_s^* < \tau_{NC}$, $r_1 \ll R$, and $s \ll 1$. These are all consequences of typical tokamak conditions in the $q < 1$ core region described by the model. We present in Figs 1-3 the initial transient behaviour of $Z = \frac{T(t)}{T_{mean}}$, $\mathrm{Log}_{10} W(t)$. The results pertain to the TEXTOR simulations considered in [2,3]. The following values of parameters were used: $\chi_{\perp eff} \simeq 10^4$ cm^{2}s^{-1}, $s \simeq 0.06$, $\tau_s^* \simeq 100$ ms, $\tau_{NC} \simeq 250$ ms, $\chi_{\parallel} \simeq 10^{11}$ cm^{2}s^{-1}. From these core parameters we obtain values for Λ and Θ: $\Lambda = 5 \times 10^4$, $\Theta = 3.6 \times 10^{-3}$. Making use of these values we calculate, using a numerical code, that $\tau_{period} = 19.2$ ms corresponding to a sawtooth amplitude, $\frac{\Delta T}{T} = \frac{T_{max} - T_{mean}}{T_{mean}} \simeq 5.5\%$, and crash time, $\tau_{crash} \simeq 190 \mu$s.

During the ramp (Fig. 3, A to B anticlockwise), W is essentially negligible in Eq.(1) and the equation can be integrated to give Z. Substituting in Eq.(2) in which F proves to be negligible, we determine the ramp time scale in terms of the amplitude. The amplitude itself is obtained by requiring continuity of the solution through the crash. Under the assumed orderings, during the fast crash (Fig. 3 B to A) we replace $Z \simeq 1$ in Eq(1) to a good approximation and divide Eq.(2) by Eq.(1) (neglecting F except for the fact that W has a maximum value of $1/\Theta$) and get a first order autonomous equation connecting W, Z. Then W is obtained as a function of Z through the crash from the first integral,

$$W + \frac{1}{W} + \frac{\tau_s^*}{\tau_{NC}}(\ln W - \frac{1}{W}) = 2\Lambda \left[(\frac{\Delta T}{T})^2 - (Z-1)^2 \right] + C \qquad (4)$$

where the constant of integration C is determined by continuity. It follows [3] that the period-amplitude relation is,

$$\tau_{period} = \frac{2\tau_s^*}{(1 - \frac{\tau_s^*}{\tau_{NC}})} \frac{\Delta T}{T} \qquad (5)$$

Evaluating the 'crash integral' at $Z = 1.W = 1/\Theta$ immediately gives the amplitude scaling law to a good approximation,

$$\frac{\Delta T}{T} \simeq \left[\frac{1}{2\Lambda}(\frac{1}{\Theta} + \frac{\tau_s^*}{\tau_{NC}} \ln \frac{1}{\Theta})\right]^{1/2}$$

$$\simeq s\left[(\frac{\tau_A}{\tau_s^*})(\frac{V_{the}R}{\chi_{\perp eff}})\right]^{1/2}$$

ie,

$$\frac{\Delta T}{T} \propto s(\frac{V_{the}R}{V_{\text{Alfvén}}L_{p0}})^{1/2} \tag{6}$$

The crash time is now straightforwardly determined. We thus get the following generalisation of our earlier results.

$$\tau_{\text{crash}} \simeq 2\tau_s^* \frac{\Delta T}{T}\Theta \ln(\frac{1}{\Theta}) \tag{7}$$

$$\tau_{\text{crash}} \simeq \frac{2}{s}\frac{R}{V_A}\frac{(RL_{p0})^{1/2}}{r_1}\left[(\frac{m_i}{m_e})\beta\right]^{-1/4} \ln(\frac{1}{\Theta}) \tag{8}$$

$$\frac{\tau_{\text{period}}\tau_{\text{crash}}}{2(\tau_s^*)^2} \simeq \frac{1}{\Lambda(1 - \frac{\tau_s^*}{\tau_{NC}})}\ln(\frac{1}{\Theta}) \tag{9}$$

Comparison with experiment and numerics

Machine	Parameter	Experiment	Numerics	Theory
TEXTOR	τ_{period} (ms)	20	19.2	18
	$\frac{\Delta T}{T}$ %	4-5	5.5	5
	$\tau_{\text{crash}}(\mu s)$	$\simeq 200$	190	200
TEXT	τ_{period} (ms)	2	2	2
	$\frac{\Delta T}{T}$ %	20	20	20
	$\tau_{\text{crash}}(\mu s)$	$\simeq 20$	18	18
JET-ICRH	τ_{period} (ms)	176	185	179
	$\frac{\Delta T}{T}$ %	$\simeq 25$	25	25
	$\tau_{\text{crash}}(\mu s)$	$100 - 200$	110	150

See [2,3] and Refs. therein for details.

4. Conclusions: The analytic model developed here gives experimentally testable scalings for period, amplitude and crash time of sawteeth. The **period**(cf. Eq.(5)) is proportional to amplitude, and core confinement timescale. It is lengthened by neoclassical losses. The model predicts complete sawtooth stabilisation in certain conditions[2]. The sawtooth **amplitude** (cf. Eq.(6)) is proportional to the shear parameter at $q = 1$ and to the fourth root of the product of the plasma β and the mass ratio (ie, to $(\frac{V_{the}}{V_{Alfvèn}})^{1/2}$). The dependence on the ratio of the major radius to the pressure

length scale is also of interest. The **crash time** (cf. Eq.(7)) is proportional to the *toroidal* Alfvén time and is modified by the shear and pressure length-scales and aspect ratio of the core. For fixed core conditions, period and crash time are inversely related (D-IIID, See [2] and reference 7 therein). We estimate the amplitude of $\Delta q(0,t)$ from toroidal Ohm's law, neoclassical resistivity and Ampère's law applied at $r = 0$ to be, $\frac{\Delta q_{max}}{q_0(0)} \simeq \frac{\Delta T}{T}$. This is consistent (modulo profile factors) with previous estimates by Hasselberg *et al* [4] who obtain, $\frac{\Delta q_{max}}{q_0(0)} = 0.7\frac{\Delta T}{T}$. Work is in progress on the problem of thermal interaction of sawteeth and alpha heating in reactor (ITER) conditions.

5. References:

[1] Haas F.A. and Thyagaraja A., Europhys. Lett. **19** (4), 285 (1992).
[2] Haas F.A. and Thyagaraja A., Plasma Physics and Controlled Fusion, **37**, 415 (1995).
[3] Thyagaraja A. and F.A. Haas, UKAEA FUS 286, May (1995).
[4] Hasselberg G., Khalil S.M., Rogister A.L.M. and Soltwisch H., Nuclear Fusion **31**, 592, (1991).

Acknowledgements: The authors thank Dr. J.W. Connor for useful suggestions. This work was funded partly jointly by the UK Dept. of Trade and Industry and Euratom.

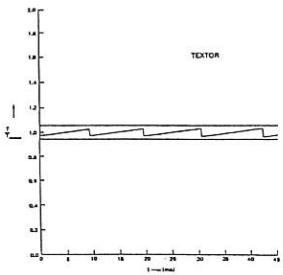

Fig. 1

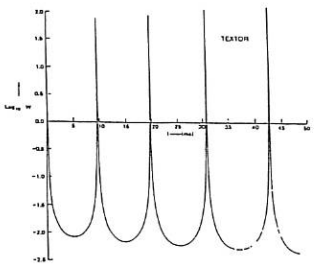

Fig. 2

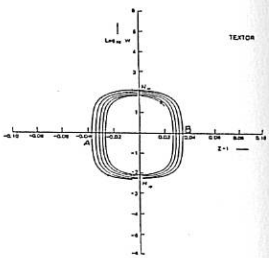

Fig. 3

Kinetic and hydrodynamic descriptions of wave scattering and transformation in plasmas

AG Sitenko
Bogolyubov Institute for Theoretical Physics, UNAS,
Metrolohichna 14b, 252143 Kiev, Ukraine

1. Introduction

Extensive applications of plasma diagnostics methods which employ electromagnetic wave scattering, has renewed the interest to the problem that had been considered many years ago [1-5]. In particular, the studies of plasma dynamics in the nuclear fusion devices made it a problem of importance to calculate the electromagnetic wave scattering spectra for nonequilibrium plasmas in strong magnetic fields. Such calculations have been made in a series of papers [6-10]; some of them [8-10] doubt the applicability of the fluid approach to the treatment of nonlinear effects even in cold plasmas. In Ref. [11], the arguments concerning the fluid approach inapplicability [9,10] are shown to be erroneous and a simple example of two-wave interaction in a plasma without external magnetic field is considered to illustrate that the results of kinetic and fluid approaches in the limiting case of a cold plasma are identical. Insofar as the approach in terms of hydrodynamic equations considerably simplifies the treatment of nonlinear processes occurring in a plasma, it is a matter of principle to substantiate the fluid approximation applicability and to reveal the relation between the results obtained by kinetic and fluid approaches. In this paper we consider the relation between the results of fluid and kinetic approaches for the case of electromagnetic wave scattering in a plasma with an external magnetic field.

2. Reduction of the Kinetic Equation to the Chain of Moment Equations

The main task in calculating the cross-sections of wave scattering or mixing is to derive from the constitutive equation an expression for the current given rise to by the incident wave nonlinear interaction with fluctuations, and determines the scattered wave field. The nonlinear constitutive equation for the plasma, and hence the scattered-wave-inducing current, may be derived from kinetic or hydrodynamic equations for the electron and ion plasma components. Since the difference between electron and ion masses is very large, the consideration may be restricted to the electron component only. The relevant kinetic equation may be written as

$$\frac{\partial F}{\partial t} + \vec{v}\frac{\partial F}{\partial \vec{r}} + \frac{e}{m}\left(\vec{E} + \frac{1}{c}[\vec{v}, \vec{B}_0 + \vec{B}]\right)\frac{\partial F}{\partial \vec{v}} = 0, \qquad (1)$$

where $F(\vec{v})$ is the electron distribution function, $\vec{B}_0$ is the external magnetic field, $\vec{E}$ and $\vec{B}$ are self-consistent electric and magnetic fields. The kinetic equation (1) is nonlinear with regard for the self-consistent electron interaction. In order to compare the results obtained by kinetic and hydrodynamic approaches, we solve the kinetic equation by the method of moments. Then nonlinear equation (1) reduces to an infinite chain of equations for the distribution function moments

$$\frac{\partial N}{\partial t} + \frac{\partial \nu_i}{\partial r_i} = 0, \qquad \frac{\partial \nu_i}{\partial t} + \frac{\partial \nu_{ij}}{\partial r_j} = \frac{e}{m}\left\{NE_i + \frac{1}{c} \in_{ijk} \nu_j (B_{0k} + B_k)\right\},$$

$$\frac{\partial \nu_{ij}}{\partial t} + \frac{\partial \nu_{ijk}}{\partial r_k} = \frac{e}{m}\left\{\nu_i E_j + E_i \nu_j + \frac{1}{c}(\in_{ikl} \nu_{jk} + \in_{jkl} \nu_{ik})(B_{0l} + B_l)\right\} \tag{2}$$

and so on, where $N = \int d\vec{v} F$ is the electron density, $\nu_i = \int d\vec{v} v_i F$ is the electron flux density, $\nu_{ij} = \int d\vec{v} v_i v_j F$ and $\nu_{ijk} = \int d\vec{v} v_i v_j v_k F$ are the second- and third-order moments. We note that

$$\nu_{ij} = \frac{\nu_i \nu_j}{N} + \Delta_{ij}, \quad \Delta_{ij} = \int d\vec{v}\left(v_i - \frac{\nu_i}{N}\right)\left(v_j - \frac{\nu_j}{N}\right) F \tag{3}$$

where Δ_{ij} is the pressure tensor. With no heat fluxes, the chain of equations (2) is cut off by virtue of the relation

$$\nu_{ijk} = \frac{1}{N^2}\nu_i \nu_j \nu_k + \frac{1}{N}(\Delta_{ij} \nu_k + \Delta_{ik} \nu_j + \Delta_{jk} \nu_i). \tag{4}$$

Having substituted this relation into the third equation of the set (2), we obtain an equation for the quantity Δ_{ij}. The plasma current $\vec{j}$ is immediately determined by the electron flux density $\vec{\nu}$, $\vec{j} = e\vec{\nu}$. (5)

The second equation (2), combined with relation (3) and equation for the pressure tensor Δ_{ij}, makes it possible to find the current and thus, together with Maxwell's equations, completely determines the electromagnetic field in the plasma. The set of simplified equations (2) derived from the kinetic equation, corresponds to the fluid approximation with regard for the thermal effects. The hydrodynamic velocity $\vec{u}$ is determined by the relation $\vec{u} = \frac{\vec{\nu}}{N}$. According to the definition (3), the quantity Δ_{ij}, in case of local isotropic equilibrium, reduces to $\Delta_{ij} = \Delta \delta_{ij}$, $\Delta = \frac{p}{m}$, $p = NT$, where p is the plasma pressure, T is the plasma temperature. Then the set of equation (2) reduces to the usual hydrodynamic equations. The current $\vec{j}$ and the hydrodynamic velocity $\vec{u}$ satisfy the nonlinear relation

$$\vec{j} = eN\vec{u}. \tag{6}$$

3. The Limiting Case of Cold Plasmas

In the cold plasma limiting case, we can neglect the quantity Δ_{ij} or the pressure ($p = 0$) in the equation for the flux density $\vec{\nu}$ or for the hydrodynamic velocity $\vec{u}$. We also disregard the nonlinear terms and obtain the constitutive equation in the form

$$\vec{j}(\vec{E}) = -i\omega \hat{\varkappa}(\omega) \vec{E}, \tag{7}$$

where $\hat{\varkappa}(\omega)$ is the dielectric permittivity tensor of a cold magnetoactive plasma. We denote the incident wave frequency and wave vector by ω_0 and $\vec{k}_0$, those of the scattered wave by ω and $\vec{k}$; the fluctuation frequency and wave vector are $\Delta\omega = \omega - \omega_0$ and $\vec{q} = \vec{k} - \vec{k}_0$. In what follows we label the quantities corresponding to the incident wave by the subscript 0; the fluctuation amplitudes are tilded. We treat both incident and scattered waves in the linear approximation. In the case of

cold plasma (when for the incident wave $\Delta^0_{ij} \to 0$ and for fluctuation excitations $\tilde{\Delta}_{ij} \to 0$), the quatity Δ_{ij} associated with the scattered wave is equal to 0. Hence, in the case under consideration, the current that induces scattered waves is determined by the equation for the flux density $\frac{\partial \vec{V}}{\partial t} + \nabla \frac{\vec{V}\vec{V}}{N} = \frac{e}{m}\left\{N\vec{E} + \frac{1}{c}[\vec{V}, \vec{B}_0 + \vec{B}]\right\}$. (8)

Taking into account the nonlinear terms (which are, however, linear with respect to the incident wave and fluctuation amplitudes), we obtain an expression for the current that induces scattered waves, i.e., $\vec{J}_{\vec{k}\omega} = -i\frac{\omega}{n_0}\hat{\varkappa}(\omega)\left\{\tilde{n}_{\vec{q}\Delta\omega}\vec{E}^0 + n^0\tilde{\vec{E}}_{\vec{q}\Delta\omega} + \right.$

$$\left. + \frac{1}{c}[\tilde{\vec{V}}_{\vec{q}\Delta\omega}, \vec{B}^0] + \frac{1}{c}[\vec{V}^0, \tilde{\vec{B}}_{\vec{q}\Delta\omega}] - i\frac{m}{en_0}((\vec{k}\tilde{\vec{V}}_{q\Delta\omega})\vec{V}^0 + (\vec{k}\vec{V}^0)\tilde{\vec{V}}_{\vec{q}\Delta\omega})\right\}. \quad (9)$$

With the continuity equation being satisfied, equation (8) for the flux density $\vec{V}$ is equivalent to the equation for the hydrodynamic velocity $\vec{u}$, i.e.,

$$\frac{\partial \vec{u}}{\partial t} + (\vec{u}\nabla)\vec{u} = \frac{e}{m}\left(\vec{E} + \frac{1}{c}[\vec{u}, \vec{B}_0 + \vec{B}]\right) . \quad (10)$$

This means that, in the cold plasma limiting case, the results of the fluid approximation reproduce the results obtained by the kinetic approach.

4. Is There Ambiguity in the Use of Fluid Equations?

The direct use of equation (10) and current definition (6) results in different from (9) expression for the scattered-waves-inducing current, i.e.,

$$\vec{J}_{\vec{k}\omega} = -i\frac{\omega_0}{n_0}\left\{\tilde{n}_{\vec{q}\Delta\omega}\hat{\varkappa}(\omega_0)\vec{E}^0 + \frac{n_0}{\omega_0}(\vec{k}_0\hat{\varkappa}(\omega_0)\vec{E}^0)\tilde{\vec{u}}_{q\Delta\omega} + \right. \quad (11)$$

$$\left. + \frac{n_0}{\omega_0}\omega\hat{\varkappa}(\omega)\left[\frac{1}{c}(\tilde{\vec{u}}_{\vec{q}\Delta\omega}, \vec{B}^0] + [\vec{u}^0, \tilde{\vec{B}}_{\vec{q}\Delta\omega}]) - i\frac{m}{e}((\vec{k}_0\tilde{\vec{u}}_{\vec{q}\Delta\omega})\vec{u}^0 + (\vec{q}\vec{u}^0)\tilde{\vec{u}}_{\vec{q}\Delta\omega})\right]\right\}.$$

In particular, the factors in the terms of equations (9) and (11) which describe wave scattering by electron density fluctuations, depend on different frequencies. The factor in (9) depends on the scattered wave frequency ω, whereas the one in (11) depends on the incident wave frequency ω_0. The difference between the expressions (9) and (11) which are derived from equivalent hydrodynamical equations (8) and (10), suggested an idea to the author of Ref. [9] that the fluid approach is inapplicable for the study of nonlinear processes in plasmas. Actually, however, expressions (9) and (11) are equivalent in the limiting case of cold plasma (this is just the case for which the hydrodynamic equations are applicable). For cold plasmas, one may disregard the thermal effects (i.e. thermal corrections in the dispersion wave equations) and the Langevin source in the constitutive equation for fluctuations.

5. Effect of Thermal Dispersion of Fluctuations

The phase velocities of the incident and scattered electromagnetic waves are much greater than the electron thermal velocity and hence thermal corrections to the dispersion of these waves may be disregarded. However, phase velocities of fluctuation excitations are of the same order of magnitude as the electron thermal velocity and

therefore, under certain conditions, their thermal dispersion may considerably influence the wave scattering. If the distribution function F is isotropic with respect to the velocity deviations from the mean vealue, then for fluctuation excitations we have $\tilde{\Delta}_{ij} = \tilde{\Delta}\,\delta_{ij}$, $\tilde{\Delta}_{\vec{q}\Delta\omega} = \frac{5}{3}\frac{T}{m}\tilde{n}_{\vec{q}\Delta\omega}$. We disregard thermal dispersion corrections for the incident and scattered waves. At the same time, in the equation for the flux density $\vec{V}$ associated with the scattered wave, we allow for the thermal correction Δ_{ij} in the second moment. This correction is proportional to the temperature and, according to (2), is determined by the equation

$$\Delta_{ij}(\vec{k},\omega) - i\frac{\omega_B}{\omega}(\in_{ikl}\Delta_{jk}(\vec{k},\omega) + \in_{jkl}\Delta_{ik}(\vec{k},\omega)) = S_{ij}(\vec{k},\omega), \tag{12}$$

where $S_{ij}(\vec{k},\omega) = \frac{5}{3}\frac{T}{mn_0\omega}(\vec{k}\vec{V}^0\delta_{ij} + k_i^0 V_j^0 + k_j^0 V_i^0)\tilde{n}_{\vec{q}\Delta\omega}$. (13)

The solution of this equation is given by

$$\hat{\Delta}(\vec{k},\omega)\vec{k} = -\frac{2\pi}{\omega_p^2}\{(\omega-\omega_B)^2\hat{\varkappa}(\omega-\omega_B)\vec{Q}_-(\vec{k},\omega) + (\omega+\omega_B)^2\hat{\varkappa}(\omega+\omega_B)\vec{Q}_+(\vec{k},\omega)\}, \tag{14}$$

where the quantities $Q_\pm(\omega)$ are defined by

$$Q_\pm(\vec{k},\omega) = \frac{\omega}{\omega\pm\omega_B}\{\hat{S}(\vec{k},\omega)\vec{k} \mp 4\pi\frac{\omega\,\omega_B}{\omega_p^2}(\vec{k}\vec{b})\hat{\varkappa}(\omega)\hat{S}(\vec{k},\omega)\vec{b} \pm i\,\hat{S}(\vec{k},\omega)[\vec{k},\vec{b}]\}\ .$$

The additional inducing current, associated with the effect of electron thermal motion on the fluctuation dispersion, is described by the expression

$$\vec{J}^T_{\vec{k}\omega} = -\frac{m}{en_0}\omega\,\hat{\varkappa}(\omega)\,\hat{\Delta}(k,\omega)\vec{k}. \tag{15}$$

Unlike the hydrodynamical current (9) which corresponds to zero plasma temperature, the thermal current (15), treated as a function of the scattered wave frequency, has singularities at multiples of the cyclotron frequency, i.e., $\omega = \pm 2\,\omega_B$. Therefore, if the incident wave frequency is close to twice the cyclotron frequency, the spectrum of incoherent scattering (associated with small frequency shifts) considerably depends on thermal dispersion of fluctuations. Singularities in the spectrum of electromagnetic wave scattering in magnetoactive plasmas were discovered in paper [9] by means of the kinetic approach.

References

[1] Akhiezer AI, Prohoba IG and Sitenko AG, *Soviet Physics JETP* **6** 576 (1958)
[2] Sitenko AG, Electromagnetic Fluctuations in Plasma, Academic: New York (1967)
[3] Sitenko AG and Kirochkin YuA, *Soviet Phys. Usp.* **9** 430 (1966)
[4] Salpeter EE, *Phys. Rev.* **120** 1528 (1960); *Phys. Rev.* **122** 1663 (1961)
[5] Farley DT, Dougherty JP and Barron DW, Proc. Roy Soc. **A263** 238 (1961)
[6] Chiu SC, *Phys. Fluids* **B3** 1374 (1991)
[7] Vahala L, Vahala G and Bretz N, *Phys. Fluid* **B4** 619 (1992)
[8] Aamodt RE and Russel DA, *Nuclear Fusion* **32** 745 (1992)
[9] Bindslev H, *Plasma Phys. Control. Fusion* **35** 1615 (1993)
[10] Bindslev H, *Физика плазмы* **20** 39 (1994)
[11] Sitenko AG, *Plasma Phys. Control. Fusion* **37** 163 (1995)

Hot Plasma Effects on the Collective Scattering off of Electromagnetic Fluctuations

J.A. Heikkinen[1] and O. Dumbrajs[2]
VTT Energy, P.O. Box 1604, FIN-02044 VTT, Finland[1]
Helsinki University of Technology, Department of Technical Physics, FIN-02150 Espoo, Finland[2]

Abstract: *From the general three-wave coupling formalism in magnetized Vlasov plasma, an expression is derived which gives the differential cross-section for the scattering of incident radiation off of thermal fluctuations induced by ions in a hot magnetized plasma. The model is valid to any order in thermal parameters, and thus generalizes the previous theory models to regimes where either the Larmor parameter $k_{s\perp}\rho_e$ or the electron cyclotron resonance can become significant for the scattered or incident waves.*

Introduction: Recently, scattering from field fluctuations with full electromagnetic plasma screening response [1-3] has been investigated in the context of α particle collective scattering diagnostics. The inclusion of electromagnetic effects has been motivated by the fact that for some scattered solid angles the fluctuations are essentially electromagnetic, as e.g. near the lower hybrid resonance with near perpendicular propagation, and for the mixed scattering from e.g. ordinary to extraordinary modes the electromagnetic effects become significant [2]. The models cited above are all based on either zeroth, first or second moment expansion of the source current $\vec{j}_s$ which makes it possible to express this current in closed form in terms of fluctuations of physical quantities like density or fields. This makes the models valid only under conditions $|k_{s\perp}v_\perp/\Omega_e| \ll 1$, $|k_{sz}v_z/(\omega_s - \ell\Omega_e)| \ll 1$ and $v_e/c \ll 1$. Here, $k_{s\perp}$ and k_{sz} are the perpendicular and parallel component of the scattered wave vector with respect to $\vec{B}$, and $v_\perp$ and v_z are the corresponding components of the electron velocity. v_e and c are the electron thermal velocity and the speed of light, respectively. Ω_e is the electron cyclotron frequency, and ℓ is an integer. In the present work, general kinetic formulae for the source current and the scattering cross-section are derived without relying on the previous assumptions.

The differential Scattering Cross Section: The incident, scattered and fluctuation electric fields are assumed as plane monochromatic waves $\vec{E}_0 = \hat{\vec{e}}_0 E_0 \exp(i\vec{k}_0 \cdot \vec{r} - i\omega_0 t)$, $\vec{E}_s = \hat{\vec{e}}_s E_s \exp(i\vec{k}_s \cdot \vec{r} - i\omega_s t)$, and $\vec{E} = \hat{\vec{e}} E \exp(i\vec{k} \cdot \vec{r} - i\omega t)$ entering or leaving a scattering volume V in a uniform magnetized plasma. The wave angular frequencies and wave vectors obey the energy and momentum conservation rules $\omega_0 + \omega = \omega_s$ and $\vec{k}_0 + \vec{k} = \vec{k}_s$. The wave polarization vectors of unit length are $\hat{\vec{e}}_0$, $\hat{\vec{e}}_s$, and $\hat{\vec{e}}$ for the incident wave, scattered wave, and the fluctuations, respectively.

In order to calculate the spectral tensor $\langle \vec{j}_s \vec{j}_s^* \rangle$ for the source current fluctuations, we obtain the identity $\hat{\vec{e}}_s^* \cdot \mathbf{\Delta}_s \cdot \vec{E}_s = -(i/\omega_s \epsilon_0) \hat{\vec{e}}_s^* \cdot \vec{j}_s$, where Δ_s stands for the dispersion tensor of the scattered wave. By expanding the Vlasov–Maxwell equations to second order in wave amplitudes, one can find from the general three-wave coupling formalism [4] an equation $\hat{\vec{e}}_s^* \cdot \mathbf{\Delta}_s \cdot \vec{E}_s = -(i/\epsilon_0) V E_0 E$, where

$$V = \sum_\sigma m_\sigma \int d\vec{v} f_\sigma(\vec{v}) \sum_{p_0+p=p_s} e^{i(p_0\theta_0+p\theta-p_s\theta_s)} \vec{A}_\sigma \cdot \vec{u}_p \tag{1}$$

and

$$\begin{aligned} \vec{A}_\sigma &= \vec{u}^*_{sp_s} \frac{\vec{k}_0 \cdot \vec{u}_{0p_0}}{\Psi_0(p_0)} + \vec{u}_{0p_0} \frac{\vec{k}_s \cdot \vec{u}^*_{sp_s}}{\Psi_s(p_s)} + \vec{k} \frac{\vec{u}_{0p_0} \cdot u^*_{sp_s}}{\Psi(p)} - \frac{i\Omega_\sigma}{\Psi_s(p_s)} \times \\ &\quad \left(\frac{k_z}{\Psi(p)} - \frac{k_{0z}}{\Psi_0(p_0)}\right)(\vec{u}^*_{sp_s} \times \vec{u}_{0p_0}). \end{aligned} \tag{2}$$

Here, p_0, p, and p_s go through all positive and negative integers including zero. The angles θ_j and velocity vectors $\vec{u}_j$ are defined from $\exp(i\theta_j) = (k_{jx} + ik_{jy})/k_{j\perp}$ and

$$\begin{aligned} \vec{u}_{jp_j} &= \frac{iq_\sigma}{m_\sigma \omega_j} \{\Psi_j(p_j) J_{p_j}\left(\frac{k_{j\perp} v_\perp}{\Omega_\sigma}\right) \mathbf{R}_j \cdot \hat{\vec{e}}_j + [(v_z e_{jz} + \frac{p_j \Omega_\sigma}{k_{j\perp}^2} \vec{k}_{j\perp} \cdot \hat{\vec{e}}_j) \times \\ &\quad J_{p_j}\left(\frac{k_{j\perp} v_\perp}{\Omega_\sigma}\right) + \frac{i v_\perp \Omega_\sigma}{k_{j\perp}^2} (\hat{\vec{z}} \times \vec{k}_j) \cdot \hat{\vec{e}}_j \frac{d}{dv_\perp} J_{p_j}\left(\frac{k_{j\perp} v_\perp}{\Omega_\sigma}\right)] \mathbf{R}_j \cdot \vec{k}_j \} \end{aligned} \tag{3}$$

with

$$\mathbf{R}_j = \frac{1}{\Psi_j(\Psi_j^2 - \Omega_\sigma^2)} \begin{pmatrix} \Psi_j^2 & i\Psi_j\Omega_\sigma & 0 \\ -i\Psi_j\Omega_\sigma & \Psi_j^2 & 0 \\ 0 & 0 & \Psi_j^2 - \Omega_\sigma^2 \end{pmatrix} \tag{4}$$

and $\Psi_j = \omega_j - k_{jz} v_z - p_j \Omega_\sigma$. $\hat{\vec{z}}$ is the unit vector in the magnetic field direction. The previous model of the coupling of the wave fields is valid provided the free electron contribution to the fluctuation of the electron distribution at $\omega, \vec{k}$ can be neglected.

From the previous equations then follows $\hat{\vec{e}}_s^* \cdot \vec{j}_s = \omega_s V E_0 E$, which can be further modified to a form $\hat{\vec{e}}_s^* \cdot \vec{j}_s = \omega_s E_0 \vec{G} \cdot \vec{E}$, where the coupling vector $\vec{G}$ is given by

$$\begin{aligned} \vec{G} &= \sum_\sigma m_\sigma \int d\vec{v} f_\sigma(\vec{v}) \sum_{p_0+p=p_s} e^{i(p_0\theta_0+p\theta-p_s\theta_s)} \frac{iq_\sigma}{m_\sigma \omega} \times \\ &\quad \{(\omega - k_z v_z - p\Omega_\sigma) J_p\left(\frac{k_\perp v_\perp}{\Omega_\sigma}\right) \vec{A}_\sigma \cdot \mathbf{R} + (\vec{A}_\sigma \cdot \mathbf{R} \cdot \vec{k}) \times \\ &\quad [(v_z \hat{\vec{z}} + \frac{p\Omega_\sigma}{k_\perp^2} \vec{k}_\perp) J_p\left(\frac{k_\perp v_\perp}{\Omega_\sigma}\right) + \frac{i v_\perp \Omega_\sigma}{k_\perp^2} (\hat{\vec{z}} \times \vec{k}) \frac{d}{dv_\perp} J_p\left(\frac{k_\perp v_\perp}{\Omega_\sigma}\right)]\}. \end{aligned} \tag{5}$$

With the help of the derived expressions, one finds the scattering cross-section

$$\frac{d^2\Sigma}{d\Omega_{k_s} d\omega_s} = \frac{k_0 k_s^3 \omega_s}{32\pi^3 \epsilon_0^4 n_e \omega_0 \omega^2} \frac{\vec{G} \cdot \mathbf{Z} \cdot (1/V\tau) \langle \vec{\vec{j}}\vec{\vec{j}}^*(\vec{k},\omega) \rangle \cdot \mathbf{Z}^+ \cdot \vec{G}^*}{(\hat{\vec{e}}_s^* \cdot \epsilon_s \cdot \hat{\vec{e}}_s)(\hat{\vec{e}}_0^* \cdot \epsilon_0 \cdot \hat{\vec{e}}_0)}, \tag{6}$$

where $\vec{E}$ has been expressed as a function of $\delta\vec{j}$ with the help of tensor $\mathbf{Z} = \mathbf{\Delta}^{-1}(\omega, \vec{k})$ from the equation $\mathbf{\Delta} \cdot \vec{E} = -(i/\epsilon_0\omega)\delta\vec{j}(\omega, \vec{k})$. Here, $\mathbf{\Delta}(\omega, \vec{k})$ is the dispersion tensor at $\omega, \vec{k}$. $\mathbf{Z}^+$ denotes the transpose of $\mathbf{Z}^*$. Equation (6) gives the cross-section as a function of the spectral tensor of current fluctuations $\langle \vec{\vec{j}}\vec{\vec{j}}^*(\vec{k},\omega) \rangle$ at $\omega, \vec{k}$ and as a function of the coupling vector $\vec{G}$. This expression is amenable for direct numerical calculation and makes no approximation with respect to the ordering parameters $|k_{\perp s} v_\perp / \Omega_s|$ or $|k_{sz} v_z / (\omega_s - \ell\Omega_\sigma)|$.

Applications to α-particle diagnostics: A code has been written which calculates the scattering cross-section from Eq. (6) by including only the ion contributions to the sum over particle species in the current correlations. The α particle distribution is assumed to have a slowing-down form with α particles assumed as magnetized. The resulting spectral function for microwave scattering off fluctuations in the frequency regime $\omega/2\pi = 0.3 - 3.5$ GHz in a D-T plasma is shown in Fig. 1 The D-T ion background is modeled with particles having a mass 2.5 times proton mass, and scattering from ordinary mode polarization to ordinary waves $(O - O)$ is considered. The angle ϕ between the magnetic field and the wave vector is 89 degrees. The result is compared with the spectral function obtained with similar parameters by Aamodt and Russell [2] in their Fig. 2b. These authors kept only the first moments of fluctuation distribution in evaluating the spectral function. The fluctuation wavelength is held fixed at $k\rho_e = 0.144$, where ρ_e is the electron Larmor radius. The spectral function $S(\omega, \vec{k})$ shown in Fig. 1 can be found in terms of the cross-section $d^2\Sigma/d\Omega_{k_s} d\omega_s$ with the help of the relation

$$\frac{d^2\Sigma}{d\Omega_{k_s} d\omega_s} / S(\omega, \vec{k}) = \frac{k_0 k_s^3 |\hat{\vec{e}}_s^* \cdot (\epsilon_s - \mathbf{I}) \cdot \hat{\vec{e}}_0|^2 \omega_0 / \omega_s}{32\pi^3 n_e^2 (\hat{\vec{e}}_s^* \cdot \epsilon_s \cdot \hat{\vec{e}}_s)(\hat{\vec{e}}_0^* \cdot \epsilon_0 \cdot \hat{\vec{e}}_0)}. \tag{7}$$

With the present parameters, this ratio is 5.5×10^{-31}. Because $|k_{0,s} v_e / \Omega_e| \approx 0.1$ in our example, a good agreement is obtained between the results of the present paper and those in Fig. 2b of Ref. [2]. The small difference close to fluctuation frequencies at the lower hybrid resonance ensues from the different expressions used in calculation of $\Delta(\omega, \vec{k})$.

Fig. 2 shows the cross-section from the present model and from the Thomson scattering limit [5] for three incident wave frequencies 140, 300, and 500 GHz with two electron temperatures 1 keV and 20 keV. Here, the perpendicular component of the fluctuation wave vector 1866 m^{-1} and the angle $\phi = 103.5$ are kept fixed. With the lower temperature, the Larmor parameter of the incident wave remains less than 0.22, while for the higher temperature it achieves 1 for $\omega_0/2\pi = 500$ GHz. A good agreement with the

Thomson model is found over all the parameter range. Similar good agreement was found even when the frequency of the incident wave or the scattered wave approached electron cyclotron frequency or its harmonics for nonperpendicular fluctuation wave vectors with non-mixed wave polarizations.

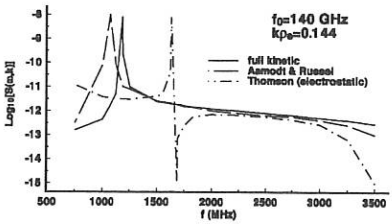

FIG. 1. *The spectral function $S(\omega, \vec{k})$ as a function of fluctuation frequency $(\omega/2\pi)$ obtained from Eq. (6).*

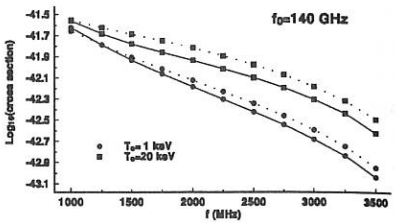

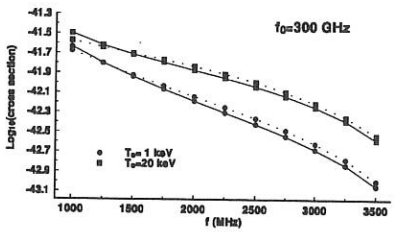

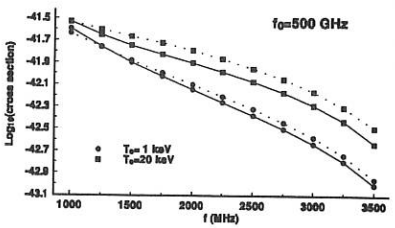

FIG. 2 *The scattering cross-section for three incident wave frequencies compared between the kinetic (solid) and Thomson (dotted) models.*

References:

[1] S.C. Chiu, Phys. Fluids B **3**, 1374 (1991).

[2] R.E. Aamodt and D.A. Russell, Nucl. Fusion **32**, 745 (1992).

[3] H. Bindslev, Plasma Phys. Contr. Fusion **35**, 1615 (1993).

[4] L. Stenflo and J. Larsson, *Three-wave Coupling Coefficients for Magnetized Plasmas*, Plasma Physics, Ed. by H. Wilhelmsson, pp. 152-158, Plenum Publishing Corporation, New York (1977); J. Larsson, J. Plasma Phys. **14**, 467 (1975).

[5] T.P. Hughes and S.R.P. Smith, Nucl. Fusion **28**, 1451 (1988).

Asymmetric Electron–Cyclotron Emission from Non–Thermal Plasmas Subject to a Generalized Kirchhoff's Law

M. Bornatici* and U. Ruffina**

* Physics Department, University of Ferrara, Ferrara, Italy, and Physics Department "A. Volta", University of Pavia, Pavia, Italy
** Department of Nuclear and Theoretical Physics, University of Pavia, Pavia, Italy

The electron–cyclotron emission (ECE) spectra characteristic of an optically thick plasma comprising a current–carrying superthermal tail for which a generalized Kirchhoff's law is valid are evaluated for both the extraordinary and ordinary mode, for perpendicular as well as oblique propagation, accounting for both higher order finite–Larmor–radius effects and harmonic overlap. With specific reference to ECE on the outboard side of the plasma, besides a spectrally narrow nonthermal feature occurring at frequencies relativistically downshifted to second and first harmonic cyclotron frequencies outside the plasma, the nonthermal ECE contributes a spectrally broad enhancement to the optically thick thermal ECE spectrum. The latter nonthermal spectral feature, in particular, is asymmetric with respect to the parallel refractive index, $N_\parallel$ and has to do with relativistically downshifted third harmonic X–mode emission and/or upshifted emission at frequencies $1 \leq (\omega/n\omega_c) \leq (1-N_\parallel^2)^{-1/2}$, the latter being dominant for $N_\parallel > 0$.

Introduction. For a plane plasma slab of thickness $2a$, and neglecting wall–reflections, the solution of the equation of radiative transfer yields for the specific intensity of the radiation from the outboard side of the plasma

$$I^{(i)}(\omega, N_\parallel) = \frac{\omega^2}{8\pi^3 c^2} \int_{-a}^{a} dx T_r^{(i)}(\omega, N_\parallel, x) \alpha^{(i)}(\omega, N_\parallel, x) e^{-\int_x^a dx' \alpha^{(i)}(\omega, N_\parallel, x')} \tag{1}$$

where $T_r^{(i)}(\omega, N_\parallel, x)$ is the **local** radiation temperature of the i–th mode, and the exponential function describes self–absorption, $\alpha^{(i)}$ being the electron–cyclotron (EC) absorption coefficient, so that $T_r^{(i)}\alpha^{(i)}$ is proportional to the (local) emission coefficient, (the index $i = X, O$, for the extraordinary (X) and ordinary (O) mode).

EC radiation for a bi–Maxwellian plasma. Let us consider the specific case of an electron distribution of the form $f = (1-\eta) f_b + \eta f_s$, where f_b denotes the (relativistic) isotropic Maxwellian distribution of the bulk (b) electrons (temperature T_b and density n_b) and f_s denotes the distribution of a low– density population of high energy electrons {hereafter referred to as superthermals (s), having temperature $T_s (> T_b)$ and density $n_s = [\eta/(1-\eta)] n_b (< n_b)$} in motion along the magnetic field with respect to the bulk electrons and such that f_s is a (relativistic) isotropic Maxwellian in the co–moving frame.[1] On account of the fact that for a bi–Maxwellian distribution Kirchhoff's law is valid for each electron population separately, the (local) radiation temperature is such that[1]

$$T_r^{(i)} \alpha^{(i)} = T_b \alpha_b^{(i)} + \frac{T_s \alpha_s^{(i)}}{\gamma_s (1 - N_\parallel \bar{v}_s)} \tag{2}$$

with $\alpha^{(i)} = \alpha_b^{(i)} + \alpha_s^{(i)}$ the total absorption coefficient, $\alpha_k^{(i)}$, $k = b, s$, denoting the absorption coefficient for the k–th electron population, and $\gamma_s \equiv (1-\bar{v}_s^2)^{-1/2}$, with $\bar{v}_s$ the drift velocity (in units of c).

The integral (1) along with (2) can be evaluated analytically in two limiting cases:

1. The superthermals are dominant with respect to the bulk,

$$I^{(i)}(\omega, N_\parallel) \simeq \frac{\omega^2}{8\pi^3 c^2} \left(\frac{T_s(x)}{\gamma_s(x)[1 - N_\parallel \overline{v}_s(x)]} \right)_{x=x_s^{(i)}(\omega,N_\parallel)} [1 - e^{-\tau_s^{(i)}(\omega,N_\parallel)}] \tag{3}$$

with $x = x_k^{(i)}(\omega, N_\parallel)$, the value for which $\widetilde{\alpha}_k^{(i)} \equiv \alpha_k^{(i)}(\omega, N_\parallel, x) e^{-\int_x^a dx\prime \alpha_k^{(i)}(\omega,N_\parallel,x\prime)}$ reaches its maximum, $\tau_k^{(i)}(\omega, N_\parallel) \equiv \int_{-a}^{a} dx \alpha_k^{(i)}(\omega, N_\parallel, x)$, the optical thickness of the i–th mode for the bulk ($k = b$), and superthermals ($k = s$).

2. The reabsorption by the bulk is dominant with respect to that by the superthermals,

$$I^{(i)}(\omega, N_\parallel) \simeq \frac{\omega^2}{8\pi^3 c^2} \left(T_b(x) + \frac{T_s(x)}{\gamma_s(x)[1 - N_\parallel \overline{v}_s(x)]} \frac{\alpha_s^{(i)}(\omega, N_\parallel, x)}{\alpha_b^{(i)}(\omega, |N_\parallel|, x)} \right)_{x=x_b^{(i)}(\omega,|N_\parallel|)} [1 - e^{-\tau_b^{(i)}(\omega,|N_\parallel|)}] \tag{4}$$

According to (4), the radiation temperature observed from the outboard side of the plasma can exhibit an enhancement with respect to the bulk temperature owing to ECE from superthermals, which is expected to be asymmetric with respect to $N_\parallel$ on account of the $N_\parallel$–asymmetry of $\alpha_s^{(i)}(\omega, N_\parallel, x)$.[1]

Numerical Results and Discussion. The evaluation of the ECE spectra is carried out on accounting for both higher order finite–Larmor–radius effects (up to 20 terms are kept in the series expansion of the relevant Bessel functions) and harmonic overlap (the first10 harmonics are included), as well as thermal corrections in the wave polarization. For reference, let us recall that the relativistic EC resonance around the n–th harmonic of the cyclotron frequency, i.e., $\gamma - N_\parallel u_\parallel - n\omega_c/\omega = 0$, where $\gamma \equiv (1+u^2)^{1/2}$, with $\mathbf{u} \equiv \mathbf{p}/mc$ the (dimensionless) electron momentum, requires that $(n\omega_c/\omega^2) - 1 + N_\parallel^2 \geq 0$, such a condition being unaffected by a streaming motion along the magnetic field.[1]

For the explicit evaluation of the ECE spectra, on the basis of (1) along with (2), we assume that i) the magnetic field has the usual $(1+\epsilon x/a)^{-1}$ spatial dependence, where a is the minor plasma radius and ϵ is the inverse aspect ratio; ii) the density, temperature and streaming velocity have spatial profiles of the form $[1 - (x/a_k)^2]^{\delta_i}$, with the indexes $i = n_k, T_k, v$; $k = b, s$ and $a_b \equiv a$, i.e., the spatial scale length of the bulk quantities is equal to the minor radius, whereas it is a_s ($\leq a$) for the superthermal component; iii) for the bulk and superthermals, $\delta_n = 1$, i.e., the density has a parabolic profile, whereas the temperature profile is somewhat steeper, namely, $\delta_{T_k} = 3/2$; for the drift velocity, $\delta_v = 3/2$ also.

Our numerical analysis refers specifically to ECE spectra of supershot plasmas in TFTR,[2] for which $a = 0.79m$, $R = 2.45m$, so that $\epsilon \equiv a/R = 0.32$; $B(0) = 51\,kG$, for which $f_c(0) = 142.8\,GHz$ and $2f_c(0) = 285.6\,GHz$; $n_e(0) = 7 \times 10^{13} cm^{-3}$, so that $f_p(0) = 75.13\,GHz$ and $(f_p(0)/f_c(0))^2 = 0.28$, $T_e(0)$ ($\equiv T_b(0)$) $= 6.5\,keV$. For these parameters, both the 2.nd harmonic X–mode and the 1.st harmonic O–mode are optically thick, even close to the plasma edge.

For reference, we show in Fig.1 the (spectrum of the) radiation temperature $(8\pi^3 c^2/\omega^2) I^{(x)}(\omega)$ of the X–mode for perpendicular propagation, for a superthermal population with temperature $T_s(0) = 3T_e(0)$ and scale length of the spatial profiles $a_s = a/2\,(= 39.5cm)$, for $\eta = 0.04\,(n_s(0) = 2.8 \times 10^{12} cm^{-3})$, both with ($\gamma_s(0) = 1.01$) and without ($\gamma_s = 1$) drift, as well as for $\eta = 0.02$ with drift ($\gamma_s(0) = 1.01$). Besides two narrow features due entirely to ECE from superthermals occurring on the low–frequency side of the spectrum,[3] (whereas the lower–frequency feature is at frequencies downshifted with respect to the upper cut–off at the outboard edge of the plasma, $\omega_c(x = a) \simeq 0.76\omega_c(0)$, the higher– frequency feature occurs at frequencies downshifted with respect to the 2.nd harmonic (cold) resonance near the outboard edge of the plasma), the emission from the bulk is somewhat enhanced by the emission from the superthermals. In particular, the downshifted 3.rd harmonic emission from the outboard of the 2.nd harmonic

thermal resonance reinforces (the high–frequency side of) the 2.nd harmonic thermal emission itself,[4] the enhancement being $\lesssim 5\%$ for $\omega \lesssim 2.2\omega_c(0)$.

The ECE spectrum for the oblique X–mode is shown in Fig. 2. The most noticeable feature with respect to the $N_\parallel = 0$–case of Fig. 1, is a significant enhancement, due to the superthermals, of the radiation temperature including the (optically thick) 2.nd harmonic, the nonthermal ECE being strongly asymmetric with respect to $N_\parallel$, cf. also Fig.3. The $N_\parallel$–asymmetry has to do with the asymmetry of the distribution function of the superthermals with respect to the parallel momentum and can thus be usable to get information on the drift motion of the superthermals. For the superthermals and with reference to the relativistic EC resonance condition, whereas for $N_\parallel < 0$ the Doppler shift adds to the relativistic frequency downshift, it is the other way about for $N_\parallel > 0$. Thus, in particular, i) the nonthermal features at downshifted 1.st and 2.nd harmonic are stronger for $N_\parallel = -0.34$ than for $N_\parallel = 0.34$; ii) around the 2.nd harmonic, the enhancement for $N_\parallel = -0.34$ has to do mainly with the downshifted 3.rd harmonic emission from the superthermals and is about 25% at $\omega \simeq 2.3\omega_c(0)$; iii) for $N_\parallel = 0.34$, the enhancement is due to ECE at frequencies $1 \leq (\omega/2\omega_c(x) \leq (1 - N_\parallel^2)^{-1/2}$, referred to as upshifted ECE,[5] from superthermals with parallel momenta of definite sign $N_\parallel u_\parallel > 0$, located in the (narrow) region

$$\frac{1}{\epsilon}\left[\left(\frac{\omega}{2\omega_c(0)}\right)^{-1} - 1\right] \leq \frac{x}{a} \leq \frac{1}{\epsilon}\left[\left(\frac{\omega}{2\omega_c(0)}\sqrt{1 - N_\parallel^2}\right)^{-1} - 1\right]$$

e.g., $-0.03 \leq (x/a) \leq 0.17$, for $(\omega/2\omega_c(0)) = 1.01$ and $|N_\parallel| = 0.34$. The resonant energy at the upper boundary being $\gamma = (1 - N_\parallel^2)^{-1/2}$, i.e., $(\gamma - 1)mc^2 \simeq 32\,keV$ for $|N_\parallel| = 0.34$, the typical energies of the emitting electrons being, in general, lower for upshifted 2.nd harmonic ECE than for the downshifted 2.nd harmonic ECE. The enhancement of the radiation temperature due to upshifted ECE is about 10% at $\omega \simeq 2\omega_c(0)$ and 15% at $\omega \simeq 3\omega_c(0)$.

As for the O–mode, the ECE spectrum for oblique propagation is shown in Fig.4.In addition to the nonthermal downshifted 1.st harmonic feature, a significant enhancement of the radiation temperature of the bulk occurs as a result of the upshifted ($N_\parallel > 0$ ECE from the superthermals.The $N_\parallel$–asymmetry in ECE is again a salient characteristic, cf. also Fig.3, and is in line with the asymmetry in wave transmission observed in the RTP tokamak.[6]

Acknowledgments. This work was supported by the Italian Ministry of University, Scientific Research and Technology (MURST).

References

[1] Bornatici M, Ruffina U, Westerhof E, *Plasma Phys. Controlled Fusion* **28** 629 (1986); Bornatici M, Ruffina U, *Phys. Fluids* **31** 2201 (1988)

[2] Taylor G, Arunasalam V, Efthimion P–C, Grek B, *Proc. 8th Joint Workshop on ECE and ECRH*, Gut Ising, Germany, (1992) (Max Planck Institut für Plasmaphysik, Garching, 1993), IPP III/186 **1** 277

[3] Airoldi A, Orefice A, Ramponi G, *Nuovo Cimento* **D13** 517 (1991)

[4] Tanzi C–P, et al., *Proc. 8th Int. Workshop on ECE and ECRH* (Gut Ising, Germany, 1992), (Max Planck Institut für Plasmaphysik, Garching, 1993), IPP III/186, **1** 265

[5] Tribaldos V, Krivenski V, ibid., 123; *Proc. 21st Eur. Conf. on Controlled Fusion and Plasma Physics*(Montpellier, France, 1994) **18B** Part III, 1228; Krivenski V, Tribaldos V, *Proc. 20th Eur. Conf. on Controlled Fusion and Plasma Physics* (Lisbon, Portugal, 1993) **17C** Part III 1045

[6] Peeters A–G et al., *Plasma Phys. Contr. Fusion* **37** 525 (1995)

Figure captions

Fig. 1 Non–thermal ECE spectra:X–mode, perpendicular observation from the outboard side of the plasma in the presence of a superthermal population with temperature $T_s(0) = 3T_e(0)$, density $\eta(\equiv n_s(0)/n_e(0)) = 0.04$, with ($\gamma_s = 1.01$) and without ($\gamma_s = 1$) drift, as well as $\eta = 0.02$ with $\gamma = 1.01$. The $\eta = 0$–curve refers to the Maxwellian case. The frequency ranges $n\omega_c(x = a) \leq \omega \leq n\omega_c(x = -a)$ for the first 5 harmonics are indicated.

Fig. 2 Non–thermal ECE spectra: X–mode, oblique ($N_\parallel = \pm 0.34$) observation from the outboard side of the plasma, in the presence of a superthermal population with temperature $T_s(0) = 3T_e(0)$, density $\eta = 0.04$, with $\gamma_s(0) = 1.01$ and without ($\gamma_s = 1$) drift. The $\eta = 0$–case (no superthermals) is also shown.

Fig. 3 The $N_\parallel$–asymmetry in the radiation temperature, $\Delta^{(i)} \equiv 1 - T^{(i)}_{rad}(-N_\parallel)/T^{(i)}_{rad}(N_\parallel)$ vs. ω, for $N_\parallel = 0.34$, for both the X and O–mode.

Fig.4 Same as Fig. 2 for the O–mode.

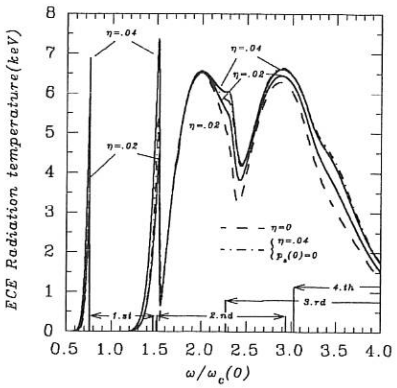

Fig. 1

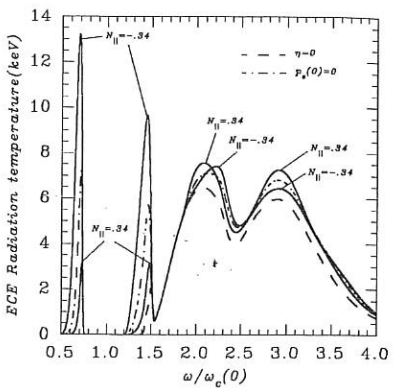

Fig. 2

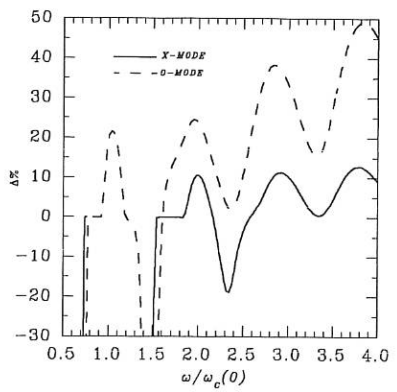

Fig. 3

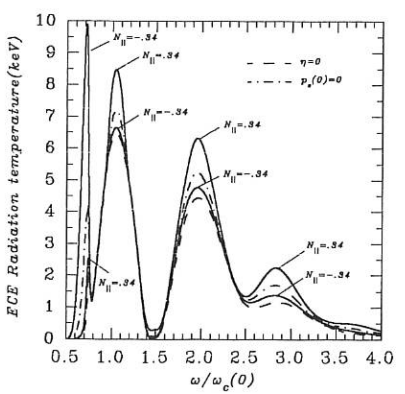

Fig. 4

Trapped Particle Precessional Drifts in Arbitrary Aspect Ratio Tokamaks with Shaping: Consequences for Stability

C M Roach, J W Connor and S Janjua[1]
UKAEA Government Division, Fusion, Culham, Abingdon, Oxon, OX14 3DB, UK, (UKAEA/Euratom Fusion Association)
(1) Bath University

Introduction

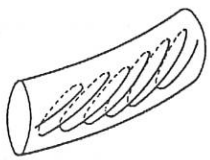

Figure 1: Trapped particle toroidal precession

Plasma equilibrium parameters affect the precessional drift frequencies $\langle\omega_D\rangle$ of trapped particles, which can significantly influence plasma stability; eg collisionless trapped electron modes (CTEM) and fishbones. Instability growth rates are maximised when $\frac{\langle\omega_D\rangle}{\omega_*} \sim 1$ [1], and minimised or stabilised when this ratio is small (or negative). We extend a circular large aspect ratio calculation of $\langle\omega_D\rangle$ [2] to calculate the bounce averaged drift frequencies for toroidally symmetric plasmas of arbitrary aspect ratio with shaped poloidal cross sections.

Our calculation [3] is applied to JET and START like flux surfaces, to investigate the suggestion [4] that favourable trapped particle drifts are responsible for improved confinement in START [5]. We find a complex dependence of $\langle\omega_D\rangle$ on equilibrium parameters, with competing effects from aspect ratio, shaping, magnetic shear and pressure gradients. Averaging over pitch angle and normalising to the diamagnetic drift frequency ω_* we characterise our results in terms of the important stability parameter $\frac{\overline{\langle\omega_D\rangle}}{\omega_*}$.

The Calculation

$\langle\omega_D\rangle$ for trapped electrons is given by ([2]):

$$\langle\omega_D\rangle = \frac{m}{e}\frac{\partial J}{\partial \Psi}\left(\frac{\partial J}{\partial K}\right)^{-1} \tag{1}$$

where m, e are the electron mass and charge, Ψ is the poloidal flux, $K = \frac{v^2}{2}$ and

$$J = \int_{\text{bounce}} v_{\|} dl = \int_{\text{bounce}} \left(2\left(K - \mu B\right)\right)^{\frac{1}{2}} dl \tag{2}$$

is the longitudinal adiabatic invariant, where $\mu = \frac{v_\perp^2}{2B}$.

To compute $\langle\omega_D\rangle$ for particles trapped on a given flux surface we need to know the geometry and magnetic field on the surface. Solving the Grad-Shafranov equation locally, by expanding about this surface, yields the local variation of the magnetic fields perpendicular to the surface [6]. This gives all the information required to evaluate equation (1), assuming that we are dealing with very narrow orbits.

The surface geometry is parameterised via:

$$\begin{aligned} R_s &= R_0\left(1+\epsilon\left(E-1\right)\cos\theta+\epsilon T\cos 2\theta\right)=R_0\hat{R} \\ Z_s &= R_0\epsilon\left(\left(1+E\right)\sin\theta+T\sin 2\theta\right) \end{aligned} \tag{3}$$

where R_0 is the plasma major radius, ϵ is the aspect ratio, E is ellipticity, T is triangularity and θ is a poloidal angle. The magnetic field on the equilibrium surface is also parameterised:

$$B_p = B_{\phi 0}\frac{\epsilon\gamma}{q}\left(1+B_{p1}\cos\theta+B_{p2}\cos 2\theta+B_{p3}\cos 3\theta+B_{p4}\cos 4\theta\right)=B_{\phi 0}\frac{\epsilon\gamma}{q}\hat{B}_p \tag{4}$$

$$B_\phi = \frac{B_{\phi 0}}{\hat{R}} \tag{5}$$

where $B_{\phi 0}$, B_{p1}, B_{p2}, B_{p3} and B_{p4} are constants appropriate to the specified surface, q is the safety factor, and

$$\gamma=\frac{1}{2\pi}\oint d\theta\frac{\hat{h}}{\hat{R}^2\hat{B}_p} \tag{6}$$

The magnetic shear $s=\frac{RrB_{p0}}{q}q'$ (where $'$ denotes the partial derivative with respect to the poloidal flux), and the pressure gradient parameter $\alpha=-\frac{2\mu_0 p'\epsilon^2R_0^2}{B_{p0}}$ are the only remaining parameters [7].

Assuming narrow orbit widths, we find from equation (1) after some algebra:

$$\langle\omega_D\rangle = -\frac{m2K}{eB_{\phi 0}R_0}\frac{q}{\epsilon r\gamma}\frac{\int_{\theta_b}^{\pi}d\theta\left(1-\hat{\lambda}\hat{B}\right)^{\frac{1}{2}}\frac{\hat{h}\hat{B}}{\hat{R}\hat{B}_p^2}\left[\left(1-\frac{\hat{\lambda}\hat{B}}{2(1-\hat{\lambda}\hat{B})}\right)\frac{r}{\hat{B}}\frac{\partial\hat{B}}{\partial\rho}-\frac{1}{\hat{R}_c}-\frac{r}{\hat{B}_p}\frac{\partial\hat{B}_p}{\partial\rho}\right]}{\int_{\theta_b}^{\pi}d\theta\left(1-\hat{\lambda}\hat{B}\right)^{-\frac{1}{2}}\frac{\hat{h}\hat{B}}{\hat{B}_p}} \tag{7}$$

where the integrals in (7) can be computed numerically, after taking care over singularities at the bounce angle $\theta=\theta_b$. The numerical evaluation of equation (7) has been checked both analytically in the circular large aspect ratio [2] and in the deeply trapped limits, and numerically for a tight aspect ratio equilibrium surface against a particle guiding centre code.

Phase space averaging and normalisation to ω_* gives a quantity which characterises stability:

$$\frac{\overline{\langle\omega_D\rangle}}{\omega_*}=\frac{1}{\omega_*}\frac{\int_0^{\pi}d\theta_b p(\theta_b)\langle\omega_D\rangle}{\int_0^{\pi}d\theta_b p(\theta_b)} \tag{8}$$

where $p(\theta_b)$ is the velocity phase space factor, and $\omega_*=\frac{1}{en}p'$.

Results

Computing a full equilibrium from a 2D Grad-Shafranov solver using the JET parameters from Table 1, we have extracted α and s and fitted the shape and magnetic field at the $q=2$ surface using parameterisations (3), (4) and (5). Figure 2 gives $\langle\omega_D\rangle/\omega_*$ as a function of θ_b.

R_0 (m)	3.00	I_p (MA)	3.0
a (m)	1.25	β (%)	1.15
κ_a	1.30	B_ϕ (T)	3.27
δ_a	0.40		

Table 1: Typical JET parameters.

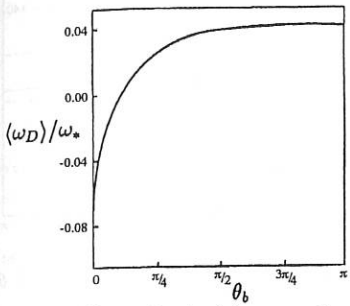

Figure 2: $\langle\omega_D\rangle/\omega_*$ as a function of θ_b for the JET $q = 2$ surface.

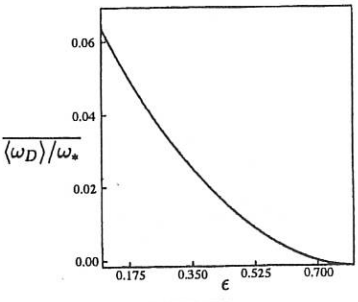

Figure 3: $\overline{\langle\omega_D\rangle/\omega_*}$ for ϵ scan.

We have calculated $\langle\omega_D\rangle/\omega_*$ for a range of equilibria, scanning in the aspect ratio parameter ϵ. Starting from the JET $q = 2$ surface we vary ϵ by adjusting R_0 and B_{p0}, keeping other parameters fixed (ie a, q, α, s, $B_{\phi 0}$, B_{p1}, B_{p2}, B_{p3} and B_{p4}). This is one of many possible prescriptions for scanning self-consistent tokamak equilibria in ϵ. For the particular scan we have chosen, Figure 3 shows that drifts become more favourable as ϵ increases, though the rate of decrease of $\overline{\langle\omega_D\rangle}/\omega_*$ with ϵ does reduce at larger ϵ.

In our scan we find that as ϵ increases, B_p becomes comparable to B_ϕ, and the plasma develops an unconventional off-axis minima in $|B|$. This has an important impact on trapped particle orbits, producing a class of trapped particles which are wholly confined above or below the equatorial mid-plane. Our calculation can compute the toroidal precession frequencies in such equilibria.

R_0 (m)	0.185	I_p (MA)	0.136
a (m)	0.135	β (%)	1.79
κ_a	1.30	B_ϕ (T)	0.59
δ_a	0.40		

Table 2: Typical START parameters.

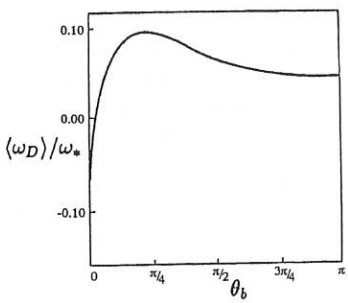

Figure 4: $\langle\omega_D\rangle/\omega_*$ as a function of θ_b for a START $q = 2$ surface.

Computing a full equilibrium with START like parameters as in Table 2, we fit the $q = 2$ surface and display the calculated $\langle\omega_D\rangle/\omega_*$ distribution in Figure 4. Surprisingly we find that $\overline{\langle\omega_D\rangle}/\omega_*$ is larger than for JET, despite higher ϵ. START has significantly higher shear than at JET however, and high s does not favour stability [2]. The character of trapped particle drifts appears to be similar in JET and in START.

We can study the effects of shear and pressure gradient by locally perturbing α and s on the surface without affecting the global equilibrium. Figures 5 and 6 show the impact of such perturbations on $\langle\omega_D\rangle/\omega_*$. Low (or negative) s and high α favour CTEM stability.

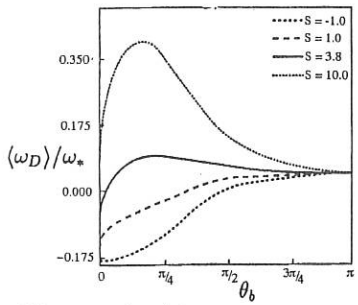

Figure 5: $\langle\omega_D\rangle/\omega_*$ as a function of θ_b for different shear values s.

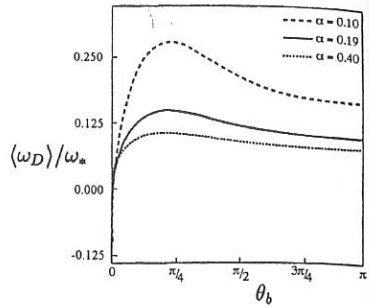

Figure 6: $\langle\omega_D\rangle/\omega_*$ as a function of θ_b for different α values.

Conclusions

In conclusion $\langle\omega_D\rangle$ has been calculated for narrow orbit trapped particles in arbitrary ϵ tokamaks with shaping of the poloidal cross section. Pressure gradients and shear are also included, so that $\langle\omega_D\rangle/\omega_*$ can be computed accurately for conventional and advanced tokamak equilibria. The calculation has been benchmarked numerically and analytically, and we have calculated $\overline{\langle\omega_D\rangle}/\omega_*$ for JET and START like plasmas. A competition between the benefits of large ϵ and the costs of higher s, gives similar drifts in both machines in our calculation. This does not provide support for the hypothesis that favourable drifts stabilise trapped particle instabilities in START, as proposed in [4]. High β (hence large α) and advanced tokamak configurations with low or negative shear do however optimise $\overline{\langle\omega_D\rangle}/\omega_*$.

Acknowledgements

It is a pleasure to thank Lynton Appel, Chris Gimblett, Jim Hastie, Guido Huysmans, Kin Kam, Simon Pinches, Greg Rewoldt and Howard Wilson for useful discussions in the course of this work, which was funded jointly by the UK Department of Trade and Industry and Euratom.

References

[1] W M Tang, Theory of Fusion Plasmas, Proceedings of the Joint Varenna-Lausanne International Workshop, Varenna, August 1990, Bologna, 1990, p 31.
[2] J W Connor, R J Hastie and T J Martin, Nuclear Fusion, **23**, 1702, (1983).
[3] C M Roach, J W Connor and S Janjua, Plasma Physics and Controlled Fusion, **37**, 679, (1995).
[4] G Rewoldt and W M Tang, International Sherwood Fusion Theory Conference, Newport, Rhode Island, March 1993.
[5] R J Colchin, Bull Am Phys Soc, **37** 1354, (1992).
[6] C M Bishop, Culham UKAEA Report, CLM-R 249, March 1985.
[7] C M Bishop, Nuclear Fusion, **26**, 1063, (1986).

The Effect of Shearless Stellarator Rotational Transform on the Tokamak Plasma Stability

M.I. Mikhailov, V.D. Shafranov and **A.A. Subbotin**
Russian Research Centre "Kurchatov Institute", Moscow, Russia

1. Introduction

We consider the stability of the straight pressureless current column with external rotational transform in stellarator approximation. The configuration in this case looks as onedimensional one and the expression for energy variation acquire the well known form (see, e.g. [1]):

$$\delta W = \frac{\pi^2 R}{m^2} \int \left\{ (Y')^2 + \frac{m^2}{r^2} Y^2 - \frac{Rj}{rB_0} \left(\frac{Y^2}{\iota - n/m} \right)' \right\} r\, dr \,. \tag{1}$$

Here $\iota = \iota_J + \iota_h$, ι_J and ι_h are the total, current and stellarator rotational transforms respectively.

2. Analytical approaches

Some useful information concerning instability of current carrying plasma column can be obtained analytically.

2.1 Uniform current density

First of all let's consider the simplest case of uniform current density, $j = \text{const}$. For this case analytical instability conditions have been obtained [1]. For $\iota_h = \text{const}$ and consequently $\iota = \text{const}$, the ideal modes are important only. Corresponding instability condition is

$$0 < m\iota(a) - n < \iota_J(a)\,, \tag{2}$$

or

$$\frac{n}{m} < \iota(a) < \frac{n - \iota_h}{m - 1}\,. \tag{3}$$

Here a is the plasma boundary radius.

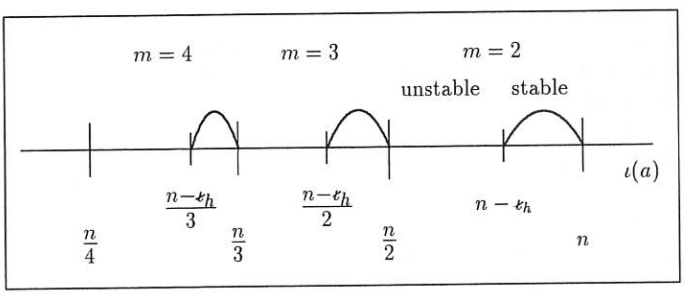

Fig. 1. The stability windows are appeared at given n in tokamak with $j = \text{const}$ at adding $\iota_h(r) = \text{const}$.

It is seen from Eq. (3) that unlike the tokamak where there is no windows of stability at $\iota_J = \text{const}$, in stellarator such windows exist for given n value (see Fig. 1) :

$$\frac{n - \iota_h}{m-1} < \iota(a) < \frac{n}{m-1} . \tag{4}$$

If the modes with different n are taking into account these gaps of stability disappear.

2.2 Nonuniform current density

For analyzing the stability of plasma column with nonuniform current density we'll use here the Principle of Successive Current Layers (SCL) suggested for tokamak by L. Zakharov [2]. For the tokamak with external rotational transform ι_h the SCL principle has been extended in [3]. For more general case of the current column with conducting shell and external rotational transform it follows from this principle that m/n mode with resonance surface in the region between the plasma boundary and the conducting shell will be stable if for any plasma small radius with nonzero current density

$$(m-1)\iota - n + \iota_h + r\,\iota_h'/2 + L\,[(m+1)\iota - n - \iota_h - r\,\iota_h'/2] > 0. \tag{5}$$

And vice versa, if the left side of Eq. (5) is always negative the mode will be unstable. Here $L = (r/b)^{2m}$, b is a shell radius.

For tokamak ($\iota_h = 0$) without conducting shell ($L = 0$) it follows from SCL principle [2] that ideal m/n modes with resonance surface in vacuum region will be unstable for any current density profile with $j > 0$ and $j'(r) < 0$ if

$$(m-1)\iota_J(0) < n . \tag{6}$$

That means, for example, that in configuration with $\iota_J(a) > 1/2$ the mode $m/n = 2/1$ is unstable if $\iota_J(0) < 1$. Taking into account this result Zakharov treats the disruptive instability as the instability of ideal 2/1 mode at $\iota_J(a) > 1/2$ when due to internal disruption the rotational transform on the magnetic axis becomes equal to unity.

Let's consider how the adding of shearless stellarator rotational transform will change this situation. For 2/1 mode in the case $b \gg a$ Eq. (5) means $\iota(0) > 1 - \iota_h$, so that with $\iota_h > 0$ there is a possibility of ideal 2/1 mode stabilization even if $\iota(0) \leq 1$ (for example, due to internal disruption). This can explain the results of the experiments on WVII-A [4], when the introduction of stellarator rotational transform have lead to disruptive-free discharges.

It can be noted from Eq. (6) that in tokamak with $\iota_J(0) < 1$ the ideal modes with resonant surface in vacuum region and $m = n + 1$ are always unstable. In stellarator this modes will be unstable if $\iota(0) < 1 - \iota_h/n$. Thus, in principle they can be stabilized even at $\iota(0) < 1$.

According to SCL principle the part of the current channel with $\iota(r) > (n - \iota_h)/(m - 1)$ is stable against m/n mode. Zakharov named this part of the column the "supporting channel". It is clear, that stellarator rotational transform expand the "supporting

channel" if $\iota_h(0) > 0$. It is seen that the flattening of the current density profile expands the "supporting channel" too.

3. Numerical Results

More detailed information about different modes stability have been obtained numerically. The diagrams of stability are calculated for the configurations with $\iota_h(r) = \text{const}$, $\iota(0) = 1$ and

$$j = j(0)\,[1 - (r/a)^k]^\gamma \,. \tag{7}$$

We consider $\iota(0) = 1$ as the possible, due to internal disruption, and the most dangerous case for external free boundary ideal modes. The current density distribution contains two parameters k and γ. At given k, ι_h and $\iota_J(a)$ the value of γ was chosen to satisfy the condition $\iota(0) = 1$. This limits us in choosing the values of $\iota_J(a)$, ι_h.

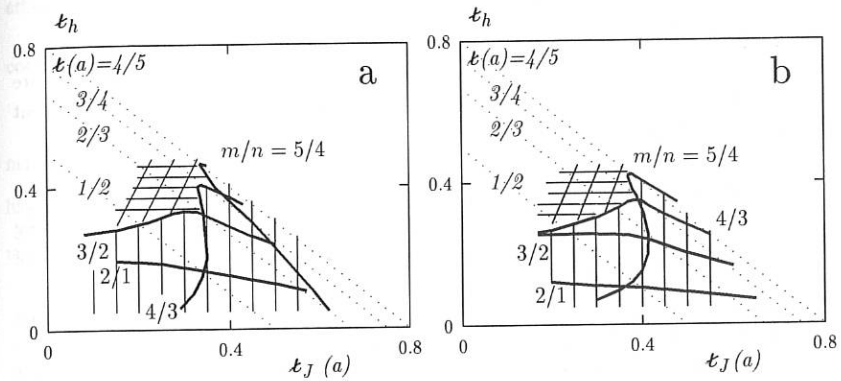

Fig. 2. The diagrams of stability of ideal and tearing modes for configurations with $\iota_h(r) = \text{const}$, $j = j(0)\,[1 - (r/a)^k]^\gamma$. *Parameter* γ *is chosen from the condition* $\iota(0) = 1$. *The boundaries of stability of ideal and tearing modes are marked by solid lines. The regions of instability are marked by vertical lines. In marked by crossed lines regions all the ideal and tearing modes are stable. By dotted lines the straights* $\iota(a) = 1/2,\ 2/3,\ 3/4,\ 4/5$ *are shown. Below these lines corresponding modes are tearing ones.* a : $k = 4$, b : $k = 6$.

The stability boundaries of the modes with $m = n + 1$ are shown on the diagrams Fig. 2. In the stability region of this modes another modes were checked too. The regions in which all ideal and tearing modes was found to be stable, are marked by the crossed lines, while the regions of instability are marked by vertical solid lines.

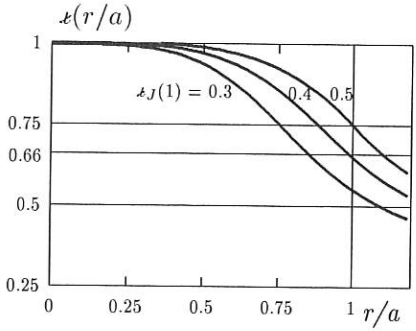

Fig. 3. Profiles of total ι for $\iota_h = 0.25$, $\iota(0) = 1$ and different values of $\iota_J(a)$. The horizontal solid lines show the resonance values for modes $m/n = 2/1, 3/2, 4/3$.

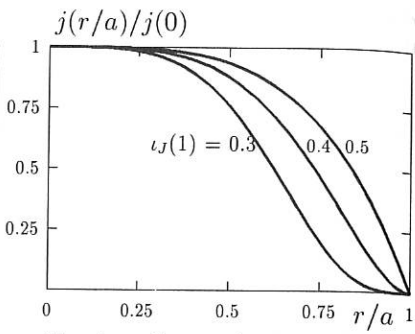

Fig. 4. Current density profiles for $\iota_h = 0.25$, $\iota(0) = 1$ and different values of $\iota_J(a)$.

As the examples the profiles of total rotational transform and current density are shown on Figs. 3, 4 for $\iota_h = 0.25$, $k = 4$ (see Eq. 7) and different values of current rotational transform on the boundary.

4. Conclusions

1. The shearless stellarator rotational transform can stabilize all the ideal and tearing modes. Needed for this purpose the stellarator rotational transform ι_h is of the order of current rotational transform ι_J : $\iota_h \sim \iota_J$.

2. Rather small stellarator rotational transform can be useful too. As it is seen from diagrams, the stellarator rotational transform of the order of $0.1 - 0.15$ can stabilize the most dangerous from viewpoint of disruptive instability mode 2/1 at different current density profiles and with $\iota(0) = 1$. This is in agreement with the WVII-A experimental results [4].

Acknowledgment

We wish to thank Professor F. Troyon for supporting this work. This work is supported by Russian Foundation of Fundamental Research, grant N 95-02-05519a.

References

[1] Miyamoto K, *Nucl. Fusion* **18** 243 (1978)

[2] Zakharov L, *Sov. J. Plasma Phys.* **7** 714 (1981)

[3] Mikhailov M and Shafranov V, *Nucl.Fusion* **30** 413 (1990)

[4] W VII-A Team, *Plasma Physics and Controlled Nuclear Fusion Research 1978 (Proc. 7th Int. Conf. Innsbruck,1978)* **2** 265 (1979)

DERIVATION OF BOHM's COEFFICIENT OF THE MAGNETIC FIELD DIFFUSION IN FRAME OF 2-D. EMHD MODEL.

O.Z.Zabaidoullin*, V.V.Vikhrev.
"Russian Research Centre Kurchatov Institute",
*Ecole Polytechnique, LPMI, France.

Like in [1] we discuss the dynamics of the magnetic field in frame of electron magneto hydrodynamics (EMHD). It was shown that in case of inhomogeneous plasma $\frac{\Delta n}{n}$ along the current lines the Joule heating up to $(\omega\tau)_{ei}\frac{\Delta n}{n}$ times higher, than Joule heating of the plasma with uniform density n along the current. For the obtained Joule heating we put into correspondence the efficient coefficients of magnetic field diffusion and conductivity. The efficient coefficient of the magnetic field duffusion $D=\frac{cT}{10eH_0}$ slightly differs from Bohm's coefficient $D=\frac{cT}{16eH_0}$.

INITIAL CONDITIONS.

At the initial moment t=0 plasma occupies the right part of the plane (x, y), and magnetic field the left part: $x \le 0$ (Fig.1). Distribution of the plasma density $n(x,y) \equiv n(y)$ has the positive constant gradient $\frac{\partial}{\partial y}\left(\frac{1}{n}\right)=\frac{n_0-n}{n_0 nL}$ at the interval [0,L] and the same but negative at the interval [L,2L] (Fig.2).

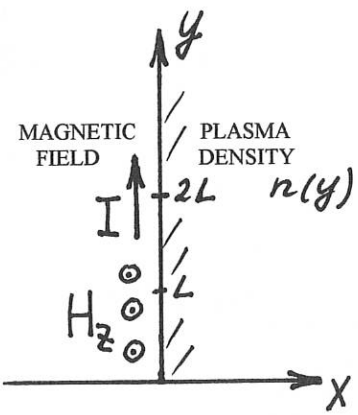

Initial distribution of the magnetic field and plasma density
FIG.1

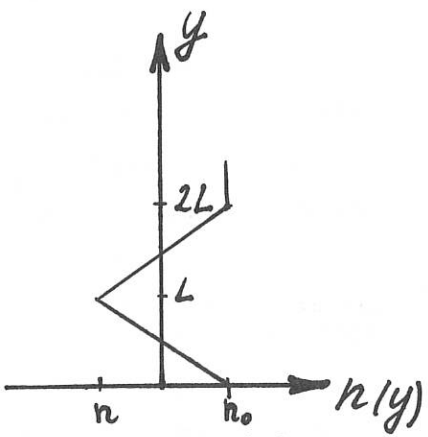

Distribution of the plasma density

FIG.2

We simulated the following equation of the magnetic field dynamics in frame of EMHD:

$$\frac{\partial H}{\partial t} = D\left(\frac{\partial^2 H}{\partial^2 x}\right) + D\left(\frac{\partial^2 H}{\partial^2 y}\right) + \frac{cH}{4\pi e}\frac{\partial H}{\partial x}\frac{\partial}{\partial y}\left(\frac{1}{n}\right) \quad (1)$$

The results of such modelling are shown on Fig.3.

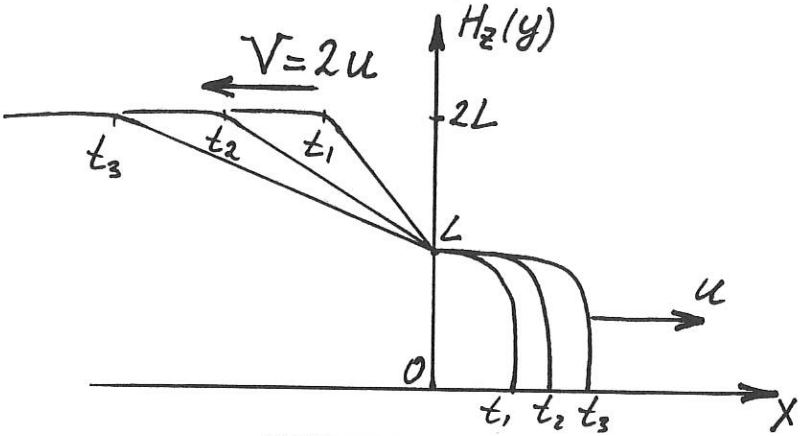

DYNAMICS OF THE MAGNETIC FIELD
FIG.3

DYNAMICS OF THE MAGNETIC FIELD AT THE INTERVAL [0,L].

For a plasma layer of width *dy* inside the interval [0,L] eq.(1) can be simplified

$$\frac{\partial H}{\partial t} = D\left(\frac{\partial^2 H}{\partial^2 x}\right) + \frac{cH}{4\pi e}\frac{\partial H}{\partial x}\frac{\partial}{\partial y}\left(\frac{1}{n}\right), \quad (2)$$

which has exact analytical solution [1] of magnetic field penetration like a shock wave into a plasma

$$H = \frac{H_0}{e^{(x-ut)/\lambda}+1} \quad (3)$$

with velocity

$$u = cH_0/8\pi e\frac{\partial}{\partial y}\left(\frac{1}{n}\right) \quad (4)$$

and characteristic width of the shock wave front

$$\lambda = \left(\frac{\sigma H_0}{2ec}\frac{\partial}{\partial y}\left(\frac{1}{n}\right)\right)^{-1} \quad (5)$$

From the system of the Maxwell's eq., neglecting the electric field energy compare with magnetic, one can obtain the eq. for changing the magnetic field energy in a given volume

$$\iiint \frac{\partial\left(H^2/8\pi\right)}{\partial t} dV = \iint P, dS - Q_{joul}. \quad (6)$$

From eq.(3) we can obtain expression [2] for current layer Joule heating per unit length

$$Q_{joul} = \frac{c^2}{4\pi\sigma}\iint \left(\partial H/\partial x\right)^2 dx = \frac{1}{4}\frac{H_0^3 c}{48\pi^2 e}\frac{\partial}{\partial y}\left(\frac{1}{n}\right) \quad (7)$$

And what is more important, that Q_{joul} ***proportional to the magnetic field in cube and does not depend from plasma conductivity*** σ ***and time*** t. The reason of such enhanced Joule heating is in significant decreasing of the shock wave width λ (5) in compare with classical skin $\left(c^2 t/4\pi\sigma\right)^{1/2}$. By this reason in the front of magnetic field penetration the diffusional term (first) in the eq.(2) and Hall term (second) have the same order.

There is another method [2] to obtain the value of Joule heating Q_{joul} directly from eq.(6). The flux of the electromagnetic energy

$$W = c/4\pi \iint \left[E_{Hall} * H\right]_y dx \qquad (8)$$

can be obtained, using the expression for the Hall component of the electric field intensity $E_{Hall} = [rotH, H]/4\pi en$. In our case

$$W = \frac{cH_0^3}{48\pi^2 en(y)}. \qquad (9)$$

And

$$\iint P, dS = \frac{\partial W}{\partial y} dy = \frac{cH_0^3}{48\pi^2 e} \frac{\partial}{\partial y}\left(\frac{1}{n}\right) \qquad (10)$$

According to the eq.(3)

$$\iiint \frac{\partial\left(H^2/8\pi\right)}{\partial t} dV = u \frac{H_0^2}{8\pi} dx. \qquad (11)$$

From the eq.(6) we can obtain the expression for Joule heating (7)

$$Q_{joul} = \frac{1}{3} u \frac{H_0^2}{8\pi}. \qquad (12)$$

For the knowing Joule heating (12), we can put into correspondance the efficient coefficients of magnetic field diffusion and plasma conductivity. Let us suppose that we do not know about the possibility of the magnetic field penetration (3) into a plasma. In this case we can consider the width of a current layer as a classical δ. So, we can estimate the current density as follows $j = \frac{c}{4\pi} rotH = \frac{cH}{4\pi\delta}$, and Joule heating as $\frac{c^2 H_0^2}{16\pi^2 \sigma\delta}$. From the equality

$$\frac{c^2 H_0^2}{16\pi^2 \sigma\delta} = \frac{1}{4} \frac{H_0^3 c}{48\pi^2 e} \frac{\partial}{\partial y}\left(\frac{1}{n}\right)$$

we can express the efficient coefficient of the plasma conductivity

$$\sigma = \left(\frac{H_0 \delta}{12ec} \frac{\partial}{\partial y}\left(\frac{1}{n}\right)\right)^{-1}. \qquad (13)$$

The efficient coefficient of magnetic field diffusion

$$D = c^2/4\pi\sigma = \frac{cH_0\delta}{48\pi e} \frac{\partial}{\partial y}\left(\frac{1}{n}\right) \qquad (14)$$

for the considered plasma distribution takes the following form

$$D = \frac{cH_0}{48\pi en_0} \frac{\delta}{L} \frac{\Delta n}{n} \qquad (15)$$

DYNAMICS OF THE MAGNETIC FIELD AT THE INTERVAL [L,2L].

At the interval [L,2L], opposite to previous part, the plasma density increases in the direction of the current. Dynamics of the magnetic field is also described by eq.(2), which has no analytical solution in this case. By this reason we studied it numerically. The results of magnetic field dynamics are presented on Fig.3. At the interval [L,2L] magnetic field goes out

from the plasma boundary with maximum velocity $V = 2u$ at the line y=2L, where u is from eq.(4).In this case the width of the shock wave δ increases proportionally to time and for simplicity we put $Q_{joul} = 0$.

So, the average Joule heating at the interval [0,2L]

$$Q^*_{joul} = \frac{1}{8}\frac{H_0^3 c}{48\pi^2 e}\frac{\Delta n}{n_0 nL} \qquad (16)$$

and the efficient coefficient of the magnetic field diffusion are twice less then at the interval [0,L]

$$D^* = \frac{cH_0}{96\pi e n_0}\frac{\delta}{L}\frac{\Delta n}{n} \qquad (17)$$

For a turbulent plasma $\frac{\delta}{L} \approx 1$ and $\frac{\Delta n}{n} \approx 1$, $D^* = \frac{cH_0}{96\pi e n_0}$.

INFLUENCE OF THE ELECTRON PRESSURE.

In this part of our work we used the results of [3], where velocity of magnetic field penetration into a plasma was obtained with account of electron pressure

$$u = \gamma c H_0 / 8\pi e \frac{\partial}{\partial y}\left(\frac{1}{n}\right), \qquad (18)$$

where γ is a plasma specific heat $3/5$. Using the relationship (12) and (16), we can write

$$Q^*_{joul} = \gamma\frac{1}{8}\frac{H_0^3 c}{48\pi^2 e}\frac{\Delta n}{n_0 nL}, \qquad (19)$$

and for efficient coefficient of magnetic field diffusion,

$$D^* = \gamma\frac{cT}{6eH_0} = \frac{cT}{10eH_0}, \qquad (20)$$

which is slightly differs from Bohm's coefficient $cT/16eH_0$ by a factor of $5/8$.

CONCLUSIONS.

It was theoretically obtained the expression of the plasma Joule heating of the current layer per unit length with density inhomogeneaty

$$Q^*_{joul} = \frac{1}{8}\frac{H_0^3 c}{48\pi^2 e}\frac{\Delta n}{n_0 nL}.$$

For this Joule heating we put into correspondence the efficient coefficient of plasma conductivity

$$\sigma^* = \left(\frac{H_0\delta}{24ec}\frac{\Delta n}{n_0 nL}\right)^{-1}$$

and magnetic field diffusion

$$D^* = \frac{cH_0}{96\pi e n_0}\frac{\delta}{L}\frac{\Delta n}{n},$$

which is in case of magnetic field-plasma equilibrium takes the following form

$$D^* = \frac{cT}{10eH_0}.$$

REFERENCES.

1. Kingsep A.S., Mohov U.V., Chukbar K.V., Fizika Plasma, 1984, vol.10, p.854.
2. Vikhrev V.V., Zabaidoulline O.Z., Preprint IAE 5797/6, 1994.
3. Kingsep A.S., Sevastianov A.A., Fizika Plasma, 1991, vol.17, p.205.

Refined Numerical Modelling of Fusion Product Measurements

G. Beikert*, B. Wolle, Z. Jauch, T. Baloui, K. Hübner

Institut für Angewandte Physik, Universität Heidelberg, D–69120 Heidelberg

*Max–Planck–Institut für Plasmaphysik, D–85748 Garching, EURATOM Association

Abstract. We present two major refinements to the usual procedure of modelling fusion product measurements. Firstly, we take into account effects of particle trapping on the ion velocity distribution. Secondly, we present a low–variance Monte Carlo modelling procedure of the fusion product emission rate with an interface to the neutron transport code MCNP.

1. Introduction

The measurement of fusion products is a powerful tool in plasma diagnostics but the analysis and interpretation often requires numerical modelling. However, several important effects are often neglected in papers which report the modelling of such measurements. In view of the increasing importance of fusion product diagnostics at future machines like ITER, there is a need for more accurate modelling. Since fusion reactivities are rather sensitive to the population of fast injected ions, the relaxation of the ions has to be modelled carefully. We take into account particle trapping and show that this leads to a significant reduction of the fusion reactivity. We model the local emission rate of fusion products without any further approximation by using the Monte Carlo method. This model of the emission rate can be used as an input to the neutron transport code MCNP which itself can be used to calculate the effects owing to neutron scattering.

2. Modelling fast ion relaxation

In the neutral beam heating of a tokamak plasma, the relaxation of the fast injected ions is described by the Fokker-Planck equation. Usually, assumption is made that all ions are well-passing. However, the fraction of trapped particles can be quite large, depending on injection and tokamak geometries.

Expanding the ion velocity distribution $f(\vec{v})$ into a series in the bounce over slowing–down time, the lowest order equation is separable in $v = |\vec{v}|$ and $\xi = \sqrt{1-(1-\mu^2)B_0/B}$, where μ is the pitch and B/B_0 is the ratio of the magnetic field over its value on the axis. The solution can be expanded in a series as $f = \sum a_n(v,t)\, C_n(\xi)$ where the C_n are eigenfunctions of the equation

$$\frac{1}{r}\frac{\mathrm{d}}{\mathrm{d}\xi}\left[\left(1-\xi^2\right)\frac{t\,\mathrm{d}C_n}{\mathrm{d}\xi}\right] + \lambda_n C_n = 0 \tag{2.1}$$

with eigenvalues λ_n and boundary conditions discussed in [1]. If the functions $r = \xi\langle Bv/B_0 v_\parallel\rangle$ and $t = \langle v_\parallel/v\rangle/\xi$ are approximated in the trapped and passing regions by their limiting values near $\xi = 0$ and $\xi = 1$, equation (1) reduces to the Legendre equation for passing ions and a similar equation for the trapped particles with eigenvalues $\lambda_n = \nu_n(\nu_n + 1)$. For small inverse aspect ratios ϵ and assuming that $\nu_n = n + \alpha_n$ with $\alpha_n \ll 1$, one can obtain approximate analytic solutions for the eigenvalues and eigenfunctions [1]. However, it turns out that these analytic solutions are valid for very small values of ϵ only. Already for $\epsilon = 0.1$, α_1, α_2 and α_3 turn out to be 0.45, 0.338 and 1.013, respectively.

Therefore, we have developped a method for calculating the eigenfunctions and eigenvalues numerically by using a shooting-method. For a given magnetic field and inverse aspect ratio, this has to be done only once. The separated equation for the coefficient functions $a_n(v,t)$ is solved by using a version of the 2D time-dependent Fokker-Planck code NRFPS [2] which is based on a finite–element method and also calculates fusion reactivities. We have carried out calculations for various inverse aspect ratios ϵ. It should be noted that the fraction of trapped particles for $\epsilon = 0.1$ is already about 0.45. Taking particle trapping into account, the neutron rate decreases in the order of ϵ, as compared to the well-passing case. This is owing to a reduction of the fast ion population which itself is in the order of $\sqrt{\epsilon}$. Thus, the slowing-down time decreases by the order of $\sqrt{\epsilon}$. For $\epsilon = 0.1$, $T_e = T_i = 5$ keV, $n_e = n_D = 2 \times 10^{19}\mathrm{m}^{-3}$ and 80 keV deuterium injection with a source rate of $2 \times 10^{19}\mathrm{m}^{-3}\mathrm{s}^{-1}$ and injection angle of 45^0 the evolution in time of the 2.45 MeV neutron rate is shown in figure 1.

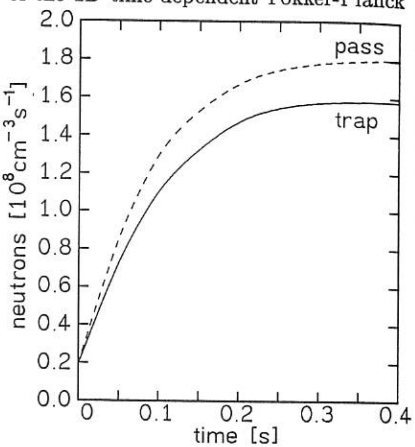

Figure 1. Time–evolution of the local neutron rates with and without particle trapping for the test case data.

3. Modelling the emission of fusion products

The emission rate of fusion products emitted at time t from a point $\vec{r}$ into the direction $\vec{\omega}$ with energy E due to fusion reactions of particles of type A and B is

$$Q(P)\, dP = \frac{n_A n_B}{1+\delta_{AB}}\, dP \iint g(P, \vec{v}_A, \vec{v}_B)\, d\vec{v}_A d\vec{v}_B \tag{3.1}$$

$$\text{with} \qquad g = f_A \cdot f_B \cdot \frac{d\sigma}{d\vec{\omega}} \cdot |\vec{v}_A - \vec{v}_B| \cdot \delta(E - E^*) \quad , \tag{3.2}$$

where (P) is shorthand for $(\vec{r}, \vec{\omega}, E, t)$. n, $\vec{v}$ and f denote the density, the velocity and the normalized velocity distribution of the reacting particles, $d\sigma/d\vec{\omega}$ is the differential cross section of the fusion reaction and E^* is determined by energy and momentum conservation. For Maxwellian ion distributions, eq. (3.1) reduces to a one–dimensional integration. For

ion distributions expanded in Legendre polynomials of the pitch angle, the local fusion reactivity $\langle \sigma v \rangle = \int g \, d\vec{v}_A d\vec{v}_B d\vec{\omega} dE$ can be computed by three–dimensional numerical integration. However, integration over the direction of emission excludes modelling of effects from anisotropic emission or modelling of fusion product spectra.

The emission rate of fusion products can be modelled in more detail by using the Monte Carlo method [2][3]. With the Monte Carlo method, the emission rate is represented by randomly selected actual phase space coordinates P^* and a weight w. If the expectation of the weight times any arbitrary function $h(P^*)$ satisfies

$$\langle w \cdot h(P^*) \rangle = \int h(P) Q(P) dP \quad , \tag{3.3}$$

(w, P^*) can be called a weighted sample of $Q(P)$. Weighted samples of $Q(P)$ can be generated by sampling P^*, $\vec{v}_A^*$ and $\vec{v}_B^*$ from an arbitrary probability density function (PDF) $p(P, \vec{v}_A, \vec{v}_B)$ and setting

$$w = \frac{n_A n_B}{1 + \delta_{AB}} \cdot \frac{g(P^*, \vec{v}_A^*, \vec{v}_B^*)}{p(P^*, \vec{v}_A^*, \vec{v}_B^*)} \quad . \tag{3.4}$$

For a particular h, $\int h(P) Q(P) dP$ can be estimated by averaging $w \cdot h(P^*)$ over a large number N of samples (w_i, P_i^*), $i = 1 \ldots N$. The central limit theorem gives the familiar Monte Carlo precision estimate of $\sigma / \sqrt{N}$, where the variance σ^2 is defined by $\sigma^2 = \langle w^2 h^2 \rangle - \langle wh \rangle^2$. The art of Monte Carlo is choosing a PDF p such that σ becomes as small as possible without substantial additional computer time or memory cost. The optimal PDF for the estimation of the integral $I = \int f(x_1, \ldots, x_N) dx_1 \ldots dx_N$ is

$$p(x_1, \ldots, x_N) = \frac{f(x_1, \ldots, x_N)}{\int f(x_1, \ldots, x_N) dx_1 \ldots dx_N} \quad . \tag{3.5}$$

Sampling from this N–dimensional PDF is equivalent to the successive sampling of the x_k^* from the one–dimensional PDF's

$$p(x_k) = \frac{\int f(x_1^*, \ldots, x_{k-1}^*, x_k, \ldots, x_N) dx_{k+1} \ldots dx_N}{\int f(x_1^*, \ldots, x_{k-1}^*, x_k, \ldots, x_N) dx_k \ldots dx_N} \quad . \tag{3.6}$$

Numerical integration of eqs. (3.6) is impractical since it is as expensive as the computation of I. However, eqs. (3.6) can be used to compute approximately optimal PDF's by analytical or numerical means. Applying this principle to $I = \int h(P) Q(P) dP$, we compute PDF's for the succesive sampling of t, $\vec{r}$, $\vec{\omega}$, $|\vec{v}_A|$, $|\vec{v}_B|$, $|\vec{v}_A \cdot \vec{v}_B|$ and the remaining coordinates of $\vec{v}_A$ and $\vec{v}_B$. Finally, E is computed from reaction kinematics. For $h(P) \approx 1$, we need only 10000 samples to estimate I with a Monte Carlo error of less than 1 %. We have modelled, as an example, for plasma data corresponding to the JET PEP discharge #26705 [4], the neutron spectrum emitted in vertical direction. In figure 2, this spectrum is compared with the spectrum measured by the time–of–flight spectrometer. The good agreement represents a validation of our method and supports the assumption that the time–of–flight spectrometer measures the vertical neutron spectrum.

4. The MCNP Interface

MCNP [5] is a widely accepted Monte Carlo code for neutron transport calculations. However, its built–in neutron source capabilities are not general enough for adequate modelling of the fusion plasma neutron source. Fortunately, it also allows the user to supply his own code for modelling the source. The subroutine `source` must generate weighted samples (w, P^*) from the source distribution $Q(P)$ and the subroutine `srcdx` must generate weighted samples (w, E^*) from the distribution $Q(\vec{r}', \vec{\omega}', E, t')$ with fixed location $\vec{r}'$, direction $\vec{\omega}'$, and time t'. We have implemented `source` and `srcdx` as described in sec. 3 and patched both subroutines into MCNP. With this interface, it is now possible to perform neutron transport calculations in tokamaks based on realistic neutron source distributions. As an illustrative example, we enclose the above mentioned model plasma with a toroidal vessel with a major radius of 3.0 m and a minor radius of 2.35 m. We have used our modelling procedure together with MCNP in order to calculate the spectral neutron flux at a point located inside the vessel in the toroidal plane 5.0 m from the torus axis. Computational results for vessel thicknesses of 0.5 cm and 5.0 cm are shown in figure 3. It is interesting to notice to which amount the total neutron flux is increased by neutron scattering.

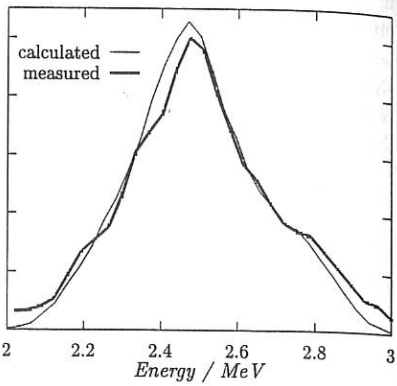

Figure 2. Measured and calculated neutron spectrum for the JET PEP discharge #26705.

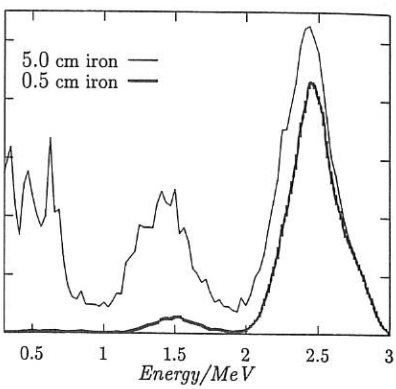

Figure 3. Neutron spectrum of the above mentioned model plasma enclosed in an iron vessel at a point near the wall for two different vessel thicknesses.

References

[1] Cordey J G 1976 *Nucl. Fusion* **16** 499
[2] Wolle B *et al* 1994 *Plasma Phys. Contr. Fusion* **36** 1051
[3] Olsson M *et al* 1993 *Plasma Phys. Control. Fusion* **35** 179
[4] Smeulders P *et al* 1995 *Nucl. Fusion* **35** 225
[5] Briesmeister J F (Ed.) 1993 *Los Alamos National Laboratory Report* LA–12625–M

THE HALL EFFECT IN PLASMAS: ENHANCED RATE OF MAGNETIC FIELD PROPAGATION AND SHORT-SCALE PLASMA-FIELD MIXING IN PLASMA FOCUS EXPERIMENTS

A.B.Kukushkin, V.A.Rantsev-Kartinov, A.R.Terentiev, and K.V.Cherepanov
RRC "Kurchatov Institute", 123182 Moscow, Russia.

1. Introduction

The Hall effect in plasmas [1], which is caused by the frozenness of the magnetic field into electron plasma and by the resulting transfer of magnetic field with electric current velocity, manifests itself in the enhanced rate, in contrast to conventional diffusion, of magnetic field propagation in plasmas in the case of electric current moving along the gradient of plasma density. This includes both the gradients at the boundaries plasma-conductor and in plasma interior. The major physical mechanism is the "braking" of magnetic field, which is transferred by the electric current, at positive gradient of electron density. This phenomenon may strongly influence plasma dynamics both in the case of electronic MHD (immovable ions) and in general case. For instance, the enhanced rate of magnetic field propagation plays an important role in the current sheath slipping along the anode in plasma focus experiments. This is confirmed by fairly good agreement between experimental results from the facility [2] and the 2D two-fluid numerical modelling [3]. The importance of allowing for the Hall effect in interpreting the fiber-initiated Z-pinch experiments is demonstrated [4] by comparing the 2D modelling with/without the Hall term. The enhanced rate effects in the current sheath formation are essential for the formation of a closed, spheromak-like magnetic configuration (SLMC) by the self-transformed magnetic field of the Filippov-type plasma focus [5]. Here, the plasma in the Z-ϑ pinch at the major axis of the SLMC exhibits peak values of power density as high as those of the dense Z-pinch, i.e. by several orders of magnitude larger than that achieved in experiments on the flux-conserver-confined spheromak as a force free configuration (cf. Ref. [6]). Analysis of unpublished experimental results from the facility [2] verifies the concept [7] and suggests the possibility of further concentrating the plasma power density by natural compressing the SLMC by the residual magnetic field of plasma focus [5].

In the present note the experimental results are presented for the short-scale (with respest to characteristic space scales of the current sheath) plasma-magnetic field mixing in plasma focus

facility [2], and a qualitative approach is outlined to describing this phenomenon in terms of the enhanced propagation rate, due to the Hall effect.

2. A qualitative theoretical approach

A qualitative approach to describing the short-scale mixing of plasma and magnetic field is based on the extension [8] of the model [9]. This approach allows to (i) reproduce a number of previous results in the theory of the electronic MHD (namely, the enhanced rate of magnetic field propagation (a) along the anode, and (b) in plasma interior in the case of monotonically/sharply growing density along the electric current velocity) and (ii) find scaling laws for the non-monotonic density profile in the electronic MHD, and for the repelling the plasma from the anode by the magnetic field in the MHD. For the scaling law of the magnetic field propagation in perpendicular direction to plasma-field boundary, with a smooth non-monotonic (one-dimensional) profile of electron density n(z) in the parallel direction, it is found [8], for a homogeneous temperature,

$$x(z,t) = \sqrt{2D_\sigma t} + \omega_e \tau_{ei} \frac{\partial \ln n}{\partial z} D_\sigma t + \mathrm{f}\left(\int_{z_0}^{z} \frac{dz'}{\omega_e \tau_{ei}} - \sqrt{2D_\sigma t} \right) \qquad (1)$$

where the first term allows for the contribution of conventional diffusion, $D_\sigma = \frac{c^2}{4\pi\sigma}$, σ is Spitzer conductivity; the second term decribes enhanced propagation rate ($\omega_e \tau_{ei} >> 1$); and the last term corresponds to the transfer of initial perturbation of the front, $x(z,0) \equiv \mathrm{f}(\mathrm{t} = 0)$.

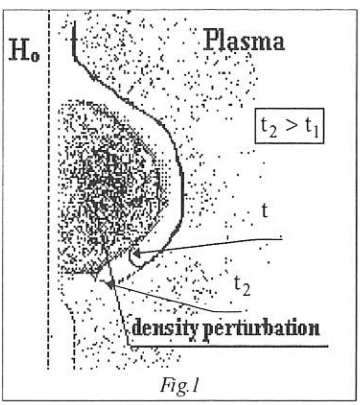

Fig.1

In the opposite case, for $\partial n(z)/\partial z \to \infty$, the front motion is close to that in the case of enhanced rate propagation along the anode, i.e. by the diffusion law with the effective diffusion coefficient $D_{eff} = (\omega_e \tau_{ei})^2 D_\sigma$ [10,3].

Application of these results to describing the propagation of the magnetic field in the case of local perturbation of plasma density at the front of magnetic field in plasma (in particular, at plasma-field boundary, Fig.1), enables us to find criteria for

the maximum space scale of plasma droplets isolated from the bulk plasma by the propagating magnetic field, in advance of suppressing such a penetration by the large-scale pressure of magnetic field, at time scales determined by the Alfven velocity. These criteria establish the links between two observed phenomena in high current gas discharges (plasma focus, Z-pinch etc.) for $\omega_e \tau_{ei} >> 1$; namely, the enhanced propagation rate, compared to conventional diffusion, of magnetic field in plasmas and short-scale mixing of the plasma and magnetic field.

3. Experimental results

The experimental setup [2] is a Filippov-type plasma focus with mushroom-shaped anode, 11 cm diameter, located inside a coaxial metallic chamber 80-cm long and 30-cm high, which acts as the cathode. The distance between the anode and the cathode along the major axis was varied between 6 cm to 12 cm. The main discharge parameters are: capacitance, 180 μF; initial inductance, 55 nG; initial voltage, 16-24 kV, varying with energy of 20-50 kJ, respectively; maximum current, 600 kA; deuterium gas pressure, 163 Torr. The pictures in Fig.2 (t= -90 ns) and Fig.3 (t= +174 ns) are the shadowgrams taken with the help of a ruby laser (0.01-J laser pulse energy; 15-ns duration; pulse direction perpendicular to the system axis). The anode is at the bottom of the diagnostic window (4 cm diam.), the plasma focus major axis coincides with the vertical axis of the window; time zero corresponds to the major (first) singularity of electric current derivative.

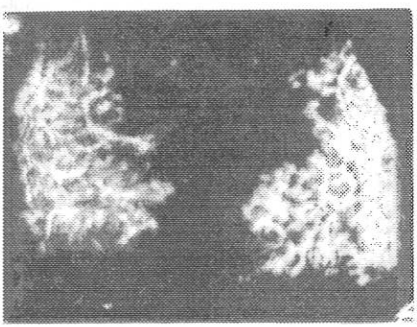

Fig.2

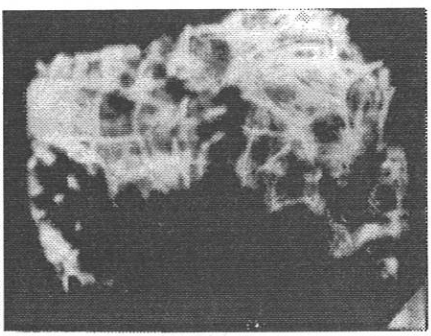

Fig.3

The numerous data exhibit cell-like structure of the plasma. This corresponds to a thin volumetric (three-dimensional) net-like structure of the magnetic field penetrating the plasma.

The local values of magnetic field inside this net found from the above mentioned criteria may exceed its values averaged over several cells up to the order of magnitude.

4. Conclusions

It follows from the analysis of experimental data in terms of the qualitative approach [8,9] that the enhanced rate of magnetic field propagation in plasmas, due to the Hall effect in plasmas [1], may be responsible for the short-scale (with respest to characteristic space scales of the current sheath) mixing of plasma and magnetic field. This mechanism of plasma-magnetic field interaction manifests itself even at not large spatially averaged values of the parameter $\omega_e \tau_{ei}$ and being combined with plasma-field inhomogeneities of larger space scale (filamentation of electric current etc.) may substanstially influence dynamics of plasma compression in a plasma focus discharge and other high current gas discharge systems.

References

[1] Morozov A.I., Shubin A.P., Zh. Eksp. Teor. Fiz. (Sov. Phys. JETP) **46** 710 (1964)

[2] Orlov M.M., Khrabrov V.A., Terentiev A.R., Fizika Plazmy (Sov. J. Plasma Phys.), **11** 1268, 1517 (1985)

[3] Vikhrev V.V., Zabaidullin O.Z., AIP Conference Proceedings #**299**, Dense Z-pinches 3rd Int. Conf., London, p.165, Eds. M.Haines and A.Knight, AIP Press, New York (1994).

[4] Sheehey P., Lindemith I.R., In Ref.3, p.157

[5] Kukushkin A.B., Rantsev-Kartinov V.A., Terentiev A.R., Transactions of Fusion Technology **27** 325 (1995); Preprint of the RRC "Kurchatov Institute", IAE 5737/7, (1994).

[6] Jarboe T.R., Plasma Phys. and Control. Fusion **36** 945 (1994).

[7] Kukushkin A.B., Rantsev-Kartinov V.A., Preprint of the RRC "Kurchatov Institute", IAE 5646/6, Moscow (1993).

[8] Kukushkin A.B., Cherepanov K.V., Preprint of the RRC "Kurchatov Institute", IAE-5832/6, Moscow, 1994 (in Russian).

[9] Kukushkin A.B., In Ref.3, p.154.

[10] Gordeev A.V., Grechikha A.V., Kalda Y.L., Fizika Plazmy (Sov.J.Plasma Phys.)**16** 95(1990).

Plasma Edge Turbulence Numerical Study with a Vlasov Eulerian Code

E. Fijalkow[1], M. Shoucri[2], G. Manfredi[3], M. R. Feix[1],
P. Bertrand[4], A. Ghizzo[4], G. Knorr[5].

Introduction

A full kinetic (electrons and ions) gyrokinetic Vlasov Eulerian Code is compared with a simpler code with ions handled by a fluid equation. The agreement is excellent.

The same code is now used to study the formation and evolution problem of charges separation at the plasma edge. It appear that if for a magnetic field tilted by 88° from the plasma sheet, the perturbation is essentially stable, for angles nearer to 90° the evolution is dominated by an inverse cascades effect, the energy condensing towards the lower k modes.

Basic equations

We consider a two-dimensional slab geometry, the x (poloidal) direction being periodic, the y (radial) direction finite. The magnetic field $\vec{B}$ is in the x, z plane and tilted by an angle θ from the x axis. We allow that the motion perpendicular to the magnetic field is described by the $\vec{E} \times \vec{B}$ and Polarisation drifts. A correction taking into account the finiteness of Larmor radius is introduced for the ions.

The equation for electrons takes then the form

$$\frac{\partial fe}{\partial t} + \nabla_\perp.(\vec{v}_\perp.f_e) + \vec{v}_{||}\cos\theta.\frac{\partial f_e}{\partial x} - \frac{e}{m_e}\vec{E}_x\cos\theta\frac{\partial f_e}{\partial v_{||}} = 0$$

$$\vec{v}_\perp e = \vec{E}\times\vec{B}/B^2 - \frac{m_e}{eB^2}\left(\frac{\partial\vec{E}_\perp}{\partial t} + \left(\frac{\vec{E}\times\vec{B}}{B^2} + \vec{v}_{||}\right).\nabla\vec{E}_\perp\right) \qquad (1)$$

For the ions two equations are to be caught in mind: equation 2 for the kinetic case, equation 3 for the fluid case.

Kinetic case:

$$\frac{\partial f_i}{\partial t} + \nabla_\perp.(\vec{v}_{\perp_i}f_i) + \vec{v}_{||}\cos\theta.\frac{\partial f_i}{\partial x} + \frac{e}{m_i}\vec{E}_x.\frac{\partial f_i}{\partial v_{||}} = 0$$

$$\text{with}\quad \vec{v}_{\perp_i} = \frac{m_i}{eB^2}\left((\vec{E}^*\times\vec{B}/B^2 + \vec{v}_{||}).\nabla\vec{E}_\perp + \frac{\partial\vec{E}^*_\perp}{\partial t}\right) + \vec{E}^*\times\vec{B}/\vec{B}^2. \qquad (2)$$

fluid case:

$$\frac{\partial n_i}{\partial t} + \nabla_\perp.(v^*_{\perp_i} n_i) = 0$$

$$\text{again with} \quad v_{+_i} = \vec{E} \times \vec{B}/B^2 + \frac{m_i}{eB^2}\left(\frac{\partial \vec{E}_\perp}{\partial t} + \vec{E} \times \vec{B}/B^2.\nabla \vec{E}_\perp\right) \tag{3}$$

The star over $\vec{E}$ and $\vec{v}_{\perp_i}$ is an operaion that accounts for the finite Larmor radius effects, and represent a smoothing by a Gaussian Kernel [1]. The star operation is carried out in k-space. The electric field is obtained solving Poisson equation, the ions density smoothed.

$$\Delta\Phi = -\frac{e}{\varepsilon_0}(n_i^* - n_e) \quad ; \quad \vec{E} = -\nabla\Phi \tag{4}$$

A normalized form of the equations, together with an explanation of the numerical method, can be found in refs [2], [3].

The numerical simulations

We start the simulation for both electrons and ions with a steep density in y:

$$N(y) = .5(1 + \tanh(1.6y))$$

so that the initial conditions for the two species are

$$f_{i,e}(x, v_{||}, t = 0) = \frac{N(y)}{\sqrt{2\Pi T_{i,e}/m_{i,e}}} \quad \exp\left(-\frac{m_{i,e}v_{||}^2}{2T_{i,e}}\right)\{1 + \varepsilon(\sin k_o x + \sin 2k_0 x + \sin 3k_0 x)\} \tag{5}$$

In the actual simulation $T_e/T_i = 1$; $m_i/m_e = 1840/$; $\frac{\omega_{c_i}}{\omega_{p_i}} = .9$; $\varepsilon = .005$ and the temperature varies as

$$T(y) = T_O[0.2 + 0.4(1 + \tanh(1.6y))] \tag{6}$$

Comparison of the two codes shows a quasi similitude in the results. As example see fig(1), showing a countour plot of the potential at $E = 28000$, $\theta = 89°$. Full kinetic in 1a, Kinetic + fluid in 1b.

The first Fourier modes of the potential are presented fig. 2 for $\theta = 88°$ and fig. 3 for $\theta = 89.5°$.
In fig. 2 still the first mode is strongly oscillating, its amplitude remains at a low level, equivalent to that of the second and the third modes. The higher modes are growing with time. The total perturbation is small and has little effect on electrons

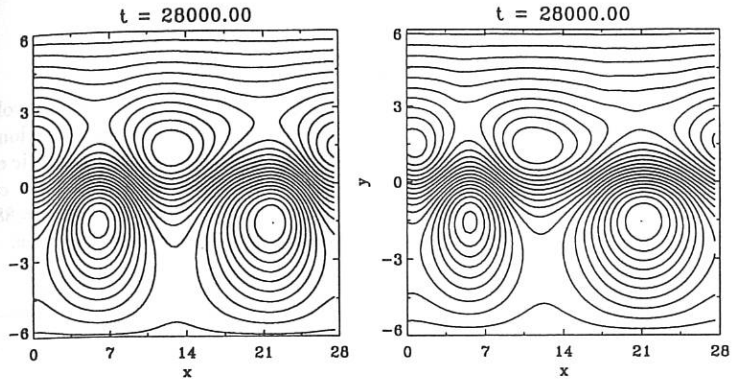

Figure 1

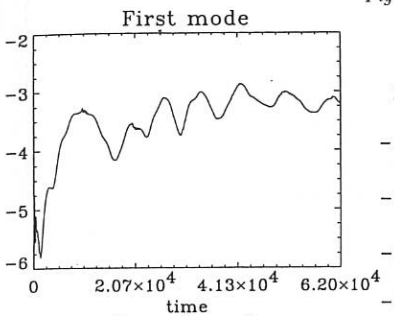

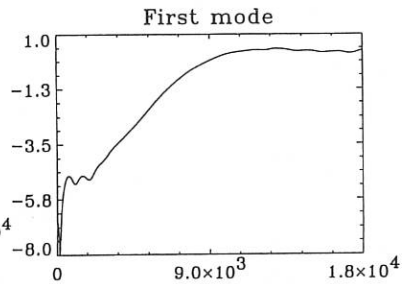

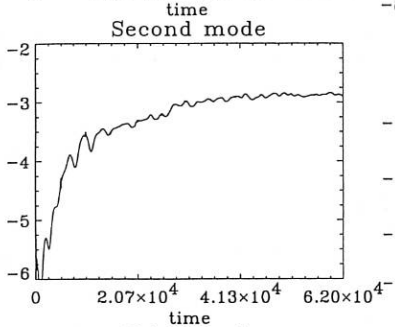

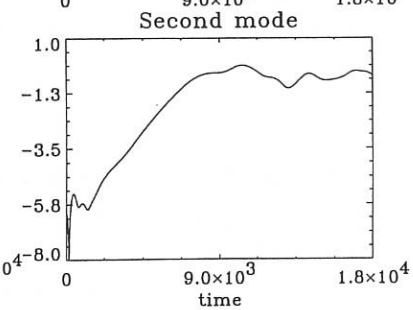

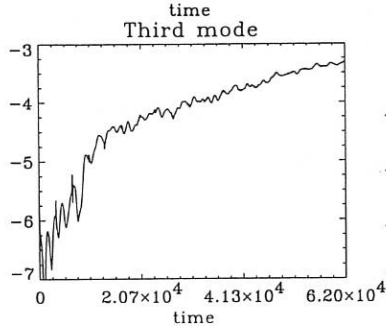

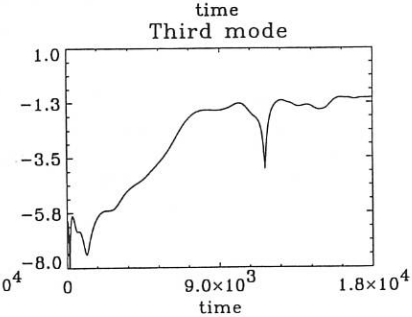

Figure 2

Figure 3

and ions density profites. In fig. 3 the first mode dominates, the whole evolution beeing characterized by an inverse cascade process, the energy flowing to the longuest wavelength. In the latter case the actual regime is no more dominated by kinetic effects and fluid behaviour is dominant. Curves of the potential (full time) and the charge (dotted line) spatially average over x for $\theta = 89°$ are presented fig. 4. If for $\theta = 88°$ the initial curve don't change, the evolution at $\theta = 89°$ tends to an cuverted shape.

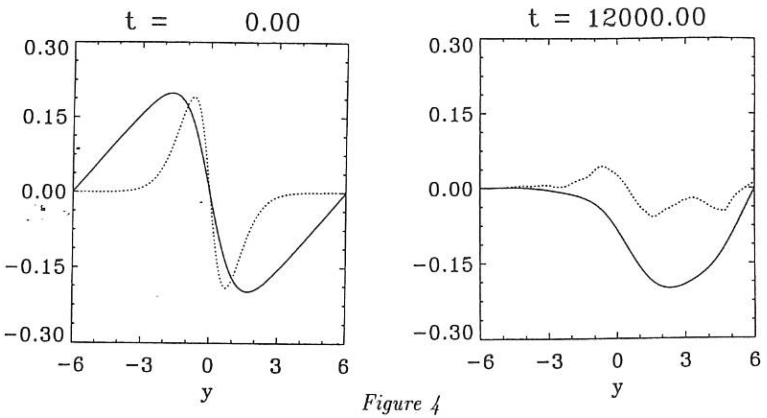

Figure 4

Acknowledgment :
The authors undebted to IDRIS (Institut du Développement et des Ressources pour l'Informatique Scientifique, CNRS, Orsay, France) for computer time allocation on the C98 computer.

References :

[1] G. Knorr and H. Pecséli : J. Plasma Physics 41, 157, 1989.

[2] A. Ghizzo, P. Bertrand, M. Shoucri, E. Fijalkow, M.R. Feix : J. Comp. Phys. 108, 105, 1993.

[3] A. Ghizzo, G. Manfredi, M. Shoucri, P. Bertrand, G. Knorr, E. Fijalkow, M.R. Feix, J. Lebas, in 15th Int. Conf Numerical Simulation of Plasmas, Valley Forge, Pen 1994.

[1] MAPMO, Université d'Orléans - BP 6759 - 45067 Orléans Cedex 2 - France
[2] CCFM, Varennes, Quebec, Canada
[3] Fusion Theory Div., Culham, Abingdon, Grande Bretagne
[4] LPMI, Université de Nancy, France
[5] Dept. of Physics and Astronomy, University of Iowa, USA.

Non-linear Heat Pinch in a Tokamak

M. G. Haines
Blackett Laboratory, Imperial College London SW7 2BZ, UK

Consultant to AEA Technology, Fusion
Culham Laboratory, Abingdon, Oxon OX14 3DB, UK

Recent experimental results on the DIII-D tokamak have demonstrated that with off-axis electron-cyclotron heating (ECH) there is a large inward electron heat flux up the temperature gradient. We propose that due to the finite drift parameter for the toroidal current, enhanced by the presence of trapped electrons, the isotropic component of the distribution function is driven non-Maxwellian. The enhanced number of energetic electrons leads to an extra and non-linear inward heat flux in quantitative agreement with experiment. Furthermore this model permits an understanding of profile consistency or resilience in tokamaks.

This work is motivated by the intriguing experimental results on the DIII-D tokamak in which ECH is absorbed half-way between the minor axis and the wall, yet electron temperature profiles are strongly peaked on the minor axis[1,2]. Indeed the electron temperature on axis is 1.7keV and only 0.5keV at the position of ECH deposition. It therefore appears that heat actually flows *up* the temperature gradient, a phenomenon inconsistent with a simple diffusive model of heat flow. Any explanation of this must of course be consistent with the Second Law of Thermodynamics; indeed the *local* generation of entropy must be positive.

If we assume that in the region of ECH deposition there is a substantial population of suprathermal electrons created, the trapped component of these will drift inwards with a convection time τ_c given by

$$\tau_c = r_1 \frac{B_\theta}{E_\phi} \tag{1}$$

where B_θ is the poloidal magnetic field and r_1 is the distance to the minor axis. The effective time τ_e for a hot electron to lose energy by electron-electron collisions is

$$\tau_e = 0.51 \frac{m_e}{n_e e^2} \frac{J_\phi}{E_\phi} \left(\frac{v}{v_T} \right)^3 \tag{2}$$

where $v_T^2 = 2T_e / m_e$ and trapped particle and other effects in Ohm's law are neglected.

Using $B_\theta \cong \frac{1}{2}\mu_0 r_1 J_\varphi$ we obtain the ratio

$$\frac{\tau_c}{\tau_e} = \frac{\omega_{pe}^2}{c^2} r_1^2 \left(\frac{v_T}{v}\right)^3 \qquad (3)$$

For DIII-D parameters, n = 2.2 x $10^{19}m^{-3}$, r_1 = 0.34m, T_e = 0.5 keV, we find that τ_c is equal to τ_e only for 1 MeV electrons. Fokker-Planck simulations[3] show that there is a negligible number of electrons with energy above 50 keV. Therefore there is no enhanced inward heat flux by suprathermal electrons generated in this localised ECH region *unless* their energy is maintained or increased. This effect is considered next.

Taking the tensor expansion of the Fokker-Planck equation[4,5] and limiting our attention to f_0 and $\underline{f}_1$ we write, where $\underline{f}_1$ is replaced by the ϕ component only, f_ϕ

$$\frac{\partial f_\varphi}{\partial t} = \frac{e}{m} E_\varphi \frac{\partial f_0}{\partial v} - \nu_0 f_\phi \frac{v_T^3}{v^3} + C_{ee\phi} \qquad (4)$$

For a Maxwellian lowest order isotropic component, ie. $f_0 = f_m = a_0 \exp\left(-v^2/v_T^2\right)$

and neglecting the $C_{ee\phi}$ and $\partial f_\varphi/\partial t$ terms (see refs.18 and 19) the condition that $|f_\phi| > f_m$

is $$v/v_T \gtrsim \left(v_T/v_d\right)^{1/4} \qquad (5)$$

where the *classical* drift velocity v_d is given by

$$0.381\frac{v_d}{v_T} = \frac{eE_\phi}{m\nu_0 v_T} \qquad (6)$$

where $E_\phi = \eta \| J_\phi = 0.506 m v_d/(e\tau_e)$ and $\nu_0\tau e = {}^3/_4\sqrt{\pi}$. The well known Dreicer condition[6] for the runaway electrons is given by the condition

$$v/v_T \gtrsim \left(v_T/v_d\right)^{1/2} \qquad (7)$$

for the unlimited acceleration of electrons.

The effect of f_ϕ on f_0 is given by[5] (8)

$$\frac{\partial f_0}{\partial t} - \frac{1}{3v^2}\frac{\partial}{\partial v}\left(v^2 \frac{e}{m} E_\varphi f_\varphi\right) = \frac{\nu_{ee}}{n_e} v \frac{\partial}{\partial v}\left[f_0 4\pi \int_0^v f_0 v^2 dv + \frac{v}{3}\left\{\frac{4\pi}{v^2}\int_0^v f_0 v^4 dv + 4\pi v \int_v^\infty f_0 v dv\right\}\frac{\partial f_0}{\partial v}\right]$$

where the RHS represents electron-electron collisions with $\nu_{ee} = \nu_{eeT} v_T^3/v^3$. If we take this term to be of order $\nu_{eeT}\frac{v_T^3}{v^2}\frac{\partial f_0}{\partial v}$ we arrive at the condition which Dreicer also found for the isotropic velocity of electrons above which Joule heating exceeds the down-scatter by electron-electron collisions,

$$v/v_T \gtrsim (v_T/v_d)^{1/3} \qquad (9)$$

We note that this is intermediate to conditions (5) and (7). The three conditions are illustrated in Fig.1.

For a tokamak in the neoclassical regime the classical values of v_d/v_T above must be modified in order that v_d^* represents the mean drift velocity of passing particles.

If we approximate J_ϕ to be $2B_\theta/(\mu_0 r) = 2B_\phi/(\mu_0 R_q)$, condition (75 is modified to

$$\frac{v}{v_T} > \left(\frac{1}{0.762}\frac{1-1.95(r/R)^{1/2}}{1-1.47(r/R)^{1/2}}\right)^{1/4}\left(\frac{v_T}{v_d^*}\right)^{1/4} \equiv \alpha \qquad (5')$$

with

$$\frac{v_T}{v_d^*} = \frac{\mu_0 Rqnev_T}{2B_\phi}\left[1-1.47(r/R)^{1/2}\right] \qquad (10)$$

For the DIII-D tokamak[1,2] in the ECH region, r/R = 0.2, R = 1.7m, B_ϕ = 1.7 tesla, q = 1.5, n = 2.2 x 10^{19} and v_T = 1.3 x $10^7 ms^{-1}$ (T_e = 500eV) we find that v_T/v_d^* is 15 and condition (5') states that for $v > 1.64v_T$ there is a strong departure of f_0 from Maxwellian.

In order to provide a realistic approximate formula for the extra non-linear heat pinch Q_{NL} we assume that for v/v_T greater that α (eq.6') the extra energy in the electrons is double that of the equivalent Maxwellian. This then gives

$$Q_{NL} = \frac{3}{2}\frac{E_\varphi}{B_\theta}1.47\left(\frac{r}{R}\right)^{1/2}\left\{\frac{4}{3\sqrt{\pi}}\alpha^3 e^{-\alpha^2} + \frac{2\alpha}{\sqrt{\pi}}e^{-\alpha^2} + erfc\alpha\right\}nT \qquad (11)$$

where, neglecting bootstrap terms,

$$\frac{E_\varphi}{B_\theta} \cong \frac{2\eta_\parallel}{\mu_0 r\left[1-1.95(r/R)^{1/2}\right]} \qquad (12)$$

In eq.(11) E_ϕ/B_θ represents the radially inward Ware pinch velocity, $1.47(r/R)^{1/2}$ represents the fraction of electrons that are trapped, and the term in brackets represents the fraction of energy for electrons with $v/v_T > \alpha$. For the DIII-D parameters eq.(11) yields $Q_{NL} = 1.63 \times 10^3 Wm^{-2}$, which is close to the experimental value.

We note however that we have ignored the empirical 'anomalous' heat flux and the linear neoclassical E_ϕ/B_θ component of heat flow which however are both outward and of a similar magnitude to this. It would appear from this rough estimate that there is a strong possibility that a non-linear heat flux associated with a non-Maxwellian distribution could explain the experimental results.

References

[1] C. C. Petty et al.
Eur. Conf. on Controlled Fusion & Plasma Physics, Vol **1**, 241 (1990)

[2] T. C. Luce, C. C. Petty & J. C. M. de Haas, *Phys. Rev. Lett.* **68**, 52 (1991)

[3] M. O'Brien, private communication

[4] T. W. Johnston, *Phys. Rev.* **120**, 1103 (1960)

[5] I. P. Shkarovsky, *Can. J. Phys.* **41**, 1753 (1963)

[6] H. Dreicer, *Phys. Rev.* **117**, 329 (1960)

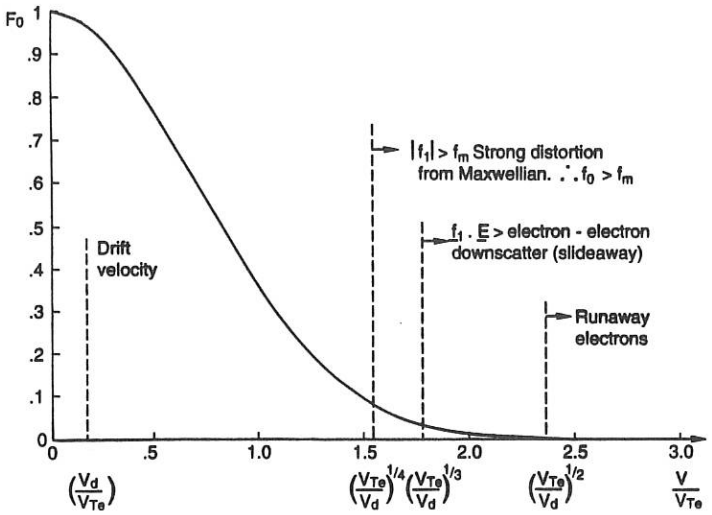

Figure 1

A sketch of a Maxwellian distribution $F_0 = \exp(-v^2/v^2_{Te})$ versus v/v_{Te} showing the values of v/v_{Te}, $(v_{Te}/v_d)^{1/4}$ which a strong distortion of F_0 from a Maxwellian will begin, $(v_{Te}/v_d)^{1/3}$ at which the Joule heating balances the electron-electron downscatter, and $(v_{Te}/v_d)^{1/2}$ at which runaway electrons occur. The value of v_d/v_{Te} is also indicated.

Neoclassical Theory of Poloidal Rotation Damping

R. C. Morris, M. G. Haines, R. J. Hastie
Plasma Physics, Imperial College, London, SW7 2BZ, United Kingdom.

1. Introduction

The rate of decay of poloidal flow $U_\theta(t)$ in a tokamak in the banana regime has been a source of contention since 1972 when the first attempt was made to determine a characteristic damping time τ_p. Since then raferences [1]-[6] have calculated the value of τ_p such that $\tau_p \sim \epsilon^n \tau_{ii}$, where $n = 1, 1.5, -.5, 0, .5, 1$ respectively. The present work attempts to unify the result as much as possible by treating the damping calculation as an initial value problem.

The tokamak is modelled in the drift regime $\delta << 1$, where δ is the ration between the ion larmor radius ρ and the plasma scale length L, and also in the banana regime $\eta << 1$, where η is the ratio between the bounce time τ_b and the ion-ion collision time τ_{ii}. Flux coordinates (ψ, θ, ϕ) are used such that the magnetic field can be written $\mathbf{B} = \nabla\phi \times \nabla\psi + I(\psi)\nabla\phi$.

2. Fluid Picture

To first order in δ the flows in a tokamak plasma are within a flux surface. The poloidal and toroidal compents of such a flow can be derived from the first order pressure balance equation to give

$$\frac{u_\theta}{B_\theta} = \frac{u_\parallel}{B} - \frac{T}{mB\Omega}\left(\frac{e\Phi'}{T} + \frac{P'}{P}\right), \tag{1}$$

$$\frac{u_\phi}{B_\phi} = \frac{u_\parallel}{B} + \frac{T}{mB\Omega}\left(\frac{e\Phi'}{T} + \frac{P'}{P}\right), \tag{2}$$

where Φ is the electrostatic potential, Ω is the ion Larmor frequency, P and T are the ion pressure and temperature and the dash implies a radial derivative $\partial/\partial\psi$.

Since the tokamak is axisymmetric equations (1) and (2) show that for a small change in the parallel flow $u_\parallel$, u_ϕ is kept constant due to a large readjustment in Φ' and it is this component of the poloidal flow which is seen to change.

3. Kinetic Picture

The parallel flow evolves according to the surface averaged parallel component of the ion, momentum balance equation given by the expression

$$m_i n_i \frac{\partial}{\partial t}\langle \mathbf{B}\cdot\mathbf{u}_i\rangle = -\langle \mathbf{B}\cdot\nabla\cdot\mathbf{\Pi}\rangle, \tag{3}$$

where $\mathbf{\Pi}$. The parallel stress can be written as a velocity moment of the gyro-averaged, ion distribution function $\bar{f}_i$

$$\langle \mathbf{B}\cdot\nabla\cdot\mathbf{\Pi}\rangle = \langle Bm\int \mathbf{dv}\, v_\parallel^2\, \hat{\mathbf{n}}\cdot\nabla\bar{f}_i\rangle. \tag{4}$$

Now $\bar{f}_i$ is found by solving the *Drift Kinetic Equation*, which is written

$$\frac{\partial \bar{f}_i}{\partial t} + (\mathbf{v}_{\|} + \mathbf{v}_d) \cdot \nabla \bar{f}_i - e(\mathbf{v}_{\|} + \mathbf{v}_d) \cdot \mathbf{E} \frac{\partial \bar{f}_i}{\partial w} = C\{\bar{f}_i\}, \tag{5}$$

where w is the kinetic energy, $\mathbf{v}_d$ is the guiding-centre drift, $C\{f\}$ is the collision operator, and $\mathbf{E}$ is the electric field. The solution of equation (5) is the subject of the next section.

4. Solution of the Drift Kinetic Equation

4.1 The Banana Constraint Equation

The distribution function can be expanded in terms of the parameters δ and η such that

$$\begin{aligned} f &= f_0 + f_1 + \cdots \quad \text{where} \quad f_1 \sim \delta f_0 \\ f_1 &= f_1^{(0)} + f_1^{(1)} + \cdots \quad \text{where} \quad f_1^{(1)} \sim \eta f_1^{(0)}. \end{aligned} \tag{6}$$

The first expansion is put into equation (5) which is solved to zeroth order in δ giving a Maxwellian distribution

$$f_0 = n \left(\frac{m}{2\pi T} \right)^{3/2} e^{-x}. \tag{7}$$

where $x = w/T$. To first order in δ and zeroth in η, the solution takes the form

$$f_1^{(0)} = -\frac{I v_{\|}}{\Omega} f_0' + g(t, x, \lambda) \tag{8}$$

where g is an integration constant independent of the poloidal angle θ and λ is a pitch angle variable defined by $\lambda = \mu/w$ and μ is the particle magnetic moment. The parallel stress can be written solely in terms of $f_1^{(0)}$ (or g), hence writing the drift kinetic equation to first order in η and bounce averaging results in the *banana constraint equation*

$$\left\langle \frac{B}{v_{\|}} \left[C\{f_1^{(0)}\} - \frac{\partial f_1^{(0)}}{\partial t} \right] \right\rangle = 0. \tag{9}$$

4.2 Analytical Solution

The initial value nature of the problem can now be exploited by performing a Laplace transform of equation (9) such that a time dependent quantity $f(t)$ transforms to $\bar{a}(s)$ where s is the Laplace variable of dimension t^{-1} taking on values $0 \leq s \leq \infty$. On very short time scales ($\nu_{ii}/s << 1$) it is clear that only the particles occupying a narrow layer of pitch-angle space adjacent to the trapped passing boundary can diffuse due to collisions into the trapped region and hence contribute to the damping process. This implies that the collision terms in the transform of equation (9) are neglected every where outside of this boundary layer. The distribution function $\bar{g}(s)$ at early times in the boundary layer can then be written

$$\bar{g}(s) = \left[1 - e^{-\sqrt{\frac{s}{\nu_{ii}}}(\lambda_c - \lambda)} \right] \left[\frac{Im}{TsD} (s\bar{\Phi}'(s) - \Phi'(t=0)) - \frac{g(t=0)}{s} \right], \tag{10}$$

where $D = \langle B/\sqrt{1-\lambda B}\rangle$. This expression is then put into equation (4) and after integrating over the whole of velocity space, it is combined with equation (3) and inverse Laplace transformed. The initial distribution function is taken to be a Gaussian in pitch angle space centred at $\lambda = \lambda_0$. The resulting damping rate of the radial potential gradient is given by

$$\frac{\partial \Phi'(t)}{\partial t} \propto \sqrt{\frac{\nu_{ii}}{t}}\, e^{-\alpha(\lambda_0-\lambda_c)^2}, \tag{11}$$

where α is an arbitrary constant.

4.3 Numerical Solution

Equation (9) is now solved numerically for arbitrary time scales so that all collision terms are retained. Cranck-Nicholson differencing is used together with a *forward recursion, back solve* technique outlined in reference [7]. Internal boundary conditions express the continuity of the distribution function and conservation of flux (in λ) at the trapped passing boundary.

The initial distribution can be varied extensively and in figure 1 we consider two contrasting initial distributions sketched in pitch-angle space. Here $\lambda_c = 1/B_{max}$ and marks the trapped-passing boundary and $\lambda_m = 1/B_{min}$ represents the far trapped region

a)

b)

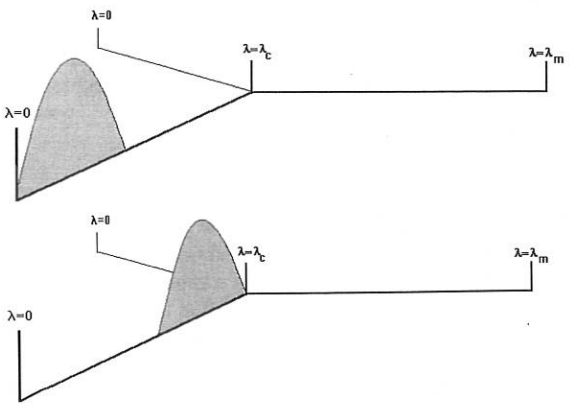

Figure 1: Two initial distributions in λ-space.

In a) the majority of the particles are situated deep in co-passing space whilst in b) the bulk are close to the trapped-passing boundary. The decay of poloidal flow for each of the initial conditions above is shown in figure 2. In each case an exponential fit has been attempted and the associated characteristic decay time τ_p is given with the figure.

For each of these runs the inverse aspect ratio ϵ was kept constant at a value of $\epsilon = 0.3$. However as parameter was varied the decay curves altered and the variation for initial condition figure 1a) is illustrated in figure 3.

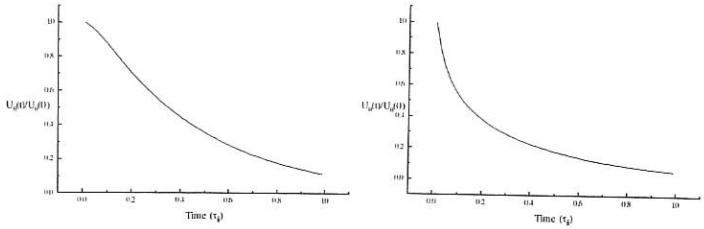

Figure 2: The poloidal flow decay curves for initial conditions of figure 1

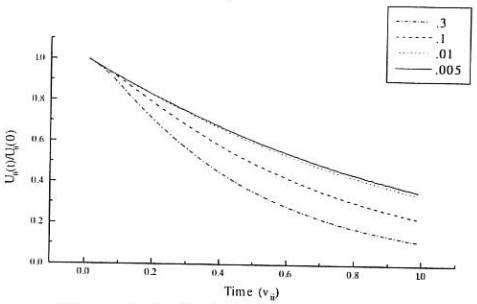

Figure 3: Variation of decay curves with ϵ.

5. Conclusions

It has been found that the decay time of the poloidal flow in a tokamak is dependent upon the pitch-angle structure of the initial distribution function. In particular the evolution is sensitive to the proportion of particles close to the trapped-passing boundary.

The parametric dependence of the decay time with the inverse aspect ratio disagrees with most of the past references. In fact an accurate functional dependence is difficult to determine but the general trend is an inverse scaling with ϵ, implying that the decay rate decreases with the proportion of trapped particles.

References

[1] Stix TH, *Phys.Fluids* **16** 1260 (1972)
[2] Hirshman SP, *Nucl.Fusion* **18** 917 (1978)
[3] Callen JD, *Culham Lab. Report* (1978)
[4] Shaing KC et al, *Phys.Fluids* **B1** 705 (1989)
[5] Taguchi M, *Plasma Phys.Controlled Fusion* **33** 859 (1991)
[6] Hsu CT et al, *Phys.Plasmas* **1** 132 (1994)

Scale-Invariant Plasma Motions Near X-Points

T. J. Schep[1], F. Pegoraro[2], B. N. Kuvshinov[1], M. Romanelli[2]

[1] FOM-Instituut voor Plasmafysica, "Rijnhuizen", Association Euratom-FOM, Nieuwegein, the Netherlands

[2] Dept. of Theoretical Physics, University of Turin, Italy

Abstract

The dynamical equations and the related topological invariants in the low frequency range have been studied for a plasma embedded in a strong magnetic field. These equations are Hamiltonian with non-canonical Poisson brackets, and involve spatial scale lengths which extend from the global MHD scale-lenghts down to the ion gyroradius and the electron skin depth. The plasma dynamics in the neighbourhood of critical points ($X-$ and $O-$ points) of the magnetic configuration is investigated, both on MHD scale and on a scale below the ion gyro-radius, in terms of scale-invariant equations. The scale-invariant solutions exhibit a collapse of an $X-$point configuration in a finite time. An explicit model that connects the solutions on both scales is presented.

Two-fluid model of a 2-D collisionless plasma

We consider a geometry with magnetic field $\vec{B} = B_0\,(\vec{e}_z + \vec{e}_z \times \nabla\Psi)$ and electric field $\vec{E} = -\nabla\phi + (B_0/c)\;(\partial\Psi/\partial t)\;\vec{e}_z$, where $\Psi(x,y,t)$ is the flux function and $\phi(x,y,t)$ the electric potential. Assuming that the parallel ion velocity is much smaller than the electron velocity v_z, Ampere's law reads $v_z \approx -J_z/en_0 = -(cB_0/4\pi en_0)\nabla^2\Psi$, where n_0 is a reference value. The parallel momentum balance and the continuity equation of the electrons are [1]

$$\frac{1}{a}\frac{\partial\Psi_e}{\partial t} + \Big[\Phi\ ,\ \Psi_e\Big] + \Big[\Psi\ ,\ \ln\frac{n}{n_0}\Big] = 0\ , \tag{1}$$

$$\frac{1}{a}\frac{\partial}{\partial t}\ln\frac{n}{n_0} + \Big[\Phi\ ,\ \ln\frac{n}{n_0}\Big] - \frac{1}{\beta_e}\Big[\Psi\ ,\ J\Big] = 0\ , \tag{2}$$

respectively. Here, $\Psi_e = \Psi - {d_e}^2\nabla_\perp^2\Psi$ is the generalized flux function, $d_e = c/\omega_{pe}$ is the electron inertial skin depth, the brackets are defined by $\Big[f,g\Big] = \vec{e}_z\cdot\nabla f\times\nabla g$, $\Phi = e\phi/T$, $J = \nabla_\perp^2\Psi$, $a = cT/(eB_0)$, and $\beta_e = 4\pi\ n_0T/{B_0}^2$. Finite electron mass effects enter through d_e. Temperatures are taken to be constant throughout the plasma. The electron density n is related to the ion density through the quasi-neutrality condition. In the limit of large and small ion gyroradii, the ion response is respectively,

$$\ln n/n_0(\vec{x}) + \tau_i\Phi = 0, \quad \ln n/n_0(\vec{x}) - \tau_i{\rho_i}^2\nabla^2\Phi = 0, \quad (\tau_i = T/T_i)\ . \tag{3}$$

In terms of the proper variables, the nonlinear equations (1) and (2) can be written in Hamiltonian form with non-canonical Poisson brackets [1,2]. Independently of the ion response, these electron equations admit the two infinite sets of Lagrangian invariants $F_{\pm}[\Psi_e \mp (\beta_e)^{1/2} d_e \ln n/n_0]$, with $F_{\pm}$ arbitrary functions. In the case of closed systems, the volume integrals of these invariant functions are the Casimirs of the noncanonical Poisson brackets. In what follows we will limit the discussion to the case $d_e \to 0$.

Invariants and self-similar solutions

The plasma behaviour in the neighbourhood of critical points, such as X- and O-points, is studied by referring to a class of solutions that leave Eqs (1) and (2) unchanged under the transformation $t \to t$, $(x, y) \to (\alpha x, \alpha y)$, This class contains solutions that describe the collapse of the magnetic configuration in a finite time [3,4]. Close to the critical point, the large ion gyroradius limit will apply. Adopting polar coordinates, the spatially self-similar solutions are of the form

$$\Psi = r^3 \hat{\Psi}(\theta, t), \qquad \Phi = r^2 \hat{\Phi}(\theta, t) \ . \tag{4}$$

Farther away from the critical point, the large ion gyroradius (MHD) limit applies and the self-similar solutions are of the form

$$\Psi = r^2 \hat{\Psi}(\theta, t), \qquad \Phi = r^2 \hat{\Phi}(\theta, t) \ . \tag{5}$$

These self-similar systems are not energetically closed and will not possess invariant integrals over a fixed domain. However, one expects that in a scale-invariant system the integrals of Lagrangian invariants that scale inversely with the volume will still be conserved. This leaves the following two invariants in the large ion gyroradius limit

$$\oint \hat{\Psi}^{-2/3} d\theta, \qquad \oint \hat{\Phi} \hat{\Psi}^{-4/3} d\theta \ , \tag{6}$$

and two invariants in the small ion gyroradius limit

$$\oint \hat{\Psi}^{-1} d\theta, \qquad \oint \hat{\Psi}^{-1} \nabla^2 \hat{\Phi} d\theta \ . \tag{7}$$

These integrals reflect the geometrical structure of the configuration. Their values are controlled by the magnetic separatrices $\Psi = 0$. It can easily be verified that, independently of the relationship between Ψ and J, these integrals are indeed constants of the motion of the respective systems. The additional invariant $\oint \hat{\Phi} d\theta$ is the remnant of the rotational invariance of the Hamiltonian of the complete system. By expanding $\hat{\Psi}$ and $\hat{\Phi}$ in a Fourier series in θ, we obtain from Eqs.(1), (2), (3), and (4) in the small scale limit a set of coupled ordinary differential equations for the Fourier coefficients $\Psi_m = \Psi^*{}_{-m}$ and $\Phi_m = \Phi^*{}_{-m}$. This infinite system becomes finite if it consists only of the harmonics $\Psi_{\pm 1}$, $\Psi_{\pm 3}$, Φ_0 and $\Phi_{\pm 2}$. These harmonics correspond to potentials Φ that are quadratic and magnetic potentials Ψ that are cubic in the Cartesian coordinates (x, y). The resulting magnetic field has either one or three real separatrices. The set of equations for the time behaviour of the Fourier

harmonics describes a finite-dimensional system with six degrees of freedom. Note that Φ_0 is a constant. This finite system is Hamiltonian with conjugate variables,

$$\{q_i\} = (\Psi_{-1},\ 1/2\ \Phi_2,\ 3^{1/2}\Psi_3), \qquad \{p_i\} = (\Psi_1,\ 1/2\ \Phi_{-2},\ 3^{1/2}\Psi_{-3})\ .$$

As is shown in [4], the system posseses three conserved quantities that are independent and in involution. Thus, the scale-invariant system in the large ion gyroradius limit is integrable. For most of the initial conditions, the potential is everywhere repulsive and the initial configuration collapses in a finite time, i.e., the magnitude of the velocity potential Φ becomes infinite with a $(t_0 - t)^{-1}$ behaviour.
In the MHD-limit, where the second Eq.(3) and Eq.(5) are valid, the Fourier expansion of $\hat{\Psi}$ and $\hat{\Phi}$ lead to a finite dimensional system for the harmonics Ψ_0, $\Psi_{\pm 2}$, Φ_0 and $\Phi_{\pm 2}$. This corresponds to potentials Φ and Ψ that are both quadratic in Cartesian variables. The corresponding magnetic field has two real separatrices. The resulting system consist of evolution equations for the time behaviour of $\Psi_0(t)$ and $\Psi_{\pm 2}(t)$ that contain $\Phi_{\pm 2}(t)$. The time dependence of the latter quantities is undetermined.
In the region where neither the large nor the small ion gyroradius limit is valid, self-similar solutions do not exist.

Collapse on MHD scale-lengths

In this Section we present a model that connects the self-similar solutions on the MHD-scale to those on the small scale below the ion gyroradius.
Since the magnetic structure away from the X-point has two separatrices, while the structure in the neighbourhood of the X-point has three separatrices, two X-points are needed in order to represent a consistent magnetic topology. The distance between the X-points is of the order of or larger than an ion gyroradius. Further we assume that the time dependence of the global solution is given basically by the small scale system. Hence, the global system is assumed to exhibit a collapse. The following model is adopted for the magnetic potential Ψ and the electric potential Φ,

$$\begin{aligned}\Psi(r,\theta,t) \;=\; & R_3(r,\theta)\{\Psi_{g1}(t)[e^{i(3\theta_1-\theta_2)} + e^{i(3\theta_2-\theta_1)}] + [\Psi_{g2}(t) + \alpha(r,\theta)\Psi_{g3}(t)]e^{i(\theta_1+\theta_2)} + \\ & + \Psi_{g4}(t)[e^{3i(\theta_1-\theta_2)} + e^{i(\theta_1-\theta_2)}] + c.c\},\end{aligned} \tag{8}$$

$$\Phi(r,\theta,t) = R_2(r,\theta)\{\Phi_{g1}(t)[e^{2i\theta_1} + e^{2i\theta_2}] + \Phi_{g2}(t)[e^{2i(\theta_1-\theta_2)} + e^{2i(\theta_2-\theta_1)}] + \Phi_{g3}(t) + c.c.\}. \tag{9}$$

The following expressions for $R_3(r,\theta)$, $R_2(r,\theta)$ and $\alpha(r,\theta)$ are adopted:

$$R_3 = \frac{{r_1}^3{r_2}^3}{1 + (r_1 - 1)^2(r_2 - 1)^2}, \qquad R_2 = \frac{{r_1}^2{r_2}^2}{1 + (r_1 - 1)(r_2 - 1)}, \tag{10}$$

and

$$\alpha(r,\theta) = (r_1 - 1)(r_2 - 1)(1 + r_1 r_2)^{-1}, \tag{11}$$

where we have introduced the local radial and angular coordinates,

$$r_{1,2} = [r^2\sin^2\theta + (r\cos\theta \mp 1/2)^2]^{\frac{1}{2}}, \qquad \sin\theta_{1,2} = \pm(r/r_{1,2})\sin\theta.$$

These functions have the correct behaviour in the large scale limit (small ρ_i) $r_{1,2} \rightarrow r \gg 1$, $\theta_1 \rightarrow \theta$, $\theta_2 \rightarrow \theta + \pi$, and in either of the small scale limits (large ρ_i) $r_{1,2} \rightarrow 1$, $\theta_{1,2} \rightarrow \pi$.

The time dependent coefficients Ψ_{gi}, Φ_{gj} are determined by matching the self-similar solutions around the $X-$points with those valid on the MHD scale-lenghts. This matching leads to a condition on the time behaviour of $\Phi_{\pm 2}$ that permits to close the system of the self-similar solution on the MHD scale.

The potentials (8) and (9), at a certain instant of time, are presented in Figs. 1 and 2 respectively. The positions of the $X-$points are indicated by crosses. The three separatrices emanating from each $X-$point are connected to each other and to the outgoing separatrices on the MHD scale. Close to the $X-$points as well as in the outer MHD region, the flow lines are hyperbolic. In the intermediate region convective cells exist.

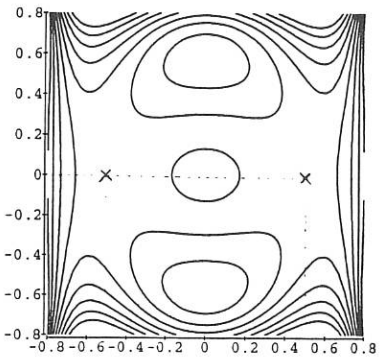

Fig. 1: The magnetic flux (8)

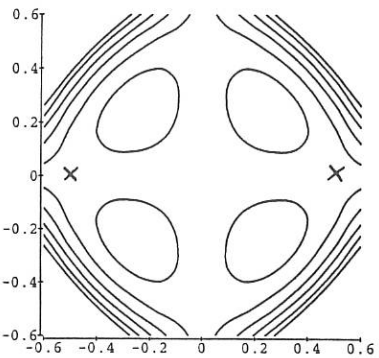

Fig. 2: The flow potential (9)

This work was performed under the Euratom-FOM Association and Euratom-CNR agreements, with financial support from NWO, CNR and Euratom.

[1] Kuvshinov, B. N., Pegoraro, F., Schep, T. J., *Phys. Lett.*, **A 191** (1994) 296.

[2] Schep,T. J., Pegoraro, F., and Kuvshinov, B. N. , *Phys. Plasmas*, **1**(1994) 2843.

[3] Pegoraro, F., Kuvshinov, B. N., Schep, T. J., Proc. Joint Varenna-Lausanne International Workshop on "Theory of Fusion Plasmas", 391 (1994).

[4] Pegoraro, F., Kuvshinov, B. N., Romanelli, M., and Schep, T. J. ,Proc. Nice International Workshop on "Small Scale Structures in Three-Dimensional Hydro- and Magnetohydrodynamic Turbulence", Nice 1995, Springer Verlag, to be published.

Investigation of low radiation collapses in stellarator plasmas

M.A.Ochando, **F. Castejón**
Asociación EURATOM /CIEMAT para Fusión, 28040 Madrid, Spain.
A.P.Navarro
Universidad Alfonso X el Sabio, Villanueva de la Cañada, 28691Madrid, Spain.

1. Introduction

Radiative collapses in the Advanced Toroidal Facility (ATF) [1] have been already studied using the predictive transport code Proctr [2], mainly during the campaign in which field errors were present [3]. At that time, no bolometric signals were fully available and the total radiated power was modelled from discrete impurity line radiation measurements. The dominant role of radiation was admitted only in discharges in which 100% of the plasma energy was radiated at the collapse time. However, shots with moderate radiation level, Prad/Pin as low as 30%, could also suffer collapse and no threshold for the maximum admissible fraction of radiative losses seemed to exist. For these reasons the radiation channel was considered of no decisive importance to trigger the thermal collapse [4]. Later, and especially during the experimental campaigns of 1990-91, both global monitors [5] and a 15-channel bolometer array [6] were used to give the complete information on total and local plasma radiative losses and the role of radiation in the occurrence of plasma collapses was then reconsidered. As the radial profile of the total radiation showed a characteristic evolution when the collapse was in progress: an emissivity peak located well inside the last closed magnetic surface moved towards the center of the plasma while increasing in intensity, a local, more than a global, breaking of the power balance was suggested as the possible origin of the thermal collapse [7]. The spatial localization of this breakdown and the existence of precursors could be used to develop methods to control these catastrophic phenomena. Together with the well known central impurity accumulation, several other scenarios have been considered as candidates for triggering a thermal collapse. Inadequate fuelling, uncontrolled recycling, off-axis absorption when combined heating is applied or the synergetic effect of local turbulence on thermally unstable regions might all lead plasmas to collapse. In a previous work we have used a simplified 1-D code to determine if a thermal instability in the outermost part of the confinement region could trigger the plasma energy collapse [8].

2. Results and discussion

In spite of the field errors were corrected and the wall conditioning was improved, during the above mentioned later operation period, collapsing discharges were obtained under a wide

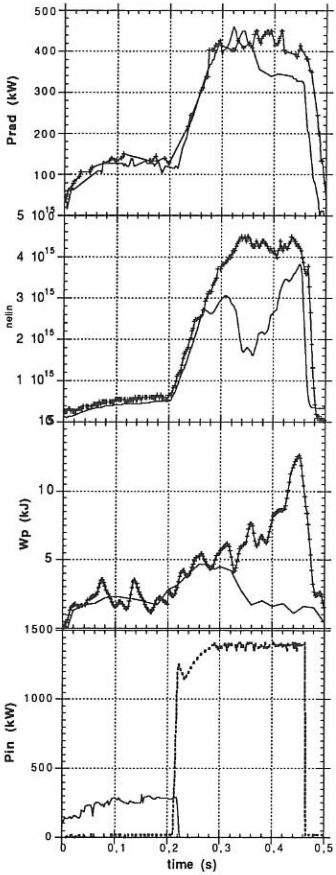

Figure 1. Experimental traces from shots #15990 (+) and #15994 (-)

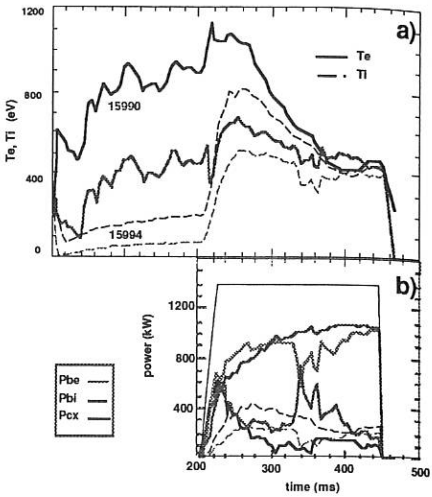

Figure 2. a) electron and ion temperatures; b) power absorbed by electrons and ions and CX losses.

variety of conditions: toroidal field, Bt: 1-2 T; ECRH only; ECHR+NBI; controlled impurity injection; pellet injection, etc.

In order to obtain possible evidences on the mechanisms involved in the collapse, the dynamics of plasma parameters have been simulated with the Proctr code. Here we are presenting the results of the comparison between two identically preprogrammed ATF shots: #15990 (no collapse) and #15994 (partial collapse). Identical initial conditions, such as magnetic field, heating models, profiles shape, transport models, fuelling procedures and plasma-wall interaction, have been assumed. Although the impurity population was uncertain, as the two discharges belonged to the same series and no titanium gettering had been applied recently, we have supposed that only oxygen and carbon were present in the considered plasmas. The shape of the total radiation radial profiles also supported this assumption.

As external inputs for the code we have used the experimental time evolutions of the line density (nelin), input power (Pin), diamagnetic stored energy (Wp) and total radiated power (Prad). In figure 1 all these mentioned signals for the two shots are displayed. As can be seen, discharge #15994 suffers an energy collapse followed by a density fall at about 350 ms and,

after 20 to 30 ms plasma density recovers just until neutral injectors are switched off. On the contrary, shot 15990 shows a monotonic increase in stored energy while power is injected into the plasma. It must be emphasized that in all the collapsing discharges, the time evolution of main plasma magnitudes presents the same behaviour as in shot #15994.

From the results of the transport code calculations, it can be said that the ECRH "conditioning phase" seems to be critical. Global parameters and profiles of the generated target plasma are of extreme importance for the neutral beam heating phase.

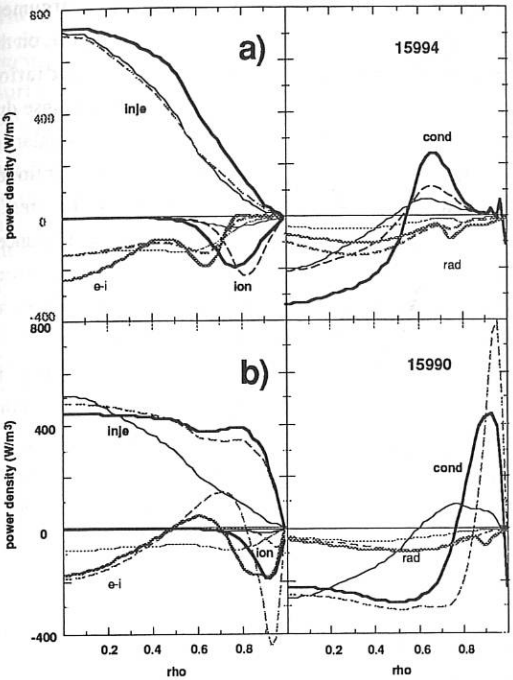

Figure 3. Radial electron power balance for a) collapsing and b) non collapsing shot.

As is displayed in figure 2a, both, average electron and ion temperatures are lower in shot #15994 than in #15990, due to its slightly higher plasma density (see fig.1). Injected neutrals, more efficient to rise density of #15994 during the early stage of the NBI, are also apparently better coupled to electrons but, as shown in figure 2b, the energy transfer to ions is notably higher than that of #15990. Figure 3a illustrates the response of the plasma bulk of #15994 trying to sustain the energy balance: heat from the core must be conducted to electrons in the central region, who are efficiently transferring their energy to ions. Besides, it can be also seen in figure 3a (thin, dashed and thick lines correspond to times before, during and after the collapse) that radiation presents a local maximum at about 0.8a which slowly propagates inwards. This is a systematic time evolution experimentally observed in all of the discharges once the collapse starts. On the contrary, in shot #15990, conducted power is only needed at the plasma periphery and radiation does not change while density is kept constant (see figs.1 and 3b). On the other hand, as electron temperature is much lower at the outer region of the plasma in shot #15994, cold neutrals can enter deeper into the plasma, favouring so an enhancement of the CX losses mostly by collisions with non thermalized ions, and also a more extended

ionisation region is established (see fig.4; labels are time in ms). For those radial locations, the electron temperature does not surpass 100 eV and radiative thermal instabilities can easily develop due to the characteristic cooling rates of the considered impurities.

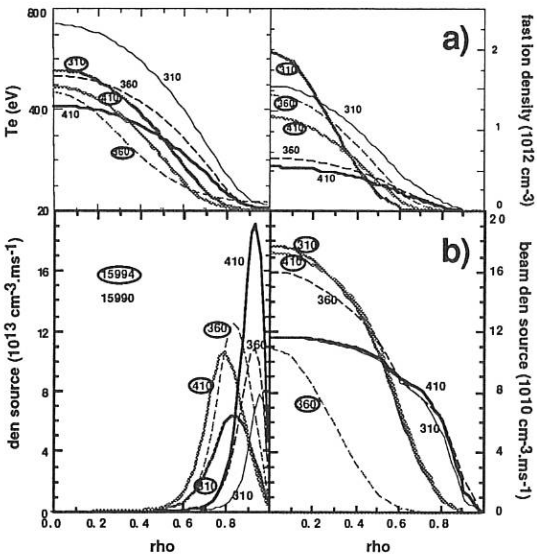

Figure 4. Radial profiles of electron temperature, fast ion density and density sources from low and high energy neutrals

This fact can be understood as a support for the argument discussed in reference 7, on the possibility of radiation triggering plasma collapse due to a local power unbalance. But, it should be mentioned that Proctr code in its present version can only yield balanced electron energy. Therefore should a local unbalace appear, Proctr simulation stops.

More simulations are in progress to go deeper into this important subject, making use of several other experimental data from the ATF torsatron.

Acknowledgment

The authors are greatly indebted to Drs. H. Howe and B.P. van Milligen and to the NIFS, Japan, for allowing the use of their computer facilities.

References

[1] J.F. Lyon et al., Fusion Technol. **17**, 33 (1990)

[2] H.C. Howe, Oak Rigde National Laboratory Report ORNL/TM-11521 (1990)

[3] H.Howe et al., 16th European Conf. Controll. Fusion Plasma Phys. **13B,** 683 (1989)

[4] R.C. Isler et al., Nucl. Fusion **31**, 245 (1991)

[5] J. Schivell, et al., Rev. Sci. Intrum. 53, 1527 (1982)

[6] S.F. Paul, et al., Rep. PPPL-2432 (1987)

[7] S.Hiroe et al. Nucl. Fusion **32**,1107 (1992)

[8] A.P.Navarro et al., Rev. Sci. Instrum., **66** (1995)

DIMENSIONAL ANALYSIS OF L-H POWER THRESHOLD SCALINGS

W. Kerner, J.G. Cordey, O. Pogutse *, and E. Righi
JET Joint Undertaking, Abingdon, Oxfordshire OX14 3EA, UK
* RRC Kurchatov Institute, Moscow, Russia

INTRODUCTION

The region where the physical effects of the open field lines become important includes part of the closed field line edge plasma as well as the scrape-off-layer (SOL) plasma. Due to the fast longitudinal losses just outside the last closed flux surface, i.e. the separatrix, steep gradients in the temperature and density build up. The near separatrix region in tokamaks provides a new length scale parameter $x_0 = (-d \ln p_o/dx)^{-1}$ being of the order of several Larmor radii. Modified drift and interchange instabilities occur in this region due to longitudinal losses. The related turbulence gives rise to perpendicular transport and regulates the width x_o. The H-mode is set up when the shear flow stabilises these instabilities leading to the condition on the normalised gyro-radius $\hat{\rho} = \rho_i/x_0 > c_1$ where c_1 is of order unity.

The ITER data base working group has studied the scaling of the L-H transition power threshold with plasma parameters and has recently presented a reasonable fit to the multimachine threshold data base [1]:

$$P > 0.025\, n_o^{0.75}\, B_o\, S \qquad (1a), \qquad P > 0.4\, n_o\, B_o\, R^{2.5} \quad , \qquad (1b)$$

where P is the power in MW, n_o the average density in 10^{20} m^{-3}, $B_o$the toroidal field in Tesla and R the major radius in m. Both forms assume that the linear B_o dependence is correct and take a quadratic dependence on the length scale or a linear dependence on the density as correct and adjust the other parameters. Our model indicates that the edge pressure gradient length x_o is the relevant length scale.

The simplified energy balance near the separatrix ($T_i = T_e = T_o$) reads (under the assumption that the density gradient is comparable or less than the temperature gradient): $\frac{\partial}{\partial t} T_0 = \frac{\partial}{\partial x} \chi_\perp \frac{\partial}{\partial x} T_0 - \frac{1}{\tau_\parallel} T_0$.

Here the $\tau_\parallel$ is the characteristic time of the longitudinal losses. Integrating this equation and inserting the total power which diffuses into the SOL as a boundary condition gives the following balance relations:

$$\frac{P}{n_0 S} \approx \frac{\chi_\perp T_0}{x_0} \approx \frac{x_0 T_0}{\tau_\parallel} \; . \qquad (2)$$

Here P denotes the total power which diffuses across the separatrix and S the tokamak surface S.

The scientific method used is dimensional analysis together with the mixing length argument. This enables us to derive the scaling of the perpendicular heat conductivity from the analysis of the edge instabilities without knowing the specific details of the physical processes. For the L-H transition the condition of shear flow stabilisation is applied. Then the product $x_o\, T_o$ can be obtained as a function of P, once $\tau_\parallel$ is known. The longitudinal losses are described by two different models. In the first regime the losses are due to classical longitudinal thermal conduction, i.e. if $\lambda < L_\parallel$, and the second one is due to free-streaming flow, i.e. if $\lambda > L_\parallel$. Here λ is the particle mean free path, $L_\parallel$ the distance along the field line between the target plates and C_s the sound speed.

$$\tau_\parallel^{th} = \frac{L_\parallel^2}{\chi_\parallel} \propto \frac{L_\parallel^2 n_0}{T_0^{5/2}} \qquad (3a) \qquad\qquad \tau_\parallel^{fs} = \frac{L_\parallel}{C_s} \propto \frac{L_\parallel}{T_0^{1/2}}\,. \qquad (3b)$$

TURBULENT TRANSPORT COEFFICIENT $\chi_\perp$ FOR THE OPEN FIELD LINES REGION

We briefly discuss the linear equations for the mutual drift and interchange modes, from which we define the dimensional parameters of the problem. The ion and electron continuity equation together with matching boundary conditions of the ion and electron current to the corresponding sheath currents can be cast into the form (as explained in detail in Ref. [2]) with ϕ' being the perturbed potential:

$$\begin{aligned} (\omega+\omega_*)\cdot(k_\perp\rho_i)^2\cdot\frac{e\phi'}{T_0}+\omega_{*g}\cdot\frac{n'}{n_0} &= -i\nu\cdot\left[(1-\xi)\cdot\frac{n'}{n_0}+\xi\cdot\frac{e\phi'}{T_0}\right] \\ \omega_*\cdot\frac{e\phi'}{T_0}-\omega\cdot\frac{n'}{n_0}+\frac{\omega_{*g}}{2}\cdot\frac{n'}{n_0} &= -i\nu\cdot\left[(-\xi)\cdot\frac{n'}{n_0}+\xi\cdot\frac{e\phi'}{T_0}\right], \end{aligned} \qquad (4)$$

where ω_* denotes the electron drift frequency, ω_{*g} the magnetic drift frequency, $\nu = C_s/L_\parallel$ and $\xi = \frac{j_{olle}}{j_{olli}}$. These equations can be solved analytically for the resistive interchange instability as well as for the drift instability. Inserting the maximum growth rate and the corresponding perpendicular wave vector the mixing length argument determines the transport coefficients:

$\chi_{\perp RI} = \chi_{GB}(L_\parallel / R)\left(\hat{\beta}\right)^\nu$ and $\chi_{\perp DR} = \chi_{GB}(L_\parallel / R)^{1/3}\left(\frac{x_o}{R}\right)^{-1/3}$, (with ν = o and 1 in special cases) where $\hat{\chi}_{GB} = \frac{cT_o}{eB_o}\cdot\hat{\rho}$ is the gyro-Bohm coefficient and $\hat{\beta} = \left(L_\parallel^{\,2} / R\cdot x_o\right)\cdot\beta$ is the normalised beta. Thus the dimensional analysis together with the mixing length arguments give the following general expression for the turbulent transport for the mutual influence of interchange and drift instabilities:

$$\chi_\perp = \hat{\chi}_{GB} \cdot f\left(\hat{\beta}, \xi, L_\parallel / R, \hat{\rho}, x_o / R\right) \approx \hat{\chi}_{GB} \cdot f\left(\hat{\beta}, x_o / R\right) = \hat{\chi}_{GB} \left(\hat{\beta}\right)^{\alpha} \left(\frac{x_o}{R}\right)^{\delta} \qquad (5)$$

THE CRITERION FOR STABILITY

As a criterion for stability we apply the condition $V_0' > \gamma_{max}$, where $V_0' = dV_0 / dx$ is the shear velocity. This condition has been derived for both the interchange and drift modes. It indicates that the perturbations have no time to develop fully and are suppressed due to the velocity shear drag. This gives the following estimate for the shear flow $V_0' \approx \frac{C_s}{x_0} \cdot \frac{\rho_i}{x_0}$. Inserting the result for the growth rates yields $\hat{\rho}_{RI} > \left(\frac{x_0}{R}\right)^{1/2}$ and $\hat{\rho}_{Dr} > \left(\frac{x_0}{L_\parallel}\right)^{1/3}$, respectively. As discussed in detail in Ref. [2] the more stringent dimensional criterion $\hat{\rho} > C_1 = 0$ (1) need to be applied. Then the marginal condition $\hat{\rho} \approx 1$ can be rewritten as $T_o \propto x_o^2 B_o^2$.

DISCUSSION

The first striking result is that a cubic dependence of the threshold power on the magnetic field is obtained for the free-streaming case, i.e. $\frac{P}{n_o S} = B_o^3 f(n_o, \alpha, \delta)$

For classical parallel losses, on the other hand, the empirical scalings can be reproduced (with $L_\parallel \alpha R$ i.e. ignoring the q_a dependence). Scaling (1a) is obtained for $\alpha = -1/2$ and $\delta = 1/6$. Then the transport coefficient scales as $\chi_\perp = \hat{\chi}_{GB} \cdot \left(\hat{\beta}\right)^{-1/2} (x_o / R)^{1/6}$. The scaling (1b) requires $\alpha = 1/3$ and $\delta = 0$ and implies $\chi_\perp = \hat{\chi}_{GB} \left(\hat{\beta}\right)^{-1/3}$.

Let us compare these findings with the experimental observations Figure 1 displays the L-H transition power threshold for many JET discharges. The data indicate a stronger than linear dependence on $n_e B_o$, in particular for low density and high power. Considering the case of SOL drift type instabilities the dependence of the L-H threshold on the net current onto the target plates provides the possibility for control. It follows that for an ion current in the instability region exceeding the corresponding electron current, i.e. $\xi < 1$, the plasma becomes more stable. Consequently the condition for L-H threshold is more favourable, i.e. lower. If the ion drift is in the direction towards the X-point then the ion current onto the target plates just outside the separatrix should be larger than in the case when the ion drift direction is away from the X-point. In contrast, the electrons stick close to the separatrix. This fact can explain the difference in the observed L-H transition power threshold.

More recent threshold data are shown in Figure 2. The best fit is obtained for a slightly nonlinear dependence $P/S \alpha n_e^{0.75} B_o^{1.20}$. Obviously, the cubic dependence on B_o in the free streaming limit (expected for low density and high

temperature) is not observed. The presented model allows to derive conclusions on detached divertor plasmas. In this case a cold layer develops in front of the target plates, which suppresses the currents onto the target plates. It is concluded that the SOL drift instability will be absent but the SOL interchange instabilities become more severe due to the absence of line-tying of the magnetic field. As a consequence the L-H threshold should increase.

CONCLUSIONS

The near separatrix region in tokamaks provides an important length scale parameter $x_0 = (-d \ln p_o/dx)^{-1}$ being of the order of several ion gyro radii. In the L-H transition both resistive interchange and drift instabilities are stabilised with increasing edge temperature thereby decreasing x_0. The H-mode is set up when the shear flow stabilisation of drift waves and of interchange modes becomes effective. The results indicate that the length parameter x_0 prompts new dimensionless quantities such as $\hat{\rho}$, x_0/R and $x_0/L_\parallel$, which should be taken into account in the empirical scalings for the transport coefficients. The other important result is that finite beta physics, in form of the parameter $\hat{\beta} = (L_\parallel^2 / x_o R)\cdot\beta$ being of order unity, plays an important role for electrostatic SOL turbulence. Classical parallel thermal heat conduction provides a threshold power scaling similar to the experimentally observed scaling.

[1] H-mode Data Base Working Group, presented by F. Ryter, 21st EPS Montpellier 1994, Vol. I p.334.

[2] J.G. Cordey, W. Kerner and O. Pogutse to appear in Plasma Phys. Contr. Fus.

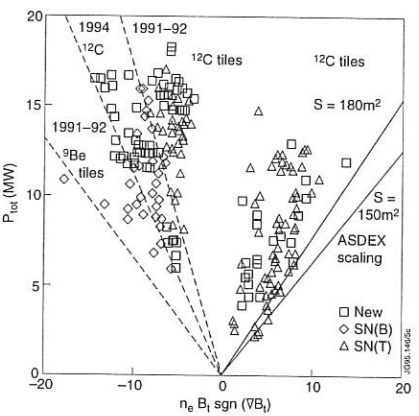

Fig. 1: H-mode operational diagram for both ion ∇B directions

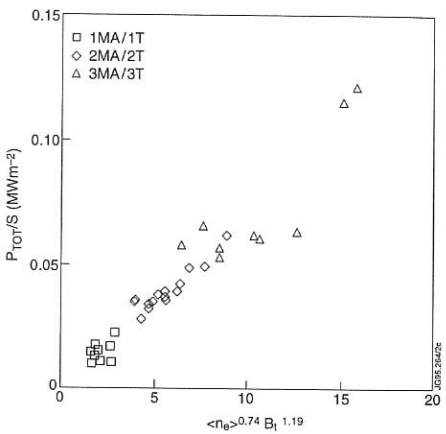

Fig. 2: Power threshold dependence on density and magnetic field; $\langle n_e \rangle$ in 10^{19} m^{-3}, B_t in Tesla.

LONG TERM APPLICATIONS OF HIGH β SPHERICAL TOKAMAKS

T C Hender, G C Counsell, C A Gardner, M R Gardner, R J Hastie,
P J Knight, O J Kwon*, D C Robinson, N P Taylor and H R Wilson

UKAEA Government Division, Fusion, Culham, Abingdon OX143DB, UK
(UKAEA/EURATOM Fusion Association)
*Dept of Physics, Taegu University, Seoul, South Korea.

Introduction The Troyon β-limit indicates the possibility of high-β at tight aspect ratio. Detailed calculations show a first stability limit $\beta \equiv 2\mu_0\langle p\rangle / B_v^2 < \beta_n I(MA) / a(m)B_v(T)$ (B_v=vacuum toroidal field at geometric axis) which increases slightly at tight aspect ratio, as shown in Fig 1.

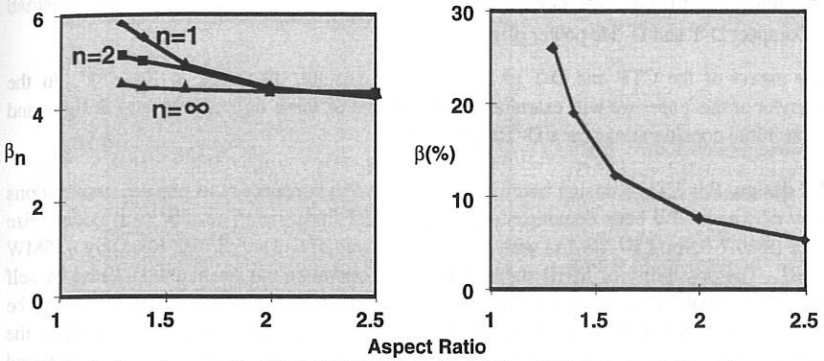

Fig 1 Variation of normalised $\beta_n(=\beta/[I(MA)/a(m)B_v(T)])$ and $\beta(=2\mu_0\langle P\rangle/B_v^2)$ with aspect ratio for q_ψ=5, q_0=1.05 and b/a=1.6. n=1 and 2 stability with no wall calculated by ERATO code.

The results shown in Fig 1 are optimised such that the pressure profile is globally marginally stable to ballooning modes using the CHEASE equilibrium code [1]. These results are for relatively modest elongation, whereas at tight aspect ratio vertically controllable high elongation (b/a~2.5) is permitted by the natural shaping, as demonstrated in the START experiment [2]. At such high elongations calculations show a first stability β-limit (no wall) in excess of 50%. Second ballooning stable configurations with monotone q-profiles have also been found at tight aspect ratio. Figure 2 shows such a case with q_0=1.9, q_ψ=5.7, β=93% and β_n=8.1.

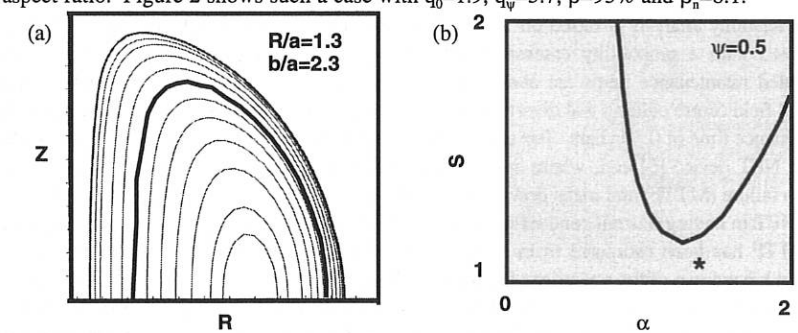

Fig 2 (a) Flux surfaces for second stable case showing (b) direct access to second ballooning on the most nearly unstable (highlighted) flux surface ($S=rq'/q$, $\alpha=-2r^2/RB_\theta^2\, dP/dR$)

To achieve second ballooning stability requires deeply hollow current profiles with large current gradients near the plasma edge, which are strongly destabilising for low-n external kink modes. For the second stable case shown in Fig. 2 a conducting shell is required at $r_{shell}/a<1.2$ to stabilise the most unstable (n=2) mode. An advantage of tight aspect ratio is the ability to achieve second stability with monotone q-profiles thus avoiding instabilities associated with low shear (infernal modes) or inverted q-profiles (double tearing).

The compact high-β nature of the spherical tokamak lends itself to several long term applications, which include:-

- Component Test Facility (CTF) for evaluating component assemblies (e.g. blanket sections) in a 14MeV neutron environment
- Compact D-T and D-^{3}He power plants

Some aspect of the CTF and D-T power plant designs are discussed in Ref [3]. In the remainder of this paper we will examine further aspects of these tight aspect ratio designs and look at initial considerations for a D-^{3}He power plant.

CTF design For CTF, a design based on conservative tight aspect ratio physics assumptions (many of which have been demonstrated in the START experiment) results in a modest size device (R=0.7-0.9m, I_p=7-10MA) with a blanket test area of 6-10m^2, driven (Q~1) by ~25MW of NBI. The possibility of MHD stable steady-state operation has been demonstrated by self consistent calculations which show that the plasma current (in magnitude and profile) may be driven by a combination of bootstrap, diamagnetic and NBI driven currents. Further the required beam power is consistent with energy balance assessed relative to physics-based confinement scalings (e.g. Rebut-Lallia). The reference CTF design is described in Ref [3]. The key features are normal conducting coils with a single turn dispersion strengthened copper (Glid-Cop [4]) centre post carrying the toroidal field current and no solenoid; the plasma being formed by a compression scheme as in START [2] with the current ramped to, and maintained in, flat-top by a combination of pressure driven currents (bootstrap and diamagnetic) and NBI current drive. For CTF an assessment of the likely fluxes and component damage has been made via a 3-D neutronics study, and the likely fluence has been determined from a statistical availability analysis.

The availability analysis is based on a detailed examination of scheduled maintenance tasks, combined with a probability assessment of unscheduled maintenance events. The main scheduled maintenance items are annual replacement of neutron damaged items such as the toroidal field centre column and divertor targets, which contribute to a total estimated scheduled maintenance time of 0.19 years. For unscheduled maintenance a detailed study has been made for the NET device [5] and, where appropriate, values from that study are used for the mean time to failure (MTTF) and mean down time (MDT) for a given system. However CTF differs from NET in having normal conducting (as opposed to superconducting) coils. For these coils the MTTF has been estimated from detailed published data and the MDT deduced from a detailed breakdown of the operations in replacing these coils. The total availability arising from unscheduled events is calculated to be 0.54. This gives an overall availability of 0.44, which translates to a fluence of 6.6MWam^{-2} over 10 years and a modest annual tritium consumption of ~0.5kg. The availability study thus indicates an acceptable fluence for CTF and has also

been very useful in isolating the critical systems whose reliability have most impact on availability, thus indicating areas for future design optimisation.

For the CTF design [3] a 3-D neutronics survey has been made using the Monte Carlo code, MCNP4. The aim of this work is to establish a detailed description of the neutron fluxes and damage to components; particularly the single turn copper centre column and the insulators of the shielded multi-turn poloidal field coils. The key components, comprising the toroidal and poloidal field coils, the centre column, the blanket test modules and all shielding materials, are all included in the Monte Carlo model. For each of the key components the nuclide composition has been specified and necessary nuclear cross-section libraries included. Finally the model is completed by specifying a realistic plasma neutron source model. The results show modest damage rates to the dispersion strengthened copper centre post (Fig 3).

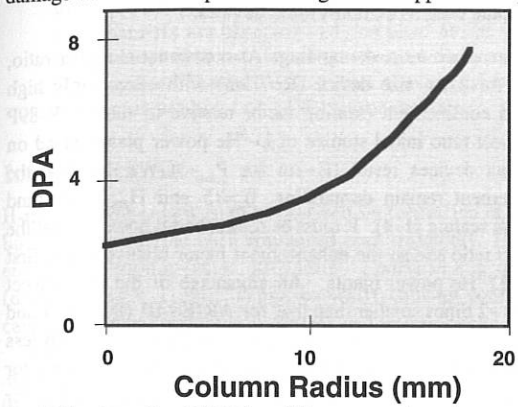

Fig 3 Displacements per atom (DPA) per full power year as a function of depth into the column. NB: since expected availability is 44% a full power year is 2.3 operational years.

Available data for Glid-Cop [4] suggest that the centre column, at its peak operating temperature of <130°C, should last several years before neutron damage necessitates replacement (showing the annual replacement assumption in availability analysis is probably pessimistic). The neutron spectrum in the CTF blanket has also been calculated. For these calculations the blanket test modules are taken to be a homogenous mixture comprised of 50% Li_2O, 40%H_2O and 10% 316 stainless steel, with natural lithium (7.42 atom% Li^6). The calculated flux spectrum is shown in Fig 4.

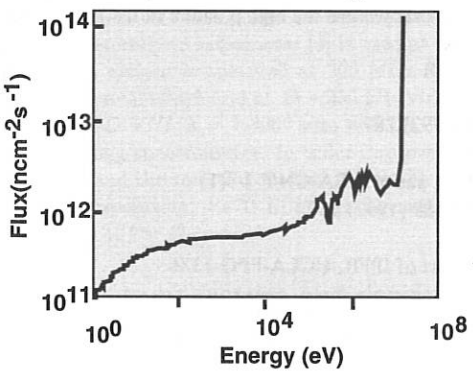

Fig 4 Volume-averaged neutron flux spectrum in blanket module

The detailed structure of the spectrum is due to the choice of blanket material, eg. the dip around 300keV is due to a resonance in ^{7}Li. Comparison of this blanket spectrum, with a spectrum at the front of the ITER shielding blanket (no Li in composition) shows good agreement in the shape, probably due to the common use of water coolant, which acts as a good neutron moderator, and the steel structure, which provides some of the detailed features of the spectra.

Power Plants For both D-T and D-^{3}He power plants the key advantage of tight aspect ratio is the ability to achieve compact devices with high mass power densities. For D-T based power plants the main issues are discussed in Ref [3]. For example studies show D-T power plants based on second stability regime (see above) result in very compact devices with R~2m at R/a=1.2. These power plants remain feasible at small unit sizes (<100MWe) making them economically attractive, in terms of capital cost, as demonstration devices.

For D-^{3}He the conditions for ignition are much more demanding. At conventional aspect ratio, the ARIES-III study [6] resulted in a moderate size device (R=7.5m) with exceedingly high requirements on stability (β_n=15) and confinement (scaling factor relative to the ITER-89P scaling law $H_{ITER89P}$=7.2). At tight aspect ratio initial studies of D-^{3}He power plants based on second stable equilibria show compact devices result (R~2m for P_{fus}~3GW), but that the requirements on stability and confinement remain demanding, β_n=15 and $H_{ITER89P}$~5 (and relative to the Connor-Lackner-Gottardi scaling H~4). It must be remembered however that the first stability β_n increases at tight aspect ratio and so the enhancement factor relative to the first stable β_n is less for tight aspect ratio D-^{3}He power plants. An advantage of the tight aspect ratio designs is that the toroidal field is ~2 times smaller than that for ARIES-III (B_t=7.6T) and the so the effects of synchrotron losses on the power balance at tight aspect ratio are much less pronounced. This means the requirements on wall reflectivity (which are very high for ARIES-III, R=0.977) can be relaxed at tight aspect ratio, thus eliminating a major problem for D-^{3}He reactors.

Summary The potential for high β at tight aspect ratio has been confirmed by detailed stability calculations. These show in the first stability regime a limit which increases as the aspect ratio decreases giving β_n~5 at R/a=1.2. Still higher β's can be achieved in the second stability regime though close fitting shells are required for low-n stability. Applications of the tight aspect ratio tokamak to a 14MeV neutron component test facility and D-T/D-^{3}He power plants are discussed. For these applications it is shown that the high β nature of the tight aspect ratio tokamak results in very compact devices.

References

[1] H Lutjens et al, Comp Phys Comm **69** (1992) 287.
[2] A Sykes et al, Nucl Fus **32** (1992) 694.
[3] R Buttery et al, IAEA paper Seville 1994, paper IAEA-CN/F-I-3(1)
[4] G Butterworth et al, Jrnl Nucl Materials **189** (1992) 237
[5] R Buende, Fus Tech (1989) 139.
[6] The ARIES-III D-^{3}He reactor study, report of IPFR, UCLA-PPG-1386

Acknowledgement We thank the Lausanne group for providing us with a copy of the ERATO stability code used in these studies. This work was jointly funded by the UK Department of Trade and Industry and EURATOM.

Effect of Edge Localized Modes (ELMs) on Edge Electron Density and Temperature Profiles and Impurity Transport in ASDEX Upgrade

W. Suttrop, K. Schönmann, J. Schweinzer, H. Zohm, M. Alexander, H. Reimerdes, ASDEX Upgrade team, NBI group, ICRH group, Max-Planck-Institut für Plasmaphysik, EURATOM Association, D-85748 Garching

Abstract

The effect Edge Localized Modes (ELMs) on the electron density and temperature as well as on *O* impurities as measured by their x-ray radiation is studied for ASDEX Upgrade H-mode discharges. Enhanced particle and heat fluxes across the separatrix are observed and described on the diffusive time scale by enhanced transport coefficients. Impurity transport simulations suggest an outward drift of *O* impurities. The turbulent nature of enhanced transport caused by type I ELMs is demonstrated by fast ECE measurements.

Introduction

H-mode confinement is characterized by formation of a transport barrier near the plasma boundary combined with improved core transport. Edge Localized Modes (ELMs) cause enhanced periodic (rate: 50-2000 s^{-1}) particle and heat loss during short time intervals (duration $\Delta t < 1$ ms). While basically causing confinement degradation, ELM activity can be beneficial for density control and to reduce the impurity level in H-mode discharges.

Following the DIII-D classification [1], based on the ELM frequency dependence on the auxiliary heating power, ELM types observed in ASDEX Upgrade are type III ($df/dP < 0$) close to the H-mode threshold or at high radiation levels and type I ($df/dP > 0$) for heating powers well above the H-mode threshold. In addition, type III ELMs are distinguished from type I ELMs in that a coherent magnetic precursor is observed for the former (e.g. [2]). This paper focuses on type I ELMs and their influence on electron and impurity transport in the bulk plasma close to the last closed flux surface. Results are presented for neutral beam heated ($P_{NBI} = 2.5 \ldots 10$ MW) discharges with ∇B-drift directed towards the X-point.

Electron temperature and density measurements are conducted using Electron Cyclotron Emission (ECE) and Li beam [3] diagnostics. For ECE measurements, a 18-channel heterodyne radiometer [4] is used at the second harmonic of the cyclotron emission. The system is operated at 300 MHz RF bandwidth corresponding to $6 - 10$ mm spatial channel width and at $15 - 250$ kHz video bandwidth (temporal resolution ≥ 2 μs). Impurity (*O VIII*, $\lambda = 1.8967$ nm, and *Cu XX*, $\lambda = 1.1386$ nm) radiation is monitored with a Bragg spectrometer. In order improve the signal-to-noise ratio of the Li beam diagnostics and the counting statistics of the Bragg spectrometer without compromising the temporal resolution, 40-70 ELMs are averaged, each aligned with respect to the nearest maximum of the D_α emission.

Electron temperature and density profiles during ELMs

Figure 1 shows electron temperature and density profiles shortly before and during type I ELMs in a neutral beam heated H-mode discharge. The profiles are plotted at the

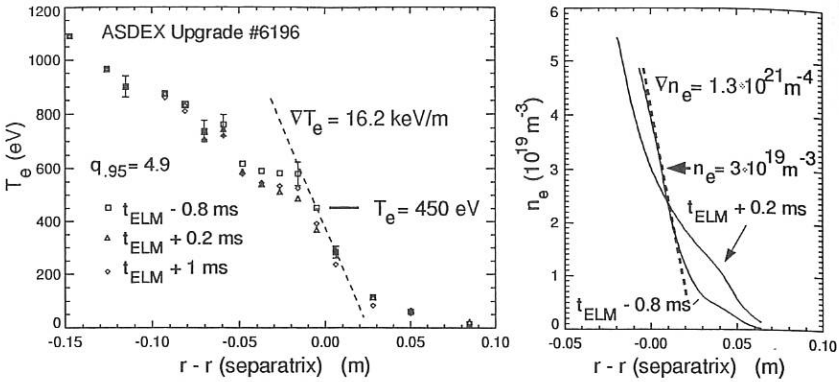

Figure 1: *T_e and n_e profiles before and during type I ELMs. An ASDEX Upgrade shot with $B_t = 2.5$ T, $I_p = 0.8$ MA, $q_{0.95} = 4.9$, and $P_{NBI} = 5$ MW is shown.*

indicated times relative to the D_α emission maximum in the divertor. The H-mode transport barrier is recognized by steep T_e and n_e profiles in a region extending from the separatrix position to 2 cm inside the plasma. During the ELM ($t = 0.2$ ms), the profiles flatten considerably and recover for times $t > 0.5$ ms until the next ELM occurs.

From the experimental T_e and n_e profiles shown in Fig. 1, the maximum electron pressure gradient is found to be $\nabla p = 172$ kPa/m. Assuming $n_e = n_i$ and $T_e = T_i$, and using $q_{.95} = 4.9$ from equilibrium reconstruction, the normalized pressure gradient is $\alpha = 2.0$. The critical pressure gradient for ballooning stability in the first stability region can be approximated for high shear ($S = 4$ in this case) by the linear relationship [5] $\alpha_{crit} = 0.57S = 2.3$. This observation confirms within our experimental accuracy limits that prior to type I ELMs, the ideal balloning limit is reached at the plasma edge.

Unlike for type III ELMs, no magnetic precursor has been found for type I ELMs in ASDEX Upgrade to date. Figure 2 a) shows traces of a differential magnetic loop, sensitive preferentially to high mode number oscillations, the divertor D_α radiation, and two ECE channels sampled at 1 MHz with the resonances located closely inside and outside the separatrix. A precursor oscillation is observed in the ECE signal at $a - 0.4$ cm but not in the magnetics.

Type I ELMs affect T_e profiles in a minor radius range extending from the separatrix to $10 - 18$ cm inside the separatrix. Fig. 2 b) shows T_e traces at different radii for a typical case. A "cooling wave" launched by a type I ELM propagates 11 cm on the time scale of 0.5 ms, indicating diffusive heat transport. Instantaneous T_e changes are limited to the first 3.3 cm in this example.

Modelling of transport modification due to type I ELMs has been attempted using either a simple one-dimensional particle and heat diffusion model in cylindrical geometry or, alternatively, by B2-EIRENE simulations [6] in full 2-D geometry based on the reconstructed equilibrium. In both models, transport coefficients $D_\perp$ and $\chi_\perp$ were found to change by factors of $3 - 10$ in radial a region extending from $4 - 8$ cm inside the separatrix into the scrape-off layer (SOL) during a time interval of $0.4 - 1$ ms during the ELM.

It should be emphasized, however, that a description of ELM induced transport by a

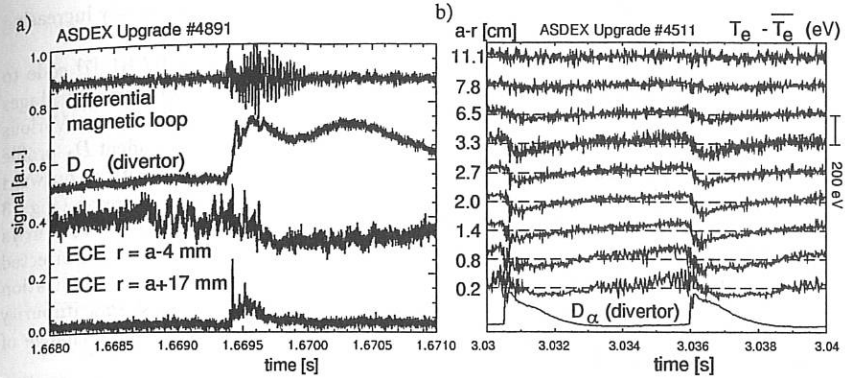

Figure 2: *a) A coherent precursor to type I ELMs is observed in ECE measurements with resonance near the separatrix but not in a magnetic loop sensitive to high poloidal mode numbers. b) In a typical case, type I ELMs affect T_e in a radial range of* 11 *cm inside the separatrix by heat diffusion. An instantaneous drop of T_e occurs within* 3.3 *cm inside the separatrix.*

diffusive model can hold only in a time-averaged sense. Sufficiently time-resolved ECE measurements in the SOL reveal that transport across the separatrix occurs in an irregular sequence of distinct outbursts of plasma, as shown by the spikes in the bottom trace of Figure 2 a).

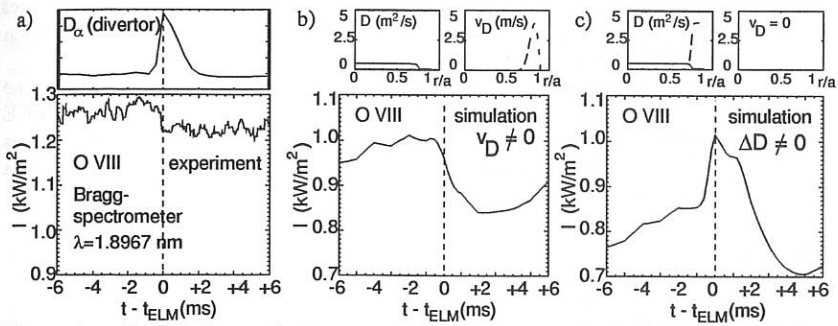

Figure 3: O VIII *line radiation measured during type I ELMs (a), and simulation of* O VIII *radiation for two transport models: b) time-independent D, peaked outward drift v_D at the edge during the ELM, c) D augmented at the edge during the ELM, no drift v_D*

ELM-related impurity transport

The effect of type I ELMs on *O VIII* impurities is demonstrated by Figure 3. The observed line radiation (Fig. 3 a) drops within 0.2...0.3 ms during the ELM by 5 – 15%

of its original value, indicating a decrease of *O VIII* concentration, then slowly increasing back to the original value before the ELM.

Impurity transport is simulated by using a modification of the STRAHL [7] code to solve a system of coupled one-dimensional continuity equations for all O ionization stages assuming profiles of the diffusion coefficient D and an optional drift velocity v_D. Various combinations of D and v_D have been attempted. Assuming a time-independent $D_\perp$ profile $D_\perp = 3\ \mathrm{m}^2/\mathrm{s}$ for $r/a < 90\%$ and $D_\perp = 0.09\ \mathrm{m}^2/\mathrm{s}$ for $r/a > 90\%$ together with an outward drift of $v_D = 4$ m/s at the edge, results in a simulated 15% intensity decrease (Fig. 3 b). If $v_D = 0$ is assumed and the edge diffusion coefficient $D_\perp$ is augmented to 4 m^2/s during the ELM, the *O VIII* radiation *increases* (Fig. 3 c) because the outward-directed oxygen concentration gradient in the ELM region causes inward-diffusion and ionization of O in lower ionization stages. As a consequence, the simulations suggest that impurity transport during ELMs implies an outward particle drift rather than a mere change of the diffusion coefficient $D_\perp$.

Summary and conclusion

The effect of type I ELMs on electron density and temperature profiles as well as on oxygen impurity transport has been studied for the H-mode of ASDEX Upgrade. ECE measurements show that T_e profiles are affected by a cooling wave propagating from the separatrix to $10 - 18$ cm inside the plasma. Instantaneous effects on T_e profiles are limited to the first $4-8$ cm. First attempts to model T_e and n_e averaged over a sequence of ELMs indicate that ELM-related transport is compatible with the assumption of transport coefficients $D_\perp$ and $\chi_\perp$ augmented by a factor of $3 - 10$ during the ELM.

Oxygen (*O VIII*) impurity radiation is found to decrease during type I ELMs. Considering the hollow oxygen concentration profile this implies that ELM effects on impurities cannot be described primarily by enhanced diffusion. Transport simulations suggest an outward particle drift during ELMs.

A fluctuating ECE signal is observed as a precursor of type I ELMs. During the ELM, heat transport is found to occur as repeated turbulent outbursts of plasma by ECE measurements with 2 μs time resolution. This indicates that transport during ELMs is closely connected to MHD activity and a simple diffusion model can be interpreted in a time-averaged sense only.

References

[1] E. J. Doyle et. al., Phys. Fluids **B3**, 2300 (1991)
[2] H. Zohm et. al., this conference
[3] J. Schweinzer et. al. , this conference
[4] N. A. Salmon, 18th International Conference on Infrared and Millimeter Waves, University of Colchester, England (1993)
[5] J. Wesson, Tokamaks, p. 156, Oxford (1987)
[6] D. P. Coster et. al., 21st EPS Conference on Controlled
Fusion and Plasma Physics Montpellier, France (1994)
[7] K. H. Behringer, Description of the impurity transport code STRAHL, JET Report JET-R(87)08, JET Joint Undertaking, 1987.

Variation of power density decay lengths in the SOL of ASDEX Upgrade measured by thermography and Langmuir probes.

A. Herrmann, V. Rohde, M. Weinlich, M. Laux,
G. Haas, A. Carlson, ASDEX Upgrade Team, NI Team

Max-Planck-Institut für Plasmaphysik, EURATOM Association, Garching and Berlin; Germany

1. Introduction

Controlled dissipation of power flowing from the core plasma into the scrape-off layer is a major problem in tokamak fusion reactors and a main topic in the research program of the ASDEX Upgrade tokamak. Some efforts were made on ASDEX Upgrade to achieve ITER relevant conditions in the divertor region and to get experimental results as a base for the ITER divertor design [1]. For this, ASDEX Upgrade is equipped with versatile diagnostics to measure the plasma parameters and the energy flow in the divertor region. In this paper we will concentrate on results of Langmuir probe measurements at different positions in the scrape off layer and data from the thermography diagnostic. We compare the power density derived from both type of measurements and will present power decay lengths at the target plate for a wide range of discharge conditions.

2. Diagnostics

A high time resolution thermography system has been used to record the power density at the divertor plates [2]. The system is based on a 256 pixels IR line camera with a highest time resolution of 130 μs (typically used: 260 μs). The spatial resolution is 2.72 mm/pixel at the outer plate and 3.4 mm/pixel at the inner plate.

The plasma parameters at the plates are monitored by a set of Langmuir probes, flush mounted into the outer and inner divertor plates at different radial and toroidal positions. Three tips are always located at the same radial position toroidally adjacent, so that they can be used as triple, double or single probes. The typical time resolution is of the order of (50..70) μs.

In 1994 a new midplane manipulator went into operation on ASDEX Upgrade. It gives the opportunity to expose different kinds of probe heads, such as collector or electrical probes, into the edge plasma near the outer midplane. For the experiments under discussion, a head with a reciprocating Mach type Langmuir probe was used. The housing and the probe tips are made from carbon. Three tips (0.9 mm dia., 2 mm length, 3 mm pin distance) viewing into the ion and electron drift direction, respectively, are arranged at a poloidal line. Two strokes can be performed per discharge, where each stroke lasts about 100 ms. Because the radial position was directly measured the radial dependence of electron temperature, density and floating potential can be derived precisely. The maximum penetration depth is limited by the power load to the probe head and, therefore, is just inside the separatrix for ohmic discharges and 1 cm outside in additionally-heated plasmas.

The flux of neutral gas is measured by ionization gauges at different toroidal and poloidal positions in the vacuum vessel [3].

3. Experiments

The shots under discussion were single null divertor discharges in hydrogen or deuterium. The thermography diagnostic, the flush mounted Langmuir probes, and the ionization gauges were routinely measuring. The midplane reciprocating Langmuir probe was used in Ohmic and L-mode shots. A negative magnetic field is the 'normal' situation on ASDEX Upgrade associated with an ion grad B — drift direction towards the bottom divertor.

4. Results and discussion

The experiments presented here deal with three subjects. The comparison of the power density decay, measured at the midplane and at the divertor plate, gives an idea of contribution of the perpendicular energy transport in the scrape-off layer (SOL). The contribution of charged particles to the power deposition onto the plates can be estimated from the ratio of the power density calculated from Langmuir data with that measured by thermography. The variation of the power decay lengths at the outer plate with the neutral density in the SOL is investigated.

The midplane probe is, due to the geometry, measuring the parallel heat flux, whereas the heat flux measured by thermography and flush mounted Langmuir probes is a projection of the parallel heat flux to the target plates. Taking the pitch angle between the target plate and the magnetic field lines into account, the parallel power density is calculated for thermography data. Additionally, the SOL spreading is considered by projecting the radial position of both diagnostics to the normalized poloidal magnetic flux (ρ_{pol}). This procedure was performed for each data point separately, using the function parametrization calculation for the magnetic configuration of ASDEX Upgrade.

For a set of ohmic discharges (I_p = 800 kA, $\bar{n}_e = (1\text{–}4)\times 10^{19} m^{-3}$, $B_t = \pm$ 2T) the midplane power flow is calculated from the measured particle flux, Γ_{ion}, and electron temperature, kT_e, based on Langmuir measurements:

$$q = \Gamma_{ion} (\gamma\, kT_e + E_{interact}) \qquad \text{Eqn. (1)}$$

where γ = 5 is the sheath transmission factor and $E_{interact}$ contributes for the net energy release per ion due to ion target interaction. For typical ion temperatures in the midplane of about 50 eV this contribution can be neglected.

Fig. 1 shows power density profiles for a high density discharge. The curves are fitted in the region near the separatrix to an exponential function, giving the decay length.

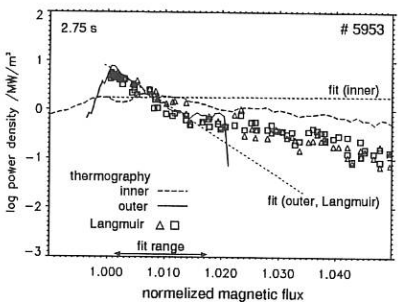

Fig. 1.: Power density profiles, measured by midplane Langmuir probes and thermography, $\bar{n}_e = 4\times 10^{19} m^{-3}$

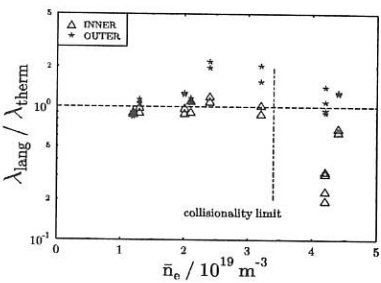

Fig. 2.: Change of the power density decay ratio (Langmuir / thermography) as a function of the line averaged density, dash dotted — collisionality limit

The power load to the inner plate is generally low and combined with a large decay length (Fig. 1), whereas the decay lengths at the outer plate and at the midplane are similar. The density dependence of the ratio of the power decay lengths at the midplane and at the plates is shown in Fig. 2 for the whole set of data.

The ratio of the power decay lengths is about unity, except the high density points for the inner plate. A ratio of unity reveals a correlation between the midplane (Langmuir) and the target power density (thermography) profile, indicating that the perpendicular heat transport, which should broaden the power density profile at the plate, is negligible within the accuracy of the measurement. Applying the criterion for collisionality in the SOL [4] shows, that at densities above $3.5\times10^{19}\mathrm{m}^{-3}$ the collisionality limit is exceeded, i.e $\lambda^{ei}_{free} \leq 3 \times L_c$. This explains the increased decay length at the inner plate at high density (Fig. 1 , Fig. 2). As we know from density limit discharges, also the outer plate detaches at densities of about $5\times10^{19}\mathrm{m}^{-3}$. A ratio well above unity is observed for the first shots after the change of the magnetic field direction where a conditioning of the ICRH limiter near the probe is expected. This may result in additional ionization processes which increase the measured decay length [5].

In the following the thermography and the flush mounted Langmuir probes will be compared, measuring the net power density deposited onto the plates and the energy release due to charged particles (Eqn. 1), respectively. An energy gain due to the recombination energy ($E_{interact}$ = 13.6 eV) is taken into account (Eqn. 1).

Moving the separatrix across the plates avoids the problem of the relatively big distances between the Langmuir tips, compared to the decay length, and gives the opportunity to measure power density profiles across the plates which can be compared with that, measured thermographically (Fig. 3).

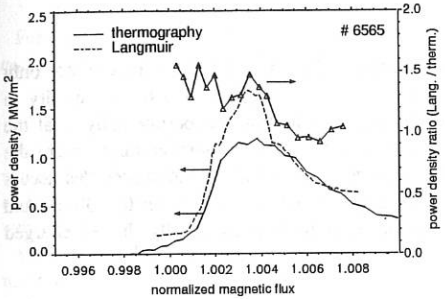

Fig. 3.: Power density profiles across the outer target plate derived from Langmuir measurement and thermography (I_p = 800 kA, B_t = -2.5 T, n_e= 5×10^{19} m^{-3}, P_{NI} = 3 MW)

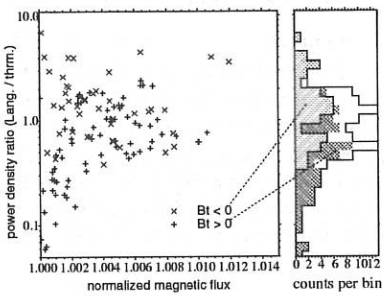

Fig. 4.: Comparison of power density ratios — Langmuir / thermography — measured at the outer target plate

The ratio is about 1.5 at the separatrix (ρ_{pol} = 1) and decreases slowly with the distance from the separatrix. Fig. 4 shows ratios for a set of 37 ohmic and L-Mode discharges (I_p = (800,1000) kA, B_t = ± (2.1–2.6) T, $\bar{n}_e$= $(1–10)\times10^{19}\mathrm{m}^{-3}$, P_{NI} = (0–3) MW).

A ratio of about unity away from the separatrix indicates that most of deposited power is due to charged particles. Close to the separatrix the ratio depends on the field direction. It is about 3 in the case of normal field direction and 1/3 for reversed field. This effect is not understood

yet. Phenomenologically it is due to different behaviour of the temperature and density profiles at the plate for the two field directions. In the case of normal field direction, the maximum of the temperature and density profile is at the same location. For the reversed field direction the temperature peak is moved away from the density peak into the direction of the private flux region [6].

In ASDEX Upgrade the neutral density in the divertor can be influenced by controlling the gas puffing and changing the pumping speed almost independent of the main plasma parameters [7]. One goal of increasing the neutral density in the divertor is to produce a dense and cold divertor plasma.

High densities and low temperatures in the divertor should result in an imbalance of pressure [8], in a broadening of the power density profiles and therefore, in a reduction of the maximum power density.

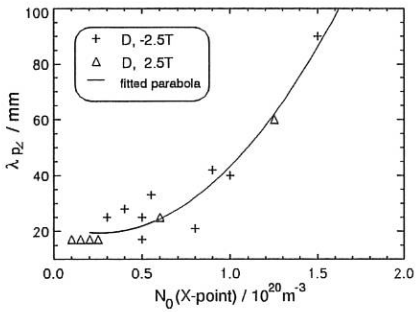

Fig. 5.: Change of the power density decay length with the neutral density below the X-point (N_0(X-point))

Investigations of the variation of the power decay lengths with neutral density for different confinement regimes (ohmic, L-, H-mode) and directions of the magnetic field have been started. In this paper only the outer target plate and stationary Ohmic and L-mode discharges as well as phases in between ELMs are considered. As shown in Fig. 5 this theory is verified by the measurements. No significant differences are obvious between the different field directions.

5. Summary

The combined use of Langmuir probes and thermography on ASDEX Upgrade is not only a meaningful tool to validate the results of both diagnostics but gives also the possibility to prove models for the energy transport in the SOL, e.g. it was found experimentally, that the perpendicular heat transport in the SOL is negligible for densities and temperatures where the collisionality is low ($\lambda^{ei}_{free} > L_c$). Further, the combined use of both methods provides access to the understanding of energy deposition onto the target plates. It was shown for Ohmic and L-Mode discharges, that the deposited power to the outer plate is essentially due to charged particles.

6. References

[1] M. Kaufmann, et al., *Plasma Phys. Contr. Fusion* 35 B205 (1993)

[2] A. Herrmann, et al., *Plasma Phys. Contr. Fusion* 37 (1) 17 (1995)

[3] G. Haas et al., *J. Nucl. Mat.* 121 151 (1984)

[4] P.C. Stangeby and G.M. McCracken, *Nucl. Fusion* 7 1225 (1990)

[5] P.C. Stangeby, *J. Nucl. Mat.* 121 55 (1984)

[6] M. Laux, et al., this conference, "Effects of field reversal in ASDEX Upgrade"

[7] K. Lackner et al., *Plasma Phys. Contr. Fusion* 36 B79 (1994)

[8] C.S. Spencer, et al., this conference, "Scrape-Off Layer Power and Pressure Balance in ASDEX Upgrade"

Scrape-Off Layer Power and Pressure Balance in Asdex-Upgrade

C S Pitcher[1], H-S Bosch, A Carlson, J C Fuchs, G Haas,
A Herrmann, H Murmann, V Rohde, J Schweinzer, P Stangeby[2],
W Suttrop, M Weinlich and the ASDEX-Upgrade Team

Max-Planck-Institut für Plasmaphysik, EURATOM Association, D-85748 Garching, Germany
1) CFFTP, Toronto, Canada , 2) UTIAS, Toronto, Canada and JET, UK

1. Introduction

In this paper we compare the predictions of a simple 1-dimensional SOL model with experimental results from the AUGD tokamak. We specifically focus on the loss of power and pressure that occurs in a SOL flux tube in its transit from the region adjacent to the main plasma down to the divertor plate. We concentrate on the flux tube that corresponds to the first radial e-folding distance in parallel power flow that starts at the outside midplane and terminates at the outer target plate. The model and experimental results are presented in greater detail in a review paper [1].

2. Model

For simplicity we assume that power enters the flux tube only at the midplane location, i.e. $q_{\|u}$, and that power flows to the divertor by electron heat conduction,

$$T_u^{7/2} - T_t^{7/2} \simeq \frac{7 q_{\|u} L}{2\kappa_0} \tag{1}$$

where L is the connection length (25 m), T is the plasma temperature (we assume $T_i = T_e$), κ_0 is a constant and 'u' and 't' denote the upstream (or midplane) and target plate locations, respectively.

We assume that the plasma pressure along the flux tube remains constant throughout the majority of the flux tube, although pressure can be lost within a thin recycling region close to the divertor plate, where friction of plasma ions on neutrals can lead to substantial plasma pressure loss. We write,

$$2 n_t T_t = f_m n_u T_u \tag{2}$$

where f_m is the pressure loss factor, as in [2].

In deriving f_m, we use analytic results from Self and Ewald [3], whose model deals with the case of hot ions within a gas discharge tube,

$$f_m = 2\left(\frac{\alpha}{\alpha+1}\right)^{\frac{\alpha+1}{2}} \tag{3}$$

where,

$$\alpha \equiv \frac{< \sigma v >_i}{< \sigma v >_i + < \sigma v >_m} \tag{4}$$

where $< \sigma v >$ are the rate coefficients for ionization (i) and momentum loss (m, including both elastic and charge-exchange collisions), given by [4]. To a first approximation, α, and therefore the pressure loss f_m, also shown in Fig. 1, depend only on the electron temperature in the recycling region, assumed to be the plate temperature T_t. The neutral density in the region does not by itself affect the pressure drop, but instead determines the scale length of the recycling region [1]. Significant pressure loss occurs only for $T_t < 5eV$.

We assume that volumetric power loss above the recycling region is due to impurity radiation [5],

$$q_{\|u}^2 - q_{\|r}^2 = \frac{1}{3}\kappa_0 c_z L_z p_u^2 (T_u^{3/2} - T_t^{3/2}) \tag{5}$$

where c_z is the impurity concentration, assumed to be constant along the flux tube, and L_z is the radiation power coefficient, also assumed to be constant (for $T > 5eV$) and zero for $T < 5eV$, in approximate agreement with data for carbon in non-coronal equilibrium [6]. $q_{\|r}$ is the power entering the recycling region and p_u is the upstream plasma pressure (ion + electron). One can see that the loss of power along the flux tube depends on the presence of a parallel temperature gradient and increases strongly with upstream pressure.

The boundary condition at the entrance of the recycling region is

$$q_{\|r} = n_t c_{St} (\gamma T_t + \epsilon_{pot} + \epsilon_{rad}) \tag{6}$$

where, c_{St} is the ion acoustic speed at the plate and $\gamma = 6$ is the sheath power transmission factor. ϵ_{pot} is the potential energy associated with each ion reaching the plate, including atomic and molecular recombination ($\epsilon_{pot} \simeq 16eV$). ϵ_{rad} is the energy radiated per recycling hydrogenic atom ($\epsilon_{rad} \simeq 15eV$).

3. Experimental Details

The model is compared with experimental results from the Asdex-Upgrade tokamak. The upstream conditions are measured with ECE, Langmuir probes, Thomson scattering and a lithium beam. The conditions at the plate are measured with built-in Langmuir probes and infra-red thermography. In addition, the plasma density and temperature just above the plate and recycling region are measured with a novel moving Langmuir probe [7]. The two-dimensional radiated power distribution across the plasma cross-section, including the divertor fans, is obtained with bolometer cameras.

4. f_m - Comparison with Experiment

In Fig. 1 we compare results from a large number of discharges with the prediction for the pressure loss factor, Eqn. 3. Upstream pressure is obtained from ECE (for T_e) and lithium beam (for n_e) profiles. Target plate values are obtained from built-in Langmuir probes. Separatrix and inter-ELM conditions are given. Experimental results are shown for an Ohmic density scan with ∇B drift away from the X-point (series of steady-state discharges), an Ohmic density ramp with ∇B drift towards the X-point, a density scan in hydrogen L-mode discharges with 3.5 MW NBI (steady-state), a low density hydrogen L-mode discharge with 3.5 MW with transient neon puff, a steady-state CDH discharge (neon) with 7.5 MW #6136 (see [8]) and finally, a transient CDH discharge with 7.5 MW with time-varying neon puff.

As expected, the pressure loss appears to be a function of the electron temperature in the recycling region immediately adjacent to the target plate. Pressure drops as small as $f_m \simeq 0.013$ at $T_t \simeq 1.5eV$ are observed and little pressure loss is found for $T_t > 5eV$.

5. Detailed Comparison with Model

The full model is compared with a subset of the experimental results shown in Fig. 1, an Ohmic density scan in deuterium with grad-B drift away from the X-point, $I_p = 0.8MA$, $B_t = 2.1T$ and with plasma density in the range $\overline{n_e} = 1.1 \times 10^{19} m^{-3}$ to $\overline{n_e} = 4.6 \times 10^{19} m^{-3}$. Again, only separatrix conditions are considered, obtained during density flat-tops lasting several seconds. Carbon is the dominant impurity. The power entering the divertor is constant with density, ($P_{DIV} \simeq 300kW$), as is the power e-folding distance $\lambda_P \simeq 4mm$ (midplane), thus giving a constant parallel power density, $q_{\|u} \simeq 13MWm^{-2}$.

In the comparison of the model with experiment, we have used $L_z = 2.3 \times 10^{-32} Wm^3$ for carbon. While this particular value was chosen to give the best fit with experiment, it lies within the error bounds of the appropriate value based on non-coronal equilibrium [6]. The carbon concentration is taken from bremsstrahlung Z_{eff} measurements, $c_z = 0.02$, and is approximately constant with density.

Fig. 2 gives the model predictions and the experimental results for the plasma temperature and total electron pressure at three locations in the flux tube—upstream, target plate and a point in between, corresponding to the location of the moving Langmuir probe, a distance of 3.5 m along field lines from the plate. At low plasma density, the SOL is nearly isothermal, pressure is approximately constant and the temperature is high, $T > 30eV$. At medium density, a significant temperature gradient develops, but pressure remains constant since $T > 10eV$ everywhere within the SOL. At high density, $T_t < 5eV$, a significant pressure loss occurs between the upstream/probe locations and the plate, due to neutral friction in the recycling region. The pressure at the probe is expected to be equal to the upstream pressure since recycling is assumed to occur below the moving probe in these discharges.

Fig. 3a gives the density at the moving probe location and at the plate. The probe density rises rapidly with discharge density whilst the plate density rises in parallel only at low and medium density, but rolls-over and decreases at high density. The decrease of n_t and T_t (i.e. of particle flux) at the plate are key elements in reducing the power flux to the plate to small levels; that is, reducing T_t by itself is not sufficient, since the power associated with the flux of potential energy ϵ_{pot} is only reduced by reducing the particle flux, $n_t c_{St}$, Eqn. 6 [2].

The strong decrease in power reaching the plate is shown in Fig. 3b. (In the model we have neglected that fraction of the radiated power which is incident on the plate.) The complementary increase in divertor radiation (i.e. radiation below the X-point) is shown in Fig. 3c, here normalized with respect to the power entering the divertor, P_{DIV}. Also included in Fig. 3c is the model prediction for the impurity radiation and that due to hydrogenic radiation. The impurity radiation rises rapidly with density, reflecting its p_u^2 dependence (Eqn. 5). The hydrogenic radiation is always relatively small.

References

[1] C S Pitcher and P C Stangeby, Plas Phys Contr Fus (1996)

[2] K Borrass and G Janeschitz, Nucl Fus 34 (1994) 1203.

[3] S A Self and H N Ewald, Phys. Fluids 9 (1966) 2486.

[4] R K Janev et al, Elem Proc in H-He Plas, Springer-Verlag, Berlin (1987)

[5] L L Lengyel, IPP Report IPP 1/191 (1981)

[6] D Post, J Nucl Mat (1995)

[7] C S Pitcher, EPS Conf. (1993) Lisbon

[8] J Neuhauser, invited review, this conference, Plas Phys Contr Fus

Fig. 1 Total Pressure Loss Factor (target/upstream)

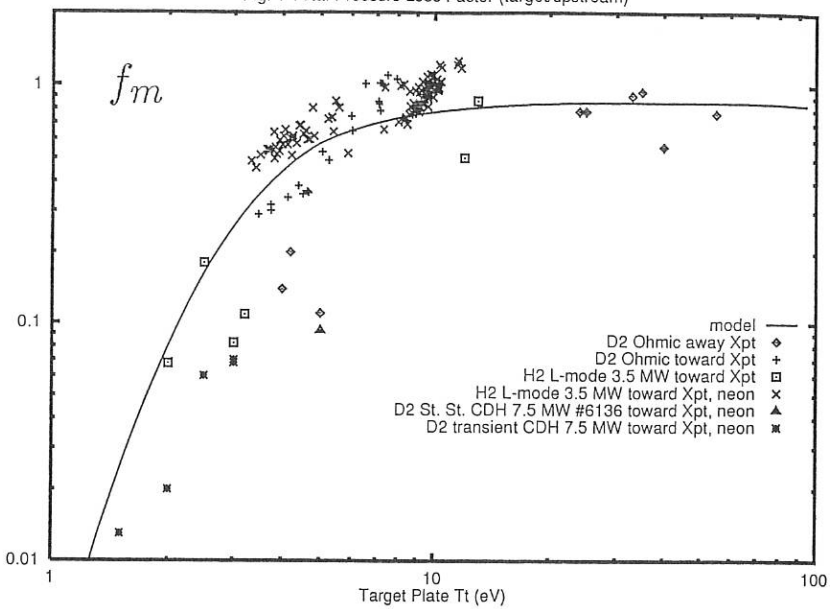

Fig. 2a Electron Temperature

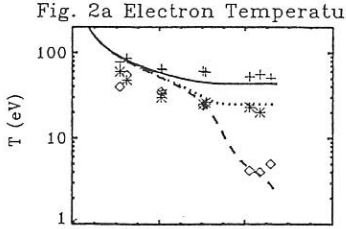

Fig. 2b Electron Pressure

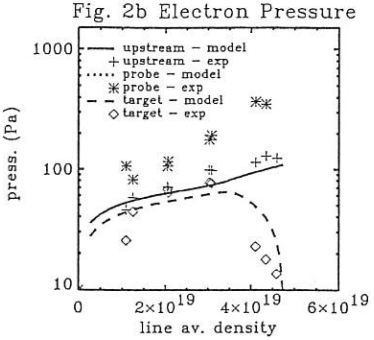

Fig. 3a Density

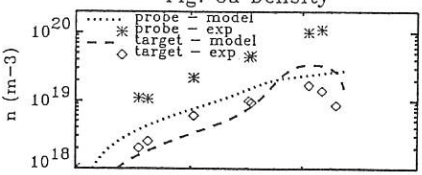

Fig. 3b Parallel Power Density

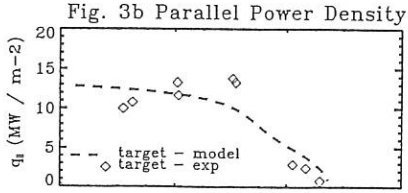

Fig. 3c Divertor Radiation

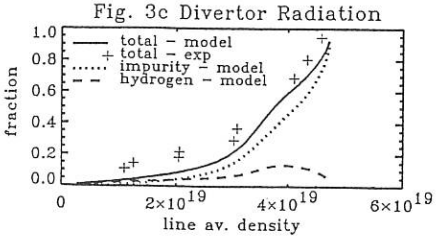

ELM-Resolved Ion Temperatures from Neutral Fluxes

J. Stober, H. Verbeek, D. P. Coster, H.-U. Fahrbach, O. Heinrich, W. Herrmann,
G. Haas, O. Kardaun, D. Reiter‡, R. Schneider, J. Schweinzer, W. Suttrop,
ASDEX Upgrade Team, NI Team, ICRH Team, and ECRH Team
Max-Planck-Institut für Plasmaphysik, EURATOM-Association,
D–85748 Garching, Germany
‡ IPP, Forschungszentrum Jülich GmbH, EURATOM-Association,
D–52425 Jülich, Germany

1 Introduction

In principle, the energy distribution of the neutrals coming out of a plasma is closely related to the ion temperature since neutrals and ions are coupled via charge exchange (CX), electron-ion recombination and electron impact ionization. The rather straight forward methods [1] that estimate the temperature at the innermost point of the line-of-sight from the exponential decay of the spectra at high energies were applicable only at low densities and small plasma radii. They can not be used for plasmas of modern tokamak devices. This paper describes the status reached so far in the ion-temperature estimation by fitting all of the measured neutral-flux data by varying the parametrisation of the temperature for stable and ELMy plasma conditons.

2 Energy-resolved neutral-flux measurement

At ASDEX-Upgrade, energy resolved neutral fluxes are measured with two methods for different energy ranges that can be analysed. Both view the plasma nearly radiallly at the outer midplane. The time-of-flight diagnostic LENA [2] covers the energy range from 30 eV to 1000 eV (Deuterium). The opening time of the chopper is 1 μs and the chopper frequency is 7 kHz. It has no mass resolution. The diagnostic CXA [3] uses a gas cell for reionization and parallel electric and magnetic fields for energy and mass selection. It has a wide energy range starting at 500 eV. However, the energy range usable for temperature evaluation during neutral injection is reduced for the injected species due to non thermal neutrals. In these cases the upper energy limit was 3 keV. The highest sample frequency used so far was 50 μs. The statistics of both diagnostics are very poor on a time scale of 100 μs which is needed to study a single edge localised mode (ELM). Therefore, a time interval with a large number of similar ELMs is mapped onto a interval with the length of the mean ELM period. Thereby, the times when the divertor D_α signal reaches its maximum are mapped to zero. So far only type-I ELMs have been investigated.

3 Ion temperature estimation

Most neutral particles leaving the plasma are due to CX processes. Therefore, the knowledge of the neutral density profile is important for the interpretation of the measured spectra. There are two different types of sources for neutrals in the plasma: the neutrals penetrating

the plasma from outside, leading to a distribution that decays roughly exponentially inside the separtrix and recombination of electrons and ions that dominates the distribution in the plasma center. The energy dependence of the neutral particle fluxes due to CX is:

$$F(E_0) \sim \int_0^L n_i \cdot n_0 \cdot < \sigma v_{rel} > \cdot \frac{\exp\left(-E_0/T_i\right)}{T_i^{3/2}} \cdot E_0^{1/2} \cdot \exp\left(-\int_0^x \frac{ds}{\lambda_{tot}(s)}\right) dx \qquad (1)$$

Obviously the knowlege of many parameters and cross sections is required to extract temperature information from the data. Since we do not have a possibility to measure the neutral density profile we calculate it self-consistently using the EIRENE code [4], which is based on a Monte-Carlo algorithm and state-of-art cross-section data. Nevertheless, profile data of the electron density, electron temperature and Z_{eff} have to be known. A minority of the measured neutrals originate directly from ion-electron recombination without undergoing further CX processes and is therefore not included in equation (1). However, these additional fluxes are calculated in EIRENE as well.

The fitting procedure uses a parameterisation for the T_i profile combined with a decay length in the scrape-off layer, that linearly interpolates adjustable T_i values at fixed radial positions. The radial coordinate is $\rho_{pol} = \sqrt{(\Psi - \Psi_{axis})/(\Psi_{sep} - \Psi_{axis})}$. The steps of the procedure are: (a) create a calculation grid from magnetic data so that radial surfaces are close to flux surfaces. (b) fill the grid with experimental plasma background data constant on radial surfaces, (c) use start values for the T_i , (d) calculate neutral density with EIRENE, (e) minimize the difference between the measured neutral fluxes and the fluxes calculated with equation (1) using a 'quasi Newton' method. In this step n_0 is taken as constant, (f) iterate (d) and (e) until χ^2 is reasonable small allready after step (d), i. e. when the profile of the neutrals is selfconsistent with the ion temperature. Errors can be estimated from the derivatives calculated during step (e), but the effects of the ion-temperature variation on the neutrals is not included.

It is important that the lines-of-sight are almost normal to the separatrix. In this case, the neutral density in a small area around the penetration point dominates as outer neutral source and the poloidal distribution of the neutrals has not to be accounted for. This would be different for more tangential lines-of-sight. In that case a detailed knowledge of the neutral sources at the vessel walls would be necessary. In our case, beside from the plasma background, there is only one parameter in the neutral density calculation, that is the source strength of the outer source which is included in step (e) of the fitting procedure. For the energy range and plasma conditions discussed here the collision rate is high enough to exclude effects due to ripple trapped particles.

4 Steady state results

Since the quality of the procedure is best studied for simple conditions, we consider here a stationary ohmic discharge (600 kA, −2 T). Fig. 1 shows the T_i profile resulting from the

fitting procedure together with the electron temperature and density profiles using LENA and CXA results [30 eV, 8000 eV]. The dashed error bars belong to the procedure described above. They come along with an error in the neutral source strength of more than a factor of two. It has been checked that for various fixed source strengths in this range, different T_i profiles are found that lead to comparable χ^2 values. Fixing the source strength leads to a significant decrease of the errors of the outer T_i parameters (small bars in Fig. 1). To determine the correct source strength we use EIRENE to calculate the total neutral fluxes 50 cm away from the plasma and adjust the source to simulate the value measured with an ionization-gauge [5] in the vincinity of the CXA diagnostic.

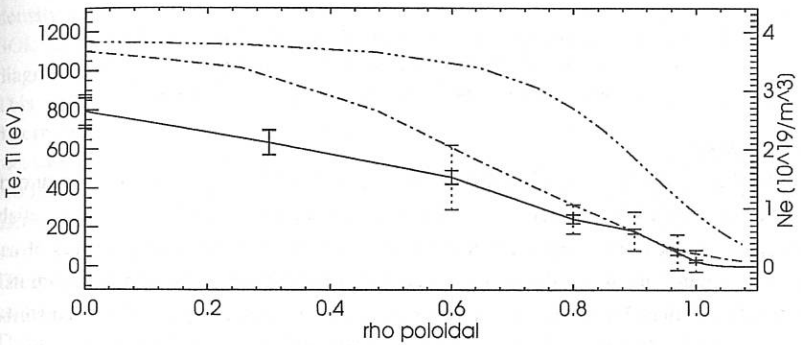

Figure 1 Ion (–) and electron (· –) temperatures as well as electron density (· · ·–) are shown for an ohmic discharge (#4783). The different errorbars (1 σ) for the ion temperature are due to variations in the fitting procedure (see text).

5 Edge localised modes

The highest time resolution with reasonable statistics obtained with the mapping procedure described in section 2 is 200 μs (LENA). On this time scale a strong variation of the shape and intensity of the energy spectra is observed. For these type-I ELMs we do not see changes in the fluxes before the start of the D_α rise, in contrast to results for type-III ELMs at JFT-2M [6]. Fig. 2 shows the ion temperature profiles obtained for a shot with long ELMy H-mode and strong gaspuffing. The period between the type-I ELMs is about 5ms. These profiles are compared with theoretical results of B2–EIRENE calculations [7]. Since only LENA data could be used for this shot, the information comes mostly from the scrape-off layer. There, experiment and modelling agree quite well.. The main feature is a temperature rise during the ELM outside the separatrix. In terms of decay length this is an increase of about a factor of two. The time resolution of the CX-temperature is 1 ms due to the limited time resolution of the electron density needed for the plasma background. This has been improved, so that we hope to present higher time resolutions in the near future.

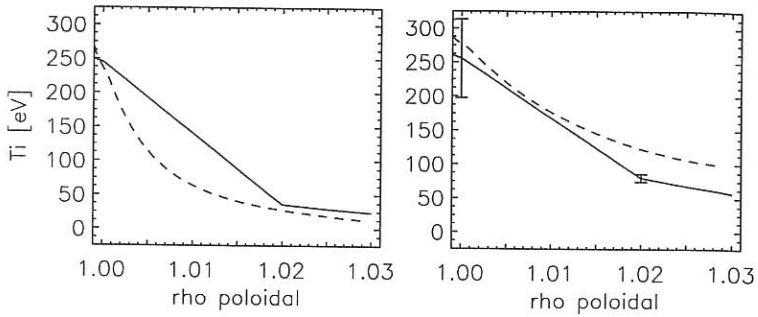

Figure 2 ELM resolved ion temperatures from CX data (solid line) and B2–EIRENE calculations (dashed). ***Left:*** *1 ms before the D_α maximum,* ***Right:*** *0.7 ms after the maximum. integration time for the experimental data is 1 ms (#4906).*

6 Conclusions

The simulation of CX-spectra is shown to be a useful instrument for ion-temperature determination in ASDEX-Upgrade. For well documented shots in stationary phases reliable temperature profiles can be obtained from the scrape-off layer to the center. In cases of neutral beam heating, the depth that can be examined is limited due to non-thermal neutrals at energies higher than 3 keV, but this might be overcome by simulating the other, undisturbed isotope as well. The accuracy at the edge is significantly improved if absolute values of neutral fluxes outside the plasma can be included.

ELM resolved CX-measurements show strong variations in shape on a timescale of 200 μs or less. The T_i Profiles (Δt = 1ms) obtained for the scrape-off layer are in good agreement with B2–EIRENE calculations: During the ELM (the first ms after the MHD event) the decay length is at least a factor of two higher than in the quiet phase 1 ms before the ELM starts.

References

[1] Wagner F., *J. Vac. Sci. Technol.*, **20**, 1211 (1982)

[2] Verbeek H., *J. Phys.*, **E19**, 964 (1986), Verbeek H., Schiavi A.,, *IPP-Report*, **9/103**, (1994)

[3] Bartiromo et al., *Rev. Sci. Instrum.*, **58**, 788 (1987)

[4] Reiter D., *KFA Jülich reports*, **Jül–1947**, (1984),, **Jül–2599**, (1992)

[5] Haas G. et al., *J. Nucl. Mater.*, **121**, 151 (1984), Klepper C. C. et al., *J. Vac. Sci. Technol.*, **A 11**, 446 (1993)

[6] Miura Y. et al., *Phys. Rev. Lett.*, **69(15)**, 2216 (1992)

[7] Coster D. P., *Proc. of the 21th EPS Conference on Controlled Fusion and Plasma Physics, Montpellier, 1994*, **2**, 846, Petit-Lancy, 1994, EPS

Density Profiles in the ASDEX Upgrade Scrape-Off Layer

J. Schweinzer[1], S. Fiedler[1], O. Gehre[1], G. Haas[1], J. Neuhauser[1], D. Wutte[2], HP. Winter[2], ASDEX-Upgrade-, NBI-, ICRH-, ECRH- Team

1) Max-Planck-Institut für Plasmaphysik, EURATOM Association, W-85748 Garching

2) Institut für Allgemeine Physik, TU-Wien, Wiedner Hauptstraße 8-10, A-1040 Wien

1. Introduction

The understanding of particle and energy transport in the scrape-off layer (SOL) of toroidal confinement devices is important for physics interpretation of ongoing experiments, and is vital for the successful engineering of any next-step configuration. In this context reliable density profiles among other SOL plasma parameters are of interest. On ASDEX Upgrade SOL density profiles in the outer midplane are measured by a 35 keV-lithium beam diagnostic [1].

This paper describes the optical detection system and the experimental difficulties to determine radial Li(2p) emission profiles from measured raw signals. These relatively measured LiI (670.8 nm) emission profiles are sufficient to determine electron density profiles [2]. The number of considered atomic Li(nl) states in the unfolding method has been increased to 10 (n = 2,3,4) in order to model more accurately the attenuation of the beam. All used atomic data has been recompiled recently in [3].

The behaviour of SOL density with varying neutral gas density in the divertor chamber will be presented.

The combination of line density measurements by means of DCN-interferometry and SOL density profiles permits to obtain accurate profiles for the full radial range. This method is applied to a NI-heated discharge with strong neon and gas puffing which leads to a H-mode where the plasma is completely detached from the target plates (CDH-mode) [4].

2. Optical Detection System and Determination of Radial Li(2p) Emission Profiles

A poloidal cross section of ASDEX Upgrade with position of both Li-injector and optical detection system can be found in [1]. Li(2p-2s) light emitted from the beam (FWHM 12 mm) is focused by an optical wedge and a system of two lenses onto an array of 3 x 35 individual quartz fibres (diameter 0.4 mm, length 40 m). A rectangular section along the beam axis, 183 mm in radial and 15 mm in toroidal extent, is covered by the detection system. A single spatial channel consists of three fibres arranged perpendicular to the beam axis guiding the light to a chain of lens / IF filter (FWHM 0.5 nm) / lens / photomultiplier. A schematic of such a channel is shown in fig. 1.

The broadness of the sensitive section is chosen similar to the beam diameter in order to discriminate efficiently between beam emission and plasma background light. However, this design requires an almost perfect adjustment of the beam relative to the sensitive section of the detection system.

Calibration of the 35 channels relative to each other is usually achieved by observing the light arising from the interaction of the beam with neutral gas right after termination of the discharge, assuming a constant beam emission over the complete radial detection range. As it

turned out, such calibration factors are very sensitive to the toroidal position of the Li-beam. The main reason for this unwanted behaviour is, that three individual fibres (cf. fig. 1) building up one spatial channel exhibit different transmission efficiencies.

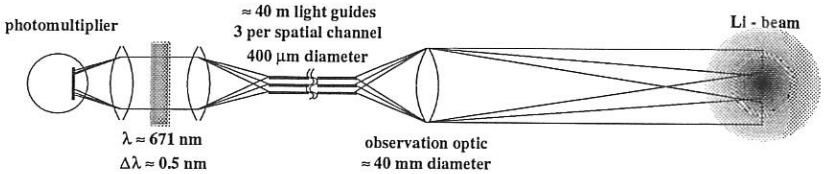

Fig. 1: A schematic of the optical detection system of the Li-beam probe.

When the Li-beam changes its toroidial position during the discharge and in the following time period where the calibration signal is gathered, this non-uniform transmission introduces considerable errors for the determination of Li(2p) emission profiles from the raw signals. Unfortunately, the Li-beam on ASDEX Upgrade is deflected by the magnetic field, although the injector is shielded by 5 cm iron and a 2 mm thick µ-metal box. A remaining vertical magnetic field of ≈ 1.0 to 1.5 mT is sufficient to shift the beam 4 to 6 mm toroidally in the section of observation.

To eliminate these errors we measure calibration factors for different beam positions right after the discharge by deflecting the beam electrically (U...deflection voltage). The calibration factors $c_i(U)$ are found by minimising the function G(U) which corresponds to maximal smoothness of the arising profiles (c.f. equation below, S_i raw signal of channel i). This requirement for determining profiles can be justified by comparing the spatial resolution of the measurement (0.52 mm) with the transition distance $\lambda_{Li} = v_{beam}\,\tau_{2p}$, which is the distance a Li atom travels during the lifetime of the excited 2p state.

$$G(U) = \sum_{i=2}^{34}\left[2\frac{S_i}{c_i(U)} - \frac{S_{i-1}}{c_{i-1}(U)} - \frac{S_{i+1}}{c_{i+1}(U)}\right]^2$$

λ_{Li} serves as a measure how steep gradients of the electron density are smeared out in the corresponding Li(2p) emission profile. For a 35 keV beam λ_{Li} is equal to 2.6 cm which is roughly five times the spatial resolution. Therefore a "scatter" of neighbouring channels in the emission profile is of no physical meaning. It should be noted that collisional deexcitation will decrease λ_{Li}, but never to such small values which could prevent to apply the described method.

In fig. 2 two emission profiles at U = 41 and U = 135 V are compared with the one for U = 83 where G(U) reaches a minimum.

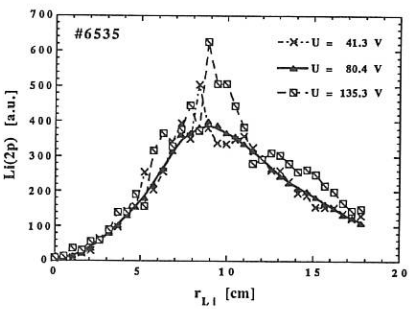

Fig. 2: Li(2p) emission profiles for three deflection voltages U.

3. SOL Density Profiles and their Relation to Neutral Gas Density in the Divertor

We have measured SOL electron density profiles 30 cm below midplane in ohmic discharges, where the neutral density in the divertor, monitored by the flux into an ionization gauge, was increased until a density limit disruption took place. Such profiles are characterised by the density n_e^{sep} at the magnetically determined separatrix (error: ± 5 mm) and by a fall-off-length λ derived by fitting an exponential to the profile over the first 4 cm outside the separatrix.

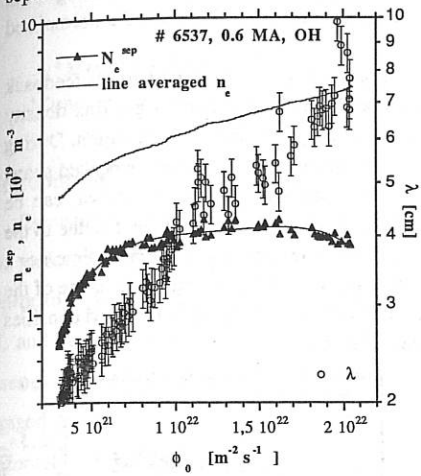

Fig. 3: Electron density n_e^{sep}, line averaged density n_e and fall-off-length λ as a function of neutral gas flux density Φ_0.

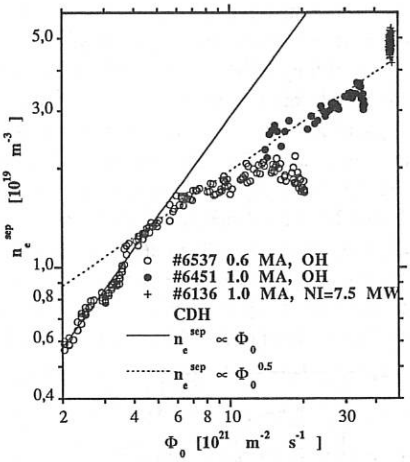

Fig. 4: Electron density n_e^{sep} as a function of neutral gas flux density Φ_0 for three different discharges.

Both parameters are shown in fig. 3 in comparison with the line averaged bulk density n_e from laser interferometry as a function of the neutral gas flux density Φ_0. For values of Φ_0 lower than 5 10^{21} m^{-2} s^{-1} n_e^{sep} increases strongly with Φ_0. While n_e is steadily increasing with Φ_0, the increase of n_e^{sep} becomes weaker and finally even a decrease is found. The fall-off-length λ increases permanently during the discharge and reaches extremely high values close to the disruption. It seems, that there exists an egde density limit which is reached long before the plasma disrupts. This is in agreement with theoretical models which predict a maximum attainable edge density for a given power flow to the SOL based on power balance considerations [5].

n_e^{sep} values of discharges with different plasma current and heating power can be ordered rather well by Φ_0. As long as the discharge stays away from the critical density limit, n_e^{sep} seems to be determined mainly by the neutral gas flux density in the divertor [6]. For high and low Φ_0, however, n_e^{sep} depends differently on Φ_0 (cf. fig. 4).

This statement has to be further supported from analysis of more discharges of different types, in order to find out whether Φ_0 is of paramount importance for n_e^{sep}, or whether other parameters as the power flux into the SOL are of comparable influence [6].

4. Density Profiles from Interferometry and Li-beam Measurements

The DCN interferometer on ASDEX Upgrade measures line densities along 8 different lines of sight, 5 oriented nearly horizontally and 3 vertically, covering mainly the inner separatrix plasma region. An unfolding method which calculates the density profile on flux surfaces from the measured line densities only, suffers from missing information about the plasma edge. Therefore we have improved this method by including SOL density profiles from Li-beam measurements in the unfolding procedure of DCN data. By combining both measurements reliable profiles over the complete radial range as a function of a normalised poloidal flux coordinate are produced.

A long-lasting CDH phase in a NI-heated discharge was obtained with simultaneous feedback control of both the radiation level (neon puff rate) and the divertor neutral gas flux density (D_2 puff rate). In this phase more than 90% of the heating power is lost by radiation. During the initial stage of the CDH phase, the density profile changes slowly to a more peaked shape (fig. 5). From fig. 6, where the ratio between central and edge density is shown, can be deduced that the shape of the profile becomes stationary for $t > 2.1$ s. This effect is due to the appearance of the (1,1) mode [4]. Neither a reduction of the energy confinement time nor a considerable increase of the central neon concentration is accompanied with the change of the density profile [4]. All measurements were time-integrated over 5 ms, thus averaged densities over the small high-frequency type III ELM´s are presented.

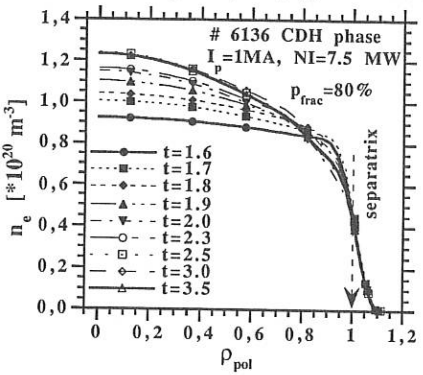

Fig. 5: Density profiles of the CDH phase as a function of normalised flux coordinate ρ_{pol}.

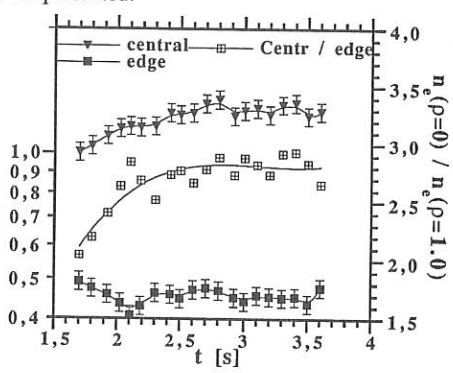

Fig. 6: Central and edge density and the ratio of both during the CDH-phase.

Acknowledgement: S.F. gratefully acknowledges support by the Austrian *Friedrich Schiedel Stiftung für Energietechnik* (project leader: HP. Winter, TU Wien).

References

[1] S. Fiedler et al. contr. paper to *21st EPS Conf. on Contr. Fusion & Plasma Phys.*, Montpellier, 1994
[2] J. Schweinzer et al. *Plasma Phys. Control. Fusion* **34** (1992) 1173-1183
[3] J. Schweinzer et al. *Comp. Phys. Com.* (1995, in print)
[4] O. Gruber et al. *Phys. Rev. Lett.* **74** (1995) 21-24
[5] J. Neuhauser et al. *Plasma Phys. Control. Fusion* **31** (1989) 1551-1568
[6] W. Schneider et al. *J. Nucl. Mater.* **121**, (1984) 178-183

The Behaviour Of Divertor And Scrape-Off Layer Parameters in JET

S.J. Davies, S.K. Erents[1], H.Y. Guo[2], A. Loarte, G.F. Matthews, K. McCormick[3] and R.D. Monk[4]

JET Joint Undertaking, Abingdon, Oxon., OX14 3EA, UK.

[1] UKAEA Fusion, Culham, Abingdon, Oxon., OX14 3DB, UK.

[2] INRS-Energie et Materiaux, Université du Quebec, Canada.

[3] Max-Planck-Institut fur Plasmaphysik, EURATOM Association, 85748 Garching, Germany.

[4] Department of Physics, Royal Holloway College, University of London, Surrey, TW20 OEX, UK.

1. Introduction

Extensive studies of the behaviour of divertor and Scrape-Off Layer (SOL) parameters have been undertaken following the installation of the new JET MkI pumped divertor. Using both reciprocating and fixed Langmuir probe systems it has been possible to simultaneously measure SOL and target profiles over a wide range of plasma parameters during ohmic, L- and H-mode phases of a pulse. The data presented in this paper were obtained from a series of pulses with line-averaged densities of (1.3-6.7)x10^{19} m^{-3} at input powers up to 10MW with (1.5-3.3)T fields. Both horizontal and vertical target configurations were used with normal ($B\wedge\nabla B\downarrow$) and reversed ($B\wedge\nabla B\uparrow$) field.

The main topics covered are comparison of SOL widths in horizontal and vertical target configurations with reversed field, scaling of horizontal/vertical configuration SOL widths in reversed/normal field and the behaviour of target scrape-off widths as a function of X-point height and connection length. The radial heat diffusivity, $\chi_\perp$, was calculated for these data using an analytical model [1] and compared with EDGE2D modelling results. Finally the scaling of JET target power scrape-off widths were compared with the empirically-derived JT-60 scaling [2]. The SOL and target widths quoted in this paper are referenced to the midplane unless stated otherwise.

2. Comparison of SOL widths in horizontal and vertical target configurations

SOL widths in reversed field for both the horizontal and vertical target configurations were measured as a function of density and input power. EDGE2D-U/NIMBUS modelling of these target configurations predicted (for a given density and input power) that the SOL would be thinner in the vertical target configuration owing to the different recycling patterns within the divertor [3].

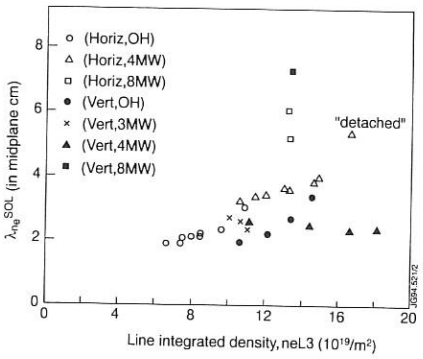

Figure 1 : Comparison between density SOL widths for horizontal and vertical target configurations.

Figure 1 compares the measured density SOL widths, λ_{ne}^{SOL}, for the two configurations as a function of line - integrated density and input power. Generally the vertical target density SOL widths are lower than for the horizontal case as predicted. Under ohmic conditions, λ_{ne}^{SOL} in the vertical target configuration increases less rapidly than for the horizontal case. The increase in SOL width with density is indicative of the approach to detachment (see, e.g., [4, 5]).

3. Scaling of horizontal/vertical configuration SOL widths in reversed/normal field

The best regressions to the horizontal configuration SOL widths in reversed field, using line-integrated density and input power as the regression variables, were obtained by fitting separately to data with input powers of <4MW and to data with input powers of (4-8)MW. The density and temperature SOL widths scaled approximately as $n_e^{0.5}\ P_{tot}^{0.25}$ for input powers of <4MW and as $n_e^{0.4}\ P_{tot}^{0.75}$ for (4-8)MW input power. Correspondingly the pressure and power SOL widths scaled approximately as n_e^{1} ($P_{tot}<4$MW) and as $n_e^{0.75}\ P_{tot}^{0.95}$ (P_{tot} (4-8) MW).

SOL widths recorded in vertical configuration, normal field pulses were scaled using line-averaged density, power to the SOL and q_{cyl} as the regression variables. This approach enables easier comparison between different tokamaks and is consistent with various modelling approaches, e.g.[6]. The regressions were performed over the whole data range and the best fit to the density SOL widths was $P_{sol}^{-(0.5\pm0.1)}\ n_e^{(0.9\pm0.2)}\ q_{cyl}^{-(0.2\pm0.2)}$. Note the small dependence on q_{cyl} and the inverse dependence on P_{sol} in contrast to the reversed field scaling above.

This series of pulses also included an investigation of the effect of top/divertor fuelling position on edge parameters. Initial observations suggest that the temperature/power SOL widths at high densities are lower for top fuelling by up to a factor of two. For divertor fuelling the best fit to the temperature SOL width was $P_{sol}^{-(0.4\pm0.1)}\ n_e^{(0.4\pm0.2)}\ q_{cyl}^{(0.95\pm0.20)}$ and for the power SOL width (which changed little over the range of plasma parameters) it was $P_{sol}^{(0.10\pm0.05)}\ n_e^{-(0.3\pm0.1)}\ q_{cyl}^{(0.23\pm0.08)}$. Little or no difference was observed as a result of top/divertor fuelling in the density SOL width or the target scrape-off widths. The changes to the SOL as a function of top/divertor fuelling is discussed more fully in [7].

4. Behaviour of target scrape-off widths for different X-point equilibria

Equilibria with different X-point height, connection lengths and consequently flux expansions but with the same main plasma parameters were developed to investigate the effect of configuration on divertor performance. The largest variation in target scrape-off widths mapped to the midplane is seen in the density and temperature profiles and is a result of the different flux expansions. The outer target power scrape-off width mapped to the midplane remained unchanged at (0.5±0.1)cm and thus was larger at the target for higher flux expansions. The comments below refer to outer strike zone profiles and the same differences were observed under OH, L- and H-mode conditions.

For the same X-point height (30cm) but different flux expansion (2.3/4.5) the density scrape-off width at the target, λ_{ne}, was the same at, for example, ≈2.7cm (L-Mode) and the corresponding power scrape-off width at the target, λ_P, was 1.4cm/1.8cm. For different X-point height (30cm/15cm), λ_{ne} was ≈2cm (H-Mode) and the corresponding λ_P was 1.1cm/3.4cm when the flux expansion differed by a factor ~3 (2.3/6). For comparable (4.5/6) flux expansions λ_{ne} was 2.7cm/3.2cm (L-Mode) whilst λ_P was 1.8cm/2.9cm.

5. Determination of radial heat diffusivity, $\chi_\perp$, from target power scrape-off widths

The target power scrape-off width at the midplane, λ_P^{Tgt}, calculated using analytical modelling [1] and modified for JET specific quantities [8], is given by

$$\lambda_P^{Tgt} = \left(\frac{2e}{7}\right)^{7/9} \left(n_e \chi_\perp A_\perp\right)^{7/9} P_{tgt}^{-5/9} \left(\frac{7L}{8\pi R \kappa_o (B_\theta / B)_u}\right)^{2/9} \quad (1).$$

$\chi_\perp$ has been calculated using (1) for the data recorded in the various configurations described in this paper and was found to have a strong dependence on power to the target as shown below.

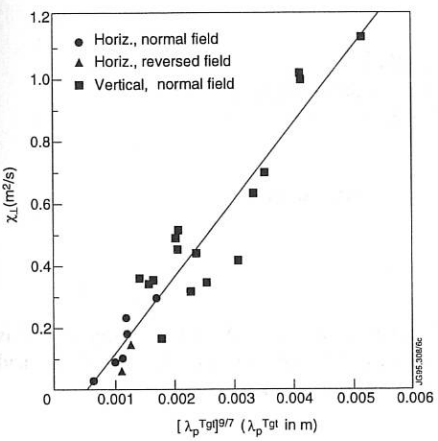

Figure 2 : $\chi_\perp$ plotted as a function of $(\lambda_p^{Tgt})^{9/7}$.

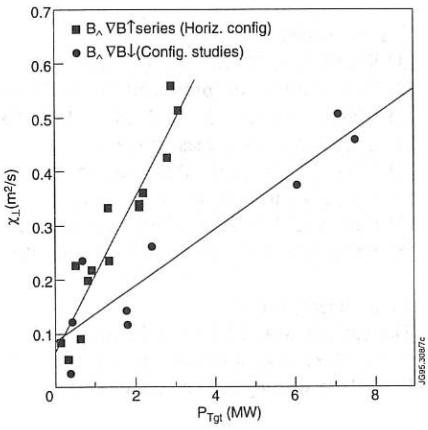

Figure 3 : $\chi_\perp$ as a function of power to target.

EDGE2D-U/NIMBUS modelling of similar low density ohmic discharges with horizontal and vertical target configurations gives a $\chi_\perp$ of 1.3 m^2/s with $D_\perp = 0.12$ m^2/s [4] which is an order of magnitude higher than that calculated here.

6. Comparison of JET target power scrape-off widths with JT-60 scaling

The behaviour of λ_P at the target within the framework of the JT-60 empirical scaling law [2] is shown in Figure 4, where $1/\lambda_P$ at the target for the reversed field, horizontal target and the normal field, vertical target series are plotted along with the JT-60 data.

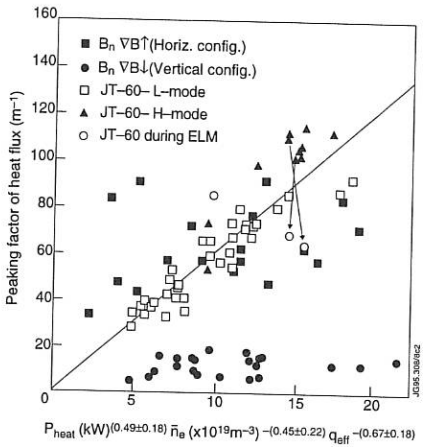

Figure 4 : $1/\lambda_P$ at the target as a function of the JT-60 empirically derived scaling law.

The horizontal target data represents the best general agreement with the JT-60 data. The effect of configuration is clearly shown by the vertical target data which should be increased by a factor of seven for direct comparison with the JT-60 data. These JET data clearly show the discrepancy with the JT-60 data. The JT-60 scaling assumes a constant $\chi_\perp$, which as the previous section has shown, is not the case. The best fit scaling of $1/\lambda_P$ for the horizontal target data was $P_{tgt}(kW)^{(0.14\pm0.04)}$ $n_e(x10^{19}m^{-3})^{-(0.85\pm0.22)}$ $q_{cyl}{}^{-(0.59\pm0.10)}$.

7. References

[1] Keilhacker, M. et al., Physica Scripta, **T2/2**, 443 (1982)
[2] The JT-60 Team, presented by M. Shimada, IAEA-CN-56/a-1-3, **1**, 57 (1993)
[3] Vlases, G. et al., J. Nucl. Mat., **196-198**, 392 (1992)
[4] Loarte, A. et al., these proceedings
[5] Monk, R. D. et al., these proceedings
[6] Itoh, S-I and Itoh, K., Plas. Phys. Control. Fus., **36**, 1845 (1994)
[7] Harbour, P. J. et al., these proceedings
[8] Stangeby, P. C., personal communication

Acknowledgements
The authors would like to acknowledge D.J. Campbell and Task Force D for their support of this work. They also acknowledge the expertise of C. Hogben, G. Kaveney, G. Neill, J. Vince and D. Wilson whose skill and commitment have made such measurements possible.

Edge Pressure Gradients and Velocity Shear Behaviour during H-modes and ELMs in the new JET Divertor Configuration.

N C Hawkes, D V Bartlett, D J Campbell, N Deliyanakis, R M Giannella, P J Lomas, N J Peacock, L Porte, A Rookes*, R I A Sartori, P R Thomas and G Vayakis

JET Joint Undertaking, Abingdon, Oxon, OX14 3EA, UK
†UKAEA Euratom Association, Culham Laboratory, Abingdon, Oxon, OX14 3DB, UK
*Imperial College of Science, Technology and Medicine, London, UK

Introduction

Improved measurements of ion and electron pressure gradients and ion rotation velocity at the edge of H-mode plasmas in JET's new divertor phase have been studied and analysed with regard to the relationship of velocity shear profile and steep pressure gradients with enhanced confinement and edge stability.

The ECE hetrodyne radiometer has been upgraded to have the best radial resolution possible, limited by the layer width needed for the plasma to become opaque. The upgraded edge change exchange diagnostic makes simultaneous measurements of impurity ion temperature, density and flow velocity. Both diagnostics have a radial spatial resolution of 1 cm or less under optimum conditions. Measurements of electron density on a corresponding scale are made with a multi-channel reflectometer.

Poloidal Velocity Measurements During Elms

During strong neon gas puffing experiments an intermittent periodic ELM behaviour is established. Taken together with the bright emission from the neon impurity these conditions yield the most sensitive measurements of the poloidal flow. Under these conditions the scatter in the poloidal velocity measurement for a chord located in the steep part of the temperature gradient, where the poloidal velocity has been found to be highest in the DIII-D measurements[1], is within $\pm 5\, km.s^{-1}$ of zero during both the ELMy and quiescent H-phases with no systematic shift between the two phases.

During these intermittent ELMs the gradients of impurity density vary significantly compared to the quiescent H-phase, whilst those of the ion temperature are almost unaffected. The resilience of the T_I profiles to ELMs is characteristic of most types of ELMs in JET.

Ion Temperature Gradients from Sweeping

During high power discharges the X-point is swept at 4 Hz across the target to reduce local heat loading. This also has the effect of moving the separatrix position at the midplane where the charge exchange observations are made. When a single chord of the diagnostic intersects the steep part of the temperature profile then the sweeping takes this chord up and down the profile, modulating the temperature measurement. The amplitude of this T_I modulation compared to the sweep amplitude provides a direct measurement of the gradient, and this is in agreement with the results from the profile measurements. Gradients of T_I up to $66\, keV.m^{-1}$ have been recorded from adjacent chord differences, where the steep gradient region lies entirely between two chords.

H-mode Ion Profile Evolution

In the new JET divertor configuration the H-mode transition is generally characterised by a gradual evolution of the D_α through an ELMy phase to a quiet H-mode. In such cases there is a slow development in the pressure profile. Several theories of the H-mode [2,3, for example] invoke a sheared poloidal $\mathbf{E}\times\mathbf{B}$ flow to account for the confinement changes. In the JET measurements there is no evidence of such a flow in the impurity ions, implying that their diamagnetic flow speed is balanced by their $\mathbf{E}\times\mathbf{B}$ (or $v_{||}$) motion. The background ion diamagnetic flow would be greater than that of the impurities (for the same pressure profiles) due to their lower charge giving, in general, a different poloidal flow speed. Therefore it becomes important to study the time evolution of the radial electric field.

The chordal charge exchange measurements allow the determination of the radial electric field from the zero order force balance of the impurity ions, $\mathbf{E} = \frac{\nabla p}{Zen} - \mathbf{v}\times\mathbf{B}$. In the slow H-transition cases, where the poloidal flow does not appear to change, the radial field evolution can be evaluated from the pressure gradients and the toroidal flows alone. In these cases a negative well in E_r develops of up to $35\,kV.m^{-1}$ at 2–3 cm inboard of the LCFS due to the pressure gradient terms on a timescale of 0.5–1 s, while 1–2 cm inboard of this minimum the field becomes positive due to the increase in toroidal rotation. The region of strong shear in the toroidal rotation therefore lies at a different radius from the region of highest pressure gradient.

Clear, direct evidence that the shear in toroidal rotation forms inboard of the maximum ion temperature gradient is seen in particular discharges where, for a chord that lies within the temperature gradient, its toroidal rotation is almost zero during the entire H-mode. For this to occur, the gradient in v_ϕ must lie at least 1 cm inboard of the gradient in T_I.

A fast H-mode transition was set up in order to study the changes in the profiles immediately before and after the H-transition with a magnetic geometry giving close to optimum diagnostic space resolution. Figure 1 shows the time evolution of D_α, impurity density, temperature and poloidal flow during such an H-mode. At 19.25 s the D_α intensity falls abruptly coincident with a sawtooth crash and the transport barrier forms, as indicated by the ramp-up of the C VI density at the inner chords (R≤3.778m). In the 100 ms before the transition there is some evidence of transition ELMs, but no steepening of the impurity pressure profiles. There appears to be a small change in poloidal flow ($\sim 5\,km.s^{-1}$, in the electron diamagnetic direction) at the time of the transition at 3.802 m, at the edge of the transport barrier—inboard of this radius there is no change within the errors.

Two radial profiles of electric field are shown in figure 2. The profiles have been obtained by averaging over 100 ms periods immediately preceeding and following the H-transition. The poloidal rotation (and errors in this measurement) dominate the total radial field, although, even 50 ms after the transition there is evidence of a negative field well appearing due to the ∇p terms. However, from the time traces (figure 1) it is clear that this source of E_r develops linearly with time following the transition and hence is not involved in the physics of the transition itself.

Edge Temperature Gradients

Steep gradients of both T_I and T_e are seen in the edge region, falling off sharply over approximately one ion poloidal gyroradius. Figure 3 shows the time behaviour of the T_I and T_e gradients. Since there is some uncertainty on the ECE radii from the calculated equilibrium fields, the maximum gradient at the edge of each profile is indicated. The two values agree quite closely, rising from $\sim 10\, keV.m^{-1}$ at the start of the main heating pulse to over $65\, keV.m^{-1}$. The gradient is not seen to follow a local (toroidal) velocity shear, but rather the velocity evolution over a wider region, peaking when v_ϕ reaches a maximum on the inner channel. At a density of $10^{19}\, m^{-3}$ this maximum gradient gives a pressure gradient $>100\, kPa.m^{-1}$. Since collisionality, ν_i^*, is low, a large parallel current density $j_{bs} \sim \epsilon^{-1/2} \nabla p / B_\theta \sim 500\, kAm^{-1}$ results from the bootstrap current. This is of the order of the central current density and so can, when fully developed, reduce local magnetic shear considerably. This must be taken into consideration when assessing, for example, ballooning and external kink stability of the edge.

Conclusions

An extensive dataset has been built up of edge impurity (C and Ne) poloidal rotation in the new JET. The evidence is that there is no such rotation in JET H-modes to within $|v_\theta| < 5\, km.s^{-1}$ within the region of the transport barrier, consistent with previous JET results[4]. Outboard of this region, the lower emission brightness results in larger errors although a slow drift in the electron diamagnetic direction is sometimes seen in the outermost channels. The E_r profile in JET develops a negative well at the transport barrier, relatively slowly as a consequence of confinement changes, not coincident with the H-transition.

Profiles of ion and electron temperature show strong gradients (up to $65\, keV.m^{-1}$). This implies the existence of a strong bootstrap current, of order of the central density, therefore considerably reducing local magnetic shear and hence affecting edge ballooning and kink stability.

References

[1] P. Gohil *et al.*, Nuclear Fusion, **34**, 1057 (1994)

[2] K. C. Shaing, E. C. Crume Jr. and W. A. Houlberg, Physics of Fluids B, **2**, 1492 (1990)

[3] H. Biglari, P. H. Diamond and P. W. Terry, Physics of Fluids B, **2** 1 (1990)

[4] N. C. Hawkes, Controlled Fusion and Plasma Physics, Proceedings of the 20th EPS, Lisboa, **17C** 7 (1993)

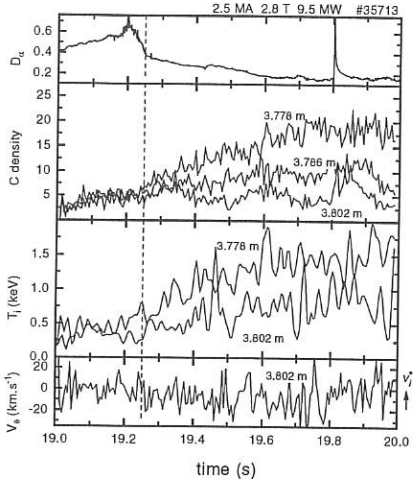

Figure 1: *Time traces of impurity density, temperature and poloidal flow during a fast H-transition. Neutral beam injection is applied from 59.0 s. The poloidal flow at the outermost radial position shows a change of about 5 km.s^{-1} between the L and H-phases. Chords further inside the plasma show no systematic change at the transition, and fluctuations in the measurements are less than 5 km.s^{-1}.*

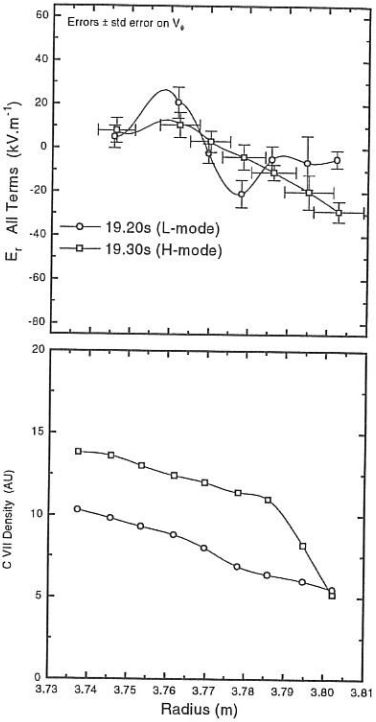

Figure 2: *Profiles of the time evolution of E_r obtained from the data of figure 1 at two times, 50 ms before and 50 ms after the H-transition with the corresponding n_z profiles. The vertical error bars are ±one standard error ($\sigma/\sqrt{N}$) and are taken from the v_θ measurements since these dominate the errors. The radial error bars represent the geometric resolution of the diagnostic. The separatrix position from EFIT is 3.843 m.*

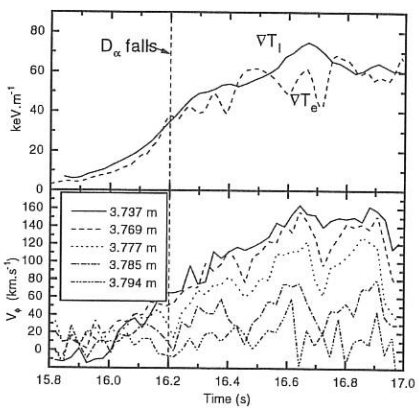

Figure 3: *Time evolution of the peak ion and electron temperature gradients and toroidal velocity profile in an H-mode discharge.*

The SOL in Diverted Discharges in the Texas Experimental Tokamak (TEXT)

William L. Rowan, Roger. D. Bengtson, Xavier Bonnin, R. V. Bravenec, T. P. Crowley,† K. W. Gentle, J. W. Heard,† P. D. Hurwitz, A. Ouroua,† P. E. Phillips, B. Richards, K. A. Schroder, P. M. Schoch,† D. J. Storek, and D. L. Winslow
Fusion Research Center, The University of Texas at Austin, Austin, Texas 78712, USA
†Rensselaer Polytechnic Institute, Troy, NY 12180, USA

1. Introduction

In the Texas Experimental Tokamak, TEXT-U, tokamak plasmas are produced in diverted or limited configurations [1] in a boronized or unboronized vacuum vessel and can be heated with 600 kW of ECRH. SOL experiments are yielding interesting results on the source of plasma turbulence, on recycling and impurity asymmetries near the divertor tiles, and on asymmetries in density fluctuations. Because electrostatic turbulence appears to be the mechanism for cross-field transport in the SOL, the main goal is to identify possible turbulence drives. SOL simulations will eventually be used to compare predicted drives to experiment. Until then, the simulations are being used to investigate up-down asymmetries near the divertor tiles.

2. Experiments to Identify the Turbulence Drives

Cross field transport in the SOL is well correlated with the transport due to electrostatic turbulence. The source of the turbulence remains elusive, but the turbulence properties have been identified. One of these may be particularly valuable. The magnitude of $k_{\|}$ relative to k_{θ} may suggest a spatial location for the drives. Since parallel wave numbers for the turbulence are small, the turbulence drives may be well separated from the point of observation -- as far away as the divertor plates or the limiter. Hence, turbulence may be due to atomic drives resulting from ionization [2] or radiation [3] near the divertor plates or limiter or due to curvature drives [4] that depend on unfavorable magnetic curvature along only one limited region of a magnetic field line.

2.1 Ionization Drive

To understand the ionization drive, simply consider the electron source, $n_e S n_0$, due to the ionization of neutrals. Clearly, a density fluctuation will act through this term to increase the level of fluctuations. The drive was examined in detail [2] to produce both a critical level of ionization for the instability to exist and a prediction of the associated particle transport.

To search for this drive, the TEXT-U experiments were conducted in a poloidally limited discharge to make the drive as large as possible. In this discharge, the local ionization produced near the toroidally localized limiter is as high as can be produced in TEXT-U. In a series of discharges, the electron density was increased shot by shot. As the density increased, the ionization increased, but the relative fluctuation level was independent of the increase. Though one conclusion is that the ionization drive does not exist, a second is that the fluctuation level is simply saturated. In a second experiment, the fluctuation level was measured in close proximity to the toroidally localized limiter and as a function of distance from it. Because the neutral density is a decaying function of distance from the limiter, this was a measurement of fluctuation level as a function of neutral density along a magnetic field line. The fluctuation level was independent of the local ionization rate. Though interesting, this result may simply reflect the magnitude of $k_{\|}$. Finally, the transport due to the ionization drive was estimated. The predicted transport is directed inward and more than an order of magnitude smaller than the measured transport which is directed outward. It is concluded that the ionization drive does not play a role in TEXT-U and may not exist at all. The latter point is consistent with a recent critique [5] of the original theory.

2.2 Radiation Drive

If the radiated power, P_{rad}, is represented in terms of the electron density, n_e, the impurity density, n_z, and the cooling rate, I_z, in the usual way as

$$P_{rad} = n_e \sum_z (n_z I_z) ,$$

then the growth rate for this instability is [3]

$$\gamma = \frac{2\, n_z}{3} \left(\frac{2\, I_z}{T_e} - \frac{\partial I_z}{\partial T_e} \right) .$$

In TEXT-U experiments, the effects of the second term were sought. Were the cooling rate to decrease with increasing T_e (as suggested in the original work on this drive [2] following results from calculation based on coronal models, [6] for example), then the instability would grow. In TEXT-U experiments, T_e in the plasma periphery was modulated with ECRH. The plasma radiation appeared to be in phase with the temperature at the plasma edge, hence the second term of the above equation is not destabilizing. Furthermore, this might almost have been expected because the inference of a destabilizing influence of that second term is based on a coronal model for impurities which, of course, omits transport.

2.3 Curvature Drive

The toroidal curvature of the magnetic field lines may be a source for turbulence in tokamaks [4]. On the open field lines in the SOL, some fluid modes may be unstable for the appropriate average curvature of the magnetic field lines with respect to the pressure gradient. In a tokamak, curvature is stabilizing on the inner side of the torus (on the high field side of the poloidal cross section) and destabilizing on the outer side (on the low field side).

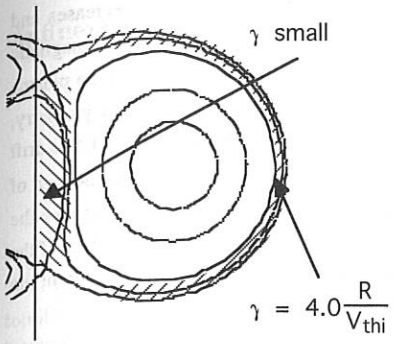

Figure 1. Curvature drive in a DN discharge

On TEXT-U, curvature drives can be studied by comparing turbulence measurements in two different configurations, poloidally limited and double null (DN). In the double null configuration (see figure 1), the SOL on the high field side (favorable curvature) is effectively isolated from that on the low field side (unfavorable curvature). The growth rate, γ, for the curvature instability at $k_{\|}=0$ in each of the two configurations can be estimated using a simple model [4] due to Garbet. The results are shown in Figure 1 where R is major radius, and V_{thi} is ion thermal velocity. For the poloidally limited configuration, $\gamma = 2.5 \frac{R}{V_{thi}}$ for the entire SOL. As shown in figure 2, the turbulence level is as predicted, higher on the low field side (LFS) than on the high field side (HFS). This is consistent with previous findings [7]. A similar experiment in a limited configuration in TEXT-U gave essentially the same fluctuations on both the HFS and on the LFS.

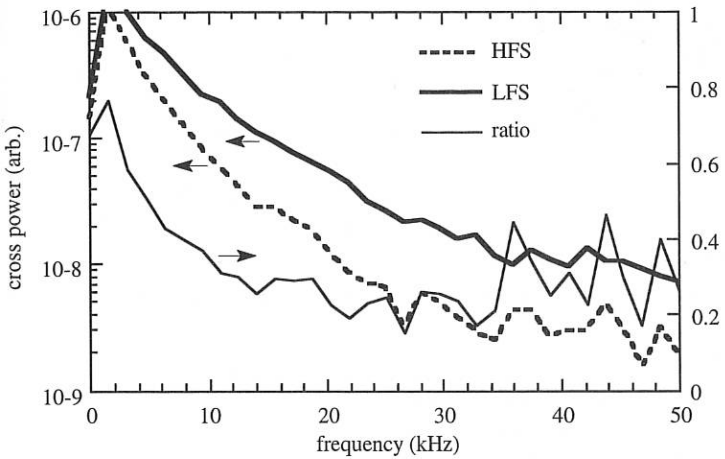

Figure 2. Comparison of HFS and LFS turbulence in a diverted discharge

3. SOL simulation. A study of up-down asymmetry.

In equatorial single-null discharges (see figure 3a), there is an up-down asymmetry in D_α and impurity emission from the vicinity of the divertor plate. The spectroscopic viewing chords are shown in figure 3a. The radiance measurements and simulations are in figure 3b. The tangent radius of 3b is measured with respect to the center of the magnetic configuration.

The degree of asymmetry is independent of plasma current direction, but decreases and eventually reverses with increasing n_e. The divertor plate construction and the magnetic configuration are up-down symmetric, so this configuration is ideal for study of the plasma drives for up-down asymmetries. In a first attempt to understand the measured asymmetry, the B2-Eirene [8] plasma simulation code was used to examine the impact of the $\nabla T \times B$ drift on D_α emission at the divertor plate. The inclusion of the drift correctly predicts the sign of the asymmetry. Addition of carbon impurities (drift + C of Fig. 3b) further enhances the asymmetry and improves agreement with the experimental data. The increased effect of the $\nabla T \times B$ drift with carbon may simply be due to enhancement of the temperature gradient via radiative losses. However, the dependence on density is not yet understood.

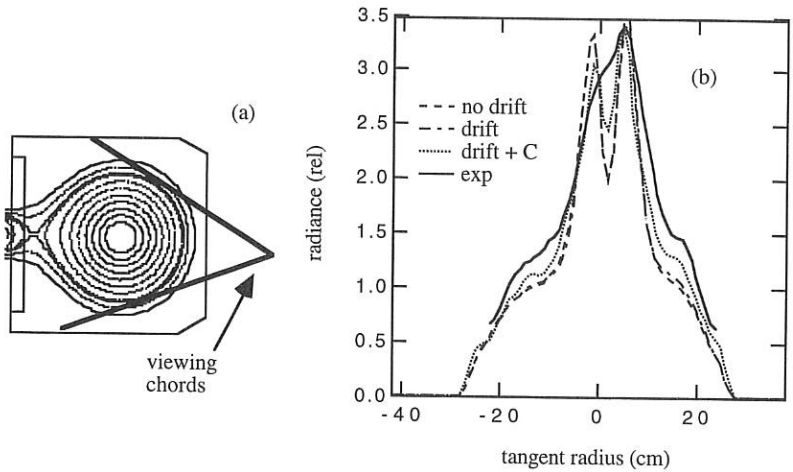

Figure 3. D_α emission: simulation and experiment.

Acknowledgements

This work was supported by the U. S. Department of Energy under grant DE-FG05-88ER-53267 to The University of Texas.

References

[1] W. L. Rowan, et al., J. Nucl. Mater. 220-222, 668 (1995)

[2] A. S. Ware, et al., Phys. Fluids B 4, 877 (1992)

[3] D. R. Thayer and P. H. Diamond, Phys. Rev. Lett. 65, 2784 (1990)

[4] X. Garbet, et al., Nuclear Fusion 31, 967 (1991)

[5] D. W. Ross, Phys. Plasmas 1, 2630 (1994)

[6] D. E. Post, et al., Atom. Data Tables 20, 397 (1977)

[7] M. Endler, et al. J. Nucl. Mater. 220-222, (1995).

[8] R. Schneider et al., J. Nucl. Mater. 196-198, 810 (1992)

Influence of L– and H–mode and Rotational Transform on the Edge Density Profiles in W7-AS

G. Kocsis[1], **S. Zoletnik**[1], S. Fiedler[2], P. Grigull[2], G. Herre[2], K. McCormick[2], J. Schweinzer[2] and W7–AS Team[2]

[1] KFKI–RMKI, P.O.Box 49, 1525 Budapest-114, H-1525 HUNGARY

[2] Max-Planck-Inst. für Plasmaphysik, EURATOM Association, D-85748 Garching

In W7-AS plasma performance is strongly affected by the three dimensional edge topology. Two principally different edge topologies can be distinguished: a) at low rotational transform ($\iota \leq 0.4$) the last closed flux surface is determined by the limiters, whereas b) at higher ι separatrix-dominated configurations are possible. For $\iota_a \simeq 0.53$ the H-mode of W7-AS is accessible above a power and density threshold[1]. Transient phenomena (dithers, ELMs) frequently appear before and after the L-H transition.

The edge electron density distribution depends sensitively on both the magnetic field topology and the confinement mode, thus its investigation can reveal phenomena leading to changes in global plasma performance. This paper presents a detailed study of the density profile behaviour for different edge topologies and confinement modes.

The experiments were done using the high-energy neutral Lithium beam diagnostic, which can measure $n_e(r,t)$ from the outer SOL to deep within the main plasma[2]. The time - ($\leq$0.2ms) and spatial -(0.6-1cm) resolution of the diagnostic permits determination of both the fast temporal variation of n_e and its fine radial structure.

Density profiles for different edge configurations. In order to get a more symmetric SOL in W7-AS, the main limiters were replaced by a set of poloidal limiters (two per field period). The structure of the edge was investigated at different rotational transforms, ECRH heating powers and line integrated densities.

Fig. 1. shows as a contour plot the density profile *vs* edge rotational transform ι_a (low β, low density, net current free, $B_0 = 1.25T$, ECRH discharges) for the separatrix dominated case ($\iota \geq 0.4$). The thick solid, dashed and dash dot lines on this figure represent the (vacuum field calculated) boundary of the scrape-off layer with a connection length of less than 50 m in the positive and negative toroidal direction, and the separatrix position, respectively. It can be clearly seen that characteristic changes in the position of these lines are accompanied by similar changes in the contour lines of the density in the SOL, justifying the reliability of the vacuum field calculation.

This figure establishes that the plasma globally shrinks for increasing ι_a values. Repeated deviations from this general trend can be observed around these rotational transform values where the natural 5/m islands appear: 0.463, 0.512, 0.57 and 0.635 (see the 2D plot of *Fig. 2.*). Moving along the ι_a axis from lower values a shoulder appears step by step accompanied by a steeper density profile outside the shoulder. Moving further in ι_a the density increases behind the shoulder, which gradually disappears this way. After this the profile moves inside until the next resonant value where a similar shoulder appears. One might explain the appearance of the shoulder with the presence of the 5/m islands[3] partly intersected by the limiters, because they introduce a radial short cut in the particle and energy transport by a strong parallel component. The radial position of the profile shoulders agree well with the position of the vacuum field calculated islands.

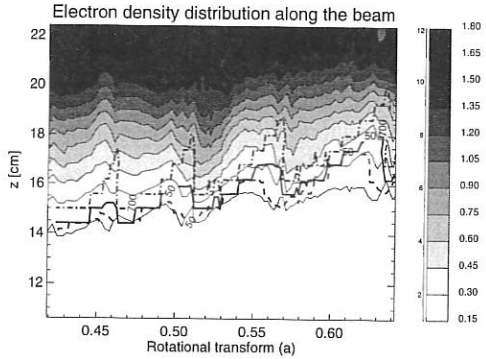

Fig. 1. Edge and SOL electron density distribution as a function of rotational transform. The scale on the right side represents the electron density in $10^{13}cm^{-3}$ units. The figure is compiled from a series of shots.

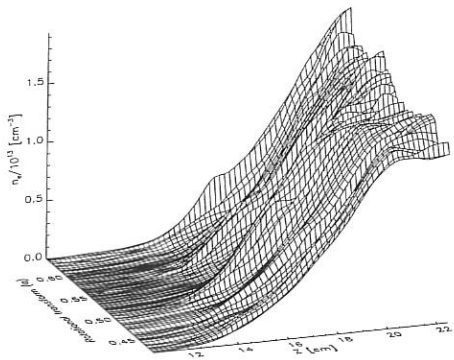

Fig. 2. Density profiles as on Fig. 1. showing the appearance of shoulders at certain rotational transform values.

For the limiter dominated case ($\iota \leq 0.4$) neither the density profile nor the vacuum field calculated connection length changes drastically in the SOL at different rotational transforms. Density e-folding lengths (in flux coordinates) in the SOL in a density scan with constant ECRH heating power (140GHz, P=460kW, B=2.5T, B_z=25mT, $\iota_a = 0.34$) and in a power scan with constant volume averaged density (70/140GHz, B=2.5T , B_z=17 mT, $\iota_a = 0.34$, $\langle n_e \rangle_{vol} = 1.48 \times 10^{13} cm^{-3}$) are shown in *Fig. 3.* The e-folding length decreases with increasing density and increases with the non radiated part of the heating power. These results are in good agreement with Langmuir probe measurements[4,5].

Density profile change at the L-H transition. L-H mode transition is achieved at $\iota \simeq 0.5$, $B_t = 2.5T$ with 140 GHz ECRH heating if the electron density of the plasma is increased above a certain threshold. The onset of the H-mode is best characterized by a sharp drop in the H_α radiation from the limiter and wall. Due to the improved confinement the line averaged electron density of the plasma increases after the transition even if the gas feed rate is reduced.

The difference between the L and H mode electron density profiles is shown in *Fig. 4.* As one can see, the profile steepens significantly around the LCFS, indicating the improvement of confinement. Analysis of the fast time evolution around the L-H transition shows that this steepening develops in about 5 ms.

The change of the density profile in the H-mode phase of the discharge during a

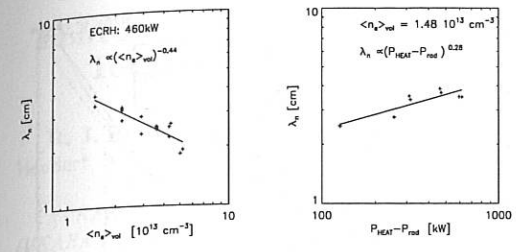

Fig. 3. SOL electron density e-folding length as a function of volume averaged density and total non radiated part of the power for series of shots.

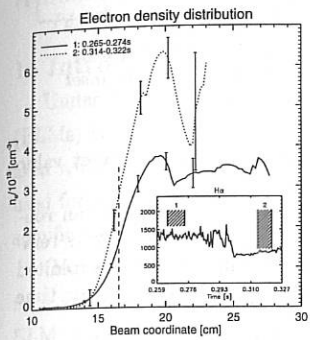

Fig. 4. L and H mode electron density profiles close to the L-H transition.

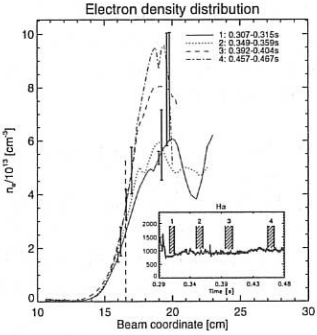

Fig. 5. Electron density profile change in H-mode during a density ramp-up.

continous increase of the line integrated density is shown in *Fig. 5.* Although the line density, and also the local density in the core plasma increases by a factor of two between the first and last profile, there is no change in the SOL density distribution. The decay length of an exponential fit to the SOL density profile shows no change opposed to the behaviour found in the L-mode at $\iota \simeq 0.3$. This "locking" of the H-mode SOL density profile is in agreement with similar tokamak measurements[6].

Transient phenomena in H-mode shots The L-H transition is preceeded by fluctuations of the H_α signals. The modulation amplitude increases towards the transition in the form of pulses with a fast ($0.5ms$) rise and a slow ($\approx 1ms$) decay time. Similar phenomena are often observed in the H-mode, at a lower frequency. The Li_{2p} light profile exhibits characteristic changes during these transients, but the calculation of the density profile change is difficult due to similar changes of the background light profile which is measured by chopping the Li-beam every 60 ms. In some cases nearly identical pulses (in the H_α signal) can be found in the same shot at close times, one during chopper time interval and the other during a beam-on interval. In these cases the background light can be subtracted from the total detected light by using the background light time evolution found during the pulse in the chopper interval. Several events have been processed this way, and a characteristic density profile change can be deduced from this measurements. *Fig. 6.* shows density profiles at different times during an H_α pulse before the final L-H transition (dithering) and in the H-mode (ELM). Both figures show the same characteristic change; the profile flattens around the LCFS and becomes closer to an L-mode profile. In this sense, there is no difference between dithering and ELMs. Observations also show, that the density profile starts to change about 200 μs before the H_α signal starts to rise.

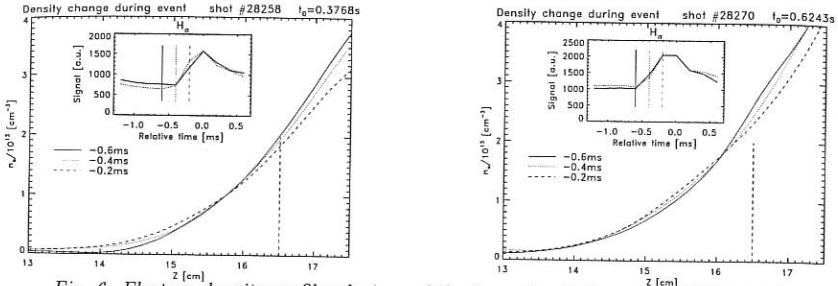

Fig. 6. Electron density profiles during a dithering pulse (left) and an ELM (right). Part of the H_α signals (for Li-beam-on and beam-off pulses) is shown as an inset for reference.

This time delay is equal to the time resolution of the diagnostic, thus its exact value cannot be determined.

Conclusions. It was found that the high energy Lithium beam disgnostic can routinely measure the edge electron density distribution of W7-AS plasmas with $0.2ms$ temporal and $\approx 1cm$ spatial resolution. However, the temporal resolution can be exploited only if a good estimate is available for the background light intensity on the same time scale.

Density profile changes in the edge and SOL are in good agreement with changes in the calculated vacuum magnetic field configuration. Local shoulders appear close to the calculated position of magnetic islands. The SOL e-folding length of the density distribution increases with the total edge power loss and decreases with increasing volume averaged density, indicating similar changes in the SOL cross diffusion coefficient. These results are in good agreement with Langmuir probe measurements[4,5].

The SOL and edge density distribution steepens at the L-H transition in about 5 ms. In the H-mode the SOL density distribution becomes independent of the line averaged density, in agreement with observations on ASDEX[6]. The density profile change during a dithering cycle, is very similar to changes during an ELM, and both have characteristics resembling an H-L backtransition. The wall H_α signal delay shows a few hundred μs propagation time for the ELM density pulse to reach the wall.

Acknowledgements. The work of one of the authors (S.F.) has been partially financed by the Austrian "Friedrich Schiedel Stiftung für Energietechnik" (project leader: Hp. Winter, Institut für Allg. Physik, TU Wien, AUSTRIA). The authors from KFKI-RMKI would like to thank the hospitality and support of IPP-Garching.

References

[1] V. Erckmann, *et al.*, *Phys. Rev. Lett.* **70** 2086 (1993)

[2] K.McCormick, et al., 21th EPS Conf., Europhy. Conf. Abs. **18b**, III–1268 (1994)

[3] J. Das, *et al.*, this conference.

[4] P. Grigull, *et al.*, *10th Int. Stellarator Conf. 22-26 May, Madrid* (1995)

[5] Y. Feng, *et al.*, this conference.

[6] G.K.McCormick et al., *J. Nucl. Mat.* **162-164** 264 (1989)

ELM Related MHD Activity on the COMPASS-D Tokamak Compared with ASDEX-Upgrade

R. J. Buttery†, D. A. Gates†, A. Colton†, H. de Blank*, S. J. Fielding†, T. C. Hender†, A. W. Morris†, M. Maraschek*, M. Schittenhelm*, W. Suttrop*, M. Valovič†, H. Zohm* and the COMPASS-D and ASDEX-Upgrade teams.

†*UKAEA Government Division, Fusion, Culham Laboratory, Oxon, OX14 3DB. UK. (UKAEA / EURATOM Fusion Association).* **ASDEX-Upgrade Team, Max-Planck-Institut Für Plasmaphysik, Euratom-IPP Association, D-85740 Garching, Munich, Germany.*

1. Introduction

Understanding the underlying physical mechanism giving rise to Edge Localised Modes (ELMs) is an important first step in controlling this phenomena which has been associated with the H-mode on numerous tokamaks. ELMs degrade confinement, but can be used for control of density rise and impurity accumulation in H mode. They also have a significant impact on peak power loads at the divertor, an important issue for ITER.

On both COMPASS-D and ASDEX-Upgrade, which have similar, ITER-like, magnetic geometry, these ELMs fall into two categories - Type I and Type III ELMS. Type III ELMs characteristically occur just above the L-H power threshold and have a repetition rate that decreases with increasing power. Type I ELMs are larger, occurring after ELM free H modes, with a lower repetition rate which increases with input power. Both these types of ELMs exhibit certain types of precursors, such as magnetic and/or temperature oscillations, and other accompanying activity. In this work, we examine the signatures of ELMs on these machines, and model them to see if the observed effects during an ELM can be explained by the magnetic modes seen to grow in the ELM precursor.

2. ASDEX-Upgrade Results

ASDEX-Upgrade (I_p =0.6-1.4MA, B_T=1-3T, R = 1.65m, a = 0.5m) is equipped with electron cyclotron emission (ECE) radiometry with good spatial (1cm) and temporal ($2\mu s$) resolution at the edge of the plasma and Mirnov coils. Infrared data and Langmuir probes provide measurements at the target plates.

There is clear evidence for a magnetic precursor to type III ELMs, with frequency $\sim$ 70kHz, which appears to be in phase with oscillations in the ECE measurements from the edge of the plasma. It is interesting to note that temperature precursors also appear to be present for type I ELMs, but at lower frequency (10-20) kHz and less coherent. However, no similar precursor has yet been observed with the Mirnov coils.

The ECE data (Fig 1) show that the ELM is localised within the outer few cms of the plasma, with the temperature perturbation propagating further in. The precursor is localised within the outer 1-2cms. During the ELM, power is ejected into the scrape-off layer. Thermography on the target plates shows a broadening of the deposition profile, suggesting increased transport in the edge.

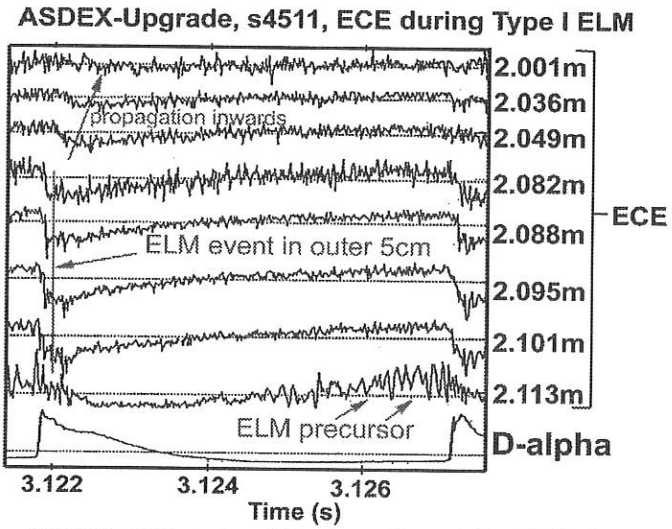

Figure 1: ECE at edge of the plasma (separatrix at 2.12m)

3. COMPASS-D Observations

The COMPASS-D tokamak (I_p =100-200kA, B_T =1-2T, R = 56cm, a = 18cm) is well equipped with three arrays of Mirnov coils (24 poloidally oriented coils per array) inside the vessel, with coils at 4 other toroidal locations. These coils are located closer to the plasma ($r/a \sim 1.3$) than those on ASDEX-Upgrade, and provide a more detailed picture of the magnetic signals from high mode number perturbations.

Like ASDEX-Upgrade, evidence for various magnetic modes during Type III ELMs is observed as well as high frequency ($\sim$ 100kHz) precursor modes. However, there are also magnetic precursors to Type I ELMs in Ohmic and ECRH discharges, with similar spatial structure to the Type III precursors. These ELMs obey the power scaling relationship for Type I ELMs mentioned above.

Signals from a type I ELM are shown in Fig (2). The long precursor of this ELM allows a clear analysis of its mode structure. Shortly before the D_α rise, this mode grows rapidly before becoming incoherent during the ELM itself. Fourier analysis shows two high frequency precursor modes (at 100kHz, 120kHz) with $n = 4, 5$, which merge (or perhaps one becomes dominant) as they grow and slow down before the ELM. Typical growth times for Type I precursor modes are $\sim 30\mu s$ compared with $\sim 200\mu s$ for Type III's.

4. Modelling of Type I Precursors

The external magnetic field during the ELM can be reconstructed by inserting numerous helical filament currents parallel to the field on the relevant flux surfaces, with current varying sinusoidally with filament number to match the mode number, n. The

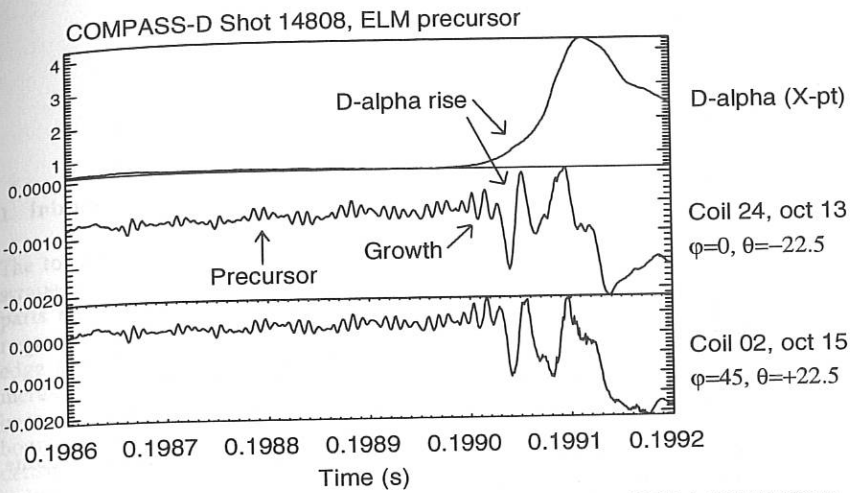

Figure 2: D_α and intergrated Mirnov signal (Tesla) traces for Type I ELM, COMPASS-D shot 14808. Arrows indicate times used in model to match the Mirnov signal.

total current in an island is matched to the observed amplitude of Mirnov signals during the ELM and the radial location of the filaments is varied to match the Mirnov oscillations observed at various toroidal and poloidal angles.

Using this technique for the modes described above on COMPASS-D, we find the $n = 4, 5$ modes are located on the $q = 2.25, 2.8$ surfaces, corresponding to $m = 9$ and $m = 14$ respectively. These surfaces intercept the outboard midplane 16mm and 8mm inside the separatrix. The current profiles used in the model have only a small effect on the location of the islands in the plasma.

The resulting field is used to calculate the electron thermal diffusivity using the Rechester and Rosenbluth formula [1],

$$\chi_r = \frac{< (\delta r)^2 >}{< \delta l >} v_{electron}. \qquad (1)$$

where δr is the change in radius for field line length, δl. It should be stressed that this is an empirical model, saying nothing about growth or rotation time scales.

5. Results of Modelling

The total island current is matched to the precursor amplitude at three times, as indicated by the arrows in Fig (2): (a) at the start of the precursor (75Amps); (b) during the growth of the mode prior to the rise in D_α (150Amps); (c) during rapid growth of the mode during the D_α rise itself, just before the mode loses coherence (500Amps).

The effects of these modes on the thermal diffusivity are shown in Fig (3). In the first stage (a), there is a modest degree of ergodicity, and hence χ_r, around the islands. This

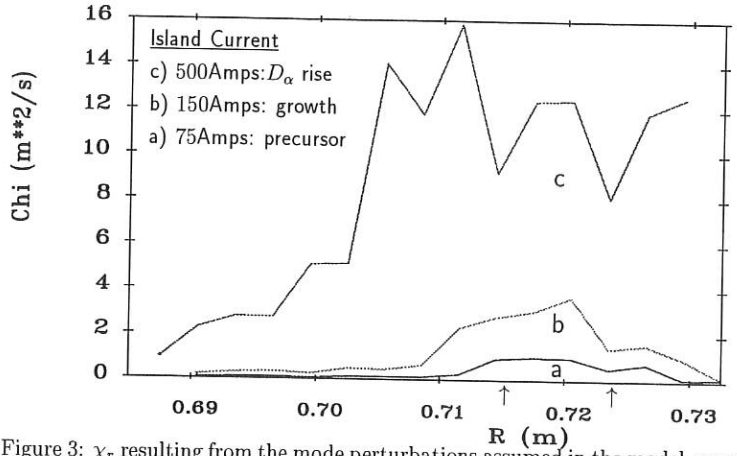

Figure 3: χ_r resulting from the mode perturbations assumed in the model, arrows indicate surfaces on which islands are placed, separatrix is at R=0.732m.

is substantially increased and broadened during the growth (b) of the mode. Finally, during the D_α rise (c), the ergodicity is enormously increased and extends beyond the separatrix.

Thus the model predicts a large loss of power during the D_α rise. A conservative estimate, based on edge ion temperature and density, assuming 2cm of plasma are lost, gives a $\sim$ 200J loss of energy, i.e. about $\sim$ 3% of plasma energy, in line with the measured losses due to type I ELMs on COMPASS-D seen with the diamagnetic loop.

Recent analyses of ECE data on ASDEX-Upgrade compare well with this, predicting an increase of χ_r to $\sim 8m^2/s$ [2] in the outer 7cm of plasma during an ELM.

6. Conclusions

Modelling of the observed helical magnetic modes during a type I ELM can account for the significantly increased transport and loss of energy from the plasma seen in experiment, based on transport enhancement due to ergodicity of the magnetic field at the plasma edge.

Acknowledgement:

The UKAEA authors were jointly funded by the UK Dept. of Trade and Industry and Euratom.

References

[1] A. B. Rechester and M. N. Rosenbluth, Phys. Rev. Lett. **40** 38 (1978).

[2] W. Suttrop, EPS paper, this conference, (1995).

Edge Modes as ELM Events

O.Pogutse*, J.G.Cordey, W.Kerner and B.Schunke
JET Joint Undertaking, Abingdon, Oxon., UK.
*On leave from RRC Kurchatov Institute, Moscow, Russia.

1. Introduction

The tokamak edge plasma includes a part of the core plasma and a part of the scrape-off-layer about a few Larmor radii inside and outside the separatrix. These parts have quite different topology with open and closed magnetic field lines, respectively. Due to MHD activity these two areas can interact. Therefore, this edge plasma plays a critical role in the behaviour of the entire plasma. With increasing edge temperature the dissipative instabilities in the edge plasma become weaker, the transport coefficients decrease and the gradients at the boundary increase. The profile of the pressure (along with temperature and density) becomes increasingly more step-like. For such steep gradients Larmor radius stabilisation and shear flow stabilisation take place, turbulence is suppressed and the H-mode is set up. Moreover, the development of a step-like pressure profile in the H-mode will lead to unstable MHD surface modes, which may explain the essential properties of the ELM phenomenon. The MHD instability first occurs near the X-point and gives rise to a precursor event. This instability throws out plasma from this region and destroys the separatrix in this point. Both these processes give a strong interaction with the end plates and the wall of the chamber. Due to this interaction the region near the X-point is filled by cold dirty plasma with low conductivity. This "new" plasma acts like an effective limiter for the main plasma just inside the separatrix, which becomes MHD unstable against surface modes. These surface modes have a relatively weak radial dependence which explains the macroscopic character of the ELM. This model gives an estimate for the ELM repetition time and explains, in addition, the occurrence of two different time scales during a giant ELM. The initial rise ends with a fast MHD event removing a plasma layer from the periphery. The second phase is determined by the diffusive refilling of the expelled layer.

2. Perturbed MHD equations near the separatrix. Coordinate System:

The magnetic field line geometry is described by the orthogonal coordinates ρ, ω, φ with line element $ds^2 = h_\rho^2 d\rho^2 + h_\omega^2 d\omega^2 + R^2 d\varphi^2$, where $h_\rho^2 = h_\omega^2 = \left(y_0^2 / 2^{5/2}\right) \cdot \left[1 - \cos(\omega) + \rho^2 / 2\right]^{-1/2}$; y_0 is the distance of the current wire from the X-point. For $\rho << 1$ this expression reduces to $h^2 = \left(y_0^2 / 4\right) \cdot [\omega^2 + \rho^2]^{-1/2}$. Introducing $R = R(\rho,\omega) = R_0 + x(\rho,\omega)$, where

$x(\rho,\omega)=\pm\left(y_0/\sqrt{2}\right)\cdot[-1+\cos(\omega)+\rho+\sqrt{2}(1-\cos(\omega)+\rho^2/2)^{1/2}]^{1/2}$, leads for $\rho << 1$ to $x(\rho,\omega)=\pm\left(y_0/\sqrt{2}\right)\cdot[\rho+(\omega^2+\rho^2)^{1/2}]^{1/2}$.

MHD ballooning equation:

Introducing the eikonal representation for the perturbed electrostatic potential: $\phi(t,\rho,\omega,\varphi)=\tilde{\phi}(\rho,\omega)\cdot\exp(-\gamma t+in\int_{\omega 0}^{\omega}q(\rho,\omega')d\omega'-in\varphi)$, where γ is the growth rate, leads to the ballooning stability equation:

$$\frac{1}{R}\left(\frac{B_\omega}{hB_0}\frac{\partial}{\partial\omega}\right)R\left(\frac{nq}{h}\right)^2(1+\zeta^2)\left(\frac{B_\omega}{hB_0}\frac{\partial}{\partial\omega}\right)\tilde{\phi}-\gamma^2C_A^{-2}\left(\frac{nq}{h}\right)^2(1+\zeta^2)\tilde{\phi}$$
$$-\tilde{\phi}\frac{4\pi}{RB_0}\left(\frac{nq}{h}\right)^2\frac{1}{h^2}\left(\frac{\partial}{\partial\rho}\frac{R}{B_0}-\zeta\frac{\partial}{\partial\omega}\frac{R}{B_0}\right)\frac{dP_0}{d\rho}\tilde{\phi}=0 \qquad (1)$$

$q=q(\rho,\omega)=\frac{B_0h}{B_\omega R}$ denotes the safety factor and $\zeta=\zeta(\rho,\omega,\omega 0)=(\frac{\partial}{\partial\rho}\int_{\omega 0}^{\omega}qd\omega)/q$ is the shear function.

3. Stability analysis

Introducing the function $u(t)$: $\tilde{\phi}(t)=\frac{1}{\sqrt{1+t^2}}u(t)$, and expanding all quantities near the X-point leads to a Schrödinger-type equation in the new variable $t=\omega/\rho$: $u_{tt}''+(E-V(t))u=0$, where $E=0$ and the "potential" $V(t)$ is: $V(t)=\left(\frac{\Gamma^2}{(1+t^2)}+\frac{1}{(1+t^2)^2}-\hat{\beta}\frac{[1+(1+t^2)^{1/2}]^{1/2}}{(1+t^2)^{3/2}}\right)$, with $\Gamma^2=\frac{\gamma^2q(\rho,\pi)^2R(\pi)^2}{C_A^2}$, and $\hat{\beta}=-\frac{\sqrt{2}32\pi R(\pi)}{y_0}\frac{q(\rho,\pi)^2}{B_0(\pi)^2}\rho^{1/2}\frac{dP_0}{d\rho}$. This equation for $u(t)$ can be derived from the variational form $W=\frac{1}{2}\int_{-\infty}^{\infty}[(u_t')^2+V(t)\cdot u^2]dt$. Choosing the trial function $u(t) = c_1$, where c_1 is constant and varying c_1 yields the condition for the growth rate $\int_{-\infty}^{\infty}V(t)dt=0$. The resulting threshold beta (for $\gamma = 0$), is:

$$\hat{\beta}_{cr}=\int_{-\infty}^{\infty}\left(1+t^2\right)^{-2}dt\Big/\int_{-\infty}^{\infty}\left[1+\left(1+t^2\right)^{1/2}\right]^{1/2}\Big/\left(1+t^2\right)^{3/2}dt=0.5\ . \qquad (2)$$

The condition for instability, $\hat{\beta}>\hat{\beta}_{cr}$, expressed through the pressure gradient near the X-point assumes the form:

$$\frac{q(\pi)^2 4\pi P_0}{B_0(\pi)^2}>\frac{y_0}{R(\pi)}\left(\frac{(\Delta x)_0}{y_0}\right)^{1/2}\propto\frac{(\Delta x)_X}{R_0}. \qquad (3)$$

We approximate $y_0 \sim b$ and $\frac{dP_0}{d\rho}$ as $\frac{P_0}{\Delta\rho}\sim\frac{P_0}{\rho}$, where $\rho\sim\Delta\rho\approx(\Delta x)_0/y_0$; $(\Delta x)_0$ is the pressure gradient length on the separatrix in the mid-plane and $B_0(\pi)$ is the

toroidal magnetic field of the magnetic axis, $(\Delta x)_X \approx ((\Delta x)_0 y_0)^{1/2}$ is the X-point gradient length. The safety factor $q(\pi) \equiv q(\rho,\pi)$ near the separatrix is related to q by the relation $q(\rho) = q(\rho,\pi)\cdot\Lambda$, where $\Lambda = 2/\pi \ln(4\pi/\rho)$. Then it holds that $q_{95} \approx 3\cdot q(0.1,\pi)$.

4. ELM model

Nonlinear evolution:

The interchange instability occurs near the X-point. Thereby a plasma tube of width $(\Delta x)_X \approx ((\Delta x)_0 y_0)^{1/2}$ is expelled onto the target plates in the time $\tau_1 \approx [(\Delta x)_X R]^{1/2} / C_s$. The related energy loss is given by $\delta_X = \frac{\Delta W_X}{W} \approx \frac{\pi(\Delta x)_X^2}{\pi ab} \frac{P_{0edge}}{<P_0>}$, and is too small to explain the loss observed in a giant ELM. For $(\Delta x)_0 \sim 0.1$m, a ~ 1m, b ~ 1.5m and $P_{0edge}/P_0 \sim 10^{-1}$, the energy loss amounts to $\delta_X \sim 10^{-3}$, i.e. it is very small. However, the expelled plasma interacts with the target plates and as a consequence the X-point region is filled with cold dirty plasma. This plasma with low conductivity acts as a "new effective limiter". The plasma inside the separatrix now obeys unfrozen boundary conditions. It becomes unstable against a flute type instability of the main plasma with a growth rate $\tau_2 \approx [(\Delta x)_0 R]^{1/2} / C_s$. This event yields the giant ELM. Eventually a refilling of the expelled plasma inside the separatrix by hot plasma from the centre takes place on the diffusion times scale $\tau_3 \approx \tau_E (\Delta a / a)^2 \approx \tau_E / (nq)^2$ (see Figs. 1 and 3).

Scaling of the ELM frequency.

Core plasma is expelled from the region inside the separatrix with an effective radial width of the order of $\Delta a \propto a/nq$. This causes the energy loss $\Delta W \approx 2\pi ab \frac{P_{0edge}}{(nq)}$, or $\delta = \frac{\Delta W}{W} \approx \frac{2P_{0edge}}{(nq)<P_0>}$. For n ~ 1, q ~ 5 one has a loss of $\delta \approx 5\%$, which is close to typical experimentally observed values. The time to restore the lost energy by heating is given by $\frac{1}{\tau} = \frac{P}{\Delta W}$, with $W = 2\pi ab<P_0>$. Using the definition $\tau_E \approx W/P$ we can rewrite τ in the following way $\tau \approx \frac{2\pi ab P_{0edge}}{(nq)P} \approx \frac{1}{nq} \frac{W}{P} \frac{P_{0edge}}{<P_0>}$. For n ~ 1, q ~ 5 and $P_{0edge}/<P_0> \sim 0.1$ this expression gives the estimate $\tau \approx 10^{-2}\tau_E \approx 1$ms. The scaling which follows from this formula for the ELM frequency is then given by:

$$f = \frac{1}{\tau} \propto nq \frac{P}{W} H_p \propto \frac{B_0 P H_p}{I^3 (\Delta x)_0^{1/2}}, \qquad (4)$$

where I denotes the plasma current, P the heating power, $H_p = <P_0>/P_{0edge} \propto P_0(0)/<P_0>$ the peakness factor of the pressure profile and $(\Delta x)_0$ the mid-plane gradient length of the pressure at the separatrix (see Fig. 2).

5. Conclusions

The separatrix changes qualitatively the condition for the existence of interchange MHD instabilities. In a plasma with a separatrix the edge perturbations mainly affect the X-point. The threshold beta for the perturbations which occur just outside the separatrix is given by (3). It is found that these perturbations are more easily destablised than the corresponding internal perturbations in the closed field line region. The internal perturbations experience the stabilising effect of the magnetic well, which is absent for external perturbations. These perturbations can remove only a small fraction of the total stored energy and only destroy the magnetic separatrix near the X-point. However, these effects lead to an influx of cold and dirty plasma into the X-point region. This plasma with low conductivity acts now like an effective limiter for the plasma tube of width $\Delta a \approx a/(nq)$ inside the separatrix. It destabilises the interchange instability of the main plasma. From this scenario we can estimate the frequency of ELMs, its dependence on the plasma current, on the heating power and on the peakness factor (4). The entire process has three stages: i) appearance of the interchange instability near the X-point and filling of this region by dirty, cold plasma; ii) triggering of the major interchange instability due unfreezing and iii) refilling of the empty region inside the separatrix by hot plasma from the centre on the diffusion time scale. A reasonable correlation between the theoretical predictions and the experiment results is found.

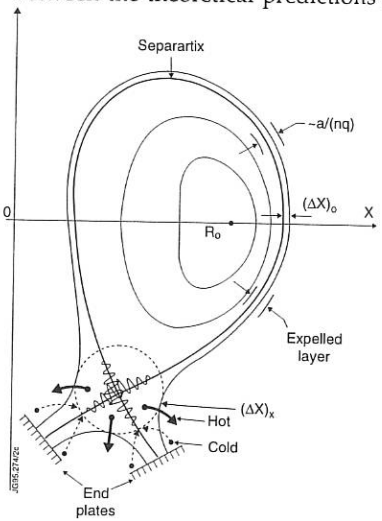

Fig. 1: Perturbations at the separatrix

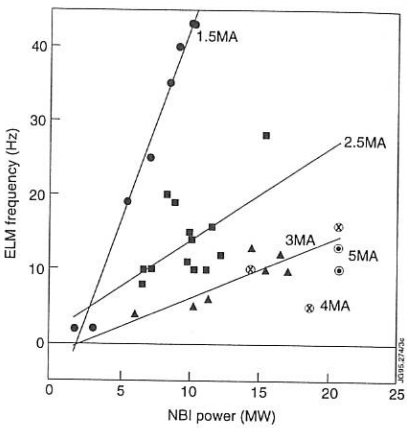

Fig. 2: ELM frequency for JET discharges

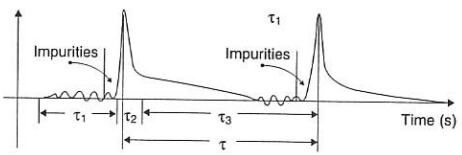

Fig. 3: Typical timescales of repetitive giant ELM's

THE EFFECTS OF ELMS ON THE PLASMA EDGE OF JET

J Lingertat, B Alper, S Ali-Arshad, P E Bak[1], A Chankin, S Clement, P Coad, I Cortes[2], N Deliyanakis, J Ehrenber, A Loarte, R Monk[3], L Porte, R Prentice and A Tabasso[1]

JET Joint Undertaking, Abingdon, Oxfordshire, OX14 3EA, UK

[1)] Imperial College, Plasma Physics Depart., Prince Consort Road, London, SW7 2BZ, UK.

[2)] Asociacion Euratom/Ciemat, 28040 Madrid, Spain.

[3)] Royal Holloway College, University of London, Surrey, TW20 0EX, UK.

INTRODUCTION - ELMs are an unavoidable ingredient of H - mode plasmas in tokamaks. They are associated with a pulse-like release of energy and particles from the main plasma into the divertor. This may adversely affect the divertor operation or in the case of high power operation, even damage the divertor target plates. On the other hand, it is well known that ELMs are beneficial in reducing the density and impurity build-up in H-mode discharges. To exploit these beneficial features of the ELMs and to avoid the detrimental ones a thorough understanding of their generation and of then energy release mechanism is necessary. This paper focuses on the details of the ELM - triggered energy and particle release into the divertor.

For analysis, mostly giant ELMs (Type I) have been used which are observed after the ELM-free phase of high performance NB-heated discharges [1].

SUMMARY OF RECENT JET RESULTS - During an ELM the release of energy and particles from the main plasma into the divertor occurs in a sequence of three phases:

- Phase I the "precursor" phase with a characteristic time of $\delta t_p \leq 100$ μs
- Phase II the "plasma edge determined" phase with a characteristic time $\delta t_e \sim 100$ μs,
- Phase III the "confinement degradation" phase with a characteristic time $\delta t_c \sim 10$ - 50 ms.

Phase I - The precursor phase is observed at the divertor as a perturbation of the floating potential measured by the target Langmuir probes. Since the floating potential is mainly determined by the electron temperature and the current flow between plasma and target, this phase may be regarded as the beginning of the increase of the power flux into the divertor caused by electron heat conduction. The total amount of deposited energy on the divertor target plates is below the detection limit ($\sim 10^4$ J).

During an ELM the perturbation of the floating voltage starts usually $\delta t_p \sim 10$ - 100 μs earlier than the density increase measured by a divertor interferometer. This feature is not observed with every ELM. Often the floating voltage precursor is correlated with precursors observed by the reflectometer and by magnetic probes.

A comparison between the time of arrival of the floating voltage perturbation on the outer and inner strike zones shows no time difference to within 20 μs. However, there is a time difference of 0.5 - 1 ms between the signals obtained by a reciprocating probe inserted near the top of the plasma and the target probes [2]. This implies that the X-point region is the origin of the perturbation [2,3,4].

Phase II - During the plasma edge determined phase, up to a few percent of the main plasma stored energy is released within $\delta t_e \sim 100$ μs into the divertor. This energy is removed from the outer region of the plasma column [5] and assumed to be transported mainly by electron heat conduction. A similar model has been proposed for type III ELMs [6].The maximum parallel power flux may reach values of $\sim 10^4$ MW/m^2. A transient connection between the target surface and a plasma of ~ 300 - 400 eV gives the right order of magnitude for the measured power flux.

The soft X-ray intensity perturbation caused by an ELM is shown in fig. 1. Here, the perturbation starts at the top of the plasma, moves down to the X-point and again up to the top. Note, however, that other ELMs have been observed which start near the X-point region. There is no evidence of the outer midplane being the origin of ELMs [7]. The fastest time scale found in this data is ~ 10 μs which may be associated with the precursor time scale δt_p. The total time of the perturbation is ~ 100 μs. This time interval is associated with the phase II time scale δt_e.

From the time evolution of the floating voltage and the surface temperature (figs.2 and 3) it is evident that during this phase the strike points of the separatrix move rapidly (< 100 μs) inwards (inner strike point) and outwards (outer strike point) by $\Delta R_S \sim 20$ cm. The energy deposition has its maximum at the new position of the inner strike point. For the inner strike point ΔR_S may be so large that the main energy is released outside the divertor target onto structures of the inner wall.

Assuming that the plasma column behaves like a rigid body the observed movement of the strike points translates into a movement of the main plasma upwards and inwards with $\Delta z \sim$ 10 - 20 cm and $\Delta R_p \sim 5$ - 10 cm. The observation of multiple peaked and broadened profiles on the divertor target reported previously [2] is caused by poor time resolution of the diagnostic instruments.

The high power flux pulse causes a release of impurities and deuterium from the affected areas which leads to the D_α - intensity peak usually associated with an ELM, to a peak in the radiated power and to an increase of the plasma density. The amount of released material and gas depends on the history of the surface hit by the power flux pulse. However, it is generally large because the target areas involved are regions with loosely bound deposition layers of non - stochiometric mixtures of impurities and gas.

Finally, the impurity/deuterium release triggers a deterioration of the global plasma energy confinement.

Phase III - During the confinement degradation phase the plasma loses particles and energy due to a drop in the relevant confinement times. This drop shows in most cases the features of an H → L transition [8].

The loss of particles leads to a decrease in the total particle content of the main plasma. The time evolution of the averaged density depends on the balance between the increase due to the injected impurities and deuterium during phase II and the subsequent decrease in the particle confinement time.

The loss of energy leads to an enhanced power flux to the target plates in a time scale of several 10 ms. This energy is deposited at the initial position of the strike points with an asymmetry of the power flux commonly observed during H → L transitions. The

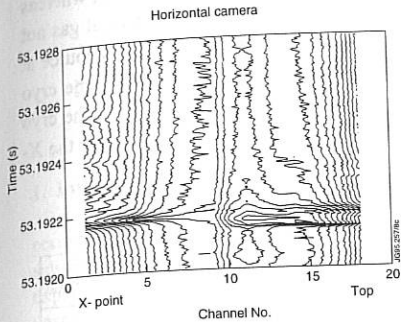

Fig. 1 Contour plot of the soft X-ray intensity as a function of time measured by a horizontal camera with 18 lines of sight, pulse 33701

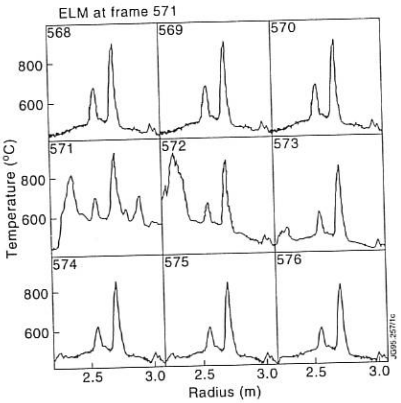

Fig.2 Evolution of the target temperature profile before, during and after an ELM, pulse 33649.

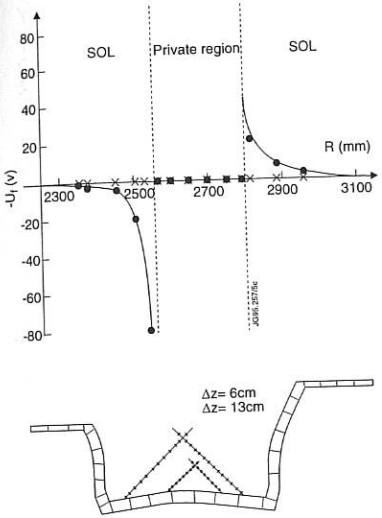

Fig.3 Reconstruction of the movement of the X-point from the measured movement of the strike points together with the floating voltage distribution on the target plate before and during an ELM, pulse 33649

total amount of energy lost during phase III depends on the extent of confinement degradation and is usually by a factor 2 - 8 larger than the energy loss during phase II (fig.4). After the H → L transition the plasma recovers within several 10 ms and goes again into the H mode. However, depending on the amount of injected impurities during phase II, the plasma may show a reduced H factor or even, after a sequence of giant ELMs, remain in the L mode.

The neutral gas pressure below the divertor target plate measured by pressure gauges [9,10] shows a spike for each ELM. Additionally, there is a "pile-up" of the base line pressure in the case of switched off cryo-pump. The D_α intensity shows the same pile-up behaviour, whereas the ion saturation current does not show this feature. The pile up is caused by neutral gas not taking part in the recycling process which indicates that there is a strong neutral gas source at the target caused by the ELMs. This additional gas can be removed by operating the cryo pump which is located below the target in the region of the outer strike point. With the cryo pump switched on the ELM frequency is reduced. Presumably, the neutral influx near the X-point region influences the ELM generation mechanism.

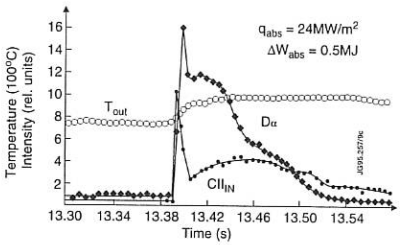

Fig.4 Time evolution of the maximum target temperature at the outer strike point T_{out}, the average of the maximum D_α intensity at the inner and outer strike point D_α and the maximum of the CII radiation intensity at the inner strike point CII_{IN} during an ELM, pulse 34458.

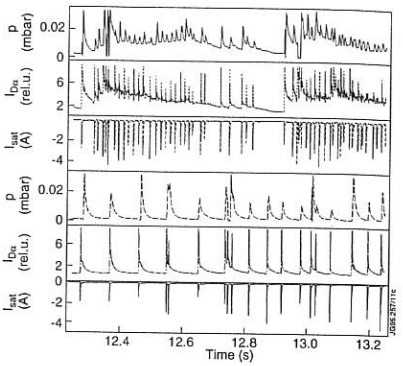

Fig.5 Time traces of the neutral gas pressure p beneath the outer target plate, the D_α intensity and the ion saturation current during two ELMy discharges with cryo pump off (pulse 32270) and cryo pump on (pulse 32285).

Acknowledgement - The support of Task Force H and the continuous help of P.Van-Belle with data processing is gratefully acknowledged.

References

1 T.T.C. Jones et al., "The Route to High Performance on JET", this conference.
2 J. Lingertat et al., "The Effect of ELMs on the JET Divertor Plasma", Proceedings of the IPP/JET/Culham Workshop on H-mode and Boundary/Divertor Physics, JET 7 - 8 Nov. 1994.
3 O. Pogutse et al., "Edge Modes as ELM Events", this conference.
4 M.F.F. Nave et al., Nucl. Fusion 35(1995)409.
5 T.C. Hender et al., "Influence of Edge Instabilities on JET High Performance", this conference.
6 H. Zohm et al., 20th EPS Conf. on Contr. Fusion and Plasmaphys., Europhysics Conf. Abstracts 17C, 19.
7 D.N. Hill et al., Nucl. Fusion 28 (1988) 902.
8 V.V. Parail et al., "The Physics of L and H mode confinement in JET", submitted to Nucl. Fusion.
9 J.K.Ehrenberg et al. "Neutral Gas Pressure Measurements in the JET Pumped Divertor", this conf.
10 G. R. Saibene et al., "Effects of active pumping and fuelling on divertor plasma discharges in JET", this conference.

Instabilities of Debye Layers in Experiments on Imitation of SOL Plasma-Surface Interactions

IV Vizgalov, GS Kirnev, **VA Kurnaev**, DV Sarichev, YuV Chernyatjev
Moscow Engineering Physics Institute, Moscow 115409, Russia

1. Introduction

A beam-plasma discharge (BPD) driven by an electron gun in a linear magnetic field permits to generate a highly non-equilibrium long-thin plasma flows with main parameters similar to those of scrape-off layer (SOL) in the present day tokamaks. In previous experiments [1] it was shown that in some particular conditions plasma-surface interaction sets unstable, and powerful RF electromagnetic oscillations arise in the collector circuit affecting energy dissipation and particle transport in imitated SOL plasma flows.

2. Experimental Conditions and Features of the Sheath Potential Drop Instability

The imitation facility with its diagnostic equipment was described in [1]. Experiments under discussion were carried out with the water cooled collector plates made of materials which can be used in candidate plasma-facing components (PFC), namely, graphite, W and Al (as a Be analogy forming oxide layer with similar to BeO secondary electron emission properties). Plasma flows were generated by BPD in hydrogen or argon with small admixtures of oxygen (1-10%, if necessary). The discharge channel was confined by a linear magnetic field varied in the range of 0.1-0.5 T. The input plasma cross-section was limited by a circular diaphragm (Ø1cm) installed in front of the collector plate. Plasma composition and energy spectra could be controlled with the built-in energy and mass analysers.

An autogeneration of electromagnetic oscillations appears in the collector circuit after a prior plasma treating of the surface, the plates made of W and Al revealing the oscillation activity more easily. Typical collector potential oscillograms along with time-averaged current-voltage characteristics (CVCs) are presented in fig.1-2. The first oscillogram (fig.1a) clearly demonstrates the prevalence of non-linear effects in generation mechanism. It is obtained at a rather low bias corresponding to the maximum of CVC (fig.2). A sinusoidally varying collector potential (fig.1b) is observed when both the working point and the range of oscillations lay inside the bias interval with CVC linear decrease. If oscillations are powerful enough, they alter the incoming plasma flow parameters along with transport processes and the surface emissivity. In this case of self-correlation collector plate oscillations obtain an amplitude-modulated character to the extent that they can die out at regular intervals with successive bursts of auto-oscillation activity (fig.1c).

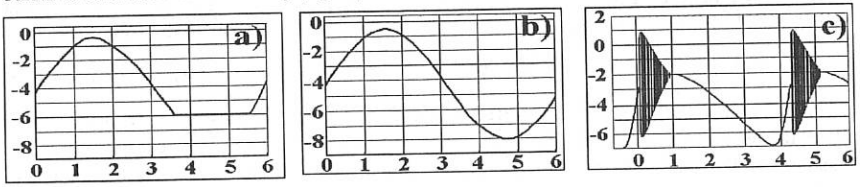

Fig.1. Oscillograms of the collector potential. a) - U_{col} =-60 V (0.02 mks/unit , 10 V/unit); b) - U_{col} =-200 V (0.02 mks/unit, 50 V/unit); c) - U_{col} =-500 V (20 mks/unit, 100 V/unit).

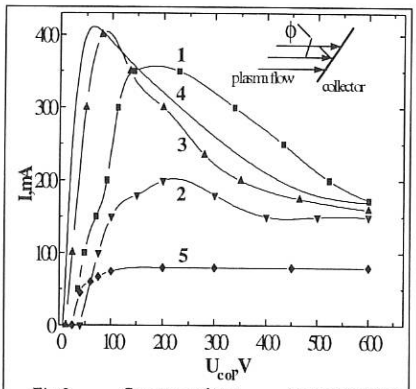

Fig.2. Current-voltage characteristics. $p=2*10^{-4}$ Torr. 1-4 - Al-collector: 1-H_2, $\varphi=30^o$; 2-Ar, $\varphi=60^o$; 3-Ar, $\varphi=0^o$; 4-Ar, $\varphi=0^o$ (computed dependence); 5-graphite collector, Ar, $\varphi=0^o$.

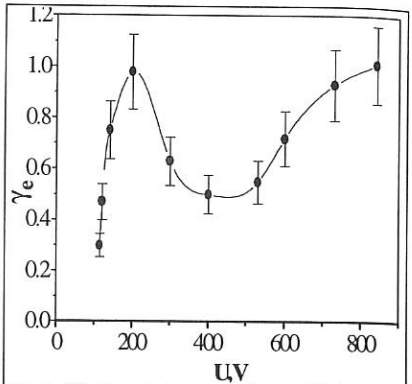

Fig.3. Effective electron emission coefficient as a function of negative collector biasing. Aluminium collector. H_2, $p=2.4*10^{-4}$ Torr.

3. Instability mechanism

The bias auto-oscillating instability is assumed to be determined by N-shaped CVC. It is most distinct for nonisothermal plasmas with pronounced superthermal "tail" in electron energy distribution. This points to significance of enhanced secondary electron-electron emission as an instability factor, for interaction of low-emissive surface with hot electrons would increase the sheath potential drop and smooth the CVC. In our imitation experiments with the use of BPD the presence of hot electrons is provided automatically due to the intrinsic mechanism of collisionless electron beam power dissipation in bulk plasma. In edge plasmas there is always a source of superthermal electrons due to their drift across a separatrix from hot regions or due to interaction with means of auxiliary plasma heating (with ICRH or ECRH antennae, for instance).

The bias dependence of effective coefficients for secondary electron emission γ_e measured by calorimetry method and referred to ion saturation current for cold Al plates is presented in fig.3. Its behaviour is similar to that for CVC. At high negative voltages γ_e is determined by the ion bombardment and corresponds to γ_e for cold cathodes with oxide layers in glow discharges. At low voltages, as one would expect, emission under surface bombardment with superthermal electrons prevails and provides the negative differential resistance in the collector circuit. This effect depends substantially both on details of electron energy distribution and on surface emissivity.

The collector current-voltage relationship can be presented in the following analytical form, when hot electrons with density n_{eh} are assumed to move normally to the solid surface:

$$I(U) = eSn_{eh}\int_{eU}^{\infty}[\sigma(\varepsilon - eU) - 1]f(\varepsilon)(2\varepsilon/m_e)^{1/2}\,d\varepsilon - I_e(U) + (\gamma+1)I_i + I_t(U_d)\,, \quad (1)$$

where the collector voltage U is referred to the plasma potential (in our experiments it was close to the ground potential), S is the collector plate area, $f(\varepsilon)$ is the energy distribution function of hot electrons, γ,σ are the energy dependent coefficients of secondary ion and electron emissions, I_i - the saturation ion current, $I_e(U)$ - the thermal electron current, $I_t(U_d)$ - the term which can appear due to other emission mechanisms, for example, there exists the

non-zero probability of direct electron tunnelling through a thin dielectric layer with potential drop U_d. This expression without the first and the last terms represents the usual probe characteristic for plasmas with moderate temperatures, when electron-electron emission can be neglected.

Computer integrations based on one-dimensional plasma model with measured energy spectra and without inclusion of direct tunnelling demonstrate good coincidence with experimental CVCs (fig.2, curves 3,4). In accordance with experimental results calculated CVCs remain monotone for graphites and pure metals which have rather low σ values (σ~1 in maximum). In the case of N-shaped CVCs for Al and W targets the coincidence with computations can be achieved only providing the use of σ and Υ energy dependencies peculiar to oxides [2, 3], the first sufficiently exceeding 1 in maximum (it is about 5 for oxides on aluminium surfaces).

It is worthy of note that varying Al or W collector bias in Ar+O plasmas one can observe hysteresis transitions between two states of the surface emissivity corresponding to appearing or removal (due to sputtering) of the oxide scale. The bias difference for forward and reverse transitions can be explained by two reasons: firstly, dielectric oxide layer is charged and its potential drop lowers the bombarding ion energy, secondly, the higher binding energy in oxides with respect to the oxygen adsorbed on the pure metal surfaces reduces sputtering. The thickness of oxide layer is determined by the equilibrium between its sputtering and growth. The former depends on the sheath potential drop along with mass-charge composition of an ion component. The latter depends both on oxygen content and on the rate of its diffusion through the layer, just as on the rate of substrate atoms counter-diffusion. In typical conditions, when CVC obtains N-form, the equilibrium oxide layer thickness is of the order of 100Å. Thus, a voltage drop through it of about 10V provides a necessary conductivity (due to tunnel effect for high-quality dielectric layers [4]). Thicker layers (something like 1000Å) need much higher voltages for surface discharging. At high biasing they become unstable because casual irreversible punctures perturb electric field distributions in the sheath. The break-down of induced surface charges leaves erosion traces of snow-flake form (3-10 mm in diameter) characterised by small central boreholes into the bulk collector material.

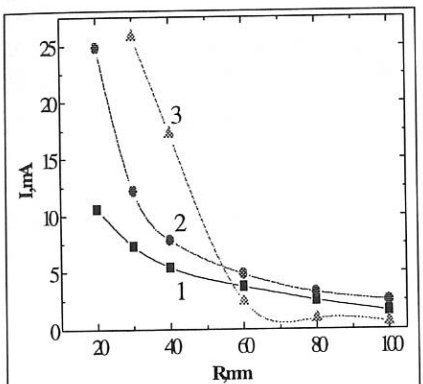

Fig.4. Radial distribution of the ion saturation current. H_2, $p=2.4*10^{-4}$ Torr. 1 - U_{col} =0V, 2 - U_{col} =-30 V, 3 - U_{col} =-300 V.

Graphite collector plates have monotone and almost unchanged with time CVC. Carbon has volatile chemical compounds with hydrogen just as with main plasma impurities and it does not exhibit an auto-oscillation activity during interaction with intensive plasma flows. Nevertheless, the carbon erosion products in specific conditions can form re-deposited synthesised layers of carbides or of a diamond-like structure with enhanced emissivity, which makes possible an auto-oscillation activity according to the discussed above instability mechanism.

In the vicinity of the floating potential the observed N-shaped CVCs have almost a stepwise current change with voltage, that is, they have a very large positive derivative. In

this case collector operates as a sort of voltage stabiliser damping potential fluctuations in the incoming plasma flow and lowering its transverse turbulent drift. In the voltage range with negative derivation of N-shaped CVC such a collector plate, in contrast, operates as an amplifier of plasma regular oscillations (ion-acoustic waves, for example) or random potential fluctuations and so stimulates the turbulent broadening of the flow. Moreover, a non-linear element with N-shaped CVC facilitates the autogeneration of electromagnetic oscillations in the effective LC-contour involving outer circuit elements along with plasma-surface capacitance. The latter is non-linear too, for it includes Debye and dielectric layers with oscillating electric fields. Experimentally observed radial contraction and broadening of the BPD channel with the change of operating bias (time-averaged in oscillation regime) are depicted in the fig.4.

4. Conclusions

Surface composition and structure generated during PFC interaction with incoming plasma flows can play the principal role in dynamics of edge Debye layers. In particular, stable thin layers of oxide, carbide or even diamond-like dielectric scales can appear on the surface contacting with hydrogen plasmas in presence of minor quantity of impurities. It crucially alters PFC emissivity in presence of hot electron component. The enhanced secondary emission from PFC can stabilise or, quite the reverse, trigger unstable behaviour of the sheath potential distribution depending on the resulting form of CVC and bias value. N-shaped current-voltage relationship corresponding to such an instability fundamentally differs from S-shaped one common to arcs. Powerful electromagnetic oscillations can arise in unstable regime. It causes the mean potential drop across a plasma sheath to step up (due to detector effect) with the overall increase of sputtering. It also drastically changes the transport processes in plasma. Corresponding self-correlated effects in plasma-surface interaction, under certain conditions, generate the regular bursts of auto-oscillation activity.

References

[1] Vizgalov IV, Dimitrov SK, Kurnaev VA, Chernyatjev YuV *Proc. 18 European. Conf. on Contr.Fusion and Plasma Physics. Berlin 1991* **3** 37-40.

[2] Yasnopolsky NL, Malisheva VS *Sov. Radiotechniques and Electronics* 9(**7**) 1293 (1962)

[3] Krutchenko OH, Chizhikov AE Sov. *Electron Techniques. Electrovacuum and Discharge Devices* **119** (**4**) 62 (1987)

[4] Dearnalley G., Stoneham A.M.,Morgan D.V. *Rep. Progr. Phys.* **33** 1129 (1970)

Effect of the toroidal field reversal on divertor asymmetries

A.V.Chankin[1], D.J.Campbell, S.Clement, S.J.Davies, A.Loarte, G.F.Matthews, R.D.Monk[2], R.Reichle, G.Saibene, M.Stamp, P.C.Stangeby[3]

JET Joint Undertaking, Abingdon, Oxon, OX14 3EA, United Kingdom
[1]*and Scientific Centre "Kurchatov Institute", INF, Moscow, Russia*
[2]*Royal Holloway College, University of London, Surrey, TW20 OEX, UK*
[3]*and University of Toronto, Institute for Aerospace Studies, Ontario, Canada*

Introduction

The study of divertor asymmetries is largely motivated by the problem of unequal power sharing between the strike zones. Excessive power load to the outer side often observed in the "normal" toroidal field direction (i.e. ion ∇B drift directed towards the target) in JET [1,2] and other machines (see e.g. refs. in [3],[4]) can aggravate the power exhaust problem for ITER. The "reversal" of the toroidal field (so that the ion ∇B drift is directed away from the target) was found to alleviate this problem by loading the two strike zones more symmetrically.

The field reversal also causes substantial changes of the asymmetries in density, electron temperature, H_α and local radiation power near the strike zones. In high recycling plasmas with additional heating, the ratio of the inner to outer side densities (the in/out n_e ratio) decreased, and the same ratio for electron temperatures (the in/out T_e ratio) increased with the ∇B reversal [3]. Such changes led to more symmetric distribution of plasma parameters in the reversed field compared to the normal one, where denser and cooler plasma with associated increase in local radiation and decrease in the target heat flux was observed at the inner strike zone.

Since the divertor asymmetries also depend on plasma core density, confinement regime, type and repetition of ELMs etc., a series of single null X-point discharges with both B_T directions was performed in JET to determine the effects caused by the field reversal.

Experimental Results

The discharges considered here are 2.7-4.2 MW NBI-heated L-modes with medium to high density. Along with B_T, the plasma current I_p was also reversed, thereby keeping the helicity of magnetic field lines and the contribution of NBI-induced momentum input to the divertor asymmetries unchanged. Pairs of pulses with similar main plasma parameters but opposite directions of B_T and I_p are compared. The results on the distribution of power to the target, the line averaged radiated power intensity and H_α radiation integrated over divertor inner and outer halves, are summarised in the Table 1. Reversed field data are shown in shaded rows.

The JET MK I target consists of rows of individual small carbon CFC (in these experiments) tiles, leading to highly non-uniform heating of the target. As the IR measurements of the target temperature were taken by a 1D array (see [5] for details), a 3D program of heat propagation within individual tiles had to be developed. The program also takes account of the exposed and shadowed areas of the tiles by incorporating the angles between the field lines and the tile surfaces. The power balance calculations are benchmarked by comparing (P_{input}-P_{rad}) with the calculated P_{target} for steady state conditions (in Table 1 0* power to the inner side means power conducted to the target less than 0.5 MW, corresponding to IR temperatures below the detection level of ≈380°C).
In/out ratios of P_{rad} and H_α from Table 1, as well as in/out ratios of the peak values of ion saturation currents at the strike zones (obtained from Langmuir probes during radial sweeps of strike-points) are plotted in Fig.1 for both field directions as functions of the safety factor at the flux surface enclosing 95% of the poloidal magnetic flux (q_{95}).

Discussion

The most clear experimental feature of the toroidal field reversal was the reversal of P_{rad}, H_α and I_{sat} asymmetries, confirming that the plasma is denser/cooler at the inner side in normal ∇B. In/out ratios of P_{rad} and H_α are above 1 for all the pulses with the normal ∇B, and below 1 for the reversed field pulses. The in/out ratios of the peak I_{sat}, plotted in Fig.1, are also higher in the normal ∇B case. The in/out ratio of T_e is generally lower in the normal field. The full extent of the T_e drop at the inner side in normal ∇B is difficult to quantify, owing to the problem in determining T_e in strongly collisional plasmas [6]. Langmuir probe measurements with standard interpretation give a figure of ≈15-20 eV. For the q_{95}=5.1 pulse with normal ∇B, the calculated powers from Langmuir probe data are 2.9 MW to the inner side and 1.3 MW to the outer side, in apparent disagreement with the power calculated from IR data (0.9 and 2.0 MW respectively).
The P_{target} asymmetry was almost always in favour of the outer side (see Table 1), and could not be significantly altered by the inclusion of local radiation. The high detection levels of the IR measurements did not allow us to cross-check the conclusion made on JT-60U that at high densities the total power asymmetry, after the inclusion of local strike zone radiation, is almost unaffected by the ∇B reversal [4].
In the reversed ∇B pulses, the q-dependence of the power distribution between strike zones [7] was confirmed, with more equal power sharing at low q_{95}. Concerning shifts in the P_{target} asymmetry caused by the ∇B reversal, an "anomalous" behaviour at q_{95}=4.2 and 5.1 was observed: more equal power sharing in normal ∇B cases. Radiation near the inner strike zone, as well as the H_α signals, were the highest in normal field discharges with q_{95}=4.2 and 5.1, suggesting high n_e and low T_e there. The parallel I_{sat} in the normal ∇B discharge with q_{95}=5.1 reached 90 A/cm^2. It is estimated that half of the measured total IR power to the inner side in this discharge (0.45 MW) can be attributed to surface

recombination of the ion flux at the target [7]. The recombination power to the target, $P_{rec} \sim 13.6eV \times n\sqrt{T_e}$, can exceed the sheath dominated power flux, $P_{sheath} \sim 7 n_e T_e^{3/2}$, at $T_e < 2$ eV. Provided that the plasma is attached to the target, constant pressure along the field lines, $P_e = const$, would imply $n_e^{in} T_e^{in} = n_e^{out} T_e^{out}$ and lead to a tendency of increased power deposition to the inner side at lowest T_e: $P_{target}^{in} \sim P_e / \sqrt{T_e^{in}}$. This contrasts with a conventional sheath dominated picture, where low T_e at the inner side results in lower power, $P_{target}^{in} \sim P_{target}^{out} \times \sqrt{T_e^{in} / T_e^{out}}$, and emphasises the necessity of the pressure drop by momentum removal in order to reduce the power conducted to the target.

To explain the effect of the ∇B reversal on the divertor asymmetries, various classical drifts were considered. According to the theories accounting for the effect of the poloidal **E×B** drift on divertor asymmetries [8,9], the in/out n_e ratio should increase with the ∇B reversal. In the experiment, however, the opposite tendency is observed - the in/out n_e, P_{rad} and H_α ratios decrease with the ∇B reversal. This can be due to the radial **E×B** drift [10], which dominates the poloidal **E×B** drift in high recycling plasmas [11]. This drift produces asymmetries in qualitative agreement with the experimental observations, due to an asymmetric particle supply and shear viscosity in the SOL [11] (see Fig.2 illustrating directions of radial and poloidal **E×B** drifts for normal ∇B).

Conclusions

Dedicated experiments in JET confirmed that in high recycling plasmas ∇B reversal affects primarily the density asymmetry between strike zones. Shift in the density distribution between the inner and outer strike zones is consistent with the effect of the radial **E×B** drift. Asymmetries in the power to the target are more complex. In high q discharges "anomalous" behaviour of the power distribution was observed (more equal power sharing in normal ∇B), which could be explained by the recombination power at the inner target for an attached plasma and very low electron temperature. In reversed ∇B discharges, the previously reported q-dependence of power sharing between the strike zones, with more symmetric power deposition at low q_{95} was validated.

References

[1] Reichle R. et al 1991 Proc. 18th Eur. Conf. on Contr. Fusion and Plasma Phys. (Berlin, 1991) vol 15C, part 3, p 105. [2] Janeschitz G. et al 1993 Proc. 20th Eur. Conf. on Controlled Fusion and Plasma Phys. (Lisboa, 1993) vol 17C, part 2, p 559. [3] Chankin A.V., Clement S., Erents S.K. et al., Plasma Phys. Control. Fusion 36 (1994) 1853. [4] Asakura N., Itami K., Hosogane N. et al, J. Nucl. Mater.,220-222 (1995) 395. [5] S.Clement et al., this conference. [6] Guenther K., this conference. [7] Campbell D.J. and the JET Team, in 15th Int. Conf. on Plasma Phys. and Contr. Fusion Research, Seville, Spain (1994). [8] Tendler M. and Rozhansky V., Comments Plasma Phys. Controlled Fusion 13 (1990) 191. [9] Cohen R.H., Ryutov D., Comments Plasma Phys. Controlled Fusion 35 (1993) 1271. [10] Hinton F.L., Staebler G.M., Nuclear Fusion 29 (1989) 405. [11] Stangeby P.C., Chankin A.V., JET-P(95)07, submitted to Nuclear Fusion.

q95	Ip (MA)	Bt (T)	$\overline{ne}$ (m-3/ e+19)	Pin (MW)	Prad total (MW)	Ptarget(MW)= inner side + outer side	Prad(MW/m2) at strike zone, inner side / outer side	H-alpha rad. (ph./e+15), inner side / outer side
2.3	2	1.5	18.0	3.8	2.2	Not available	0.12/0.11= 1.1	2.3/1.4= 1.64
	-2	-1.5	12.0	5.3	1.4	3.4 = 1.7+1.7	0.080/0.105= 0.76	2.8/3.8= 0.74
2.6	3	2.4	10.6	4.1	1.0	2.5= 0*+2.5	0.08/0.042= 1.9	1.85/1.25=1.48
	-3	-2.4	9.5	5.7	1.1	4.5= 1.7+2.8	0.054/0.061=0.89	1.66/1.93=0.86
3.6	3	3.3	8.0	5.0	1.1	3.8= 0*+3.8	0.1/0.056= 1.79	4.2/2.3= 1.83
	-3	-3.3	8.3	5.2	1.05	3.7= 0.9+2.8	0.068/0.096=0.71	1.6/2.0= 0.8
3.7	2	2.4	7.5	4.7	1.3	2.8= 0*+2.8	0.112/0.007= 1.6	8.8/3= 2.9
	-2	-2.4	7.8	5.0	1.2	3.7= 0.9+2.8	0.062/0.108=0.57	1.7/2.7= 0.63
4.2	2	2.8	8.3	5.1	1.8	2.8= 0.5+2.3	0.142/0.136=1.04	15.5/4.5= 3.4
	-2	-2.8	8.2	4.7	1.2	2.3= 0*+2.3	0.092/0.107=0.86	2.25/3.75= 0.6
5.1	2	3.3	8.0	4.5	1.6	2.9= 0.9+2.0	0.13/0.087= 1.5	20/4.5= 4.4
	-2	-3.3	7.5	4.8	1.5	3.1= 0*+3.1	0.097/0.133=0.73	2.0/4.0= 0.5

Table 1: Comparison between normal (positive B_T and I_p) and reversed (negative B_T and I_p) field discharges.
** - surface temperature from the IR camera is below the background level.*

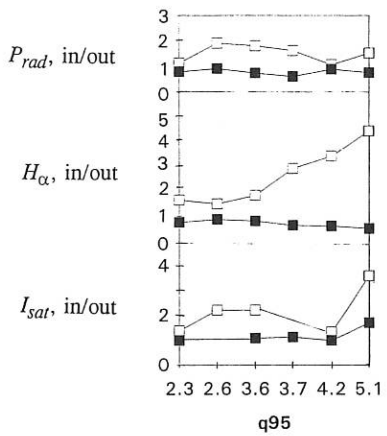

Fig.1: q-dependence of in/out asymmetries in local radiated power, H_α intensity and peak ion saturation current density: □ - ∇B normal, ■ - ∇B reversed.

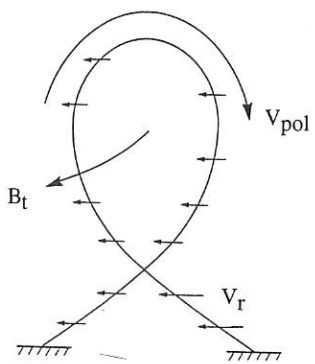

Fig.2: Directions of radial and poloidal E×B drifts for the case of ion ∇B drift towards the target. These directions reverse for the reversed ∇B.

Divertor Plasma Detachment in JET

R. D. Monk[1], D.J. Campbell, S. Clement, S.J. Davies, J. Ehrenberg, S.K. Erents[2], H.Y. Guo[3], L. D. Horton, A. Loarte, C.G. Lowry, J. Lingertat, G. F. Matthews, R. Reichle, G. Saibene, A. Tabasso[4] and G.C. Vlases.

JET Joint Undertaking, Abingdon, Oxfordshire, OX14 3EA, United Kingdom.
[1]Royal Holloway College, University of London, Surrey, TW20 OEX, United Kingdom.
[2]UKAEA Fusion, Culham, Abingdon, Oxfordshire, OX14 3DB, United Kingdom.
[3]INRS-Energie et Materiaux, Université du Québec, Canada.
[4]Imperial College, University of London, SW7 2BZ, United Kingdom.

1. Introduction

Given the large power exhaust expected from a reactor plasma (such as ITER) it is evident that the divertor target will not survive without some additional means to dissipate a significant fraction of the power. By creating a cold and dense plasma in the divertor it is possible to access a "detached" regime [1] whereby atomic physics loss mechanisms, such as charge exchange and hydrogenic radiation provide significant reductions in the particle, momentum and energy fluxes to the target plates. Experiments have been carried out in the JET tokamak using the new Mk. I pumped divertor to investigate plasma detachment under a wide range of conditions. This paper outlines the results from discharges where only the intrinsic impurities (e.g. carbon and beryllium) are present, radiative divertor experiments with impurity seeding are described elsewhere [2,3].

2. Detachment in Ohmic and L-Mode Discharges

As the main plasma density is increased by gas puffing during ohmic and L-mode discharges the following features are generally observed (see figure 1) :-

- Ion saturation current (I_{sat}) measured by Langmuir probes, D_α photon flux and neutral pressure increase more than linearly with density - the "high recycling" regime.
- Approaching $< \overline{n}_e > \approx 3 \times 10^{19}\,m^{-3}$ the I_{sat} reaches a peak value and begins to "roll-over".
- While D_α and neutral pressure continues to increase, the I_{sat} falls to low values indicating that "detachment" has occurred.
- Finally, if the plasma density is further increased a MARFE enters the main plasma with a characteristic drop in the divertor D_α signal, usually ending in a density limit disruption.

During the "high recycling" phase, the electron temperature at the divertor plates falls from around 20eV to 10eV and the Be-II or C-II emission decreases indicating a reduction in the sputtered impurities (see figure 2). However, divertor probe I-V characteristics under these high density conditions tend to exhibit low electron to ion saturation current ratios (in some cases <1) which is reflected in an overestimation of T_e [4]. As the D_α intensity profile

increases across the divertor, a large peak in the outer I_{sat} is seen to emerge from the broader exponential profile (figure 2). Simultaneous probe measurements in the divertor and main SOL (see figure 3) indicate that during this phase there is electron pressure balance along the field lines. Measurements from probes mounted in the side panels of the divertor target shows no evidence for enhanced cross-field losses of ions during detachment.

As the plasma detaches, the I_{sat} near the separatrix drops by an order of magnitude and the T_e falls to approximately 2eV at the inner plate and 3eV on the outer. During this phase there is a large decrease in the electron pressure at the divertor (figure 3) which remains fairly constant in the main SOL although the e-folding width, λ_p^{sol}, increases from 2.5 to 7.2cm. At detachment, the D_α profile has a peak in the vicinity of the x-point rather than the strike points. This is also observed in the radiated power distribution determined from the bolometers [3]. Measurements of the bremsstrahlung radiation in the infrared indicates a region of very high density ($>10^{20}m^{-3}$) in the vicinity of the x-point in agreement with the interferometer. Detachment is observed to be a gradual process rather than a bifurcation and develops as a function of the density rise, typically over a timescale of seconds.

Steady-state detached discharges of >5s have been produced on carbon and beryllium divertor targets with 3-4MW of neutral beam heating. In general, it is observed that the "roll-over" and density limit scale weakly as a function of the input power. Increased flux expansion appears to allow access to detachment at lower main plasma densities although the density limit is similarly reduced. However, wall clearance and plasma purity are critical in achieving a favourable split between divertor and bulk radiation (typically 2:1) and consequently maintaining a high density limit. Use of the in-vessel cyropump lowers the divertor neutral pressure [5] and requires a higher main plasma density to achieve the same degree of detachment as an unpumped discharge. Density limits occur when the radiated power fraction exceeds ~70% (carbon target) or ~85% (beryllium target). Otherwise, the behaviour of the carbon and beryllium targets with respect to detachment is very similar. The comparison of horizontal and vertical plate operation with respect to detachment is discussed elsewhere [6].

In terms of divertor detachment, the behaviour with the reverse toroidal field direction (ion ∇ B drift away from the target) is similar to the normal field case with the I_{sat} roll-over occurring at similar main plasma density. However, in ohmic discharges, the density limit and consequently the operating window for detachment, is reduced by approximately 30% compared to the normal field case.

3. High Density H-Mode Discharges

With increased D_2 gas puffing into ELMy H-modes it is observed that the ELM frequency increases and the energy confinement time is degraded (typically from an ITER89-P L-mode

factor of 2 down to 1.4). At radiated power fractions of $P_{rad} / P_{in} \approx 50\%$ there is a transition back to L-mode which determines the H-mode density limit. At the highest densities compatible with H-mode operation, the I_{sat} between ELMs can be reduced. However, it is highlighted in [7] that when operating close to the H-mode power threshold, the net effect of increasing the density is to *increase* the peak target temperature measured by IR thermography. This is due to the degraded energy confinement and reduced power spreading characteristic of the high frequency "grassy" ELMs.

4. Divertor and Edge Plasma Instabilities on the Approach to Detachment

During L-mode high density discharges, periods of oscillatory behaviour in the divertor and edge plasma parameters are commonly observed (figure 4). These phenomena are characterised by a sharp drop in I_{sat}, D_α and P_{rad} at the strike zones followed by an increase in the edge plasma density and increased D_α and P_{rad} in the vicinity of the x-point. This "detached" phase lasts for approximately 10ms and then there is a large increase in I_{sat} that resembles an ELM followed by the plasma re-attaching to the divertor plate. The oscillations are observed to occur over a reproducible range of input power and density. The frequency of the oscillations decrease with the level of power flowing into the scrape-off layer and cease during the detached phase. Such periodic detachment may be driven by the requirement to maintain the principal impurity source (i.e., the interaction of the divertor plasma with the target). The observed increase in edge density with detachment is associated with the ionisation in the main plasma of the neutral particles that were previously confined to the divertor region. Further work is underway to ascertain the driving mechanism for these phenomenon.

5. Conclusions

Steady-state detached plasmas with 70-85% radiated power can be achieved with D_2 injection for ohmic and L-mode plasmas. During detachment the electron pressure is observed to fall by over an order of magnitude at the divertor target. During high density H-modes the divertor ion flow can be reduced in-between ELMs although the confinement is degraded and reverts to L-mode at around $P_{rad} / P_{in} \approx 50\%$. The operating window for detachment with the ion ∇B drift direction away from the divertor target is narrower than for the normal field case. During high density L-mode plasmas a form of oscillatory detachment is observed.

References

[1] G.F. Matthews, Journal of Nuclear Materials **220-222** (1995) 104.
[2] G.F. Matthews et al., these proceedings.
[3] R. Reichle et al., these proceedings.
[4] K. Günther, these proceedings.
[5] G. Saibene et al., these proceedings.
[6] A. Loarte et al., these proceedings.
[7] S. Clement et al., these proceedings.

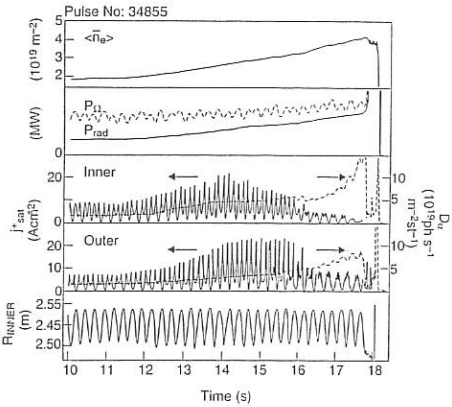

Figure 1 : Characteristics of divertor plasma detachment during an ohmic discharge.

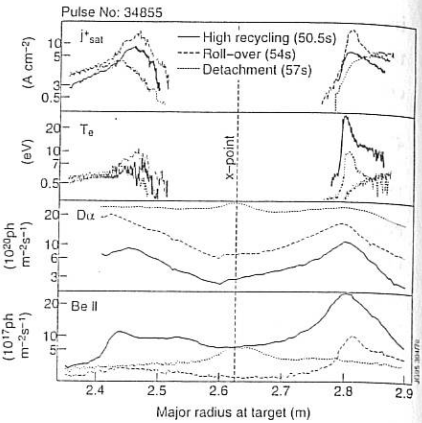

Figure 2 : Spatial profiles of I_{sat}, T_e, D_α and Be-II photon fluxes across the divertor target.

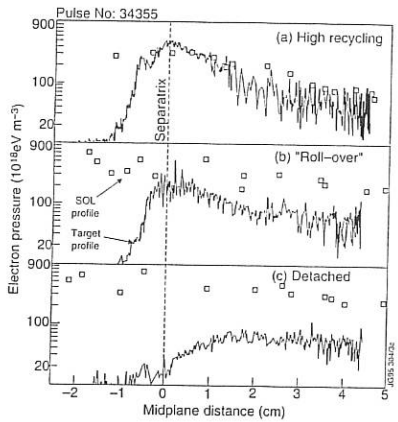

Figure 3 : Electron pressure profiles in the main scrape-off layer and divertor plasma during the approach to detachment.

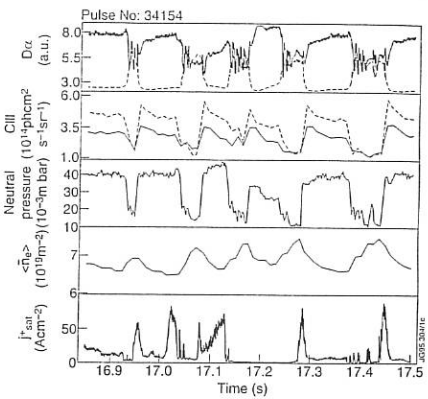

Figure 4 : Experiment evidence of unstable divertor and edge plasma behaviour during an L-mode discharge.

The Location of the Separatrix in the JET divertor and SOL

S K Erents*, S J Davies, J J Ellis, H Y Guo°, K McCormick+, G F Matthews, R D Monk⊥, D O'Brien and W Zwingmann
JET Joint Undertaking, Abingdon, Oxon, OX14 3EA, United Kingdom
* U K A E A Culham Laboratory, Abingdon, Oxon, OX14 3DB
° INRS-Energie et Materiaux, University du Quebec, Canada
+ Max-Planck-Institut fur Plasmaphysik, EURATOM Association, 85748 Garching, Germany
⊥ Royal Holloway College, University of London, Surrey, TW200FX, United Kingdom

1. Introduction

Verification of tokamak scrape-off layer models requires measurement of plasma parameters at the divertor target plates and upstream in the SOL. Because of the very short scrape-off thicknesses of these parameters at the plasma mid-plane, typically 10 - 30 mm, it is important to know the position of the separatrix with an accuracy much better than this. A solution to this problem is essential if meaningful multi-machine scalar edge databases are to be constructed for ITER. Apart from recent high resolution spectroscopy and lithium beam measurements, (P Breger et.al., these proceedings), current methods for determination of the separatrix position in JET plasmas are:

- Use of magnetic codes EFIT [1] and XLOC [2].
- The behaviour of upstream reciprocating probe floating potential near to the separatrix.
- The location of a maximum in particle flux to fixed probes in the divertor during a radial sweep of the separatrix.
- The use of pressure balance between target probes and upstream reciprocating probes.

2. Use of the magnetic codes EFIT and XLOC

The magnetic codes use data from an array of pick-up coils located around the inside of the vessel to construct the magnetic flux surfaces, often presented as a 2 D poloidal cross section of the plasma. A typical expected accuracy, determined primarily by mesh size, would be ± 20 mm at the torus mid-plane. Due to field line expansion to the probe locations at the top of the vessel, and in the divertor region, accuracy at these positions is only ± 50 mm. This is

useless for modelling purposes, where separatrix upstream and target parameters are required with an accuracy of better than ~ 10 mm.

Figure 1 shows the position of the separatrix calculated from the magnetic codes for a series of 2 MA, L-mode discharges. Input powers are between 2 - 8 MW, and line average densities are in the range 2 - $4x10^{19}$ m^{-3}. Toroidal fields, B_T, vary between 1.5 and 3.4 T. Also shown in this figure is the position of the separatrix from probe data using pressure balance, reported below.

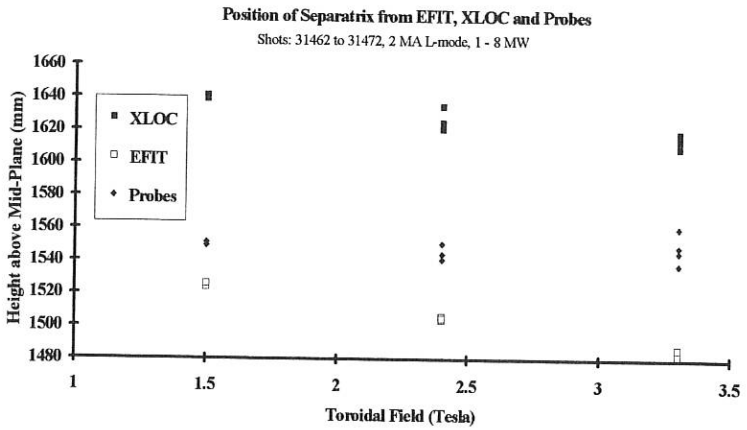

Figure 1 The location of the separatrix determined from magnetics, and from probe pressure balance.

There is no change in separatrix position as indicated by the probes with either input neutral beam power or B_T, although the codes suggest a dependence on B_T.

3. The Floating Potential near to the Separatrix

The floating potential V_f is observed to fall close to the separatrix, and in the past on JET this has been used as an indicator of the separatrix position. However it is now clear that much of this fall is associated with heating and sublimation of the carbon reciprocating probe, sometimes seen as an increase in CII light and in radiation. The hysteresis in $T_e(r)$ and $V_f(r)$ due to heating of the reciprocating probe as it moves in then out of the plasma, is shown in figure 2. The general fall in $V_f(r)$ reflects the increasing electron temperature $T_e(r)$, since the plasma potential $V_p = V_f + 2.5\ kT_e$, remains fairly constant. The use of the electric field, $E_r = \partial V_p / \partial r$, to give an indication of separatrix position, as used by other groups [3], is clearly not applicable for these L-mode discharges due to these hysteresis effects.

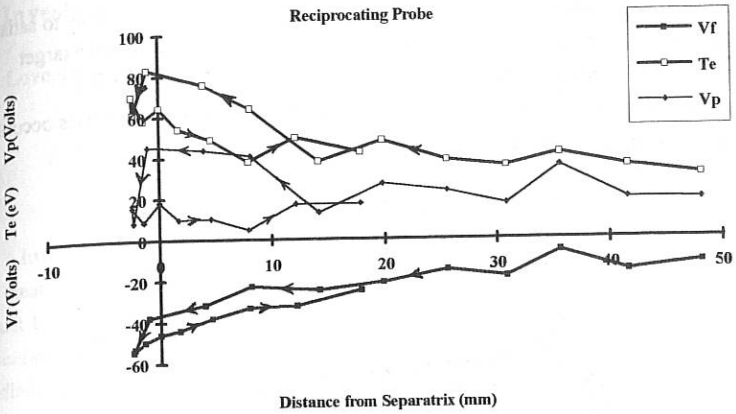

Figure 2 Radial profiles of floating potential, electron temperature and plasma potential

4. Use of Pressure Balance to determine the Upstream Separatrix position.

Pressure balance between upstream and target probe pressures, P_u, P_T, which in the simplest model is total electron pressure $P_u = 2\ P_T$, may be used to establish the position of the separatrix position upstream. This technique can be used for sheath limited (T_e = constant) and also high recycling mode (∇ // T_e large) plasmas, but *not* for detached plasmas. The technique relies on the good identification of the separatrix position, to within ~ 3 mm, as provided by a maximum particle flux j_{sat} on probes in the divertor during a sweep of the separatrix, figure 3. Edge codes suggest that this maximum in j_{sat} is indeed within a few mm. of the separatrix.

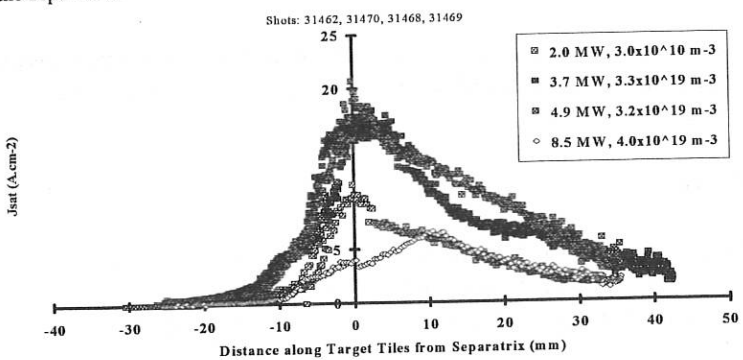

Figure 3 Radial profiles of particle flux, j_{sat}, in the divertor, showing maxima at separatrix

Radial profiles of target pressure, with the upstream pressure profiles moved radially to satisfy $\overline{P}_u = 2.\overline{P}_T$, are shown in figure 4. Due to an uncertainty in the effective area of the target probe used for these measurements, this area has been calibrated using absolute D_α measurements. The technique fails if the strike zones are bifurcated, which sometimes occurs at high densities, (i.e. the 8.5 MW example).

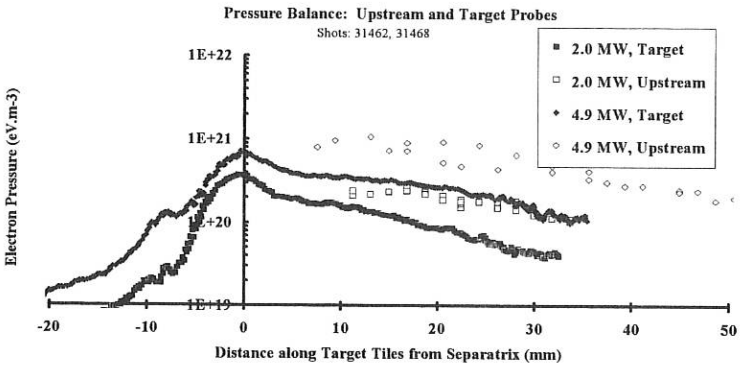

Figure 4 Radial profiles of electron pressure to fixed target and upstream reciprocating probes

5. Summary

- The magnetics codes, EFIT and XLOC on JET cannot determine separatrix positions with the accuracy required for modelling of the edge plasma using target probes and upstream reciprocating probes.
- Changes in floating potential near to the separatrix are not a good indicator of separatrix position.
- Pressure balance between target and upstream reciprocating probe measurements can be used to determine the separatrix position provided the target plasma is not close to detachment.

6. References

[1] D P O'Brien, L L Lao, E R Solano, M Garribba, T S Taylor, J G Cordey and J J Ellis, Nucl. Fus. 32 No. 8 (1992), 1351 -1360.

[2] D P O'Brien, J J Ellis and J Lingertat, Nucl. Fus. 33 No. 3 (1993), 467 - 480.

[3] P Gohil, K H Burrell, R J Groebner, J Kim and R P Seraydarian, Proc. 21st. EPS, Montpellier, 27 June 1994.

Investigation Of Opacity In The JET Tokamak Divertor Region

T Lovegrove[1], L D Horton, R W T König, J Lingertat, A C Maas, C F Maggi, R D Monk, M F Stamp, P J Storey[1] and A Tabasso

JET Joint Undertaking, Abingdon, Oxfordshire, OX14 3EA, United Kingdom.
1] University College London, Gower Street, London, United Kingdom.

1. Introduction

In creating the ideal environment for thermonuclear fusion, every aspect affecting its parameters must be considered. A greater understanding of the plasma's opacity will lead to a more accurate estimation of the power losses occurring in the tokamak due to the absorption of radiation.

The probability of light absorption occurring is in direct proportion with increasing density of absorbers. In JET these are the conditions necessary to reduce sputtering of material from the wall of the pumped divertor. It is therefore possible that opacity effects are great enough to alter the plasma's power balance.

2. The Theoretical Investigation

Opacity increases linearly with absorber density. Normally, in an "attached" divertor, the peak densities occur at the targets, where Langmuir probe measurements are available.

There are two types of divertor plasma model being used to simulate "detached" plasmas, these being an onion skin model of the SOL [1] and a full two dimensional fluid code, EDGE2D [2]. The first of these models is available for a wider range of shots and, when used to simulate the plasma, obtains the expected result of peak densities at the target [see Fig.1]. However, at high densities, such as those in the divertor region, studies show that a momentum loss is caused by collisions of ions with recycling neutrals [3]. This results in higher plasma pressures above the target plates, increasing the density in this region and often culminating in a peak density away from the targets.

The onion skin model has been modified to incorporate the momentum loss due to the ion-neutral collisions as calculated by the Monte Carlo neutral code NIMBUS [4]. For detached plasma simulations, this modified model does show an increased density just away from the target as predicted [see Fig.1a]. However the density increase does not reproduce the measured level of bremsstrahlung in the divertor.

More detailed calculations using the fluid code predict a larger momentum loss and better reproduce the experiment [see Fig.1b]. The discrepancy in the two simulations is thought to be related to errors in electron temperature measurements with the target Langmuir probes and is under investigation [ref. Guenther, this conference].

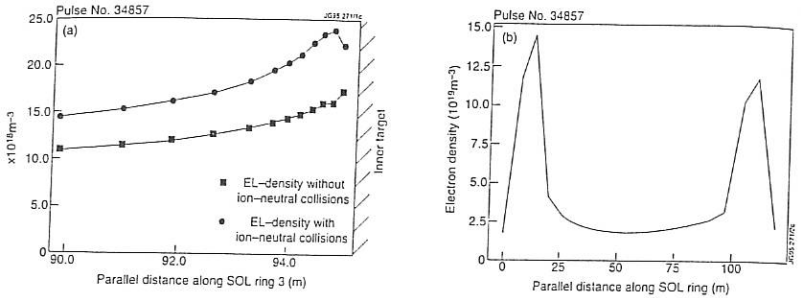

Fig.1a) Onion skin and b) fluid, model simulations of a detached plasma showing the effect of ion-neutral collisions in the SOL.

To estimate the extent of radiative absorption in the divertor plasma we have used a collisional radiative model of deuterium level populations. This utilises a first order escape probability method [5] to evaluate the line escape probabilities and gives a self consistent model of the level populations and radiation field in a plane parallel slab of uniform temperature and density.

In an initial model of the JET divertor, data from a fluid code simulation of a high density JET shot is used. The plasma parameters from the simulation, up to a selected height vertically above the target and between the separatrix and the wall are averaged and fed into the population code to form the uniform slab of plasma. The height of the slab is varied as a parameter, trading off extra plasma depth with lower average densities in the slab.

This model shows that for a photon being emitted at the midpoint of a slab of height 3cm, the Lyα and Lyβ lines have optical depths of approximately 2.0 and 0.31 with corresponding line escape probabilities of 0.42 and 0.81, respectively. This result shows that divertor plasmas produced in JET are close to the region where opacity effects become important.

Recently, the model has been improved so that it better imitates the changing environment in the divertor plasma by using a finite stack of uniform rectangular slabs, each with different plasma parameters. Emission and absorption profiles are assumed to be Doppler broadened and the code allows for a variation in the profile width from slab to slab. Doppler shifts between slabs, caused by neutral velocity gradients, are accounted for in all three dimensions. The slabs are of finite length with the slab stack base running parallel to the separatrix rather than to the target plate. The single flight escape probability from the entire stack, for a photon emitted at an arbitrary point, is calculated by numerically averaging over all frequencies and angles of emission.

3. The Experimental Investigation

Two ohmic density ramp pulses are examined, both very similar, their main difference being that for the first the strike points hit the vertical plate of the divertor whereas for the second the strike points are on the horizontal plate of the divertor. Lyβ and Dα emission are measured along a line of sight through the inner divertor leg using a combined visible/VUV spectrometer [6]. The precise lines of sight of the visible and VUV channels of this spectrometer are uncertain. In addition, spatial profiles of Dα are available across the horizontal target from a flux camera.

For the two shots, Lyβ and Dα line profiles from the visible/VUV spectrometer have been fitted to give total intensities. The Lyβ has an estimated fitting error of 10% and the Dα has a smaller error given in Fig.2. The ratio of these lines has been taken and can also be seen in Fig.2.

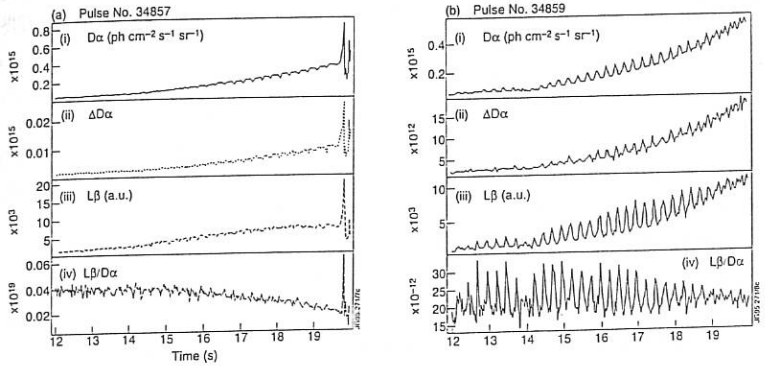

Fig.2 Line integrated signals for pulses with the strike point on a) the vertical target and b) the horizontal target. (i) Balmer-alpha emission, (ii) uncertainty in the fit to the Balmer-alpha emission, (iii) Lyman-beta emission, and (iv) the ratio of the two signals as a measure of the divertor's opacity.

It can be seen that for the first shot there is a notable drop in the ratio of approximately 50%, well outside the fitting errors described above. In the second shot, both the Dα and Lyβ show oscillations as the strike points are swept across the horizontal target. The oscillations in the UV signal are larger than those in the visible, due to the fact that the two systems have different acceptance cones and the resulting ratio then also oscillates making interpretation difficult.

The fact that the Dα emission is seen to oscillate less than the Lyβ emission as the plasma strike point is swept suggests that the acceptance cone for the visible channel of the visible/VUV spectrometer is greater than that for the UV channel. Using the radial profile of Dα emission from the flux camera, it is possible to assess the effect of geometry of these signals. These

profiles have been averaged over a 20cm spot size for the visible signal and a 10cm size for the UV.

Changes occur in the ratio of these averages as the plasma is swept which explains the variations seen in the horizontal target shot (see Fig 2b). Nevertheless, using the same averaging process, the ratio of averages for the vertical case does not reproduce the drop seen in the experimental ratio of Lyβ/Dα (see Fig.2a).

It must be said that the characterisation of the UV spectrometer is not complete. In particular, shifts in the wavelength position of spectral lines have been observed during a shot. This may be due to underfilling of the grating, which would be most apparent in horizontal plate discharges where the spectrometer views large spatial emission gradients. It is not clear how this would affect the effective calibration of the UV system.

Nevertheless, it seems most likely from these studies that the change in the ratios of Lyβ/Dα are due mainly to a decrease in the Lyβ emissivity and therefore to absorption of this spectral line.

4. Comparing Theoretical And Experimental Results

Using the altered population code with fluid model simulations of a recent plasma pulse has given very promising results. For a slab stack of height 20cm the Lyα and Lyβ escape probabilities are 0.48 and 0.87, respectively. For the original single slab model, covering the same area, the Lyα and Lyβ escape probabilities are 0.67 and 0.91, respectively.

The line of sight of the spectrometer is at a 45 degree angle to the separatrix and slab base. This increased line of sight could lower the escape probabilities further. Therefore, to make a direct comparison between theoretical and experimental results, the improved population code has been used to estimate the opacity along the same line of sight. This results in a 6% drop in the Lyβ to Dα ratio as a function of time. Although this result is not nearly as dramatic as the 30%-50% drop in the ratio from the experimental investigation, it is still within the error bars of the theoretical study due to the uncertainty in electron temperature and density profiles in existing models of detached plasmas.

5. Conclusion

Calculations show that radiative absorption is on the point of being significant in the JET divertor. Experimental measurements of the Lyβ to Dα ratio, which show a drop as the divertor density is increased (and temperature decreased), support this theoretical study.

References

[1] Taroni, A., et al., *Contrib. Plasma Phys.* **32** 438 (1992)

[2] Stangeby, P.C., Elder, J.D., *J. Nucl. Mater.* **196-198** 258 (1992)

[3] Stangeby, P.C., *Nucl. Fusion* **33** 1695 (1993)

[4] Cupini, E., Dematteis, A., Simonini, R., *NET Report EUR* 324 **XII** (1984)

[5] Hummer, D.G., Rybicki, G.B., *Astrophys. J.* **254** 767 (1982)

[6] WOLF, R.C.,et al., submitted for publication in Rev. Sci. Instrum.

The Influence of Divertor Geometry on JET Discharges

A. Loarte, D.J. Campbell, S. Clement, S.J. Davies, S.K. Erents[1], H-Y. Guo[2], P.J. Harbour, L. Horton, J. Lingertat, C. Lowry, G.F. Matthews, K.Mc Cormick[3], R.D. Monk[4], D. O'Brien, G.Saibene, R. Simonini, G.J. Radford, A. Taroni, G. Vlases

JET Joint Undertaking, Abingdon, Oxon., OX14 3EA, UK

[1] UKAEA Fusion, Culham Laboratory, Abingdon, Oxon., OX14 3DB, UK

[2] INRS-Energie et Materiaux, Université du Québec, Canada

[3] Max Planck Institut für Plasmaphysik, Garching, Germany

[4] Royal Holloway College, University of London, Surrey, TW20 0EX, UK

1. Introduction

The JET Mark I pumped divertor can be operated with the strike zones either on the horizontal or vertical section of the divertor target, allowing a study of the influence of divertor geometry on the scrape-off layer (SOL) and the main plasma. Predictive modelling for JET [1,2] had shown large differences between the characteristics of the SOL and divertor plasma for the two configurations, associated with their different recycling patterns. The horizontal divertor directs the recycling neutrals towards the outer part of the SOL, while the vertical divertor should concentrate them towards the separatrix. For the vertical target, this effect should lead to lower neutral leakage from the divertor, more peaked density profiles in divertor and main SOL, and inverted electron temperature profiles at the divertor, with lower separatrix electron temperature than for the horizontal targets. These characteristics should also lead to detachment of the separatrix divertor plasma at lower main plasma density for the vertical divertor than for the horizontal one. A series of experiments has been carried out in JET to test these predictions (typical magnetic configurations are shown in Fig. 1), comparing plasmas in all confinement regimes, toroidal field directions, with/without cryopump and for a wide range of plasma densities. We only consider here discharges without cryopump to differentiate between purely geometrical effects and those associated with differences in pumping for the various configurations [3].

2. Measured Ion Flow and Temperature Profiles at the Divertor Plate.

Ion flow profiles at the divertor plate for low density Ohmic and L-mode discharges are more peaked when the separatrix is on the lower part of the vertical plate, compared to the horizontal divertor, and similar to the horizontal for the upper part of the vertical plate (see Fig. 2). The difference in the shape of the electron temperature profiles is less clear but the uncertainty of this measurement is larger. As the density increases, the horizontal plate ion flow profiles develop a peak near the separatrix, becoming more similar to the vertical case (upper and lower). The temperature profiles become very flat for both configurations, but the simple interpretation of these measurements becomes questionable under such conditions [4]. If the

density is increased further, divertor detachment is obtained at similar densities for horizontal and lower vertical plate configurations. A difference found between horizontal and vertical divertor is that, while for horizontal plate discharges strike point sweeping does not affect detachment (i.e. the detached divertor plasma profiles follow the strike point movement), for vertical plate configurations the degree of detachment depends on which part of the target the strike point lands, being greater for the lower vertical plate than for the upper part (see Fig. 3). Similar observations are found for H-mode discharges, although the comparison of the detailed shape of the profiles at the divertor target is more uncertain because of the distortion caused by the presence of ELMs.

3. Main Scrape-off Layer Density Profiles

Predictive modelling has shown that a vertical plate divertor should lead to a narrower density profile in the main SOL. This effect is associated with the intrinsic recycling pattern of a vertical divertor, which concentrates the recycling neutrals near the separatrix, depleting the outer part of the SOL. This prediction has been observed in the experiment, but the difference in density e-folding lengths depends very strongly on the plasma density and input power, the difference being largest (up to a factor of 2) for L-mode discharges with 4MW of NBI additional heating.

4. Effects of Divertor Geometry on the Main Plasma

Although some of the predicted profile modifications due to the divertor geometry are observed at the divertor and the scrape-off layer, the main plasma parameters are very similar for equivalent discharges in the two configurations. Radiation levels and patterns are similar in both configurations apart from the trivial differences associated with the location of the divertor strike zones. No clear correlation has been found between the level of recycling, as determined by the D_α intensity in the main chamber (which should reflect the level of neutral leakage from the divertor) and the strike zones being on the horizontal or the vertical section of the plate. Fig. 4 shows the main plasma parameters and divertor ion flow for two additionally heated (4 MW) L-mode discharges on the horizontal and vertical target. No noticeable difference between these discharges is observed (similar examples exist for Ohmic and ELMy H-mode discharges).

5. Modelling of Divertor Geometry Effects

EDGE2D-U/NIMBUS [5] modelling of discharges (assuming purely diffusive perpendicular particle transport) on the horizontal and vertical divertor plate has been performed for the discharges described in sections 2 and 3. The values for the perpendicular diffusion coefficients have been obtained from detailed modelling (assuming a pure plasma and a non-coronal approximation for impurity radiation or with full fluid treatment of all carbon ionisation stages) of low density Ohmic discharges : $D_\perp = 0.12\ m^2/s$, $\chi_{\perp e,i} = 1.3\ m^2/s$. These coefficients are kept constant for all the simulations and the value of the separatrix density, power into the SOL and

divertor radiation adjusted to match the experiment. The results for the ion flow profiles at the plate for L-mode conditions are shown in Fig. 5. The agreement between modelling and experiment is good in the lower density range of Ohmic and L-mode discharges but as the density increases (before detachment starts in the experiment) the model predictions diverge from experiment. The predicted main SOL density e-folding lengths exceed those measured by more than a factor of 2 and the peak ion flows at the plate are underestimated by a similar factor. Modelling does not describe the experimental approach to detachment for the vertical and horizontal divertors. From these calculations, the main plasma density at which detachment starts (ion flow at divertor drops with increasing main plasma density) should be a factor 2 to 3 lower for the vertical plate divertor. This is not supported by the experiment, where detachment is observed at the same densities for both horizontal and vertical divertors.

Work is in progress to explain the discrepancies between model and experiment along the following lines (presently, none of them provides a satisfactory explanation for all differences observed) : a) Existence of a particle pinch in the SOL [6], b) Unsatisfactory baffling of the structures surrounding the divertor, c) Neutral recirculation caused by the 3-D structure of the JET Mark I divertor (not included in the modelling presented here), d) Inadequate modelling of impurity dynamics in the SOL and divertor for highly radiative divertors.

6. Conclusions

Detailed experiments have been carried out in the JET Mark I divertor to assess the effect of divertor geometry on the divertor SOL and divertor plasma. While steeper SOL density and ion flow profiles at the plate are observed in the experiment, as expected from modelling predictions, no significant differences in the main plasma parameters are correlated with the discharges being diverted on the horizontal or vertical plate. In particular, the predicted (with a purely diffusive model for perpendicular particle transport) access to detachment at lower densities for the vertical plate divertor does not take place in the experiment. Whether this disagreement is due to the recirculation of hydrogen neutrals in the experiment being strongly influenced by the real 3-D structure of the divertor (not included in the model) or to SOL transport processes, is not clear. It is of paramount importance to assess this point quantitatively, as the physical basis of all advanced divertor designs relies on the strong influence of divertor target geometrical effects which has not been corroborated by the JET Mark I divertor experiments.

7. References

[1] JET Team, 14th IAEA Conf. Plasma Phys. & Control. Fus. Res., Würzburg, FRG, 1992.
[2] Taroni, A., et al., Jour. Nuc. Mat **220 - 222** (1995) 1086.
[3] Saibene, G., et al., These Proceedings.
[4] Günther, K., These Proceedings.
[5] Simonini, R., et al., Contrib. Plasma Phys., **34** (1994) 368.
[6] Taroni, A., et al., These Proceedings.

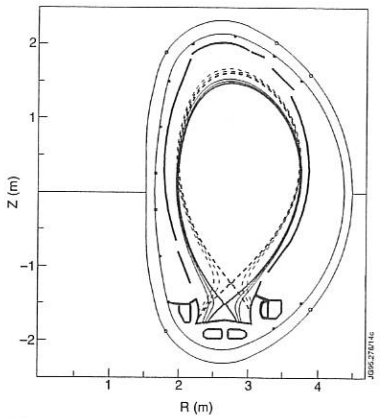

Fig. 1. MHD equilibria for two representative discharges on the horizontal and vertical section of the divertor target

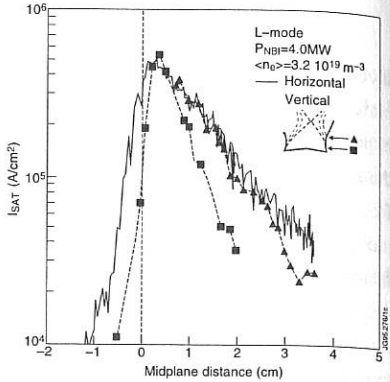

Fig. 2. Ion flow profiles for similar low/medium density discharges on the horizontal and vertical plates versus midplane distance.

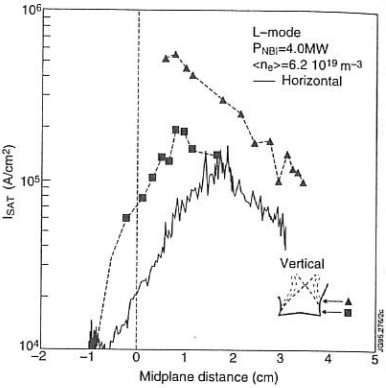

Fig. 3. Ion flow profiles for similar high density discharges on the horizontal and vertical plates versus midplane distance.

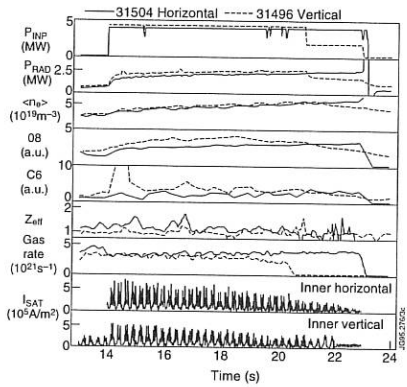

Fig. 4. Main plasma and divertor parameters for two similar discharges on the horizontal and vertical plates

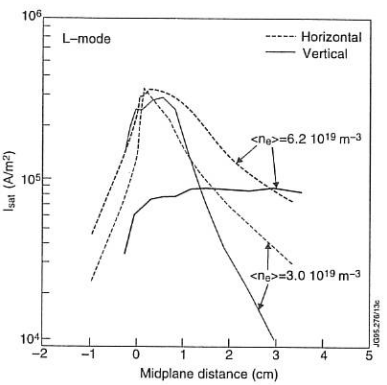

Fig. 5. Modelled horizontal and vertical divertor ion flow profiles for medium and high density L-mode conditions.

Power deposition studies in the JET Mk I pumped divertor

S Clement, D J Campbell, A Chankin, J P Coad, L Horton, A Loarte, J Lingertat, R Monk[1], A Tabasso[2] and R Viola[3]

JET Joint Undertaking, Abingdon, OXON, OX14 3EA, UK

[1]Department of Physics, Royal Holloway College, University of London, Surrey, TW20 OEX, UK.

[2]Imperial College of Science, Technology and Medicine, London, SW7 2BC, UK.

[3]Joint Research Centre, Petten, NL.

1/ INTRODUCTION. The study of divertor performance under steady-state conditions at high power is a central goal of the JET Pumped Divertor programme. Particular care has been taken in the design and installation of the Mk I divertor target so as to optimise its power handling, in particular by avoiding exposure of tile edges, which, in previous JET divertor configurations, limited the range of heating power due to the occurrence of carbon blooms. In addition, the strike points can be swept over the target plates at 4 Hz with an amplitude of up to 20cm so as to increase the effective wetted area of the target. The Mk I JET divertor has shown an excellent power handling capability during the current experimental campaign. In the first part of the experimental campaign, the Mk I divertor target plates consisted of small fibre-reinforced carbon tiles clamped to a cooled support; in March 1995, Be tiles replaced the CFC tiles. The performance of the target has been investigated over a wide range of plasma conditions, at powers of up to 28MW and in steady-state H-modes lasting up to 20s.

2/ EXPERIMENTAL. The surface temperature of the divertor tiles is measured by an infrared thermography system, consisting of a linear array of InGaAs diodes oriented along the radial direction of the divertor and sensitive in the 1.6 μm region. The spatial resolution along the radius is 3 mm; the signal is averaged toroidally over the width of 4 pairs of tiles. In this way, the temperature measured underestimates the maximum temperature in each averaged region, and has to be subsequently corrected for the real wetted area of the tiles. The time resolution of 2ms permits (marginally) the study of fast events such as ELMs. The minimum detectable temperature is 350 to 560°C; the initial temperature of the tiles given by thermocouples imbedded in the tiles. One video camera and 3 spectroscopic CCD cameras (Dα, Be II or C II, and Bremsstrahlung filters) are focused on the same area as the IR camera, and an extra CCD camera coupled with a light source is used between shots to observe the target. The power conducted to the tiles and the corrected temperatures are calculated by a dedicated parallel processor system.

The problems encountered in the interpretation of the IR data arise not only from the 1D toroidal averaging for a very non-symmetrical tile geometry, but also from the contributions of non-thermal emission to the signal, and from thermal radiation emitted by re-deposited layers and loose flakes that have poor thermal contact with the bulk material.

modes: in a typical hot ion mode case (#34230) with a long ELM-free period, P_{cond}=10MW, and 1D power calculation with the corrected temperatures gives P_{innner}=4.5MW, P_{outer}=3.5MW, hence P_{target}=8±2 MW. Langmuir probes however find only ~1MW conducted in the electron channel [4]. This is attributed to the high SOL ion temperature in this regime. In high performance Elm-free H-modes the power sharing between inner and outer strike zones is more balanced than in L-mode in the same configuration.

The effect of giant ELMs is twofold [5]: first, a fast (<1ms) power deposition occurs in the inner divertor, away from the strike zone, with typical energies around 100kJ; then a back-transition to L-mode confinement is often observed, during which energy is deposited at the strike points (already hot); this second phase has caused melting in the Be tiles). The power distribution inner/outer clearly changes between ELMs.

High frequency ELMs are produced in discharges with medium to high gas fuelling. These ELMs also tend to deposit power in the inner divertor target during the fast event, and at the high repetition rates obtained, the net effect is a broad power deposition profile on the target. Combining gas fueling and sweeping, a 20s H-mode has been obtained, at medium injected power (8.5 MW, 120 MJ), where the tile temperature stayed below 550°C. However, high gas fueling at powers near to the H-mode threshold can cause a back-transition into L-mode, where the benefits of the ELMs are lost (fig4).

5/ SUMMARY AND CONCLUSIONS. a) The Mk I divertor targets have shown a very good power handling capability both in the CFC and Be versions. In CFC, 140MJ have been injected, of which more than 100MJ were conducted to the horizontal target. For the side plates the values are 85 and 50MJ respectively. The Be target sustained more than 60MJ conducted to the horizontal target, and more than 20MJ on the side plates. With the CFC tiles, in no case has a carbon bloom limited the performance as in the past. The more limited power handling capability of the Be tiles has nevertheless permitted the high current/high power programme to be carried out by using the sweeping capability.

b) Within the uncertainties of the measurements of the IR thermography, a satisfactory global power balance (≈80%) is found in quiescent discharges, both in L- and ELM free H-modes. **c)** Frequent ELMs are extremely effective in alleviating the heat load on the strike zones, by spreading the power over a large surface area of the divertor target, but the penalty is the uncontrolled deposition of power in zones which may have a poor power handling capability. In the case of giant ELMs, the increased power deposition on the strike zone associated with the frequently observed back-transition to L-mode confinement cancels out the benefit of the initial power spreading. **d)** The largest uncertainties in the thermography measurements arise from the existence of loosely bound re-deposited layers on the target surface, that have a poor thermal contact with the bulk material. The

Furthermore, the emissivity of the Be surfaces changes significantly when power is deposited on the tiles. JET Neutral Beam test bed results shows emmisivity changing between 0.2 and 0.8, with a strong dependency on temperature and thermal cycling [1].We attempt to address these problems by using a careful reconstruction of the wetted areas and 3D modelling of the temperatures, measuring the bremsstrahlung profile at the same location, and analyzing the cooling rates to distinguish between bulk material and loosely bound materials. Nevertheless, temperature measurements on the Be tiles have a high uncertainty due to the changing emmissivity and loose flake effects.

3/ POWER HANDLING OF THE CFC TARGET. A quantitative analysis of the power deposition on the Mark I divertor tiles has been carried out with TILO [2], a code that computes the power density on the tile surfaces, taking into account the shadowing patterns, and allows further thermo-mechanical analysis of the tile(s) considered. Four inputs are needed: the magnetic geometry of the plasma, given by the equilibrium code PROTEUS; the power conducted to the divertor tiles, calculated from measured plasma parameters as $P_{cond}=P_{in}-P_{rad}-dW/dt$; the decay length of the power density λ_p, measured with the IR camera; and the geometry of the divertor tiles, which is imported from a CAD system. The resulting power density on the target is then input to ABAQUS and the calculated time evolution of the peak target temperatures at the strike points can be compared with those measured with the infrared thermography [fig2].

A simple case has been chosen: the shot #30909, with $I_p=3.2MA$, $B_t=3.2T$, 6MW of NBI heating, L-mode confinement (hence no ELMs) and no sweeping of the strike regions. In this shot, $\lambda_p=1cm$ at the midplane, and $T_{initial}$ (thermocouples)$=40°C$.

The results of the simulation are: $P_{in}=0.85$ ($1/2\ P_{cond}$)$=0.425\ P_{cond}=2.3MW$, $P_{out}=1.40$ ($1/2\ P_{cond}$)$=0.7\ P_{cond}=3.85MW$. The calculated conducted power is 112% of the measured conducted power: this is a satisfactory power balance, considering the error of 10-20% in the experimental values, and the uncertainties in the material properties of the tiles. P_{out}/P_{in} differs only by 10% from the value of $T_{out}/\ T_{in}$, which means that the tiles behave like a semi-infinite solid to a reasonable approximation, and that the peak temperature values can reasonably be compared to make power imbalance assessments. The result of the TILO simulation shows that the tiles are handling ≈20% more power than predicted from the design parameters [3]. Sweeping the strike regions further enhances the power handling capability of the target. Comparison between two similar shots with and without sweeping show that, for a ratio of λ_p/sweep amplitude$=0.44$, the effective power seen by the target is $P_{swept}<0.66P_{unswept}$, in agreement with the calculated increase of the wetted area with sweeping [3].

4/ POWER BALANCE AND DISTRIBUTION IN DIFFERENT REGIMES. A good global power balance is found in L mode regime, and also in quiescent ELM-free H-

redeposition pattern has been observed to vary on a shot by shot basis [6]. The analysis of the cool down characteristics, coupled with careful modelling, can help to identify the bulk heat transmission processes.

Special thanks are due to Mr. P van Belle.

[1] H Falter et al, to be published.
[2] R. Viola. TILO USER'S MANUAL (JET).
[3] C G Lowry, private communication.
[4] K McCormick et al, these proceedings.
[5] J Lingertat et al, these proceedings.
[6] H Guo et al, these proceedings.

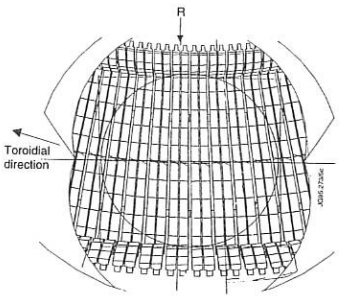

Fig.1. View of the divertor target for the IR camera, and various 1D and 2D CCD cameras, from a vertical port in the JET vessel.

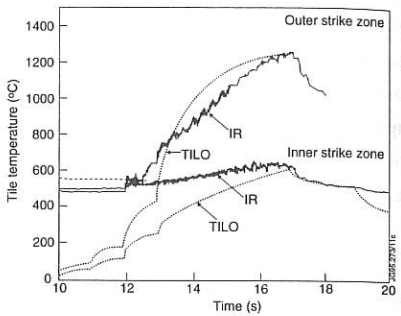

Fig.2. Measured peak temperatures in the strike zones and results of the TILO calculations.

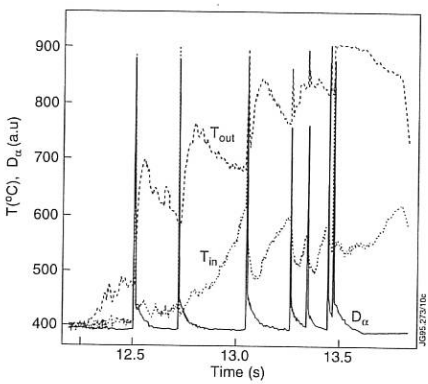

fig 3. Maximum temperatures in each divertor side,and D_α, in shot 34460.

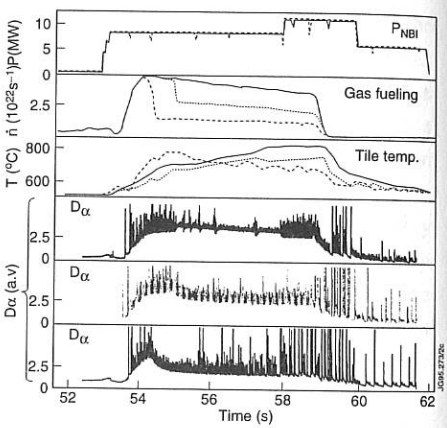

fig.4. Effect of gas fuelling in three similar discharges with different fueling rates (shots #31862 (1), #31863 (3) and #31865 (2)).

Divertor Similarity and Multi-machine Scaling Experiments

G. C. Vlases, I. H. Hutchinson[1], and Z. A. Pietrzyk
Jet Joint Undertaking, Abingdon, Oxon OX 14 3EA, England
[1]M. I. T. Plasma Fusion Center, Cambridge, Massachusetts, USA

1. Introduction

In this paper we address the question of whether experiments can be carried out in existing and planned tokamaks in which the appropriate dimensionless parameters in their divertors can be matched to those expected in the ITER divertor. This question is an extension of the question of whether a toroidal ITER divertor simulator could be built, as discussed first by Lackner [1] and subsequently by Hutchinson and Vlases [2]. The second reference also developed the question of what can be done in existing tokamaks, which is expandedupon in the present paper.

2. Divertor Similarity- Unconstrained

In order to have divertor similarity in the strictest sense, all relevant dimensionless parameters, and the geometry, must be the same in the simulator as in ITER. Lackner showed that similarity of all binary atomic collision processes (including radiation) is achieved if the absolute temperature, T, is the same in both devices. He further showed that exact similarity of the entire tokamak, i.e. core, edge, and divertor regions, is not possible, and was thus led to analyze the conditions for similarity of the divertor as an isolated system, arguing that the important processes such as charge exchange and radiation might be modelled independent of the tokamak driving the divertor. He chose to maintain exact geometrical similarity, and showed that the similarity parameters temperature, T, parallel collisionality, $\nu^* = L/\lambda_{e\text{-}i} \sim nL/T^2$, and a perpendicular relative neutral penetration distance, $\nu^o = \lambda_o/\Delta \sim n\Delta/f(T)$ could all be matched if the power entering the SOL was given by the relation $(P/R)_{sim} = (P/R)_{ITER}$, which requires values of P higher than those possible in existing or planned tokamaks. The required divertor depth (x-point to strike point) is determined by the required geometrical similarity. Here Δ is the SOL width and L the field line length. In principle, $\beta = 2\mu_o nkT/B^2$ could also be matched, but the magnetic fields would have to be higher than those in ITER, which is difficult to achieve. $\rho^* = \rho/\Delta$ (ρ is the gyroradius; note that this is not the "core" definition of ρ^*) cannot be matched.

Hutchinson and Vlases showed that if the field line pitch angle, $\alpha_d = \tan^{-1}(B_p/B_T)$ were allowed to be shallower than that in ITER, then all five divertor similarity parameters listed above, T, ν^*, ν^o, ρ^*, and β, could all be matched simultaneously. The matching of β requires $B_{sim} = B_{ITER} = 6$ T. The power required is considerably lower than that given by the "P/R scaling", and goes roughly as $P^{1.5}$. They showed that a tokamak driven simulator with R = 1m and a midplane SOL width half that of ITER would require only P = 18 MW, n equal 1/2 that of ITER, and a divertor depth of 1 m. The perpendicular (to B) motion of neutrals is correctly modelled. The penalty for relaxing the field line angle is that the neutrals emitted from the plate and going "directly back" along flux surfaces and reionized, do not have the ratio

$\lambda_{o.pol}/d_x$ preserved, where d_x is divertor depth, measured along the separatrix from x-point to target and $\lambda_{0,pol,||}$ the neutral mean free path in the direction parallel to poloidal flux surfaces. The fraction of such neutrals, however, is expected to be quite small in detached divertors, particularly those with steeply inclined targets as envisaged for ITER, and thus their "mismatch" should be unimportant.

We note that simulating an "isolated divertor" such as we are doing here ignores certain phenomena in the main plasma edge, in particular ELMs and the L-H transition, which affect divertor performance. Thus, any results obtained in such similarity experiments must be treated with caution.

3. Approximate Similarity in Todays Divertors - with Constraints

We turn now to the question of how closely existing tokamaks can approximate ITER divertor similarity parameters. The approach adopted in ref [2] is first to calculate the similarity parameters in the divertor of a given tokamak, relative to the values in ITER (the ratio is in the rest of this paper denoted by an underscore, i.e. $\underline{B} = B_{sim}/B_{ITER}$) by using a simple two point model. The input or "control" parameters, which are BL, P, f_e, and d_x, are then varied to minimize the mismatch between the simulator and ITER values of the similarity variables, which can be weighted in an arbitrary fashion. The two point model uses Bohm, gyrobohm, or stochastic scaling of the perpendicular diffusivity. In all existing or planned tokamaks it is impossible to achieve the idealized matching of all five similarity variables as described above because of various constraints, the most common of which are limited magnetic field strength, flux expansion (f_e) capability (which determines α_d), and divertor depth (d_x). In the following examples we choose to match T, ν^*,ν^o, and ρ^* at the divertor entrance and target, and not to try to match β.

Table 1 shows the results of such an optimization for the case of Bohm diffusivity. The safety factor is taken to be the same as in ITER ($\underline{q} = 1$). The first eight rows list the input parameters which were assumed. The next eight rows (light shading) show the fits obtained to the ITER similarity parameters for the various devices; a value of 1.0 is a perfect match. Rows 19 and 20 (darker shaded) show the heating power and the midplane density. JET is capable of matching the ITER parameters within about 25%, with C-mod and TPX being the next closest. The powers required are in general around the maximum available from the various devices, but considerably below that which would be required using the geometry preserving "P/R" scaling. The last two rows show the values of b and a parameter measuring the mismatch of directly reionized recycling neutrals, $\underline{n_t d_x} \sim (\, l_{0,pol,||} / d_x)^{-1}$.

The match can be improved by operating the simulator at twice the safety factor of ITER ($\underline{q} = 2$). This has the effect of lengthening the field lines in the divertor. The results, using the same input as for table 1 except for the changed safety factor, are shown in Table 2. It can be seen that the fit to virtually all of the dimensionless variables, for all of the devices, in improved considerably. In addition, the power required has decreased to relatively moderate levels. The principal instance where the fit worsens is in the $\underline{n_t d_x}$, which is expected to be unimportant.

	ITER	JET	AUG	JT-60	DIIID	C-MOD	TCV	TPX
BT (T)	6	3.4	3.5	4	2.1	9	1.4	4.0
R (m)	8	3	1.6	3.3	1.67	.67	.88	2.25
fe	2.5	5	4	4	7.5	5	10	3.8
d_x (m)	2	.6	.25	.3	.45	.22	.3	.6
BL m	1	.213	.117	.275	.073	.125	.026	.187
fe	1	2	1.6	1.6	3	2	4	1.5
dx	1	.3	.125	.15	.225	.11	.15	.3
Ld/Lm	1	1.6	1.0	.58	3.2	2.62	5.45	1.6
Td	1	.76	.56	.51	.78	.88	.76	.80
vd	1	.80	.97	1.20	.60	.67	.48	.82
ndΔd	1	1.11	1.24	1.42	1.04	.97	1.0	1.04
ρ_d^*	1	1.07	1.59	0.97	1.32	1.51	1.74	1.51
Tt	1	.74	.58	.60	.68	.76	.60	.75
vt	1	.88	.86	.72	.93	1.03	.98	1.0
ntΔt	1	1.14	1.19	1.19	1.20	1.13	1.26	1.11
ρ_t^*	1	1.05	1.63	1.06	1.23	1.41	1.55	1.46
p	1	.364	.33	.35	.22	.37	.15	.47
nmLm	1	.33	.31	.45	.16	.26	.084	.375
P (MW)	300	41	19.8	43	14.0	9.3	5.0	40.
nm	1	.88	1.55	1.09	.76	3.1	.76	1.3
β	1	1.83	2.53	1.47	3.5	.93	6.5	2.1
ntdx	1	.26	.19	.16	.17	.34	.11	.40

Table 1. ITER Matching for q = 1 and restricted f_e and d_x

	ITER	JET	AUG	JT-60	DIIID	C-MOD	TCV	TPX
BLm	1	.42	.23	.55	.14	.25	.05	.375
Td	1	.88	.65	.58	0.90	1.02	0.88	.93
vd	1	.80	.98	1.20	0.60	0.66	0.48	.81
ndΔd	1	1.08	1.21	1.38	1.01	0.95	0.97	1.00
ρ_d^*	1	0.79	1.17	0.71	.97	1.11	1.28	1.11
Tt	1	0.86	0.68	0.70	0.79	0.88	0.70	87
vt	1	0.86	0.85	0.71	.91	1.01	0.96	.98
ntΔt	1	1.11	1.15	1.15	1.17	1.09	1.22	1.07
ρ_t^*	1	0.78	1.20	0.78	.91	1.04	1.14	1.08
p	1	.44	.40	.42	.27	.45	.18	.57
nmLm	1	.44	.41	.61	.21	.34	.11	.50
P(MW)	300	24.7	12.0	26	8.5	5.6	3.0	24
nm	1	.59	1.02	.74	.50	2.0	.50	.90
β	1	1.4	1.95	1.13	2.68	0.71	5.0	1.6
ntdx	1	.17	.13	.11	.11	.22	.075	.26

Table 2. ITER matching for q = 2. All other input same as table 1.

We next consider only a set of existing tokamaks, and take ASDEX as the representative "standard case". Each of them has a different divertor geometry. We now constrain only the divertor depth to the maximum available, except for the three JET cases representing different divertor depths. The results are shown in Table 3. It is seen that JET, DIII D, and ASDEX-UG can be operated in such a way as to achieve nearly identical values of the important divertor similarity variables. This suggests the possibility of carrying out "matched" ϵ ‹periments in the three devices to attempt to understand the influence of the varying geometry.

	AUG	JET $d_X = .6$	JET $d_X = .45$	JET $d_X = .35$	JT-60	DIIID	C-MOD	TCV
BLm	1	1.82	1.82	1.82	2.36	.63	1.07	.22
fe	1	.77	.75	.75	.67	1.25	.96	2.04
p	1	1.59	1.43	1.30	1.40	0.79	1.37	.52
nmLm	1	1.54	1.56	1.58	1.95	0.70	1.01	.31
Td	1	1.20	1.03	.90	.82	1.03	1.47	1.29
v_d^*	1	1.03	1.15	1.26	1.47	.86	.77	.54
ntΔd	1	0.91	1.0	1.08	1.16	.97	.79	.81
p_d^*	1	1.03	.96	.90	0.84	1.06	1.18	1.30
Tt	1	1.17	1.08	1.00	0.97	0.97	1.25	1.0
vt	1	1.10	1.02	.94	0.89	1.02	1.24	1.17
ntΔt	1	0.93	.96	.98	0.98	1.02	0.93	1.05
p_t^*	1	1.01	.98	.95	0.92	1.03	1.09	1.14
P(MW)	8	23.8	21.4	19.5	23.1	6.6	4.6	2.3
nm	1	.82	.83	.84	.94	.67	2.4	.56
β	1	1.03	1.01	.96	.78	1.73	.44	3.0
ntdx	1	1.96	1.49	1.17	1.12	.80	2.11	.67

Table 3. Matching to A-UG.

4. Conclusions

We have considered the similarity of the divertor as an isolated system, as developed by Hutchinson and Vlases [2], and applied their technique to optimization of todays tokamaks. When current devices are operated at twice the value of the ITER safety factor, i.e. at q ~ 6, several of them are capable of producing similarity parameters, other than β_{div}, which are quite close to those expected in ITER. As a second example, we have considered the comparison of parameters within the group of existing tokamaks, and found that JET, A-UG, and DIIID can produce nearly identical parameters, thus isolating the effects of their differing geometries and main plasma edge conditions. It should be emphasized, however, that matching of these similarity parameters in the divertor, while necessary, may not be sufficient due to the differing main plasma edge properties which influence divertor performance.

References

1. K. Lackner, Commments on Plasma Physics and Controlled Fusion (1994)
2. I. H. Hutchinson and G. C. Vlases, JET Report JET-P(94)32 (to be published)

Power and particle flux to the neutraliser plates of the Tore Supra ergodic divertor

A. Grosman, Ph. Ghendrih, S. Féron, D. Guilhem,
T. Loarer, B. Meslin, F. Nguyen, H. Garcin, K. Mony, J.Y. Pascal, S. Vartanian
Association EURATOM-CEA, DRFC, Centre d'Etudes de Cadarache
F-13108 St Paul lez Durance (FRANCE)

1. Introduction

In order to investigate steady state regimes, the ergodic divertor of Tore Supra [1] must control the power flux to its neutraliser plates while ensuring a sufficient pumping capability. The physics of these processes is the same as that of conventional divertors although the geometry is somewhat more involved. The ergodic divertor offers therefore a means to examine ITER relevant problems with different geometrical constraints. The energy deposition is monitored by calorimetric measurements which are complemented by bolometry and infrared imaging. The imaging of an actively cooled plate with a low thermal time constant yields a precise map of the 2-D patterns of the power flux [2]. Although the average power deposition remains constant, one finds that the power flux pattern on one neutraliser is sensitive to minor changes of the plasma magnetic equilibrium such as a modification of the edge safety factor by about 2%. This property is analysed in ohmic plasmas and good agreement is found with patterns computed with the field line tracing code Mastoc. Langmuir probes give access to the plasma parameters at the plate location but without a detailed map of the particle influx.

2. Energy transport and deposition : theory and experiments.

2.1 Theoretical considerations : A first step in the analysis of heat deposition with the ergodic divertor has been to rule out the naive picture of wall components wetted in an ergodic way (meaning uniformly) by the field lines. Indeed the naive picture of the ergodic heat deposition assumes a purely diffusive motion of the field lines, with a diffusion coefficient of the order of $D_{FL} \sim 10^{-4}$ m^2 / m. This random walk process is based on a large number of steps, hence infinite field lines. The intersection with wall components clearly violates this assumption. In this case, the very last step in the random walk determines essentially the intersection point. Starting from the energy sink which characterises the plasma interaction with the wall, one can draw in the parallel direction a coherent flux bundle which bares the memory of the interaction. In the domain where coherence properties prevail, the so-called laminar region, the transport process is dominated (by definition) by the parallel transport with a small effect of the transverse transport. Such a transport scheme is generic of divertor configurations. The experimental evidence of the corresponding structures of the heat deposition have already been reported for the deposition on the modular limiter located in the

mid plane. The field line tracing code (MASTOC) clearly exemplifies these results [3]. Obviously, this computation has shown that field lines experience a radial "jump" from one magnetic surface to another (the magnetic surfaces referred to are the unperturbed magnetic surfaces) only at the location of the divertor coils. Consequently, the computation of the field lines radial penetration with the code MASTOC gives a generic pattern of the heat deposition on a divertor module. An analysis of the energy deposition at a sufficient level of precision must account for all magnetic perturbations to the axisymmetric magnetic equilibrium, the largest being the ripple modulation of the toroidal field. It should be noted that the amplitude of its radial component is at maximum slightly larger than the one due to the ergodic divertor coils themselves. A local calculation of the total radial component between the bars has been achieved and has been appended to the MASTOC code to allow an accurate comparison between its results and the experimental observations.

2.2 Comparison with experiments : At first, one should examine the overall splitting of the conductive and radiative fraction of the heat outflux. This will allow one to take into account the deposition on other plasma-facing components than the ED modules themselves. Then, a first order analysis indicates that the heat deposition is modulated according to the poloidal structure of the magnetic perturbation. On a more detailed basis, one must investigate the effect of the perturbation on the connection properties. In fact, the energy deposition pattern exhibits fine structures which translate into a non homogeneous deposition on the neutraliser plates themselves. The size of these structures are a significant fraction of the total surface each of the neutraliser plates (~ 0.10 x 0.05 m^2).

This is analysed in a series of shots such that the magnetic configuration of the plasma is slightly modified by decreasing the major radius on a shot to shot basis (table 1). Calorimetry measurements of the water-cooled elements, in figure 1, indicates the splitting of the conductive-convective and radiative (including charge-exchange) power to the neutraliser plates and front face of the ED modules and to the inner bumper limiter. The latter intercepts a significant fraction of the conductive power with an e-folding length of about 0.02 m in the high-field side, i.e. λ_q = 0.01 m on the low-field-side. On the contrary the conductive power increases, despite a growing mismatch between the plasma minor radius and the radius of the modules, 0.8 m. The conductive power to the ED modules remain equally shared between the neutraliser plates and the front face. Calorimetry also allows one to analyse the partition between the six toroidally spaced modules as done in [4].The radiative outflux is noteworthy a little higher in the vicinity of the ED modules. On the dedicated neutraliser plate for infrared imaging, the low thermal time constant (about 5 ms, i.e. less than the lapse of time between two successive thermal images) of its thin boron carbide layer allows one to translate approximately the temperature map into the heat flux map . The structures are clearly visible and appear to exhibit the highest degree of modification for a variation of the edge safety factor by about 2% as shown in figures 2a and 2b. The very high degree of sensitivity on the

magnetic configuration is also found in experiments where $\beta_p+l_i/2$ increases due to auxiliary heating .

An application to the experimental case mentioned above allows one to link the heat deposition to the flux tubes connection to the plasma. In figures 3a and 3b, the maximum radial penetration of the flux tubes for 3 toroidal turns (approximately, the thermal conduction correlation length) is displayed. It compares well with the experimental images especially as far as the general shape and its radial variation by changing the safety factor q is concerned. This seems to confirm that the major reason to explain the inhomogeneity is the large probability (about 40% [4]) that a field line leaving the ED modules intersects it after only one poloidal turn. Only the longer flux tubes yield significant heat fluxes on the neutraliser plates. The analysis of thermal images allows one to derive a peaking factor for the heat flux on a neutraliser plate. In appropriate cases with q about equal to 3, the heat flux is rather evenly distributed as the peaking factor is about 2 if the whole surface is concerned and would be restricted to 1.7 if only the wetted area is taken into account. A sweeping capability exists for such a deposition scenario by inducing very modest changes of the plasma current and of the magnetic equilibrium.

3. Particle fluxes to the divertor neutraliser plates

The particle flux to the neutraliser plate has been deduced from Langmuir probes mounted on the neutraliser plates. It is not possible to study the inhomogeneities that way. Nevertheless, an interesting observation can be made : the local density remains small (lower than 10^{19} m^{-3}) for the series of shots studied hereabove. The lack of local condensation should be related to the rather high electron temperature measured within the edge region by a reciprocating Langmuir probe (see figure 4). The simple fact that the radial modulations affect much more the electron temperature profile than the density profile, shows that the dominant heat transport is in the parallel direction whereas the particle source is certainly more evenly distributed in this layer due to an increased transverse transport.

4. Conclusions

The heat flow to the plasma facing components in the ED configuration of Tore Supra is essentially determined by the parallel transport along a thermal correlation length, i.e. about one toroidal turn : this allows one to use a field line tracing code (MASTOC) to derive the general shape of the heat deposition.

References :

[1] P. Ghendrih et al., Plasma. Phys. and Cont. Fus., 34(1992)2007-2014.
[2] D. Guilhem et al., Europhys. Conf. Abstracts, Vol 18 B, II-750 (1994).
[3] F. Nguyen, Ph. Ghendrih and A. Samain, Report EUR-CEA-FC-1539 (1975).
[4] Ph. Ghendrih, A. Grosman and F. Nguyen, J. Nucl. Mat., 220-222(1995)511.

Table 1 : Shot characteristics

Shot#	q(a)	R(m)	a(m)	B_t(T)	Ip(MA)	Idiv(kA)	βp+li/2
15518	2.96	2.398	0.775	3	1.465	38.5	0.72
15519	3.01	2.39	0.775	3	1.465	38.5	0.73

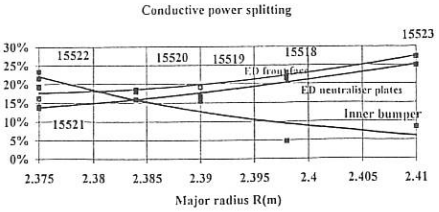

Figure 1 : Conductive power splitting between the ED elements and the inner limiter

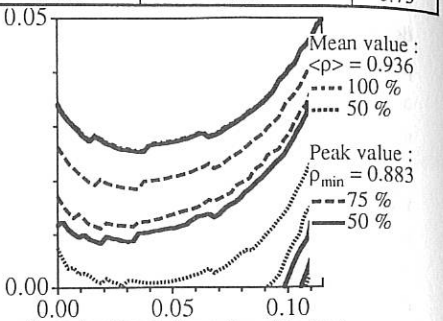

Figure 3a : Penetration radius of the field lines leaving the neutraliser in shot # 15518 same axis as in figure 2

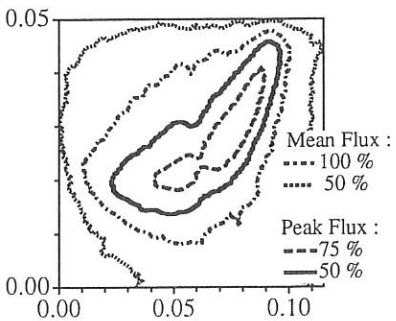

Figure 2 a : Power deposition on the ED neutraliser plate in shot # 15518 ; abcissa : poloidal, ordinate : radial

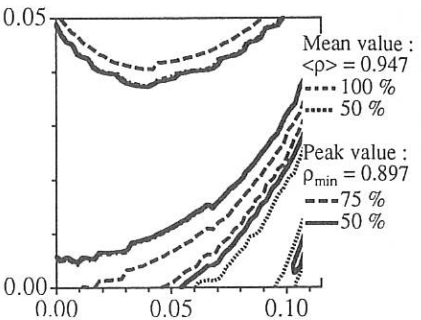

Figure 3b : Penetration radius of the field lines leaving the neutraliser in shot # 15519 same axis as in figure 2

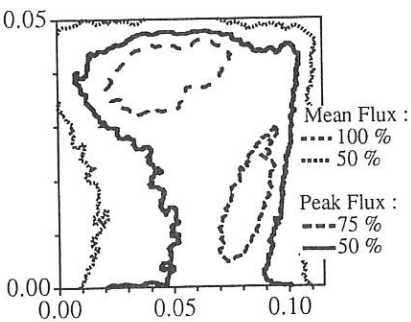

Figure 2 b : Power deposition on the ED neutraliser plate in shot # 15519 same axis as above

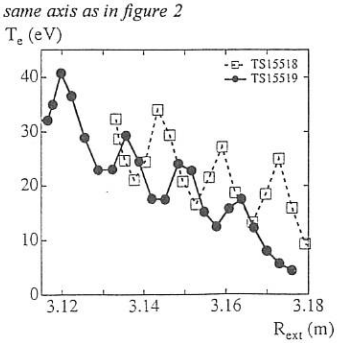

Figure 4 : Electron temperature profiles measured by a reciprocating Langmuir probe in shots 155518-15519

Analysis of Particle Flow in the DIII-D SOL and Divertor[1]

G. D. Porter, M. Rensink, T. Rognlien, G. Smith, and the DIII-D team[2]
Lawrence Livermore National Laboratory, Livermore, CA, 94550 USA

1. Introduction

The scrape-off layer (SOL) and divertor plasma in the DIII-D tokamak has been modeled using the 2-D fluid code UEDGE[1][2][3]. The resulting simulated plasmas are compared in detail with the numerous diagnostics available on the device. Good agreement is obtained between the experimental measurements and the simulations when relatively small values of the assumed anomalous perpendicular transport coefficients are used. We use a purely diffusive model for perpendicular transport, with transport coefficients which are constant in space. The value of each of these transport coefficients is varied in the simulation to match the measured upstream density and temperature profiles. The resulting plasma parameters are then compared with all other diagnostics which measure parameters at various poloidal locations in the SOL.

One of the difficulties in this procedure arises from experimental uncertainty in determining the total particle flux from the closed flux surfaces into the SOL. One can gain confidence that the thermal diffusivities which are used to obtain consistency of the upstream temperature profiles between simulation and experiment are also consistent with the experimentally inferred power to the SOL, i.e., not only do the assumed diffusivities produce consistency in the upstream radial profile of the temperature, but the power across the separatrix, determined from a diffusive model and hence dependent on the temperature gradients, is also consistent with the power into the SOL determined experimentally. Analogously, one could test the particle diffusivity used to simulate the density profiles by comparing with the total particle flux into the SOL. Unfortunately, the particle flux is not well determined experimentally. Furthermore, the simulated density profile is determined by at least three parameters; the particle diffusivity, and the recycling coefficients for both neutrals and ions at the walls of the vessel (including the divertor plates). None of these parameters are well known. We discuss the effect of the particle flux and recycling in this paper. We begin by briefly discussing the expected particle flow channels in the plasma, and the experimental estimates of the particle flux across the separatrix in Section 2. We compare the simulations of a specific DIII-D discharge with experimental data in Section 3. We finish with discussion in Section 4.

2. Experimental estimate of particle flux

There are at least three sources of particles inside the last closed flux surface of a tokamak plasma: (1) high energy neutrals introduced by neutral beam heating; (2) neutral gas injected outside the SOL plasma to control the plasma density; and (3) neutral gas produced by recycling of ions impinging on the divertor plates. (We

[1]Work supported by U.S.DOE under LLNL Contract W-7405-ENG-48 and GA contract DE-AC03-89ER51114
[2]General Atomics, La Jolla, CA, USA

speak here only of the primary gas species, not impurity species.) The ionization source rate of energetic neutrals from the heating systems is typically a few hundred amps (5–20 $\times$ 10^{20} /s). The second source of particles, injected cold gas, is usually turned off in the H-mode plasma operation considered here. The final particle source, recycling gas, is the major source of uncertainty in determining the particle flux into the SOL. A small fraction (typically no more than a few percent) of the neutral gas which originates from recycling of the ions impinging on the divertor plates will be ionized inside the last closed flux surface, and hence be a source of particles flowing from the core into the SOL. Thus the core ionization source from recycling depends not only on the recycling coefficient at the divertor, but also on the probability of a neutral penetrating to the core and hence on the detailed plasma parameters in the SOL. At steady state all ions created by ionization of neutrals inside the separatrix must flow into the SOL and be removed. Hence the particle flux into the SOL must be equal to the total ionization rate in the core plasma.

Experimentally one can estimate the total ionization rate from all sources by examining the behavior of the density at a plasma transition such as the L- to H-mode transition. Using temporally fixed values for all parameters except the density (particle confinement time, divertor recycling coefficient, wall neutral particle albedo, and penetration probability for neutral gas sources into the core plasma), the temporal behavior of the total number of particles inside the separatrix is given by[4]

$$N_{core}(t) = N_{core}(\infty) + \left[N_{core}(0) - N_{core}(\infty)\right] \exp\left\{\frac{-t}{\tau_p^*}\right\} \quad (1)$$

Where τ_p^* is the core confinement time corrected to include sources from divertor recycling, and the equilibrium particle content, $N_{core}(\infty)$, is determined by the total ionization rate in the core plasma. One can estimate the total ionization source inside the separatrix by fitting the temporal behavior of the particle content observed at the L- to H-mode transition to Equation 1. Typically we find the experimental particle content, obtained from Thomson scattering data with the assumption of constant density on flux surfaces inside the separatrix, is described well by Equation 1 throughout the period from the transition until density equilibrium has been achieved after the onset of Edge Localized Mode (ELM) activity, suggesting that the assumptions inherent in deriving this equation are reasonable. The total ionization source inferred by this process is a few kA, or a few times 10^{22}/s, approximately an order of magnitude higher than expected from neutral beam sources.

3. Comparison of simulation and experiment

We explore the nature of recycling physics by simulation of a specific discharge on the DIII-D tokamak; a 1.6 MA lower single null configuration with neutral beam heating of approximately 6 MW. Inversion of the radiated power profile obtained from two bolometer cameras indicate 1 MW of power is radiated on the closed flux surfaces, and an additional 1.9 MW is radiated in the SOL and divertor regions. Application of the analysis described in the previous section indicates an ionization rate inside the separatrix of about 2.7 kA (1.7×10^{22}/s), decreasing rapidly as one

moves inward from the separatrix. The simulation is done over a radial region between a normalized poloidal flux of 0.98 and 1.125. We assume a fixed power and density at the inner flux surface, and adjust the thermal diffusivities to match the electron temperature and density profile measured by the Thomson system, and the ion temperature profile measured by Charge Exchange Recombination. We assume the ion recycling coefficient at the divertor plate is unity except in the region which corresponds to the entrance to the pumping chamber under the outer ring of the DIII-D divertor, where we assume that only 90% of the ions are recycled as neutrals. Finally, we assume a neutral particle albedo of 0.95 on both the outer wall and the private flux wall which provides particle removal. Upon matching the upstream density and temperature profiles, the consistency between the simulation and experiment is determined by comparison of the power deposited in the divertor, measured with an IRTV system; H_α emission measured with a 7 channel array which views the divertor from above the machine; radiation profiles measured with two bolometer camera arrays; and the ion saturation current at the plate measured with a Langmuir probe array.

We consider two simulations which differ in the value of the particle diffusivity. The first case has a diffusivity of $D_\perp = 0.15\ m^2/s$ with a corresponding particle flux across the separatrix of 2.2 kA, and obtains the best overall fit to the SOL data. The upstream density and temperature profiles are well matched to that obtained experimentally. The simulated peak power at the outer strike point on the divertor floor is within about 10% of that obtained from the IRTV, although the simulated power profile is somewhat narrower than measured. The simulated peak power at the inner strike point is about a factor of 4 higher than measured, and is dominated by recombination of the large ion current. The simulated ion current to the inner strike point is indeed larger than measured with the Langmuir probe array. This discrepancy suggests significant departure in the model of recycling from the behavior of the experiment. We compare the simulated H_α photo diode signals with experimental results in Figure 1. The simulated signal on the channels nearest the strike points is about 70% high on the outside, and a factor of 2 high on the inside. The simulated signals on the three channels which view the private flux region are a factor of 2 to 5 lower than the experiment. These results suggest that the mean free path for recycled neutrals is too short in the simulation,

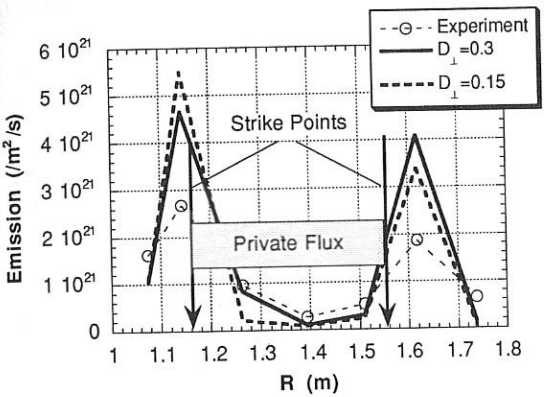

Figure 1: Comparison of simulated and measured H_α emission measured with a photo diode array viewing the divertor from above. The particle diffusivity is given in units of m^2/s.

leading to a larger particle flux amplification from the mid plane to the plate, and low neutral densities in the private flux region.

The simulated H_α signals for a second case with a particle diffusivity of 0.3 m^2/s and resulting particle flux of 3.9 kA across the separatrix is also shown in Figure 1. The large increase in the particle flux increases the convective power across the separatrix to the point that it dominates the power flow. Since the simulation is done with a fixed power, the upstream electron temperature at the separatrix has dropped from about 160 eV to about 120 eV. The combination of lower electron temperature and increased particle flow to the SOL has resulted in a significant drop in the electron temperature at the plate, particularly the inner plate. As a consequence the location of the electron temperature at which ionization of the recycling neutrals occurs (approximately the 5 eV contour) has moved a few centimeters off the inner plate for the high diffusivity case. This in turn permits penetration of the recycling neutrals into the private flux region and increases the emission seen on the photo diodes viewing this region, as seen in Figure 1. Likewise, there is better penetration of recycled gas to the SOL side of the inner divertor region, producing a cooler SOL, and in general a narrower SOL profile. All of these effects depend critically on the electron temperature at the inner plate being very low, less than 1 eV in the simulation. In contrast, interpretation of the Langmuir probe data indicate the plate temperature is 5–10 eV.

4. Discussion

Design of future divertor configurations rely upon control of recycled neutral particles, hence it is important to better model this phenomenon. The results presented here suggest we can better model the neutral particle recycling at the divertor plates, as measured by the H_α emission, with simulations which obtain plate electron temperatures below 1 eV. Such low temperatures provide a long ionization mean free path region for recycled neutrals, permitting neutral penetration around the inner strike point, and more accurate simulation of the measured emission is obtained. The existence of such low temperature regions is inconsistent with Langmuir probe data which indicate plate temperatures of 5–10 eV. Thus it would appear the Langmuir probe and H_α diagnostics are in conflict. The neutral model used in the UEDGE simulations discussed here was a simple diffusive fluid model which did not account for momentum removal via neutral interactions. As indicated here, this model overestimates the ion current to the plates, and hence overestimates recycled neutral densities. This simple model has now been upgraded to include neutral momentum effects, and is expected to permit more accurate modeling of the recycling phenomena. Validation of this improved model will require resolution of the apparent diagnostic conflict.

References

[1] Porter, G. D., et.al., Innsbruck EPS meeting

[2] Porter, G. D., et.al., Varenna PET meeting

[3] Rognlien, T. , et.al., Monterey PSI meeting

[4] This work was originally done by G. Jackson, private communication, General Atomics.

An Investigation of the Extent of Divertor Detachment in Alcator C-Mod

B. Lipschultz, J.A. Goetz, I.H. Hutchinson, B. LaBombard, G. M. McCracken, A. Niemszewski, J.L. Terry, S.M. Wolfe

Plasma Fusion Center, Massachusetts Institute of Technology, Cambridge Ma. 02139 U.S.A.

Introduction

Understanding divertor detachment is essential to predicting the operation of future diverted tokamaks. The current plan for ITER operation assumes that the plasma is detached from the divertor, that $\bar{n}_e$ be near the Greenwald limit [1] and that the main plasma is not diluted by impurities. However, we do not know whether these conditions can be achieved simultaneously. In this set of experiments the core plasma parameters have been varied systematically in order to determine when divertor detachment starts, how the radial extent of detachment grows and how the detachment process can be controlled. Various divertor geometries have been studied in Alcator C-Mod, with most emphasis on equilibria with strike points on the vertical plates[2,3] as shown in Figure 1.

In general, the threshold density for divertor detachment of Alcator C-Mod plasmas has been found to be linearly dependent on the input power for ohmic plasmas [4]. T_e at the divertor plate is ~ 5 eV for flux surfaces about to detach. Under ohmic conditions the core density at the divertor detachment threshold is $\bar{n}_e \sim 0.25 \times n_{Greenwald}$. Other tokamaks, with more open, flat-plate divertor geometries, typically find that the detachment threshold is closer to the Greenwald density limit ($0.5\text{-}0.9 \times n_{Greenwald}$)[5]. More detailed characteristics of divertor detachment and the available diagnostics are found elsewhere [2,4,6].

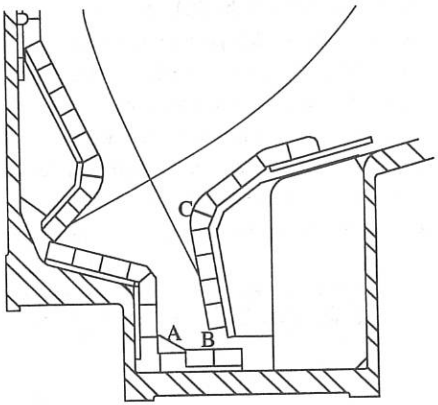

Figure 1: The Alcator C-Mod divertor configuration. A representative equilibrium with outer strike point on the vertical section of the plate is shown.

Density dependence of detachment

The detachment of plasma on a particular flux surface from the outer divertor plate has been determined by comparing the plasma pressure profiles at the target to upstream values in the SOL outside the divertor. Each flux surface is labeled by its distance outside the separatrix on the midplane (ρ in mm). The absolute uncertainty of this mapping is ± 1-2 mm but the relative uncertainty, shot to shot, is ~ 1 mm. Figure 2 shows the growth of the radial extent of detachment for typical ohmic 0.8 MA (5.3 Tesla) plasmas. Included are data from discharges

with outer divertor strike point on the vertical section (figure 1; region B-C) and with the strike point on the floor (figure 1; region A-B) - the so called 'slot-divertor' configuration. From this data it is clear that the radial extent of detachment is a strong function of $\bar{n}_e$ until the divertor pressure deficit reaches the 'nose' of the outer divertor (figure 1, point C). We have varied the density over the widest range for the vertical plate geometry and the detachment extent does not increase beyond the divertor nose (ρ=6 mm) even for densities 2.5 x the detachment threshold.

The effect of the divertor detachment on radiation in the divertor is similarly abrupt. Below the detachment threshold, divertor radiation is peaked near the inner and outer plate surfaces and the magnitude of the radiative loss increases with density. As the detachment of flux surfaces extends up the divertor face to the nose, the majority of the radiation in the divertor region moves inside the separatrix to just above the x-point. The emission distribution does not change as the density is increased further.

The detachment process can cause very large drops in pressure at the divertor surface. Figure 3a illustrates the density dependence of pressure ($2n_eT_e$) at different locations along the vertical plate for the discharges shown in figure 2. The pressure loss at the plate in the private flux region and at the separatrix is very large. Moving further out in the SOL, the effect of detachment on the plate pressure is gradually reduced up to the divertor nose (ρ = 6 mm). In the regions of the outer divertor plate beyond the nose the pressure increases with density, independent of the detachment. There may be some variation among the flux surfaces in the rate of pressure loss with respect to $\bar{n}_e$ (e.g. the

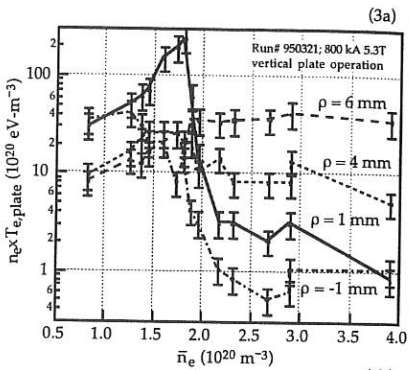

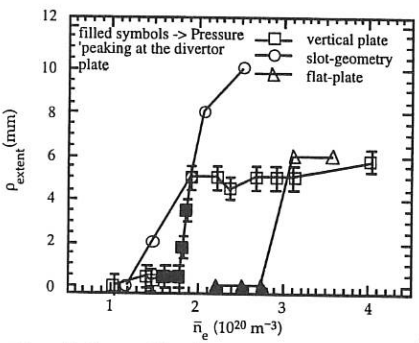

Figure 2: Extent of detachment at the outer divertor for 3 different geometries. ρ corresponds to the midplane radius of the detachment front.

Figure 3: Effect of Detachment on outer divertor plate plasma pressure for vertical plate 800 kA ohmic case of figure 2: a) Plate pressure at different radii; b) Plate pressure normalized to corresponding SOL value.

plasma pressure at $\rho = 4$ mm drops more slowly than in the separatrix and private flux regions).

The plasma pressure loss at the divertor surface can also be viewed as a pressure deficit with respect to the SOL outside the divertor. Figure 3b replots the data of 3a normalized to the pressure upstream on the same flux surface. The level of pressure deficit in the divertor ($2n_eT_{e,plate}/2n_eT_{e,SOL}$) is not necessarily a simple function of density. Often, a small pressure enhancement or `densified region' ($\rho = 1$ mm curve) can appear before detachment spreads across the vertical section. The 'radial' width of this region is small (ρ = 1-2 mm).

Dependence of detachment threshold on divertor geometry

Some aspects of the Alcator C-Mod divertor geometry appear to have a strong effect on the characteristics of divertor detachment. As discussed above, the differences between vertical plate and slot operation are minimal in the onset of detachment. Another common feature is that the extent of detachment is limited to below the divertor nose; $\rho = 6$ mm for the vertical plate data shown and $\rho = 10$ mm for the slot geometry data. For all strike point locations in the region B-C of figure 1, the detachment density threshold does not vary, nor the observation of the localized pressure enhancement prior to detachment. As the strike point is moved closer to the divertor nose (location C) from below, the 'fraction' of the flux surfaces detached from the divertor surface and the fractional pressure loss are reduced.

In an effort to compare C-Mod results with divertor detachment characteristics in other devices a third mode of divertor operation was developed. The plasma is raised such that the inner and outer strike points are located above the divertor noses. Then the angle of separatrix intersection with the divertor plate and access of recycling neutrals to the SOL and core plasmas is similar to the more open, flat-plate divertor geometry found in other tokamaks. Field line lengths in the region below the x-point are decreased. Several differences emerge from this study: The $\bar{n}_e$ required for divertor detachment is increased by 50-80% above that found for equivalent (core conditions, input power, plasma current,...) vertical plate operation (see fig. 2); the pressure deficit at the plate is much smaller ($2n_eT_{e,plate}/2n_eT_{e,SOL} \sim 0.1$ compared to .01 for vertical plate). The extent of detachment increases as the density is increased with the initial pressure loss occurring at ρ =2 mm. The occurrence of a pressure enhancement before detachment initiates is also still observed for the flat-plate configuration.

Modification of the detachment threshold

Core parameters other than density can have a significant effect on the divertor detachment threshold. P_{SOL} (the power flowing across the separatrix), Ip and $B_{Toroidal}$ have all been varied as part of this study. It appears that the density threshold for detachment increases with P_{SOL} and decreases with increasing q. The strongest dependence is on q. Further experiments need to be carried out to test these preliminary results.

We have also studied the efficacy of lowering the detachment threshold by injecting neon gas. The detachment threshold has been reduced to ~ 60% of the non-neon value. Following

divertor detachment, impurity screening of impurities from the core plasma degrades[4,7], increasing both puffed and intrinsic impurities levels there. In these neon puffing experiments Z_{eff} rose from 1.2 to 1.8.

Summary

We find with vertical divertor plate divertor operation that the radial extent of detachment increases strongly with increasing density until the detachment process reaches the 'nose' of the outer divertor, outside which the divertor plate is more horizontal. The detachment extent does not increase beyond the divertor nose even when the core density is more than doubled. Without auxiliary heating or addition of impurity gases, the detachment onset corresponds to $\bar{n}_e \sim 0.25 \times n_{Greenwald}$. The detachment threshold increases with P_{SOL}, 1/q and moving the outer strike point above the divertor nose. It can be reduced through the addition of neon.

Discussion

The divertor nose plays an important role in limiting detachment (vertical plate geometry) and affecting the detachment threshold. One possible reason is that neutrals which recycle from regions of the divertor plate below the nose can repetitively travel back and forth between the private flux zone and the plate, each time participating in momentum loss processes. Neutrals originating from the divertor surface above the divertor nose are likely to travel to other regions (core, midplane or private flux vacuum regions) thus not repetitively removing ion momentum.

The q dependence of the detachment threshold can possibly be explained in terms of increased radiating volume with longer field line length in the divertor. The increased losses (along a flux surface) will reduce $T_{e,plate} \sim 5$ eV and bring on detachment. Increased P_{SOL} has the opposite effect.

Acknowledgements

The authors would like to thank the Alcator group for their assistance in acquiring this data and achieving the needed equilibria. This work is sponsored by the U.S. Department of Energy under contract No. DE-AC02-78ET51013.

References

[1] Greenwald, M., Terry, J.L., Wolfe, S.M., Ejima, S. et al, *Nucl. Fusion* **25** (1988).

[2] Hutchinson, I.H. et al, *Physics of Plasmas.* **1** 1511 (1994).

[3] LaBombard B., Lipschultz, B., Kochan, S. *Proceedings of the 14th IEEE/NPSS Symposium on Fusion Engineering* p 40, (1991).

[4] Lipschultz, B., Goetz, J.A., LaBombard, B., McCracken, G.M., Terry, J.L. et al, *J. Nucl. Materials* **220-222** 50 (1995)

[5] ITER divertor experts meeting Garching Germany, February 1995.

[6] LaBombard, B *Physics of Plasmas* **2** 2242 (1995)

[7] McCracken G.M. et al, *J. Nucl. Materials* **220-222** 164 (1995)

Electron energy distribution function in edge plasmas of TF-2 tokamak

L.M. Bogomolov, V.P. Budaev, V.N. Sychev.

Institute for High Temperatures of Russian Academy of Sciences

Scientific Station in Bishkek, 720049, IVTAN, Bishkek, Kyrgyzstan, CIS.

1. Introduction.

Measurements of electron temperature fluctuations with high temporal resolution [1,2] have put a new light on edge turbulence. Determination of Te by means of swept probe technique or by method of double harmonic involves exponential current-voltage characteristics, describing nonlinear Cunkel-Guillary resistance of Debye layer. Using such characteristics is equivalent to the assumption that Electron Energy Distribution Function (EEDF) does not differ strongly from Maxwellian. However this assumption is questionable for sheath and presheath plasmas in SOL where Maxwellization time is not large enough compared to electron lifetime in presheath. Present paper is devoted to the investigation of EEDF in edge plasmas of small research tokamak TF-2. Simultaneously we try to improve the method of determination on the basis of detector effect. Corrections due to drift polarization currents have been taken into account. It will be shown that Te fluctuations at frequency region above 200 kHz (exceeding typical frequency of density fluctuations) are caused by overthermal electrons from the tail part of distribution function.

2. Theoretical principles.

In isotropic nonmagnetized plasmas EEDF is defined by Druyvesteyn formula for second derivative of probe current over voltage [3].

$$d^2I_e / dW^2 = 2\pi e^3 \quad m^{-2} \; S_p \; f(W) \;, \qquad (1)$$

Where I_e - electron current, S_p -probe area. Similar expression appears to be valid for spherical probes in magnetized plasma provided W is treated as retarding potential difference on Debye layer rather than biasing voltage U [4]. Current-Voltage Characteristics (I-V Ch) of single probe underlying all measurements of Te results from the same theory that expression (1) when EEDF is Maxwellian.

In tokamaks the probe current must close its circuit across strong magnetic field. This means that the probe voltage supplied by external generator is devided between sheath/presheath drop and drop on plasma layer, $U = V + \xi$ (See fig.1). At high frequency $\omega > \omega_p = \omega_{ci} \; S_p / \rho_i L_{||} \sim 10^5$ 1/s ion polarization current is capable to close the most part of probe current, the voltage drop on layer (effective polarization capacitance) being small [5].It has been demonstrated in[5] that

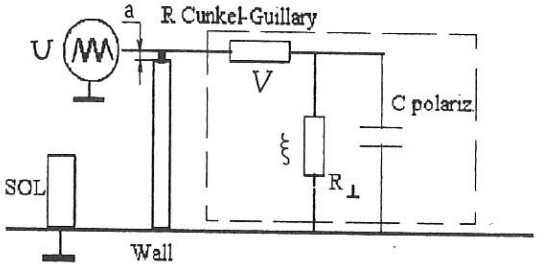

Fig 1. Langmuir probe in edge plasma: geometry and electric layout.

Dynamical I-V Ch obtained with the help of powerful generator (P > 1 kWt, $U_{max} \geq 100$ V, ramping time is about 2 μs) is very similar to usual I-V Ch of Langmuir probe in nonmagnetized plasma. For example, the ratio of electron saturation current to ion saturation one reachs 35 at high frequencies, whenever this ratio is about $4 \div 6$ at quasystationary biasing. So, polarization currents make possible to define EEDF with high temporal resolution. During short measuring interval turbulent fluctuations, which perturb the probe current, play no role.

We substitute second derivative in (1) by time derivatives of probe current and voltage. The voltage drop ξ is of order of small parameter ω_p/ω and it may be taken into account as first order correction. The expression defining EEDF is as follows

$$f(U - \xi) \sim \ddot{I}/\dot{U}^2 \, [1 - 2\dot{\xi}/\dot{U}] - \dot{U}\dot{I}/\dot{U}^3 \, [1 - 3\dot{\xi}/\dot{U} + \ddot{\xi}/\dot{\xi}] \qquad (2)$$

The correction ξ results from ion inertia effect. Using the expression for polarization current and equivalent layout (fig.1) one may evaluate ξ by the formula [5]

$$\xi = T_e \, \omega_p \, I_s^{-1} \int I \, dt = \omega_{ci} \, B_T \, (2\pi L_{||} \, e \, n)^{-1} \int I \, dt, \qquad (3)$$

Where I_s - ion saturation current, B_T - toroidal field, $L_{||}$ –connection lenth of magnetic line. Actually the expression in right side (2) defines the detector effect of occurrence the double harmonic in probe current, while the probe voltage is pure sinusoidal and has moderate amplitude $U_{max} < Te$. It follows from Taylor expansion of I-V Ch that the relation between double harmonic amplitude h_2, base harmonic amplitude h_1, electron temperature Te and parameters forming the right side (2) may be written as

$$T_e = h_2 U_0 (4h_1)^{-1} = \dot{U} \, [\ddot{I}/\dot{I} - \dot{U}/\dot{U}]^{-1} \qquad (4)$$

(Corrections ~ ξ are omitted for the sake of simplicity; for TF-2 conditions the corrections due to polarization currents are less than 15 %). In (4) the derivatives are assumed to be taken in "floating" point, where $I \approx 0$.

3. Experiment and results

Experiments have been held on TF-2 tokamak with ring poloidal limiter (R= 23,5 cm; a= 3,5 cm; $B_T \equiv 1$ T; $I_{pl} = 6 \div 10$ kA). Typical density and electron temperature of plasma near limiter tip are respectively $n \cong 5\ 10^{12}$ cm^{-3} , Te = 10÷ 20 eV). Some moveable Langmuir probes (collecting area 3 mm) have been installed in different toroidal cross-sections. A ramping generator and sinusoidal AC generator have been used for biasing, the voltage amplitude being 30 ÷ 50 V, the frequency being varied from 100 kHz to 750 kHz. The capacitor system forming 200 V powerful pulse of ramping voltage has been used also to control the accordance between output of source and fluctuating load (the probe immersed to edge plasma). Signals from Langmuir probe have been recorded by conventional 4 K ADC with time discretization 25 ns. The delay between measuring channels of current and voltage is tested to be less than 50 μs. Measurements have been made in discharges with low and moderate level of MHD -activity, the factor q being respectively 4,3 and 3,3.

Fig.2 represents the plot of EEDF of a plasma at 2mm depth from the limiter tip. The global plot appears to be reproducible in different measurements during a shot and in different shots with 30% accuracy. At energy region W< 20 eV EEDF plotted in fig.2 is similar to Maxwellian distribution function, but the tail of EEDF is absent. This may be related to end losses of fast electrons leaving plasma for limiter. Even week perturbation results in arising of EEDF second spike that corresponds to hot electrons (fig.3). The lifetime of electrons with enhanced energy is observed to be about 5 μs. The most probable reason for occurrence of overthermal electrons is flute perturbations mixing SOL plasma electrons and that from SOL outside. The EEDF of a plasma outside SOL is shown on the fig.4, the probe being located at 1,5 mm depth from Last Closed Flux Surface. The behavior of main plasma EEDF plot is not so reproducible as that of SOL plasma. Particularly, distribution with smooth maximum at plato type region at energy interval 15 ÷ 50 eV has been observed often. After choosing shots with EEDF like Maxwellian distribution we define by (5) the electron temperature. Fig.5 gives the example of Te time dependence. High frequency spike of Te is related to arising - disappearing of a group of hot electrons. The 25% level of Te fluctuations is comparable with the level of density fluctuations. This may be explained by the properties of edge flute instability specified in [6]. The cross-correlation between temperature and density fluctuations does not exceed 0.5.

The research described in this publication was made possible in part by Grant No N51000 from the "International Science foundation"

References

[1] Hidalgo C, Balbin R,*Phys Rev. Lett* ,**69 (8)** 1205 (1992)

[2] Hidalgo C, Balbin R et.al.,19 th EPS Conf.on Contr. Fusion and Plasma Phys., Innsbruck, pt.II, 783 (1992).

[3] Druyvesteyn M.L, *Zs. fur Phys.*,**64,** 781 (1930)

[4] Mal'kov M.A., *Fizika Plazmy* **17 (7)** 837 (1991).

[5] Bogomolov L.M.,Nedospasov A.V. et.al., *Proc. of 21st Int. Conf. on Phenomena in Ionized Gases*, pt.II, 353 (1993), Bochum.

[6] Bogomolov L.M. *Contrib. to Plasma Phys.*,**32 (4)** 331(1992)

Fig.2 - Fig4 Examples of energy distribution functions of edge plasma electrons.

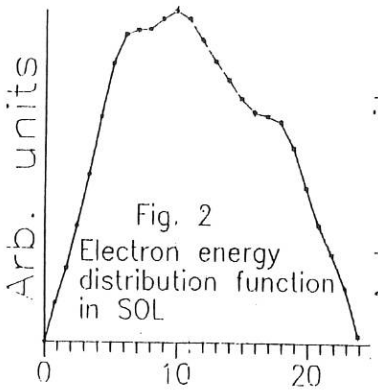

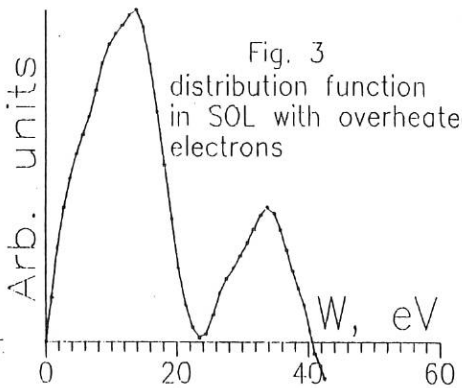

Fig.5 Time dependence of electron temperature obtained from I-V Ch by means of eq.(4)

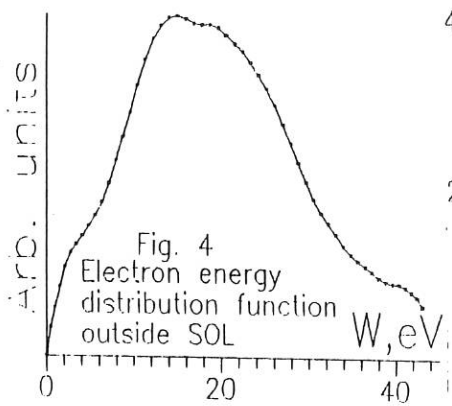

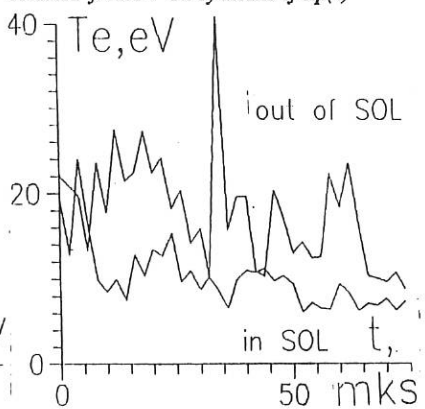

LOW FREQUENCY PLASMA HEATING AND CURRENT DRIVE REGIMES FOR IGNITOR

P. E. Moroz

Lodestar Research Corporation, Boulder CO, USA
and University of Wisconsin, Madison WI, USA

Abstract. Analysis of low frequency plasma heating and current drive (LFCD) regimes is given for the first time for the high density plasmas, typical for the Ignitor tokamak. Numerical calculations are carried out via the 2D toroidal full-wave hot-plasma code, ALFA. The 3D distributions of RF fields obtained, as well as distributions of absorbed power and driven current are discussed. It is shown that LFCD methods are efficient for the high density plasmas and can be used for current profile control and for generation of the seed for the bootstrap current.

Introduction.

The powerful system of ICRF heating is an essential part of the Ignitor design [1-3]. It allows to shorten substantially the time to ignition and save valuable Volt-sec (up to 6 Vs [3]) of the ohmic current transformer. Also, it allows the attainment of ignition at relatively low plasma current of 10 MA and to obtain high levels of performance at lower than standard fields and currents [3]. An ICRF system with a frequency range, 100 MHz < f < 210 MHz, has been considered in Refs. [1-4].

In this paper we extend the analysis to lower frequencies, 40 < f < 100 MHz. Also, we extend the analysis to the current drive problem. In our calculations, the main parameters of the machine and the plasma have been taken to be: toroidal magnetic field at the axis, B_o = 12 T, ohmic current, I_{oh} = 10 MA, central electron density, $n_{eo} = 10^{21}$ m^{-3}, central temperature, $T = T_{eo} = T_{io}$ = 15 keV. The main conclusions, however, are correct not only for Ignitor but for other large tokamaks with high plasma density and temperature.

The global 2D full-wave code, ALFA [5,6], is used in our analysis of wave penetration, power deposition and current drive. This code features general toroidal geometry with the poloidal magnetic field included, and uses Bessel functions in the hot plasma dielectric tensor to correctly account for the large Larmor radius effects.

Antenna system.

The RF antenna system, consisted of 6-strap antennae, is considered in our analysis. The total input RF power of up to 24 MW is suggested. The 6-strap phased antenna is required to produce the narrow spectrum of excited toroidal wave numbers, n, which is necessary for high CD efficiency. For plasma heating, however, there is no need in so narrow spectrum and more simple 4-strap antenna works satisfactorily. Normally, in Ignitor (as well as, in the other large tokamaks with the hot and dense plasma) the fast waves do not penetrate far in toroidal direction from the antenna. As a result, neighboring antennae practically do not "feel" each other, and can be considered separately. That is why, in our studies, we focus on field distribution, wave absorption, and current drive produced by one antenna. The full picture of wave fields in the plasma can be obtained by superposition of contributions (which are practically do not intersect) from all antennae.

Plasma heating.

The low frequency region considered includes frequencies corresponding to the ion cyclotron resonances for all ion species: for deuterium, $\omega = \Omega_D$, for tritium, $\omega = \Omega_T$, and for α-particles, $\omega = \Omega_\alpha$. As a result, a variety of essentially different plasma heating regimes can be identified which have the potential for various applications in Ignitor. One can find the heating scenarios when RF power is absorbed preferentially by any particular ion component: D, T, or α-particles. Also, the ion-ion hybrid resonance is usually present in the plasma, which extends the possible heating and current drive schemes to ones that include mode conversion to the ion Bernstein wave (IBW). For example, at frequencies, f $\approx$ 60-70 MHz, it is easy to find scenarios when most of RF power goes to T-ions, and at frequencies, f $\approx$ 80–90 MHz, -- to D-ions or α-particles. To demonstrate this feature, Fig. 1 shows contours for RF power deposition at f = 66 MHz. Equal concentrations of D and T-ions, and concentration of α-particles of 2%, are suggested. The bulk of absorption (75%) is due to T-ions at the major radius, R $\approx$ 1.2 m, corresponding to $\omega = \Omega_T$. Remaining power is absorbed mainly directly by electrons (13.5%) and through the mode conversion to IBW (10%).

Current drive.

The steady-state operation of a fusion reactor is, probably, absolutely necessary to make the electricity production cost competitive. RF current drive together with the bootstrap current is one of the possible means to reach the steady operation. In this paper we show that low frequency current drive methods can be used for high density plasmas, $n_{eo} = 10^{21}$ m^{-3}, typical for Ignitor.

An interesting regime is found at Alfven frequencies, i.e. $\omega < \Omega_i$ for all plasma species. As an example, below we present results for f = 42 MHz. The single-pass absorption in this case is about 50% and RF power is absorbed by electrons alone. The toroidal Fourier spectrum of the 6-strap antenna with phasing $\Delta=\pi/4$ between adjacent straps is given in Fig. 2. One can see two distinguished peaks, one for n = -10 to 0, and another for n = 30 to 40. The peak at large n is parasitic because the coupled power can drive the current in opposite direction. However, the antenna geometry and phasings were chosen such that this peak has little contribution to the antenna loading (Fig. 3) and even less to current drive. The first peak has typical n $\approx$ 5 corresponding to the strongest electron absorption ($\zeta_e \approx 1$, where $\zeta_e = \omega/k_{\|}v_e$). The importance of the condition, $\zeta_e \approx 1$, for LFCD was first mentioned in Ref. [7]. The distribution of the vertical component of the RF electric field, $Re(E_z)$, in the poloidal cross-section is shown in Fig. 4, and in the equatorial plane of the torus in Fig. 5a and Fig. 5b. The latter shows the details of the near-antenna field. These figures confirm the above mentioned statement that fast wave does not penetrate far from the antenna in the toroidal direction. Note also that even the contributions from each separate strap are not mixed and can be clearly seen on a distance from the antenna. The contours for the power deposition are given in Fig. 6. Most power is absorbed in the central region. However, some insignificant power is absorbed near the plasma edge on the high-field-side (HFS) via the Alfven resonance. The radial profiles of the total absorbed power (dashed curve) and RF driven current (solid curve) are presented in Fig. 7. The current profile is more peaked than the power deposition profile due to the electron trapping effects.

Discussion.

The total driven current at f = 42 MHz is found to be 360 kA for $n_{eo} = 10^{21}$ m^{-3}. This is a significant result if one takes into account that CD efficiency usually scales as $1/n_e$. This current, although is not enough to sustain the plasma equilibrium by itself, is important as a seed for the bootstrap current. Also, it can be used for the current profile control.

There are other regimes at higher frequencies, f ≈ 66 MHz and f ≈ 90 MHz, also efficient for current drive (antenna strap phasing or/and spacing has to be changed with frequency to satisfy the requirement, $\zeta_e \approx 1$). In those cases, the D-T hybrid layer plays the role of a reflecting wall. Better CD results are obtained for smaller T-concentrations when the ion-ion hybrid layer is located further on HFS leaving more space for wave penetration and electron absorption. The main competitor to the electron absorption at f ≈ 66 MHz is T-ion absorption, and at f ≈ 90 MHz it is D-ion absorption. At T-concentrations of around 25% the power absorbed by electrons in these regimes can reach 70%, and the CD efficiency is acceptably high.

Acknowledgment.

The author would like to thank Dr. R. E. Aamodt for attracting his attention to the problem of efficient RF plasma heating and CD in the dense plasmas. This work was supported by the U.S. DOE Grant Nos. DE-FG02-88ER53263 and DE-FG02-88ER53264.

References.

[1] B. Coppi, P. Detragiache, S. Migliuolo, et al., Fusion Tech. **25**, 353 (1994)
[2] J. Jaquinot, "ICRH Heating in Ignitor", 6th Boulder Workshop, Boulder, CO (1993).
[3] F. Carpignano, B. Coppi, et al., in *Radio Frequency Power in Plasmas,* AIP Conf. Proc. **289**, 10th Top. Conf., Boston MA, 1993, AIP, NY, p. 425 (1994).
[4] J. Jacquinot, Lodestar Research Corporation Report LRC-92-33 (1992).
[5] P. Moroz, 15th Int. Conf. on Num. Sim. of Plasmas, Valley Forge, PA, 3B2 (1994).
[6] P. Moroz et al., 11th Top. Conf. on RF Power in Plasmas, Palm Springs (1995).
[7] P. Moroz, D. Batchelor et al., in *RF Power in Plasmas*, AIP Conf. Proc. **289**, 10th Top. Conf., Boston MA, 1993, AIP, NY, p. 218 (1994).

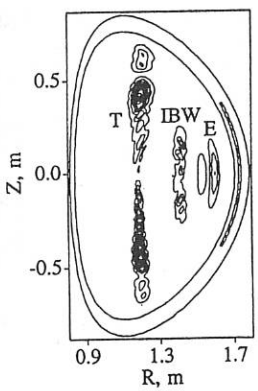

Fig. 1. Contours of the power deposition at f=66 MHz ($n_D=n_T$).

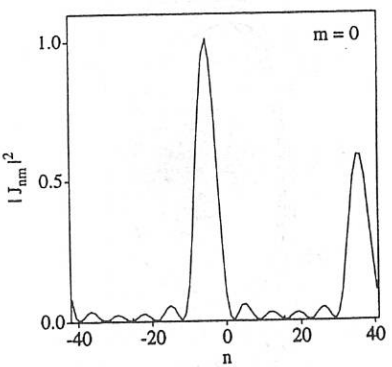

Fig. 2. Toroidal Fourier spectrum of the 6-strap antenna.

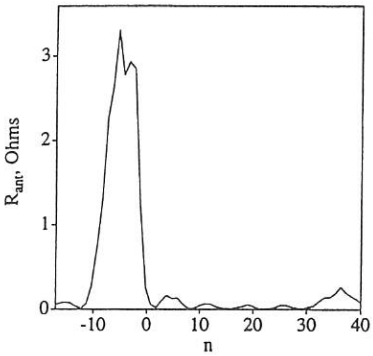

Fig. 3. Antenna loading resistance.

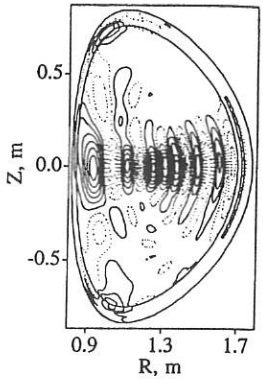

Fig. 4. Contours of $Re(E_Z)$ in the poloidal cross-section.

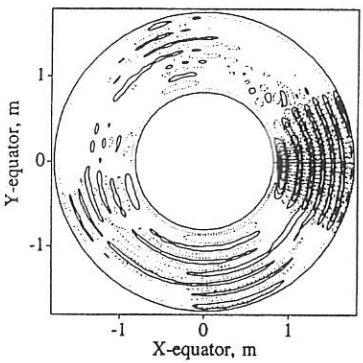

Fig. 5a. Contours of $Re(E_Z)$ in the equatorial plane of the torus.

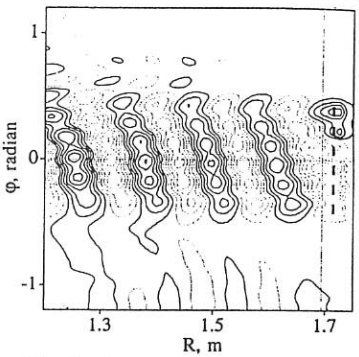

Fig. 5b. Same as Fig. 5a but the near antenna region is shown.

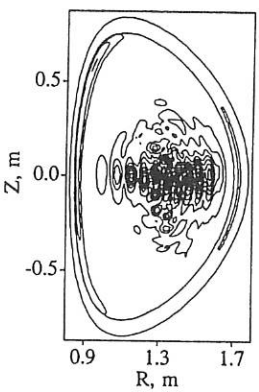

Fig. 6. Contours for power deposition (electron absorption) at f=42 MHz.

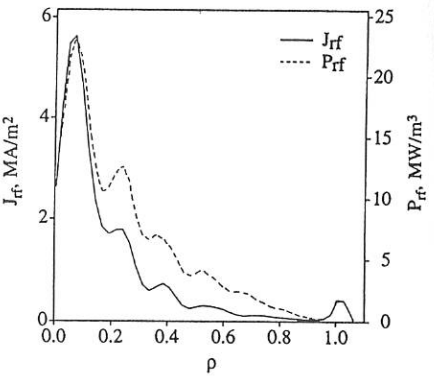

Fig. 7. Radial profiles of power deposition and driven current at f=42 MHz.

Toroidal velocity and ripple losses in Tore Supra with LH, ICRF, and combined additonal heating

P.Platz, V.Basiuk, B.Saoutic, R.Arslanbekov and J.Carrasco

Association EURATOM-CEA, C.E. Cadarache
13108 St.Paul-lez-Durance,France

Abstract. Observations from a high-resolution crystal spectrometer and from collector arrays for ripple- lossed fast particles (electrons or ions) show a strong correlation between the toroidal plasma velocity and the nature of the particles leaving the plasma. The velocity is in the direction parallel to (opposite to) Ip, when the net charge leaving the plasma is negative (positive). We observe $\Delta v / \Delta I = 22\text{-}36$ km s^{-1}/100mA (Δv=toroidal velocity; ΔI=net current collected in one out of the 18 magnetic wells).

Analysis of X-ray line spectra. On Tore Supra, high resolution line spectra from the n=2-n=1 transitions in He- and Li-like ions of intrinsic impurities are recorded with a multi-crystal spectrometer [1]. The present study is based on the strong Fe and Cr spectra in the 1.85 - 2.2 Å region. A typical spectrum from Fe is shown in fig.1. The spectrum contains the lines w, x, y, and z from Fe24+; the remaining lines are from Fe23+ (n≥3 designates a group of low-intensity lines). The spectra are taken at a rate of 5 or 10 per second. The spectrum shown in fig.1 is the result of a summation over 1.5s.

The solid line through the w, n≥3 and j lines is the result of χ^2 - fitting of a (partial) synthetic spectrum. The lines j and n≥3 are produced by di-electric recombination, and their intensities (relative to the intensity of w), are known functions of Te (decreasing with increasing Te).Ti is obtained from the width of the line w, corrected for natural and instrumental broadening (Voigt profiles). Finally, the shift of the line w from its position during the ohmic heating phase, gives the (differential) toroidal plasma velocity, Δv.

The spectra of Cr , such as the one shown in fig.2, are treated in the same way, but the fit includes the line z because of the partial overlapping with j.

As an example, fig.3 illustrates qualitatively the effects we observe when LH is replaced by ICRF: Te decreases (the intensities of the n≥3 lines go up), Ti increases, and the spectrum shifts to shorter wavelengths (given the geometry of observation, the plasma is accelerated in the direction opposite to Ip).

In the following, all quantities are relative to the ohmic phase (Δv, ΔTe, ΔTi). The uncertainties of these quantities (fitting errors) may be quite low. For spectra with a good S/N we have typically δv = 1 - 2 km/s (occasionnally 2 - 4 km/s for low intensity "ohmic" spectra) and δTe , δTi = 0.05 - 0.1 keV.

Ripple-loss diagnostic. This diagnostic consists of two arrays of twelve polarisable graphite collectors on the top and on the bottom of a vertical port. They act as probes for the low-density plasma in the port, and as collectors for the high-energy, collisionless particles, locally trapped in the magnetic well and drifting into the port (electrons down, ions up) [2,3]. In the present experiment, all collectors are set at +100V (in order to recollect possible secondary electrons). Consequently, the

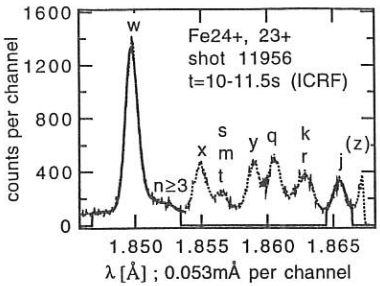

Fig.1 Spectrum of Iron (dotted) and χ^2 - fit (solid line)

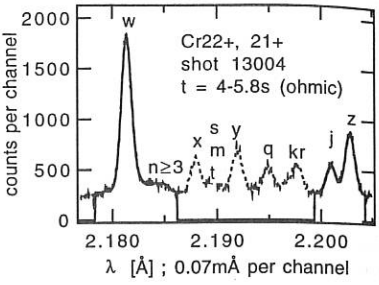

Fig.2 Spectrum of Chromium (dotted) and χ^2 - fit (solid line)

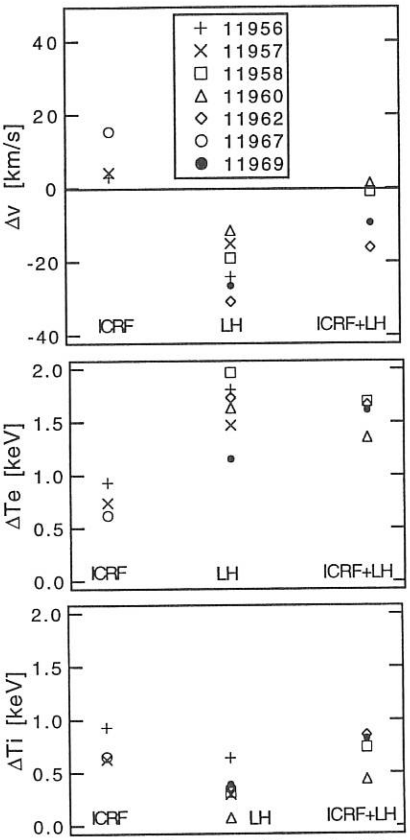

Fig.4 a,b,c. Δv, ΔTe, and ΔTi from shot series I

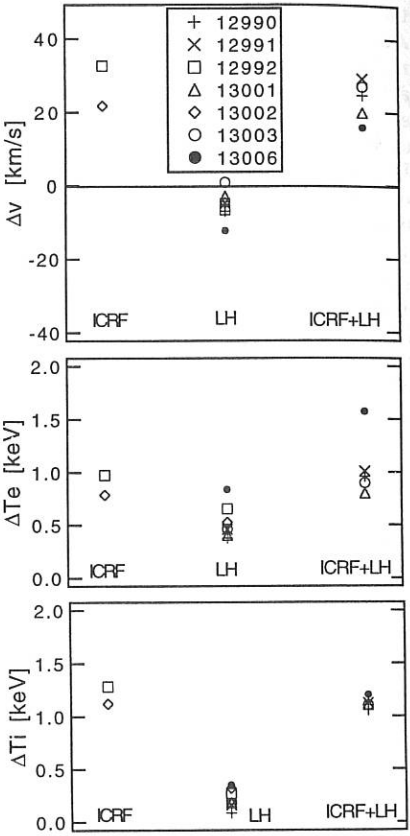

Fig.5 a,b,c. Δv, ΔTe, and ΔTi from shot series II

bottom array collects thermal and fast electrons, and the top array collects thermal electrons and fast ions. The net ripple current collected in the port (i.e. in one out of the 18 magnetic wells) is defined by

$$\Delta I = |I_{add} - I_{ohm}|_{top} - |I_{add} - I_{ohm}|_{bottom} = \Delta I_i - \Delta I_e \qquad (1)$$

with subscripts add (ohm) for additional (ohmic) heating. Consequently, $\Delta I>0$ (<0) indicates a net positive (negative) charge leaving the plasma in the port (the total current should be 18 times this value). Finally, from a large data base of shots with LH, we have obtained the following scaling law:

$$\Delta I_e[mA] = 820^* P_{LH} * (nl)^{-2} * I_p/Bt + - 10 ; \quad [MW, 10^{19}m^{-2}, MA, T] \qquad (2)$$

Experiments. We discuss the results from two series of shots:

series I: shots 11956-11969, low density plasma, nl=2.5 $10^{19}m^{-2}$
I_p=0.8MA, P_{LH}=2.7-2.9MW, P_{ICRF}=1-3MW (H-minority heating)
spectrometer set on Fe24+, 23+

series II: shots 12990-13006, high density plasma, nl=6 $10^{19}m^{-2}$
I_p=1.51MA, P_{LH}=1.8-3.8MW, P_{ICRF}=3.6-5MW (H-minority heating)
spectrometer set on Fe24+, 23+ for shots 12990 and12991
spectrometer set on Cr22+, 21+ for shots 12992-13006

Common discharge parameters are: a=0.77m, R=2.34m, B=3.7T, He filling.Typical electron and ion temperatures prior to the additional heating are 2.4keV and 2keV, respectively.The results for Δv, ΔTe, and ΔTi obtained from the two series are shown in fig.4 and 5. First we notice that, as expected, the LH additional power favours electron heating, whereas the ICRF additional power goes to electrons and ions. ΔTe and ΔTi attain 2keV and 1.3keV, respectively. Secondly, we observe that when ICRF is applied, the plasma is accelerated in the direction opposite to the plasma current ($\Delta v >0$); with LH applied, the acceleration is in the direction of Ip ($\Delta v<0$). Finally, with both heating methods present, we observe the sum velocity.

The correlation of the sign of Δv with the species of heated particles suggests the existence of a relation between the toroidal rotation and the electric charge leaving the plasma. In fig.6 we have plotted Δv against ΔI for series II. Obviously, the correlation is quite strong, i.e. the plasma is accelerated in the direction parallel (opposite) to I_p, when the net charge leaving the plasma is negative (positive), creating an outward (inward) radial electric field. For the shots of series I, the electron -loss diagnostic (bottom array) was not in operation. In spite of this, we get interesting results from this series too , by proceeding in the following manner: i) for the "ICRF only" time- slices , the ion current always dominates and, consequently, ΔI is not affected by the missing electron array; ii) for the "ICRF+LH"-time- slices we can calculate a correction using the scaling law, eq.(2), for ΔI_e; iii) for the "LH only" time slices, ΔIi =0, and ΔI = - ΔIe, with ΔIe again calculated from eq.(2). The result of this approach is shown in fig.7 (the "horizontal" error bars of + - 10mA follow from the use of eq.(2)). Although there is much scatter in the points, it is again obvious that high electron losses are on a par with $\Delta v<0$. A quantitative relation is obtained by looking on individual shots as shown in fig.8 (which is a a zoom on the data of fig.7).

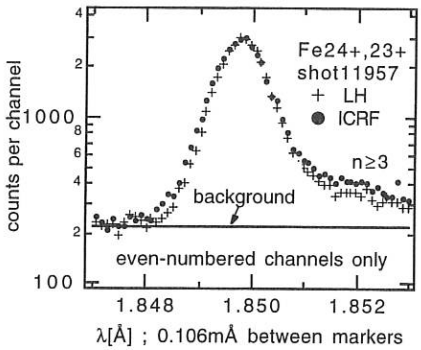

Fig.3 Line w of Fe24+ with LH or ICRF

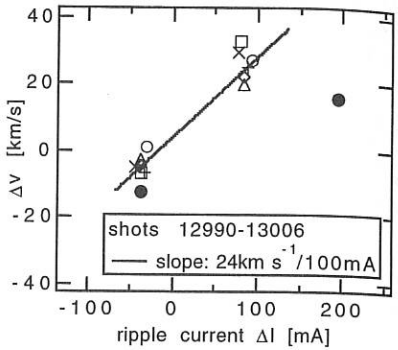

Fig. 6 Δv versus ΔI for shot series II

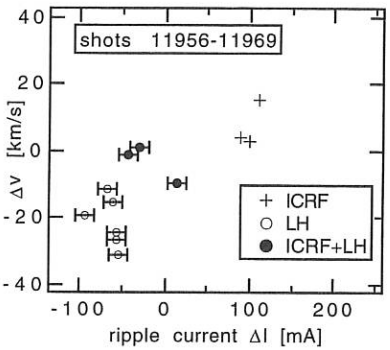

Fig.7 Δv versus ΔI for shot series I

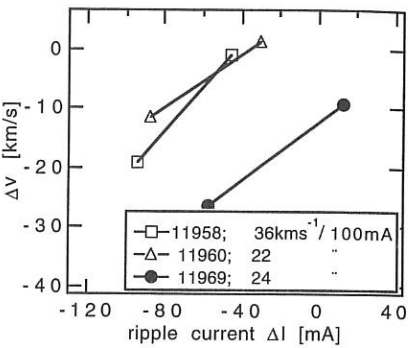

Fig.8 Partial data from series I

In view of the data presented here, the correlation of ripple losses and toroidal rotation seems quite well established. A further argument in favour of this relation is expected from another RF heating scheme used on Tore Supra, the direct fast wave electron heating (FWEH) [4], with typical parameters : 48MHz, Ip=0.4-1MA, Bt= 1.5-2.2T. Both experiment and theory [4,5] show a strong heating of bulk electrons without the creation of fast particles. Therefore, no toroidal rotation is expected. However, the electron temperature (1.2keV at 2T) of the ohmic plasma (serving as the reference) is too low to produce Cr or Fe spectra with good photon statistics. These experiments, with FWEH, will be repeated using Titanium or Argon.

References

[1] P.Platz et al.; 20th EPS Conference, Lisbon 1993, Vol. 17C, Part III, p.1083
[2] V.Basiuk et al.;19th EPS Conference, Innsbruck 1992, Vol. 16C, Part I, p.175
[3] J.Carrasco et al.;21st EPS Conference,Montpellier 1994, Vol. 18B, Part I, p.278
[4] Equipe Tore Supra, presented by B.Saoutic; invited paper; 21st EPS Conference Montpellier 1994; Plasma Phys.Control.Fusion 36 (1994) B123-B132
[5] A.Bécoulet et al., Phys.Plasma, Vol.1, No 9,p.2908 (1994)

ICRF Preionization and Plasma Production in TEXTOR

A.I.Lyssoivan[1], B.Giesen[2], **R.Koch**[1], F.Durodié[1], P.Hüttemann[2], G.Van Oost[1], J.Winter[2], S.V.Kasilov[3], H.R.Koslowski[2], L.Könen[2], A.Messiaen[1], V.E.Moiseenko[3], O.Neubauer[2], V.V.Plyusnin[3], H.Reimer[2], R.Van Nieuwenhove[1], M.Vervier[1], G.Waidmann[2]

[1] - Laboratoire de Physique des Plasmas - Laboratorium voor Plasmafysica, Association "Euratom-Belgian State", Ecole Royale Militaire - Koninklijke Militaire School, B-1040 Brussels, Belgium

[2] - Institut für Plasmaphysik, Forschungszentrum Jülich Gmbh, Association Euratom-KFA, D-52425 Jülich, Germany

[3] - Institute of Plasma Physics, National Science Centre "Kharkov Institute of Physics and Technology", 310108 Kharkov, Ukraine

1. Introduction and overview of the problem

To perform low voltage tokamak start-up in a reliable manner, save volt-seconds and reduce the generation of runaway electrons, non-inductive preionization and plasma production are desirable. It may even be mandatory in the next generations of machines, like ITER.

In the present paper, the first successful production of plasma in a tokamak using RF power in the ion cyclotron range of frequencies (ICRF) is reported. The increased interest in this frequency band (1÷100 MHz) is explained by the following facts. The same RF technology may be used for ICRF plasma production as well as for normal RF heating (RF generators, transmission lines and antennas without Faraday shields (FS), like in the case of TEXTOR [1]). The powerful, reliable and inexpensive RF generators operated in quasi-steady regime are widespread now. Dense plasmas ($n_e > 10^{13}$ cm^{-3}) of a parabolic profile were reliably produced in a wide range of toroidal magnetic field and gas pressure values in magnetic devices of different types: open traps [2-3], stellarators and torsatrons [4-6] and toroidal machines without rotational transform [4]. The capability to perform in one scenario the RF plasma start-up, preheating and current ramp-up as well was also demonstrated [7]. At last, the qualitative theory of plasma production in ICRF and numerical models were developed too [8-10].

A crucial fact to start the experiment on ICRF plasma production in TEXTOR was the presence of a screenless double loop antenna. Along with the RF magnetic field required to excite efficiently fast wave (FW) during the plasma heating phase [1], the antenna without FS generates also the RF parallel electric field ($\tilde{E}_{\parallel}$) between the antenna central conductors and the side protection limiters. According to theory [8], the RF $\tilde{E}_{\parallel}$ field is responsible for neutral gas ionisation and plasma build-up by electron impact during the gas breakdown phase ($\omega > \omega_{pe}$) and during the slow wave (SW) excitation phase ($\omega < \omega_{pe}$).

2. Experimental conditions

TEXTOR is a medium size tokamak with R_o=1.75 m and a=0.46 m equipped with a pumped toroidal belt limiter. Both double loop antennas, one without FS (A1), the other with a FS (A2), which have been designed for normal ICRF heating experiments were employed for the present studies. Being installed at toroidally diametrically opposite locations, the antennas were fixed at standard radial positions meaning that the current straps were at $r_{A1}=r_{A2}=0.51$ m. Keeping the standard value of the toroidal magnetic field B_T =2.25 T, two scenarios of RF plasma production were tested:

(i) - $\omega > \omega_{ci}$ (f=32.5 MHz, deuterium);

(ii) - $\omega < \omega_{ci}$ (f=25 MHz, hydrogen).

Each pair of the current straps in both antennas was fed either in phase (*zero*-phasing) or out-of phase (π-phasing) with typical (generator) RF power in the range ~100÷300 kW. In the case where the loading resistance could be measured, about 50% of the power was found to be coupled to the plasma. However, in most cases a reliable evaluation of the power radiated in the plasma was not possible (most probably due to a high level of harmonics in the transmission lines affecting the measured voltage levels). All experiments reported here were performed either in pure RF regime (no loop voltage) or in combined RF and Ohmic heating (OH) regime.

To improve plasma confinement in pure toroidal geometry at the RF preionization phase (before OH discharge start), a small correction poloidal magnetic field was also used [11].

3. Results of the first experiments

3.1 Deuterium RF plasma production, $\omega>\omega_{CD}$

In this frequency range, the SW is strongly evanescent and the power is expected to be collisionally dissipated in the ion Bernstein wave (IBW), coupling taking place directly at the antenna or at the 2nd harmonic layer where the evanescent FW can convert to IBW. Other mechanisms or waves linked to the fact that the plasma is only partially ionised might play a role. Absorption and coupling by non-linear mechanisms is also possible [12].

To find the range in B_T, where RF plasma production would be possible and reliable, the first series of RF only discharges was performed in multi-pulse regime, while B_T was ramped down in time (Fig.1). Two antennas were excited in sequence (A1: *zero*-phasing, A2: π-phasing) with time overlapped RF pulses. Deuterium plasma was easily produced in a wide range of B_T (1.3 ÷2.4 T) at a gas pressure ranging from 10^{-6} to 10^{-4} Torr starting with ≥50 kW of RF generator power. No restriction in RF plasma production performance was observed in this operational parameter range. Therefore, the subsequent experiments have been performed at the standard B_T value when both antennas were operated in single long RF pulses.

It was found that RF plasma production was also possible for A1 and A2 antennas operated separately. However, the screenless antenna produced plasma more efficiently. The antenna phasing also has an influence on plasma production. For example, to obtain the same plasma (~10^{11}cm^3), twice the power was needed in π-phasing as compared to *zero*-phasing (A1 antenna in both cases). This is thought to be due to better antenna coupling and power deposition at low $k_{||}$'s.

The highest density so far (up to about 10^{12} cm^{-3}) has been achieved with simultaneous operation of both antennas (Fig.2a). During pure RF phase the density of plasma had a broad and mainly central profile (Fig.3a). However, the easiness of producing the RF plasma and the quality of the plasma produced (density, position of formation, etc.) were sensitive to the poloidal correction field and the inductor stray field during the OH start-up phase (Figs.2a,3a).

3.2 Hydrogen RF plasma production, $\omega<\omega_{CH}$

In this case, plasma production was realised using the Alfvén heating scenario [13] at standard value of B_T =2.25 T. The screenless antenna fed in *zero*-phasing produced plasma more efficiently at the same RF power level as compared with the case $\omega>\omega_{CD}$. The highest density was again achieved by simultaneous operation of both antennas (Fig.2b). The profile of RF plasma density was initially peaked at the centre of the vessel like in the case of deuterium plasma production (Fig.3b).

Unfortunately, the programmable dynamic correction of poloidal magnetic field and gas pressure were not well adjusted enough to perform low loop voltage (≤ 7 V) OH start-up assisted by RF. It led to decreasing of antenna coupling, plasma cooling and disappearance of the RF discharge either before applying the loop voltage (Fig.2) or during its application (Fig.4). Figure 4 also shows the "plasma current" I_p. In reality apart from the short time-period (0.17s<t<0.34s) during which a plasma is present, I_p is in fact the current flowing in the liner. When the plasma is present I_p increases by ~2 kA which represents a true plasma current. The

fact that the plasma current does not start increasing once started probably indicates that the plasma channel is too resistive.

4. Numerical modelling

To analyse plasma build-up scenarios for the present antennas installed in TEXTOR and optimise the RF start-up process for more adapted antennas, we use a numerical simulation that combines self-consistently two codes: the 1-D RF code [9] and the 0-D Transport code [8].

This simulation provides the time-evolution of the plasma density and temperature under the action of a given amount of RF input power, taking into account that only a fraction is coupled to the plasma, the other part being dissipated ohmically on the antenna. Comparisons with the present experiments remain to be done. However, the code predicted a much better coupling for the "crankshaft" antenna [9], as compared to more conventional antenna types and the "crankshaft" antenna was successfully tested recently in the URAGAN-3M torsatron. First computations for the TEXTOR case indicate a strong sensitivity of the coupling to deviation from 90° of the angle between the RF current and the total magnetic field which would favour operation at moderate vertical magnetic field ($B_V \approx 0.01 \div 0.02$ T). For too large values ($>0.01 \div 0.03$ T) of the vertical field the code predicts a strong deterioration of the plasma confinement.

5. Conclusions

The results obtained can be summarised as follows:

1. RF plasma has been successfully produced in ICRF for the first time in a tokamak.
2. A plasma density up to about 10^{12} cm^{-3} with broad and central profile has been achieved.
3. The plasma has been produced in a wide range of toroidal magnetic fields (1.3÷2.4 T) without retuning of RF generators, in deuterium ($\omega > \omega_{CD}$) and hydrogen ($\omega < \omega_{CH}$) at a gas pressure ranging from 10^{-6} to 10^{-4} Torr.
4. The plasma has been produced with unshielded and shielded antennas. The unshielded antenna produced plasma more efficiently, especially in the case of Alfvén heating scenario.
5. The electron temperature was probably too small for plasma current start-up. A more optimised dynamic programming of poloidal magnetic field and gas pressure will be needed, to realise the low loop voltage OH start-up assisted by RF.

Acknowledgements

We thank everyone in the TEXTOR Team and the ICRF technical staff who have contributed to the present experiments. The numerical modelling described in this paper was made possible in part by Grant No U32000 from the International Science Foundation.

References

[1] Van Nieuwenhove R et al, *Nucl.Fusion* **32(11)** 1913 (1992)
[2] Shvets O M et al, *Zh.Tekh.Fiz.* **35** 2185 (1965) (in Russian)
[3] Golovato S N et al, *Phys.Fuids* **31** 3744 (1988)
[4] Shvets O M et al, *Nucl.Fusion* **26(11)** 23 (1986)
[5] Nishimura K et al, *Proc. 7th Int. Workshop on Stellarators,* IAEA, Vienna (1990) 265
[6] Demirkhanov R A et al, *Proc.9th Int.Conf.on PPCNFR,* Vol.2, IAEA,Vienna (1983) 91
[7] Dikij I A et al, *Proc.15th EPS Conf. on CFPH, Dubrovnik 1988,* Vol.12B, Part 2, 734
[8] Lyssoivan A I et al, *Nucl.Fusion* **32(8)** 1361 (1992)
[9] Moiseenko V E et al,*Proc.21st EPS Conf.on CFPP,Montpellier 1994,* Vol.18B,Part2,980
[10] Moiseenko V E et al, *Fusion Engineering and Design* **26** 203 (1995)
[11] Parail V V et al, *Proc. 10th Int. Conf. on PPCNFR,* Vol.1, IAEA, Vienna (1985) 605
[12] Korzh A F et al, *Sov. J. Plasma Phys.* **13** 164 (1987)
[13] Moiseenko V E, *Proc. 8th Int. Workshop on Stellarators,* IAEA, Vienna (1991) 207

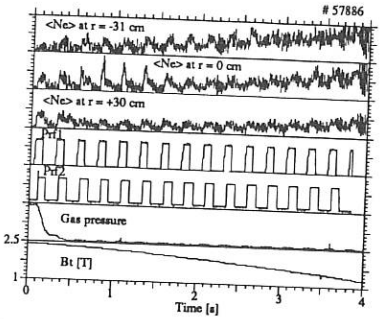

Fig.1: The multi-pulse regime of deuterium RF plasma production (#57886) (A1 : 0-phasing, A2 : π-phasing, $P_{rf1} = P_{rf2} = 150$ kW, $f_1 = f_2 = 32.5$ MHz, $p \approx 10^{-4}$ Torr, $B_V = 0$ G)

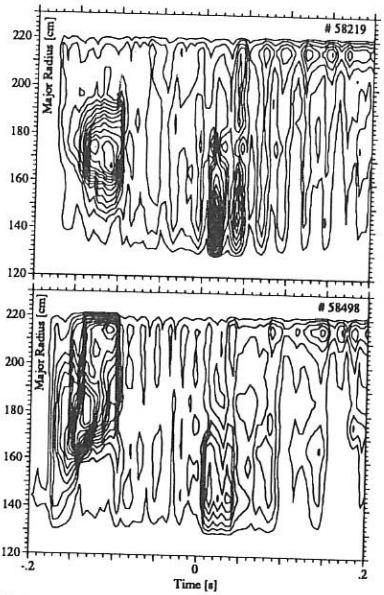

Fig.3: The time history of n_e level curves during RF only and (RF + OH)-phases of discharges #58219 and #58498

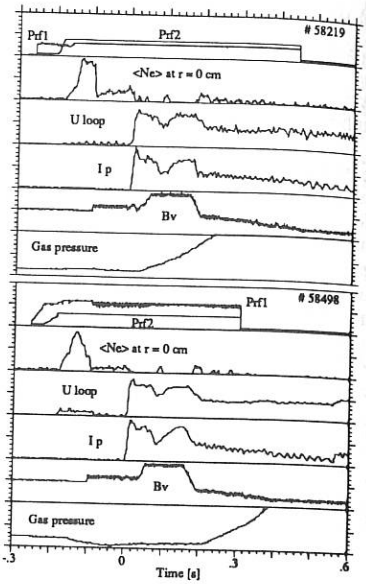

Fig.2: The time evolution of (RF + OH)-discharges in deuterium (#58219, A1, A2 : π-phasing, $f_1 = f_2 = 32.5$ MHz, $P_{rf1} = 200$ kW, $P_{rf2} = 150$ kW) and in hydrogen (#58498, A1 : 0-phasing, A2 : π-phasing, $f_1 = f_2 = 25$ MHz, $P_{rf1} = 150$ kW, $P_{rf2} = 50$ kW), $B_T = 2.25$ T, $p \approx 10^{-4}$ Torr

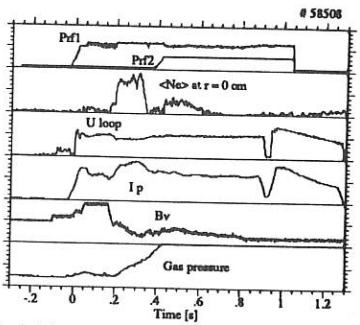

Fig.4: The time traces of measurements for shot #58508 in hydrogen (A1 : 0-phasing, A2 : π-phasing, $f_1 = f_2 = 25$ MHz, $P_{rf1} = 150$ kW, $P_{rf2} = 50$ kW, $B_T = 2.25$ T, $p \approx 4\ 10^{-5}$ Torr

Auxiliary heating experiments with a tungsten test limiter in TEXTOR 94

G. Van Oost[1], A.M. Messiaen[1], V. Philipps[2], R. Koch[1], A. Krämer-Flecken[2], K. Ohya[3], J. Ongena[1], A. Pospieszczyk[2], J. Rapp[2], M. Rubel[4], U. Samm[2], N. Schoon[1], B. Schweer[2], T. Tanabe[5], G. Telesca[2], M. Tokar[2], Y. Ueda[5], B. Unterberg[2], G. Van Wassenhove[1], M. Wada[6], J. Winter[2]

[1]Laboratoire de Physique des Plasmas - Laboratorium voor Plasmafysica - Association "EURATOM-Belgian State", Ecole Royale Militaire - Koninklijke Militaire School, B-1040 Brussels - Belgium [2]Institut für Plasmaphysik, Forschungszentrum Jülich GMBH, Association EURATOM-KFA, Germany [3] University of Tokushima, Japan [4] Royal Institute of Technology, Physics Department-Frescati, Association EURATOM-NFR, Stockholm, Sweden [5]Faculty of Engineering, Osaka University, Suity Osaka 565, Japan [6]Dep. Electronic Engineering, Doshisha University, Kyoto 602, Japan

1. Introduction

At present, plasma-facing components belong to the most difficult design issues for ITER. The main concerns for the utilization of high-Z materials as plasma-facing materials (PFM's) are [1]: (1) key issue: impurity production and accumulation (very low tolerable high-Z impurity concentration due to strong line radiation), (2) hydrogen recycling in the high recycling regime, (3) materials performance under high heat load conditions, and (4) metal impurities during ICRH [7].

Since TEXTOR is dedicated to the study of plasma-surface interactions and PFM's, and is particularly well edge-diagnosed, a high-Z test limiter programme has been initiated [2, 3] to broaden the poor database for the evaluation of the suitability of high-Z materials as PFM's. Neutral beam and ICRF heating experiments with a tungsten test limiter were conducted to find operational conditions suitable for the use of tungsten PFM's.

2. Experimental Set-up

The test limiter experiments were performed under standard TEXTOR conditions with boronized walls (ALT-II belt limiter at 46 cm, B_t = 2.25 T, I_p = 350 kA) in L-mode discharges (NBI-Co, $H^o \rightarrow D^+$; ICRH: 32.5 MHZ, screenless antenna, H-minority heating). A solid tungsten test limiter was inserted through a limiter lock at the bottom of the vessel up to a minor radius r = 44 cm. The limiter was made of highly purified W and had dimensions of 10 cm in toroidal direction, 6 cm in poloidal direction and 5 cm in height (toroidal curvature 8.5 cm and poloidal curvature 6 cm). The plasma-facing area of the test limiter represents only about 1/500 that of ALT-II (3.3 m^2). Hence, the major part of the plasma still interacts with the graphite belt limiter which dominates the general impurity behaviour.

Heat fluxes representative of ITER divertor target conditions were reached. The surface temperature was determined from IR thermography. The local impurity release was studied

by visible spectroscopy. Edge electron temperature and density profiles were measured using He- and Li-beams. High-Z contamination of the plasma was observed by Bremsstrahlung and radial profiles of the radiated power from bolometry. Graphite collector probes at (r = 47.5 cm) were used in the SOL to trace tungsten and other impurity fluxes [2].

3. Experimental Results

Recent experiments on TEXTOR with molybdenum [2, 3, 4] and tungsten [4, 5] test limiters have demonstrated that in ohmic discharges the radiated power increment due to high Z impurities increases with density. Accumulation of Mo-or W-impurities occurs when the density exceeds a critical value n_{cr} (see discussion). During the experiments discussed here, in the OH phase of discharges with the W-limiter at 44 cm and a central line-average density $\bar{n}_{eo}$ higher than a critical value of about 2.5×10^{13} cm^{-3} accumulation of W in the plasma centre was observed. This leads to a strong central radiation, peaked density profiles, centrally flattened electron temperature profiles, suppression of sawteeth, and eventually to a minor disruption (thermal instability) [5].

In discharges heated by a sufficiently high ICRH power the impurity behaviour as a function of density is totally different from that in thermally unstable OH discharges. In both cases the relative strength of the W-impurity source is dominated by physical sputtering by impact of carbon and oxygen impurities [4] and decreases with increasing plasma density (corresponding to a decreasing edge temperature). Under high edge density conditions with auxiliary heating, sputtered W-atoms are efficiently screened by prompt redeposition. Details of the local impurity release and screening are discussed in [5]. At high density the influence of the tungsten limiter on the plasma impurity content and the plasma performance becomes negligible [4, 6].

An ICRH power scan in a series of (L-mode) discharges showed that in OH target plasmas with a density above n_{cr} the central radiation disappears and the W-concentration falls by at least on order of magnitude some hundreds of ms after the onset of ICRH (see Fig. 1) if the RF power level is above a threshold value varying between roughly 0.7 MW and 1.1 MW depending on the plasma density. The radiated power profiles peak at the outer plasma regions. Preliminary experiments had already demonstrated such an RF-induced expulsion of W from the centre [6].

For ICRH power levels below threshold tungsten accumulates in the centre. Its influence on the discharge (Fig. 2) is similar to that in OH discharges with density above the critical value and a thermal instability occurs. The central W-concentration $c_w(o)$ reconstructed [4, 5] from central radiated power, $n_e(0)$, $T_e(0)$ and calculated values for impurity radiation under the assumption of corona equilibrium, is on the order of 10^{-4}, in good agreement with the relative W-deposition rate on the collector probes [4, 6]. Measurements of Bremsstrahlung in the visible range indicate that within the error bars the accumulation of W in the centre does not significantly increase Z_{eff} and hence the dilution. This is consistent with a W-concentration on the order of 10^{-4}.

A thermal instability in the presence of ICRH (below threshold) occurs several times during a discharge (Fig. 2) and can develop in different ways. For the discharge shown in Fig. 2

at t = 3.25 s the accumulation process evolves as in the OH case [5] above n_c: $c_w(o)$ rises, $n_e(r)$ peaks, radiation grows and Te(r) flattens until the situation becomes unstable and a minor disruption occurs. At t = 2.0 s, starting from a higher $c_w(o)$, $c_w(o)$ rises, Te(r) flattens but $n_e(r)$ also flattens this time (and over a broad radial range). When auxiliary heating delivers sufficient power to heat, the central plasma, Te(r) peaks, $n_e(r)$ flattens and the thermal instability is stopped (Fig. 3). The Te(r) profiles become stable and sawtoothing sets in, (t=2.5 s in Fig. 1) but only after the central radiation decreased.

The influence of tungsten was also investigated in NBI-Co heated discharges at different densities and at a power level of 1.3 MW (no power scan). No impurity accumulation was observed, and the phenomena observed during stabilization of a thermally unstable OH target plasma are similar to those in target plasmas heated by ICRH power above the threshold level. The W/D flux ratio [2] in front of the W.limiter as well as its surface temperature were found to be higher with NBI than with ICRH. However, values of Z_{eff} (about 1.5 at $\bar{n}_{eo} = 4 \times 10^{13}$ cm^{-3}) estimated from visible Bremsstrahlung do not show any measurable difference (no measurable plasma dilution) between ICRH- and NBI-heated discharges.

In the OH as well as in the auxiliary heated case Te(r) flatting always sets in at the high field side (maybe due to the lower heat conductivity). In both cases a heat pulse is emitted shortly before a minor disruption. After the heat pulse an m = 2 mode is developing with a frequency of about 2.3 kHz.

4. Discussion and Summary

The behaviour of tungsten is found to be very different in the ohmic- and the auxiliary heated phase of the discharge. In the ICRH phase the behaviour depends on the RF power level.

In the OH phase the radiated power increment due to W-impurities increases with density (although the impurity source intensity decreases), leading to a plasma thermal instability if the density exceeds a critical value n_{cr}. If in ohmic target plasmas with density above n_{cr}, ICRH at a power level above a threshold value (which increases with increasing density) is added, the thermal instability is suppressed.

The mechanisms provoking the thermal instability in OH discharges and the relaxation of the plasma core are discussed by Tokar et al. [8] (see also [2]). The critical density can be explained by the fact that impurity radiation and neoclassical (NC) transport of W-impurities increase with density. In stationary state the NC-flux is balanced by the flux due to anomalous diffusion. A central Te(r) flattering due to radiation by accumulated tungsten causes the NC inward flux of W to dominate (temperature screening disappears), leading to an instability.

In auxiliary heated discharges at sufficiently high power levels anomalous transport dominates over NC transport and W-accumulation is prevented. The threshold auxiliary power level can be interpreted in terms of n_{cr} which increases with increasing central temperature, anomalous diffusivity,and heat conductivity [8]. The critical density above which a thermal instability sets in increases with auxiliary heating power.

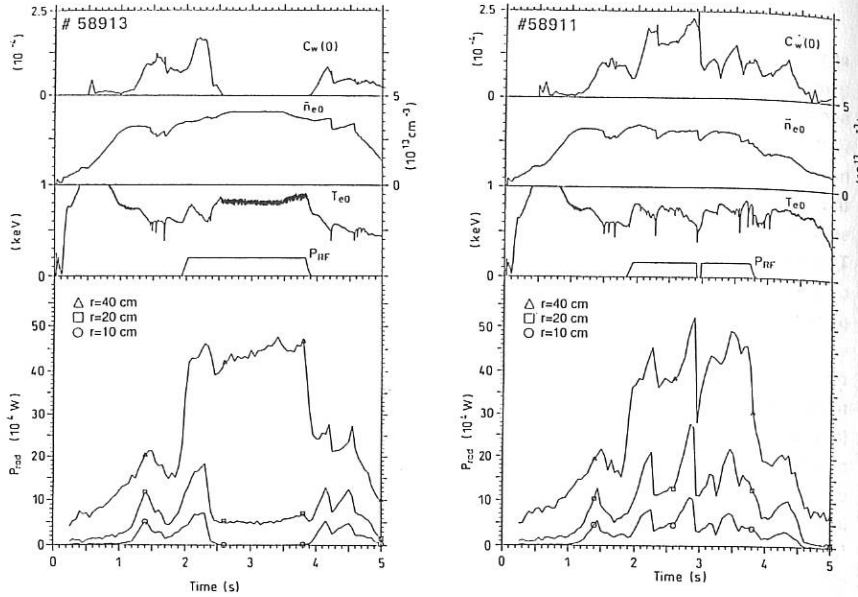

Fig. 1,2 Time evolution of central W-concentration, central line-average density, central electron temperature, RF-power, and radiated power (inside r = 10, 20 and 40 cm) (# 58913 no W-accumulation, #58911: W-accumulation)

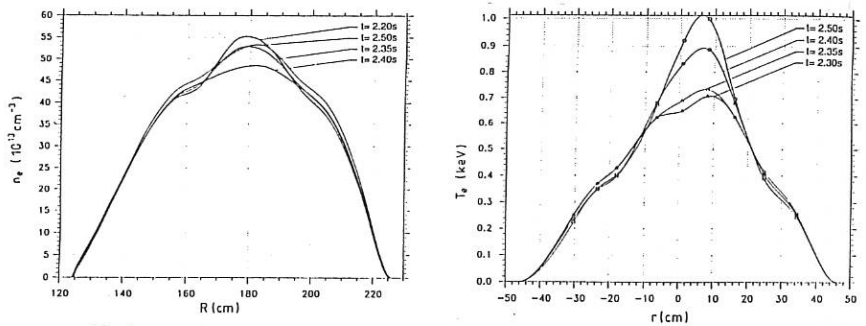

Fig. 3 Evolution of (n_e/r) and Te(r) profiles during ICRH stabilization of thermal instability (#58913)

References

[1] Tanabe T. et al., *J. Nucl. Mater.* **196-198**, 11 (1992)

[2] Philipps V. et al., *Nucl. Fusion 34*, **1417** (1994)

[3] Ueda Y et al., *J. Nucl. Mater.* **220-222, 240** (1995)

[4] Philipps, V. et al., *IAEA Conf., Sevilla 1994, Paper* (N-60/A2/4-P-19)

[5] Philipps V. et al., *this conference*

[6] Van Oost G. et al., *Proc. 21st EPS, Europh. Conf. Abstr.* **18 B, II**, 1020/1994)

[7] Noterdaeme J.M. and Van Oost G., *Plasma Phys. Control Fusion* **35**, 1481 (1993)

[8] Tokar M.Z. et al., *this conference* (Invited paper)

The Nonlocal Drift-Kinetic Quasilinear Theory of Radiofrequency Heating in Magnetic Traps[1].

S.V.Kasilov, A.I.Pyatak, K.N.Stepanov
Institute of Plasma Physics, National Science Center "Kharkov Institute of Physics and Technology", Akademicheskaya str. 1, 310108, Kharkov, Ukraine

1. Introduction

At the present moment the quasilinear theory of radiofrequency heating (cyclotron and Cherenkov) with monochromatic waves is almost complete. It provides the consistent account of the non-local effects at wave-particle interaction due the magnetic field nonuniformity along the magnetic field lines (m.f.l.) and the coherence of RF-field (the finitness of wave packet size) as well as of the effects of wave-particle decorrelation due to Coulomb collisions. The resulting from this theory bounce-averaged quasilinear equation (QLE) is extensively used for the numerical studies of the RF-heating. One of the basic assumptions used for the derivation of bounce-averaged QLE is that the unperturbed particles motion provides sufficient relaxation of the distribution function over all canonical angles, so that the distribution function stays constant on the magnetic (or drift) surface [1,2]. This assumption is obviously not valid for all collisionality regimes. In particular case of heating with toroidally localized wave packets in tokamak it means that the collision frequency should be less than banana toroidal rotation frequency and may be violated even in "collisionless" confinement regime. This situation can be modelled by 2D QLE averaged over the parallel motion, with the effects of the magnetic drift being either neglected or retained in the equation in the form of the drift of trapped orbit as a whole [3,4]. Obviously the direct effect of resonance interaction on neoclassical transport (see e.g. Ref.[1]) is omitted in this approximation. From the other hand the for the purposes of Monte-Carlo modeling of quasilinear effects of plasma heating in systems with complicated magnetic field geometry, such as stellarators, it is convenient to have the kinetic equation in the local form rather than in averaged one that permits the direct integration of particles stochastic orbits. Such an equation is present in implicit form in the literature, and our purpose is to present it explicitly that demands the explicit description of the wave-particle decorrelation. In particular case of "collisionless" regime we consider with the help of its bounce averaged form (not a surface-averaged) the effect of additional transport at ion cyclotron minority heating in tokamak due to the toroidal nonuniformity of wave packet.

2. Basic equation

Following Ref. [5] we introduce the guiding center variables $z^i = (\varepsilon, \mu, \phi, \vec{R})$ being the total energy, magnetic moment, gyrophase and guiding center position, using the momentum $\vec{p} = \vec{p}_0 + e\vec{A}/c$ where $\vec{p}_0$ is the kinetic momentum and $\vec{A}$ is RF-field vector potential. The drift-kinetic QLE takes the form

$$\frac{\partial f}{\partial t} + \vec{V}_g \nabla f = \hat{L}_C f + \frac{1}{J_y}\frac{\partial}{\partial z^i} J_y \left(D^{ij}_{QL} \frac{\partial f}{\partial z^j} - F^i_{QL} f \right) \qquad (1)$$

where $\vec{V}_g$ is guiding center velocity $\hat{L}_C$ is a Coulomb collision operator, J_y is the Jacobian of phase space coordinates. The components of the symmetric diffusion tensor are given by

$$D^{ij}_{QL} = \frac{1}{4} \mathrm{Re} \sum_{m=-\infty}^{\infty} \int_{-\infty}^{t} dt' \left(a^i_m{}^*(\vec{R}) \cdot a^j_m(\vec{R}') + a^j_m(\vec{R}) \cdot a^i_m{}^*(\vec{R}') \right) \cdot \exp\left(-i \int_{t}^{t'} dt'' \left(\omega + m\omega_c(\vec{R}'') \right) + \delta\Phi_m(t,t') \right) \qquad (2)$$

[1]Sponsored in part by International Science Foundation, Contract ISF N U32000.

where $\vec{R}'$ and $\vec{R}''$ are unperturbed characteristics for time values t' and t'' respectively, ω and ω_c are the wave and relativistic cyclotron frequencies and $\delta\Phi_m$ is collisional decorrelation function obtained explicitly in Ref.[6]. The amplitudes of Fourier series over gyrophase of the acceleration components are expressed through noncanonical Poisson brackets of Ref. [5] as

$$a^i_m = \frac{1}{2\pi}\int_{-\pi}^{\pi} d\phi \cdot \exp(-im\phi)\cdot\left\{z^i, \tilde{H}_1\right\},$$

where $\tilde{H}_1$ is complex amplitude of the linear over RF-field part of the perturbed Hamiltonian

$$\tilde{H} \equiv m_0c^2\left(\sqrt{1+\left(\vec{p}-e\vec{A}/c\right)^2/m_0^2c^2} - \sqrt{1+p^2/m_0^2c^2}\right) = \mathrm{Re}\left(\tilde{H}_1\exp(-i\omega t)\right) + \tilde{H}_2 + O\left(\tilde{A}^3\right).$$

Here m_0 is the mass of resting particle and the gauge $\varphi = 0$ is assumed for the RF-field.
For the components of quasilinear force one has

$$F^i_{QL} = \left\{z^i, K\right\} + \delta F^i,$$

where the ponderomotive Hamiltonian K is given by

$$K = \frac{1}{4}\mathrm{Re}\sum_{m=-\infty}^{\infty}\left(im\omega_c\left(\frac{\gamma}{B_0}\frac{\partial}{\partial\mu} + \frac{\partial}{\partial\varepsilon}\right)\cdot\tilde{H}^*_{1m}\hat{H}_{1m} + \left\{\tilde{H}^*_{1m}, \hat{H}_{1m}\right\}\right) + \left\langle\tilde{H}_2\right\rangle_{t,\phi}, \qquad (3)$$

$$\hat{H}_{1m} = \int_{-\infty}^{t} dt'\cdot\tilde{H}_{1m}\left(\vec{R}'\right)\cdot\exp\left(-i\int_{t}^{t'} dt''\left(\omega + m\omega_c\left(\vec{R}''\right)\right) + \delta\Phi_m(t,t')\right)$$

and angular brackets mean the averaging over time and gyrophase. Here $\tilde{H}_{1m}$ are the amplitudes of Fourier expansion of $\tilde{H}_1$ over gyrophase γ is a relativistic factor and B_0 is the main magnetic filed. The nonadiabatic part of the force δF^i is in general case of the same order with adiabatic part, however in the considered case of small collision frequency $\nu_c \ll \omega$ it is rapidly oscillating with phase-space variables and gives a negligibly small contribution to the distribution function, therefore it is omitted in the following.
In the particular case when the resonance interaction is absent and the RF-field has a form of a quasi-plane wave the main contribution to the time integral in Eq.(3) comes from the upper limit, where the decorrelation function is negligibly small. In this case the ponderomotive Hamiltonian coincides with given in Ref.[5]. Note that the phase-space variables used here are not the oscillation center variables introduced in Ref.[5]. As the consequence even in non-resonant case the fake diffusion is present in the equation together with the resonant one.
In the particular case of the cyclotron resonance heating ($\omega = n\cdot\omega_c$) in collisionless confinement regime ($\nu_{\alpha t}\tau_b \ll 1$ for the trapped particles, where τ_b and $\nu_{\alpha t}$ are bounce time and collisional detrapping frequency resp., and $\nu_c\tau_b \ll P_h$ for passing particles, where P_h is the probability to pass the cyclotron interaction region during one poloidal rotation (this quantity can be small for the heating with localized wave packets)) the drift kinetic QLE can be averaged over the parallel motion. Neglecting in collisional and quasilinear terms in Eq.(1) the derivatives over the guiding center position responsible for the neoclassical transport and assuming the trajectories $\vec{R}'$ and $\vec{R}''$ being along the magnetic field lines one gets

$$\frac{\partial f}{\partial t} + \frac{1}{J_b}\frac{\partial}{\partial x^i}J_b\left\langle V^i_d\right\rangle_b f = \left\langle\hat{L}_C\right\rangle_b f + \frac{1}{J_b}\frac{\partial}{\partial z^i}J_b\left\langle D^{ij}_{QL}\right\rangle_b\frac{\partial f}{\partial z^j}, \qquad (4)$$

where $x^i = \left(x^1, x^2\right)$ are guiding center coordinates aligned to the magnetic field lines ($\vec{B}_0\nabla x^i = 0$). The other notation is

$$J_{bt} = \int_{\vartheta_-}^{\vartheta_+} d\vartheta\cdot J_x\cdot J_y, \quad \left\langle V^i_d\right\rangle_{bt} = \frac{1}{J_b}\int_{\vartheta_-}^{\vartheta_+} d\vartheta\cdot J_x\cdot J_y\cdot\vec{V}\nabla x^i, \quad J_{bp} = \frac{1}{\delta V}\int_{\delta V} d^3R\cdot J_y, \quad \left\langle V^i_d\right\rangle_{bp} = 0$$

where subscripts "t" and "p" mean trapped and passing particles resp., ϑ is the coordinate on given magnetic field line, $\vartheta_\pm$ are the particle turning points, δV is the volume between the two

close magnetic surfaces and $J_x \equiv \partial\left(x^1, x^2, \vartheta\right) / \partial\left(R^1, R^2, R^3\right)$. The components of the diffusion tensor can be expressed in terms of "time" average

$$\left\langle D_{QL}^{ij} \right\rangle_b = \lim_{T\to\infty} \frac{1}{T} \int_0^T d\tau \cdot D_{QL}^{ij}\left(\vartheta'(\vartheta,\tau)\right), \tag{5}$$

where $\vartheta'(\vartheta,\tau)$ is the trajectory starting from ϑ at $\tau = 0$. The ponderomotive force is averaged of the equation due to $\{\varepsilon, K\} = -\partial K/\partial\tau$ and $\{\mu, K\} = 0$. The diffusion tensor (5) formally differs from obtained with the assumption of resonance overlapping (see e.g. Ref.[3]) by the presence of the rapidly oscillating terms of the same order, which give negligibly small contribution to the distribution function. In this approximation the distribution function of passing particles stays constant on given magnetic surface , while for the trapped particles this symmetry can be destroyed eighther by the asymmetry of the main magnetic field or of the RF-field.

3, Localized ICRH induced transport.

For the simplest case of the fundamental minority cyclotron resonance heating with toroidally localized wave packet in tokamak the relativistic and finite Larmor radius effects can be neglected and the averaged equation for trapped particles takes the form

$$\frac{\partial f}{\partial t} + \Omega_\alpha \frac{\partial f}{\partial \chi} = \frac{2\pi q R P(\chi)}{m_\alpha n_\alpha \left|v_p\right|\tau_b} \frac{1}{v_\perp} \frac{\partial}{\partial v_\perp} v_\perp \frac{\partial f}{\partial v_\perp} + \left\langle L_C \right\rangle_b f \tag{6}$$

where v_p and $v_\perp$ are parallel and perpendicular components of particle velocity in the cyclotron resonance point, Ω_α is the banana toroidal rotation frequency, $\chi = \zeta - q\vartheta$,ϑ,ζ are the poloidal and toroidal angles, q, R, m_α, n_α are safety factor, torus major radius, minority mass and density respectively, and $P(\chi)$ is the RF-power density averaged over one poloidal revolution of the magnetic field line with given χ. The correspoding equation for passing particles is obtained from Eq.(6) by putting $\Omega \to 0$ and $P(\chi) \to \int_{-\pi}^{\pi} P(\chi)/\pi$. For the simplicity we take Krook model for the collision operator and assume the minority distribution to be close to Maxwellian f_M. Using Fourier series expansion as given by $P(\chi) = \sum P_l \exp(il\chi)$, for the amplitudes of the distorted part of the trapped particles distribution function we get

$$f_l = \frac{2\pi q R f_M}{n_\alpha T_\alpha \left|v_p\right|\tau_b} \left(\frac{m_\alpha v^2}{T_\alpha} - 2 \right) \frac{P_l}{\nu_{\alpha t} + il\Omega_\alpha}.$$

The increase of the trapped particles population in the region of wave packet creates the ambipolar potential

$$\varphi_l(\vartheta) = \frac{\pi \varepsilon_t^{1/2} Z_\alpha P_l}{2^{3/2} e n_e \left(1 + Z_{eff}\right)\left(\nu_{\alpha t} + il\Omega_\alpha\right)} \int_{\kappa_0} d\kappa \cdot \frac{\kappa}{K(\kappa)} \left(\kappa^2 - \sin^2\frac{\vartheta}{2}\right)^{-1/2} \left(\kappa^2 - \sin^2\frac{\vartheta_r}{2}\right)^{-1/2},$$

where Z_α, Z_{eff} are minority and effective charge, n_e is plasma density, $K(\kappa)$ is elliptic integral of 2-nd kind, κ_0 is defined by the square root domain and ϑ_r is the cyclotron resonance point. Here we assumed smallness of toroidicity ε_t and independence of detrapping and rotation frequencies on velocity space variables. The toroidal asymmetry of the electrostatic potential causes the drift of bulk plasma trapped particles with radial velocity $V_r = \left(cq/rB_0\right)\partial\langle\varphi\rangle_b/\partial\chi$, resulting in additional diffusion with coefficient

$$D_\perp = \varepsilon_t^{5/2} \nu_\beta F\left(\vartheta_r\right) \left(\frac{qcZ_\alpha}{Re\, n_e B_0 \left(1 + Z_{eff}\right)} \right)^2 \sum_l \frac{l^2 P_l^2}{\left(\nu_\beta^2 + \varepsilon_t^2 l^2 \Omega_\beta^2\right)\left(\nu_\alpha^2 + \varepsilon_t^2 l^2 \Omega_\alpha^2\right)}. \tag{7}$$

Here $\nu_\alpha, \Omega_\alpha, \nu_\beta, \Omega_\beta$ are collision and toroidal rotation frequencies of minority and bulk particles, $F\left(\vartheta_r\right) \approx 1$. Estimating $\Omega_{\alpha,\beta} \approx qcT/\left(2e_{\alpha,\beta} B_0 \varepsilon_t R^2\right)$ for the tokamak with R = 3 m, q = 2, B = 3 T, $n_e = 3\ 10^{19}$ m^{-3}, $T_\alpha = T_\beta =$

5 KeV heated with 10 MW of ICRH power localized within the radius r = 0.5 m and angle $\Delta\zeta$ = 90°, we get $D_\perp \approx 0.01$ m^2/s, that is higher than neoclassical ion thermal conductivity.

References

[1] Osipenko M.V. and Shurygin R.V. Fizika Plazmy 16 (12) 1425 (1990).
[2] Becoulet A. et al. Phys. Fluids B3 (1) 137 (1991).
[3] Timofeev A.V. and Tokman M.D. Plasma Physics Reports 20 (4) 376 (1994).
[4] Sakharov A.S. and Tereshchenko M.A. Plasma Physics Reports 21 (2) 99 (1995).
[5] Grebogi C. and Littlejohn R.G. Phys.Fluids 27 (8) 1996 (1984).
[6] S.V. Kasilov, A.I. Pyatak, K.N. Stepanov. Intern. School on Plasma Physics Piero Caldirola "Theory of Fusion Plasma", Varenna, Italy, 27-31 August, 1990. Ed. J. Vaclavic, F. Troyon, E. Sindoni. SIF, Bologna, 1990, p.301.

Fokker-Planck Solver With Spatial Diffusion Of The Driven Currents*

I.P. Shkarofsky** and M.M. Shoucri

Centre canadien de fusion magnétique, Varennes, Québec, J3X1S1, Canada

1. Introduction

To calculate the currents driven in a tokamak by a dc electric field or by lower-hybrid or electron-cyclotron waves, the Fokker-Planck equation is solved [1,2] to first derive the form of the electron momentum distribution function. Thereafter, one can calculate both the driven current density and the X-ray emission spatial profiles. However, the fast electrons which are generated during current drive can diffuse the spatial current density profile. The spatial diffusion that occurs depends on the form assumed for its dependence in space and also in momentum. We solve relativistically the Fokker-Planck equation in two dimensions (2D) in momentum (p) space and with one radial (r) dimension (1D) in configuration space. In [1], we developed a fast Fokker-Planck solver without spatial diffusion. It is capable of predicting the actual line-integrated bremsstrahlung energy spectrum up to hundreds of keV [3]. It uses an accelerated method through a solution of an elliptic equation. However, when spatial diffusion is included, we have to solve numerically the Fokker-Planck equation as a diffusion parabolic equation on the much slower collisional time scale. Here we provide the new version of the solver, with evolution on a collisional time scale, which includes spatial diffusion. Previous efforts were those in [4], and Cairns et al [5] who use a simplified model.

2. Analysis

We solve for the distribution function, f, with a diffusion term, $D(r,p)$:

$$\frac{\partial f}{\partial t} + \nabla_p \cdot S = I(f_m, f_1 \cos\theta_p) + \frac{1}{r}\frac{\partial}{\partial r}\left[rD(r,p)\frac{\partial f}{\partial r}\right] \qquad (1)$$

where S includes effects, explicitly given in [1], due to a dc electric field (ε), quasi-linear rf fields (lower-hybrid (D_{LH}), fast wave and electron-cyclotron, see [2]), electron-ion collisions and part of electron-electron collisions, and I includes the remaining electron-electron collision part which is an integral over f_1. The variables are normalized as in [1], with the additional parameter $D(r,p)$ normalized to νa^2, where ν is the collision frequency. Using a

collisional relaxation time step Δt, we alternate by solving Eq. (1) without spatial diffusion,

$$\partial f/\partial t + \nabla_p \cdot S = I(f_m, f_1 \cos\theta_p) \tag{2}$$

and then solving Eq. (1) with only spatial diffusion but setting the terms $S = I = 0$.

$$\frac{\partial f}{\partial t} = \frac{1}{r}\frac{\partial}{\partial r}\left[rD(r,p)\frac{\partial f}{\partial r}\right] \tag{3}$$

This corresponds to the method of fractional steps for solving Eq. (1). For the calculations, two simplifications are used, although the numerics can handle more general cases. First since both parallel and perpendicular velocities are included in the 2D solution, we took the spatial diffusion coefficient to be a function of the magnitude of the velocity or momentum, rather than of only the parallel velocity component. Thereby, we also get around the problem of how to handle the negative parallel velocity side. Secondly, since the suprathermal electrons induce the spatial diffusion, the spatial diffusion operator acts only for velocities above thermal. This is simulated by assuming a dependence proportional to the factor ($v - v_{th}$) with $v > v_{th}$ where $v_{th} = [T(r)/m]^{1/2}$ is the local thermal velocity.

3. Results

We provide results from the Fokker-Planck solver of the diffused current profiles for several examples of $D(r,p)$. Comparisons with experimental results of TdeV (shot number 23870, with a = 0.25 m, R = 0.86 m, B_T = 1.5 T, Z_{eff} = 3.5, line averaged n_e = 1.4 x 10^{19} m^{-3}, $n_\parallel$ = 2.5) and with an analysis [5] are presented. The adopted density and temperature profiles are:

$$\begin{aligned} n_e\,(10^{19}\,m^{-3}) &= 1.95\,[\,1 + 0.3712\,(r/a)^2 - 2.98\,(r/a)^3 + 1.6963\,(r/a)^4\,] \\ T_e\,(keV) &= 1.878\,[\,1 - (r/a)^{1.5}\,]^2 + 0.03\,, \quad T_i = T_e/2 \end{aligned} \tag{4}$$

All other space dependent variables (e.g. v_{th} and v) are also referred to their values obtained with $n_{ec} = 10^{19}$ m^{-3} and T_{ec} = 1 keV. The lower-hybrid rf power input is given in terms of the normalized D_{LH}, which is assumed to vary in space as $D_{LH} = 0.5[sin^2(\pi r/0.425a)]$ for $r/a \leq 0.425$, zero for $r/a > 0.425$, and D_{LH} is applied between the local $v_1 = 3\ v_{th}$ and $v_2 = 8\ v_{th}$. This shape mimics the form of the hot electron population $\int (f - f_{Maxw})\ d^3p$. We first show results without spatial diffusion [$D(r,p) = 0.0$] subject to no electric field ($\varepsilon = 0.0$), but to the above D_{LH}. The resultant current density profile, derived from integrals over the distribution function at spatial radial points, is shown in Fig. 1, plot a. This profile is hollow in the

centre, but can fill up by including appropriate $D(r,p)$ or $D(r,v)$ radial diffusion. In plots b to f, $D(r,v) = c\ (v - v_{th})$ in m^2/s (not normalized), where respectively c = 0.01, 0.05, 0.1, 0.2 and $0.05[1 + 3.5(r/a)^2]$. Note that the central region gets filled up and that the profile broadens for larger constant values of c. When c = 0.2, the central value is about 0.19, decreasing monotonically to zero at about r/a = 0.8. In Fig. 2, we plot the normalized hot electron population, $\int (f - f_{Maxw})\ d^3p$. The theoretical plots a to f correspond to the same a to f cases as in Fig. 1. In plot g (dashed curve), we show TdeV experimental data whose values, indicative of the hot population, are obtained from the 10-20 keV range of the X-ray emission profile divided by $n_e(r)$. There is reasonable agreement between the experimental and the theoretical curve for c = 0.2. Plot h of Fig.2 plots the result from the simplified model in Cairns et al [5], indicating qualitative agreement between the latter and plot e. Cairns et al use $D(r,v_{\parallel}) = 0.2\ v_{\parallel}$, limited to positive parallel velocity $v_{\parallel}$ within the plateau region, and apply an averaging procedure which reduces the calculation of the spatial profile in the plateau region to a simple diffusion equation in r. Our 2D analysis has a much larger range of applicability covering all of 2D (including perpendicular and negative parallel) velocity space in a continuous fashion, and allowing more complicated solutions, such as partial current drive with a net electric field existing. The current density profiles for such a case with $\varepsilon = 0.13/(2\pi R)$ are shown in Fig.3. Curves a to d correspond to values of c = 0.05, 0.1, 0.2 and $0.05[1 + 3.5(r/a)^2]$. In Fig. 4, curves a to d, we plot the corresponding results for the normalized hot electron population, $\int (f - f_{Maxw})\ d^3p$ and plot e shows again the experimental curve. These examples show the versatility of the code. The cpu time on a unix DEC Alpha machine, OSF1 v.3.2, is about 2 hours for 20 radial points and 400 iterations.

* Supported by the *Centre canadien de fusion magnétique* with funds from AECL, Hydro-Québec and INRS. ** Also at MPB Technologies Inc., Pointe Claire, Québec, Canada.

References

[1] Shoucri M. and Shkarofsky I., Computer Phys. Communications **82** 287 (1994)

[2] Shoucri M. and Shkarofsky I., Computer Phys. Communications **78** 199 (1993)

[3] Peysson Y. et al, 11th Topical Conf. on RF Power in Plasmas, Palm Springs, CA. (1995)

[4] Rax J.M. and Moreau D., Nucl. Fusion **29** 1751 (1989); O'Brien M.R. et al, Nucl. Fusion **31** 583 (1991); Giruzzi G., Plasma Phys. Contr. Fusion **35** A123 (1993); Kesner J., Nucl. Fusion **33** 1085 (1993); Fuchs V. et al, Nucl. Fusion **29** 1479 (1989)

[5] Cairns R.A. et al, To be published in Nucl. Fusion

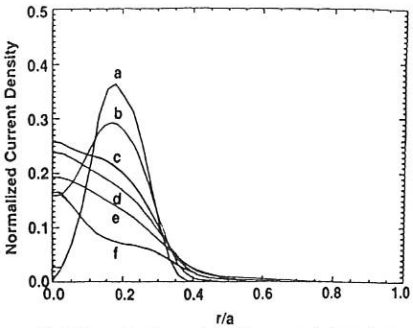

Fig.1: Normalized current density versus r/a for various values of the spatial diffusion coefficient. For curves a to f, c=0.0, 0.01, 0.05, 0.1, 0.2 and 0.05[1+3.5(r/a)^2] respectively. The normalized electric field ε= 0.0 here.

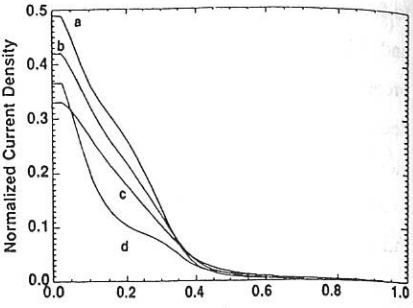

Fig.3: Normalized current density versus r/a for various values of the spatial diffusion coefficient. For curves a to d, c=0.05, 0.1, 0.2 and 0.05[1+3.5(r/a)^2] respectively. The normalized electric field ε=0.13/(2πR) here.

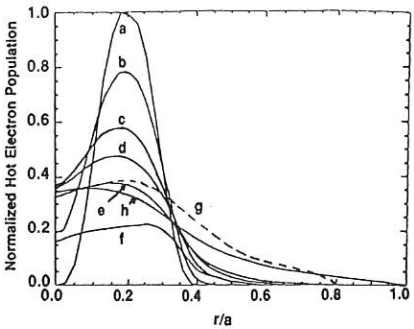

Fig. 2: Normalized hot electron density population versus r/a for the a to f values of the spatial diffusion coefficient given in Fig.1 with ε=0.0. Curve g plots normalized experimental values for the X-ray emission in the 10-20 keV range divided by electron density. Curve h is Cairns et al's [5] approximate analysis.

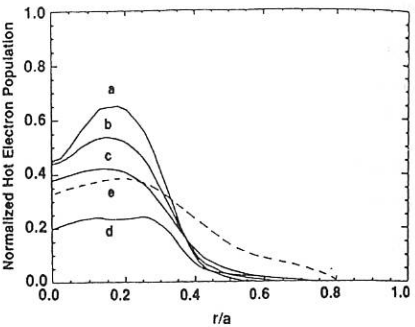

Fig. 4: Normalized hot electron density population versus r/a for the a to d values of the spatial diffusion coefficient given in Fig 3 with ε=0.13/(2πR). Curve e plots again the experimental values shown in Fig.2.

SIMULATIONS OF FILLING THE SPECTRAL GAP WITH LOWER HYBRID WAVES

P. Bertrand[1], A. Ghizzo[1], S. J. Karttunen[2], **T. J. H. Pättikangas[2]**, R. R. E. Salomaa[3], M. Shoucri[4], and I. Shkarofsky[4]

[1]Universite Henri Poincaré Nancy I, L.P.M.I.–C.N.R.S. URA 835, B.P. 239, 54506 Vandœuvre, France
[2]VTT Energy, P. O. Box 1604, FIN-02044 VTT, Finland
[3]Nuclear Engineering Laboratory, Helsinki University of Technology, FIN-02150 Espoo, Finland
[4]Centre Canadien de Fusion Magnétique, Tokamak de Varennes, Varennes J3X 1S1, Québec, Canada

1. Introduction

Using two spectra of lower hybrid (LH) waves with different values of $n_{\|}$ offers interesting possibilities for controlling the absorption profile of LH waves in tokamaks. Previously, the synergy between a fast and a slow spectrum of lower hybrid waves has been experimentally studied at ASDEX [1] and JT-60U [2]. At ASDEX, local control of the current profile was achieved. At JT-60U, filling of the spectral gap by the slower wave was investigated.

In this report, the absorption of a spectrum of fast ($v_{ph} \simeq 6v_e$) lower hybrid waves is investigated via numerical simulations. The enhancement of the absorption caused by filling the spectral gap by simultaneously launched slower waves with $v_{ph} \simeq 4.3v_e$ is studied. The electron motion is solved from a two-dimensional drift-kinetic Vlasov equation [3] and the ion motion from the fluid equations. The electrostatic field is obtained from the Poisson equation. The absorption profile of the waves is solved, and the time evolution of the LH spectrum is investigated.

2. Drift-kinetic model

In our numerical simulations, the distribution function $f_e(x, y, v_{\|}, t)$ for the electrons is solved from the two-dimensional drift-kinetic Vlasov equation [3]

$$\frac{\partial f_e}{\partial t} + (v_{\|}\cos\theta + \frac{E_y \sin\theta}{\omega_{ce}})\frac{\partial f_e}{\partial x} - \frac{E_x \sin\theta}{\omega_{ce}}\frac{\partial f_e}{\partial y} - E_x \cos\theta \frac{\partial f_e}{\partial v_{\|}} = 0, \tag{1}$$

where the magnetic field is in the $x - z$ plane making an angle $\theta = 10°$ with the x direction. The ion kinetic effects are neglected and the ion density $n_i(x, y, t)$ is solved from a fluid equation, and the field components E_x and E_y are solved from the two-dimensional Poisson equation [3].

The initial density and temperature profiles are assumed to be parabolic in y direction: $n_e(y) = n_{e0}[1 - (y/L_n)^2]$ and $v_e(y) = v_{e0}[1 - (y/L_v)^2]^{1/2}$. In the periodic x direction, the initial temperature and density are homogeneous.

The LH waves are launched into the plasma by a 'grill' formed by an oscillating external charge

$$\rho_{ext}(x, y, t) = S(t)w(y) \sum_{i=s,f} \sum_{k_x} \rho_{ext,k_x} \cos(k_x x + k_y y - \omega_i t), \tag{2}$$

where $w(y)$ is a Gaussian that is localized around $y_g = -286\lambda_{De}$. The step function $S(t)$ grows from zero to one between $\omega_{pe}t = 0$ and 300. The frequencies ω_s and ω_f correspond to the slow and the fast part of the spectrum, respectively. The wave numbers in Eq. (2) are calculated from the linear dispersion relation.

3. Single Spectrum of fast LH Waves

The modes launched by the 'grill' have the frequency $\nu_f = 3.7$ GHz, and are centered at the parallel refraction index of $n_{||} = 3$. The corresponding parallel phase velocity near the 'grill' is $v_{ph||} = 6.15v_e$. Initially, the spectrum contains nine modes with parallel refraction indices varying from $n_{||} = 1.67$ to 4.33. In this simulation, the peak temperature and density of the plasma were $T_{e0} = 1.5$ keV and $n_{e0} = 2 \times 10^{19}$ m^{-3}, respectively.

The evolution of the $n_{||}$ spectrum of the LH waves is shown in Fig. 1 at time $\omega_{pe}t = 800$ at different positions. As the wave amplitude at the 'grill' increases and the LH wave propagates deeper inside the plasma, the spectrum becomes slightly wider and modes with higher values of $n_{||}$ are excited. At time $\omega_{pe}t = 800$, a small second maximum is formed in the spectrum at the second harmonic wavenumber of the excited waves at $n_{||} \simeq 6$.

Deep inside the plasma, the spectrum becomes asymmetric because of the strong absorption of the modes with large values of $n_{||}$. During the propagation, the maximum of the spectrum is also shifted towards smaller values of $n_{||}$ as can be seen in Fig. 1. At $y = -150\lambda_{De}$, the maximum of the spectrum is at $n_{||} \simeq 3$ but at $y = 150\lambda_{De}$ it has shifted to $n_{||} \simeq 2$.

Formation of a hot tail in the electron distribution is illustrated in Fig. 3(a). Close to the 'grill', at $y \simeq -200\lambda_{De}$, the temperature of the tail begins to increase at time $\omega_{pe}t \simeq 300$, and a tail is formed at $\omega_{pe}t \simeq 500$. Deeper inside the plasma, at $y = -100\lambda_{De}$ and $y = 0$, a tail is formed later at time $\omega_{pe}t \simeq 700$ and 800, respectively. At $y = 150\lambda_{De}$, the velocity distribution is not changed during the simulation even though the amplitude of the field is rather large there at the end of the simulation. The field in this region is dominated by modes with high parallel phase velocities because the modes with small phase velocities have already been absorbed close to the 'grill'.

4. Filling the Spectral Gap with Slower LH Waves

The effect of filling the spectral gap by waves with smaller phase velocities is investigated by launching a compound spectrum of lower hybrid waves into the plasma. The spectrum consists of a slow part centered at the parallel refraction index of $n_{||} = 3$ and of a faster one at $n_{||} = 2$. The corresponding parallel phase velocities near the 'grill' are $v_{ph||} = 4.35v_e$ and $v_{ph||} = 6.53v_e$ for the slower and the faster wave, respectively. Both the slow and the fast part of the spectrum have parallel wave numbers centered at $k_{||}\lambda_{De} = 0.0150$, but the frequency of the faster part is $\nu_f = 5.55$ GHz and the frequency of the slower part is $\nu_s = 3.7$ GHz. The corresponding parallel refraction indices for the fast part of the spectrum vary from $n_{||} = 1.111$ to 2.889 and for the slow part from $n_{||} = 1.667$ to 4.333. In this simulation, the peak temperature and density of the plasma were chosen to be $T_{e0} = 3$ keV and $n_{e0} = 4 \times 10^{19}$ m^{-3}, respectively.

The compound spectrum of the LH waves is shown in Fig. 2 at time $\omega_{pe}t = 564$ at different positions. The spectra have again been obtained by performing a spatial Fourier transform of the field in the x direction. The bottom axis has then been scaled

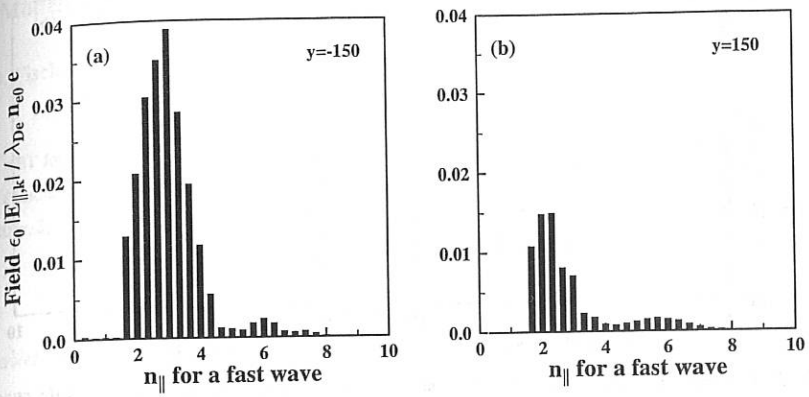

FIG. 1. Parallel refraction index spectrum of a single spectrum of fast LH waves at time $\omega_{pe}t = 800$ *at positions (a)* $y = -150$ *and (b)* $y = 150$.

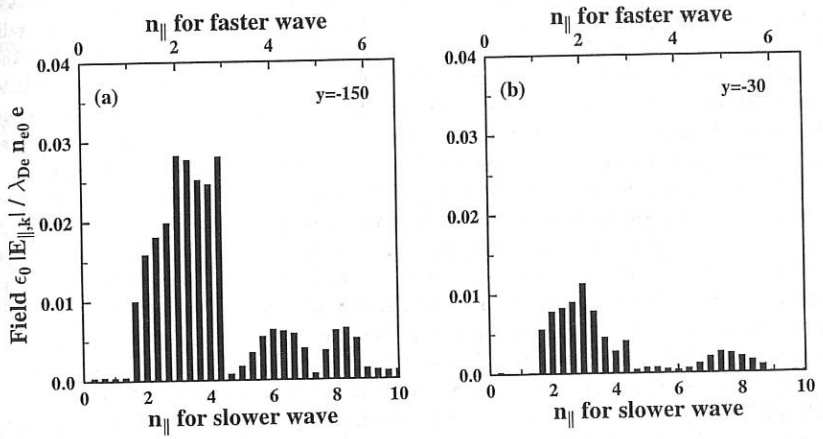

FIG. 2. Parallel refraction index spectrum of a compound spectrum of LH waves at time $\omega_{pe}t = 564$ *at positions (a)* $y = -150$ *and (b)* $y = -30$.

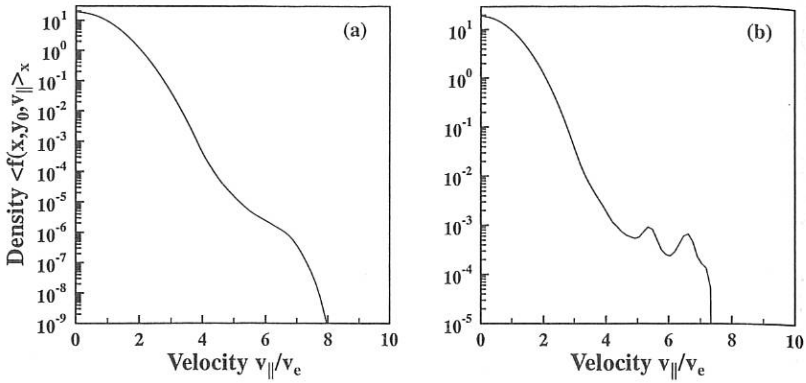

FIG. 3. Electron velocity distribution averaged over x when we have: (a) a single spectrum of LH waves, $\omega_{pe}t = 800$, $y = -200\lambda_{De}$, (b) a compound spectrum of LH waves, $\omega_{pe}t = 800$, $y = -196\lambda_{De}$.

by the frequency of the slow part of the spectrum and the top axis by the frequency of the fast part of the spectrum in order to obtain the $n_{||}$ scales.

Strong absorption of the waves with large $n_{||}$ values can be seen in the spectra shown in Fig. 2, where the amplitudes of the slow part of the spectrum around $n_{||} \simeq 3$ decrease when the waves propagate deeper inside the plasma. The spectrum broadens again towards higher values of $n_{||}$, and modes with the second harmonic wavenumber of the originally excited modes appear. For the slower part of the spectrum this corresponds to refraction index $n_{||} \simeq 6$ and for the faster part $n_{||} \simeq 4$. The amplitudes of these second harmonic modes are much higher in the case of the compound spectrum than in the case of a single spectrum even though the amplitudes of the modes are somewhat smaller.

The evolution of the electron velocity distribution is illustrated in Fig. 3(b). The interaction of the electrons with the compound spectrum of LH waves is much stronger than with the single spectrum having high phase velocities. The height of the plateau obtained at $y = -200\lambda_{De}$ with the combined spectrum of waves is more than two orders of magnitude higher than the one obtained with the single spectrum (cf. Fig. 3(a)). This of course means that a much higher current is obtained with the combined spectrum. The plateau of the distribution function shown in Fig. 3(b) has also positive values of the slope at $y \simeq -200\lambda_{De}$, which is a sign of energy transferring back and forth between the LH field and the fast electrons. This is in strong contrast with the smooth quasilinear plateau found in the case of a single spectrum in Fig. 3(a).

[1] F. X. Söldner, F. Leuterer, R. Bartiromo, et al., Nucl. Fusion **34** (1994) 985.

[2] S. Ide, O. Naito T. Kondoh, Y. Ikeda and K. Ushigusa, Phys. Rev. Lett. **73** (1994) 2312.

[3] A. Ghizzo, P. Bertrand, M. Shoucri, E. Fijalkow and M. Feix, J. Comput. Phys. **108** (1993) 105.

Modelling of LH Current Drive and Profile Control Experiments on JET

B. Fischer, Y. Baranov, A. Ekedahl, C. Gormezano, M. Lennholm, V.V. Parail[1], V. Pericoli-Ridolfini[2], Y. Peysson[3], F. Rimini, P. Schild, F. Smits[4], F.X. Soldner, E. Springmann

JET Joint Undertaking, Abingdon, Oxon, OX14 3EA, UK, 1) permanent address: Kurchatov Institute of Atomic Energy, Moscow, Russia, 2) C R E Frascati, Associazione Euratom-ENEA sulla Fusione, Frascati, Italy, 3) CEA, Centre d'Etudes de Cadarache, France 4) FOM-Instituut voor Plasmafysica "Rijnhuizen", PO Box 1207, 3430 BE Nieuwegein, The Netherlands

Abstract

Lower Hybrid Current Drive (LHCD) experiments on profile control with sawteeth suppression and shear reversal have been modelled with the transport code JETTO using LH deposition profiles from the Baranov ray tracing code. Both modelling and Fast Electron Bremsstrahlung (FEB) diagnostic show a wide range of LH current deposition profiles in these experiments with variation from hollow to centrally peaked profile shapes. Parameter scalings of local emission are deduced from inverted FEB profiles. LH current deposition profiles from the ray tracing plus 1D and 2D Fokker Planck codes are validated by comparison with FEB profiles. The modelled plasma current redistribution and heating is compared with the experiment on the basis of the evolution of the q-profile, internal inductance, loop voltage and total energy content.

Parameter dependences of LH deposition profiles

The FEB camera [1] is a multichord system providing line integrated emissivity profiles of 4 equal energy windows in the range of 133-400 keV. Parameter scalings of LH deposition have been deduced from inverted local emissivity profiles of the lowest energy window normalised to thermal electron density. Full LH current drive pulses in X-point configurations at various plasma parameters have been investigated: The peak of the FEB profiles is more off-axis for higher plasma current of I_p=3MA than for I_p=2MA for $B_T \geq 2.8$T. (Fig.1,2). The profile maximum is shifted off-axis with increasing density in the range of $\langle n_e \rangle = 0.8 - 2 \times 10^{19} m^{-3}$, where the maximum position is observed in the range of (r/a)=0.35-0.6. An effect of the electron temperature was a tendency of off-axis shift with increasing temperature for the present experiments in the range of $\langle T_e \rangle = 1 - 3$ keV. No change of the FEB profile with the

launched $N_{\parallel}$-spectrum in the range of $N_{\parallel}$=1.4-2.3 has been observed. This can be explained by multipass absorption dominating the present LHCD experiments.

Profile control experiment and simulation of sawteeth stabilisation

A full current drive LH pulse of 5MW power on a 2MA discharge (B_T=2.8T, $<T_e>$=1.8keV, T_{eMAX}=4keV, $<n_e>$=1.5x10^{19}m^{-3}, n_{MAX}=2.3x10^{19}m^{-3}, Z_{EFF}=1.9) in excess of 10s of duration with subsequent ohmic ramp from 2 to 3MA has been performed to raise q(0) as much as possible. Long pulse times are required in order to obtain steady-state conditions after a redistribution of the current profile on a long diffusive time scale. Sawteeth have been suppressed from the very beginning of the LHCD pulse. The current profile is frozen after LHCD and I_p-ramp with ICRH heating (Fig.3). The calculated total LH current is 1.7MA. Differences between the 1D and 2D Fokker Planck code [2,3] are within 10%. Very similar current deposition profiles are found from both codes. They are in good agreement with the FEB measurement (Fig.2). Using experimental temperature profiles as input in JETTO, the transport code results show that q(0) is sufficiently increased above 1 to explain the experimentally observed sawteeth suppression. The central q remains above 1 during ICRH heating, the current profile is nearly frozen and relaxes slowly. The simulation shows even shear reversal, which is not yet indicated by a simple equilibrium reconstruction, i.e. without several constrains such as polarimetry. The temporal behaviour of internal inductance and loop voltage (Fig.4) is well reproduced by the simulation. Using the Bohm-like JET L-mode transport model [4] in JETTO reveals the same results as stated above until the late second current ramp. Modelling of the second phase has yet to be done. The plasma energy content is well reproduced by the simulation for more than 10s of LH heating (Fig.5). The ohmic heating in this phase is negligible and the dominant power deposition is due to LH.

Shear reversal with LHCD and ohmic ramp up in the initial plasma phase

Shear reversal has been built up with LHCD + ICRH in a rapid ohmic ramp of 1MA/s and n_e < 1.5x10^{19}m^{-3} [5]. The hollow current profile has been frozen at higher density by high additional power and subsequent electron heating. Very peaked LH deposition profiles have been found from both FEB diagnostic and ray tracing together with Fokker Planck calculations in the early ohmic ramp up phase (Fig.6). The early ramp up has been simulated imposing the experimentally validated LH current profile. The shear reversal, indicated by the equilibrium reconstruction, is found to be in reasonable agreement with the simulation.

Summary and future plans

The FEB diagnostic is essential for the LH deposition analysis and the experimental validation of LH deposition profile modelling. Using experimentally validated LH deposition profiles the transport code simulation reproduces the plasma current redistribution and plasma heating in good agreement with the experiment. The equilibrium reconstruction has to be upgraded with a polarimetry restraint in order to obtain more reliable central q values from the experiment. LH and transport code modelling will be applied to find scenarios for experiments on current profile control in parameter regimes which are more sensitive with respect to the launched $N_{\parallel}$-spectrum and the available time duration of the JET plateau in current..

References

[1] P.Froissard et al., Proc. of 18th EPS Conf., Berlin (1991).

[2] Y.Baranov et al., 20th Europ. Conf. on Contr. Fusion and Plasma Physics, Lisbon (1993).

[3] M.Shoucri et al., Computer Physics Communications 82, 287 (1994).

[4] V.V.Parail et al., Proc. of 15th IAEA Conf., Seville (1994).

[5] F.X.Soldner et al., Proc. of 15th IAEA Conf., Seville (1994).

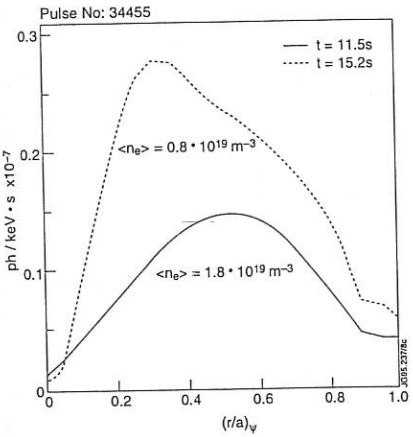

Fig.1: Local emissivity profiles normalised to density (<T_e> =1.7keV, I_p=3MA, B_T=3T).

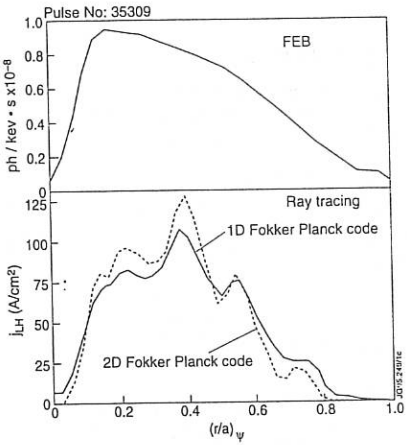

Fig.2: Profile shapes from FEB and LH codes (<n_e>=1.5x10^{19}m^{-3}, <T_e>=1.8keV, I_p=2MA, B_T=2.8T).

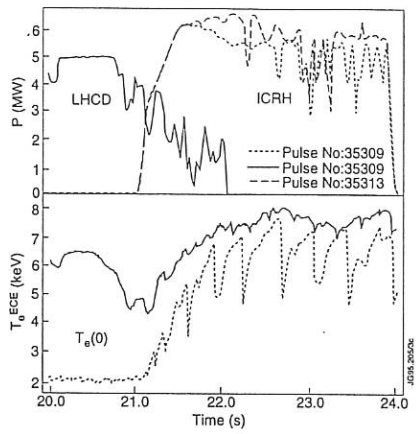

Fig.3: Sawteeth stabilisation (#35309) after LHCD compared to a reference pulse (#35313)

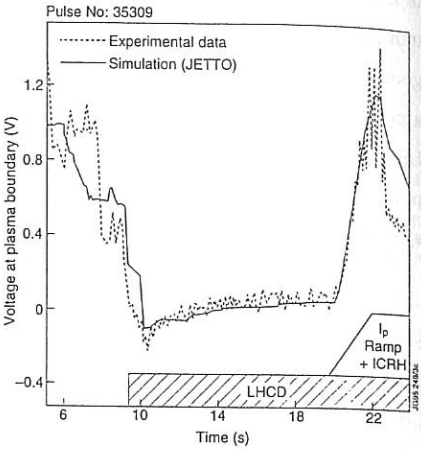

Fig.4: Evolution of surface loop voltage.

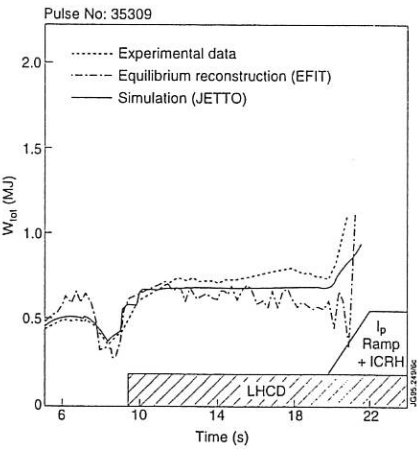

Fig.5: Energy content during LH pulse.

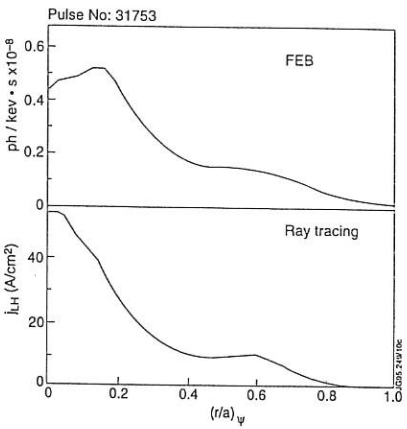

Fig.6: Current profile shapes from FEB diagnostic and LH modelling.

ICRF Heating and Current Drive Experiments in TFTR

R. Majeski, C. K. Phillips, J. H. Rogers, G. Schilling, J. R. Wilson, D. Batchelor,*
S. Batha, D. Darrow, A. England,* N. Fisch, M. C. Herrmann, J. C. Hosea,
D. Ignat, F. Jaeger,* F. Levinton, E. Mazzucato, M. Murakami,* R. Nazikian,
D. Rasmussen,* G. Taylor, E. Valeo, J. C. Wright, S. Zweben, and the TFTR Group

Princeton Plasma Physics Laboratory, Princeton, New Jersey 08543 USA
*Oak Ridge National Laboratory, Oak Ridge, Tennessee 37831 USA

1. Introduction

Since the inception of the deuterium-tritium (D-T) phase on TFTR, radio-frequency (RF) experiments in the ion cyclotron range of frequencies (ICRF) have focussed either directly on the leading candidate for RF heating of reactor grade plasmas, heating at the second harmonic of tritium, or on heating and current drive techniques which are applicable to D-T plasmas. Many aspects of ICRF heating at the second harmonic of tritium ($2\Omega_T$) have now been investigated, including power deposition and transport in RF heated supershot plasmas. The second class of experiments includes direct electron heating and current drive by the ion Bernstein wave (IBW), excited via mode conversion at the ion-ion hybrid layer from the launched fast magnetosonic wave. The mode converted IBW has been shown to heat electrons and drive current both on and off axis, and to couple strongly to fusion products. Finally, direct fast wave current drive in reactor relevant regimes has been demonstrated.

2. Second harmonic tritium heating.

Up to 6 MW of RF power has been applied to second harmonic tritium ($2\Omega_T$) heating. With 5.5 MW of ICRF power coupled to a D-T target plasma formed by 23 MW of neutral beam injection (NBI), the central ion temperature increased from 26 to 36 keV, and the central electron temperature from 8 to 10.5 keV.[1] A small amount (2%) of ^{3}He was added to the discharge in this case to increase the single pass absorption. During RF modulation experiments[1] with 60% tritium NBI and no ^{3}He minority, up to 65±13% of the RF power was deposited directly on the tritium. As shown in Fig. 1, similar discharges with 4.4 MW of RF power (unmodulated) and 23 MW of NBI, again with 60% in T and no ^{3}He, exhibited power deposition profiles for ions and electrons which were highly peaked on axis, as determined by TRANSP analysis.

3. Mode conversion electron heating and current drive.

The theory of efficient single-pass mode conversion with a low field side wave launch in a multiple ion species plasma has been discussed in detail.[2,3] These experiments compliment earlier work with a high field side launch in TFR.[4]

The magnetic fields (<5.2T), frequencies (43 or 64 MHz), and allowable gas species in TFTR restrict the ion species mix for mode conversion to D (or ^{4}He) - ^{3}He at 43 MHz, with the possible addition of tritium to increase fusion reactivity. We find experimentally that heating is localized to the mode conversion surface ($n_{\parallel}^2$=S, where S is defined by Stix[5]). The position of peak electron power deposition has been varied with the magnetic field and ion species mix.[6] For a ^{3}He fraction greater than 15-20%, 60-80% of the total RF power coupled to the plasma is found in the electron heating channel at the mode conversion surface. Off axis heating with 4.4 MW of RF at r/a=0.15 has produced transiently hollow electron temperature profiles.[7] When the mode conversion surface was located on the Shafranov-shifted axis, 4 MW of ICRF was sufficient to raise the central electron temperature of the ohmic target plasma from 3 to over 10 keV, the highest electron temperature produced by RF alone in TFTR. For comparison, the highest electron temperature attained in the sawtooth-stabilized hydrogen minority regime is less than 8 keV, with over 10 MW of RF power.

For current drive experiments, the two strap TFTR ICRF antennas were driven at either 90^o (co-) or -90^o (counter-) relative phase. Co- and counter- are referred to the direction of ohmic electron current. In Fig. 3 (a,b) we display the time evolution of the surface loop voltage for two such discharges. In these discharges, the electron temperature and temperature profiles were substantially the same from 3.3 - 4.0 seconds, with $T_e(0)$=5.5 keV. The central electron density was 4 x 10^{19} m^{-3} in ^{4}He, ^{3}He, and D. For the counter- discharge $Z_{effective}$ = 3.2 at 3.75 seconds; while for the co- discharge $Z_{effective}$ = 3.5. The difference in the loop voltage just prior to beam injection implies a noninductively driven current of ±120 kA. Analysis of $\partial T_e(r)/\partial t$ at the termination of the RF pulse indicates that the power deposition was on-axis. The mode conversion process is selective in parallel wavenumber[2], so that near 100% directivity of the mode converted wave is expected. Modelling with the FELICE[8] code combined with the Ehst-Karney[9] parameterization yields a predicted current of ±100 kA.

Off-axis currents, at r/a up to 0.2, have also been driven. The maximum RF-driven off-axis current in these experiments was 100 kA, with 3.4 MW of power coupled to a plasma with a central density of 5.5 x 10^{19} m^{-3}, and central electron temperature of 6 keV, in ^{4}He, ^{3}He, D, and T. The predicted current for this pair of discharges was 90 kA. RF-driven evolution of the current profile was observed with the motional Stark effect diagnostic, with a 50% increase in q_0 for the off-axis co- discharge relative to the counter- discharge.

In cases where the mode conversion layer is located precisely on the Shafranov-shifted plasma axis, a strongly enhanced loss of fusion products has been seen with the escaping fusion product detectors, with driven loss rates approaching 50% of the fusion product birth rate. D-D fusion products (tritons) are primarly observed, due to the relative positions of the mode conversion and $2\Omega_T$ layers. Losses show evidence of strong heating (up to 50% above the birth energy). The implied diffusion rate approaches 1 Mev^2/sec. This rate of energy diffusion is expected to be sufficient to investigate aspects of alpha channeling.[10,11]

Recently, driven losses of DT fusion alpha particles have also been observed when the mode conversion layer is sufficiently close to the alpha particle cyclotron layer, as shown in Fig. 4.

4. Fast wave current drive.

Experiments in fast wave current drive have principally utilized a ^{4}He target plasma at a toroidal field of 2.7 T. ICRF at 43 MHz is applied to indirectly heat electrons in an H-minority regime, while current drive utilizes a frequency of 64 MHz to couple directly to the electrons.[12] Results are shown in Fig. 5(a and b). The central electron temperature and density were 4 keV and 3.5×10^{19} m^{-3} respectively, with 1.4 MA of plasma current. The directivity of the launched fast wave spectrum was maximized by increasing the antenna-plasma separation, and is estimated at >60%. If symmetric co- and counter- current drive is assumed, then the observed loop voltage difference implies a driven current of ±70 kA for 2 MW of current drive power. This is in approximate agreement with the estimated current drive using the Ehst-Karney parameterization, which is 40-150 kA over the range of 60-100% in antenna directivity.

Acknowledgments

This work was supported by U.S. DoE Contract DE-AC02-76-CH0-3073.

References

[1] C. K. Phillips et al., *Physics of Plasmas* **2** 2427 (1995)

[2] R. Majeski, C. K. Phillips, and J. R. Wilson, Phys. Rev. Lett. **73** 2204 (1994)

[3] V. Fuchs et al., *Physics of Plasmas* **2** 1637 (1995)

[4] Equipe TFR, in *Plasma Physics and Controlled Nuclear Fusion Research,* Proceedings of the 9th Conference on Plasma Physics and Controlled Nuclear Fusion, Baltimore, 1982 (IAEA, Vienna, 1983), Vol. 2, p. 17

[5] T. H. Stix,*Waves in Plasmas* (American Institute of Physics, New York, 1992)

[6] R. Majeski et al., to appear in *Plasma Physics and Controlled Nuclear Fusion Research,* Proceedings of the 15th Conference on Plasma Physics and Controlled Nuclear Fusion, Seville, Spain, 26 September - 1 October 1994

[7] R. Majeski et al., to appear in *Radio Frequency Power in Plasmas*, Proceedings of the Eleventh Topical Conference, Palm Springs, California, 19-21 May 1995

[8] M. Brambilla, Nucl. Fusion 28, 549 (1988)

[9] D. A. Ehst and C. F. F. Karney, Nucl. Fusion 31, 1933 (1991)

[10] N. J. Fisch and J. M. Rax, *Phys. Rev. Lett.* **69** 612 (1992)

[11] N. J. Fisch et al., *Physics of Plasmas* **2** 2375 (1995)

[12] J. H. Rogers et al., to appear in *Radio Frequency Power in Plasmas*, Proceedings of the Eleventh Topical Conference, Palm Springs, California, 19-21 May 1995.

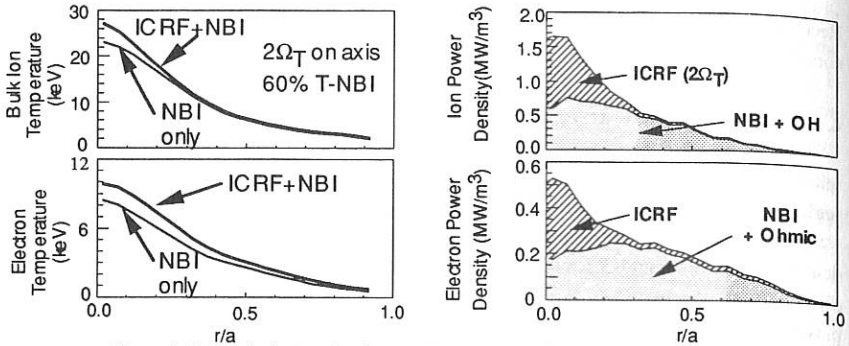

Figure 1. Ion and electron heating profiles are centrally peaked during $2\Omega_T$ heating. $n_e(0)=6 \times 10^{19}$ m^{-3}, 4.8 T, I_p=1.8 MA. Results from TRANSP analysis.

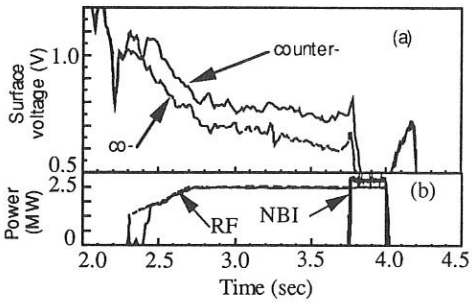

Figure 2. Loop voltage (a) and injected power for two discharges during mode conversion current drive, one with wave launch co-parallel to the ohmic electron current and one with a counter-parallel wave launch.

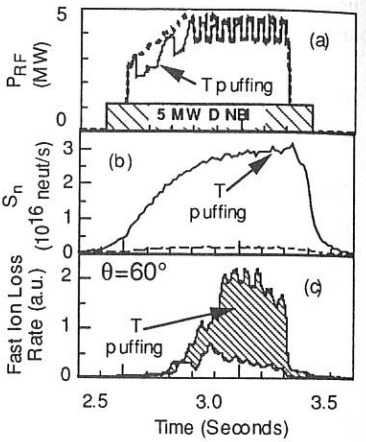

Figure 3. Injected power (a), neutron rate(b), and fast ion loss signal during on-axis mode conversion. Aditional losses during tritium puffing appear to be due to IBW-alpha particle coupling.

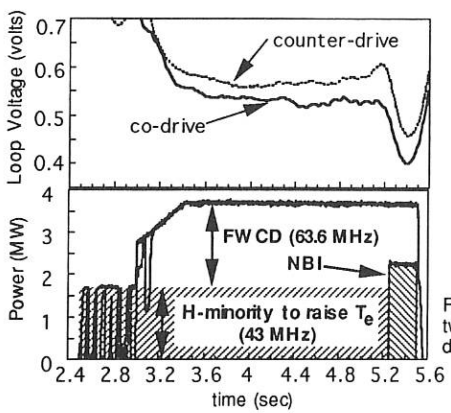

Figure 4. Loop voltage and injected power for two discharges, one with co- fast wave current drive and one with counter current drive.

FIRST RESULTS FROM LHCD IN COMPASS-D

C.D. Warrick, B. Lloyd, S.J. Fielding, M.R. O'Brien, G. McArdle, A.W. Morris, P.R. Simpson and M. Valovic.
UKAEA Government Division, Fusion, Culham, Oxon OX14 3DB UK
(UKAEA/Euratom Fusion Association)

Introduction

A 1.3GHz lower hybrid current drive (LHCD) system has been installed on the COMPASS-D tokamak. The system is designed to deliver up to 400kW into COMPASS-D for 1.5s using two klystrons coupled simultaneously to a single transmission line via a combiner network which also allows operation of one klystron in isolation. System modifications are underway to allow sequential operation of the klystrons to provide ~200kW for up to 3s. The ~60m transmission line feeds a conventional eight-waveguide grill antenna via a power splitting and phasing network. The radial position of the antenna is remotely adjustable. The resonant alumina windows are brazed at the front of a titanium waveguide assembly which was wire-eroded from a solid block. The position of the windows ensures that all cyclotron resonances are located in the pressurised part of the transmission system. The stainless steel antenna mouthpiece is shaped both poloidally and toroidally and the internal surfaces are gold-coated to inhibit breakdown. The individual waveguide dimensions are 165.1mm x 14.75mm with 2mm septa giving a peak $N_{||} \sim 3.25$ and 2.1 for a relative waveguide phasing of $\Delta\phi = -90^\circ$ and -60° respectively, with a spectrum width $\Delta N_{||} \sim 1.75$ (FWHM) and good directivity (70 - 80%).

Coupling Studies

Extensive coupling studies have been undertaken for a range of grill phasings (-90°, -60° and +60°), a variety of plasma configurations (ie. circular and ITER-like single null divertor (SND) discharges, varying I_p and B_ϕ directions) and a wide range of plasma parameters. Magnetic reconstructions of the plasma configuration indicate a clear improvement in coupling when the grill mouth and plasma shape are well matched, the plasma is vertically centred and the distance between the antenna and the last closed flux surface (LCFS) is minimised. Most striking, however, is the observation of a preferred I_p/B_ϕ configuration for optimum coupling (I_p and B_ϕ in the same direction and such that LH provides co-current drive) which typically reduces the reflected power by a factor of 2 compared with all other configurations for similar plasma parameters. If $\Delta\phi$ is changed from +60° to -60°, the directions of both I_p and B_ϕ must be changed to maintain optimum coupling. Thus the conditions for good coupling correspond to co-current drive together with a preferred field line tilt in front of the antenna. The explanation for this behaviour is not yet clear. The reflected power level increases only quite weakly with decreasing electron density and increasing plasma-antenna separation provided that the latter is

not too large. Even in conditions in which the coupling is not optimised, continuous power injection can be maintained through an L→H transition albeit with a ~50% increase in reflected power at the transition. Comparison of the measured reflection coefficients in the individual waveguides with predictions of the SWAN coupling code [1] suggests the presence of an underdense region ($\omega > \omega_{pe}$) in front of the grill for a wide range of conditions in COMPASS-D, consistent also with the fact that coupling is improved when the phasing is changed from $\Delta\phi = -90^\circ$ to $\Delta\phi = -60^\circ$. Similarly, the presence of modest levels of 60GHz ECRH power (100-150kW) can significantly improve the coupling at densities below the LH density limit/ECH cut-off ($1.5\text{-}2.0 \times 10^{19}/m^3$) if the ECRH resonance ($\omega = 2\omega_{ce}$) is located towards the outboard side of the tokamak. This is presumably due to an increase in the scrape-off layer density in front of the grill with ECRH as has been previously measured in DITE [2]. At lower toroidal magnetic fields, when the resonance is located towards the inboard side of the vessel, there is no noticeable improvement in LH coupling with ECRH. By optimisation of the plasma configuration and antenna radial position, good coupling (R ~ 15-20%) is routinely achieved in SND plasmas even in the absence of ECRH. This corresponds to R ~ 2-4% from a multijunction grill.

Current Drive

LHCD at modest power levels (~100kW) has enabled COMPASS-D discharges to be extended to >1s (I_p ~ 100kA, B_ϕ ~ 1.7T, $\bar{n}_e$ ~ $3\text{-}4 \times 10^{18}m^{-3}$). At higher injected powers full non-inductive current drive has been observed (I_p = 135kA, B_ϕ = 1.4T) at line-averaged densities $5\text{-}6 \times 10^{18}m^{-3}$ (P_{LH} = 120kW) and $7\text{-}8 \times 10^{18}m^{-3}$ (P_{LH} =140kW) corresponding to current drive efficiencies in the range $\eta_{20} = n_e I_{LH} R_0 / P_{LH}$ ~ 0.035 - 0.04 ($\times 10^{20}$) $AW^{-1}m^{-2}$ (Fig 1). At such low toroidal fields the poor accessibility of the low $N_{||}$ components of the launched spectrum limits the current drive efficiencies achievable but these are adequate for proposed experiments in COMPASS-D. Due to inductive effects, the loop voltage is initially driven significantly negative (~ -0.1V) recovering to zero as the current profile evolves towards its final state. By the end of the 100ms LH pulse the measured internal inductance is almost constant and the inductive contribution to the measured loop voltage is calculated to be small (< 0.05V). The measured primary current (Fig 1) indicates significant transformer recharging during the LH pulse. Simple theoretical estimates of the current drive efficiency based on the expression [3]:

$$\eta_{20} = \frac{4}{(5 + Z_{eff})} \frac{31}{\ln \Lambda} \frac{1}{\langle N_{||}^2 \rangle} \qquad AW^{-1}m^{-2}$$

where [4],

$$\frac{1}{\langle N_{||}^2 \rangle} = \frac{\int_{N_{||_{acc}}}^{+\infty} P(N_{||}) / N_{||}^2 dN_{||} - \int_{-\infty}^{N_{||_{acc}}} P(N_{||}) / N_{||}^2 dN_{||}}{\int_{-\infty}^{+\infty} P(N_{||}) dN_{||}}$$

give values ~ (1.5-2.0) $\times \eta_{20}$(exp.) depending on the values assumed for Z_{eff} and $N_{||acc}$, which must be considered reasonable agreement in view of the large number of assumptions implicit in this theoretical formulation [5]. Calculations using the BANDIT3-D Fokker Planck code [6] give closer agreement with experiment but exhibit a fairly strong sensitivity to electron temperature. The LHCD density limit in COMPASS-D, above which no current drive is observed, is typically $\bar{n}_e$ ~ 1.5 - 2.0 $\times 10^{19}m^{-3}$. In common with observations on other devices, there is evidence of improved particle confinement during LHCD in COMPASS-D in contrast to the reduced particle confinement typically observed during ECRH.

At power levels for which the full current was driven non-inductively, a short period of m=2 activity was observed shortly after LH turn-on and sawteeth were stabilised (Fig 2). The m=2 activity quickly decreased again as the current profile evolved further. The m=2 mode was accompanied by a burst of hard x-ray emission (visible also on the soft x-ray detectors) indicating that appearance of the mode led to a loss of fast electrons. At lower LH powers (~50-100kW) continuous m=2 activity is generated during the LHCD pulse; this has been stabilised using high power modulated ECRH [7].

Summary

LHCD at modest power levels has enabled COMPASS-D discharges to be extended to >1s and full non-inductive current drive has been achieved (I_p ~ 135kA) at line-averaged densities up to $\bar{n}_e$ = 7-8 $\times 10^{18}m^{-3}$ with a current drive efficiency in good agreement with theory. Stabilisation of sawteeth is observed. Extensive coupling studies have revealed a surprising dependence on the plasma configuration and in particular on the direction of field line tilt in front of the antenna. Optimisation of coupling has resulted in reflected power levels ~15% in ITER-like SND plasmas.

Acknowledgements

The loan of equipment from IPP Garching and CEA Cadarache is gratefully acknowledged. This work was jointly funded by the UK Department of Trade and Industry and EURATOM.

References

[1] D. Moreau & T.K. Nguyen, Report EUR-CEA-FC-1246, Grenoble (1984).

[2] B. Lloyd et. al., Proc. 17th Eur. Conf. on Contr. Fusion and Plasma Heating, Amsterdam, **III** (1990) 1283.

[3] C.F.F. Karney & N. Fisch, Phys. Fluids **28** (1985) 116.

[4] J.E. Stevens et al, Nucl. Fusion **28** (1988) 217.

[5] F. Leuterer et al, Nucl. Fusion **31** (1991) 2315.

[6] M.R. O'Brien et al., Proc. IAEA Technical Committee Meeting on Advances in Simulation and Modelling of Thermonuclear Plasmas, Montreal 1992, p527.

[7] G. McArdle et al, Proc. of the EC-9 Workshop, Borrego Springs, January 1995.

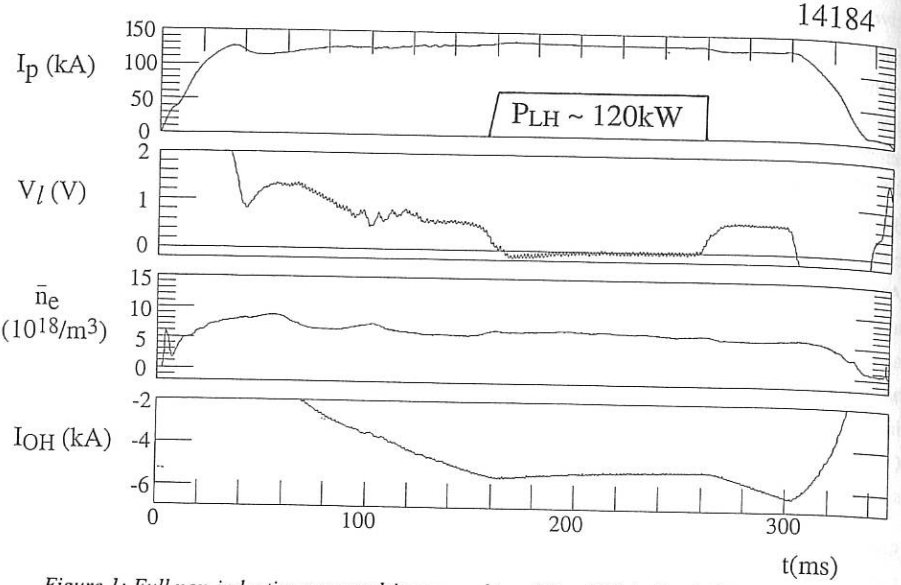

Figure 1: Full non-inductive current drive was achieved (I_p=135kA, B_ϕ=1.4T) at $\bar{n}_e$ ~ 5-6 × $10^{18}/m^3$ with P_{LH} = 120kW. Significant transformer recharging was observed.

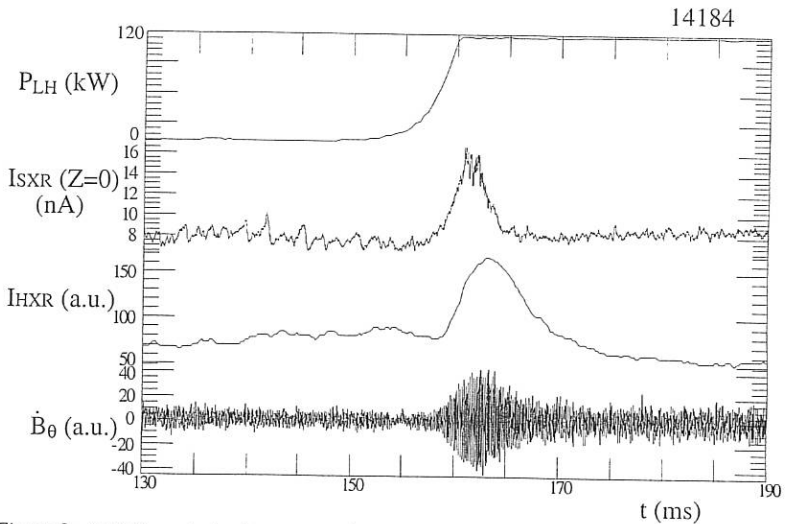

Figure 2 : At full non-inductive current drive, a short burst of m=2 activity and hard x-ray emission was observed, indicating a loss of fast electrons. Sawteeth were stabilised.

"Advanced Tokamak" current density profiles for non-inductive TORE SUPRA operation

F. Kazarian-Vibert, X. Litaudon, R. Arslanbekov, P. Bibet, P. Froissard, M.Goniche, G.T. Hoang, E. Joffrin, D. Moreau, Y. Peysson, G. Rey

Département de Recherches sur la Fusion Contrôlée,
Centre d'Etudes de Cadarache, 13108 Saint-Paul-Lez-Durance, France

1. Introduction

The improvement of the Tokamak concept has received increasing interest in fusion research. The so-called "advanced Tokamak" concept is characterised by self consistent hollow current density profiles which should provide an enhancement of global energy confinement and improved stability, an attractive behaviour for a non-inductive steady state operation of a fusion reactor. The main objective of the Lower Hybrid (LH) experiments performed on Tore Supra is to define and realise such scenarios [1-2]. Various LH driven plasma regimes have been studied. In this paper two different types of experiments are presented.
4 Tesla discharges have been obtained using feed-back control of the primary circuit voltage (V_{oh}) such that the transformer flux was kept constant and so, the loop voltage was maintained exactly zero. A model of coupled plasma-poloidal field (PF) coils system is used to describe this operation mode. Moreover, a reversed shear, improved confinement regime has been investigated at low toroidal magnetic fields (Bt < 2T) when the core plasma is inaccessible to the LH waves. A 1-D current diffusion simulation is performed with CRONOS [2]. The importance of the non-inductive current profile shape on the time evolution of the discharge is discussed as well as on the electron heat transport by a local analysis.

2. "Constant-flux" Tore Supra Experiments

The Tore Supra coupled plasma-PF coils system has been fully modelled using equivalent circuit equations, where the inductance matrix of the poloidal field circuits were numerically calculated with a finite element equilibrium code (CEDRES) [3]. Early experiments in which V_{oh} was kept constant were performed during the 1992 campaign and have since been analysed. The good agreement between theoretical simulations and the measured variation of the primary coil current as a function of I_p validated the assumptions in the model [4]. Thus, it was used as a tool to test various feed-back schemes. It has been found that an alternate and promising scheme was a feedback control of V_{oh} such that the transformer flux is imposed, and consequently, a zero loop voltage is obtained faster. Indeed the calculated equilibrium time constant (τ_{eq}) in that case was shorter than the resistive time (τ_p), $\tau_{eq} = \tau_p (1 - \mu^2)$, where μ the coupling coefficient is close to 1 in Tore Supra. During the last experimental campaign, that "constant-flux" operation mode has been explored.
A stable fully non-inductive plasma current of 0.8 MA has been sustained during 15 seconds in the 4-Tesla Lower Hybrid enhanced confinement regime (LHEP) [5-6] (Fig. 1.a). The standard LHEP mode is characterized by (i) a flattening of the central q_ψ-profile (r/a <0.3) together with (ii) an increase of the internal inductance (li) which leads to global improved confinement. The phase shift in the LH antenna was -30 deg. ($n_{//o} = 1.8$ where $n_{//o}$ is the parallel index at the peak of the launched spectrum). The electron thermal energy content was about 40 % above the Rebut Lallia Watkins prediction [7]. By applying the LH power (≈ 3.7 MW), q_o varied from 1 to 1.4, while the internal inductance l_i was larger than in the ohmic phase. The inductance matrix of the poloidal field circuits was calculated by CEDRES [8] taking into account the characteristics of the discharge. A comparison was then possible between the model predictions and the experiment. A good agreement with the model predictions was obtained [4] and

confirmed that the current in the poloidal field coils reached an equilibrium on a time scale of 6s (fig. 1.b.c).

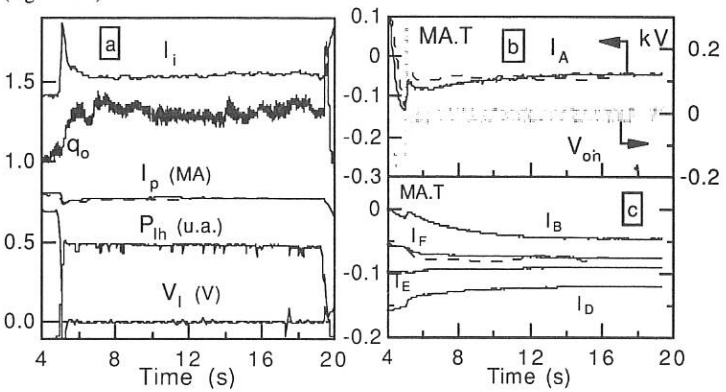

Fig. 1: Time evolution of plasma parameters during shot 16379. The dashed curve represents a theoretical calculation.
a) Plasma current (I_p), LH power (P_{lh}), loop voltage (V_l), safety factor on axis (q_o) and self inductance (l_i).
b) and c) Time evolution of the poloidal field coils currents ($I_{a,b,d,e,f}$) and primary circuit voltage (V_{oh})

The current diffusion code CRONOS allows to assess the time evolution of the electric field and the LH current deposition profiles by comparing theoretical and experimental time evolutions of the plasma parameters (Fig. 2). The electric field is stationary after time of the order of 3 s which is 10 times shorter than the typical plasma resistive time. In fact, by maintaining the loop voltage exactly zero at the edge and by cancelling the on-axis electric field with a central and broad LH current deposition profile, the electric field profile is forced to reach an equilibrium with a short time constant.

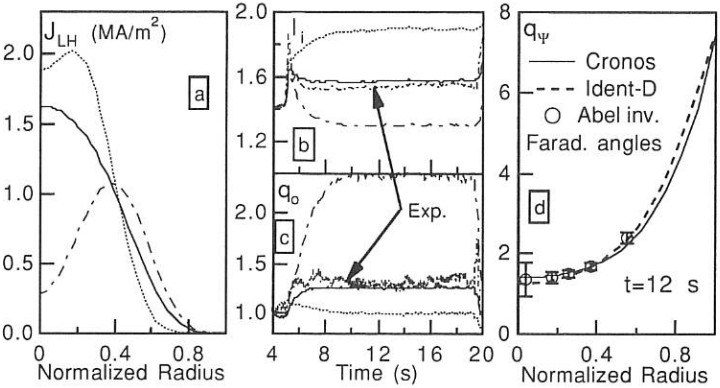

Fig. 2: Effect of the LH current density profiles on the time evolution of l_i and q_o: (a) assumed LH current profiles, (b-c) measured l_i and q_o versus time and simulations d) $q\Psi$ profiles determinated with CRONOS and compared with magnetic reconstruction (Ident-D) and Abel inversion of the polarimetry measurements.

Therefore, in these plasma conditions and antenna phasing a stable fully non-inductive equilibrium state has been reached for the thermal energy, impurity content, current and pressure profiles and finally the electromagnetic fields of the poloidal system. The duration of that type of shots can therefore be extended, and this provides a scenario for studying continuous operation (heat exhaust, plasma-wall interaction, etc...).

3. Stationary shear reversal LH Experiments

Another similar improved confinement regime has been observed at low toroidal magnetic field ($B_t < 2$ T) when the plasma core is inaccessible to the waves [2]. The plasma parameters were chosen so that the LH wave propagation behaves as in high-density/4 Tesla plasmas for which steady-state operation would demand more LH power. In the cold-plasma approximation, the accessibility limit for the local parallel wave index depends mainly on the ratio of the electron plasma frequency (f_{pe}) to the cyclotron frequency (f_{ce}), which scales as n_e/B_t^2 (n_e is the electron density). For instance, the local accessibility criterion is conserved by decreasing the electron density and magnetic field by a factor 4 and 2, respectively. Furthermore, to keep the edge safety factor (q_a) constant the current is varied together with the magnetic field. Experiments have been performed in standard ($q_a \approx 3$, high current) and "advanced-tokamak" ($q_a \approx 6$, low current) operation. To simulate high-density steady-state discharges, $n_{eo} \geq 10^{20}$ m^{-3}, $B_t = 4$ T, I_p = 1.6-0.8 MA ($q_a \approx 3$-6), the plasma parameters are typically n_{eo}=3-4 10^{19} m^{-3}, B_t=2T, I_p=0.8-0.4 MA.

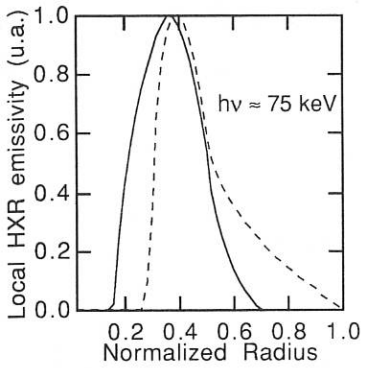

Fig. 3: Abel inversion of the experimental hard-X-ray profiles in "self-similar" experiments. Full lines and dashed lines correspond respectively to the high-density/4T (shot 16467) and low-density/2T plasmas (shot 12910).

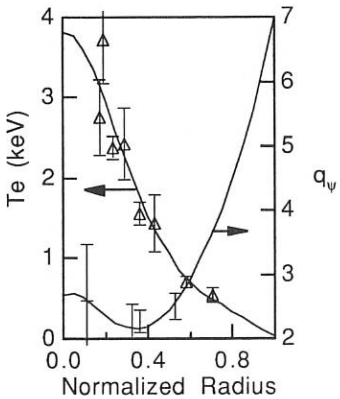

Fig. 4: Te and q_ψ-profiles for low-density/2T LH experiments

As far as experiments are concerned, the local hard-X-ray emissivity profiles measured during high-density/4T and low-density/2T discharges present the same hollow shapes (Fig. 3), which confirms the relevance of the "self-similar" experiments. In the "advanced-plasma" configuration (0.4 MA/2T), stable, fully non-inductive discharges were obtained with an electron thermal energy contents exceeding the Rebut-Lallia-Watkins prediction by a factor $H_{rlw} \approx 2$ at $\beta_p \approx 0.8$ and a safety factor on-axis (q_o) increasing above 2 when the LH power is applied. Polarimetry measurements indicate that the magnetic shear is negative within the surface $r/a \leq 0.3$ with a minimum q value above 2 (Fig. 4). Despite the off-axis power deposition profile inferred from the hard-X-ray emission data, the central temperature rises from 1 keV to 3.5 keV (Fig. 4).

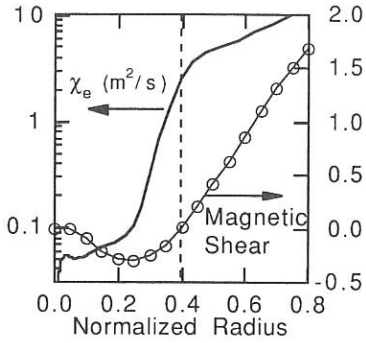

Fig. 5: Electron heat diffusivity (LOCO) and magnetic shear profiles in LH similarity experiments (#14409).

The off-axis LH power deposition profile is validated through hard-x-ray emission data, ray-tracing/2-D Fokker-Planck calculations [9-10] in agreement with Wave-Diffusion/Fokker-Planck (WDFP) simulations [11], and finally with the full simulation of the time evolution of the current-profiles (CRONOS).

Therefore local transport analyses (LOCO) [12] indicate that the electron thermal diffusivity is significantly reduced in the reversed magnetic shear region (Fig. 5). The formation of such a "transport barrier" is also invoked to explain the temperature transition in some of the 4-Tesla LHEP discharges (hot core LHEP phase [2]) although the magnetic shear is only marginally reversed.

4. Conclusion

A new operation mode where a zero loop voltage is imposed by a feed-back control through V_{oh} has been studied theoretically and experimentally. The feasability of the "constant-flux" operation mode is demonstrated. By choosing an appropriate $n_{//}$ launched spectrum, a fully non-inductive and stable discharge has been obtained durind 15 s. Furthermore, using this scheme, the transition to the LHEP regime has been reproduced.

In addition, a new improved confinement regime with a reversed-shear has been obtained at 2-Tesla when the core-plasma is inaccessible to the LH waves. In this case, the off-axis power deposition is assessed, and a transport barrier in the reversed magnetic shear region is observed.

In the next experimental campaign, the "constant-flux" operation mode will be fully used with possibly other non-inductive methods such as fast wave current-drive together with a larger self-generated bootstrap current component. Steady-state high-density LH similarity experiments will also be pursued using this operation scheme.

Acknowledgements

The authors would like to thank G. Martin and T. Wijnands for their interest in this work and their direct implication in the implementation of the Tore Supra feedback system.

References

1. Equipe Tore Supra (presented by D. Moreau), Plasma Physics and Controlled Nuclear Fusion Research, Proc. 15th Int. Conf., Seville, 1994
2. Equipe Tore Supra (presented by X. Litaudon), Proc. of 11th Topical Conference on RF Power in Plasmas, Palm Springs, California, 1995, to be published.
3. Y. Stefan, J.P. Allibert, J.M. Ané, S. Bremond, et al., private communication.
4. F. Kazarian,X. Litaudon , D. Moreau et al., Proc. 21th EPS Conf. on Controlled Fusion and Plasma Physics, Montpellier, France, (1994) 1058
5. D. Moreau, et al., Plasma Physics and controlled Nuclear Fusion Research, Proc. of 14th Int. Conf., Würzburg, 1992 (IAEA,Vienna,1993), Vol. **1**, p. 649.
6. G.T. Hoang, et al., Nucl. Fusion, **34**, (1994) 1
7. P. H. Rebut, P. P. Lallia, M. L. Watkins, Plasma Physics and controlled Nuclear Fusion Research, Proc. 12th Int. Conf., Nice, 1988 (IAEA,Vienna,1989), Vol. **2**, p. 191.
8. S. Bremond, private communication.
9. Y. Peysson, R. Arslanbekov, et al., Proc. of 11th Topical Conference on RF Power in Plasmas, Palm Springs, California, to be published.
10. R. Arslanbekov, X. Litaudon, Y. Peysson, these proceedings.
11 K. Kupfer, D. Moreau, X. Litaudon, Phys. Fluids B, **5** (1993) 4391.
12. G. R. Harris, et al., Nucl. Fus., **32** (1994) 1967.

ITER Plasma Diagnostics

A E Costley, L Johnson, **L de Kock***, T Matoba†, V Mukhovatov, D Orlinski‡, P E Stott$^{\Delta}$, S Yamamoto*, K M Young$^{\approx}$ and the ITER Joint Central Team and Home Teams

ITER Joint Central Team, San Diego Joint Work Site, CA, USA
* ITER Joint Central Team, Garching Joint Work Site, Garching, Germany
†JAERI, Naka, Japan
‡ Kurchatov Institute, Moscow, Russia
$^{\Delta}$JET Joint Undertaking, Abingdon, UK
$^{\approx}$Princeton Plasma Physics Laboratory, Princeton, NJ, USA

1. Introduction

In order to safely operate, control and optimise ITER at high levels of fusion power (~1.5 GW), it will be necessary to measure accurately and reliably a wide range of plasma parameters. Key parameters which describe the condition of the first wall and divertor will also have to be measured. The measurements will be made with an extensive set of plasma diagnostics.

The implementation of the diagnostics on ITER is a substantial task because of the combined requirements to operate in high levels of radiation, through limited access, in some cases with long transmission paths, and to achieve very high levels of availabilty and reliability. Many of the measurements will be used for machine protection and plasma control and will require an operational reliability considerably above that presently achieved. A good starting point for the designs is the experience gained on exisiting large tokamaks such as JET, JT60 and TFTR but the extrapolation to ITER conditions is substantial and it is already obvious that it will not be possible to apply some of the established techniques. For some measurements new approaches are required: for example, it is planned to use Faraday rotation measurements in the mid-plane for the measurement of the line integrated density rather than multichord transmission interferometry which does not appear feasible on ITER.

Work on ITER diagnostics is a combined effort of the ITER Joint Central Team and the Home Teams. Thus far the required measurements, parameter ranges, accuracies and resolutions have been determined; the problems of diagnostic access have been examined; and a preliminary choice of diagnostic techniques has been made. Also, an extensive programme to establish the effects of radiation on diagnostic materials and components is in progress. In this paper, we summarise the work carried out thus far and present the plans for the future activities.

2. Required Measurements

As on existing machines, the measurements will play different roles in the operational programme. They can be grouped into three broad categories: (i) those necessary for machine protection and plasma control; (ii) those necessary for optimising and evaluating the plasma performance; and (iii) those required for understanding important physical phenomena which may limit ITER performance. All measurements in categories (i) and (ii) are regarded as essential for ITER operation. A thorough consideration of the ITER requirements has led to the measurements in each category as shown in Table1.

Table 1 Summary of Required Measurements

Category (i): Measurements for Machine Protection and Plasma Control	Category (ii): Measurements for Performance Evaluation and Optimization.	Category (iii): Additional Measurements for Physics Understanding
Plasma Current	Electron Temperature Profile†	Pellet Penetration
Plasma Position and Shape	Electron Density Profile†	PFC Material Erosion
Loop Voltage	q(r)†	Density Fluctuations
Beta	Zeff Profile†	Edge Turbulence
Radiation	Fishbones, TAE Modes†	MHD Activity in Plasma Core
Plasma Line-Averaged Density	Ion Temperature Profile	T_e Fluctuations
Total Neutron Flux and Em. Prof.	He Density in Plasma Core	E field and E fluctuations
Locked-modes	Escaping Alphas	
m=2 MHD Modes, Sawteeth	n_H/n_D in Plasma Core	
Plasma Rotation	Confined Alpha-Particles	
n_T/n_D	Escaping Alphas	
Impurity Species Identification	Impurity Density	
Zeff (Line-Averaged)	Edge n_T/n_D	
ELMs, L/H Mode Indicators	Neutron Fluence	
Hard X-ray Emission	Impurity & D/T Influx in Div.	
Key Divertor Parameters: Plate Temp*,Rad. Power, Plate Ablation,Ionization Front Posn. Gas Pressure*	Ion Saturation Current in Divertor; n_e, T_e at Divertor Target	
Edge Light & First Wall Temp*	Rad. Power (Edge and Div)	
Base Pressure*	Radiation Profile in Divertor	
Gas Pressure in Duct*	Heat Loading Profile in Div.	
In-vessel viewing*	Divertor Helium Density	
Halo' Currents*	n_T/n_D,n_H/n_D in Divertor	
	n_e, T_e and T_i of Div. Plasma	
Toroidal Magnetic Field*	Divertor Plasma Flow	
* *Imp.Eng.Parameters*	† *Potential Category (i) Meas.*	

3. Selected Diagnostic Techniques and Key Design Requirements

The measurements will be made with an extensive set of diagnostic systems which is expected to be very similar to that on existing large tokamaks. Most of the individual systems will be based on established techniques; however in some cases the established technique can not be applied and a 'new concept' diagnostic is being considered. For convenience we group the diagnostics into seven generic groups: magnetics, neutron systems, optical/ir systems, bolometric systems, spectroscopic and NPA systems, microwave diagnostics, and plasma facing and operational diagnostics.

The principal magnetic systems will be a series of loops and coils mounted inside and outside the vacuum vessel including coils in the divertor region. In order to get a high frequency response it will be necessary to have a set of coils mounted close to the plasma in the blanket and the design and installation of these is particularly challenging. The key design requirements are for radiation resistant coils and loops and integrators capable of operating with the long ITER pulses (1000s). The main neutron diagnostics will be radial and vertical neutron cameras, neutron flux monitors, neutron spectrometers and an activation system. Here the major design difficulties are obtaining the necessary views of the plasma within the constraints of the ITER ports and mounting the collimators and spectrometers close to the tokamak. Measurement of the lost alpha particles will be important and will require the development of a new concept technique. Measurement of the confined alpha particles is also important and the principal technique under consideration is collective scattering. Many factors are involved in choosing the optimum wavelength and this choice has not yet been made. Separate Thomson scattering systems are being considered for measurements in the core, edge, X-point and divertor regions. LIDAR systems are preferred but in order to achieve the required spatial resolution in the edge region (5 mm), a conventional imaging system is being considered. A key design issue is the potential radiation damage to the plasma facing optics, especially the components which transmit the high power laser beam. Measurement of the electron density by conventional multichord transmission interferometry is not feasible because vertical transmission is not possible and mirrors mounted on the inside wall will probably not survive the thermal and radiation loads. Transmission in the equatorial plane is being considered with the simultaneous measurement of both the phase delay (inteferometer measurement) and the Faraday rotation. Two bolometer arrays are planned: one for the main plasma and another for the divertor region. The key design requirement is for radiation resistant bolometer heads and an important question is whether a sufficiently high signal/noise can be achieved in the measurement in the presence of the intense neutron and gamma background.

An extensive set of spectroscopic diagnostics is foreseen. There will be a series of viewing systems and spectrometers operating in the visible and uv regions. A high resolution x-ray crystal spectrometer system will be included for measurements of the ion temperature and plasma rotation using highly ionised impurity ions. An array of sight-lines will view the

plasma along many chords and the intensity of the visible continuum will be measured for the determination of the Z_{eff} profile. Key design areas are the systems used for transmitting the radiation to the spectrometers and detectors, and the location of these components. Two new concept systems are under consideration: a two photon Ly-alpha fluorescence technique for the measurement of the n_D/n_T and n_H/n_D ratios, and laser induced fluorescence for the measurement of the helium density in the divertor. Active measurements with neutral beams are also planned. MSE measurements are in principle possible using one of the high energy heating beams, but for CHERS measurements a lower energy beam is required. Preliminary estimates show that the optimum energy is about 100 keV/amu and the required beam power is about 5 MW. It is probable that a dedicated neutral beam will be included for diagnostic purposes. Both active and passive NPA measurements are planned. ECE and reflectometer systems are planned for the measurement of the electron temperature and density profiles. For ECE a key matter is the possible degradation of the measurement capability due to the enhanced relativistic and Doppler broadening at the high electron temperatures in ITER. For reflectometry an important question is whether measurements of the central plasma region are possible with such a large plasma and the expected broad density profile. The possibility of using reflectometry with the magneto-sonic wave is being considered as a possible method for measuring the profile of the species mix and/or the line integrated mass density. Microwave scattering is being considered as a technique for obtaining the bulk plasma rotation.

Measurements of the plasma in the divertor region and measurements of the condition of the divertor target plates are especially difficult because of the very limited access. Two types of special divertor diagnostic cassette are planned. One will be instrumented with the magnetic coils, pressure gauges, bolometers and Langmuire probes and will be located at both sides of each remote handling port. The other will be infront of each remote handling port and will provide access for optical and microwave diagnostics viewing through slots and channels.

4. Required Design Levels and R&D

During the EDA it is not necessary to design in detail every part of each diagnostic system: the construction phase of ITER is about eight years and there will be time to complete the diagnostic designs. However, it is necessary to establish the feasibility of the chosen techniques and to determine the characteristics of the main diagnostic components. The interfaces with the large machine components, which are planned to proceed to procurement immediately following the EDA, need to be designed in detail. The requirements for space and services need to be specified. The determination of the required design levels is an important part of the present design activities. It is also necessary to establish a data base of radiation effects on relevant materials and on diagnostic components so that the designs can be finalised. This is being established in the supporting radiation effects R&D programme. The combination of the design and R&D activities should allow a diagnostic system which can meet the demanding ITER diagnostic requirements to be provided.

MULTIPLE NEUTRON SPECTROMETER DIAGNOSTIC FOR ITER

J Källne, L Ballabio, S Conroy, G Ericsson, J Frenje, PU Renberg, and E Traneus
Department of Neutron Research, Uppsala University, S-75121 Uppsala, Sweden

G Gorini and M Tardocchi
Department of Physics, University of Milan, I-20133 Milano, Italy

1. Introduction

The initial definition of required diagnostic functions for ITER has now been presented as part of ongoing EDA work. In response to this, a new neutron diagnostic is proposed. It is conceived as a 3-arm system of high resolution neutron spectrometers viewing the ITER plasma along horizontal lines of sight intersecting the plasma axis normally (radially, R) and tangentially (T); the latter includes two directions being counter to each other (co and counter to the plasma current, T1 and T2). The measurement objective is to acquire data of very high and controlled quality that will permit unfolding of or compensation for direction dependent vector and scalar factors in the neutron emission. Vector dependent factors might arise, for instance, due to toroidal rotation. Scalar dependent factors can be caused by plasma profiles giving different line integration values along the chords of sight lines used. The acquisition of multiple sight line data makes it possible to obtain plasma information that goes beyond single line measurements in scope, range and quality.

The basis for this diagnostic is simultaneous measurement of several neutron emission components and the use of this information in a comprehensive way. Especially, it is the purpose to extract the plasma information contained in the differences of measured quantities. These differences are often small relative to the values of the quantities measured. This diagnostic therefore rests crucially on the ability to perform measurements with very high accuracy in absolute and relative terms. Especially, the relative instrumental errors must be very small for the quantities used for the extraction of difference based diagnostic information.

What is proposed is a three ray ion advanced diagnostic (TRIAD) to provide four essential ITER diagnostic functions with regard to (i) ion densities, (ii) ion temperature, (iii) the fast α-particle population, and (iv) the plasma toroidal rotation. Each arm of the instrument is equipped with a spectrometer system to measure the neutron spectrum in the regions of 14- and 2.5-MeV to which the d+t->α+n and d+d->^{3}He+n reactions, respectively, contribute. These reactions constitute, for a thermal plasma, a spectrum of two peaks whose intensity, location and shape are to be measured. The main function of the 2.5-MeV spectrometers is to measure intensity which is needed for the density determination while the 14-MeV spectrometers are used for full peak determination. The diagnostic potential and the instrumental feasibility of this new concept has been explored based on results from the

ongoing development work on neutron diagnostics for burning plasmas [1]. A neutron spectrometer utilizing the magnetic proton recoil (MPR) technique is under construction as a prototype for ITER. The MPR techniques is envisaged to be used in TRIAD.

2. The neutron emission spectrum

The main features of the neutron emission spectrum of a DT-plasma consists of the 2.5- and 14-MeV peaks mentioned (Fig. 1). A third broad distribution of neutrons (centered at around 14 MeV) is predicted to arise due to reactions involving deuterons or tritons whose velocity distribution has been made super-thermal by collisions with the α–particles existing as a slowing down population (typically, E_α<4 MeV). In addition, the spectrum will contain unavoidable background contributions but this is not crucial for the diagnostic principles. All features are sufficiently separated from each other to be suitable for the intended diagnostic uses. The most detailed information is derived from the 14-MeV peak and it is used below to illustrate the extraction of the scalar and vector dependencies in the neutron emission.

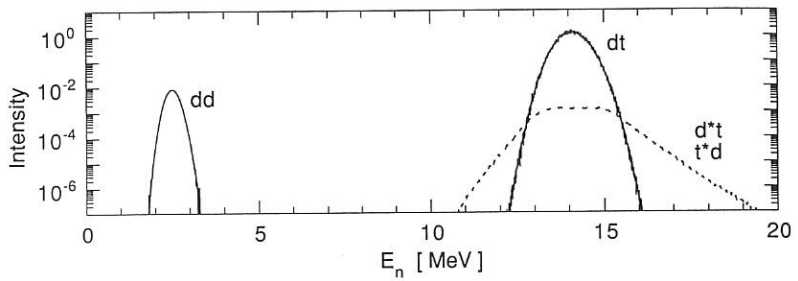

Fig. 1. Schematic spectrum of the neutron emission from a DT plasma in steady state condition of temperature T_i=20 keV. The peaks at 2.5 and 14 MeV are due to the thermal ion reactions d+d→^{3}He+n, d+t→α+n:.The broad distribution is due to d+t→α+n plus d+t* →α+n involving supra thermal ions (d* and t*) created through knock on by the fast α–particles.*

3. Shape and location dependencies of neutron emission peaks

The neutron peak (P) is a superposition of Gaussians determined by the temperature T_i with weight factors g_i, i.e., $P_R=\Sigma_i\,(g_R)_i\cdot\Gamma(T_i)$, $P_{T1}=\Sigma_i\,(g_{T1})\cdot\Gamma(T_i)$ and $P_{T2}=\Sigma_i\,(g_{T2})\cdot\Gamma(T_i)$. The factor g is the observed neutron flux per fixed ΔT_i, i.e., a neutron emission distribution as a function of temperature. The tangential sight lines are assumed to be identical apart from the co/counter directions so that $g_T=g_{T2}=g_{T1}$. The above is true for observations made with three spectrometers having no off-sets in the energy calibration ($\varepsilon_R=\varepsilon_{T1}=\varepsilon_{T2}=0$) and for a plasma with no toroidal plasma rotation ($v_T=0$). With $v_T\neq0$, there is a Doppler energy shift of $\pm\Delta E_{Ds}$ affecting the neutrons observed along T1 and T2 but rno rotation effects on R-line data.

The plasma rotation is determined from the difference between the peaks P_{T1} and P_{T2} which we can express, for the sake of illustration, as a peak position difference $\Delta E_T = E_{T1} - E_{T2} = 2\Delta E_{Ds} + \varepsilon_{T1} - \varepsilon_{T2}$. The Doppler shift ΔE_{Ds} is proportional to v_T and amounts to 0.27 keV ($\Delta E/E = 4 \cdot 10^{-5}$) at $v_T = 1$ km/s (the ITER lower limit diagnostic requirement), or a measured difference of $2\Delta E_{Ds} = 0.54$ keV. It is not feasible to attempt an energy calibration of the T1 and T2 spectrometers at the 10^{-5} level. Instead, the acquired data for different plasma conditions should be used to find the limit (ΔE^{min}) of lowest values of $|\Delta E_T|$ and use ΔE^{min} as an estimate for the calibration difference, i.e., $2\Delta\varepsilon_T \equiv \varepsilon_{T1} - \varepsilon_{T2} \approx \Delta E^{min}$ as $2\Delta\varepsilon_T \rightarrow \Delta E^{min}$ for $v_T \rightarrow 0$ (assuming mono-directional V_T for small values). One can now derive v_T from $\Delta E_{Ds} = (\Delta E_T - \Delta E^{min})/2$ and the measurement of ΔE_T. This leads to a systematic overestimation of the true rotation value amounting to the minimum rotation that the plasma can have in the core for conditions of sufficient neutron flux to be observed.

Next we wish to use also the radial view data. Applying the correction $\pm\Delta\varepsilon_T$ to the observed positions of the P_{T1} and P_{T2} peaks and taking out the Doppler shift as determined (to eliminate the vector dependence), one obtains reduced data (P'_{T1} and P'_{T2}). The tangential data sets have now the same energy off-set of ε'_T, and the radial data have ε_R. These two off-sets can be empirically related to each other through an observable that is independent of the R and T viewing directions. The maximum of the T_i-profile (T^o) is such a quantity which can be used to determine the off-set difference $\Delta\varepsilon = \varepsilon'_T - \varepsilon_R$ using the measured spectral position for the $\Gamma(T_i = T_o)$ component of the composite peaks P_R, P_{T1} and P_{T2}. With all spectra on the same energy scale, one can study the peak shape differences in terms of the weight factors g_R and g_T which, in turn, reflect line integrals sampling the neutron emissivity profiles (depending on the density and temperature profiles) along the tangential and radial plasma chords.

4. Instrumental considerations.

The MPR-method is suitable for precision energy measurements as it is based on charge particle deflection in a magnetic field. While the absolute energy determination may be limited to $\Delta E/E = 10^{-3}$, what matters for the intended applications is the relative calibration stability of the TRIAD system. A stability of better than 10^{-5} is routine under amenable laboratory conditions which at a tokamak could be upset mainly by stray magnetic fields. These would be controlled as far as possible by passive shielding. The field variations that leak through can be counteracted with active field compensation to obtain a constant field in the spectrometer or the field must be monitored for application of corrections to the data. In principle, it is possible to keep a system calibration stability at the 10^{-5} level for the TRIAD spectrometers. The feasibility of achieving this depends on the magnitude of the stray fields at the diagnostic location and the arrangement of the spectrometers relative to each other. A note of comfort is the fact that the requirements on stray field handling are no more exacting for the TRIAD diagnostic than those for the neutral beam injection systems in successful use. The

MPR spectrometers for TRIAD would be of dedicated design while the crucial stability performance can be assessed based on the work with the prototype.

5. Diagnostic out-put

The potential diagnostic out-put of TRIAD is as follows noting the special rôles of the R, T1 and T2 spectrometers. TRIAD provides information on the peak ion temperature and the temperature dependence of the line integrated neutron emissivity. The peak temperature is preferentially sampled by the T-lines while the temperature dependence is more readily observed along the R-line; with combined use the T- and R-lines give enhanced information on T_i-dependence. The fuel ion densities n_d and n_t can be determined with the R-line spectrum but the signal intensity, both in absolute terms and relative to background, is enhanced by a factor of 3.5 by using the T-line. The plasma rotation is obtained by the combined use of the T1- and T2-lines while the R-line can be used for analysis consistency check. The α-particle population can be probed with either of the three lines. The α-particle and fuel density measurements are the diagnostics for which low count rate is the limiting factor. For a spectrometer of the MPR type, the count rate increases with neutron flux which is about a factor 3.5 higher for the T-lines compared to the R-line. Therefore, the TRIAD is 8 times better than a single R-line with respect to count rate which can be translated into a corresponding increase in statistical accuracy or time resolution, and also increased sensitivity in the case of an α-particle probe.

6. Conclusion

The proposed TRIAD neutron spectrometry diagnostic can potentially provide four essential diagnostic functions for ITER. The tangential sight lines are required for plasma rotation measurement which, in practice, is also true for obtaining the fuel densities. For all functions, the diagnostic quality and range are significantly enhanced for TRIAD compared to using a single sight line. Suitable instrumentation, with potential capability to meet the high accuracy standards identified, is identified and can provide the starting point for studying the feasibility of the diagnostic measurements proposed and of the technical solutions required.

References.

[1] J Källne and H Enge, "Magnetic proton recoil spectrometer for fusion plasma neutrons", Nucl. Instr. Meth. **A311**(1991)595, and, J Källne et al, "Neutron physics for fusion research", Uppsala Univ. Neutron Physics Report, UU-INF **94#8** (Oct. 94).

Diamond Detector Application for ITER SXR-imaging.

Andrey G.Alekseev, Vladimir N.Amosov, Anatoliy V.Krasilnikov, Dmitry V.Portnov, Albert Yu.Tsutskikh, Evgeniy G.Utjugov.

Troitsk Institute of Innovations & Fusion Research,

Troitsk, Moscow Region, Russia

Technical Approach and Methodology

Electron temperature in ITER is expected to vary up to 20keV. This range is too wide to cover with system based on one kind of detector. Te spectral response of detector should be within a range approximately 2-5Te, to achieve appropriate image contrast (discussed later). For measurements of low temperature plasma (Te<8keV) diamond detector can be proposed.

Diamond Detector Properties

Soft X-ray radiation flux measuring system based on diamond sensitive elements have been developed for the purposes of high temperature thermonuclear plasma diagnostics and X-ray dosimetry. In comparison with well-known Si and CdTe semiconductor sensors, diamond detectors proved to be more preferable due to their outstanding features: low leakage currents (<1pA at V= 100 V and low radiation background conditions) providing extremely low level of intrinsic current noises and therefore high signal/noise ratio (commonly defined by preamplifier input current noise), high radiation damage level (~10^{14} DT-neutrons/cm^2), etc. Entrance window being properly chosen, corresponding detector spectral response can be obtained in the range from UV to10keV photons. Lower cut-off energy of the order of 500eV is provided by outer metal contact absorption (20 nm-thick gold layer) at the absence of any window, while the diamond crystal thickness (300 mcm for a given sample) limits the upper edge of spectral curve.

Insertion of the second diamond layer of the same thickness provides "two-color" sensitivity of the detector (Fig. 1).

Comparative tests of diamond, Si and CdTe X-ray detectors with similar dimensions have been performed at the T-10 tokamak (Kurchatov's Atomic Energy Institute, Moscow) [1]. Definitely higher S/N-ratio (by more than the order of magnitude) approximately at the same value of current sensitivity have been proved in diamond detector- based measurements. Besides it, the CdTe detector shows essentially lower sensitivity in $h\nu < 2.5$keV spectral range. Expectations of more severe operation conditions (background radiation, high electromagnetic fields and acoustic noises, etc.) forced a further developments of the device. It was divided into two parts: remote detector head including the diamond sensor with entrance window (beryllium foil as usual) and first preamplifier stage (low-noise FET or nouvistor, if high radiation damage level is needed), and basic amplifier unit with the systems of dc bias, leakage current and/or thermal output voltage drift compensation, frequency and noise correction, detector power supply filtering, optoelectronic isolation, etc.

Table 1. Diamond detector specification

Spectral range	**0.5 - 10 keV**
Entrance window (removable)	**30 mcm-thick Be foil**
Sensitive area	**0.1 ÷ 0.2 cm^2**
Dark current	**< 1 pA**
Dynamic current range	**10^{-12} ÷ 10^{-6} A**
Response time	**< 10^{-8} s**
Detector voltage supply	**-100 V**

Figure 1 shows the response of diamond detector with and without 30mcm Be entrance window and the response of second layer of "two-color" detector.

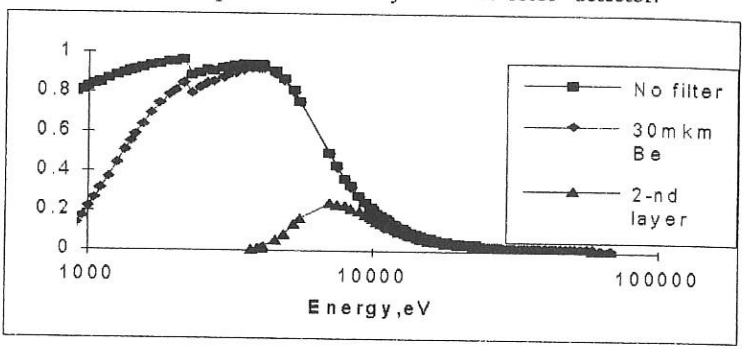

Figure 1. Diamond detector SXR-absorption

This dependence is typical for detector with narrow spectral range in comparison with Te. The temperature contrast of narrow spectral band detector can be estimated as following:

$$\frac{dJ}{J} \Big/ \frac{dT}{T} \approx E/T - 1$$

where E is average energy of detector spectral response.

So diamond detector can be used for imaging of plasma in the spectral range up to 8 keV. It can be useful for investigations of the beginning and the end of discharge (first 100 s), on outer magnetic surfaces, for divertor plasma, in the region of X-point, near divertor ionization front.

Diagnostic precision

Table 2 shows signal/noise estimation for diamond detector, with time resolution not worse than 0.1 ms. To improve detector shielding curved glass capillary bundles should be used. Spatial resolution in the case will be limited with angle of SXR-reflection (≈5mrad) and distance to plasma from bundle entrance edge (3m), that is about 2cm. The displacement of detector from direct neutron beam will be about 2-5 cm, so

neutrons should pass all shield layers to reach detector. Curved bundles should be arranged in channels in blanket. In Table 2:

- I corresponds to measurements of outer plasma region, DT -phase
- II central chord, first 100 ms of discharge
- III central chord, DT-phase

Table 2. Diamond detector diagnostic parameters.

Parameter	*I*	*II*	*III*	*Units*
<Te>	*1*	*2.5*	*11.8*	*keV*
Detector sensitive area	0.1	0.1	0.1	cm2
Field of view	4E-05	4E-05	4E-05	ster.
Input SXR-power on first wall	0.05	0.5	15	W/cm2
SXR-Power on detector	3E-08	3E-07	1E-05	W
Absorped power	1E-08	1E-07	3E-06	W
Signal current	96	1115	28662	pA
Neutron flux on first wall	1E+14	1E+11	1E+14	1/cm2s
Neutron flux	1E+07	1E+04	1E+07	1/cm2s
Neutron count	5000	5	5000	1/s
Average neutron energy	2	2	2	MeV
Neutron induced current	16	0.02	16	pA
Noise current	1.0	1.0	1.0	pA
Signal/Noise, no neutron	96	1115	28662	
Signal/Noise	6	1115	1788	

For measurements of plasma near X-point and ionization front in divertor the special planar diamond detector should be used with spectral sensitivity band from several eVs to several keVs. It's quite difficult to expect that temperature measurements are possible for that region, because of the predomination of radiation in impurities peaks. The location of ionization front can be estimated due to large changes in concentration and temperature near it, see Figure 2.

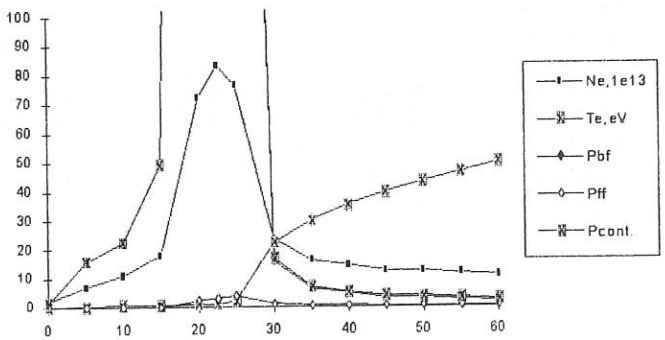

Figure 2. SXR-emission near ionization front in divertor

Here Pff - bremstraghlung emission, W/cm^3, Pbf-recombination in very rough estimation. Emission in peaks is significant but wasn't taken into account and not

shown on this graph because of poor information about plasma impurities composition expected. Obviously imaging system can observe bands of high emission near the X-point. To improve signal/noise ratio curved microchannel SXR-conductor can be used. Glass capillary bundles (about 1 cm diameter ant 4m length) can be assembled in focusing configuration along plasma magnetic axes to increase signal. The radius of bundles curvature (above 8m) is enough to shift detector to reduce neutron flux reaching it passing through all shielding layers. Such capillaries showed attractive SXR-transmission features (see Fig. 3), bending radius ~ 9 m.

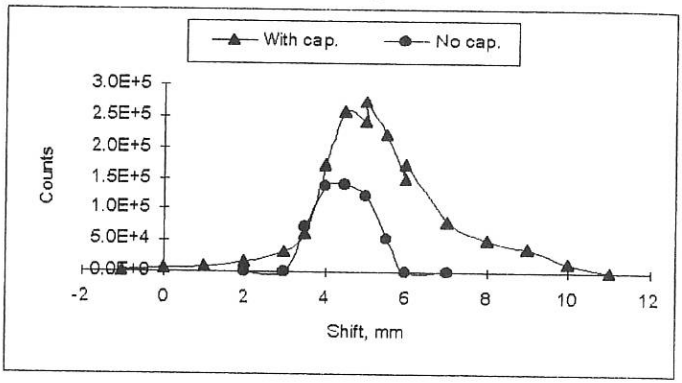

Figure 3. Comparison of capillary transmission

The power of SXR-flux was increased more than 2 times after insertion of 30cm - long, 0.5mm inner diameter capillary into optical path that can be explained by increasing of solid angle field of view. It's possible to manufacture special capillary concentrators that can increase initial SXR-flux hundreds times [2]

References

[1] G.A.Bobrovskiy, D.V.Portnov et. al. "Internal disruption study in T-10 plasma" in 12 EPS Conference on Contr. Fusion and Plasma Physics, Budapest, 1985, v.1, p.142. and A.V.Vasilyev, K.A.Grinuk, V.S.Khrunov et. al. "Investigation the radiation resistance of CdTe and diamond detectors" Thesis report in 5 Soviet Meting of High Temperature Plasma Diagnostics, Minsk 1990, p.159-160, in russian.

[2] Kumakhov M. et al., "Application of rentgenooptical systems for X-ray diagnostics", Plasma Physics (in russian) 18(4) 496 (1994).

IMPURITY INDUCED NEUTRALIZATION OF ALPHA PARTICLES AND APPLICATION TO ITER DIAGNOSTICS

A.A. Korotkov, A.M. Ermolaev[+]
A.F.Ioffe Institute, St.Petersburg, Russia
+ University of Durham, Durham DH1 3LE, England, UK

1. Introduction

Charge exchange between ICRF-driven protons and hydrogen-like main impurity ions in JET plasmas (Impurity Induced Neutralization) has been recently established as the dominant neutralization process for MeV-energy protons [1]. The same process could underlie a passive diagnostic of alphas at the core of ITER plasma unaccessible for a probing beam or pellet injection. The neutralization of alphas in ITER plasmas will occur due to double capture of electrons from the helium-like main impurity ions:

$$He^{2+} + A^{(z-2)+}(1s^2) \rightarrow He(1s^2) + A^{z+} \qquad (1)$$

where $A^{(z-2)+}$ - [He]-ions of beryllium and carbon or atoms of helium ash. The cross-section of the reaction (1) is quite reliably established in the case of helium atoms, but not known for [He]-ions. We have estimated these cross-sections as well as densities of the impurity donors in ITER plasmas. The calculations allow to determine the main plasma parameters having an influence on the neutralized alpha particle fluxes and consider a feasibility of the diagnostics based on the measurement of these fluxes.

2. Cross-sections for double charge exchange of alphas with [He]-ions

$1s^2$ - $1s^2$ transition in (1) is the main one in fusion plasmas because of the low population of the excited ionic states and because a final $He(1s^2)$-state has the most close bound energy to the initial $A^{(z-2)+}(1s^2)$-state. We have calculated the cross-section of the reaction (1) for Be^{2+} and C^{4+} using a model of the independent electrons (IEM). IEM is expected to give a reliable estimation if $1s^2$ -$1s^2$ is the main transition and $Z_p, Z_t > 1$ or $v > \sup\{Z_p, Z_t\}$ [2] as in our case (Z_p,Z_t - projectile and target nuclear charges, v - relative velocity in atomic units). In IEM we have $\sigma_{cxcx} = 2\pi \int |P_1(\rho)|^4 \rho \, d\rho$, where $P_1(\rho)$ is a probability of a single charge exchange from the initial state to the ground state of the He^+, ρ - impact parameter. $P_1(\rho)$ has been computered using the modified two-orthogonal state expansion method (TSEM) [3] at energies near the cross-section maximum and at higher energies - the first-order continuum distorted wave approximation (CDW1) [4]. The initial state of the [He]-ion is described by the Hartree-Fock orbital [5] in CDW1

calculations and by the orbital of the Hylleraas type in TSEM. The final orbital is a hydrogenic one. The results presented in Fig.1 quite well match each other in the intermediate energy range. Fig.2 shows the obtained cross-sections (including helium atom case) used in further calculations. To estimate the uncertainty of the cross-sections due to IEM we have calculated the combined cross-section taking into account an electron-electron interaction in the final channel: $\tilde{\sigma}_{cxcx} = (\xi\ \sigma^{r}_{cxcx} + \sigma_{cxcx})/(1 + \xi)$, where σ^{r}_{cxcx} is for the relaxation of the electrons in the final state, $\xi = v_o/v$, v_o - orbital electron velocity in the ground state of He^+. σ^{r}_{cxcx} has been computered using Hartree-Fock or Hylleraas type orbital for the helium ground state. We obtained: $0.5\ \sigma_{cxcx} \le \tilde{\sigma}_{cxcx} \le \sigma_{cxcx}$ for Be^{2+} and $0.7\ \sigma_{cxcx} \le \tilde{\sigma}_{cxcx} \le \sigma_{cxcx}$ for C^{4+}. More elaborated theoretical methods are in progress for the determination of the uncertainties due to application of TSEM and CDW1 themselves.

3. [He]-ion densities and neutralization probability of alphas at ITER plasma center

We consider an ignited ITER plasma with parameters presented in [6]: $n_e(m^{-3}) = 1.3 \times 10^{20}(1-x^2)^{0.5}$, $T_e=T_i(keV) = 20\ (1-x^2)$, B = 5.7 T, P_{fus} = 1500 MW, x = r/a, a = 3 m, plasma elongation - 1.55. We adopt a classical alpha particle distribution function f_α in the absence of the particle losses which gives 0.3% of the slowing-down alphas at the plasma center. Three impurity compositions were considered: 1) 20% He, 1% Be, Z_{eff}= 1.55; 2) 15% He, 6% Be, Z_{eff}= 2.05; 3) 20% He, 1% Be, 1% C, Z_{eff}= 1.82. Impurity donor densities have been computered using a model of the impurity ion balance which was developed earlier to describe the IIN of MeV-energy protons in JET plasmas [1]. Radial ion transport in the model is described by an empirical confinement time τ_z taken to be equal for all species. The calculations show that τ_z is a critical parameter for the [He]-ion densities (n_{z-2}). The steady state ion densities at ITER plasma center are presented in Fig.3 versus τ_z (in the relation to the bare ion densities n_z). With good accurecy: $n_{z-2} = n_z/(n_e\ I_{z-2}\ \tau_z)$, where I_{z-2} is a rate coefficient for the ionization of [He]-ion by electron impact. A great number of the experiments at different confinement modes give the impurity ion diffusion coefficient in the plasma center in the range $0.1 \le D_z(m^2/s) \le 1.5$ independently on the ion species. Therefore we expect for ITER τ_z in the interval $1 \le \tau_z(sec) \le 20$ for the plasma area $x < 0.5$. Fig.4 presents the IIN probability $P_\alpha = \sum_z \sigma_{cxcx} v_\alpha n_{z-2}$ as a function of the alpha particle energy at τ_z= 5 sec. Neutralization probability due to helium probing beam P_{beam} (E_b= 400 keV, I = 7 A) proposed for the neutral particle diagnostics in [7] is also shown. P_α far exceeds P_{beam} even at a half of the plasma radius. The neutralization is determined by the helium ash at $E_\alpha \le 0.5$ MeV and by Be^{2+} at $E_\alpha \ge 1$ MeV. Contribution of C^{4+} becomes important at $E_\alpha \ge 2$ MeV if carbon density approachs 1% (composition 3).

4. Feasibility of the diagnostics using passive neutralized alpha particle flux

Neutralized alpha particle fluxes from the plasma center in the radial Φ_α^R and vertical direction Φ_α^v at $\tau_z = 5$ sec are shown in Fig.5. $\Phi_\alpha = f_\alpha P_\alpha \gamma$, where γ is an attenuation factor. The importance of the flux attenuation is clearly seen. Note that electron loss throw excited helium states [8] results in 20 - 40% and 30 - 50% decrease of γ for the Φ_α^R and Φ_α^v correspondingly when alphas energy varies from 3 to 0.5 MeV. We have also calculated the alpha particle count rates for the measurement of the energy distribution $d\phi_\alpha/dE_\alpha$ with neutral particle analyzer (NPA) GEMMA-2M used on JET [7]. The results are presented in Fig.6 for the NPA geometric factor 3.7 $\times 10^{-4}$cm^2 str and 2 $\times 10^{-4}$ cm^2 str for the Φ_α^R and Φ_α^v correspondingly (source area in the plasma is 40 $\times$ 40 cm^2). Count rate for the background neutrons has been calculated for the total neutron flux $\Phi_n = 5 \times 10^7$ cm^{-2} s^{-1} [9] at the NPA detector position. The most promising diagnostic approach is a multichord measurement of the Φ_α^R. The alphas count rate far exceeds the neutron one in this case at $E_\alpha > 0.5$ MeV. The f_α - analysis with energy resolution 30% and statistic accuracy 10 - 20% is provided at required time $\Delta t = 0.1$ sec and space resolution of 30 cm in the energy range $0.5 \le E_\alpha(\text{MeV}) \le 3$ if $\tau_z = 5$ sec. For any other τ_z $\Delta t = 0.02 \times \tau_z$.

5. Conclusion

The analysis predicts that IIN will provide the neutralized alpha particle fluxes sufficient for the measurement of the alphas energy spectrum at the core of ITER plasma with required space and time resolution and accuracy. The problem of the τ_z measurement has to be solved for the alphas density determination. The measurements of the fast helium fluxes in the ^{3}He ICRF heating or dt- experiments on modern tokamaks with simultaneous control of the light impurity densities are of highly priority as well as a development of the relevant atomic data base.

References

[1] Korotkov AA and Gondhalekar A, 21-st EPS Conf. Abstracts **18B** 266 (1994)

[2] Jain A et al, Phys.Rev. **A39** 1741 (1989)

[3] Yu Rang Kuang, J.Phys **B24** 1645 (1991)

[4] Belkić Dž et al, Comp.Phys.Communication **30** 193 (1983)

[5] Clementi E and Roetti C, At.Data Nucl.Data Tables **14** 177 (1974)

[6] 'ITER Physics and Plasma Operation Studies', ITER TAC-3-03 (1993)

[7] Afanasiev et al, 'Proposal on the Neutral Particle Diagnostics for ITER', ITER Documentation GSS IP58 94-06-16F

[8] Korotkov AA, Nucl.Fusion A+M Supplement **3** 79 (1992)

[9] 'ITER Diagnostics', ITER Documentation Series **33**, IAEA, Vienna (1990)

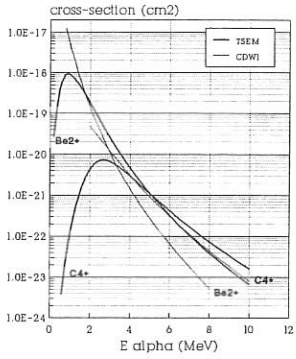

Fig.1:IEM double capture cross-section for alphas

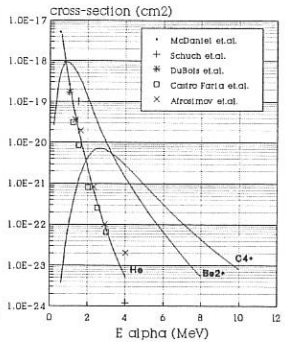

Fig.2:Used double capture cross-sections for alphas. Points-helium experimental data

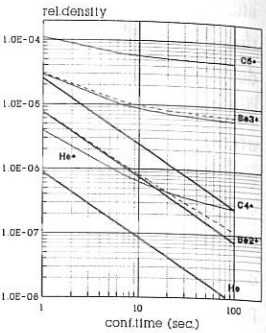

Fig.3:Impurity donor densities versus Imp.conf.time Dotted lines- with He beam at x=0.5

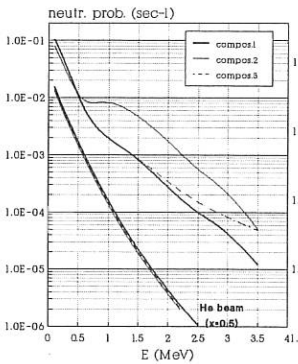

Fig.4:IIN and beam induced neutralization probability of alphas versus their energy

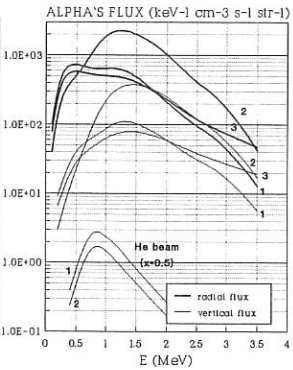

Fig.5:Neutralized alphas flux from ITER plasma center due to IIN

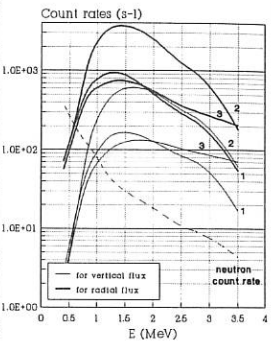

Fig.6:Alphas and neutron NPA count rates at dE/E=10%

Advances in Neural Network Applications for COMPASS-D and ITER

C. G. Windsor, T. N. Todd, M. E. U. Smith and D. L. Trotman
UKAEA Government Division, Fusion, Culham, OX14 3DB, UK
(UKAEA/EURATOM Association)

1. Introduction

Neural networks have become a standard part of the armoury of methods available for control systems since the development of the multilayer perceptron (MLP) method ten years ago [1]. Recent reviews have been given in the book "Neural Networks" [2]. The problem of solving the Grad-Shafranov equation to derive the plasma parameters from the diagnostic signals is too complex to perform on line with present-generation digital processors, but can be solved numerically for a particular case. Alternatively, as in the neural network implementation used here, a series of numerical simulations in which the predicted diagnostic signals are calculated off-line for a series of possible plasma positions and shapes can be used to form a training database. The neural network thus operates by performing a non-linear mapping between the multi-dimensional input space of the various diagnostic variables to an output space containing the desired parameters to be controlled.

2. Real time plasma shape and position control on COMPASS-D

The plasma position and shape on the COMPASS-D tokamak have been controlled simultaneously using a 75kHz bandwidth hard-wired real time neural network. The primary network operates with up to 48 selected magnetic inputs and has been used in the vertical position control loop to control the position of the upper edge of the plasma at the radius of a reciprocating Langmuir probe and, for example, to keep this constant during a programmed plasma shape sequence as shown in figure 1[3].

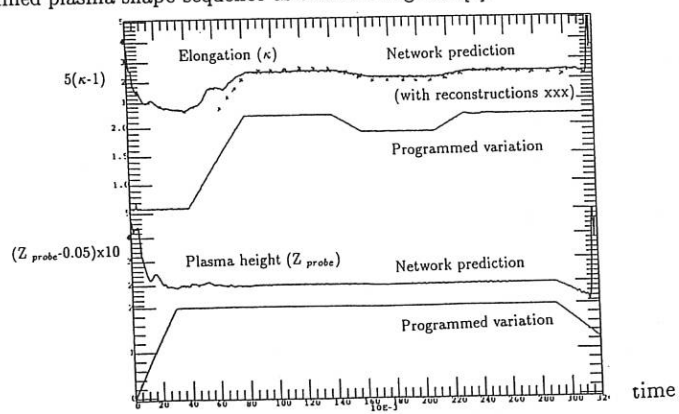

Figure 1: *The control of both plasma shape and position of COMPASS-D for shot 13804. The upper traces show the elongation given by the network compared with the programmed variation. The lower traces show the corresponding values for the vertical position of the plasma boundary at the radius of the reciprocating probe. The crosses represent the output of a filament code (DFIT) matched to the measured data.*

3. A network to combine magnetic, control current and soft X-ray data

One of the main advantages of neural networks is their ability to combine different types of diagnostics Two coupled networks are now ready for use as shown in figure 2. A dedicated soft X-ray network uses inputs from 16 vertical and 16 horizontal camera channels. With just four hidden units it is able to determine accurately three output signals defining the plasma core radius, vertical position and elongation. These outputs are fed to the primary network along with selected magnetic inputs, and four control current inputs, to display the plasma boundary. The core data is expected to help characterise the equilibrium by providing information on the Shafranov shift and gradient of elongation, related to the equilibrium parameters $\beta_p + l_i/2$ and l_i.

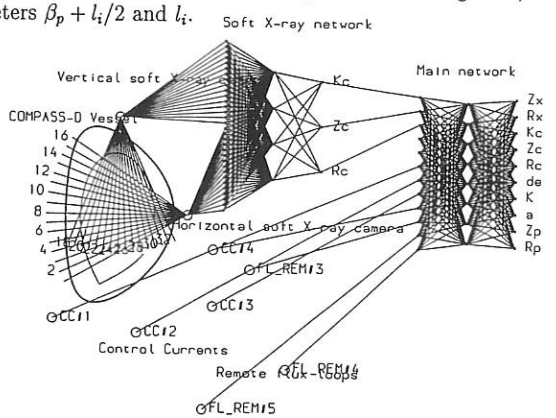

Figure 2: *The layout of the double network as simulated on COMPASS -D.*

4. A ten parameter plasma boundary and profile display

The plasma boundary for circular plasmas and the upper section of the single-null X-point plasmas is described by the conventional function of poloidal angle θ as a function of the plasma radius, R_0, vertical position Z_0, minor radius a, elongation κ, and triangularity δ.

The lower section of an X-point plasma is described by an approximate polynomial function evaluated so that the boundary goes through the desired R_x,Z_x and through the inner radius with the calculated curvature $(1 + \delta)$ / A $^2\kappa^2$. This prescription gives a fair description of the plasma boundary, as shown in figure 3.

5. COMPASS-D as a test bed for ITER

Although smaller than ITER by a factor of about 15, the COMPASS-D tokamak is well suited to trial studies of plasma position control. It mimics ITER in featuring a strongly asymmetric single-null divertor configuration. ITER's long pulses and high fast neutron radiation levels mean that magnetic diagnostics close to the plasma may not be reliable in the long term. Neural networks are here used to consider the alternatives of control current inputs, remote flux loops and soft X-ray emission. Random noise of 2% was added to all inputs and in the case of soft X-ray values this was increased to 10% with a minimum spread of around 10% of the peak intensity. The 251 equilibrium training examples in the database were presented for over 10,000 iterations to the network and the performance

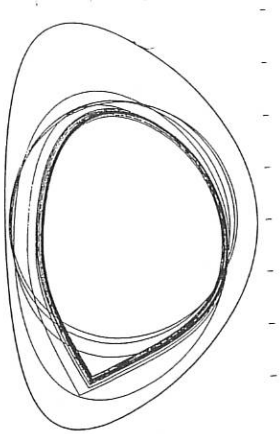

Figure 3: *The plasma boundary as a function of time in 0.01 sec intervals, predicted using a double network from magnetic, control current and soft x-ray experimental data from shot 14776 on COMPASS-D.*

quoted here was evaluated for the 250 test examples in the database. 8 hidden units were generally used. The mean accuracy in the profile boundary, in the X-point position and in the core position has been determined for various networks including 5 flux loop inputs (FL), 4 poloidal field control current inputs (CC) and 32 soft X-ray inputs (SX). The accuracy of the network mapping itself may be gauged from the precision of the network boundary parameters compared with the exact values from the database. The results confirmed many intuitive concepts. The 5 flux loops alone gave a benchmark boundary accuracy of order 5.4 mm. Soft X-rays alone were very poor for the boundary determination, and failed to show the X-point, but gave the core dimensions to 1.5 mm, a factor of 4 better than the flux loops alone.

This provides the rationale for the double networks illustrated in figure 2. The first network analyses only the soft X-rays and has just three output parameters, defining the core major radius, vertical position and elongation. These combined networks give 0.7 mm core accuracy with a 1.9 mm boundary accuracy. When scaled to ITER dimensions this corresponds to a 25 mm boundary error, not too far from the ITER D93 specification of 20 mm.

The application of the networks to real experimental data is another matter. Experimental errors caused by integrator drift, soft X-ray leakage currents, calibration errors and noise are now necessarily included. There is in addition the problem that the "true answer" is no longer to hand, and must be evaluated approximately from some numerical code with its own attendant errors. In this case it has been evaluated using the filament code DFIT.

Generally the precision of the results is very much worse than in case of the pure simulations. The boundary error from flux loops is roughly doubled to 11.7 mm, and the core error in a double network increases to 11.1 mm. However the present preliminary results are being refined. In particular it is necessary to consider the time dependence through the shot of any accuracy parameters, especially those involving soft X-rays. At both early and late times this is very low and good results cannot be expected. Around the middle

of the shot when the plasma pressure is high, the signals are large and much better results are achieved. This is illustrated in figure 4 which shows the three spread parameters for networks with inputs from flux loops, soft X-rays and control current.

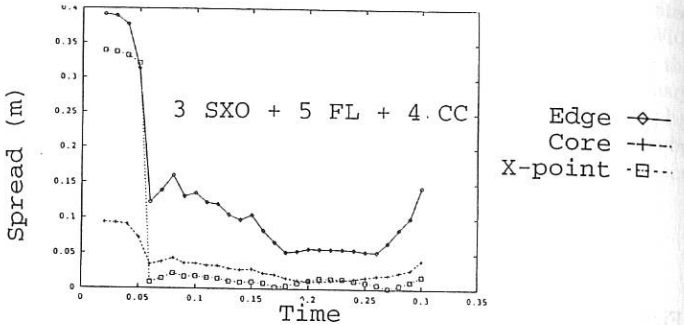

Figure 4: *The average accuracy of the parameters defining the boundary, X-point and core dimensions, in mm, as a function of time for the double network, showing the much better performance in the middle period of the shot when the soft X-ray intensity is high.*

6. Conclusions and work in progress

Simulations from the database show clearly that the neural network method would be capable of determining the ITER plasma boundary to the required accuracy given that the experimental diagnostic inputs to the network were of an adequate accuracy.

The inclusion of soft X-ray data gives much improved accuracy to the boundary prediction. Also demonstrated is the feasibility of the neural network method to include independent diagnostic techniques besides the magnetic field and flux measurements.

The use of real experimental data shows all too clearly the difficulties of obtaining diagnostic data to the accuracy needed to make full use of the neural network method.

The real time soft X-ray network is now installed on COMPASS-D and giving its first results. The remote flux loops are now collecting data, however their analysis must await a new database with an extended spatial grid.

Acknowledgment

This work was supported by the UK Department of Trade and Industry, EURATOM.

References

[1] D.E. Rumelhart, G. Hinton and G. Williams, "Parallel Distributed Processing",MIT Press Cambridge, Massachusetts, 1986.

[2] C.M. Bishop, P.S. Haynes, M.E.U. Smith, T.N. Todd and D.L. Trotman, "Real-time control of a high temperature plasma using a hardware neural network", in "Neural Networks" Ed.J.G. Taylor, Unicom Ltd (1995)

[3] C.G. Windsor, P.S. Haynes, D.L.Trotman, M.E.U. Smith, T.N. Todd and M. Valovic, Nucl. Energy, 34, 85-91, 1995.

TPX Diagnostics for Tokamak Operation, Plasma Control and Machine Protection.

P. H. Edmonds, S. S. Medley[a], K. M. Young[a], G. H. Neilson[b], R. J. Goldston[a], M. G. Bell[a], D. W. Johnson[a], F. M. Levinton[c], G. Renda[a], G. Gettelfinger[a], N. L. Bretz[a], S. J. Zweben[a].

Fusion Research Center, University of Texas at Austin, TX 78712

[a]Princeton Plasma Physics Laboratory, Princeton, NJ 08543 USA

[b]Oak Ridge National Laboratory, Oak Ridge, TN 37831

[c]Fusion Physics & Technology, Inc., Torrance, CA 90503

Introduction

The Tokamak Physics Experiment (TPX) is planned to be an advanced performance, high beta, steady state, high heat flux, double null divertor tokamak [1, 2, 3, 4]. Machine parameters are: R_0=2.25 m, a_p=0.5 m; A=4.5; κ~2; δ~0.8; B_T=4 T and I_p=2 MA. Operation in both hydrogen and deuterium is planned. The design is required to incorporate end-of-life tritium capability. The experiment includes 8 MW of neutral beam power, 6 MW of ion cyclotron and 3 MW of lower hybrid rf power for auxiliary heating and current drive. Experimental scenarios include non-inductive current drive with an initial 1000 sec long pulse mode and an upgrade to steady state (10^5 sec), divertor heat loads of up to 7.5 MW/m^3 and maximum neutron rates up to 7.5x10^{16}/sec. First plasma is scheduled for mid-2001.

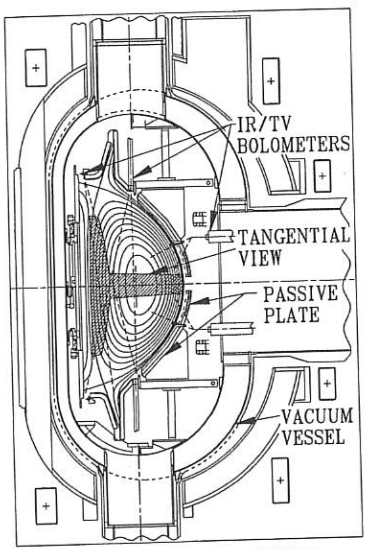

Figure 1. Elevation View of TPX Core including IR TV locations and view of plasma through stabilizer plates

Diagnostics are required for real time plasma control, physics measurements and machine protection. Fundamental to initial operation are measurements of plasma equilibrium and position, basic plasma properties, current density and pressure profiles, surface heat loads on plasma facing components and

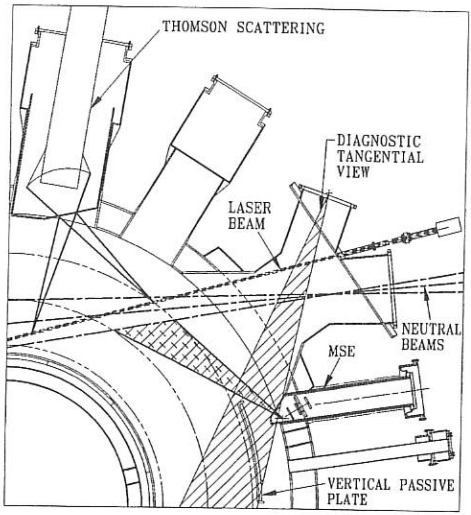

Figure 2. Plan view of TPX quadrant showing representative MSE re-entrant port, NB trajectory, Thomson scattering beam and view lines, and typical tangential mid plane view.

Plasma Parameters	Baseline	Upgrade(a)
$n_e(0)$ (m^{-3})	0.9×10^{20}	2.0×10^{20}
τ_E (ms)	300	400
$T_e(0)$ (keV)	14	21
$T_i(0)$ (keV)	14	23
β_N (%), β.a.B_0/I_p (T-m/MA)	4	5.5
Bootstrap Fraction, F_{BS}	0.72	0.73
Peak DD neutron rate (s^{-1})	5×10^{16}	7.5×10^{16}

Table I *Selected TPX Parameters*

provision for disruption avoidance. An extensive set of diagnostics is planned, divided between a baseline set required for the first phase of operation and an upgrade set which includes fluctuation diagnostics as well as those required for extended pulse length operation [5]. Present diagnostic design is concentrated on the first phase diagnostics. Preliminary designs for the magnetics, Thomson scattering, motional Stark effect and divertor infra-red imaging diagnostics are described.

TPX diagnostic design, construction, installation and operation will be a national effort, with participation by National Laboratories, industry and universities under the direction of the TPX project.

TPX Device Description

An elevation view of the TPX machine core is shown in Fig. 1 and a partial plan view in Fig. 2. Stability against MHD modes at high beta requires close fitting stabilizer plates. These consist of upper and lower toroidal rings with a resistive gap and vertical plates located at the four vessel weld planes. These plates will have narrow mid plane slots for tangential viewing. A projection of a representative tangential view is included in Fig. 1. Selected physics parameters for the baseline and upgrade configurations are given in Table I.

The primary neutron shielding will consist of boronized cooling water in the double jacket vacuum vessel, external shields and plugs installed in vessel penetrations will provide further shielding. Remote maintenance will be required for all in-vessel components; this radiation zone includes many diagnostic elements, fiber optics,

windows, etc. Where necessary this requirement is included in the diagnostic design. To minimize this need, a design preference is that diagnostics should be robust, redundant and remotely insertable.

The combination of high heat flux and long pulse accentuates the issues of thermal heating and erosion/deposition for plasma facing diagnostic components, such as windows and mirrors and of the degradation of window and fiber-optic transmission quality due to radiation induced absorption and scintillation effects.

TPX Diagnostics Description

Shape, Position and Magnetic Configuration Measurements.

The TPX magnetic set is based on conventional inductive sensors with advanced hybrid integrators [6]. Real time processing of the data for equilibrium reconstruction is needed for plasma profile control and for integration with the MSE and pressure diagnostics for current profile control. Additional sensors will measure currents in the plasma facing, vacuum vessel and other structural components. Remote maintenance of the magnetic diagnostics is unlikely and the diagnostics will be required to survive for the life of the machine.

Current Profile Measurements.

The plasma current profiles will be measured by the Motional Stark Effect (MSE) diagnostic. The diagnostic requires a tangential view intersecting a neutral beam path. The planned installation, shown in Fig 2, provides a spatial resolution of about 2 cm [7]. Each beam line contains three sources, only one is used for the MSE diagnostic, beam modulation will be required to discriminate against signals from the two other beams. For extended pulse length operation (>> 1,000 sec) two beam lines will be utilized for plasma heating and current drive, these will alternate during the long pulse to allow for cryopump regeneration. A second MSE system will be added, viewing the second beam line, to supply continuous current profile information.

Thomson Scattering.

The goals for the Thomson scattering system include a repetition rate of 100 Hz and spatial resolution of 3 cm in the core and 3 mm in the edge. Technical and performance requirements favor imaging systems over LIDAR techniques [8]. The proposed configuration utilizes radial imaging of a tangential laser beam line. A separate viewing system will be used for the high resolution view of the mid plane edge plasma. The viewing and laser sightlines are indicated in Fig. 2.

Divertor Imaging

The divertor tile temperature will be monitored using visible/IR TV systems. The imaging elements will be located in-vessel at top and bottom locations as shown

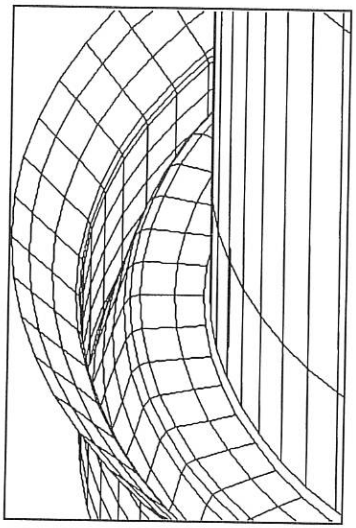

Fig. 3. Non-perspective divertor view from auxiliary port (outboard camera in Fig. 1.)

in Fig. 1. A non-perspective divertor view from the outboard auxiliary port is shown in Fig. 3. Fiber optic and lens/mirror relay optics will deliver the signal to cameras located in a low radiation environment outside the vessel. Beam splitting mirrors will allow simultaneous viewing in the infra-red and visible. Complete coverage of the high heat flux tiles is desired. A preliminary study of the divertor IR/TV diagnostic has been completed [9].

Summary

The diagnostics for TPX are at an early design phase, with emphasis on the diagnostic access interface with the major tokamak components. Account has to be taken of the very severe environment for diagnostic components located inside the vacuum vessel. The placement of subcontracts for the design and fabrication of the diagnostic systems is in progress.

Acknowledgment

This work was supported by the U.S. Department of Energy under contract No. DE-AC02-76CH03073.

References:

[1] K. I. Thomassen, D. B. Batchelor, J. Bialek, et al., Plasma Phys. and Contr. Nucl. Fus. Res, Wurzburg, Vol. 3, p. 279, (1992).

[2] J. A. Schmidt, K. I, Thomassen, R. J. Goldston, et al., J. Fusion Energy **12**, 3, 221, (1993).

[3] G. H. Neilson, D. B. Batchelor, P. K. Mioduszewski, et al., Fusion Tech., **26**, Vol. 3 Part 2, 343-349, (1994).

[4] R. C. Davidson, R. J. Goldston, et al., Phys. Plasmas 2 (6), 2417 (1995).

[5] S. S. Medley, Rev. Sci. Instrument, **66** (1), 297-302, (1995).

[6] Paul Anderson, et al., General Atomics Report No. GA-21533, (1993).

[7] F. M. Levinton, TPX Report No. 62-941216-FP&T/FLevinton-01, (1994).

[8] D. Johnson and B. Grek, TPX Report No. 62-950205-PPPL/DJohnson-01, (1995)

[9] G. Renda, TPX Report No. 62-941220-PPPL/GRenda01, (1994).

Tomographic reconstruction of the radiation distribution during neon puff experiments in ASDEX Upgrade and JET

J.C. Fuchs, K.F. Mast, R. Reichle*
ASDEX Upgrade Team, NI Team, JET Team*

MPI für Plasmaphysik, EURATOM Association, D-85748 Garching, Germany
*JET Joint Undertaking, Abingdon, Oxon, OX14 3EA, United Kingdom

Introduction

Bolometric measurements of experiments with controlled puffing of neon impurities into a deuterium plasma in order to achieve a radiating boundary are analyzed for ASDEX Upgrade and JET. Radiation losses are recorded by several bolometers with crossed lines of sight. A twodimensional poloidal reconstruction of the local radiation power density is performed with a tomographic algorithm based on an anisotropic diffusion model. The radiation profiles for some shots with and without injection of neon and other impurities are compared for both ASDEX Upgrade and JET plasmas.

Bolometric diagnostic

In the ASDEX Upgrade tokamak radiation losses are recorded by 88 bolometers placed in six pinhole cameras and two collimators which are mounted around one poloidal cross section of the plasma inside the vacuum vessel (Fig. 1). The bolometers are miniaturized, low noise metal resistor bolometers [1] which are excited by a 50kHz sine wave and effectively suppress thermal drift and electromagnetic interferences. Radiation from the X-point and divertor region and the upper boundary of the plasma is observed by two 'horizontal' cameras with a high spatial resolution (3cm), whereas the radiation from the center part of the plasma is registrated by a 'horizontal' camera with a resolution of 10cm. A vertical camera with 24 channels measures the radiation from the entire plasma cross section along basically vertically arranged lines of sight.

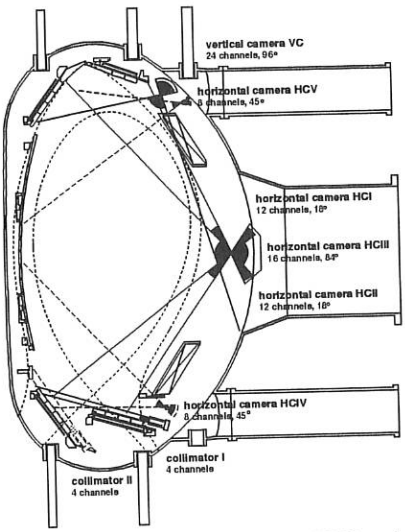

Fig. 1: Bolometer cameras on ASDEX Upgrade

The divertor camera HCIV with 8 channels and the two collimators with 4 channels over each target plate were taken into operation lately. However, cooling effects by gas puffing and other disturbances have not yet been quantified, so the reconstruction of the radiation distribution is still performed without the measurements of these channels.

In JET there are 34 channels in the old bolometer system with crossed lines of sight, placed in two 'horizontal' and one 'vertical' camera and 84 channels in the new system of which up to 16 have been used simultaneously, leading to a good resolution in both the main plasma and the X-point and divertor region [2].

Tomographic reconstruction of the radiation emissivity

Bolometers measure the radiated power integrated along their lines of sight. In order to obtain the distribution of the local radiation emissivity in a poloidal cross section of the plasma, the measured line integrals therefore must be unfolded. This is done with a new algorithm for tomographic reconstruction of the two dimensional distribution of the emissivity, which is not limited to closed flux surfaces, but also works on open flux surfaces, e.g. around the X-point and in the divertor region [3].

The algorithm is based on the fact that the variation of the emissivity along magnetic field lines is much smaller than perpendicular to them. In order to describe this behaviour, we make the ansatz that the distribution of the radiation emissivity is generated by an anisotropic diffusion model with strongly different values of the diffusion coefficients $D_{\|}$, $D_{\perp}$ along and perpendicular to the magnetic field lines. The solution with minimized sources and sinks of this diffusion process and considering the constraints of the measured line integrals represents the poloidal distribution of the emissivity $\epsilon(R, z)$.

Volume integration of the emissivity over the whole plasma or some parts of it gives the total radiated power and the radiated power from the divertor region or the main plasma.

The radiation profiles presented in this paper have been obtained using a grid with 26×48 grid points. This corresponds to a spatial resolution of about 5cm for ASDEX Upgrade plasmas and 8cm for JET plasmas. The ratio of the diffusion coefficients was chosen to take values $D_{\perp}/D_{\|} = 0.1$ in the main plasma and up to 0.8 in the divertor region. Also the absolute values of $D_{\perp}$ and $D_{\|}$ were chosen smaller around the X-point than in the main plasma because here one expects a larger variation in the radiation profile.

Results

Fig. 2 shows the comparison of the radiation distribution for two ASDEX Upgrade shots with $I_p = 1\text{MA}$, $\overline{n_e} \approx 1\text{e}20/m^3$ and 7.5MW neutral beam injection heating. On the left hand side the radiation profile is shown for a shot without any neon, on the right hand side for a shot with an additional neon puff, where the amount of the neon injection was feedback controlled with the fractional radiated power P_{rad}/P_{heat}.

In the case without any neon the radiation profile is strongly peaked in the X-point and divertor region. About 55% of the heating power is lost by radiation, and the X-point radiation (unsymmetric part of the radiation profile around the X-point) is about 60% of the total radiated power. With additional neon injection the radiation from the main plasma and especially from the boundary increases, which is also proved by model calculations [4]. The radiation profile develops a more uniform layer around the boundary region of the plasma. The total radiated power increases to ca 80% of the heating power, whereas the X-point radiation is only ca 25% of the total radiated power.

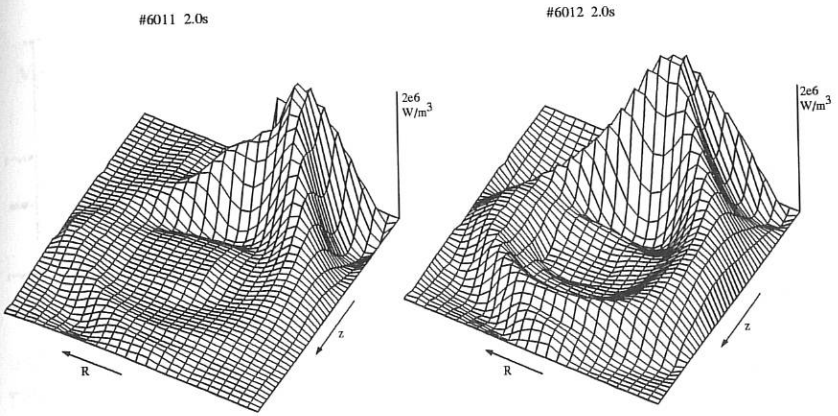

Fig. 2: Radiation profile for two ASDEX Upgrade shots, with view from the top of the plasma towards the X-point. Left: no neon. Right: additional neon injection

JET plasmas show a similar behaviour: Fig. 3 shows the reconstructed radiation profiles for two similar shots, one without neon, the other with a strong neon puff. Again the radiation profile develops a more radiative boundary with neon injection in comparison to shots with neon. The total radiated power raises to ca 55% of the heating power, in comparison to 35% in the case without neon. The emissivity profile on the divertor region also shows a decrease of radiation over the strike zones during the neon injection.

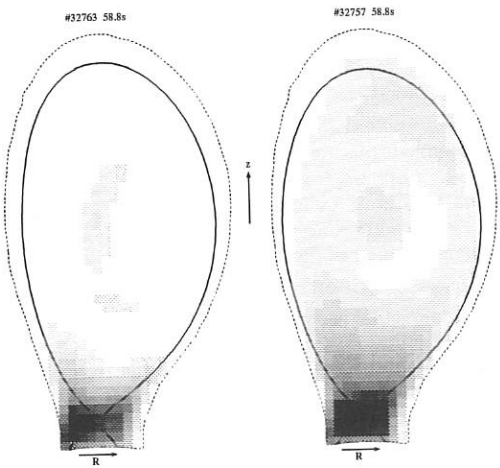

Fig. 3: Radiation profile for two JET shots. Left: no neon. Right: additional neon injection

The development of the radiation profile during neon injection depends also on the location of the gas valve. Fig. 4 shows the comparison of the time evolution of some measured line integrals of radiation for two ASDEX Upgrade shots with neon puffing into the main chamber or into the divertor respectively. In the case of neon injection into the divertor the radiation from the main plasma and the upper boundary increases more slowly than for neon injection into the main chamber, but reaches almost the same levels. Correspondingly, the radiation profile at the beginning of the neon puff shows much less radiation from the main plasma and upper boundary for injection into the divertor.

The measured line integrals of the collimator over the inner target plate show also that the radiation directly over this plates decreases quickly to a very low level for shots with neon injection into the main chamber, whereas for shots with injection into the divertor the radiation decreases more slowly.

The radiation profile is also influenced by additional puffing of deuterium into the plasma. In ASDEX Upgrade, deuterium puffing results in an increase of the radiation, especially in the divertor region.

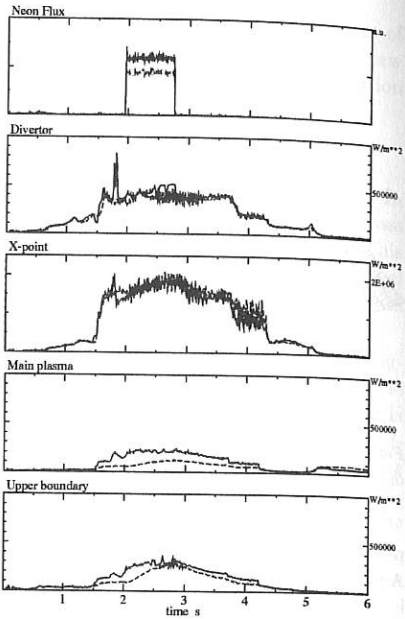

Fig. 4: Line integrals of radiation from divertor region, X-point, main plasma and upper boundary for two shots with neon injection into the main chamber (solid lines) and into the divertor (dashed lines)

Injection of nitrogen or argon instead of neon results also in similar radiation profiles. However, nitrogen radiates more in the edge and argon more towards the center of the plasma than neon [5], as can be seen both in the measured line integrals and in the reconstructed radiation profiles.

Conclusions

Bolometric measurements of experiments with controlled puffing of neon impurities into a deuterium plasma have been analyzed. For both ASDEX Upgrade and JET plasmas neon injection results in an increase of the radiation from the main plasma and the boundary, the radiation profile develops a more uniform boundary layer. Neon injection into the divertor instead of the main chamber leads to a slower increase of the radiation in the upper boundary. Additional puffing of deuterium also influences the radiation profile.

References

[1] K.F.Mast, J.C.Vallet, C.Andelfinger et al., Rev.Sci.Instrum. **63**(3) (1991),p 744
[2] R. Reichle et al., this conference
[3] J.C. Fuchs, K.F. Mast, A. Hermann, K. Lackner et al., Contrib. 21st EPS, Montpellier, France, 1994, p1308ff
[4] R. Dux et al., this conference
[5] A. Kallenbach et al., this conference

Spatial Distribution of Electron Density Fluctuations Measured Using CO_2 Laser Phase Contrast Method on Heliotron E

S Kado, K Muraoka, K Kondo†, F Sano†, T Mizuuchi†,
K Nagasaki†, H Okada†, S Besshou†, T Obiki†
Interdisciplinary Graduate School of Engineering Sciences,
Kyushu University, Kasuga 816, Japan
†Plasma Physics Laboratory, Kyoto University, Uji 611, Japan

The Laser Phase Contrast Method, which has so far been a line-of-sight measurement, is improved to obtain spatially resolved information along the probe beam path. A counter propagating pair of waves, electron mode and ion mode, were observed. Phase velocities of these modes and their parametric dependencies are discussed.

1. Introduction

The Laser Phase Contrast Method (LPC Method) for measuring electron density fluctuations in a magnetically confined high temperature plasma was first proposed and applied by Weisen[1,2], the detailed discussions were made by Matsuo et al. [3], and the trial for identifying the turbulence occurring in Heliotron E was performed by Tanaka et al. [4]. The LPC method basically utilizes the merit of imaging optics: i.e. the wavenumber and frequency in the plasma are directly represented on the detection plane. In order to achieve this, the phase disturbance of the probe beam due to the fluctuating density is converted to an amplitude disturbance by situating a $\pi/2$ phase plate on the beam-focused point where the diffracted and undiffracted beam are separated, so that the signals become detectable by a photo-conductive detector. Thus, the LPC method has such merits as simplicity in optical setup, ease of port access, quite high time resolution, capability of measuring longer wavelength fluctuation than using the conventional Bragg scattering measurement, etc. However, the conventional LPC method only yields line-of-sight integrated signals along a probe beam chord.

In this paper, we present results from a new LPC system which is capable of measuring spatial distributions of fluctuations in toroidally confined plasmas. The basic principle of this measurement is similar to the collective scattering experiment on the Tore Supra tokamak[5] in utilizing the perpendicularity of the propagation direction of fluctuations to the magnetic field. By virtue of the sheared magnetic field, the observable regions along the beam chord can be restricted by selecting the particular diffraction directions of the probe beam which are parallel to the propagation directions of fluctuations[6]. This is achieved by attaching a slit to the phase plate.

2. Measurements and results

Figure 1 shows the schematics of the LPC system installed on the Heliotron E device. A TEM_{00} mode CW-CO_2 laser having a wavelength of 10.6 μm and output power of 11W was

used and the dimensions of the beam just before the input port were set to be 160 mm and 50 mm, respectively. A 16 ch HgCdTe detector array was used to detect the signal from any 40 mm wide section of the beam in the plasma. The ranges of the detectable frequency and wavenumber were 2.5-314 kHz and 0.18-1.3 mm^{-1}, respectively. The wavenumber-frequency spectrum S(K,f) was derived by the Fourier transform in terms of time and space.

Figure 2 shows the spectrum of an ultrasonic wave (40 kHz) which simulated the density fluctuation in plasmas. The transducer was placed just below the output port. For such a monochromatic wave, the spectrum had a peak at the wavenumber corresponding to the phase velocity of the test wave. Here, the positive and the negative frequencies correspond to propagation towards the inboard and the outboard sides of the torus, respectively. For the turbulent spectrum, like generally observed fluctuations, the ridges found in the contour plot of the spectra show the dispersion relations of the plasma waves, and thus the phase velocities can be determined.

Figure 3 shows the spectra for the plasma discharges displayed as a contour plot separated by 3 dB. The conditions in this series were as follows: B=1.9 T, produced by 53 GHz ECH systems, "ECH phase" (270 kW), and sustained by an additional NBI heating, "NBI phase" (0.6MW), yielding a central electron density of $n_e(0) \sim 2 \times 10^{19}$ m^{-3}. In the NBI phase, additional ECH systems were superimposed, "2nd ECH phase" (53GHz 250kW + 106GHz 200kW). The system detected the wave vectors perpendicular to the probe beam, so that the poloidal component, K_θ, at the top and bottom, and radial component, K_r, at the midplane were measured.

We first analyzed the NBI phase. In the spectra for K_θ in the edge region ($|r/a| > 0.6$ for $K_\theta > 0.4$), Fig. 3(a) and (c), a counter propagating pair of waves were observed. Higher level ridges (solid lines) of the spectra represent the propagation in the electron diamagnetic direction (the electron mode) having the phase velocities of about (a)1500 and (c)1600 m/s. Lower level ridges (dashed line) represent the ion modes whose phase velocities were about (a)5000 and (c)3600 m/s. In the spectrum for K_r in the central region, Fig. 3(b), however, it is hard to find the ridges. In other words, fluctuations under these discharge conditions do not seem to propagate radially, or do so slower than a few hundred m/s. Reproducibility of the spectra between shots was not very good especially in the ion mode, but during one discharge, the spectra corresponded well with the plasma behavior, discussed in the following section.

A similar procedure was followed over a period of a discharge including the 2nd ECH phase to yield temporal evolution of phase velocities of electron and ion modes as shown in Fig. 4(a). The "net average" phase velocity is discussed in the following section.

3. Discussions

In this section, we intend to deduce further information about the characteristics of measured fluctuations from the following two points: namely, phase velocity and parametric dependencies. For the former, we estimated the phase velocity of electron drift wave in the NBI phase from $V_d = (Te[eV]/B[T]) \times (Ln[m])^{-1}$ [m/s], where $Ln = 1/(\nabla n/n)$. Here, we

used the values of Te, B and Ln obtained using Thomson scattering, numerical calculation and FIR interferometry, respectively. The calculated phase velocities in this region are between 700(r/a~0.7) and 2400(r/a~0.8)m/s, which do not disagree with the measured value of that for the electron mode.

On the other hand, the temporal evolution of electron and ion temperature measured by ECE(r/a ~ 0.5) and NPA(line average), respectively, are shown in Fig. 4(b). The change of Ln over this region was comparatively small so that we concentrated on the dependence of the phase velocities on Te or Ti. The electron mode corresponds well with the temporal change in Te, following even with the small change after 360 ms caused by the change in the input power of 106GHz ECH. However, the ion mode deceleration also corresponds with Te, having no dependence on Ti. Therefore, it seems more likely that the waves were affected by a change in a plasma poloidal rotation, than by changes in Te. In fact, the mean value of v_{pi} and v_{pe}, "net average" in Fig. 4(a), in which the effect of the rotation is eliminated, does not seem to depends on Te. Therefore, the electron mode observed here does not seem to have a characteristic of an electron drift wave. The estimated increase in bulk plasma velocity during 2nd ECH phase is about 1000 m/s in the electron diamagnetic direction. This might be caused by the shift in the value of a radial electric field towards the negative direction. However, the shift in rotation velocity of an MHD wave estimated from measurements using a magnetic probe indicates the opposite direction. Hence, a more detailed discussion is necessary, hopefully based on direct measurements of radial electric field and/or plasma rotation.

4. Conclusions

The LPC method has been improved to obtain spatially resolved signals of fluctuations. In the low power NBI discharges in Heliotron E, the following facts are observed.

1)The spectrum is quite different between the center (K_r) and the edge (K_θ). The former seems incoherent, while the latter seems to be a coherent propagating mode.

2)A counter propagating pair of waves are observed in the edge region.

3)The phase velocity of the electron mode dose not seem to have a dependence on Te, which would be expected for a drift wave.

From now on, detailed natures in each spatial region and of each mode should be investigated, together with the information of the radial electric field and/or plasma rotation, in order to identify the instabilities and to clarify the phenomena occurring in the varieties of plasma discharges.

References

[1] Weisen H, *Plasma Phys. Contr. Fusion* **28** 1147 (1986).

[2] Weisen H, *Rev. Sci. Instrum.* **59** 1544 (1988).

[3] Matsuo K, Tanaka K, Muraoka K and Akazaki M, *Jpn. J. Appl. Phys.* **30**1102 (1991).

[4] Tanaka K et al, *J. Phys. Soc. Jpn.* **62** 3092 (1993).

[5] Truc A et al, *Rev. Sci. Instrum.* **63** 3716 (1992).

[6] Kado S et al, submitted to *Jpn. J. Appl. Phys.*

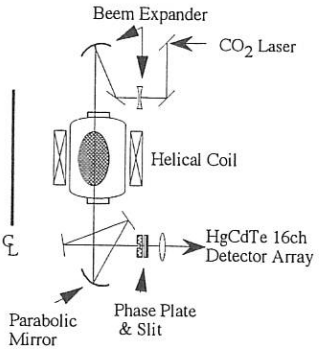

Fig. 1. Optical system of the Laser Phase Contrast Method installed on the Heliotron E device.

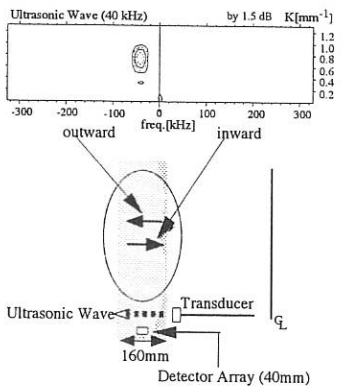

Fig. 2. S(K,f) spectrum for a ultrasonic wave having the frequency of 40 kHz. Transducer is placed towards the inboard side of the torus.

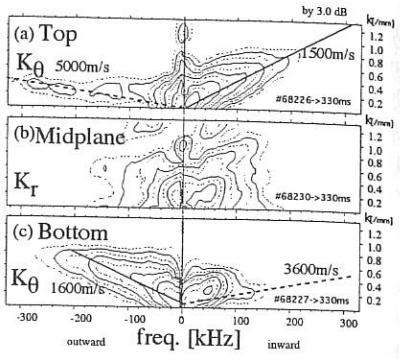

Fig. 3. S(K,f) spectra. Each position is centered at (a)r/a=+0.9, (b)r/a=0, and (c)r/a=-0.9.

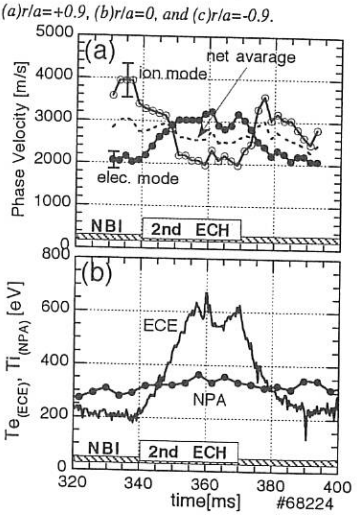

Fig. 4. Temporal evolution of parameters over a period including the 2nd ECH phase. (a) phase velocities of electron and ion modes. "net average" is a mean value of these two modes. (b) Te(ECE), and Ti(NPA).

Spectroscopic Determination of Ion Temperatures in the Divertor of ASDEX-Upgrade

G. Lieder°, K. Behringer*, Ch. Dorn*, St. Hirsch*, B. Napiontek*, M. Niethammer
U. Schumacher, A. Field*, K. Hirsch, S. de Peña*, A. Kallenbach*, S. Pitcher†
Ph. Verplancke‡, M. Weinlich*, NI Group* and ASDEX Upgrade Team*
Institut für Plasmaforschung der Universität Stuttgart, Pfaffenwaldring 31, 70569 Stuttgart
**MPI für Plasmaphysik, Garching und Berlin; †CFFTP, Toronto; ‡Belgian N.F.W.O.*
° now at OSRAM GmbH, Hellabrunnerstr. 1, 81536 München

1. Introduction

The knowledge of the detailed plasma parameter distributions, the plasma behaviour and the dominant processes in the divertor region of toroidally confined plasmas play an increasingly important role in fusion research. High resolution spectroscopy in the divertor of ASDEX-Upgrade aims predominantly at determining the ion temperatures (from Doppler widths [1-4]), the streaming velocities along the magnetic field lines (from Doppler shifts), the divertor plate erosion mechanisms (from molecular spectra), and the impurity transport in the divertor region [5-6] (from absolutely calibrated line emission measurements).

2. High resolution visible spectroscopy in the ASDEX-Upgrade divertor

For sufficiently high spatial resolution in poloidal and toroidal direction the ASDEX-Upgrade divertor is equipped with 32 poloidal lines of sight that predominantly scan the region above the outer divertor plate, while about 50 toroidal lines of sight aim at the observation of the radiation which is emitted nearly parallel or antiparallel to the magnetic field lines. They will be installed during the opening period in summer 95. The poloidally oriented lines of sight view parallel to the outer target plates at distances of 1 to 100 mm with a spatial resolution as low as 1 mm near to the tiles and about 5 mm at greater distance thus covering the X-point area. The scheme of the lines of sight in ASDEX-Upgrade is given in Fig. 1. The plasma emission is integrated along the lines of sight by quartz lenses, collected onto quartz fibres, and fed to the detector systems. There are two spectrometers with low spectral resolution in operation, a 1 m spectrometer equipped with a 2D CCD camera for survey spectroscopy and an interference filter device coupled to two photomultiplier arrays for

measuring the spatial emission profile with high time resolution. The high resolution instrument is a 1.5 m Echelle spectrometer fitted with an intensified 2D CCD camera. Its resolution is about $\lambda/\Delta\lambda \approx 10^5$, which gives a $\Delta\lambda$ of 2 pm at the low end of the wavelength range of 220 nm to 850 nm to be observed. This allows to determine ion temperatures down to about $T_i \approx 20$ meV and ion streaming velocities as low as $v_i \approx 500$ m/s. Here we report on the first results of the poloidal system, which is already in operation.

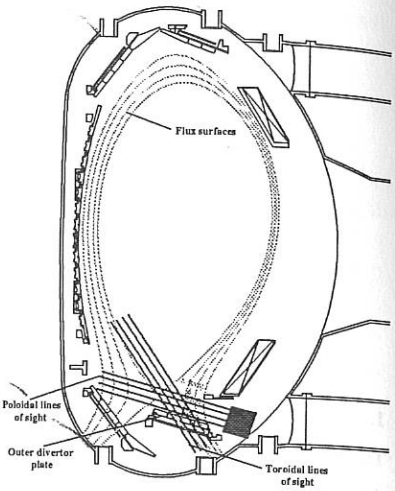

Fig.1: Scheme of poloidal and toroidal lines of sight in the ASDEX-Upgrade divertor

3. First results

The first measurements from high resolution spectroscopy near to the outer divertor plate in the poloidal plane offer informations on the isotope ratio of hydrogen, on the ion temperature distribution, on the erosion mechanisms and on the local magnetic field strength.

The high spectral resolution allows not only to determine the important isotope ratio of H to D but also to analyze the hydrogen energy distribution. Fig. 2 shows an example of the measured spectrum of D_α and H_α in the ASDEX-Upgrade divertor together with the fit composed of the convolution of the instrumental profile onto the fine structure components and the line splitting by the

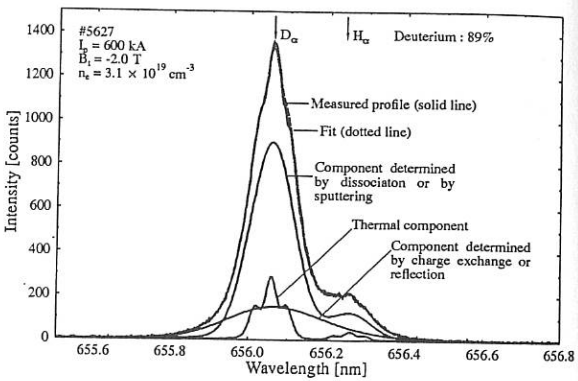

Fig.2: High resolution measurement of hydrogen isotopes

Paschen Back effect. These multiple splitted line profiles will be convoluted by Gaussian functions for three temperatures fitted onto the measurements by optimizing these temperature components. The three temperatures are related to the thermal component (thermally released hydrogen atoms from the plasma facing surface), the component given by the molecular dissociation or by sputtering as well as to the component determined by charge exchange or by reflection (high energy part). These results from measurements on atomic line intensity are supported by the measurements of molecular bands as those of CD and CH for determining the isotope ratio, CD and C_2 for investigating the erosion mechanisms.

Since the ion temperatures T_i near to the divertor plates are relatively low (according to the aim) the choice of spectral lines for these Doppler profile measurements has to be quite careful. A good candidate for the determination of T_i from spectral emission profiles is the singlet line of C III ($2p\ ^1P^o$ - $2p\ ^1D$) at 229.687 nm because of its simple Zeeman pattern and of its Doppler width dominating clearly the line profile. In contrast, other spectral lines show the importance of Zeeman and Paschen-Back splitting. Furthermore, the C III ions will have the kinetic deuteron temperature, since their ionization times at typically $T_e \leq 40$ eV in the divertor are longer than the equilibration times. Fig. 3 gives an example of the measured line profile of the C III spectral line at 229.687 nm. On the basis of the correction with respect to the instrumental profile and the Zeeman splitting the Doppler width and hence the ion temperature can be inferred, which is demonstrated by the excellent agreement between of the measured and calculated profiles.

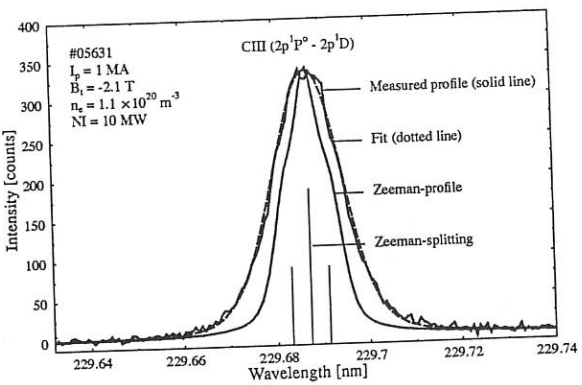

Fig.3: Measured C III line profile with its Gaussian fits including the Zeeman splitting

By this method spatial T_i profiles were determined from regions close to the target tiles up to the X-point. During discharges with additional heating only a slight increase of T_i less than a factor of 2 was observed towards the X-point.

Special emphasis was put on the investigation of H-mode discharges with feedback-controlled radiative boundary layers by means of Ne and D_2 puffing in the midplane. Fig. 4 shows an example of the ion temperature distribution in the divertor region with and without Ne puffing demonstrating the cooling of the divertor plasma by controlled impurity injection. By means of Ne injection, T_i decreases over the entire profile due to the enhanced radiative power losses during this CDH-mode operation [7]. The maximum drop is at the X-point, where T_i approximately halves.

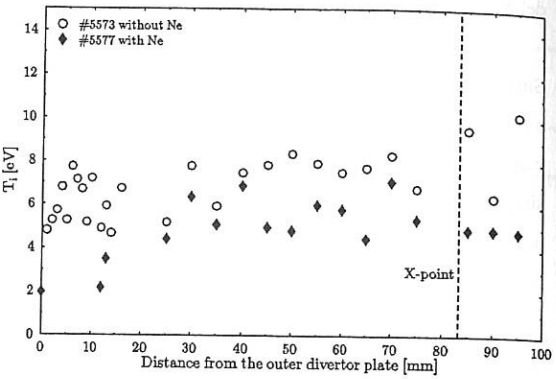

Fig.4: Ion temperature deduced from Doppler widths of C III versus the distance from the outer divertor plate with and without Ne puffing

The presented results together with those from the high resolution spectroscopy using the toroidal lines of sight in the ASDEX-Upgrade divertor in combination with the divertor modelling will certainly contribute to a better understanding of the divertor physics and the CDH-mode operation.

References:

[1] G. Fußmann et al., J. Nucl. Mat. **128** & **129** 350-358 (1984)
[2] P. Bogen, D. Rusbüldt, U. Samm, J. Nucl. Mat. **162-164** 345-349 (1989)
[3] J.D. Hey, Y.T. Lie, D. Rusbüldt, E. Hintz, Contr. Plasma Phys. **34** 725-747 (1994)
[4] A.R. Field, G. Fußmann, J.V. Hofmann, Report IPP III/165 (Dec. 1990).
[5] G. Lieder et al., Europhys. Conf. Abstr. **17C**, Part II, 579-582 (1993)
[6] G. Lieder et al., Europhys. Conf. Abstr. **18B**, Part II, 222-225 (1994)
[7] O. Gruber et al., Phys. Rev. Lett. 74 4217 (1995)

Multichannel YAG Thomson Scattering on CHS

I Yamada, K Narihara, T Minami, K Yamauchi, R Akiyama, A Ando*, A Ejiri,
M Fujiwara, K Ida, H Idei, H Iguchi, S Kubo, R Kumazawa, K Matsuoka, T Morisaki,
S Morita, S Muto, K Nishimura, S Ohdachi, S Okamura, T Ozaki, S Sakakibara,
C Takahashi, K Tanaka, J Xu, and T Watari
National Institute for Fusion Science, Nagoya 464-01, Japan

1. Introduction

Thomson scattering is one of the most reliable methods and widely used for the measurements of electron temperature and density of laboratory plasmas. We have installed a multichannel YAG Thomson scattering [1] on the Compact Helical System (CHS). A unique optics arrangement with oblique backward scattering has been adopted to keep experimental flexibility in the helical magnetic configuration. The whole electron temperature and density profiles of CHS plasmas can be obtained at every 4 msec during a single shot. The YAG Thomson scattering and its first application to CHS plasmas are described.

2. CHS YAG Thomson Scattering

The CHS YAG Thomson scattering device is mainly composed of five Nd:YAG lasers, photon collection optics, twenty four polychromators and CAMAC based data acquisition system, as shown in Fig.1.

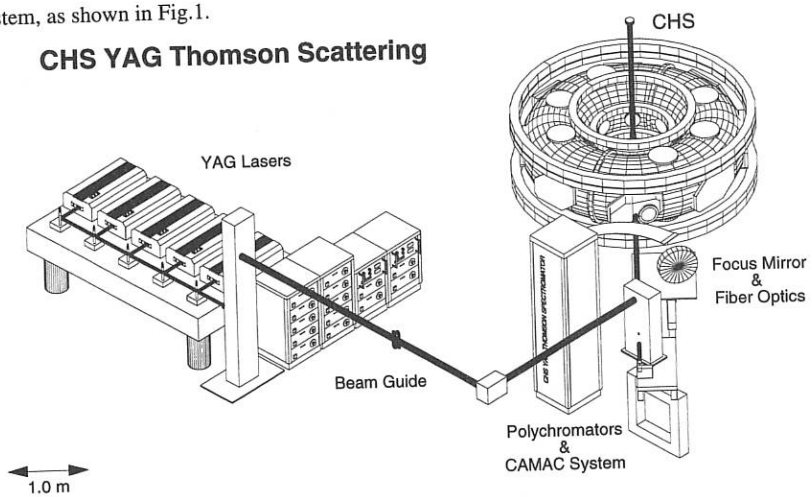

Fig.1: CHS YAG Thomson scattering

As geometrical configurations of helical systems are complicated, we have selected an oblique backward scattering configuration (163° at the plasma center). Both laser entrance and viewing windows are located on the same horizontal port on CHS.

2.1. YAG Laser

Five Nd:YAG lasers with the repetition rate of 50 Hz, the pulse energy and width of 0.5 J and 10 nsec, respectively, are used. We have designed a beam packing mirror like the multilaser system in the Doublet-III Thomson scattering [2]. This mirror can be mounted on a high-resolution mirror mount. A dielectric 14x20 mm^2 elliptic mirror is formed on an AR-coated glass of 80 mm diameter, and the position of the mirror area is different for each laser to allow upstream laser beams to pass through. In the regular operation, the five lasers are triggered successively at every 4 msec, i.e., the five lasers are used as a single 250 Hz laser. By adjusting the trigger sequence, various operational modes are possible.

2.2. Photon Collection Optics

In CHS experiments, flexible magnetic configurations are possible, for example, the major radius of vacuum magnetic axis is 92 cm in the standard configuration, and the axis position can be widely shifted from 89 to 102 cm. Backward scattering configuration is suited for getting wider observation range. However, the spatial resolution becomes worse on the contrary. We have selected the scattering angle to be 163° at the major radius after consideration. In the configuration, we can observe the whole electron temperature and density profiles from the end to end along the laser beam with the spatial resolution of about 20 mm at the plasma center.

A large (500 mmϕ) Au-coated mirror is utilized to collect feeble Thomson scattered photons efficiently. The solid angle is about 50 msr for the plasma center. To minimise the aberrations for all viewing positions over 600 mm, the mirror is set so that the center of the mirror sphere is located at a CHS viewing port (200 mmϕ), which serves as a pupil. The collected photons are transmitted to polychromators through twenty four optical fibers.

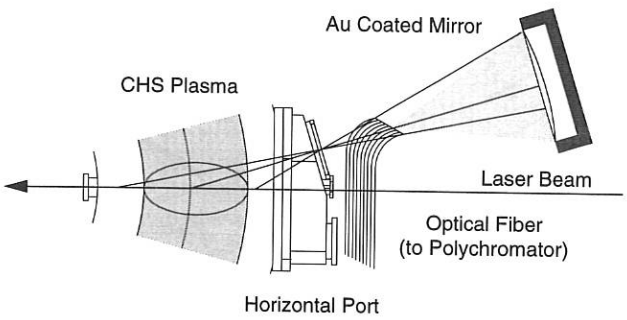

Fig.2: Schematic diagram of the collection optics (top view)

2.3. Polychromator

A filter polychromator with three wavelength channels, similar to the system for the Doublet-III Thomson scattering [3], has been developed. There are four different filter combinations optimised for the temperature ranges: 5-50, 20-200, 100-500 and 200-2000 eV. Avalanche photo diode detectors with high quantum efficiency (80-40 % at λ=900-1060 nm) and wide bandwidth (25 MHz) are used for photon detection. The relative spectral sensitivities for each wavelength channel in a polychromator have been calibrated with a tungsten standard lump and monochromator.

Stray photons are successfully suppressed owing to the high cut-off filter used, whose rejection rate against the incident laser wavelength is below 10^{-5}. In addition, the wavelength shift in backward scattering is larger than that in right-angle scattering, contributing to the stray light suppression. Typical signal to noise ratio is about $10\text{-}10^2$ for intermediate temperature and density plasmas heated by NBI (~300 eV and ~3×10^{13} cm^{-3}), which depends mainly on the observation position (inner region worse).

The relative error of measured temperature is estimated to be less than 5 % from the calculation based on the model spectra of Thomson scattering which takes account of the relativistic blue shift, and spectral sensitivities for each wavelength channel.

2.4. Raman Calibration

For absolute measurements of electron densities, we have calibrated the YAG Thomson scattering by using anti-Stokes rotational Raman scattering in molecular hydrogen [4][5]. The calibration has been carried out at several pressures up to 400 Torr at room temperature . A clear liner dependence of the Raman intensities on sample pressure has been obtained. The calibration factor has been determined from the gradient of the pressure dependence and spectral sensitivity for each channel. Because the three polychromators for the lowest temperature range have no wavelength channel which observes the Raman transition, the factors have not been obtained. The angular distribution of Raman scattered photons differs form that for Thomson scattering, resulting in the difference of effective collection efficiencies of scattered photons. The correction to it has been also taken into account. The measured electron densities are reasonably consistent with those by an HCN interferometer. However, some improvements are needed for higher reliability and accuracy.

3. Application to the CHS Plasmas

Fig.3 demonstrates an example for the measurements of the temporal evolutions of electron temperature, T_e, and density, N_e, profiles of CHS plasmas. In the discharge, a target plasma produced by ECH was heated by NBI (1.0 MW) at 25-145 msec. The magnetic field and axis were set at 1.7 T and 92 cm, respectively. The plasma stored energy of about 2 kJ was sustained from 50 msec to the end of the discharge, resulting in nearly constant β-value of 0.18 % during the time. It is clearly observed that the electron temperature profile is nearly

parabolic while the density profile has a broad double peaked 'hollow' profile. The respective peaking factors for the temperature and density profiles defined by,

$$\frac{T_e(R_{ax})}{\frac{1}{w}\int T_e(R)dR} \quad \text{and} \quad \frac{N_e(R_{ax})}{\frac{1}{w}\int N_e(R)dR}$$

where w is the width between both ends, are 1.54 and 1.15 at 120 msec. Both the center axes of the profiles have been observed to be slightly shifted outward from the vacuum magnetic axis due to the Shafranov (finite-β) shift [6]. The observed axis shift of about 1 cm at 120 msec agrees with that calculated by the 3D equilibrium code VMEC.

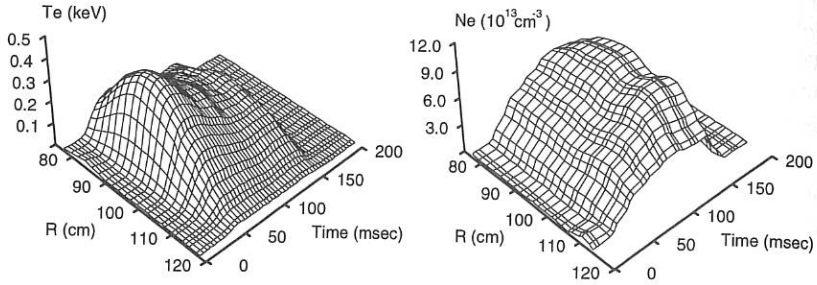

Fig.3: An example for the temporal evolutions of the electron temperature T_e and density N_e profiles of an NBI heated plasma measured with the YAG Thomson scattering

4. Summary

The multichannel-multilaser YAG Thomson scattering has been successfully applied to the measurements of the temporal evolutions of the electron temperature and density profiles of the CHS plasmas. Finally, it is noted that the CHS YAG Thomson scattering is also served as a prototype for the Large Helical Device.

References

[1] Narihara K *et al.*, *Rev. Sci. Instrum.*, to be published (1995)

[2] Trost P K *et al.*, *Rev. Sci. Instrum.* **61** 2864 (1990)

[3] Carlstrom T N *et al.*, *Rev. Sci. Instrum.* **61** 2858 (1990)

[4] Röhr H, *Phys. Lett.* **81A** 451 (1982)

[5] Yamaguchi T and Yanagisawa I, *Jpn. J Appl. Phys.* **24** 1528 (1985)

[6] Yamada H *et al.*, *Nucl. Fusion* **32** 25 (1992)

* Present address: Faculty of Engineering, Tohoku University, Sendai 980, Japan.

In Situ Measurement of a Neutral Beam Divergence Using the Spectral Asymmetry in Motional Stark Effect in a Toroidal Plasma

J.Xu, K.Ida, T.Kawachi[#], H.Ogawa[##] and J.Fujita

National Institute for Fusion Science, Nagoya 464-01, Japan

\# Institute of Physical and Chemical Research (RIKEN), Hirosawa, Wakou, 351-01, Japan

\## Japan Atomic Energy Research Institute, Naka-gun, Ibaraki, 319-11, Japan

1. Introduction

Due to the importance of the measurement of the beam divergence angle to determine the energy deposition profile of a heating beam and the spatial resolution of the plasma diagnostics using the neutral beam, several methods have been developed to measure it. The calorimetry is the most common tool on this aspect and the spectroscopic method[1] to measure the Doppler width of the beam emission is also often applied to determine the beam divergence angle before the plasma discharge. A recent example of the measurement was given by an experiment carried out on TEXTOR[2], where the total beam profile was measured using a carbon graphite plate inside the torus and the beam emission spectrum was measured for the deduction of the power ratio and the two-dimensional divergence angle of the three beam species. As to determine the beam divergence angle in a toroidal plasma, only one method is available so far [3] because the spectrum of the beam emission is complicated due to the motional Stark effect (MSE).

Recently, it has been recognized in our research that all fine components on both sides of the central σ_0 component of the MSE spectrum in the plasma are asymmetric owing to the finite beam divergence angle[4]. The difference of the wavelength width of the two π or σ lines on both sides of the σ_0 line is proportional to the beam divergence angle if the magnetic field in the viewed region is uniform and the beam attenuation is negligible in the plasma. The difference will be enlarged if the variation of the magnetic field is taken into account. This effect is useful to determine the divergence angle by comparison of a simulation and a measured spectrum of the beam emission in a toroidal plasma.

2. Brief overview of the simulation of beam emission in a plasma

In a plasma, the Balmer α line of an injected beam emission is mainly split into nine components and is polarized by an induced Lorentz electric field $\mathbf{E} = \mathbf{v} \times \mathbf{B}$[5]. The π component shows parallel polarization when it is observed transversely and the σ component is polarized perpendicularly to the electric field. The polarization direction of the σ component in the simulation is given by vector $\mathbf{G} = \mathbf{E} \times \mathbf{s}$ and that of the π component is obtained by rotating the vector around the viewing line by 90°. Here, $\mathbf{s}$ is a unit vector along the viewing line.

Because the beam is made up of a lot of beamlet, the simulation of the beam emission is based on the considerations for each beamlet. Considering that the optical system consists of a polarizer and a spectrometer, the spectrum of the beam emission, $I(\lambda)$, is given by

$$I(\lambda) = \sum_{m} \sum_{j=1}^{3} \sum_{k=1}^{9} \int\int_{V,\Omega} \left(U^{mjk}(\lambda') \cos^2 \alpha_{mk} \right) L(\lambda - \lambda') d\Omega dV . \qquad (1)$$

Here, the integration is over the region of (V, Ω, k, j, m). V is the volume of the viewed region of the beam emission and Ω is the solid angle of an object lens. 'k', 'j' and 'm' label the k-th

component of the MSE spectrum, beam species with the j-th energy of the full energy beam and the beamlet output from the m-th aperture of the grid of the beam ion source, respectively. α_{mk} is the tilted angle of the polarization direction of the k-th MSE line of the m-th beamlet emission at the observed position with respect to the transmission direction of the polarizer. 'L' is the instrumental function of the spectrometer. $U^{mjk}(\lambda')$ is the emissivity of the line with the wavelength of λ' per unit solid angle in the direction of the line of sight and is determined by

$$U^{mjk}(\lambda') = b_k n_{mj} n_e Q_{eff}, \qquad (2)$$

where all of the parameters are those at the position of the beam emission. b_k is the branch ratio of the transition of the k-th line per unit solid angle in the direction of the line of sight, which is a function of the angle between the induced electric field and the viewing line, and n_e is the electron density, which is assumed to be equal to the density of the bulk ion. Q_{eff} is the effective excitation rate of the beam including the contributions of the ion and electron impact. n_{mj} is the beam density of the j-th species of the m-th neutral beamlet and is expressed as

$$n_{mj} = \frac{J_{mj}}{\pi e v_j d_m^2 \varepsilon_j^2} \exp\left(-\theta_m^2/\varepsilon_j^2\right) \exp\left(-\int_0^{l_m} \sigma_j n_e dl\right), \qquad (3)$$

where J_{mj} is the total current of the j-th species of the m-th beamlet and ε_j is the divergence angle of the j-th species of all beamlets, θ_m and d_m are the angle of the beam path with respect to the beamlet axis and the distance between the m-th hole of the beam ion source and the point of the beam emission, respectively. 'e' is the charge of an electron. The final exponential term in the formulas (3) describes the beam attenuation in the plasma, where σ_j is the total ionization cross section due to the charge exchange, ion and the electron impact. λ', the Doppler shifted wavelength of the k-th MSE line of the j-th beam species emission of the m-th beamlet at the considered location, is given by

$$\lambda' = \lambda_0 (1 + \frac{v_j}{c} \cos\beta_m)(1 + a(k) v_j B \lambda_0 \sin\zeta_m). \qquad (4)$$

Here, ζ_m and β_m are the angle between the beam and the magnetic field and the angle between the beam and the line of sight, respectively. a(k) is the coefficient for the k-th line splitting[5], λ_0 is wavelength of the H_α line (6562.79 Å) and c is the light velocity.

3. Determination of the divergence angle of a hydrogen beam in JFT-2M

The experiment is performed using a hydrogen beam on the JFT-2M tokamak[6]. Figure 1 shows the experimental setup. The major radius of the tokamak is 1.31 m and the minor radius is 0.29 m. The toroidal magnetic field is 1.3 T and the total plasma current is 227.8 kA. The beam, 32 keV, consists of 1050 beamlets (ϕ4) and intersects the magnetic field at 40.3° at the plasma center. The diameter of the beam at the grid of the beam ion source is 0.185 m and the focal length is 2.80 m. The optical system consists of a 20mm-diameter lens, 0.1mm-diameter fiber, a polarizer, tilted by 90° with respect to the horizontal direction, and a spectrometer with the instrument function of full width at half maximum (FWHM), $\Delta\lambda_s$, of 0.76 Å. The viewing line is aligned by intersecting the beam at 29.9° at major radius of R_0.

Figure 2 shows a measured π spectrum of the beam emission in the plasma after subtraction of background of the plasma H_α emission including that of the charge exchange recombination

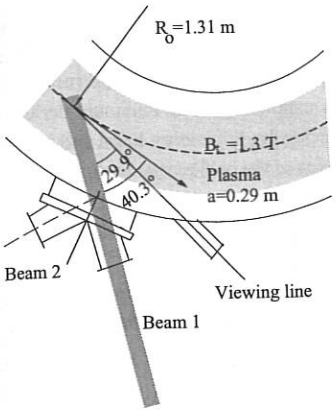

Fig. 1 The schematic of the experiment arrangement on JFT-2M.

of the plasma ion. The impurity emission of C II ion

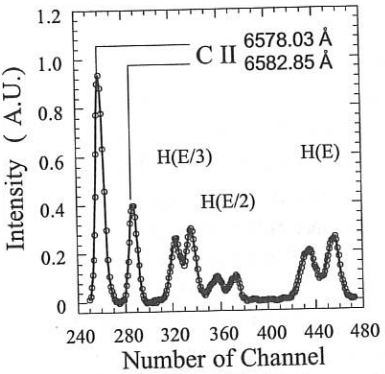

Fig. 2 The observed π manifolds of the beam emission using a polarizer tilted by 90° horizontally.

from the plasma edge is also shown in the Figure 2, from which the wavelength dispersion of 0.176 ± 0.001Å per channel of the spectrometer is obtained in the interested wavelength region. Due to the large Doppler shift, the beam emission is well separated into the three parts corresponding to those of the three species, H(E), H(E/2) and H(E/3), of the beam with full, half and one third energy. The separations of the MSE lines are small, all of the π components are grouped into the two manifolds on both sides of the central σ_0 line.

The measured spectrum were compared with a simulation. It is assumed that i) the profile of the plasma current density is a cube of parabola, ii) current of the all beamlets is same and the energy variation of the beam is negligible and iii) the instrumental function of the spectrometer is

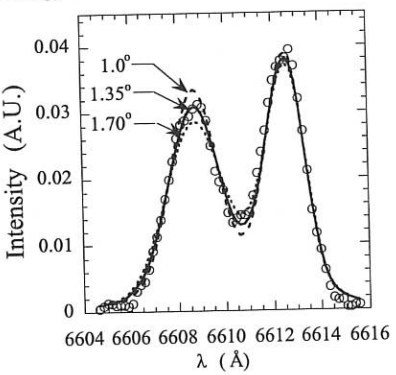

Fig.3 The comparison of the measured π spectrum of full energy beam emission and simulation with the beam divergence angle as the indicated.

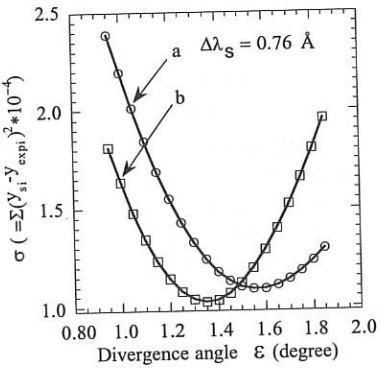

*Fig.4 The derivation in the normalized spectrum between the simulation and measurement. The curve **a** is that for the spectrum of H(E/3) and the **b** is that for the spectrum of H(E).*

a Lorentz function. The measured plasma electron temperature and density profile are used to calculate the beam attenuation and excitation in the plasma. Figure 3 shows a comparison of the

measured and simulated spectra of the full energy beam emission with the indicated divergence angles. The beam divergence angle is obtained from the best fit. Figure 4 depicts the deviation between the normalized spectrum of the measurement and the normalized spectrum of the simulation vs. the beam divergence angle. The value corresponding to the minimum derivation is taken as the expected beam divergence, which is 1.35° for the full energy beam and is 1.55° for the one third energy beam. Because the photon statistics of the half energy beam emission is not good enough, it is found difficult to determine its angular divergence.

4. Uncertainty in the determination of the divergence angle

The uncertainties of the determined divergence angle may come from the assumptions in our simulation. Since the observed position of the beam emission is at the plasma center, the spatial resolution of the measurement is about 4.0 cm, the uncertainty induced by the assumption i) is negligible. The accuracy of the divergence angle depends on the current uniformity of all the beamlets and the accuracy of the wavelength resolution of the spectrometer. In the case that the current of edge beamlet is smaller than that of the beamlet in the central region of the ion source, the divergence angle will be enlarged for the best fit. Our simulation shows that the divergence of the full and the third energy beam is enlarged by about 4% in an extreme case that the width of the beam ion source is reduced by 5%. The uncertainty of the divergence angle is 0.05° and 0.08° for the two beams, respectively, if the uncertainty of the FWHM value of the spectrometer is 5%. The error bars of the beam divergence related to the quantity of the photon statistics of the spectrum are also estimated, which are 0.01° and 0.03° for the two beams, respectively.

5. Summary

The work of *in situ* determination of the divergence angle of a neutral beam in a toroidal plasma is presented in this paper. The spectral asymmetry of the π manifolds of the beam emission is demonstrated to be sensitive to the beam divergence angle by our simulation using a newly developed code involving the detailed knowledge of the atomic physics. By comparing the simulation and the measured spectrum of the beam emission in the JFT-2M plasma, the value of the divergence angle of the full energy beam and that of the one third energy beam are obtained and the uncertainties in the determination of the beam divergence are analyzed.

Acknowledgements

One of the authors (J.Xu) would like to express thanks to Professor M. Fujiwara for his encouragement during this work, Professor T. Kuroda for the many beneficial discussions and Dr. A. Ejiri as well. This work is supported by Grant-in-Aid for Science Research (B) from Ministry of Education, Science and Culture, Japan.

References

[1] G. Bracco, C. Breton, C. de Michelis, M. Mattioli, and J. Ramette, J. Opt. Soc. Am. **71**,1318 (1981).

[2] H. Euringer and Ph. Verplancke, Rev. Sci. Instrum. **65**, 2996 (1994).

[3] R. C. Wolf, D. Ciric and R. W. Konig, JET-P 68(1994).

[4] J. Xu, K. Ida and J. Fujita, NIFS-**349**(1995).

[5] E. U. Condon and G. H. Shortley, The Theory of Atomic Spectra (Cambridge University, Cambridge, 1963).

[6] S. Takatoshi et al, JAERI-M 87-005

First results with the rotating polarization polarimeter at RTP

J.H. Rommers, J. Howard[1], M. Drabbe, F.A. Karelse, A.J.H. Donné

FOM–Instituut voor Plasmafysica, P.O. Box 1207,
3430 BE Nieuwegein, The Netherlands
[1] Permanent address: Plasma Physics Laboratory, Australian
National University, Canberra A.C.T. 0200, Australia

Introduction

The current density distribution in tokamak plasmas plays a crucial role in determining the plasma equilibrium and its stability. The current profile can be derived from a measurement of the Faraday rotation of the plane of polarization of far-infrared laser radiation transmitted through the plasma (polarimetry). Other methods, such as measurement of the Zeeman splitting of ionic energy levels, tangential Thomson scattering, or the motional Stark effect, have also been attempted but only the last one is used routinely at present.

Many schemes have been proposed for the difficult measurement of the typically small Faraday rotation angles[1]. Nowadays, the development of new methods is directed towards techniques that actively modulate the polarization vector, before sending the beam through the plasma. This offers the advantage that both the interferometer phase shift and the Faraday rotation can be measured using a single detection element for each probing beam - an almost essential requirement in multi-beam systems.

At the Rijnhuizen Tokamak Project (RTP) a new polarimeter scheme has recently been developed and implemented[2], which is similar in spirit to earlier schemes by Dodel and Kunz[3] and by Rice[4]. The problem of crosstalk from the polarimeter into the interferometer data, which existed in both of these schemes, is now eliminated, and in principle a very high temporal resolution can be obtained.

Method description

In the method recently developed and implemented at RTP, a total of three far-infrared (FIR) lasers has been applied. Two of the laser beams are used for probing the plasma, whereas the third one acts as a local oscillator. A slight frequency difference between all three lasers is introduced, such that after detection three frequency multiplexed beat signals are obtained.

Since the RTP polarimeter is intended for current density measurements, the geometry is such that the probing beams propagate nearly perpendicular to the total magnetic field. As a consequence, the characteristic propagation modes of the beams in the plasma are to a good approximation counter-rotating circularly polarized waves, each experiencing a slightly different refractive index. By setting the polarization of each of the probing beams equal to one of the characteristic polarizationsof the plasma, it is then possible to measure both refractive indices simultaneously. Due to the frequency offsets, the information on the two refractive indices is spectrally resolved and can be retrieved by separating the carriers after detection and performing a separate phase measurement on each.

As stated above, the detected spectrum will consist of three frequency bands, that need to be well separated. Two of the bands are due to mixing of the local oscillator beam

with each of the probing beams. The phase change of these beams can be averaged to give the interferometer phase change, or be substracted to give twice the polarimeter phase change. The third spectral band carries direct information on the difference between the two refractive indices and thus on the Faraday angle.

Experimental setup

The RTP tokamak (R_o = 72 cm, a = 16.4 cm, $I_p \leq$ 150 kA, $B_t \leq$ 2.5 T) is equipped with a heterodyne FIR interferometer operating at 432.5 μm. This interferometer has recently been extended with a three-laser polarimeter. Separate cavities, pumped by a single CO_2 laser, are used for generating the probing beams and the local oscillator beam. The probing beams are combined and then expanded using parabolic optics to fill the RTP ports. Up to 20 Schottky diode corner-cube mixers are used for polarization sensitive detection of the slab beam. The width of the laser transition allows frequency offsets (IF) up to several MHz between the various laser beams to be obtained by slightly detuning the relative cavity lengths.

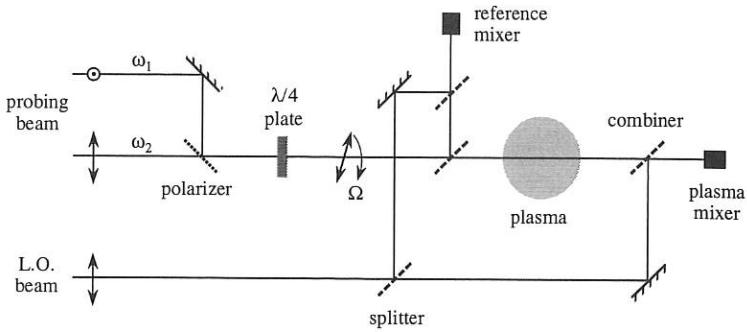

Figure 1: Schematic one-channel depiction of the three laser setup recently implemented at RTP. The two probing beams are made orthogonally linearly polarized, and are then combined using a polarizing grid. Then the beams are sent through a half wave plate, oriented at 45° to either polarization, so that counter-rotating circularly polarized waves are obtained.

The measured signals are directly acquired at a digitization rate of 500 kHz without any electronic signal processing other than amplification and bandpass filtering (200-5000 kHz). For the data presented here, the laser IF's were set such that both probe-L.O. mixing peaks were in the 500-750 kHz region. As a result the mixing between the two probes gave a much lower beat frequency, that was strongly filtered and therefore, not used. Due to the relatively slow sampling rate, the frequency peaks were aliased down. Care was taken that this did not lead to an overlap between the peaks, so that all information was preserved. The two peaks were then computationally isolated using bandpass filters and separately demodulated. The phases were extracted by dividing the corresponding analytic signals[5].

First results

For calibration and testing purposes a stepper-motor driven rotating half wave plate can be inserted in the probing arm to simulate a stepwise increase of the Faraday rotation. The results of this calibration for several channels are given in Fig. 2.

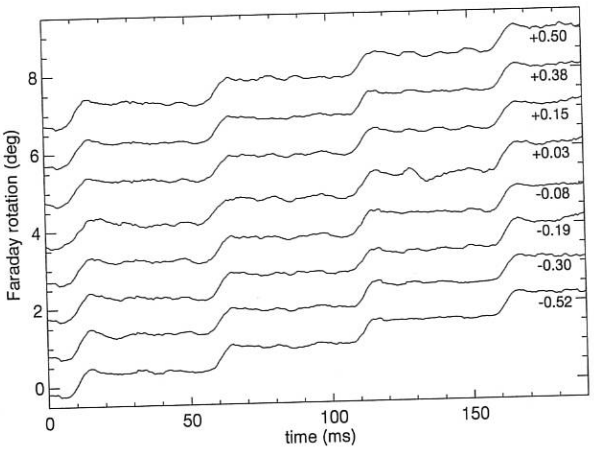

Figure 2: Calibration traces for a few polarimeter channels at various radial positions. For each trace the r/a ratio is indicated. Filtering has been performed at $\approx$ 400 Hz.

The waveplate movement is clearly visible on all channels. The strong filtering was needed to eliminate some disturbance peaks that are believed to be due to the aliasing. The spectrum namely suffers from peaks at the second harmonic of the mixer signals, due to the non-linear diode characteristic. Even though these peaks are over 40 dB down, the spectrum is somewhat disturbed. With better frequency stabilization of the laser and possibly electronic signal analysis this problem will be solved in the future, making a much higher temporal resolution possible.

Some first measurements on the RTP plasma have been performed. Using the 110 GHz gyrotron, 400 kW of additional heating was deposited at half the minor radius (Ohmic input $\leq$ 200 kW). In this way the temperature and current profile were strongly reshaped, since much current was expelled from the plasma centre. A strong decrease of the central slope of the current profile was indeed observed (Fig. 3).

In conclusion it may be stated that a new method for doing polarimetry has been developed and implemented at RTP. This method, although not yet optimally functioning, has the potential of high temporal resolution polarimetric and interferometric measurements, limited only by the natural linewidth of the laser line. In practice this resolution will be limited by the S/N that is desired, and is expected for the RTP system to be of the order of 10 kHz for a measurement accuracy of 0.1 degrees. If the algebraic equations underlying the method are evaluated, it is clear that crosstalk problems are not to be

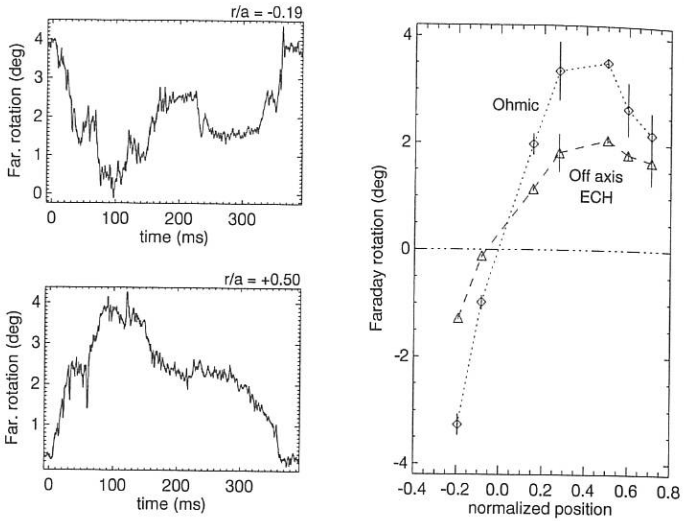

Figure 3: Time traces and Faraday rotation profiles for a discharge where 400 kW of ECH power was deposited at half the minor radius between 150 and 225 ms. The profiles were determined by averaging over 20 ms at 100 and at 200 ms. Other measurements (e.g. Thomson Scattering) show a slightly hollow temperature profile, from which a q-value on axis of just below 4 could be determined. (I_p = 80 kA, $n_{e,o}$ = 6-9 $\cdot 10^{19}$ m^{-3})

expected, in contrast to earlier methods[2]. Furthermore only one detector per channel is required.

Acknowledgement

It is a great pleasure to acknowledge Scott Burns for his expert technical advice on the construction of a triple far-infrared laser.

This work was performed as part of the research programme of the association agreement of Euratom and the 'stichting voor Fundamenteel Onderzoek der Materie' (FOM) with financial support from the 'Nederlandse organisatie voor Wetenschappelijk Onderzoek' (NWO) and Euratom.

References

1. A.J.H. Donné, Rev. Sci. Instrum. **66 (6)**, 3407-3423 (1995).
2. J.H. Rommers and J. Howard, *in preparation.*
3. G. Dodel and W. Kunz, Infrared Phys.; 18, 773-776 (1978).
4. B.W. Rice, Rev. Sci. Instrum. **63 (10)**, 5002-5004 (1992).
5. J. Howard, Infrared Phys. **34**, 175-189 (1992).

Diagnosis of nonthermal ECE by means of combined LFS ECE, HFS ECE and ECA measurements

J.F.M. van Gelder, E. Westerhof, A.J.H. Donné and RTP-Team
FOM-Instituut voor Plasmafysica "Rijnhuizen", Association Euratom-FOM,
P.O. Box 1207, 3430 BE Nieuwegein, The Netherlands

1 INTRODUCTION

To investigate the behaviour of the 2^{nd} harmonic electron cyclotron emission (ECE) and absorption (ECA) in the RTP tokamak, a 20-channel heterodyne radiometer is being applied. The electron cyclotron emission can be measured from both the high field side (HFS) and the low field side (LFS). LFS ECE X-mode and ECA are measured simultaneously. A comparison of HFS and LFS X-mode emission provides information on the nonthermal ECE. Macor viewing dumps at either side of the vessel eliminate multiple-pass reflections of the ECE and standing waves between the two antennae. When viewed from the LFS, the nonthermal EC emission is reabsorbed at the thermal resonance layer. As the nonthermal population itself is optically thin, nonthermal radiation can travel freely towards the HFS antenna. This implies that the radiation temperatures T_{hfs} and T_{lfs} are given by:

$$T_{hfs} = T_e \cdot \left(1 - e^{-\tau}\right) + I_{sth}, \tag{1}$$

$$T_{lfs} = T_e \cdot \left(1 - e^{-\tau}\right) + I_{sth} \cdot e^{-\tau}, \tag{2}$$

and therefore,

$$I_{sth} = \frac{T_{hfs} - T_{lfs}}{1 - e^{-\tau}}, \tag{3}$$

where T_e is the electron temperature, τ the optical depth and I_{sth} the suprathermal radiation intensity. The combination of LFS ECE, HFS ECE and ECA allows a clear identification of the EC emission contribution from the nonthermal part of the electron distribution. The effect of ECRH on the creation of suprathermals is regarded.

2 EXPERIMENTAL SETUP

The antenna system of the ECE/ECA setup, consists of an open-ended circular waveguide at the low field side (LFS) and a hog-horn antenna at the high field side (HFS) of the torus, mounted in the equatorial midplane [1]. The HFS and LFS antennae are connected to the radiometer through a switch board. By means of waveguide switches, three different ECE-measurements can be performed: 1) LFS X-mode ECE, 2) LFS O-mode ECE (using a grid polarizer) and 3) HFS X-mode ECE. For the purpose of measuring ECA, two sweepable sources, which cover the overall bandwidth of the radiometer, are connected to the HFS transmission line. The radiometer is calibrated using a fast magnetic field ramp in a

thermal discharge with sufficiently high density. This is a relative calibration method. The absolute temperature is obtained by scaling the top of the resulting profile with the temperature obtained from Thomson scattering. The HFS ECE signals are calibrated against the LFS signals in the ohmic phase of two comparable thermal discharges. To get a clear view on the effect of ECRH on the creation of nonthermal populations, only discharges were selected, that did not show such a population in the preceding ohmic phase.

3 RESULTS AND DISCUSSION

ECRH is injected from the HFS (60 GHz, X-mode, 125 kW), with a launching angle of 0^o and 25^o. In order to diagnose nonthermal ECE, alternate HFS ECE and LFS ECE+ECA measurements are performed on a shot-to-shot basis. Figure (1) shows nine pictures. From top to bottom (A to C) measurements are presented with line averaged densities of $\overline{n}_e = 1.2$, 1.2 and 0.8 $\times 10^{19}\ m^{-3}$, respectively. The top graphs (A) are measured with an ECRH launching angle of 25^o, the other graphs (B and C) with an angle of 0^o. The left plots show the radiation temperature profiles, measured in the ohmic and ECRH phase. The solid lines depict the LFS view, the dotted lines represent the HFS view and the dots indicate the radiation temperature calculated from Thomson scattering data. During the ohmic phases the radiation temperature profiles viewed from the HFS and the LFS are similar, which indicates a thermal plasma. For $\rho > 0.4$, it can be seen that T_{lfs} surpasses T_{hfs}, which is due to the influence of wave dispersion. The centre plots show the optical depth profiles as measured with ECA in the ohmic and ECRH phase (solid lines) and τ calculated from Thomson scattering data during ECRH (dots). It should be stressed that the LFS ECE spectra and the ECA τ-profiles are measured simultaneously, with a single radiometer, which provides a reliable tool for evaluating eq.(3). The agreement with the τ-profiles deduced from Thomson scattering is good. The right plots show the suprathermal radiation, I_{sth}, as calculated with eq. (3) (solid lines: ohmic; dashed lines: ECRH). For $\overline{n}_e = 0.8 \times 10^{19}\ m^{-3}$ and an ECRH launching angle of 0^o (graph C), the plasma emissivity increases rapidly at ECRH switch-on, although only a weak temperature enhancement occurs of approximately 20% in the centre. The suprathermal radiation shows a maximum of 2.3 keV at $\rho \approx 0.25$. This may correspond to suprathermal electrons with an energy of 20 to 30 keV on the central axis. For $\overline{n}_e = 1.2 \times 10^{19}\ m^{-3}$ (graph B) only a small increase of suprathermal radiation during ECRH is observed. Although a decrease of I_{sth} for increasing density is reported in literature [2, 3], the rate at which the decrease occurs here is much faster. The magnification of the small amount of suprathermals created by ECRH may be caused by an additional influence of the toroidal electric field, which is stronger for low density discharges. In the case of an ECRH launching angle of 25^o (graph A), the plasma is heated much more efficiently.

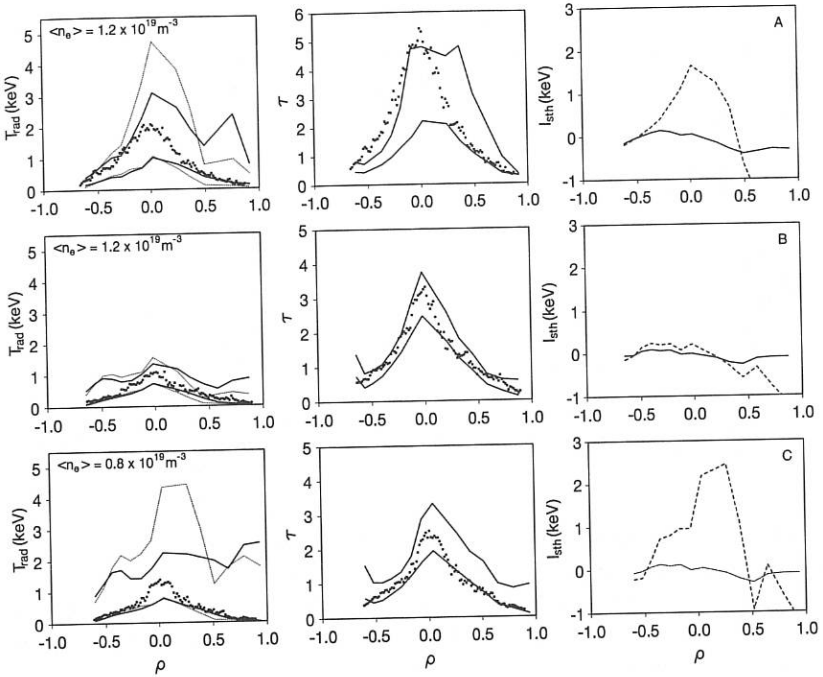

Figure 1: *A: comparison of LFS and HFS ECE for* $\overline{n}_e = 1.2 \times 10^{19}\ m^{-3}$ *and an ECRH launching angle of 25°. The left graph shows the radiation temperature measured with LFS ECE (solid line), HFS ECE (dotted line) and Thomson scattering (dots). The centre graph represents the optical depth measured with ECA (solid lines) and Thomson scattering (dots). The right plot shows* I_{sth} *as calculated with eq. (3). B: same plots with* $\overline{n}_e = 1.2 \times 10^{19}\ m^{-3}$ *and an ECRH launching angle of 0°. C: same plots with* $\overline{n}_e = 0.8 \times 10^{19}\ m^{-3}$*. Throughout the graphs, the lower curves correspond to the ohmic phase and the higher curves to the ECRH phase.*

A suprathermal population is created as a result of ECRH. The nonthermal radiation shows a maximum of 1.6 keV on the central axis. The determination of the responsible electron population from the nonthermal ECE is an ill-posed problem. To address this problem, the measurement is compared with theoretical ECE spectra obtained on the basis of bounced-averaged Fokker-Planck simulations. Figure (2) shows the simulated and measured temperature profiles. The markers represent the measurements. The solid lines indicate the simulated spectra, when no radial transport is taken into account. The dashed lines denote simulations assuming a radial transport, resulting in a heat conductivity $\chi = 0.5\,m^2/s$ in the centre to $\chi = 2.0\,m^2/s$ at the edge. It can be seen

that a large discrepancy exist between the LFS measurement and the simulation. Since $\tau \approx 5$ the LFS observation should be comparable with a thermal spectrum. The found discrepancy can not be explained. The HFS spectra agree fairly well, both qualitatively as quantitatively.

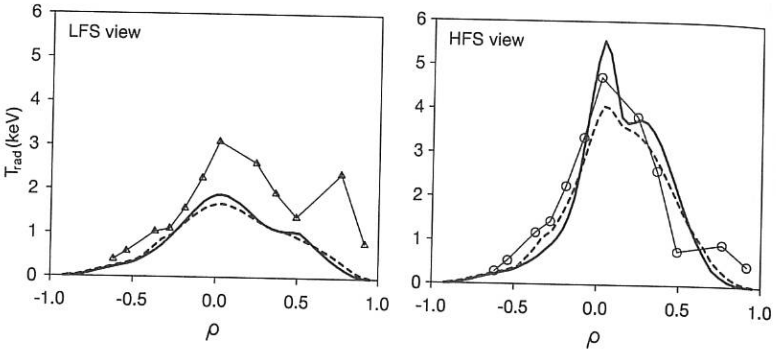

Figure 2: *The left and right picture show simulated and measured temperature profiles, viewed from the LFS and HFS, respectively. For both pictures, the markers represent measurements. The solid lines indicate the simulated spectra, when no transport is taken into account. The dashed lines denote simulations assuming a radial transport, resulting in a heat conductivity* $\chi = 0.5\,m^2/s$ *in the centre to* $\chi = 2.0\,m^2/s$ *at the edge.*

ACKNOWLEDGEMENTS

This work was performed under the Euratom-FOM association agreement with financial support from NWO and Euratom.

References

[1] J.F.M. van Gelder, K.C.E. Husmann, H.S. Miedema, A.J.H. Donné, *The heterodyne radiometer at RTP for Electron Cyclotron Emission and Absorption Measurements*, Rev. Sci. Instr. **66** (1), 418 (1995).

[2] TFR Group and I. Fidone, *Asymmetric electron cyclotron emission from superthermal electrons in TFR tokamak*, Phys. Rev. A **24** (5), 2861 (1981).

[3] M.E. Austin, R.F. Gandy, J.Y. Chen, G. Cima, V. Krivenski, P.E. Phillips, D.C. Sing, *Evidence of Non-Maxwellian Distributions During ECH from ECE Measurements on TEXT*, Bull. Am. Phys. Soc., **35** (9), 2026 (1990).

Modulational Instability of Electromagnetic Waves in Collisional Dusty Plasmas

S. V. Vladimirov and **P. K. Shukla**

Institut für Theoretische Physik, Ruhr-Universität Bochum, D-44780 Bochum, Germany

1. Introduction

Dusty plasmas [1] are characterized as a low–temperature ionized gas whose constituents are electrons, ions and extremely massive micron–sized dust particulates. The latter are usually negatively charged due to the attachment of the background plasma electrons on the surface of the dust grains via collisions. In the presence of waves the plasma currents reaching the surface of the grains assume oscillatory character. Because of the imbalancce of the electron and ion currents, there appears dust charge fluctuations [2,3].

In low-temperature space and laboratory plasmas the electron collisions with heavy charged particles are rather frequent and it turns out that when the frequency of the plasma slow motion is comparable with the electron collision frequency, then enhanced electron temperature perturbations caused by the differential Joule heating [4] of electrons ought to be incorporated in the study of the modulational instability of HF electromagnetic waves. Subsequently, nonthermal density and temperature fluctuations could be simultaneously driven on account of the combined effects of the ponderomotive force and the differential Joule heating nonlinearities. In a collisional dusty plasma, Joule heating nonlinearity might exceed the ponderomotive force nonlinearity.

In this paper, we present an investigation of the modulational interaction between large amplitude electromagnetic waves and quasi-stationary plasma slow motions by incorporating the effects of the dust charge perturbation in an unmagnetized collisional dusty plasma. The quasi-stationary plasma slow response, as considered here, has extremely low phase velocity (in comparison with the electron and ion thermal velocities) and could have a typical frequency of the order of the charging frequency [3], $\nu_{ch} = e(|I_{e0}|/C)(1/T_{e0} + 1/w_0)$, where e is the magnitude of the electron charge, I_0 is the equilibrium electron current reaching the surface of the grains, C is the grain capitance, $w_0 = T_{i0} - e\phi_{f0}$, $T_{\alpha 0}$ is the unperturbed temperature of the particle species α (α equals e for electrons, i for ions, and d for dust grains), and ϕ_{f0} is the is the steady state floating potential of the grains.

2. Formulation

We consider the nonlinear propagation of intense electromagnetic waves in a three–component unmagnetized plasma whose constituents are electrons, ions, and massive ($m_d = \infty$) negatively charged dust grains. The latter are assumed to be point charges and their sizes as well as the inter–grain spacing (r_0) are supposed to be much smaller than the effective Debye radius (λ_D) of the dusty plasma. We neglect the effects of a background inhomogeneous electric field since, in what follows, we shall be considering the low-frequency dusty plasma slow response with a characteristic period much smaller than $1/\sqrt{\mu_i} q_0 \lambda_D \omega_{pi}$. Here, $\mu_i (<< 1)$ is the ratio between the potential energy of the plasma particles in the spatially nonuniform stationary electric field and the ion thermal energy, q_0 is the correlation length of the static dust grains in the plasma, $\omega_{pi} = (4\pi n_{i0}/m_i)^{1/2}$ is the ion plasma frequency, n_{i0} is the unperturbed ion number density, and m_i is the ion mass. In equilibrium, we have $en_{i0} = en_{e0} - q_{d0} n_{d0}$, where n_{e0} is the unperturbed electron

number density, $q_{d0} = -eZ_{d0}$ is the equilibrium dust charge, Z_{d0} is the number of charge residing on a dust particle, and n_{d0} is the unperturbed dust number density.

The momentum equations for inertialess electron and ion fluids can then be written as

$$0 = -en_{e0}\nabla\phi - T_{e0}\nabla n_{e1} - n_{e0}\nabla T_{e1} - \frac{n_{e0}e^2}{2m_e\omega_0^2}\nabla|\mathbf{E}|^2, \tag{1}$$

$$0 = en_{i0}\nabla\phi - T_{i0}\nabla n_{i1} - n_{i0}\nabla T_{i1}, \tag{2}$$

where $n_{\alpha 1}(<< n_{\alpha 0})$ is the perturbed number density of the particle species α, $T_{\alpha 1}(<< T_{\alpha 0})$ is the perturbed temperature, ϕ is the ambipolar potential associated with dusty plasma slow motions, $\mathbf{E}$ is the electric field vector of the HF electromagnetic waves, and the last term on the right-hand side of (1) is the usual ponderomotive force contribution. Furthermore, $\omega_0^2 = \omega_{pe}^2 + k_0^2c^2$ is the squared electromagnetic pump wave frequency, $\omega_{pe} = (4\pi n_{e0}/m_e)^{1/2}$ is the electron plasma frequency, $\mathbf{k}_0$ is the pump wavevector, and c is the speed of light. The electron and ion collisional drags have been neglected because the wavelengths of the dusty plasma slow motion are assumed to be much smaller than $(T_{e0,i0}/m_{e,i}\nu_{e,i}\Omega)^{1/2}$, where $\nu_e(\nu_i)$ is the electron (ion) collision frequency.

The energy balance equations can now be written as

$$\frac{3}{2}\partial_t T_{e1} - \frac{\chi_e}{2}\nabla^2 T_{e1} + \frac{1}{\tau_e}(T_{e1} - T_{i1}) - \frac{T_{e0}}{n_{e0}}\partial_t n_{e1} = \frac{2\nu_e e^2}{m_e\omega_0^2}|\mathbf{E}|^2, \tag{3}$$

$$\frac{3}{2}\partial_t T_{i1} - \frac{\chi_i}{2}\nabla^2 T_{i1} - \frac{1}{\tau_e}(T_{e1} - T_{i1}) - \frac{T_{i0}}{n_{i0}}\partial_t n_{i1} = 0. \tag{4}$$

We note that the right–hand side of (3) represents the differential Joule heating [3] of electrons caused by the electromagnetic wave energy in collisional plasmas. Here, χ_α is the coefficient of the thermal conductivity of the particle species α, and τ_e is the electron energy relaxation rate.

The charging equation in dusty plasmas for our purposes reads

$$\partial_t q_d = I, \tag{5}$$

where q_d is the average charge of the dust grains and I is the average plasma current flowing into the dust grains [3].

For small amplitude perturbations of the dust charge (viz. $q_{d1} << q_{d0}$), we linearize Eq. (5). Assuming that the charge fluctuation q_{d1} is proportional to $\exp(i\mathbf{K}\cdot\mathbf{r} - i\Omega t)$, where Ω and $\mathbf{K}$ are, respectively, the frequency and wavevector associated with quasi-stationary plasma slow motions, we obtain

$$(-i\Omega + \nu_{ch})q_{d1} = -|I_{e0}^{eq}|\left[\frac{n_{e1}}{n_{e0}} - \frac{n_{i1}}{n_{i0}} + (1+2z)\frac{T_{e1}}{2T_{e0}} - \frac{\tau - z}{\tau + z}\frac{T_{i1}}{2T_{i0}}\right], \tag{6}$$

where $\tau = T_{i0}/T_{e0}$, $z = -eq_{d0}/aT_{e0}$, and $n_{i0} = n_{e0} + n_{d0}|q_{d0}|/e$. The expression for the equilibrium electron current is given by

$$I_{e0}^{eq} = -\frac{4\pi a^2 e n_e}{\sqrt{2\pi m_e}}\sqrt{T_e}\exp\left(-\frac{Z_d e^2}{aT_e}\right). \tag{7}$$

Here, we have assumed that $|\partial_t + \nu_e| \ll v_{t\alpha}|\nabla|$ so that the effects of collisions on electron and ion charging currents are negligibly small.

The nonlinear coupling of an intense HF electromagnetic pump $(\omega_0, \mathbf{k}_0)$ with the quasi-stationary plasma slow motions, as described above, $(\Omega << \omega_0, \mathbf{K})$ gives rise to HF electromagnetic sidebands, which are governed by [4]

$$\varepsilon_\pm \mathbf{E}_\pm - \frac{c^2}{\omega_\pm^2}\mathbf{k}_\pm \times (\mathbf{k}_\pm \times \mathbf{E}_\pm) = \frac{n_{e1}}{n_{e0}}\frac{\omega_{pe}^2}{\omega_\pm^2}\mathbf{E}_{0\pm}, \tag{8}$$

where $\omega_\pm = \Omega \pm \omega_0$ and $\mathbf{k}_\pm = \mathbf{K} \pm \mathbf{k}_0$ are the frequency and the wavevector of the sidebands, respectively, and $\varepsilon_\pm = 1 - \omega_{pe}^2/\omega_\pm^2$, $\mathbf{E}_{0+} = \mathbf{E}_0$, $\mathbf{E}_{0-} = \mathbf{E}_0^*$. Here, the subscript $\pm(0)$ stands for the upper–and lower– sidebands (pump) and the asterisk stands for the complex conjugate.

3. Nonlinear dispersion relation

In order to obtain the dispersion relation for our purposes, we derive an expression for n_{e1}. Thus, we assume that $n_{\alpha 1}$ and $T_{\alpha 1}$ are proportional to $\exp(i\mathbf{K}\cdot\mathbf{r} - i\Omega t)$. Accordingly, by assuming $T_{e1} \sim T_{i1}$, we obtain from (3) and (4)

$$\begin{aligned}\left(-3i\Omega + \chi K^2\right)\left(T_{e0}n_{e1} + T_{i0}\frac{n_{e0}}{n_{i0}}n_{i1}\right) - 2i\Omega\left(T_{e0}n_{e1} + T_{i0}\frac{n_{e0}}{n_{i0}}n_{i1}\right) \\ = -\left(-3i\Omega + \chi K^2 + 4\nu_e\right)\frac{n_{e0}e^2|\mathbf{E}|^2}{2m_e\omega_0^2}.\end{aligned} \tag{9}$$

Combining (9) with the charging equation (6) in the quasineutral approxiation, we readily obtain

$$\left[(-i\Omega + \frac{1}{3}\chi K^2)c_a^2(\Omega) - \frac{2}{3}i\Omega c_s^2(\Omega)\right]\frac{n_{e1}}{n_{e0}} = -\frac{e^2|\mathbf{E}|^2}{2m_e m_i\omega_0^2}\left[-i\Omega + \frac{1}{3}\chi K^2 + \frac{4}{3}\nu_{eff}\right], \tag{10}$$

where

$$c_a^2(\Omega) = \frac{T_{e0}}{m_i} + \frac{T_{i0}}{m_i}\frac{1}{1+\mu}\left[1 + \frac{\nu_{ed}[\mu + \delta(1+\mu+\tau)]/(1+\mu)}{-i\Omega + \nu_{ch} + \nu_{ed}[1-\tau\delta]/(1+\mu)}\right], \tag{11}$$

$$c_s^2(\Omega) = \frac{T_{e0}}{m_i} + \frac{T_{i0}}{m_i}\frac{1}{1+\mu}\left[1 + \frac{\nu_{ed}[\mu + \delta(1+\mu+\tau)]/(1+\mu)}{-i\Omega + \nu_{ch} + \nu_{ed}[1-\tau\delta]/(1+\mu)}\right], \tag{12}$$

and

$$\frac{\nu_{eff}}{\nu_e} = 1 + 2\kappa\frac{-3i\Omega + \chi K^2}{-i\Omega} + 2\kappa. \tag{13}$$

In Eqs. (11) and (12), we have denoted $\mu = n_{d0}|q_{d0}|/n_{e0}e = Q_{d0}/Q_{e0}$, where $Q_{d(e)0}$ is the total charge accumulated on the dust (electron) plasma component, and $\nu_{ed} = n_{d0}|I_{e0}|/n_{e0}e = \nu_{ch}P(\tau+z)/(1+\tau+z)$ is the frequency of the electron capture by the dust grain [3], where $P = n_{d0}aT_{e0}/n_{e0}e^2$. Furthermore, we have

$$\delta = \frac{-i\Omega/2}{-3i\Omega + \chi K^2}\left(1 + 2z - \frac{1}{\tau}\frac{\tau - z}{\tau + z}\right), \quad \kappa = \frac{\nu_{ed}\tau\delta/(1+\mu)}{-i\Omega + \nu_{ch} + \nu_{ed}(1-\tau\delta)/(1+\mu)}. \tag{14}$$

It appears that the dust charge fluctuation leads to a "renormalization" of the collision frequency ν_e as well as of the sound speed. If we set $\delta = 0$, we obtain the result without the temperature fluctuations in the charging equation.

Equation (10) can now be combined with Eq. (8) in order to derive a general dispersion relation for the modulational instability of intense HF electromagnetic waves in dusty plasmas. However, for illustrative purposes, we consider the case in which the Joule heating nonlinearity far dominates the ponderomotive force in a collisional dusty plasma. Hence, for $\nu_{eff} >> |\Omega + i\chi K^2|$, we have the following dispersion equation (cf. Eq. (6) of Ref. [4])

$$\Omega = i\frac{\Omega_0^3}{K^2u^2(\Omega)}, \qquad \Omega_0 = \left(\frac{8\nu_{eff}\omega_{pi}^2V_0^2}{3c^2\Delta}\right)^{1/3}. \tag{15}$$

Here, $\Delta = 1 + 4\omega_0^2\Gamma^2/K^2c^2$, $\Gamma = \nu_{eff}\omega_{pe}^2/2\omega_0^2$ is the collisional damping of the electromagnetic sidebands (we note that in this case we have a "renormalized" collision frequency according to Eq. (13)), $V_0^2 = e^2|\mathbf{E}_0|^2/m_e^2\omega_0^2$, and $u^2(\Omega) = c_a^2(\Omega) + 2c_s^2(\Omega)/3$. A close inspection of (15) reveals that the character of the modulational instability is altered in comparison with that reported in Ref. [4] (when $\Omega \ll Kc_a$). Specifically, Eq. (15) predicts an oscillatory instability.

4. Conclusion

In this paper, we have considered the parametric coupling of large amplitude HF electromagnetic waves with non–resonant quasi-stationary electrostatic perturbations by employing the multi–component dusty plasma model which incorporates the effect of the dust charge perturbation. In the presence of the latter, we have a new type of plasma slow response to electromagnetic waves. The wavelength of the quasi-stationary modulations is assumed to be much smaller than the collisional mean path of the plasma so that the usual charging equation holds for our purposes. The newly derived electron number density perturbation associated with quasi-stationary plasma slow motion is combined with the electromagnetic sideband equations in order to obtain a nonlinear dispersion relation in a collisional regime in which the modulation frequency is much smaller than the effective electron collision frequency. Accordingly, the differential Joule heating nonlinearity dominates over the radiation pressure. An examination of the dispersion relation reveals some new features of the modulational instability.

Acknowledgments

The authors gratefully acknowledge fruitful discussions with M. Nambu. One of the authors (S. V. V.) would like to thank the Japan Society for the Promotion of Science for financial support and M. Nambu for hospitality. The work of P. K. S. was partially supported by the Human Capital and Mobility program of the European Union (Brussels) through the Network "Colloidal Plasmas" under contract no. CHRX-CT94-062.

References

[1] D. A. Mendis and M. Rosenberg, Annu. Rev. Astron. Astrophys. **32**, 419 (1994).

[2] R. K. Varma, P. K. Shukla, and V. Krishan, Phys. Rev. E **47**, 3612 (1993).

[3] S. V. Vladimirov, Phys. Plasmas **1**, 2762 (1994).

[4] P. K. Shukla and S. V. Vladimirov, J. Geophys. Res. **99**, 4023 (1994).

Modulational Instability of Packets of Lower–Hybrid Waves

Sergey I. Popel
Institute for Dynamics of Geospheres, Leninsky pr. 38, Building 6,
117979 Moscow, Russia

The self–consistent description of a large number of collective modes is very important in plasma physics. Among nonlinear effects influencing the wave evolution the modulational instabilities are of particular interest. The modulational instability of a single monochromatic pump mode is now fairly well investigated both for collisionless as well as for collision–dominated, magnetized, *etc.*, plasmas [1]. However, for adequate description of many real situations in space and astrophysical plasmas, plasmas of earth's ionosphere and planetary atmospheres, as well as in laboratory plasmas, the modulational instability of broad spectra should be considered. Its character signuficantly differs from that of a monochromatic pump. For description of the modulational instability of broad Langmuir wave spectra in collisionless unmagnetized plasmas two approaches [2,3] have been used. The former one [2] (see also [4]) is based on the WKB ansatz while the latter [3] uses the theory of weak plasma turbulence. Unfortunately, these approaches can be used advantageously only for the description of near–threshold behaviour of the modulational instability of Langmuir waves [4,5]. For the Langmuir wave modulational instability developed (when the characteristic inhomogeneity scale is determined by the modulational processes) the theory of weak plasma turbulence has severe applicability limits, and the WKB approximation cannot be used. Here we study the case of broad spectra of lower–hybrid (LH) waves in magnetized plasmas. LH oscillations are the short–wavelength ($|\mathbf{k}|c \gg \omega_{pe}$) quasielectrostatic oscillations with the following dispersion (see, *e.g.*, [1])

$$\omega_{\mathbf{k}} \approx \omega_{LH}\left(1+\frac{m_i}{m_e}\cos^2\theta\right)^{\frac{1}{2}} \quad \text{if} \quad (m_e/m_i)^{1/2} \le |\cos\theta| \ll 1, \tag{1}$$

and

$$\omega_{\mathbf{k}} \approx \omega_{LH}\left(1+\frac{1}{2}\frac{m_i}{m_e}\cos^2\theta+\frac{1}{2}|\mathbf{k}|^2R^2\right) \quad \text{if} \quad |\cos\theta| \ll (m_e/m_i)^{1/2}. \tag{2}$$

Here, $\omega_{\mathbf{k}}$, $\mathbf{k}$ are the frequency and the wave number of LH wave, respectively, $m_{e(i)}$ is the electron (ion) mass, $\omega_{LH}=\omega_{pi}/(1+\omega_{pe}^2/\omega_{Be}^2)^{1/2}$ is the frequency of LH resonance, $\omega_{pe(i)}$ is the electron (ion) plasma frequency, ω_{Be} is the electron gyrofrequency, c is the speed of light, θ is the angle between the wave propagation and an external magnetic field $\mathbf{B}_0$,

$$R^2=\begin{cases}3(T_i/T_e)r_{De}^2, & \text{if } \omega_{Be}\gg\omega_{pe},\\ 3(v_{Te}/\omega_{Be})^2(1/4+T_i/T_e), & \text{if } \omega_{Be}\ll\omega_{pe},\end{cases} \tag{3}$$

$T_{e(i)}$ is the electron (ion) temperature, r_{De} is the electron Debye length, v_{Te} is the electron thermal speed. Consideration of the nonlinear processes with participation of LH waves is very important for theoretical description of the nonlinear stage of the loss–cone instability in the open traps, of the rf plasma heating on frequencies close to the frequency of

LH resonance, of LH current drive, *etc.* It has also astrophysical applications (*e.g.*, the problem of the structure of the transverse shock wave).

Let us find applicability limits of the weak turbulence theory for description of the modulational instability of broad LH wave spectra. This theory is valid for the systems with developed stochasticity [5,6] when the so–called stochasticity parameter S is sufficiently large,

$$S \equiv \Delta V / \delta V \geq 1. \tag{4}$$

Here ΔV is the island width (the width of the trapping region of a particle by a wave) in the velocity space, δV is the velocity spacing between adjacent wave—particle resonances. For the case of LH waves the latter are simply Čerenkov resonances, $\omega_{\mathbf{k}} - k_{\|} v_{\|} = 0$, where $\mathbf{v}$ is the electron velocity; the subscript $\|(\perp)$ denotes the vector component parallel (perpendicular) to the external magnetic field.

For the mode with the wave number $\mathbf{k}$ the width of the trapping region is $\Delta V = 4\left(2e\varphi_{\mathbf{k}}/m_e\right)^{1/2}$. Here $-e$ is the electron charge, $\varphi_{\mathbf{k}}$ is the amplitude of the mode potential. The energy density of the mode $W_{\mathbf{k}}$ and the potential $\varphi_{\mathbf{k}}$ are related by $W_{\mathbf{k}} \sim \left(\mathbf{k}^2 |\varphi_{\mathbf{k}}|^2 / 8\pi\right) \left(\omega \partial \varepsilon(\omega, \mathbf{k}) / \partial \omega|_{\omega=\omega_{\mathbf{k}}}\right)$ where $\varepsilon(\omega, \mathbf{k})$ is the dielectric function.

Let us consider a packet of LH waves with spectral width $\Delta k_{\|(\perp)}$ in the parallel (perpendicular) direction with respect to the external magnetic field. We assume that this packet is isotropic in the plane perpendicular to the external magnetic field (*i.e.*, the spectrum $W_{\mathbf{k}}$ depends on $k_{\|}$ and $|\mathbf{k}_{\perp}|$ only). In this case the energy density in the packet can be estimated as $W \sim N W_{\mathbf{k}} \sim \left(\Delta k_{\|} \Delta k_{\perp} / \delta k_{\|} \delta k_{\perp}\right) W_{\mathbf{k}}$, where N is the number of modes in the wave packet, $\delta k_{\|(\perp)}$ is the wave number spacing between adjacent modes in the parallel (perpendicular) direction to the external magnetic field. We note that the value of δV can be presented as $\delta V \approx \delta k_{\|} (v_{g\|} - v_{ph\|}) / k_{\mathrm{ch}\|}$ where $v_{g\|}$, $v_{ph\|}$, $\mathbf{k}_{\mathrm{ch}}$ are the characteristic values of $\partial \omega_{\mathbf{k}} / \partial k_{\|}$, $\omega_{\mathbf{k}} / k_{\|}$, and the wave number in the LH wave spectrum, respectively.

Inequality (4) can be rewritten in the form (we assume $\mathbf{k}_{\mathrm{ch}} \sim \Delta \mathbf{k}$)

$$\left(1 + \frac{m_i}{m_e} \cos^2\theta\right)^{\frac{3}{4}} \left(\frac{m_i}{m_e} \cos^2\theta\right)^{\frac{1}{4}} \left(\frac{v_{Te}}{v_{ph\|}}\right)^{\frac{1}{2}} \left(\frac{W}{n T_e}\right)^{\frac{1}{4}} \frac{\left(L_{\|} k_{\mathrm{ch}\|}\right)^{\frac{3}{4}}}{\left(L_{\perp} k_{\mathrm{ch}\perp}\right)^{\frac{1}{4}}} \geq 1, \tag{5}$$

where $L_{\|(\perp)}$ is the characteristic plasma inhomogeneity scale in the parallel (perpendicular) direction with respect to the external magnetic field, n is the electron density. For a developed modulational instability the values $L_{\|}$ and $L_{\perp}$ can be estimated as the characteristic lengths of plasma modulations: $L_{\|(\perp)} \sim L_{\mathrm{mod}\|(\perp)} \sim 1/k_{\mathrm{mod}\|(\perp)}$, where $\mathbf{k}_{\mathrm{mod}}$ is the characteristic wave number of the modulational perturbations.

If $|\cos\theta| \ll (m_e/m_i)^{1/2}$ then the modulational instability results in self–contraction of LH waves in some regions of a plasma with characteristic inhomogeneity scales (see, *e.g.*, [7])

$$L_{\perp} \sim R \sqrt{\frac{m_e}{m_i} \frac{n T_e}{W}} \frac{\omega_{Be}}{\omega_{pe}}, \quad L_{\|} \sim \frac{L_{\perp}^2}{R} \sqrt{\frac{m_i}{m_e}}. \tag{6}$$

Substituting (6) in inequality (5) and taking into account that $|\cos\theta| \sim L_\perp/L_\parallel$ we find for the case $T_e \sim T_i$

$$\frac{W}{nT_e} \leq (k_{\mathrm{ch}\perp}R)^{\frac{22}{3}} \left(\frac{m_e}{m_i}\right)^{\frac{5}{3}} \left(\frac{\omega_{Be}}{\omega_{pe}}\right)^{\frac{10}{3}}. \tag{7}$$

Condition (7) shows that for the case $|\cos\theta| \ll (m_e/m_i)^{1/2}$ the weak turbulence theory is of limited usefulness for description of the modulational instability of broad LH wave spectra, even though initially LH wave phases can be considered as random. Similar to the case of Langmuir waves [6], this is connected with the amplification of wave phase correlations in the process of the instability development even at very low turbulence levels and is caused by the LH wave dispersion (2) [which is reminiscent of that of Langmuir waves].

A different situation arises with the case $(m_e/m_i)^{1/2} \leq |\cos\theta| \ll 1$. In this case for the estimation of the characteristic scale $L_\perp$ we use the results of the investigation of the instability of a monochromatic LH wave in the limit of long–wavelength pumping (in the case considered this is the limit $|\mathbf{k}_{\mathrm{mod}}| \gg |\mathbf{k}_{\mathrm{ch}}|$). We have (see, *e.g.*, [1])

$$\frac{W}{4nT_e} \sim \frac{|\mathbf{k}_{\mathrm{mod}}|v_{Te}}{\omega_{\mathbf{k}_{\mathrm{mod}}}} \left(\frac{m_e}{m_i}\right)^{\frac{1}{2}} \left(1+\frac{\omega_{Be}^2}{\omega_{pe}^2}\right)\left(\cos^2\theta + \frac{m_e}{m_i}\right). \tag{8}$$

For a fixed W and $|\mathbf{k}'| \geq |\mathbf{k}_{\mathrm{mod}}|$ [where $\mathbf{k}'$ is the wave number of the modulated perturbations, $\mathbf{k}_{\mathrm{mod}}$ is determined by (8)] the instability of a monochromatic pump develops most efficiently. Determining $L_\perp \sim |\mathbf{k}_{\mathrm{mod}\perp}|^{-1} \approx |\mathbf{k}_{\mathrm{mod}}|^{-1}$ from Eq. (8) and using $|\cos\theta| \sim L_\perp/L_\parallel$ we obtain from inequality (5)

$$\frac{W}{nT_e} \leq \left(\frac{m_i}{m_e}\cos^2\theta\right)^5 \left(\frac{v_{Te}}{v_{ph\parallel}}\right)^4 \left(1+\frac{\omega_{Be}^2}{\omega_{pe}^2}\right)^2 \left(\frac{m_e}{m_i}\right)^2. \tag{9}$$

The latter condition is significantly weaker than that (7). For example, for the data of the experimemnt on LH current drive [8]: $n \approx 5\cdot 10^{12}$ cm^{-3}, $|\mathbf{B}_0| \approx 4.5$ T, $T_e \approx 2$ keV, $v_{ph\parallel} \approx c/1.7$, we find [from dispersion law (1)] $\cos\theta \approx 4.2(m_e/m_i)^{1/2}$ and obtain [from inequality (9)] $W/nT_e \leq 10^{-1}$. Thus if initially the phases of LH waves with $(m_e/m_i)^{1/2} \leq |\cos\theta| \ll 1$ can be considered as random, the theory of weak plasma turbulence can be used to describe the modulational processes for sufficiently wide range of levels of turbulence in a plasma [determined by inequality (9)].

A nonlinear formalism suitable for description of the modulational instability of broad spectra consisting of random LH oscillations is developed in much the same manner as in the case of random Langmuir waves [3]. In particular, we separate the random (turbulent) and regular components of the electric field $\mathbf{E}$ and of the distribution functions of plasma particles. To obtain the basic equations for the description of the modulational instability, we use Poisson equation in which the terms up to the third order in electric field are taken into account. Furthermore, we present the random electric field $\delta E^\pm$ as a sum of the initial random field $\delta E^{\pm(0)}$ (which obeys the equations of the weak turbulence theory in the absence of the modulational interaction) and the field of the modulational perturbations $\delta' E^\pm$. Here the superscripts "+" and "−" denote the positive–

and negative–frequency harmonics of the electric field, respectively. Equations describing the modulational instability can be written for the correlation functions:

$$G^{+}_{k,k'} = \left\langle \delta' E^{+}_{k+k'} \delta E^{-(0)}_{-k} \right\rangle \quad \text{and} \quad G^{-}_{k,k'} = \left\langle \delta' E^{-}_{-k+k'} \delta E^{+(0)}_{k} \right\rangle , \tag{10}$$

where $k = \{\omega, \mathbf{k}\}$, the right–hand side of expressions (10) contains Fourier components of the electric fields, the angular brackets $\langle\rangle$ denote the averaging over statistical ensemble. These equations take the form

$$\begin{aligned}
\varepsilon_{\pm k+k'} G^{\pm}_{k,k'} = &- \int \Sigma^{\text{eff}}_{\pm k+k', \pm k_1, \mp k_1} G^{\pm}_{k,k_1} |E^{+(0)}|^2_{k_1} \, dk_1 \\
&- \int \Sigma^{\text{eff}}_{\pm k_1, \pm k+k', \mp k_1} G^{\pm}_{k,k_1} |E^{+(0)}|^2_{k_1} \, dk_1 \\
-|E^{+(0)}|^2_k \int G^{\pm}_{k_1,k'} &(\Sigma^{\text{eff}}_{\pm k_1+k', \pm k, \mp k_1} + \Sigma^{\text{eff}}_{\pm k, \pm k_1+k', \mp k_1}) dk_1 \\
-|E^{+(0)}|^2_k \int G^{\mp}_{k_1,k'} &(\Sigma^{\text{eff}}_{\pm k, \pm k_1, k' \mp k_1} + \Sigma^{\text{eff}}_{\pm k_1, \pm k, k' \mp k_1}) dk_1 .
\end{aligned} \tag{11}$$

Here

$$\begin{aligned}
\Sigma^{\text{eff}}_{k_1,k_2,k_3} = &- \frac{ie^2 (\mathbf{k}_2 + \mathbf{k}_3)^2 \varepsilon^{(i)}_{k_2+k_3} (\varepsilon^{(e)}_{k_2+k_3} - 1)}{8\pi m_e^2 |\mathbf{k}_1| |\mathbf{k}_2| |\mathbf{k}_3| \varepsilon_{k_2+k_3}} \\
\times \left[\frac{k_{\parallel} k_{1\parallel}}{\omega^2} + \frac{i(\mathbf{k}_\perp \times \mathbf{k}_{1\perp})_{\parallel}}{\omega \omega_{Be}} \right] &\left[\frac{k_{2\parallel} k_{3\parallel}}{\omega^2} - \frac{i(\mathbf{k}_{2\perp} \times \mathbf{k}_{3\perp})_{\parallel}}{\omega \omega_{Be}} \right]
\end{aligned} \tag{12}$$

is the effective third–order nonlinear response for the case of LH waves (see, *e.g.*, [1]); $\left\langle \delta E^{+(0)}_{k_1} \delta E^{-(0)}_{k_2} \right\rangle = -|E^{+(0)}|^2_{k_1} \delta(k_1 + k_2)$; the superscripts "$(e)$" and "$(i)$" identify the electron and ion parts of the dielectric function ε_k. Investigation of the modulational instability on the basis of equations (11) and (12) allows us to conclude that the instability of broad LH wave spectrum is suppressed comparing with that of a monochromatic pump of the same energy.

In closing, we emphasize that in most cases when the modulational instability of LH waves is important, LH waves constitute broad spectra. In this connection the proposed nonlinear formalism could be useful for description of real situations occurring in laboratory and astrophysical plasmas.

References

[1] Vladimirov S.V., Tsytovich V.N., Popel S.I., and Khakimov F.Kh., *Modulational Interactions in Plasmas* (Kluwer, Dordrecht, 1995).

[2] Gailitis A.K., *Thesis*, P.N. Lebedev Inst. (1964); *Izv. Latv. SSR Ser. Phys. Techn. Nauk* **4** 13 (1965).

[3] Popel S.I., Tsytovich V.N., and Vladimirov S.V., *Phys. Plasmas* **1** 2176 (1994).

[4] Vladimirov S.V. and Popel S.I., *Phys. Rev. E* **51** 2390 (1995).

[5] Krommes J., in *Basic Plasma Physics*, Vol. II (North–Holland, Amsterdam, 1984).

[6] Popel S.I. and Vladimirov S.V., *Phys. Lett. A* **200** 156 (1995).

[7] Shapiro V.D. and Shevchenko V.I., in *Basic Plasma Physics*, Vol. II (North–Holland, Amsterdam, 1984).

[8] JT-60 Group, *Plasma Phys. Contr. Nucl. Fusion*, Vol. 1, p.11 (IAEA, Vienna, 1987).

Combined Diagnostic Methods of non-LTE Dense Pulsed Plasma

IL Babich, AI Cheredarchuk, AN Veklich, **VA Zhovtyansky**
Radiophysics Dep., Taras Shevchenko University, Kiev 252017, Ukraine

1. Introduction

It is generally agreed the local thermodynamic equilibrium (LTE) takes place in the dense plasma. Individual authors have been investigated deviation from LTE in noble-gas plasma in electric arcs owing to diffusion processes or overpopulation of the base atoms level due to resonance radiation [1]. Nevertheless LTE-assumption has been universally accepted. However results of investigations of electric arc plasma between evaporated copper electrodes in such assumption exhibit the significant non-physical copper vapour content at the arc periphery at every its section. Such increasing in our opinion [2,3] is unexplained as a result of demixing as it was expected in other authors' papers [4].

Our previous investigations [2] of the pulse electric arc plasma between copper electrodes have been shown its deviation from LTE. It is the result of radiation transfer in the nonuniform plasma. Really, the temperature gradient takes place at least near the boundary of any real plasma. The comprehensive calculation allows to specify the overpopulation extent of the atom copper resonance level with respect to the ground one at various distances away from the arc axis. This effect has been sufficiently universal for any dense plasma. It is most manifested at the periphery of the specified plasma source. That is why it went largely unnoticed under ordinary observations along the axis chord of the plasma volume, excluding tomographic procedure.

This paper deals with diagnostic of such non-LTE plasma. Addition problems are unstable position of the plasma bulk owing to electrodes' processes and the self-absorption of the typical for copper plasma diagnostic spectral line 510.5 nm. They are solved, too.

2. Experiment

Fast scanning compact tomographic spectrometer of a high spectral resolving power and aperture ratio is created on the base of Fabry-Perot interferometer, special monochromator and the image dissector of electrostatic type [5]. The dissector's advantage among another scanning photodetectors is providing a cycle of measurements over a single event of an investigated pulsed high-speed process. The spectrometer ensures practically simultaneous recording of spectral line shapes in various space elements of plasma as well as space distribution of the spectral line emission and absorption. Last improvements permit to use this device as a tomographic spectrophotometer for investigation of the single high-speed processes under the condition of the substantial radiance absorption. The image was focused in such a way that the range of space instability of the plasma bulk should not be exceeded the size of dissector's photocathode.

The wide-spread pair of spectral lines of copper atom 510.5 and 521.8 nm are chosen for temperature measurements by the method of relative intensities. It should be primarily taken into account the possibility of measured intensity's distortion in the result of self-absorption for spectral line CuI 510.5 nm having slight exciting energy 1.39 eV of lower level. It is directly shown in our experiment based on the laser absorption spectroscopy technique [6]. That is why

the temperature measurements obtained in the experiment may be estimated only as first order approximation.

The methods of electron density measurements independent on temperature are preferable. One of them is measuring of Stark width of the spectral line 515.3 nm. Another possibility is measuring of the absolute intensity of spectral line, radiated from high-exited level of atom. It is easily provided in atom of copper owing to its system of shifted levels. The ionization potential of exited s-electron terms consists of E_i=7.724 eV. As the energy of shifted upper level $^4D_{7/2}$ for spectral line CuI 465.1 nm consist of E_s=7.74 eV, the exponential temperature dependence may be usually neglected in measurements of radial profiles N_e:

$$I \sim N_e^2\, T^{-3/2} \exp[(E_i - E_s)/kT] \sim N_e^2\, T^{-3/2}. \qquad (1)$$

The problem is the possibility of autoionization depopulation of shifted levels, which may be resulted in its nonequilibrium with s-terms. Fortunately, the autonization from levels $^4D_{7/2}$ is foreboded. The calibration of absolute electron density values being carried out with the reference to high-temperature ($4*10^4$ K) source of continuum radiation.

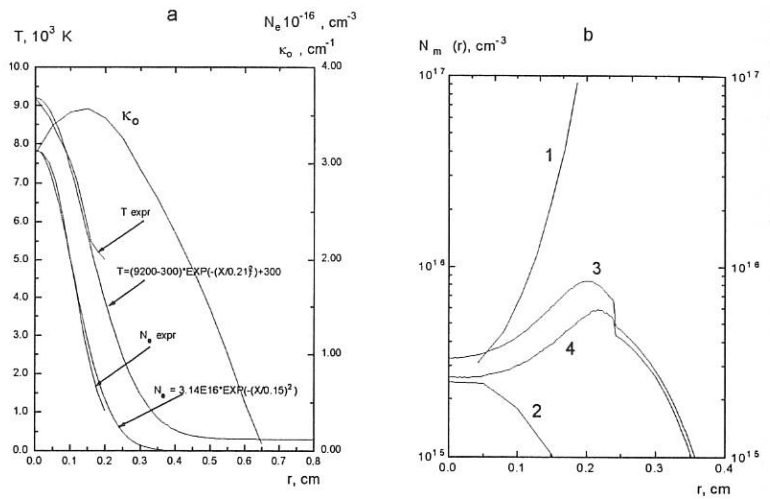

Fig. 1. Experimental data (a) and estimated populations N_m of metastable level (b): 1 - in LTE-assumption with experimentally obtained $N_{e\ expr}$ and T_{expr}; 2 - in LTE-assumption with experimentally obtained κ_o and T_{expr}; 3 - non-LTE without account of self-absorption; 4 - non-LTE optically thick plasma.

The example of temperature T(r) and electron density $N_e(r)$ obtained in the case of interelectrode distance L = 2 mm and the current impulse i = 30 A are shown in the Fig.1. They have typical for free-burning electric arc the radial profiles. Their approximations are presented in this figure, too. The main peculiarity of data obtained is "catastrophic" increasing of the copper vapour density at the arc periphery if it is determined from T(r) and $N_e(r)$ with Saha and Dalton equations. It's corresponds to essential increasing of calculated in LTE-assumption the metastable level population with r increasing in Fig.1. Such tendency is in full disagreement with experimentally observed radial profile of the absorption coefficient $k_o(r)$ in

the center of the spectral line 510,5 nm, which with a precision of spectral line width $\Delta\lambda$ determines the metastable level population N_m:

$$k_0 \sim N_m/\Delta\lambda. \qquad (2)$$

That is why we had abandoning of the LTE-assumption thereafter.

It must be noticed some authors explained periphery increasing of a copper density as a result of demixing due to ambipolar diffusion [4]. We have specially examined this viewpoint by simulation of the axially symmetric diffusion problem [3]. The conclusion is the demixing does not essential effect in electric arc plasma.

3. Radiation transfer

We consider the adequate explanation for obtained results is evident from the partial LTE-assumption (PLTE) in such plasma. The PLTE is caused by resonance radiation transfer. This radiation from the hot arc core is able to overpopulate the resonance level of Cu atoms at the arc periphery, where the temperature is relatively small. The overpopulation is identified by collision-radiative model with account of radiation transfer. Such simulation includes iteration processes until the Dalton equation and PLTE model be satisfy simultaneously at each point of arc radius. The result is illustrated by a curve 3 in Fig.1. It's essentially more corresponds to experimental values of $k_0(r)$ in Fig.1. Below is this simulation procedure have been included in simulation-adaptive spectroscopy method.

4. Simulation-adaptive spectroscopy method

A deficiency of temperature data presented in Fig.1 is neglect of self-absorption of the spectral line 510.5 nm. This problem with account of PLTE is solved by suggested method. The next

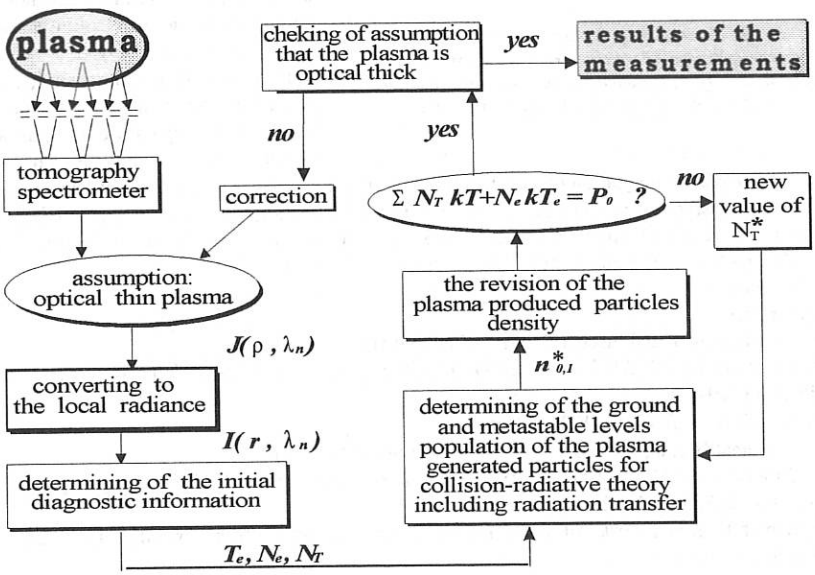

Fig. 2. The diagram of the simulation-adaptive spectroscopy method.

idea of simulation-adaptive procedure of the plasma optical diagnostic is proposed (see Fig.2). Starting with the LTE-assumption plasma parameters including heavy particle's density are calculated. In this case observed radial profiles of plasma radiance (integrated along spans) as a function of distance r in a number of spectral ranges $J(r,\lambda_n)$ are used as initial data. In the result of inverse problem solving they are transformed to radial distribution of the emission $I(r, \lambda_n)$ in the assumption of optically thin plasma. Next stage includes iterative process of collision-radiative population of the ground and metastable levels of plasma particles with account of radiation transfer in resonance lines. The calculated plasma parameters are to be satisfied simultaneously the supposed model of the non-LTE plasma and initial values $J(r,\lambda_n)$. Boltzman, Saha and Dalton equations were used in determining of the plasma condition. The last operation in this cycle is checking of plasma optical thickness in diagnostic spectral lines. The simulation is over if the plasma is optically thin. In the contrary case the initial values $I(r,\lambda_n)$ would be corrected to new values $I_k(r,\lambda_n)$ and temperature T_k. Further previous cycle would be repeated until the result of integration of radial distribution of the emission along spans with account of radiation transfer will be coincide with initial experimental data $J(r,\lambda_n)$. This iterative process is over if the result of optical thickness checking corresponds to calculated temperature and level's population. The efficiency of this procedure is illustrated in Fig.3.

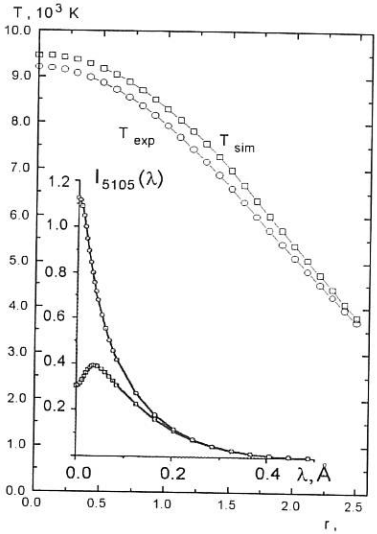

Fig. 3. The illustration of the self-absorption effect on the plasma temperature measuring T(r) and contours I(λ) of the spectral line 510.5 nm radiated from the arc axis: o - without account of self-absorption; □ - optically thick plasma.

References

[1] Uhlenbusch JF and Fischer E, *Proc. IEEE* **59(4)** 578 (1971)

[2] Zhovtyansky VA, *XIIth ESCAMPIG. Abst. Inv. Lectures and Contr. Pap. The Netherlands* **18E** 254 (1994)

[3] Babich IL et al, *Ibid* **18E** 310 (1994)

[4] Cheminat B et al, *J. Phys. D: Appl. Phys.* **20(4)** 444 (1987)

[5] Zhovtyansky VA, *Journal of Engineering Physics and Thermophysics (translated from Russian)* **62(5)** 545 (1992)

[6] Babich IL et al, *Journal of Applied Spectroscopy (translated from Russian)* **51(4)** 1028 (1989)

Nonlinear effects in the coupling of electrostatic waves

C Riccardi, A Penso, E Agostini, M Fontanesi
Dipartimento di Fisica dell'Università' di Milano
Via Celoria 16- 20133, Milano- ITALY

1. Introduction

The efficiency of wave coupling in a plasma depends on the launched wave and the launching system and can be experimentally obtained by measuring the reflection coefficient and/or the plasma loading. So that analysing the impedance of the antenna-plasma system it is possible to establish what kind of wave is coupled and when its coupling is efficient; it also allows to evaluate the presence of some undesired waves which can be coupled, and the presence of non-linear phenomena, due to high power injected through the same antenna system. In the past experimental measurements on ES waves coupling, as Electron Plasma Wave (EPW) coupling, performed evaluating the reflection coefficient, have been subject of several studies in small devices [1].

Subsequently measurements of impedance performed in tokamak devices (Alcator C, DIII D) [2,3] in the low frequency range, ES (electrostatic) waves, gave anomalous loading [2-4]. The presence of this anomalous loading is actually explained involving surface plasma waves (SPW) but should be due also to non-linear effects.Our work, on this line, concerns the experimental analysis of plasma loading, in order to establish the presence of bulk and/or surface waves and some non-linear effects involved when ES waves are coupled. Waves are coupled in a magnetised homogeneous plasma in the range of the ion cyclotron frequencies and both the Electron Plasma Waves (EPW) and the Ion Bernstein Waves (IBW) coupling are experimentally analysed with respect to the impedance of the slow-wave antenna used to excite them [5,6].

The experimental analysis is carried out measuring both the reflection coefficient and the impedance of the plasma-slow wave antenna, through an automatic computerised system, in the experimental apparatus "Thorello" where many basic plasma physics experiments are possible [5-6]; the data are compared with a simple theoretical model giving the plasma loading for homogeneous plasma.[5]

2. Experimental Setup

The experiment is performed on the toroidal device "Thorello", with major radius $R = 40$ cm, minor radius $a = 8$ cm, $B_{toroidal} \cong 2$ kGauss, $B_{vertical} \cong 1$-5 Gauss [6]. It produces hydrogen magnetised plasmas by hot-filament emission and voltage-induced acceleration, and the typical plasma parameters are: $T_e \cong 1$ eV, $T_i \cong 0.1$ eV, edge plasma

density $\cong 10^8$ cm^{-3}, center plasma density $\cong 10^{10}$ cm^{-3}, neutral gas pressure $P = 8 \cdot 10^{-5}$ mbar. The launching system is composed of four thin metallic blades placed on the outer side of the vacuum chamber at a distance $\delta = 5$ mm from the wall. Each blade has a surface $S = 1$ dm^2 and is fed with a sinusoidal signal of angular frequency $\omega = 2\pi f$, with a variable phase shift φ between signals feeding two consecutive blades ($0 \leq \varphi \leq \pi/2$). We use a launched power in the range 0-30 dBm and frequencies in the range 3-30 MHz (the ion cyclotron frequency is about 3.4 MHz), launching waves with the wave vector component parallel $k_{//}$ to the toroidal magnetic field of about 0.1 cm^{-1}; the wave phase velocity is smaller than the light speed in vacuum, so that the analysis concerns the coupling of electrostatic waves [5]. Details of the power antenna spectrum are given in the following section.

To evaluate and graph both ρ and Z in the complex domain as a function of the relevant parameters (frequency, power) we have developed an automatic detection system composed of a generator and a vector analyser, interfaced to a PC and a program which give simultaneously ρ and Z in real time.

3.Experimental Results

The analysis of non-linear effects due to high power is given in Fig.1, where the reflection coefficient ρ is plotted as function of wave power in the case of EPW coupling. The reflection coefficient is a measure of the amount of power which is transferred into the plasma and depends, as Z, for given wave frequency and wave vector values, only on the plasma parameters in front of the antennas, i.e. on density and temperature. The linear regime, in which the reflection coefficient is constant with power, is below $P = 30$ mW, while above this threshold the reflection coefficient increase its value with power. This phenomena is not due to SPW but to a decrease in plasma density in front of the antenna, caused by the presence of ponderomotive forces. In the Figure 2 the density measured by Langmuir probe is plotted varying the injection power. From the theory, the perturbed density decreases exponentially following this formula:

$$n = n_0 \exp(-V_{pm}/T_e) \tag{1}$$

where n_0 is the density imperturbed and V_{pm} is the ponderomotive potential given by:

$$V_{pm} = \left[\frac{\omega_{pi}\omega}{\omega^2 - \Omega_i^2}\right]^2 \frac{E_\perp^2}{8\pi} + \left[\frac{\omega^2_{pi}}{\omega^2 - \Omega_i^2}\right] \frac{E_\parallel^2}{8\pi} \tag{2}$$

If, for a given electron temperature T_e value, V_{pm} exceeds T_e the density turns out to be perturbed. When the density decreases the theoretical Z given by the theory increases, according to Fig.3, so that Z takes values higher than that given by the linear theory (800 ohms instead of 200 ohms). Therefore we can say that the presence of ponderomotive

effects drastically reduce the transmitted power diminishing ρ at a few percent and increases the value of Z respect to that given in linear conditions. It turns out to be that in non-linear condition, i.e. when the power rises the threshold given in Eq.(2) the plasma loading results higher, anomalous, due to the effect of the ponderomotive forces.

Indeed while at low power injection , for frequencies $f < f_{lh}$, we can excite the IBW, at higher power, due to a decrease of the density in front of the antenna, the inequality $f < f_{lh}$ is not yet satisfate, so that we couple EPW not IBW. A similar result was obtained in the high power IBW experiment on DIII-D [1,3].

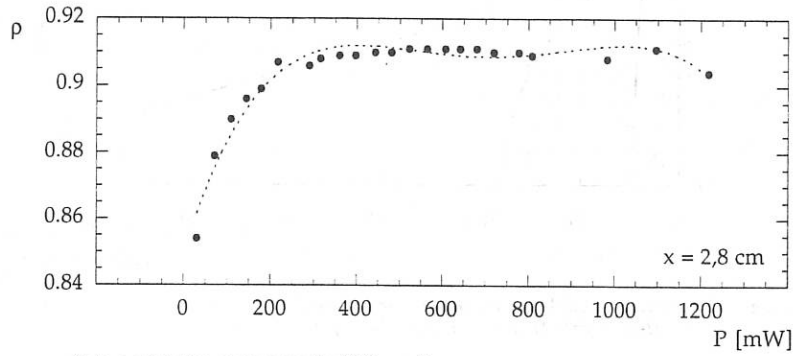

fig.1: ρ plotted vs. wave power for EPW coupling.

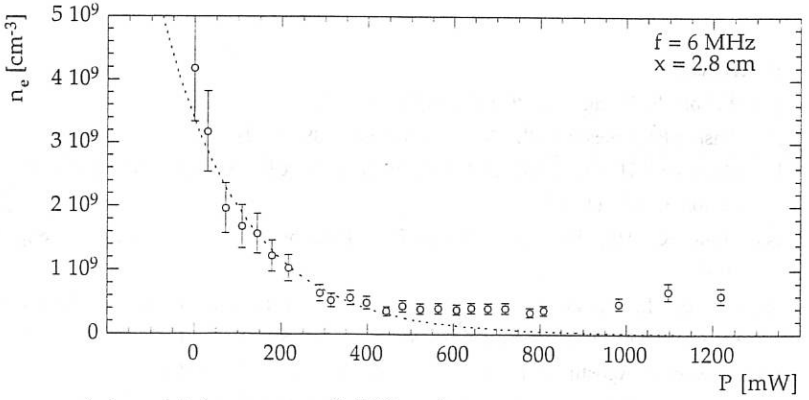

fig.2: n_e plotted vs. wave power for EPW coupling.

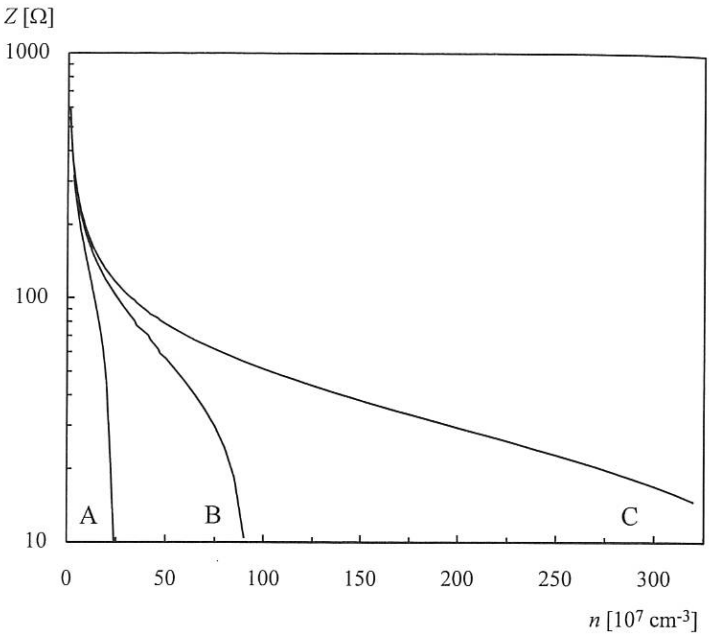

fig.3: Theoretical Z for EPW coupling plotted vs. the plasma density; φ=90°, A: f=8 MHz , B: f=10 MHz , C: f=12 MHz , $B_{toroidal}$= 2 kGauss .

References

[1] Wilson JR, Wong KL, *Phys.Fluids* **25,** 675 (1982)

[2] Pinsker RI, Colestock PL, *Nucl. Fusion* **32**, 1789 (1992)

[3] Mayberry MJ, Pinsker RI, Petty CC, Porkolab M, Chui SC, Cary WP, Prater R, *Nucl. Fusion* **33**, 627 (1993)

[4] Myra JR, D'Ippolito DA, Forslund DW, Brackbill JU, *Phys.Rev.Letters* **66,** 1173 (1991)

[5] Ferrucci L, Casanova MR, Maglione V, Montiron G, Riccardi C, Barisoni D, Fontanesi M, Galassi A, Sindoni E, *Rev.Sci.Instr.*, **66**, 2888 (1995)

[6] Riccardi C, Agostini E, Fontanesi M, *Plasma Physics* **37**, (1995)

[7] Van Nieuwenhove R, Koch R, Van Oost G, Proceedings *14st EPS Conference on Contr. Fusion and Plasma Phys.*, Madrid 1987, (European Physical Society, Ed.: F.Engelmann,J.L.Alvarez Rivas, Bochum 1987) 928.

The Condition of the Existence of the Electrostatic Waves in an Electron Beam-Plasma System

Y Nejoh
Hachinohe Institute of Technology,
Myo-Obiraki, Hachinohe, 031, Japan

1. Introduction

Nonlinear waves may play important roles in the situations ranging from rarefied space plasmas in the Earth's auroral zone[1-2], the physics of solar atmosphere and other astrophysical plasmas. Observations confirm the facts that stationary nonlinear ion-acoustic waves are usually formed when an electron beam is injected into a plasma[3]. In the actual situations, electron beam component are frequently observed in the region of space where large amplitude ion-acoustic waves exist.

In this paper, we make an attempt to theoretically study the existence of large amplitude ion-acoustic waves under the influence of an electron beam in a plasma consisting of warm ions and hot isothermal electrons. We demonstrate the region of the existence of the large amplitude ion-acoustic waves and study the dependence of the region of the existence on the electron beam temperature, the concentration of the beam density, and so on[4].

2. Basic Equations and formulation

We assume a plasma consisting of warm ions and hot isothermal electrons traversed by a warm electron beam, and consider one-dimensional propagation. We apply the fluid equations for the ions and beam electrons. The continuity equation and the equation of motion for ions are described by,

$$\frac{\partial n}{\partial t}+\frac{\partial}{\partial x}\left(nv\right)=0 \tag{1.a}$$

$$\frac{\partial v}{\partial t}+v\frac{\partial v}{\partial x}+\frac{3\sigma}{\left(1+\alpha\right)^{2}}n\frac{\partial n}{\partial x}+\frac{\partial \phi}{\partial x}=0 \tag{1.b}$$

Here, $\sigma=T_i/T_e$, and $\alpha=n_{b0}/n_0$, where the subscripts i , e and b denote the ion, electron and beam, respectively.

We have the following two equations, for the beam electrons,

$$\frac{\partial n_b}{\partial t}+\frac{\partial}{\partial x}\left(n_b v_b\right)=0 \tag{2.a}$$

$$\frac{\partial v_b}{\partial t}+v_b\frac{\partial v_b}{\partial x}+\frac{\nu}{\mu}\frac{1}{n_b}\frac{\partial n_b}{\partial x}-\frac{1}{\mu}\frac{\partial \phi}{\partial x}=0\,. \tag{2.b}$$

We have assumed an isothermal equation of state for the beam electrons. Here, $\mu=m_e/m_i$,

$\nu = T_b/T_e$, where T_b is the beam electron temperature. The electron density follows the Boltzmann distribution, $n_e = \exp(\phi)$. The Poisson's equation is given by

$$\frac{\partial^2 \phi}{\partial x^2} = n_e + n_b - n \,. \tag{3}$$

where we used the usual normalization.

In order to solve the above equations, we introduce the variable $\xi = x - Mt$ which is the moving frame with the velocity M. Integrating eqs.(1)-(3) and using the boundary conditions, $\phi \to 0$, $n \to 1+\alpha$, $n_b \to \alpha$, $v \to 0$, $v_b \to v_0$ at $\xi \to \infty$, we obtain the reduced Poisson's equation as follows,

$$\frac{d^2\phi}{d\xi^2} = \exp(\phi) + \frac{\alpha}{\sqrt{1 - \dfrac{1}{1-(\mu/\nu)(v_0 - M)^2}\dfrac{2\phi}{\nu}}} - \frac{1+\alpha}{\sqrt{1 - \dfrac{2\phi}{M^2 - 3\sigma}}} = -\frac{dV(\phi)}{d\phi} \,, \tag{4}$$

where $V(\phi)$ denotes the pseudopotential. Integration of (4) gives the *Energy law*,

$$\frac{1}{2}\left(\frac{d\phi}{d\xi}\right)^2 + V(\phi) = 0 \,. \tag{5}$$

The pseudopotential $V(\phi)$ becomes

$$-V(\phi) = \exp(\phi) - 1 - \alpha\nu\left[1 - (\mu/\nu)(v_0 - M)^2\right]\left[\sqrt{1 - \frac{1}{1-(\mu/\nu)(v_0 - M)^2}\frac{2\phi}{\nu}} - 1\right]$$
$$+ (1+\alpha)(M^2 - 3\sigma)\left[\sqrt{1 - \frac{2\phi}{M^2 - 3\sigma}} - 1\right] \,. \tag{6}$$

The oscillatory solution of the large amplitude ion-acoustic waves exist when the following two conditions are satisfied:

(i)The pseudopotential has a minimum if $d^2V/d\phi^2 < 0$ at $\phi = 0$.

(ii)Ion-acoustic waves exist only if $V(\phi_M) \geq 0$. This implies that the inequality

$$(1+\alpha)(M^2 - 3\sigma)\left[1 - \sqrt{1 - \frac{\nu}{M^2 - 3\sigma}}\right] \leq \alpha\nu + \exp(\nu/2) - 1 \,,$$

is hold. This condition determines the maximum Mach number. Figure 1 illustrates the maximum Mach number depending on the beam density α, in the case of $\sigma = 0.4$ and $\nu = 0.2$. We

understand that the Mach number decreases as the concentration of the beam density increases.

3. The region of the existence of large amplitude ion waves

We show a bird's eye view of the pseudopotential when ν=0.2, in Fig.2, in the case of v_0=1.25, M=1.30, σ=0.4 and μ=1/1836. In this case supersonic waves can propagate. Figure 3 illustrates the dependence of the pseudopotential on the electrostaticpotential when α=0.27 and ν=0.2. From Figs.2 and 3, we can understand the following: If $0.086<\alpha<0.280$, the pseudopotential forms the potrntial well. In the potential well, large amplitude ion-acoustic waves can propagate. The potential well becomes deep as α decreases. In the range of $\alpha>0.280$ and $0.086>\alpha$, the potential well is not formed.

We can illustrate the region of the existence of large amplitude ion waves depending on α and ν, in the case of v_0=1.25, M=1.30, σ=0.4 and μ=1/1836. In addition, we show the region of the existence of ion waves in $\phi-\alpha$ plane in Fig.4-(a), (b) and (c), for the case of ν=0.2, 0.3 and 0.4, respectively. Large amplitude ion-acoustic waves exist in the lower region of the curves. It turns out that large amplitude ion-acoustic waves can exist under proper conditions, mentioned above.

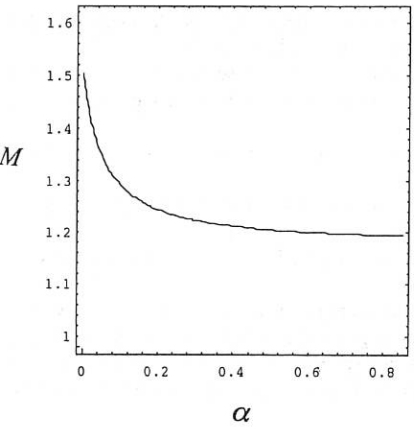

Fig.1 The maximum Mach number depending on the beam density α, *in the case of* σ=0.4 and ν=0.2.

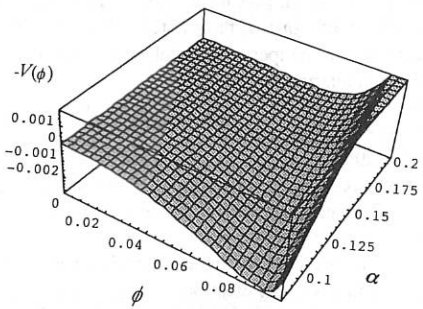

Fig.2 A bird's eye view of -V when ν=0.2 *and* σ=0.4.

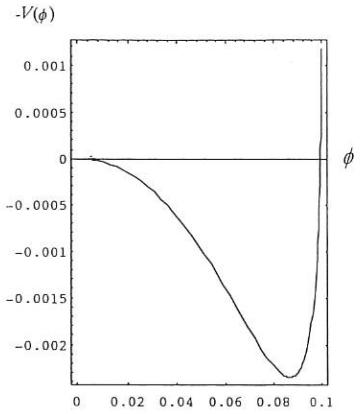

Fig.3 Pseudopotential as a function of the electrostatic potential when α =0.27 *and* ν=0.2.

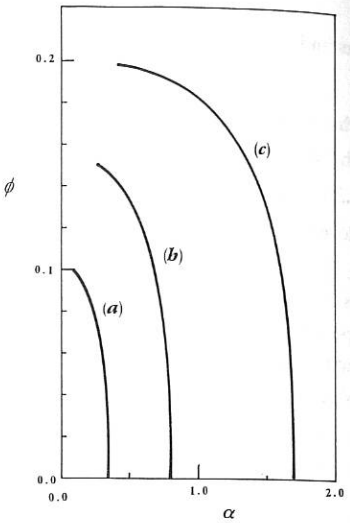

Fig.4 The region of the existence of ion waves. (a); ν=0.2, (b);ν=0.3, (c); ν=0.4.

4. Concluding discussion

We have presented the region of the existence of ion waves on the basis of the fluid equations for an electron beam-plasma system. The results are briefly summarized as follows:

(i) The conditions of the existence for large amplitude ion-acoustic waves sensitively depend on the density, the temperature of electron beams and also the ratio of the bulk ion temperature to the electron temperature.

(ii) The allowable range of the concentration of the electron density becomes wide as the beam temperature decreases.

(iii) Although supersonic ion-acoustic waves can propagate, the concentration of the electron beam density reduces the propagation speed of the large amplitude ion-acoustic wave.

(iv) The electrostatic potential-beam density plane where large amplitude ion waves exist spread as the beam temperature increases.

The present investigation predicts new findings on large amplitude nonlinear ion-acoustic waves in plasmas with an electron beam. In actual situations, large amplitude ion wave events associated with electron beams are frequently observed in interplanetary space. Hence, referring to the present studies, we can understand the properties of large amplitude ion waves in space where the electron beam exists.

References

[1]Bostrom R et al., *Phys. Rev. Lett.* **61** 82 (1988)
[2]Block L P and Falthammer C G, *J. Geophys. Res.* **95** 5877 (1990)
[3]Nejoh Y, *Proc. 4th Symp. Solar Terrestrial Environment*, Nagoya University, (1994)
[4]Nejoh Y and Sanuki H, *Phys. Plasmas* **2** (1995)

Computational Studies on Generation and Control of Ion Source Plasmas

Shunji Ido and Takeshi Kageyama
Faculty of Engineering, Saitama University
255, Shimo-Okubo, Urawa, Saitama 338, Japan

1. Introduction

Ion beam technology has become very important in recent scientific and industrial fields. The bucket-type ion source has been used to realize a uniform plasma and large size of the ion beam.

The performances of a bucket-type ion source depend on the motion of electrons in the ion source. Ohara *et al.* developed a simulation code to calculate the trajectories of electrons in an ion source using the collisionless model [1]. Because the mean free path of electrons is typically shorter than the total path of electrons, we developed a simulation code taking account of collision phenomena [2]. In the code with collisions, we could calculate the distribution of ionization points by tracing primary electrons emitted from filaments until they lost their energy or escaped to the wall and the grid [3,4].

In this study, we calculate the distribution of ionization points and the number of ionization collisions on gas pressure and the initial energy of primary electrons. And we calculate the life time of primary electrons. Further, we calculate two scattering models, anisotropic and isotropic scattering, on collisions between electrons and neutral gas atoms and discuss the availability of the isotropic scattering model. We apply this code to analyze the design optimization of a bucket-type ion source.

2. Simulation Model

2.1 Physical model of a bucket-type ion source

Figure 1 shows the schematic view of a reference bucket-type ion source. The size of the arc chamber is 500mm × 230mm × 200mm. Twenty-six permanent magnets are arranged to form a cusp field near the wall of the arc chamber. The residual flux density of the permanent magnets is 4kG. Ten filaments are installed in the arc chamber. Filament current is 10A. Arc discharge occurs between the filaments that work as the cathode and

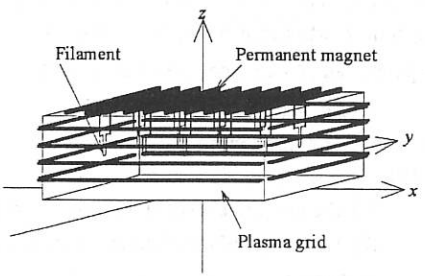

Fig.1 The schematic view of a bucket-type ion source.

the arc chamber walls that work as the anode. The neutral gas filled into the arc chamber will be ionized and become a weakly ionized plasma. The plasma is expected to exist uniformly throughout the arc chamber, because the cusp field formed by surrounding magnets reflects the charged particles. Ion beams are extracted through the plasma grid.

2.2 Calculation model

Electrons are emitted from the filaments and move in the magnetic field which is created by the surrounding magnets and the filament currents. Electrons collide with neutral atoms elastically or inelastically. In the case of inelastic collisions, electrons ionize or excite the atoms.

The motion of an electron is calculated by solving the equation of motion as follows.

$$m \frac{dv}{dt} = q\, v \times B + F_{col} \,, \tag{1}$$

where m is mass of the electron, q is charge, v is the velocity vector and B is the vector of magnetic flux density. The electric field is neglected in the above equation because it is neglibly small over the entire plasma regions anisotropic to be examined as compared with the electric field in the very narrow region near the filaments. The second term on the right-hand side F_{col} is the force term by the collisions. We get the trajectries of the electrons by solving Eq. (1) by using the Runge-Kutta-Gill method as the initial value problem.

In this studies, the gas is Ar. The collision cross sections and differential cross section, we quoted from Ref. [5,6]. The kinds of collisions are ionization, excitation and elastic collision.

The magnetic field created by permanent magnets is calculated by 3D analytical solution based on the magnetic charge model [1]. The magnetic field created by the filament currents is calculated by using Biot-Savart's law [1,5]. The typical configuration of magnetic field is shown in Fig. 2. The line cusp field can be seen along the chamber wall.

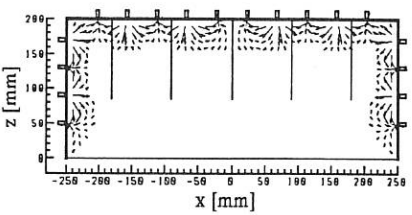

Fig. 2 The magnetic field in the x-z plane at y=0.

A calculation of the trajectory of an electron is terminated when the conditions as follow are satisfied.

(1) The electron arrives at the chamber wall.

(2) The energy of the electron becomes below 16eV (the least ionization energy of Ar atoms).

(3) The electron gets out of the grid.

We assume that the neutral atoms have no kinetic energy, because their thermal energy is

much less than that of electrons. An example of trajectory is shown in Fig. 3, where gas pressure is 5 mTorr, the initial energy of primary electrons is 80 eV and the filament current is 10 A. In this figure, the dots show the ionization points.

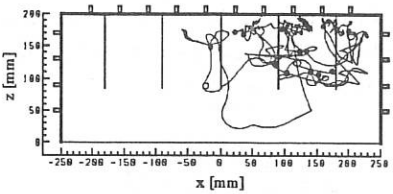

Fig.3 The electron orbits projected on x-z plane.

3. Results and Discussions

3.1 Collisions and lifetime of primary electrons

Figure 4 shows the number of ionization collisions which occur in the flight paths of electrons as a function of gas pressure. In these gas pressures, the number of electron collisions increases with the increase in the gas pressure and the initial energy of electrons. In the low pressure of 1 mtorr, electrons have the less ionization collisions for any initial energy of electrons, because the number density of Ar atoms is small. The electrons that have the small initial energy, for example 30eV, generate the less ionization collisions.

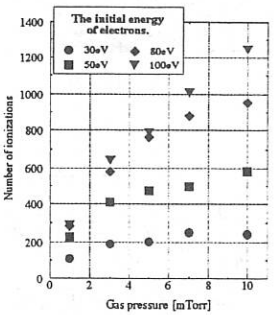

Fig.4 Number of ionization collisions shown as a function gas pressure.

Figure 5 shows the average energy of electrons as a function of time. At 1×10^{-7} sec, electrons still have sufficint energy to ionize neutral atoms in the case of gas pressure of 5 mTorr and 10 mTorr. This means that the present simulation is good for obtaining more realistic physical result than the former simulation [1,5].

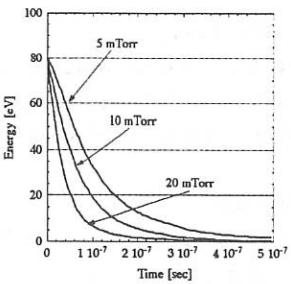

Fig.5 The average energy of electrons shown as a function of time.

3.2 Effects of isotropic scattering

Figure 6 (a) and (b) show the angular distribusions of anisotropic and isotropic scattering. The total cross section is same. In the anisotropic case, the scattering about the inclimation angle is calculated using the value of the differential cross sections where most electrons are scattered forward.

Figure 7 (a) and (b) show the ionization points projected on the x-z plane. Gas pressure is 5 mTorr and the initial energy of primary electrons is 80 eV. The distribusion of ionization points in the isotropic case is quite localized in the upper point as compared with that in the anisotropic case. This fact means that electrons escape more rapidly near the grid

(the lower edge) in the isotropic case because of larger diffusion. In the earlier studies [7], it was found that the distribution of ionization points well approximates plasma density distribution. Therefore, anisotropy of scattering collision affects the distribution of plasma generation in the ion souce.

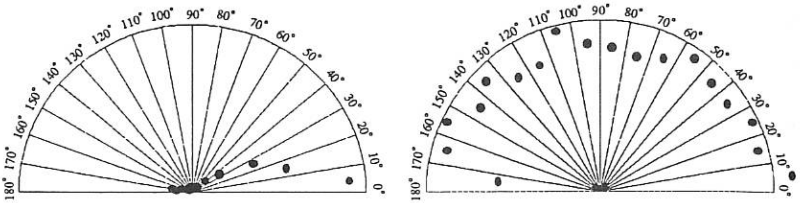

(a) Anisotropic (b) Isotropic

Fig.6 The angular distribusions of scattering electrons.

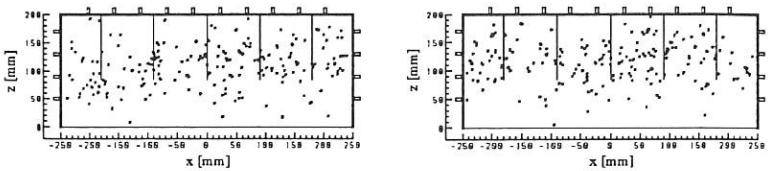

(a) Anisotropic (b) Isotropic

Fig.7 The ionization points projected on x-z plane.

4. Conclusions

We have developed a simulation code to trace primary electrons and to analyze the ionization points in plasmas of a bucket-type ion source. It was found that collision between primary electrons and neutral gas atoms are essential to examine the plasma features.

References

[1] Y. Ohara, M. Akiba, H. Horiike, H. Imai, Y. Okumura and S. Tanaka, J. Appl. Phys. **61** 1323 (1987).

[2] S. Ido, H. Hasebe and Y. Fujita, Jpn. J. Appl. Phys. **32** 4761 (1993).

[3] S. Ido, H. Hasebe and A. Shibata, Journal of Plasma and Fusion Reseach **70** 77 (1994) [in Japanese].

[4] S. Ido and H, Hasebe, Jpn. J. Appl. Phys. **33** L380 (1994).

[5] F. J. de Heer, R. H. J. Jansen and W. van der Kaay, J. Phys. B **12** 979 (1979).

[6] S. Ido and M. Ishine, Kakuyugo Kenkyu **66** 69 (1991) [in Japanese].

[7] S. Ido and K. Nakamura, Jpn. J. Appl. Phys. **32** 5698 (1993).

The Operational Characteristics of a Molten and Damaged Beryllium Divertor Target in JET

B.J.D. Tubbing, A. Chankin, S. Clement, P. Coad, E. Deksnis,
J. Lingertat, A. Loarte, C. Lowry
JET Joint Undertaking, Abingdon, OXON, OX14 3EA, UK.

1. Introduction

In the final phase of the 1994/95 experimental campaign, the Carbon Composite target in the JET Mk-1 divertor was replaced by a Beryllium target. The typical plasma facing dimensions of the target components are 30 x 80mm. To relieve thermal stresses the Beryllium surface is castellated with squares of 6mm. Most of the experimental work on the Beryllium tiles was carried out such that gross melting was avoided. Generally, sweeping of the strike zones was used to reduce the heatfluxes, and heating pulse lengths were relatively short. It was observed that in most respects operating on a Beryllium target did not differ significantly from that on a Carbon target [1].

In addition, a specific experiment was carried out to address the question of operation on Beryllium at higher heatfluxes and with gross melting, and the question how melt damage affects subsequent operation. An important motivation for these experiments was to test the speculation that in ITER a Beryllium target would 'self-protect' against excessive heatfluxes in off-normal operational conditions [2]. In this scenario, evaporating Beryllium would lead to high radiative power losses and thus reduce the heatflux to the target. This effect is often referred to as the 'vapour shield', although Beryllium vapour as such plays no role. The reference heatload for the ITER off-normal event is 25MW/m^2.

The configuration was a single-null divertor discharge, at toroidal field 2.4T and plasma current 2.5MA for most of this programme. With the full NBI heating power of 17.5MW, and with stationary strike zones, heat fluxes to the target are nominally 25MW/m^2. Most of the melting was made with stationary strike zones. Gas puffing rate was a primary variable in these experiments, because of its key role in establishing radiative divertor conditions. Reference discharges were taken before and after the melting in three standard JET regimes: 1. elmy H-mode without gas puff, 2. elmy H-mode with strong gas puff, 3. radiative divertor with Nitrogen impurity seeding.

2. Initial melting and results with and without gas-puff.

The experiments were conducted with the strike zones on a part of the divertor target that had not been damaged by prior operation. Figure 1 shows the sequence of discharges that led to the initial melting in these experiments. These were done with a constant gas puff rate of 2.5 $10^{22}s^{-1}$ electrons. NBI power was 12MW. The temperatures quoted are the maximum temperatures in the field of view of an infra-red CCD camera. The target was pre-heated by a phase with sweeping strike zones. Then, at 17s, the sweeping is stopped, and the maximum target temperature is seen to rise. The integrated heat flux to the target in this series is increased by delaying the time of resumption of the sweeping (19s, 20.5s and 21.5s respectively). With increasing heat flux, clear signs of Beryllium influxes are observed, from the Be II line emission. After the third discharge, an in-vessel camera view revealed clear signs of melting, on the outer strike zone. It was not easy to distinguish melting from the evaporation of the solid near the melting point. This issue will be analysed further.

After the discharges shown in figure 1, the power and duration of the unswept phase were further increased, and significant melting was observed. Nevertheless, the radiated power did not exceed 50% of the input power. Elmy H-mode operation was retained, and no degradation of plasma stored energy or D-D reaction rate with rising target temperature was evident. It was remarkable that the Be influxes into the discharge were significantly larger during the swept phases on a cold target, than during the unswept phases on the hot target. Presumably, this is due to the accumulation of Beryllium material that was re-deposited during the previous shot(s).

A similar approach to melting, using entirely unswept discharges, was carried out without gas puff (except for the normal density feedback). In these discharges melting was observed both on the outer and on the inner strike zone. Figure 2 shows one of these discharges, with a total energy input by NBI of 75MJ. The radiated power was observed to rise from about 50% to about 70% over a period of several seconds, while further detorioration of the target damage was clearly visible. The H-mode of these discharges was severly degraded. These non gas-puffed high power discharges were the only cases in which the radiated power fraction was seen to increase beyond about 50% by Beryllium influx. While a moderate degree of 'self-protection of the target is thus evident, this was not sufficient to prevent further tile damage.

3. Post-melting reference discharges, unswept.

After the melting, the reference discharges were repeated. These discharges are now unswept, with the strike zones located precisely on the molten regions. In figure 3 a comparison is shown between a pre- and post-melt elmy H-mode without gas puff. The post-melt discharge is clearly degraded. H-mode is not obtained. The discharge disrupts as a result of a density limit disruption, caused by the Be influx.

In contrast, pre- and post melt discharges in elmy H-mode with gas puff are rather similar, as shown in figure 4. After an initial transient, at the same level of NBI power, the same radiated power levels and stored energy are obtained. The D-D reaction rate is slightly higher in the post-melt discharge, due to the somewhat lower density. There is no evidence for large Be influxes. Similarly, the behaviour of Nitrogen seeded radiative divertor discharges before and after the melting is nearly identical, after an initial transient. Both discharges are elmy H-modes. We conclude that, with the exception of the low density, no gas puff regime, the penalty from operation on a damaged Beryllium target is not severe.

4. Recovery of normal, swept operation.

Subsequently, a series of discharges was executed in which the strike zones were swept over the damaged zones. The first of these had no gas puff. It disrupted, due to excessive Beryllium influxes. However, subsequent conditioning of the damaged zones was achieved in a series of gas puffed discharges. A steady recovery was seen. After three such gas puffed pulses, a further attempt was made at the non gas puffed case. This was now successful. Elmy H-mode was recovered, although the stored energy and D-D reaction rate were still degraded (about 20% and 40% respectively).

5. Long pulse swept operation at high input power.

Two high power, long pulse discharges, with sweeping strike zones (about 60mm) were performed at toroidal field 2.8T and plasma current 3MA, and with strike zones on a previously undamaged part of the target. Total plasma input energies (ICRH, NBI and ohmic power) were 120 and 180MJ respectively. Soon after the heating is switched on there is an

initial Be influx lasting about 0.5s, presumably due to accumulation of re-deposited material. After that, conditions are relatively stationary until Beryllium melting starts (after about 5s at 20MW total input power). Then a strong Beryllium influx is observed, the radiated power increases, and the D-D reaction rate drops dramatically. Significant further damage to the target was observed to result from these discharges.

6. Final state of the target.

Figure 5 is a photograph of a sector of the target near the outer strike zone, taken after the experiment. Three annuli of damage are visible. The inner damage existed already before this experiment. It was the result of a giant elm in high power operation, and of a particular discharge in the divertor assessment programme. The middle ring of damage is due to the unswept melting, while the outer ring is due to the high power swept operation. In the middle ring, significant formation of drops and bridging of tile gaps (about 10mm) is observed. Tiles are eroded to a depth of 2 to 3mm. There is little spreading of droplets or damage to neighbouring areas. All damage exhibits full toroidal symmetry around the machine.

7. Conclusions and implications for ITER.

A controlled experiment to assess operation on a molten and damaged Beryllium divertor target was carried out. The heatfluxes in these experiment are nominally 25MW/m^2. This corresponds to the ITER reference value for the off-normal heatflux to the ITER target.

The radiated power fraction in all these experiments remained below 50%, with the exception of the high power, unswept, non gas-puffed discharges, where it was seen to rise to about 70% over a period of seconds. Although this level of radiated power represent a certain degree of 'self-protection' of the target, it is clearly insufficient to prevent gross damage.

Post melt reference discharges showed that operation with strike zones on the damaged areas with gas-puffing and with Nitrogen seeding is essentially the same as on pristine tiles. Only discharges without gas-puffing were disruptive and / or degraded. Normal elmy H-mode operation, with strike zones sweeping over the damaged areas, could be re-established after some conditioning discharges.

The implication for ITER is that at this level of heatflux significant damage to a Beryllium divertor target can be done, while only a moderate degree of 'self-protection' is evident. Damage to the divertor target at the level observed here does not lead to loss of operation, but may be expected to lead to a rapid failure of the exposed component. It may therefore be preferable to design and implement an active safety device to protect against off-normal conditions, rather than to rely on the 'self-protection' of a Beryllium divertor target.

References

[1] M. Keilhacker and JET Team, 'JET results with the new Pumped Divertor and Implications for ITER', this conference.

[2] Y. Igitkhanov et. al., 'Effect of Slow High-power Transients on ITER Divertor Plates and Limiter Components', this conference.

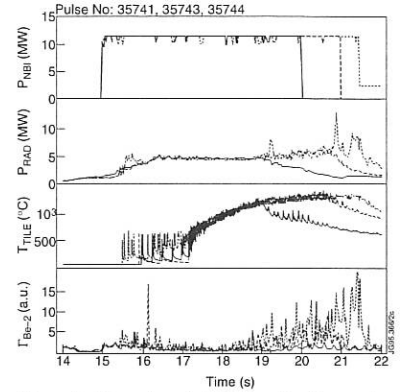

Figure 1: The series of discharges leading to the initial melting.

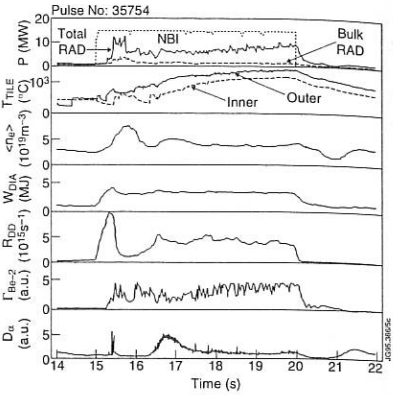

Figure 2: High power discharge without gas puff.

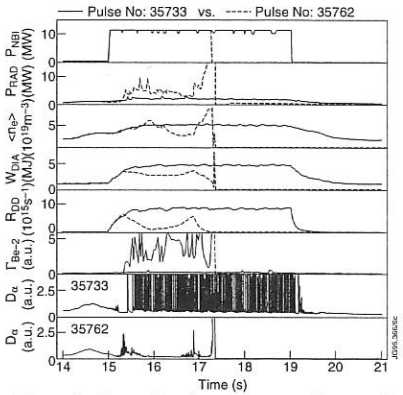

Figure 3: Comparison between pre- and post melt elmy H-mode discharges without gas puff.

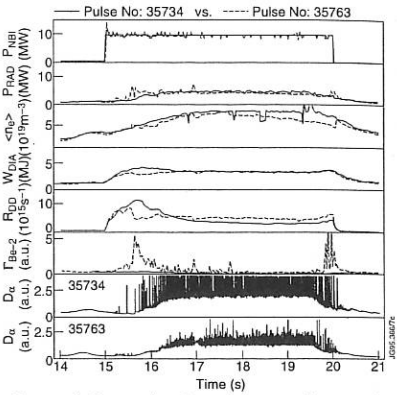

Figure 4: Comparison between pre-and post melt elmy H-mode discharges with gas puff.

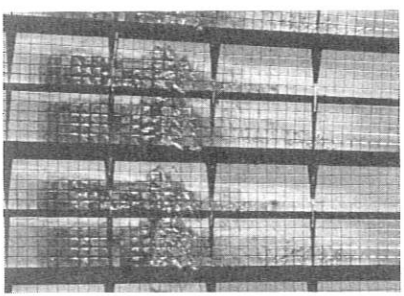

Figure 5: Photograph of a section of the outer target after the experiment. Horizontal corresponds to the radial direction, vertical to the toroidal direction.

Resistivity profile effects in numerical magnetohydrodynamic simulations of the reversed-field pinch

H.-E. Sätherblom, S. Mazur and P. Nordlund

Division of Fusion Plasma Physics (Association EURATOM-NFR), Alfvén Laboratory, Royal Institute of Technology, S-100 44 Stockholm, Sweden

Experiments on the Extrap T1 reversed-field pinch have shown that the magnetic fluctuation level and the input power dissipated by fluctuating components are strongly influenced by variations in the resistivity profile [1]. In this paper we present results from numerical investigations of the influence of variations in the resistivity profile on the plasma dynamics, using the 3-dimensional magnetohydrodynamic code DEBS [2].

The DEBS-code [2] solves the force-free resistive MHD equations in a cylinder, periodic in the poloidal θ and toroidal ϕ directions. The code uses a semi-implicit method which adjusts the code time step to the dynamic activity in the code, thus the output data is unevenly sampled and for the temporal spectral analysis discussed in this paper the Lomb method is used [3]. For the present calculations we use 161 radial grid points. Poloidal mode numbers ranges from $m = 0$ to 3 and toroidal mode numbers from $n = -21$ to 21. We use a Lundquist number of 10^4 and a viscosity of 1.5. The aspect ratio is set to 2.2. We use a resistivity profile of the form $\eta(r) = (1+9r^\gamma)^2$, where r is the normalised minor radius. We vary the shape of the resistivity profile and the resistivity in the edge region by changing γ from 30 to 10. The profile is not evolved in time. The code is set-up to hold the toroidal current and the pinch parameter $\Theta = B_\theta(a)/\langle B_\phi \rangle$ constant in time by adjusting the toroidal loop-voltage. The toroidal flux is kept constant by a perfectly conducting shell. The code was run for approximately 3000 Alfvén times in both cases in order to achieve quasi-stationary states.

This modest modification of the resistivity profile turns out to have a strong influence on the plasma dynamics. The case with the narrow, high edge resistivity profile ($\gamma = 10$) is characterised by higher fluctuation levels and a more shallow reversed quasi-stationary state than the low edge ($\gamma = 30$) resistivity case, as previously reported consistent with experimental results [1]. Thus, when changing γ we observe a factor of two increase in the volume integrated energy of the fluctuating radial magnetic field ∂B_r (see Fig. 1) accompanied by a broadening of the mode spectra. In the $m = 1$ mode spectra the energy in the core resonant modes $n = 4$ and 5 are doubled and a secondary peak is caused by the four-fold increase of energy in the $n = 7$ mode. The energy of the $m = 2$ modes is approximately doubled with a slight spectral broadening whereas the energy increase in the $m = 0$ modes is less pronounced but the peak is shifted from the $n = 2$ to the $n = 3$ mode. The fluctuation induced electric field $\mathbf{E}_f = \langle \mathbf{v} \times \mathbf{b} \rangle$ changes accordingly, strengthening its effect of suppressing axial current on the

axis and driving poloidal current at the edge. However, the parallel current $j_{\|}$ at the edge is nonetheless reduced, due to the higher edge resistivity, and the quasilinear effect of the $m = 0$ modes at the reversal surface is suppressed. The enhanced suppression of parallel current in the core results in a hollow time-averaged $\mu(r) = \mu_0 (\mathbf{J}\cdot\mathbf{B})/B^2$ profile in the central region. The resulting increase in the Spitzer input power - associated with ohmic dissipation of the mean current - is less than ten percent, whereas the anomalous input power P_a, which is dissipated by the fluctuations, increases more than a factor of two. The total loop voltage V_ϕ increases about 30%. The time averaged field reversal parameter $F = B_\phi(a)/\langle B_\phi \rangle$ changes from -0.26 to -0.12.

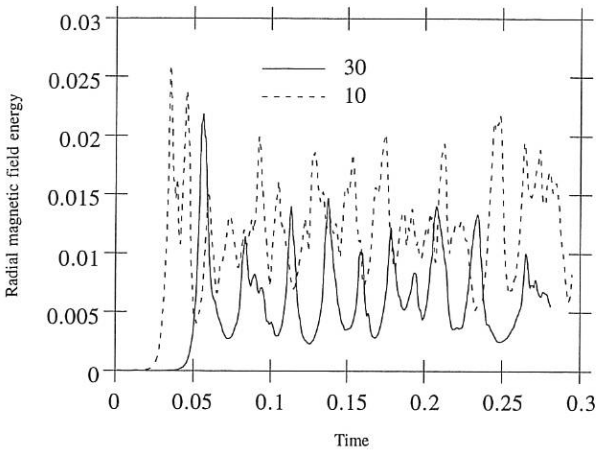

Fig 1.: The volume-integrated radial magnetic field energy vs. time normalised to resistive diffusion time

Furthermore we find that the narrowing of the resistivity profile has a strong influence on the time-scale of the RFP dynamics. From Fig. 1 we see that the bursts in magnetic energy due to relaxation events occur more frequently and less coherent in the $\gamma = 10$ case than with $\gamma = 30$. The corresponding Lomb periodogram [3] verifies this picture, showing a broad temporal power spectrum with significant frequency components of over $f = 200$ in the $\gamma=10$ case, whereas for the $\gamma=30$ case the spectrum shows one dominant peak at about $f = 40$ and no significant components above $f = 100$. Here f is in units of *1/(resistive diffusion time)*. The spectra of the on axis value $q(0)$ of the safety factor $q = rB_\phi/RB_\theta$, where R is the major radius, and F, show similar pictures although the maxima of f are different, being about 1000 and 500 for $q(0)$ and less pronounced for F, where we find maxima of $f = 140$ and 100, for $\gamma = 10$ and

$\gamma = 30$, respectively. Thus the dynamics are proceeding at up to a factor two higher rate in the narrow resistivity profile case.

In Fig. 2 the safety factor is shown as function of minor radius and time normalised to resistive diffusion time. We see that the $\gamma = 10$ case gives rise to a more rapid edge field diffusion, which causes relaxation events, characterised by the rapid peaking of q on axis, to occur with a rate which is over 50% higher than in the $\gamma = 30$ case.

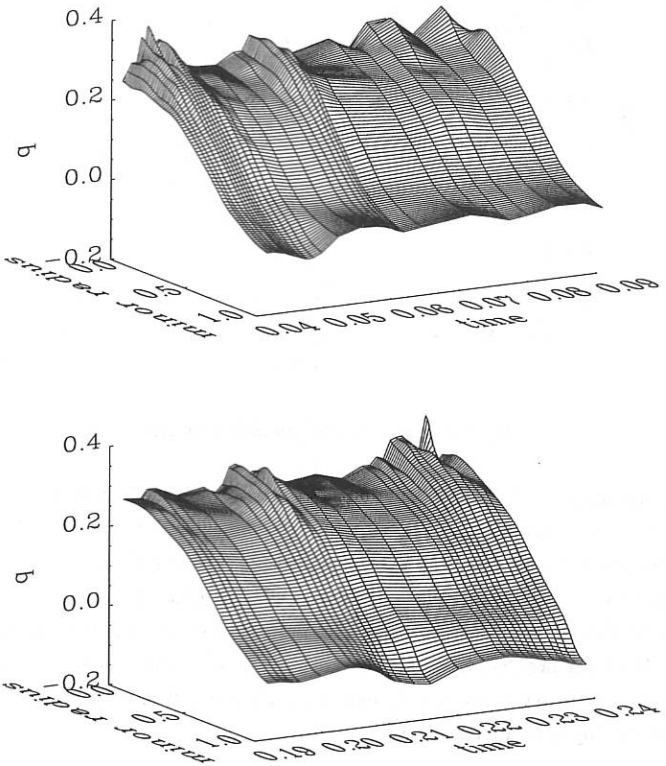

Fig 2.: The safety factor q vs. the normalised minor radius and time normalised to resistive diffusion time for the $\gamma = 10$ case (top) and the $\gamma = 30$ case (bottom)

The higher V_ϕ characterising the $\gamma = 10$ case is equivalent to proportionally higher energy and helicity input rates. In spite of this, the $\gamma = 10$ case approaches a state characterised by a slightly lower total magnetic energy W and total helicity $K = \int (\mathbf{A} \cdot \mathbf{B}) dV$. Fig. 3 shows

K vs. V_ϕ for the two cases. The starting points $t = 0$ are at the upper left of the diagram. It is seen that as time increases the systems approach different regions in the diagram. The plot of W versus V_ϕ is similar. The time-average values of the Taylor ratio W/K differ less than one percent between the both cases.

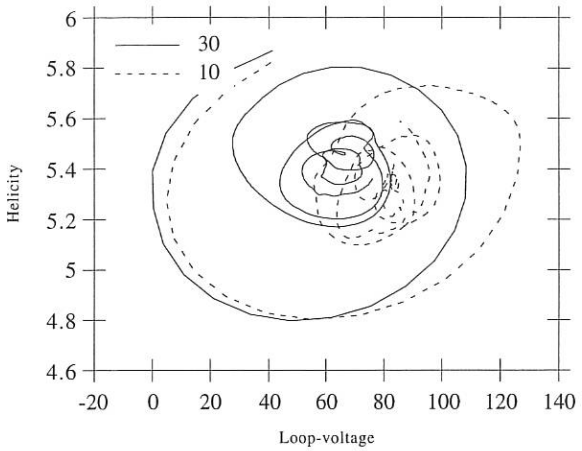

Fig 3.: The helicity vs. the toroidal loop-voltage

In summary, with a more narrow resistivity profile the fluctuation level and the fluctuation induced electric field increases. However, the enhanced dynamo action does not suffice to totally counteract the effect of the increased edge resistivity, resulting in reduced $j_\parallel$ at the edge and a more shallow reversal F . The enhanced edge resistivity increases the edge field diffusion rate, forcing the system to increase its field conversion rate, reducing the dynamic time scale. With a higher edge resistivity the final state of the system is characterised by higher loop-voltage, slightly lower values of the total magnetic energy W and the magnetic helicity K and almost unchanged Taylor ratio W/K.

This work was supported by the European Communities under an association contract between EURATOM and the Swedish Natural Science Research Council. NSC at Linköping is acknowledged for the access of the CRAY YMP.

[1] Nordlund P., Mazur S., Sätherblom H.-E. et. al., to appear in *Plasma Physics and Controlled Nuclear Fusion Research*, 1994 (Proc. 15th Int. Conf. Seville 1994), IAEA

[2] Schnack D.D. et. al., *Comput. Phys. Comm.* **43** 17 (1986)

[3] Lomb, N.R., *Astrophysics and Space Science*, **39(2)** 447 (1976)

Index

Abramova KB II-165
Adams JM II-037, II-053, III-057,
Adler HG II-401
Afanassiev VI II-057
Agostini E III-441
Aizawa M II-137
Akhmetov TD II-181
Akiyama R I-153, III-413, IV-149, IV-153
Albrecht M III-249, IV-413
Alejaldre C II-149, II-157
Alekseev AG III-385
Alexander A IV-089
Alexander M III-001, III-237
Alexeev IS I-049
Ali-Arshad S III-281, IV-021, IV-141
Aliaga-Rossel R II-173
Alladio F I-237
Allen SL III-105
Alonso J II-157
Alper B IV-061
Amemiya H I-397
Amery G I-449
Amosov VN III-385
Anabitarte E I-405
Anderson D I-093
Ando A I-153, III-413, IV-149
Andrejko MV I-033
Andrew P II-301
Ane JM IV-069
Anikeev AV IV-193
Anton M II-389, III-113, IV-081
Antoni V IV-181
Antozzi P III-381
Apicella ML II-121
Appel LC II-261
Appert K II-245, IV-233
Arber T I-257
Arslanbekov R III-373, IV-065, IV-393
Ascasibar E II-149, II-153, II-157, IV-157
Ashall JD IV-213
Askinazi LG I-033
Asmussen K I-065
Axon KB IV-213
Azumi M III-029, IV-237
Babich I III-437
Badalec J II-373
Baelmans M IV-309, IV-321, IV-329
Bagdasarov AA I-049

Bagryansky PA IV-193
Baity FW I-381
Bak PE I-013, II-441, IV-061, IV-405
Bakos JS II-421
Balbin R I-301, I-305, II-157, IV-157
Baldzuhn J III-141, III-145
Balet B I-009, I-013, II-069, IV-061, IV-141
Ballabio L III-381
Baloui T III-201
Bamford RA II-133, III-033
Barabaschi P IV-009
Baranov Y III-361, IV-393
Barnes CW III-013
Barnsley R I-081, I-097, III-121, IV-465
Barsilio ZA I-289
Barth CJ II-129
Barth K II-009, II-121
Bartlett DV III-085, III-261, IV-021, IV-425
Basiuk V III-337, IV-125
Bastasz R IV-049
Batchelor DB II-333, III-365, IV-121
Batha S II-113, III-365
Bayley JM II-173
Baylor L I-113
Bazylev B II-277
Beaumont B IV-397
Becker G I-025, II-193, IV-285
Becoulet A IV-353
Beg F II-169
Behrendt H II-297
Behringer K I-069, III-409
Behrisch R II-301
Beidler CD III-129, III-149
Beikert G III-201
Bell MG II-109, II-329, III-397
Bell RE II-113, II-357, III-013
Belov AM I-421
Bengtson RD I-001, I-281, III-265, IV-097
Bergmann A I-425
Bergsaker H I-173, III-157, IV-277
Berk HL II-233
Bernabei S II-357
Bers A IV-353
Bertrand P III-209, III-357, IV-197
Bertschinger G II-381
Bessenrodt-Weberpals M I-065, IV-133
Besshou S I-137, I-145, I-149, I-157, I-161, III-405
Bettenhausen M II-325
Bettini P IV-185
Beurskens MNA II-129

Bhatnagar VP II-069, II-329, IV-001
Bibet P III-373
Bickley AJ II-009, II-125
Birk G T I-441
Biskamp D IV-205
Blackwell BD II-141
Blow G IV-213
Boedo JA I-057, I-293
Bogomolov LM I-277, III-329
Bohmeyer W II-297
Boivin R II-341
Bolzonella T IV-177, IV-181
Bombarda F II-313, II-341, III-017
Bond DS II-053, III-057
Bondarenko IS II-117
Bondeson A I-213, I-241, III-165, IV-209
Bonnin X III-265
Bonoli P II-341, IV-121
Borba D II-237, II-261, III-081
Borg G II-141
Bornatici M III-185
Borner P IV-321
Borovsci BV I-277
Borrass K I-341
Bosch HS I-321, III-093, III-097, IV-041
Boucher C III-101
Boucher D III-169
Boucher I IV-409
Box FMA II-129
Braams BJ IV-285, IV-305
Bracco G III-021
Brañas B ..... II-157, III-141, IV-157, IV-161, IV-165, IV-429, ... IV-433
Bravenec RV I-001, III-265, IV-097
Breger P II-377, IV-001
Breizman BN II-233, II-261
Bretz NL III-013, III-397
Breun R IV-381
Brooks JN IV-305
Brooks NH II-281, IV-049
Brouchous D IV-381
Brower DL I-001, IV-097, IV-129
Brunner S IV-241
Brunsell P III-157, IV-277
Bruschi A I-361, IV-369
Brzozowski JH I-173, I-177, III-157, III-153
Buchl K I-349, III-097
Budaev VP I-277, III-329
Budnikov VN II-085, IV-385
Budny RV I-409, II-105, II-109, III-013

Buhlmann F I-417
Bulanin V II-089
Buratti P I-361, III-021
Bures B IV-141
Bures M II-329, II-353
Burgos C II-153
Burhenn R III-145
Burmasov V I-445
Burrell KH IV-137
Bush CE II-113, III-013
Bustamante EG I-405
Buttery RJ III-233, III-273, IV-213
Caldas IL I-289
Callis RW I-381
Campbell DJ I-309, II-009, II-073, II-121, II-125, III-081, III-085,
..... III-289, III-293, III-305, IV-001, IV-009, IV-465
Candy J II-237
Cantu P I-453
Cao L II-409
Cappello S IV-181
Carlson A I-425, III-097, III-245
Carolan PG II-025, II-133, II-209, III-033
Carraro L II-317, III-161, IV-177
Carreras B IV-165
Carter M II-333
Cary WP I-381
Casarotto E II-309, II-317
Castejon F II-157, III-041, III-225, IV-269
Castro RM I-289
Cauffman S II-405
Cecil E II-037
Challis CD II-069, III-005
Chamouard C III-109, IV-349
Chan V I-377
Chance M I-193
Chang Z II-113, III-013, III-045
Chankin A III-289, III-309, IV-021
Chashchina GI II-085
Chatelier M I-317, II-041
Chen H I-081
Cheredarchuk A III-437
Cherepanov KV III-205
Chernyatjev Yu V III-285
Cherubini A I-013
Cherubini C II-213
Chistiakov VV I-049, I-369
Chitarin G IV-181, IV-185
Chittenden JP II-173
Chiu SC I-109, I-377, I-381
Chodura R I-425

Choe W II-093
Chrien RE II-061
Christensen C II-341
Christiansen JP I-009, IV-061, IV-141
Christou C I-137, I-145, I-157, I-161
Chu CC I-129, II-013, II-129
Chu MS I-241, IV-137
Chutov Yul IV-453
Cima G I-001, I-005, IV-097
Cirant S I-361, IV-369
Claassen HA IV-293
Clairet F IV-101, IV-409
Clement D III-133
Clement S I-309, II-125, III-281, III-289, III-293, III-305,
..... III-309
Coad JP II-273, III-309
Coda S I-297
Coffey IH I-081, III-121
Colas L I-041, IV-101
Collarin P IV-181
Colton A II-025, III-273
Condrea I IV-289
Connor JW I-089, I-261, II-205, III-189, IV-201
Connor K I-001
Conroy S III-381
Conway NJ II-133
Cooper WA II-145, III-133
Coppi B I-461, III-017, IV-025
Corboz M III-113
Cordey JG I-013, II-073, III-229, III-277
Correa-Restrepo D II-189
Corrigan G IV-297
Coster DP III-093, III-249, IV-285, IV-329
Costley A III-377
Cote A II-361, III-101
Cote C II-361
Cottrell GA II-229, II-405
Counsell GC II-205, III-233, IV-365
Cox M II-265, IV-365
Crowley TP I-001, III-265
Cupido L IV-413, IV-425
da Cruz DF I-129, II-013
Da Silva R I-289
Dalla S II-033
Dangor AE II-169, II-173
Darrow D II-105, III-365
Das J IV-313
Daughton W III-017
Davies SJ II-125, III-257, III-293, III-297, III-305, IV-465
Davydova TA I-437

de Angelis R I-053
de Baar M I-385
de Blank HJ I-233, II-029, III-273, IV-133
de Esch H IV-001, IV-061, IV-141
de Haas JCM I-009, II-009, II-069, II-073, II-453
de Kock L III-377
de Kloe J I-129
de la Cal E II-157
de la Luna E II-157, III-141, IV-161, IV-429, IV-433
De Lorenzi A IV-185
De Luca F I-053, II-013, III-009
de Michelis C I-085, III-109
de Peña S III-409
de Pena Hempel S II-005
De Ploey A I-221
de Rover M IV-261
de Vries PC III-053, IV-029
Decoste R III-101
Degrassie JS I-381
Degtyarev L I-217
Deichuli PP IV-193
Deksnis E I-309
Deliyanakis N I-013, I-029, I-053, III-009, III-081, III-121, III-261, IV-061, IV-141, IV-405
Demchenko V IV-377
Dementjev GN I-277
Demers Y II-361
De Michelis C II-385, IV-345
Dendy RO I-185, II-229, II-241, II-405, IV-201
Denne-Hinnov B I-085
Denner T I-057
De Ridder G I-241
Deschenaux Ch IV-081
Detragiache P IV-025
Devynck P IV-101
Di Marco JN IV-181
Diebold DA IV-381
DIII-D Team III-105
Ding N II-225
D'Angelo F I-265
Dobbing JA III-081
Doczy M IV-381
Doloc C II-041
Dong JF III-073
Donne AJH III-421, III-425, IV-029, IV-337
Dorn Ch III-409
Doyle EJ I-105, I-109
Drabbe M III-421
Drake JF IV-205
Drake JR I-169, I-173, I-177, III-157

Dreher J I-441
Dreval VV IV-401
Dryagin Yu A I-429
Dubois MA IV-249
Dudok de Wit T I-085
Dumbrajs O III-181
Duong HH I-409
Durodie F III-341
Duroua A IV-097
Durst RD I-001, IV-097
Dutch MJ II-097, II-101, II-389, III-113, IV-077, IV-081
Duval BP II-097, III-113, IV-081
Dux R I-065, I-069, II-005, IV-285
Dyachenko VV II-085, IV-385
ECRH Group III-129
Edenstrasser J I-269
Edery D I-249, IV-065, IV-073
Edlington TE IV-425
Edmonds P I-001, III-397
Edwards AM II-021, IV-061
Edwards ME IV-117
Efthimion PC I-373, III-013
Ehrenberg J I-309, II-121, III-085, III-281
Ejiri A I-153, III-413, IV-149, IV-153
Ekedahl A III-361
Elfimov A IV-381
Emmoth B III-137
Endler M I-301
England A III-365
Erba M I-013, II-213, IV-061
Erckmann V I-353, I-357, I-389, I-429, III-037
Erents SK II-125, III-117, III-257, III-297, III-305
Eriksson L-G I-009, I-093, II-033, II-069, I-209, II-253, II-353,
..... III-381, IV-001
Ermolaev AM III-389
Ernst D III-013
Esipov LA II-085, IV-385
Esposito B II-037
Esser HG IV-281
Esterkin AR IV-389
Estrada T II-149, II-153, II-157, IV-157, IV-161, IV-165,
..... IV-429, IV-433
Euringer H I-057, I-061, II-397
Euripides P IV-045
Evans TE IV-049
Fahrbach H I-025, III-249
Fall T III-157, IV-277
Fanack C IV-409
Fasoli A III-081, IV-085
Fechner B II-329, II-353

Federici G IV-333
Feix MR III-209
Feng Y IV-325
Fenstermacher ME III-105, IV-305
Fernandes J IV-417
Feron S III-317
Ferreira JG III-033
Fiedler S III-253, III-269
Field AR I-069, II-289, II-293, III-097, III-409
Fielding SJ I-097, I-345, II-001, II-025, III-125, III-273,
..... III-369, IV-213
Fijalkow E II-429, III-209
Filippas AV I-281
Filippov AN IV-169
Filippov NV IV-169
Finken KH I-057, I-061, I-133, I-293, II-397, IV-093, IV-341
Fiore C II-341, III-017
Fiorentin P IV-181, IV-185
Fisch N III-365
Fischer B II-037, II-353, III-361, IV-113
Fisher RK I-409
Fishpool G IV-141
Fitzpatrick J II-233
Fivaz M IV-233
Fonck RJ I-001, III-013, IV-097
Fontanesi M I-453, III-441
Forest CB I-381, IV-125
Fraiman AA I-429
Framer-Flecken A II-321
Frances M II-157, IV-429, IV-433
Franzoni G IV-289
Fredrickson E III-045
Frenje J III-381
Froissard P II-037, III-373, IV-397
FTU Team IV-289
Fu BZ III-073
Fuchs CH I-025, III-097, IV-037, IV-285
Fuchs G III-053, IV-341
Fuchs JC I-065, I-069, II-005, III-085, III-401
Fuchs V IV-353, IV-361
Fujii T II-057
Fujisawa A I-001
Fujisawa N IV-009
Fujita J III-417
Fujiwara M III-413, IV-149
Fukuyama A I-205, IV-229, IV-237
Funaba H I-157, I-161, I-285
Furno I II-253
Fussmann G II-297
Gabellieri L I-077, IV-289

Gadeberg M II-069, IV-021
Galambos JD II-333
Galechyan GA II-165
Gandini F IV-369
Gandy R I-001
Gao QD III-073
Garbet X IV-101, IV-253
Garcia L IV-165
Garcia-Cortes I I-305, II-157, III-281
Garcia-Rosales C III-241
Gardner CA II-265, III-233
Gardner HJ II-141, II-145
Gardner MR III-233
Garnier D II-341
Garribba M II-125, IV-009
Garzotti L IV-177
Gasquet H IV-129
Gates DA I-345, II-001, II-025, III-273, III-369, IV-117
Gauthier E I-413
Gehre O I-021, I-025, III-253
Geist T I-429, IV-161, IV-433
Gentle KW I-001, I-005, I-021, III-265
Gerhauser H IV-293
Gernhardt J I-025
Gerstel U II-009
Geruzzi G I-001
Gervais F III-061, IV-101
Gettelfinger G III-397
Ghendrih Ph III-109, III-317, IV-349
Ghizzo A III-209, III-357, IV-197
Giannella R I-053, I-081, I-085, I-089, II-073
Giannone L I-301, IV-265
Giesen B III-341, IV-341
Gill RD IV-061
Gimblett CG II-241
Girka IA IV-357
Giruzzi G I-101, IV-189
Gnesotto F IV-181
Goedbloed JP I-221, IV-085, IV-113
Goetz JA II-313, II-341, III-325
Golant VE I-033
Goldston R III-397
Golovato S II-341
Gondhalekar A II-033
Goniche M III-373, IV-397
Goodall DJH II-017, III-033, III-117
Goossens M I-221
Gordeev OA II-117
Gorini G I-053, II-013, III-009
Gormezano C I-009, II-069, II-329, II-353, III-005, III-081, III-361,

..... IV-001, IV-113
Gott Yu V II-369, IV-221
Gottardi NAC III-085
Gowers CW I-009, II-069, III-005
Graf M II-313, II-341, III-017
Granata G IV-301
Granetz R II-341
Granucci G I-361, IV-369
Gray DS I-057, I-293
Green JM I-241
Greenwald M II-341, III-017
Gregory BC III-101
Grek B III-013
Gresillon D IV-101
Grigull P IV-325
Griscom DL II-401
Grisolia C III-109, IV-349
Grosman A III-109, III-317
Grossman S IV-105
Grote H II-297
Gruber O II-185, III-001, III-093, III-097, III-241, IV-037,
..... IV-089
Gryaznevich M II-017, II-205, III-033, III-117
Guarnieri M IV-181
Guasp J II-157
Guilhem D I-317, III-317, IV-345, IV-397, IV-473
Guirlet R II-385, III-109, IV-345
Guiziou L I-037, I-041, IV-101, IV-253
Gunn JP III-101
Gunther K I-433, II-077
Guo GC III-073
Guo HY I-309, II-273, III-257, III-297, III-305
Gusakov E IV-389
Haas FA III-173
Haas G I-309, I-321, I-325, II-005, III-097, III-241,
..... III-245
Hacker H III-145
Haddad E III-101
Haines MG II-169, II-173, III-213, III-217
Hallock G I-001
Hamada T I-137, I-157, I-161
Hamada Y I-125
Hamamatsu K II-057
Hanatani K I-137, I-161
Harano H II-061
Harbour PJ I-309, II-073, II-121, III-305, IV-465
Harmeyer E III-129, III-149
Harris JH IV-397
Hartfuss HJ I-353, I-357, III-037, IV-161, IV-265, IV-433
Harvey BM II-241

Harvey RW I-381
Hastie RJ I-185, II-241, III-217, III-233
Hawkes NC I-097, II-073, II-125, III-085, III-121, III-261
Haynes PS III-393
Heard JW I-001, I-005, III-265, IV-097
Hedin G I-177, III-157
Hedqvist A III-157
Hegna CC I-261
Heijnen SH IV-441
Heikkinen JA II-349, III-181
Heinrich O III-249
Heliotron-E Group I-141
Hellberg M I-449
Hellblom G I-173, III-157
Heller MVAP I-289
Hender TC I-029, II-017, II-021, II-261, III-233, III-273,
..... IV-061, IV-117, IV-213
Hennequin P III-061, IV-101
Herranz J II-149, II-157
Herre G IV-313
Herrmann A II-005, II-293, III-097, III-241, IV-037
Herrmann MC III-365
Herrmann W I-333, I-349, III-097, III-249
Hershkowitz N IV-381
Hess WR II-385, III-109, IV-345
Hesse M II-385
Heuraux S II-337, IV-409
Hicks JB III-117
Hidalgo C I-301, I-305, I-405, II-117, II-157, IV-157, IV-165
Hidekuma S I-161
Hildebrandt D II-289, IV-325
Hill DN III-105, IV-305
Hillis DL I-061, II-009
Hirano Y I-181
Hirsch K III-409
Hirsch M III-141, IV-161, IV-165, IV-433
Hirsch S II-005, III-097, III-409
Hirt A III-113
HL-1 Team I-273
Hoang GT I-037, I-041, III-373, IV-065, IV-073, IV-101, IV-393
Hoek M II-061
Hoekzema J A II-445
Hoenen F IV-041
Hoffmann C I-349
Hofmann F I-417, II-097, II-101, III-113, IV-077, IV-081
Hofmann JV IV-313
Hogan JT I-325, IV-345, IV-397, IV-473
Hogeweij GMD II-013, III-037
Hokin S I-181
Holakovsky J I-329

Holties HA II-237, III-081, IV-085, IV-113
Holtrop KL IV-049
Holzhauer E I-429
Hone MA II-053, III-057
Hong B IV-469
Horling P I-177, III-157, IV-277
Horne S II-341
Horton L I-309, II-009, II-077, II-121, II-125, II-273, III-085,
..... III-301, III-305, IV-297, IV-465
Hosea JC III-365
Hou L II-437
Houlberg WA I-113
Howard J II-141, II-413, III-421
Howarth PJA III-057
Howe H III-225
Howell DF I-257
Howman AC II-009, II-125, II-453
Huang L II-225
Hubbard A II-341, III-017, IV-121
Hubner K III-201
Hugenholtz CAJ IV-441
Hugill J II-017, II-025, III-033, III-125
Humphreys DA IV-049
Hurwitz PD I-001, III-265
Hutchinson IH II-341, III-313
Huttemann P III-341
Hutter T IV-125, IV-397
Huysmans GTA I-029, I-201, I-341, I-221, II-069, II-237, II-261,
..... III-005, IV-061, IV-085, IV-113
Hwang YS II-093
Hyatt AW IV-049
Ida K I-125, I-161, III-413, III-417, IV-149, IV-153
Idei H I-153, IV-149, IV-153
Ido S II-257, III-449
Igitkhanov Yu IV-317, IV-333
Ignacz P I-065
Ignat D III-365
Iguchi H I-153, III-413, IV-149, IV-153
Ijiri S I-137
Ijiri Y I-145
Ikamura S I-153
Ikezi H I-109, I-381
Imre K II-065
Ingesson LC IV-337
Innocente P IV-177
Intrator T IV-381
Ioffe AF II-081
Irby J II-341, III-017
Irzak MA II-085, IV-385, IV-389
Isayama A I-141, I-157, I-161

Isei N III-029
Ishida S I-017, IV-033
Ishida SI II-069, III-005
Isler RC IV-345
Isobe IV-153
Itoh K I-205, IV-237
Itoh S I-205, IV-229, IV-237
Its ER II-085, IV-385
Ivanov A IV-193
Ivanov N III-077, IV-017
Jablonski D II-341
Jacchia A I-053, II-013, III-009
Jackel HJF I-053, II-069
Jackson GL I-325, II-281
Jacquinot J II-329, III-081
Jaeckel HJ III-085, IV-465
Jaeger EF II-333, III-365
Jagger J I-001
Jakubka K IV-373
Jakubowski L II-161
Janeschitz G IV-317, IV-329, IV-333
Janjua S III-189
Janos A III-045
Jarmen A I-253
Jaroshevich SP I-033
Jarvis ON II-037, II-053, III-057, IV-141
Jasegawa IV-153
Jaspers R IV-093
Jauch Z III-201
Jaun A II-245, III-081
Jenkins I II-017, III-033, III-117
Jernigan TC I-113
Jiang Y I-001, IV-129
Jimenez JA II-149, II-157
Joffrin E III-373, IV-073, IV-125
Johner J IV-069
Johnson DW II-401, III-013, III-397
Johnson LC III-013
Johnson M IV-009
Jones I IV-045
Jones TG II-093
Jones TTC I-029, II-053, II-077, IV-061, IV-141
Joye B IV-081
Junker W III-097
Kabantsev A I-393
Kado S I-161, III-405
Kakurin AM III-077, IV-017
Kallenbach A ..... I-025, I-069, I-321, II-005, III-097, III-409, IV-285, ... IV-413
Kallstenius T III-157

Kalmykov SG II-081, IV-057
Kam K II-241
Kamada Y I-017, III-029, IV-033
Kamelander G II-185, IV-377
Kammash T IV-345
Kamo Y I-125
Kanaev BI IV-017
Kandaurov IV I-445
Kappler F II-277
Kapralov VG I-117
Karakin MA IV-169
Kardon B II-421
Karelse FA III-421
Karpushov AN IV-193
Kartsev Yu A IV-401
Karttunen SJ III-357
Karzhavin Y I-001, IV-097
Kashiwagi M II-257
Kasilov SV III-341, III-349
Kasparek W I-429
Kass T IV-041
Kassab MM I-269
Kastelewicz H II-217
Kaufmann M III-093
Kawabe T II-177, IV-173
Kawachi T III-417
Kawakami I II-137
Kawashima H I-073
Kawasumi Y I-125
Kaye A II-329
Kaye SM I-373, II-357
Kazarian-Vibert F III-373, IV-065, IV-073, IV-393
Kellman AG IV-049
Kerner W I-201, I-221, II-069, II-237, II-261, III-081, III-229,
..... III-277, IV-001, IV-085
Kessel C IV-121
Khlopenkov KV I-117
Khrebtov SM II-117
Kick M III-137
Kikuchi M I-017
Kim JS IV-097
Kim YB IV-137
Kimura H II-057
Kinoshita T I-157, I-161
Kirneva NA I-369
Kirnev GS III-285
Kishinevsky M IV-381
Kislov D I-369
Kisslinger J III-129, III-149
Klepper CC I-325, IV-345

Kletecka P IV-373
Klima R IV-373
Knight PJ III-049, III-233
Knoll DA IV-305
Knorr G III-209, IV-197
Kobayashi S I-137, I-145
Koch R II-337, II-397, III-341, III-345, IV-341
Koenen L III-345
Koenig R II-053, IV-061
Kogler U II-281, II-321, IV-281
Koide Y I-017, III-029
Komori A I-153
Kondo K I-137, I-145, I-149, I-157, I-161, I-285, III-405
Kondoh T II-057
Konen L III-341
Konig RWT I-029, II-009, II-077, II-125, II-377, II-453, IV-141
Korneev DO II-089
Kornejew P II-297
Kornev VA I-033
Korotkov A III-389
Koslowski HR I-133, II-321, III-053, III-065, III-341
Kostrukov AYu I-121
Kotelnikov IA II-181
Kovrov PE III-077, IV-017
Kozlovskij SS II-057
Kramer-Flecken A III-345
Krasai I-073
Krasilnikov A III-385
Kraux VI IV-169
Kravchenko AYu IV-453
Krejci A II-393
Krieger K II-289
Krikunov SV I-033
Krlin L I-329, IV-373
Krämer-Flecken A I-045
Kruglyakov EP I-445
Krupnik L II-117
Kryska L IV-373
Källne J III-381
Kubo S I-153, III-413, IV-149, IV-153
Kubota T IV-229
Kujanov A I-365
Kukushkin A III-205, IV-317, IV-329
Kumazawa R III-413, IV-149, IV-153
Kupfer K I-381, IV-393
Kupschus P IV-021
Kurimoto Y I-149, I-157, I-161
Kurnaev V III-285
Kurz C II-341
Kurzan B III-069

Kusama Y II-057, II-061
Kuteev BV I-121, IV-057
Kuvshinov BN III-221
La Haye RJ IV-053, IV-137
LaBombard B II-313, II-341, III-017, III-325
Lachambre JL III-101
Lackner K III-093
Lalousis P II-285
Lam N II-325
Lamalle PU II-329, II-353
Landman L II-277
Lang PT I-021, II-449
Lao LL IV-137
Lapshi VI IV-357
Laqua H I-353, I-357, I-389
Larsson D III-157, IV-277
Lashkin VM I-437
Lashkul S II-085, II-085, IV-385
Lashmore-Davies CN II-229, II-405, IV-361
Lasnier CJ III-105
Lauro-Taroni L I-081, I-089, II-009, III-121, IV-465
Laux M III-097, III-241
Lavanchy P III-081
Laviron C IV-101
Lawson KD I-081, II-077, III-121, IV-061, IV-141
Lazarus A IV-137
Lazzaro E IV-449
Lebas J IV-197
Lebedev AD II-085, IV-385
Lebedev S I-033
LeBlanc B III-013
Leclert G II-337, IV-409
Ledl L III-145
Ledyankin AI IV-345
Lee JH I-109
Lee P II-169
Lee RL II-281, IV-049
Lengyel L II-285
Lennholm M II-329, III-361
Leonard AW III-105
Lev ML II-165
Levin LS I-033
Levinton FM II-113, III-365, III-397
Lewandowski JLV II-141
Li GX I-173, I-177, III-157
Li XL II-273, II-345
Liang R I-125
Lieder G I-425, II-289, II-293, III-097, III-409
Lierzer J IV-129
Lin-Liu YR I-381, IV-137

Lingertat H II-125, IV-465
Lingertat J I-309, II-273, III-281, III-305, III-309, IV-297
Liniers M II-157
Lipin BM I-033
Lipschultz B II-313, II-341, III-325
Lister JB II-097, III-081, III-113, IV-081
Litaudon X III-373, IV-065, IV-073, IV-125, IV-393, IV-397
Litwin C IV-381
Liu Y III-073
Llobet X IV-081
Lloyd B I-345, II-001, II-021, II-209, III-369, IV-117
Lo D II-341
Lo E II-093
Loarer T I-317, III-317
Loarte A I-309, I-313, II-121, II-125, II-273, III-257, III-305, IV-297, IV-465
Lok J I-129, I-385
Lomas PJ I-029, I-313, II-077, IV-061, IV-141
Long YX II-225
Lopes Cardozo NJ I-129, II-013, II-129, III-037, IV-093, IV-261
Lopez-Fraguas A II-149, II-157
Lopez-Sanchez A II-157
Lorenz A II-173
Loughlin MJ II-053, II-069, III-057
Lovegrove T III-301
Lowry CG I-309, II-121, III-305
Luce TC III-025
Luciani JF I-189
Luetjens H I-241
Luhmann NC I-109
Lutz T I-317
Lyadina E IV-061
Lysoivan A III-341
Lütjens H I-189
Maas AC II-077, IV-141
Maassberg H I-353, I-357, I-389
Mace RL I-449
Maddison G III-117, IV-309
Maggi CF II-377
Magyar G I-085
Mahdavi MA I-317, I-325
Mai HH III-101
Mailloux J III-101
Maingi R I-113, I-325
Majeski R II-405, III-365
Makashin IN I-421
Maksimov Yu S IV-017
Malinova P I-253
Mancuso A I-237
Manfredi G III-209, IV-197, IV-201

Manhood SJ III-049, III-033
Mank G I-057, I-061, I-133, I-293, IV-341
Mansfield DK I-409, II-109
Manso ME IV-413, IV-417
Mantica P I-053, II-013, III-009
Mantsinen M II-249
Marakami M I-381
Maraschek M III-125, III-273, IV-041
Marchand R III-101
Marchenko VS II-221
Marchiori G IV-185
Marcus FB I-029, II-037, II-053, II-077, III-057, IV-061, IV-141
Marmar E II-109, II-341
Marrelli L IV-185, IV-437
Martin G II-041, II-045, IV-349
Martin P I-181, IV-185, IV-437
Martin R II-017, II-157, III-033, III-117
Martin TJ I-185, II-241
Martin Y II-097, III-113, IV-081
Martines E IV-181
Martini S IV-177, IV-181
Martynov AA I-217, I-369
Martynov DA III-077, IV-017
Masiello A IV-181
Mast KF I-069, II-005, III-097, III-401, IV-285
Masuda S IV-149, IV-153
Matoba T III-377
Matsuoka K I-153, III-413, IV-149, IV-153
Matsuura H I-137
Matthews GF ..... I-309, II-273, III-085, III-257, III-297, III-305, ... IV-297, IV-465
Mattioli M I-085, II-385, III-109
Mau TK I-109
Mauel ME IV-137
Maximov VV IV-193
May M II-341
Mayaux C II-009, II-121
Mayer M II-301
Mazur S I-169, I-173, I-177, III-157, III-457
Mazurenko A II-341
Mazzitelli G I-077
Mazzucato E III-013, III-365, IV-109
McArdle G I-345, II-021, III-369
McCarthy KJ II-153, II-417
McCarthy P IV-133
McChesney JM I-409
McClements KG I-185, II-229, II-405
McCool S I-001
McCormick K ..... I-309, I-313, II-077, II-125, III-257, III-269, III-297, ... III-305

McCracken GM II-313, II-341, III-325
McCune D II-105
McGinnity P I-081, III-121
McGuire KM III-045
Medina F II-149, II-157, III-041
Medley SS I-409, III-397
Medvedev S I-217
Meigs A IV-465
Meijer FG II-409
Meisel D I-321
Melnick IM I-097, II-133
Melnikov AV II-117
Menard J II-093
Mendonca JT IV-217
Meo F III-101
Mertens V II-005, III-097
Meshkov OI I-445
Meslin B III-317
Messiaen A I-133, III-341, III-345
Meyer W III-105, IV-137
Michaud D III-101
Micozzi P I-237
Migliuolo S IV-025
Mikhailov MI III-193
Miller RL I-241, I-377, IV-137
Minami T I-153, III-413, IV-149, IV-153
Minardi E IV-449
Miner W I-001
Mioduszewski PK I-317, I-325
Mirnov S I-421
Mishizawa A I-125
Mitchell IH II-173
Miura Y I-073
Mizuno N IV-173
Mizuuchi T I-137, I-145, I-149, I-157, I-161, I-285, III-405
Moiseenko VE III-341
Moller A I-173, III-153, III-157
Monier-Garbet P III-109, IV-345
Monk RD I-309, I-313, II-121, II-125, II-273, III-085, III-257,
..... III-281, III-293, III-297, III-305, IV-465
Montvai A IV-261
Moravec J II-373
Moreau D III-373, IV-065, IV-393
Moreau P IV-101
Morera JP IV-065
Moret JM I-417, II-097, II-101, III-081, III-113
Moret RA IV-081
Morgan PD II-401, IV-465
Mori M I-017
Morioka A II-057

Morisaki T I-153, III-413, IV-149
Morita S I-153, III-413, IV-149, IV-153
Moriyama S II-057
Moroz PE II-049, III-333
Morris AW I-345, II-001, II-021, II-025, III-049, III-125, III-273, III-369, IV-117
Morris R III-217
Mukhovatov V III-377
Murakami M III-365
Muraoka K I-161, III-405
Murari A IV-437
Murmann H III-245
Muto S IV-153
Mutoh S IV-149
Mutoh T IV-149
Myrnas R I-085
Nagasaki K I-137, I-141, I-145, I-149, I-157, I-161, I-285, III-405
Nakajima N IV-143
Nakamura Y I-225, IV-143
Nakasuga M I-137, I-161, I-285
Nakayama T I-285
Nanobashvili S IV-373
Napiontek B II-293, III-097, III-409
Narihara K I-125, I-153, III-413, IV-149, IV-153
Nascimento IC I-289
Naujoks D II-297, II-321
Navarro AP III-225
Nave MFF I-013, I-029, II-053, IV-061
Navratil GA IV-137
Nazikian R III-013, III-365, IV-109
Nedzelskij IS II-117
Neilson GH III-397
Nejoh Y II-433, III-445
Nemoto M II-057
Neu R I-065
Neubauer O III-341
Neudatchin S III-029
Neuhauser J II-217, III-093, III-097, IV-285
Nevins WM IV-121
Neyatani Y I-017, I-225, IV-033
Nguyen F II-329, II-353, III-317
Nicolai A IV-341
Niedermeyer H I-301
Nielsen P II-009, II-073
Nielson GH IV-305
Niemezewski A II-341
Nieswand Ch II-097, III-113, IV-081
Niethammer M III-409
Niffikeer SL II-169

Nikitin AN IV-097
Nishimura K I-153, III-413, IV-149, IV-153
Nishitani T II-061
Noll P IV-009
Nonn P IV-381
Nordlund P I-169, I-173, I-177, I-181, III-157, III-457
Noterdaeme JM I-349
Notkin GE IV-057
Novikov A Yu III-077, IV-017
Nowak S IV-369
Nygren RE I-317
Obert W II-009, II-121
Obiki T I-137, I-145, I-157, I-161, I-285, III-405
Ochando MA II-149, III-041, III-225
Odblom A I-093
Ogata K I-149
Ogawa H I-073, III-417
Ohdachi S I-153, III-413, IV-149
Ohya K II-321, III-345
Okabayashi M II-357
Okada H I-137, I-145, I-149, I-157, I-161, I-285, III-405
Okamoto M IV-143
Okamoto T I-285
Okamura S III-413, IV-149, IV-153
Ongena J I-133, II-321, II-397, III-345
Ono M II-093
O'Brien D I-029, I-309, III-297, III-305, IV-465
O'Brien MR I-345, II-265, III-233, III-369, IV-117
O'Connell R II-133
Oomens AAM I-129, II-013
O'Mullane MG I-097, III-121
O'Shea P II-341
Orefice A IV-369
Orlinski D III-377
Orsitto F I-401
Ortolani S IV-009
Osanai Y I-165
Osborne TH IV-137
Ottaviani M I-245
Ouroua A I-001, III-265
Ouroua H I-005
Ozaki T I-017, I-153, III-413, IV-033, IV-149, IV-153
Paccagnella R I-265
Pacher HD IV-317, IV-333
Pakyari A IV-245
Pan YD II-345
Pan'kin A Yu II-221
Parail VV I-013, I-053, II-213, III-361, IV-061, IV-113, IV-257
Paris P II-393
Paris RB II-437

Park H III-013
Parks PB I-409
Parlange F II-045
Pasch E II-297
Pasqualotto R IV-177, IV-181
Pastor I II-149
Patel A I-097
Pattikangas T III-357
Paul SF III-013, IV-105
Paume M IV-101
Pautasso G IV-037
Pavlenko VP IV-209, IV-245
Pavlo P IV-373
Pavlosky D I-001
Pavlov YuD IV-057
Peacock AT II-301
Peacock NJ I-081, I-097, III-121, III-261
Pecoul S II-337
Pecquet AL I-249, IV-073
Pedrosa MA I-305, II-149, IV-157
Peebles WA I-105, I-109
Pegoraro F III-221
Pegourie B IV-301
Pekker M II-233
Penningsfeld FP III-137
Penso A III-441
Pereverzev G II-365, III-001
Pericoli-Ridolfini V III-361
Peruzzo S IV-181
Pestchanyi S II-277
Peters M II-013, III-037
Peterson BJ I-137, I-145, I-157, I-161, I-285
Petrie TW III-105
Petrov SY II-057
Petty CC I-109, I-381, III-025
Peysson Y III-361, III-373, IV-065, IV-393
Pfirsch D II-189
Phelps DA I-381
Philipps V II-305, II-309, II-321, III-345, IV-473
Phillips CK III-365
Phillips PE I-001, I-005, III-265, IV-129
Piazza G II-277
Pickalov VV IV-337
Pieroni L IV-289
Pietrzyk ZA II-097, II-377, III-313
Piffi V II-373, II-393
Pijper FJ I-129, II-013, II-129
Pinches SD II-261
Pinsker RI I-109, I-381
Piovan R IV-181, IV-185

Pitcher CS II-289, III-097, III-241, III-245
Pitts RA II-097, III-113, IV-081
Platz P II-385, III-337
Plyusnin VV III-341
Pochelon A II-097, III-113, IV-081
Pod'minogin AA IV-193
Podushnikova KA II-085, IV-385
Pogutse O III-229, III-277
Polevoi AR II-205
Polman RW I-385
Pomaro N IV-181, IV-185
Popel SI II-425, III-433, IV-445
Porcelli F I-245, II-233, II-253, III-169
Porkolab M I-297, II-341, IV-121
Porte L I-013, I-029, I-053, II-073, III-009, III-081, III-085,
..... III-261, III-281, IV-001, IV-021, IV-061
Porter G III-321
Portnov DV III-385
Pospieszczyk A II-305, II-309, II-321, III-345
Post Zwicker AP I-061
Powers EJ I-001, I-281
Prater R I-381
Preinhaelter J IV-373
Preische S I-373
Prentice R III-281, IV-425, IV-465
Price M II-017, III-117
Probert P IV-381
Prozesky V II-301
Prut VV IV-017
Puiatti ME II-317, II-317, III-161, IV-177
Puri S I-457, II-197
Pyatak AI III-349
Qin J II-149, II-153
Qin YW II-345
Qiu M II-225
Quemeneur A III-061, IV-101
Rachlew-Kallne E III-157
Radford GJ III-305, IV-297
Radobarin GT I-033
Ram A IV-353
Ramsey AT II-401
Ramström E III-381
Ran Li Bo I-273, III-073
Rantsev-Kartinov VA III-205, IV-221
Rapp J I-057, II-321, III-345
Rasmussen D III-365
Ratel G III-101
Rau F III-129, III-149
Raus J II-393
Razumova KA I-369

Reardon J II-341
Redi M II-105
Reichle R I-309, II-125, III-085, III-401, IV-297, IV-465
Reimer H III-341
Reiner HD II-297
Reiter D III-249, IV-285, IV-321, IV-329
Rem J IV-457
Renberg PU III-381
Renda G III-397
Renner H III-149
Rensink M III-321, IV-305
Resendes DG IV-217
Rettig CL I-105, I-109
Rey G III-373, IV-397
Rhodes TL I-105, I-109
Ribeiro C II-017, III-033
Riccardi C I-453, III-441
Rice BW IV-049, IV-129, IV-137
Rice JE II-313, II-341, III-017
Richard N III-101
Richards B I-001, III-265
Riedel KS II-065
Righi E II-073, II-125, II-329, II-353, III-229, IV-001
Rimini FG I-009, II-069, II-353, III-005, III-361
Roach CM II-205, III-189
Roberts DR I-001, I-101, IV-097, IV-129
Robinson DC III-233, IV-117
Rodriguez-Rodrigo L III-041, IV-269
Rogers JH III-365
Rogister A IV-341
Rognlien TD III-321, IV-305
Rogozin AI IV-193
Rohde V III-097, III-241, III-245
Romanelli F I-089
Romanelli M III-221
Rome M I-353, I-357, I-389
Rommers JH III-421
Rookes A III-121, III-261, IV-061, IV-465
Roquemore AL I-409
Rosenbluth MN III-169, IV-009
Ross DW I-001, IV-129
Rossi A II-121
Rost C II-341
Rowan W I-001, I-005, III-265
Rozhansky V I-117, I-337, II-285
Rozhdestvensky VV I-033
Rubel M III-345
Rudakov DA II-141
Rudyj A I-301
Ruffina U III-185

Rust N III-137
Ruzic DN IV-305
Ryter F II-005, III-097, III-125, IV-089
Sabbagh SA II-113
Sabot R IV-249
Sadler G II-037, II-053, II-069, II-269, III-057, IV-001
Sadowski M II-161
Safonova MB IV-017
Sagara A IV-153
Saibene G I-309, II-009, II-121, II-125, III-305, IV-465
Saigusa M II-057
Saito K I-165
Saito KH II-137
Saito KN II-137
Sakakibara S I-153, III-413, IV-149
Sakakita H I-125
Sakamoto K I-137, I-145
Sakamoto M I-125
Salisbury MW IV-425
Sallander J III-157
Salomaa RRE II-249, III-357
Samain A I-249
Samm U I-057, II-201, II-305, II-321, III-345, IV-321
San Jose MAG I-405
Sanchez E IV-157, IV-165
Sanchez J II-149, IV-157, IV-161, IV-429, IV-433
Sander M I-133
Sanin AL I-445
Sannazaro G IV-141
Sano F I-137, I-145, I-157, I-161, I-285, III-405
Santagiustina A IV-461
Saoutic B I-037, III-337, IV-125, IV-353, IV-397
Sardei F IV-325
Sarichev DV III-285
Sarkissian AH III-101
Sartori R II-077, II-121, IV-141
Satherblom H-E I-169, III-457
Sato KN I-125
Sato M III-029
Satoh M II-057
Sattin F II-317
Sauter O I-241, IV-077
Scarin P II-317, III-161, IV-177
Schachter J II-341
Schaffer MJ I-325
Scharer J II-325
Scheffel J I-169
Schep TJ III-221, IV-457
Schild P III-361
Schilling G III-365

Schissel DP II-065
Schittenhelm M III-273
Schivell J II-105, III-013
Schmidt GL II-113, IV-021
Schneider R II-217, III-093, III-249, IV-285, IV-329
Schneider W III-125, IV-037
Schoch PM I-001, III-265
Schonmann K I-065, I-069, III-237
Schoon N III-345
Schram DC IV-337
Schram PJJM IV-453
Schroder KA III-265
Schuller FC IV-029, IV-093, IV-261, IV-441
Schultz SD IV-353
Schumacher U III-409
Schunke B I-029, II-053, II-065, II-077, IV-061, IV-141
Schweer B II-305, II-309, II-321, III-345
Schweinzer J I-233, III-237, III-245, III-249, III-253, III-269
Schwelberger J I-293
Scott B I-229
Scott SD II-109,, III-013, IV-105, IV-109
Scoville JT IV-053
Seidel U IV-037
Semenets AM I-421
Semenov AA II-165
Semenov IB I-421
Senju T I-137, I-145
Senties JM I-405
Sergeev V Yu I-049, II-081, IV-057
Serianni G IV-181
Serra FM IV-413, IV-417
Sesnic S II-357
Shafranov VD III-193
Sharapov S II-237, II-261, III-081
Sharp LE II-141
Shats MG II-141
Shcherbinin ON II-085, IV-385
Shevchenko V IV-421
Shiina S I-165, II-137
Shikhovt'sev IV IV-193
Shirai H I-017, III-029
Shkarofsky IP III-353, III-357, IV-393
Shmaenok LA II-409
Shoji T I-073
Shoucri M III-209, III-357, III-353, III-361, IV-197, IV-201,
..... IV-393
Shukla PK I-441, III-429, IV-217
Shurygin VA II-369, IV-013
Shybaev SA IV-017
Sibley II-329

Silva A IV-413, IV-417
Silva F IV-417
Simonetto A I-361, IV-369
Simonini R I-309, III-305, IV-297
Simpson PR I-345, III-369
Sing DS I-001, IV-129
Singleton MA I-097
Sipila S II-349
Sips ACC II-069, III-005, IV-001, IV-113
Sitenko AG III-177, IV-273
Sklyarova EM II-165
Skovoroda AA I-365
Smeulders P I-029, II-053, IV-061, IV-141
Smirnov AI I-033
Smith MEU III-393
Smith RJ IV-425
Smits F III-361
Snipes J II-109, II-341
Sokoll M IV-133
Solano E I-001
Solari G I-361, IV-369
Soldatov SV IV-401
Soldner FX III-361, IV-001, IV-113
Solis RM II-037
Soltwisch H III-065
Sonato P IV-181, IV-185
Spathis P II-285
Spence J I-313, IV-297
Springmann E I-013, I-053, II-213, III-361, IV-113
Stabler A I-349, IV-089
Stallings DC II-333
Stamp MF I-309, I-313, II-009, II-077, II-121, II-273, III-089, IV-021, IV-465
Stangeby PC II-273, IV-465
Stansfield BL III-101
Start DFH II-073, II-329, II-353, IV-001
Steenbakkers MFM II-129
Steimle RF I-001, I-101
Stek P II-341
Stepanov AYu II-085
Stepanov KN III-349, IV-357
Steuer KH I-069, I-349, III-069
Stober J III-249
Stockel J I-329, IV-373
Stodiek W III-065
Storek DJ III-265
Storey P III-301
Stork D I-309, II-009, II-121, II-125
Stott PE III-377
Strachan JD II-109, III-013

Strait EJ IV-137
Streibl B III-093
Stroth U I-389, III-037, III-137, IV-265
Stuart A II-033
Stubberfield P I-009
Stupishin NV IV-193
Stutman D II-093
Subbotin A III-193
Sudo S I-161
Sugihara M IV-317
Sugiyama LE I-461, III-017, IV-121
Summers DDR II-377
Summers HP II-377
Sund R II-325
Sushkov AV I-049, I-369
Suttrop W I-233, III-069, III-237, III-245, III-249, III-273
Suvorov E I-429
Suzuki Y I-161
Svoboda V I-329
Sychev VN I-277, III-329
Sykes A II-017, II-205, III-033, III-117
Synakowski EJ III-013
Tabares F II-149, II-153
Tafalla D II-153
Takahashi C I-153, III-413, IV-149, IV-153
Takase Y II-341
Takeji S IV-033
Takizuka T I-017, III-029
Talvard M I-249, II-357
Tamai H I-073
Tanabe T II-321, III-345
Tanaka K I-153, III-413, IV-149, IV-153
Tanga A IV-009, IV-021
Tanzi C II-029
Taroni A I-013, I-053, I-309, I-313, II-213, III-009, III-305, IV-113, IV-141, IV-297, IV-465
Tatarakis M II-169
Taylor G III-013, III-045, III-365
Taylor P IV-049
Taylor TS IV-137
Tebaldi C I-245
Telesca G III-345, IV-293
Terentiev AR III-205
Terreault B III-101
Terry D I-001
Terry JL II-109, II-313, III-325, II-341
Tessarotto M I-193, IV-225
Teubel A I-349, IV-089
TEXTOR and ERM/KMS Teams I-057
Theimer G I-301

Thomas PRT I-029, II-077, IV-061, IV-141
Thompson E II-121
Thompson SJ IV-137
Thomsen K II-073, IV-061, IV-141
Thyagaraja A III-173
Tighe W II-401
Timms M II-329
Tobin S IV-345
Toda S I-205
Todd TN II-001, III-393
Tohrisawa K II-177
Tohshi K I-137, I-145
Toi K I-125, I-153, IV-149, IV-153
Tokar M II-201, II-321, III-345, IV-321, IV-341
Tokman MD I-365
Tokuda S IV-033
Tolkach V II-277
Tomas J III-033
Tonetti G I-417, II-097, III-113, IV-081
Tramontin L IV-277
Traneus E III-381
Trevisan F IV-181, IV-185
Trofimenko YuV II-117
Trostell B III-381
Trotman DL III-393
Truc A III-061, IV-101
Tsaun SV IV-401
Tsitrone E IV-301
Tsuji S I-017
Tsukahara Y II-057
Tubbing BJD II-069, III-005, III-453, IV-001,
..... IV-113
Tudisco O I-361, III-021
Tukachinsky AS I-033, IV-385
Turlur S I-249, IV-065, IV-073
Turnbull AD I-377, IV-137
Tykshaev VP IV-169
Uckan T I-317
Ueda Y II-321, III-345
Uehara K I-397
Uglum J I-001
Ulrich M IV-037
Umansky M II-341
Unger E III-145
Unterberg B I-057, II-201, II-305, II-321, III-345
Ushakov AA I-337
Vaclavik J II-245, IV-233, IV-241
Valeo E III-365
Valisa M II-317, III-161, IV-181, IV-177, IV-185
Vallet JC IV-073

Valovic M ..... I-097, I-345, II-001, II-025, III-049, III-125, III-273, ... III-393, IV-117
van Belle P II-037, II-269, III-057
Van der Linden RAM I-221
Van Eester D II-397
van Gelder JFM III-425
Van Houtte D II-045, IV-349
van Milligen B Ph II-153, III-225, IV-157, IV-165
Van Nieuwenhove R III-341
van Oost G I-133, III-341, III-345, IV-431
Van Wassenhove G II-397, III-345
Varela P IV-413, IV-417
Vavovic M III-369
Vayakis G I-013, IV-405
Vega J II-153
Veklich A III-437
Verbeek H III-249
Veres G II-421
Verplancke P I-425
Vershkov VA I-049, IV-005, IV-401
Vervier M III-341
Veseleva I II-285
Vikhrev VV III-197
Villar Colome J IV-069
Villard L II-245
Viola R III-309
Vizgalov IV III-285
Vladimirov SV III-429, IV-445
Vlases G I-313, III-305, III-313, IV-297
Voitsekhovitch IA IV-257
Volkov VV III-077, IV-017
Vollmer O IV-089
von Goeler S II-357
von Hellerman M ..... II-009, II-073, II-125, II-377, II-453, III-085, III-089, ... IV-465
Voronin AV II-165
Voskoboynikov SP I-337
Vukovic M IV-381
Vyacheslavov LN I-445
Vyas P III-049
Wada M II-321, III-345
Wade MR I-113, I-325, II-009
Wade TJ II-329
Wahlberg C I-213
Waidmann G I-045, III-053, III-341, IV-029
Wakatani M I-161, I-285
Walsh MJ II-017, II-205, III-033, III-117
Walter H III-137
Wang CY II-333
Wang EY III-073

Wang ZH III-073
Ward DJ II-069, III-005, IV-077
Warr G II-141
Warren R III-273
Warrick CD I-345, II-209, III-369, IV-117
Watanabe K I-161, IV-143
Watari T III-413, IV-149, IV-153
Watkins JG III-105
Watkins N II-037, II-053, III-057
Watterson R II-341
Watts C I-001, I-005, IV-097
Weinlich M I-425, III-097, III-241, III-245
Weisen H II-097, II-389, II-393, III-113, IV-081
Welander A I-173, III-153, III-157
Welch BL II-313, II-341
Weller A I-357, III-145
Wenzel U I-069, III-097
Werley KA IV-305
Weschenfelder F II-281
Wesley J IV-009
West WP II-281
Westerhof E I-385, II-129, III-425
White RB I-193, II-105
Whitehurst GA I-345, IV-117
Whyte D III-101
Wienhold P II-281
Wijnands TJ II-045
Wilson HR I-089, I-261, II-205, III-033, III-233
Wilson JR III-365
Wilson KM II-173
Windsor CG III-393
Winslow D I-001, III-265
Winter Hp III-253
Winter J II-281, II-321, III-341, III-345, IV-281
Winz G IV-381
Wobig H III-129, III-149
Wolfe S II-341, III-017
Wolle BKR III-137, III-201
Woloch F II-185
Wong HV II-233
Wood AD II-437
Wood RD III-105
Wootton AJ I-001, I-005, IV-097, IV-129
Worley JF II-173
Wright JC III-365
Wukitch S IV-381
Wunderlich R IV-285
Wurden GA II-061
Wurz H II-277
Wutte D III-253

Xie H X III-165
Xu DM I-273
Xu J I-125, I-153, III-417, IV-149, IV-153
Xue SW II-345
Yagi M I-205, IV-229, IV-237
Yaguchi K I-137, I-145
Yamada H I-153, IV-149, IV-153
Yamada I I-153, III-413, IV-149, IV-153
Yamaguchi Y II-177
Yamamoto S III-377
Yamauchi K III-413
Yamauchi T I-073
Yamazaki K IV-143
Yan LW III-073
Yang G III-073
Yankov VV IV-209
Yevdokimov DV IV-017
Yoshino R I-225
Young KM III-377, III-397
Yu MY II-425
Yu Q I-197
Yurchenko EI IV-221
Zabajdullin OZ III-197
Zacek F IV-373
Zagorodny AG IV-273
Zaitsev FS II-265
Zarnstorff MC II-105, II-113, III-013
Zastrow KD II-009, II-453
Zehrfeld H IV-133
Zeiler A IV-205
Zeng L IV-129
Zerbini M III-021
Zhang BC I-001, II-141
Zhang W III-101
Zheng LJ I-193, IV-225
Zheng S-B I-001
Zhong GW I-273
Zhong YZ III-073, III-073
Zhovtyansky V III-437
Zhuravlev V IV-161, IV-429, IV-433
Zimeleva A II-117
Zinchenko VF IV-169
Zohm H I-233, II-005, III-097, III-125, III-237, III-273, IV-041
Zoletnik S III-269, III-269
Zou XL I-041, IV-101, IV-409
Zurro B II-149, II-153, II-417
Zushi H I-137, I-141, I-145, I-157, I-161, I-285
Zuzak W III-101
Zweben SJ II-105, III-365, III-397
Zwingmann W IV-085